TURBOMACHINERY PERFORMANCE ANALYSIS
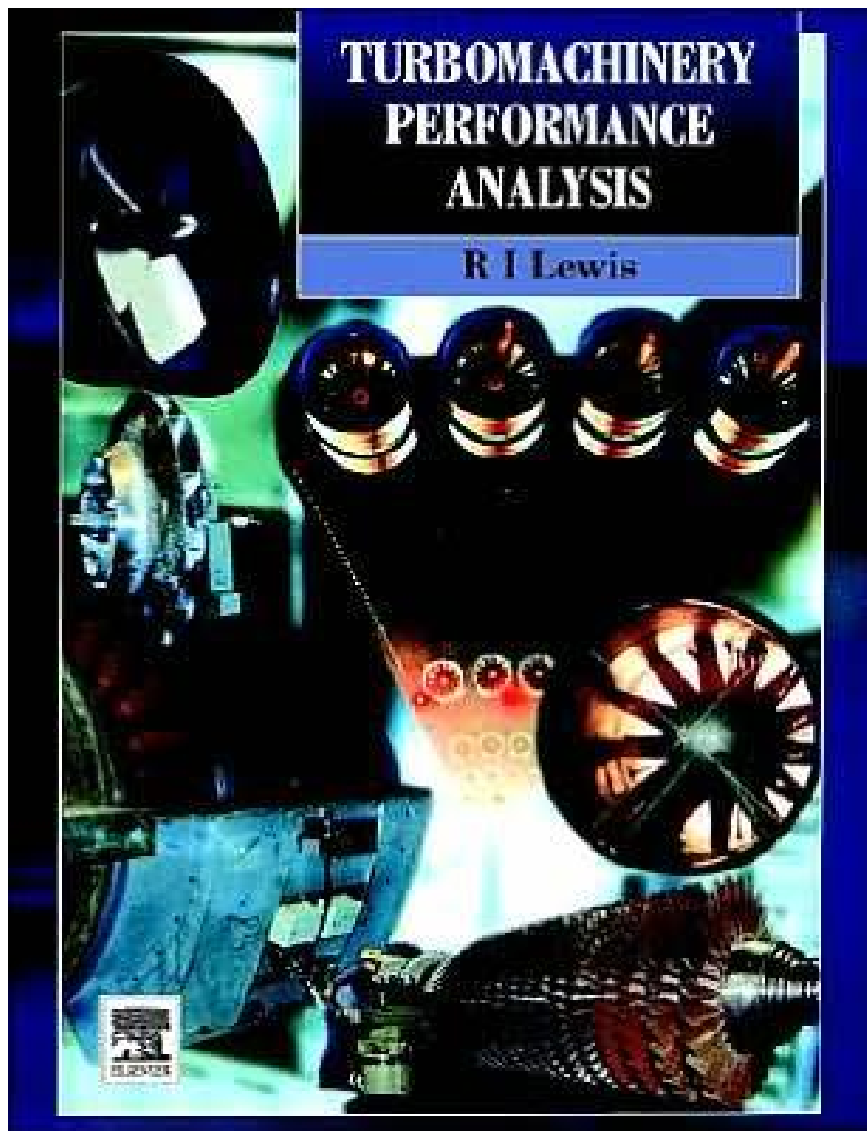
R I Lewis

- ISBN: 0340631910

- Publisher: Elsevier Science & Technology Books

- Pub. Date: May 1996

Preface

The advent of the gas turbine engine during the second world war demanded rapid developments in aerodynamic design and analysis techniques linked to wind tunnel and model testing, particularly for the evolution of high performance compressors. In response to this the field of 'Internal Aerodynamics' was born and has expanded with remarkable speed and complexity over the intervening half-century. In addition to a prolific literature of published papers portraying great diversity and impressive advances in this field, several textbooks have provided extremely helpful organisation and focus for the student or designer, including the works by Horlock (1958, 1966, 1978), Dixon (1975), Gostelow (1984), Cumpsty (1989) and Lewis (1991).

We should not forget that this activity was predated by the successful development of the steam turbine in the previous half-century, stemming largely in this country from the famous patent taken out by C. A. Parsons in 1884. The development of distributed electrical power through national or state grid systems led to an enormous growth in steam turbine technology within a competitive framework, leading to (a) progressive gains in performance, (b) a variety of design techniques, (c) an accumulation of company performance correlations, and (d) a remarkable expansion in unit size, e.g. from 30 MW to 660 MW since 1945. In parallel with this the gas turbine engine advanced rapidly as the major prime mover for both civil and military aircraft. The fields of internal aerodynamics for both steam and gas turbomachines have consequently come much closer together during the last 25 years. Similar developments of internal aerodynamics have also taken place during this period in the fields of mixed-flow and centrifugal pumps and fans, hydraulic turbines, ducted propellers and even wind generators, involving in many cases extremely erudite computer codes. Parallel developments in computer hardware and numerical methods have provided the incentive for ever-increasing power and sophistication of these important design tools whose use is now validated by considerable experience.

On the other hand turbomachinery performance correlations have tended to be less public and to develop in more individualistic ways, largely due to the different approaches within engineering companies towards the use of dimensional analysis for correlation of previous experience or for performance optimisation. Traditionally dimensional analysis has been the province of scale model testing, to provide, for example, data banks for the systematic development of families of related turbo-machines such as pumps, fans and hydraulic turbines. As will be illustrated in Chapter 1, the normal tradition is then to make use of *global* dimensionless groups linking, for example, model tests to predicted operation of the full scale prototype. The paper by S. F. Smith (1965) was of special historical significance in revealing the way forward to a more universal approach to performance analysis, in this case for axial turbines, by adopting *local* dimensionless performance variables (namely the flow coefficient ϕ and the work coefficient ψ) which led to the specification of dimensionless velocity

triangles. The outcome was a powerful correlation of the available family of Rolls-Royce model turbines at their best efficiency points, which will be the principal subject addressed in Chapter 3. The subsequent publication of a steam turbine correlation by Craig and Cox (1971) mapped on the same basis confirmed that steam and gas turbines, although subject to obvious differences regarding the properties of their working substances, are in fact close relatives within the family of rotodynamic machines. The main outcome of these studies was a clear demonstration that the efficiency of an axial turbine is at least as dependent upon the chosen performance (ϕ, ψ) duty as it is upon the blade profile aerodynamics. As will be outlined in Chapter 3 for axial turbines and in later chapters for other turbomachine types, the dimensionless velocity triangles and thus the operating environment of the blade profiles are largely shaped by the chosen (ϕ, ψ) duty.

In the intervening period since the paper by S. F. Smith (1965), although there has been intensive effort to conquer the increasingly demanding design problems of internal aero-thermodynamics to cope with advances in size and performance of both steam and gas turbines, there has been less emphasis upon the unifying methodology of dimensional analysis implied by his paper. During the early part of this period, however, the present author and his colleague Dr T. H. Frost addressed the important matter of how to teach the subject of axial turbine performance analysis and stage selection at first degree level linked to the Rolls-Royce correlation or 'Smith' chart. The author also extended this general approach at Master's degree level to cover axial fans, compressors, pumps, propellers, ducted propellers and also mixed-flow turbomachines in order to provide a universal approach to performance analysis embracing a wide range of turbomachine types. Much of this work has been published in the research literature but is now drawn together in the present book in a form suitable for the student or the designer. Three major computer programs have also been provided on the accompanying disc to facilitate student project activity at the professional designer's level. The first of these, FIPSI, enables the user to attempt the complete thermodynamic layout of a multi-stage free-vortex gas turbine, checking the chosen stage duty (ϕ, ψ) against the published 'Smith' chart, while keeping an eye on total-to-total efficiency, stage reaction at the hub and Mach number levels. The second PC program, CASCADE, provides a simple tool for blade profile selection to meet required inflow and efflux velocity triangles. The third program, STACK, provides the means for creating the geometry of up to ten blade profile sections from hub to tip with facility to stack the sections as required, for example on their centres of gravity, and for calculation of their geometrical properties such as area, centre of gravity, principal axes and second moments of area, for blade stressing purposes. The author has used these extensively with large classes of first degree students to introduce them to overall design requirements, performance analysis and prediction of multi-stage axial turbines. These major programs are provided as executable codes only. Source codes have also been provided on the PC disc for a range of other, simpler problems as a supplement to some of the teaching material within the text.

Inevitably, Turbomachinery Performance Analysis cannot be undertaken without reference to some of the underlying fluid-dynamic processes central to the rotodynamic energy exchange. In view of this four chapters have been devoted to such material. Thus Chapter 2 concentrates on cascade analysis while Chapter 5 deals with simplified meridional flow analysis. Chapter 6 is devoted to the important subject of vorticity production in turbomachines and its influence upon meridional flows. Finally in Chapter 9, selected supporting fluid dynamic analyses are presented relevant to some of the computer codes provided on the accompanying PC disc. User

manuals for FIPSI, CASCADE and STACK are provided as Appendices I, II and III. The remaining chapters are devoted to the development of detailed performance analysis methodology for axial turbines (Chapter 3), axial compressors and fans (Chapter 4), mixed-flow and radial turbomachines (Chapter 7) and ducted propellers and fans (Chapter 8).

Acknowledgements

I would like to acknowledge the outstanding contributions to the various aspects of the thermo-fluid-dynamic design and performance analysis of turbomachines made by the authors quoted in this book and many others. In particular I would like to pay tribute to my colleague Dr T. H. Frost who first developed final year teaching material during the 1960s based upon the correlation of Rolls-Royce model turbine tests published by S. F. Smith (1965) and which largely inspired Chapter 3. I am extremely grateful to several other close colleagues both at Newcastle University and in industry, and to my many research students during the past three decades, whose research contributions to turbomachinery fluid dynamics over many years have contributed to the material developed in this book. Sincere thanks are due to Roberta Stocks who has provided superb secretarial support for the research team during this period and for her help with the production of the early chapters. I would also like to pay tribute to several generations of Master's degree students and final year first degree students whose keen interest and feedback enabled me to develop the performance analysis methodology expounded in this book. In particular I am extremely grateful to final year students for their enthusiastic and intelligent use of the PC disc for design assignment activity, providing feedback and insights crucial to the development of these programs as computer-aided learning tools at professional level. Above all I wish to thank my wife and family for their continual encouragement over many years and more recently during the writing of this book.

R. I. Lewis

Table of Contents

1
Basic equations and dimensional analysis

Introduction

As its title suggests, the principal aim of this introductory chapter is to present an overall framework for the thermo-fluid dynamic design and performance analysis of turbomachines and thus to set in context the various analytical developments of the subsequent chapters. Turbomachines are often referred to as rotodynamic devices because they are specifically designed to tranfer energy to or from a so-called working fluid through the action of forces generated fluid-dynamically by a rotor. In most turbomachines the working fluid is guided in steady flow through an annular duct comprising a hub and casing as illustrated in Fig. 1.1 for (a) a single stage mixed-flow fan and (b) a multi-stage axial turbine. In the case of the fan shown here stator blades have been introduced at entry to generate a swirling flow upstream of the rotor. Fluid deflection in passing through the stator blade row is produced in Newtonian reaction to blade lift forces akin to those of an aerofoil. In the same manner, the rotor blades also generate lift forces which further modify the swirl distribution, thus producing rotor torque and therefore a demand for shaft input power. In this manner energy is transferred from the rotor to the fluid in the case of a fan, pump or compressor, resulting in an overall rise in specific enthalpy and an associated pressure rise. The reverse occurs in a turbine, which delivers shaft power in exchange for thermal energy taken from the working fluid resulting in a reduction of its specific enthalpy and an associated pressure drop.

Whether it be a fan, pump, compressor or turbine, it is evident then that the design and performance analysis of a turbomachine must invoke principles of mass flow continuity, steady flow energy transfer and finally momentum changes and their associated reaction forces. Consequently for a full statement and analysis of such rotodynamic problems we must appeal to the following laws and related study fields of thermo-fluid dynamics:

(1) The Continuity Equation.
(2) The Steady Flow Energy Equation (which is in fact a statement of the First Law of Thermodynamics for steady flow systems).
(3) Newton's Second Law of Motion.
(4) The Second Law of Thermodynamics.
(5) The laws of Aerodynamics or Hydrodynamics.
(6) Dimensional analysis.

The first three of these relate to the foregoing discussion. Due to thermodynamic irreversibilities such as frictional losses originating from fluid viscosity, the energy transfer processes will be less than perfect, requiring us to invoke also the Second Law of Thermodynamics, item (4).

In principle items (1) to (4) provide a full statement of the underlying laws of the
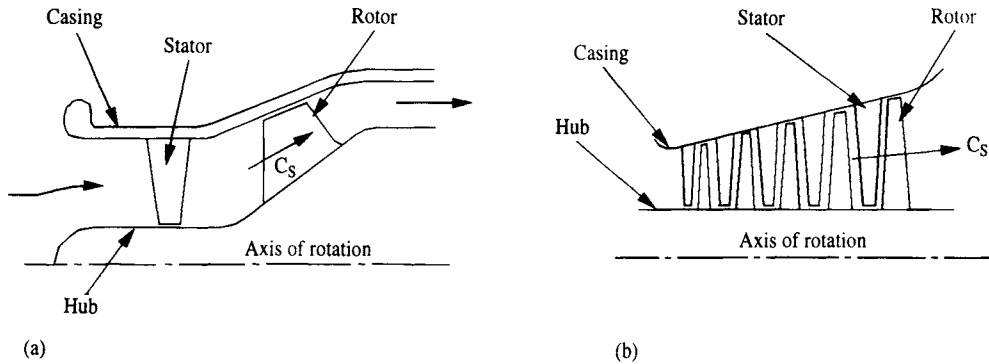
Fig. 1.1 Mixed-flow fan and axial turbine: (a) mixed flow fan; (b) multi-stage axial turbine

thermo-fluid dynamics of turbomachines. In addition to these, however, two other extremely important and useful fields of particular study have been introduced, namely (5) aerodynamics or hydrodynamics and (6) dimensional analysis, since these provide an enormous range of helpful practical engineering tools emerging from applications of the basic laws of thermo-fluid dynamics. Item (5) focuses specifically upon techniques for the selection of fluid-dynamically suitable blade profile shapes to achieve the rotodynamic energy transfer correctly and with good efficiency for a very wide range of turbomachine types. Dimensional analysis, item (6), provides quite different perspectives for the designer which are central to the main theme of this book and may be summarised as follows:

(a) To enable reduced scale model laboratory tests to be used as predictive tools for complete turbomachines, model stages or local blade elements.

(b) To provide a systematic framework for the development of families of related turbomachines as the basis for subsequent selection of the optimum overall configuration at the initial design or tendering stages (e.g. axial, mixed-flow and radial pumps).

(c) To provide a unifying framework for the whole design process of a turbomachine, linking the prescribed design flow and head duties to velocity triangles and thus onward to aerodynamic detailed design.

In the half-century following the second world war there has been an enormous volume of imaginative and creative effort invested in the relatively new field of *Internal Aerodynamics*, resulting in the production of an impressive array of numerical tools for aerodynamic design or analysis of turbomachines. Many of these techniques have been abstracted from the literature and have been presented in helpful interpretive textbook form for the designer by authors such as Horlock (1958, 1966), Dixon (1975), Gostelow (1984), Cumpsty (1989) and Lewis (1991). Such developments have been spurred on by rapid advances in computer processing, memory and language power and friendliness combined with parallel progress in flexible numerical methods. Thus in the 1960s engineering analysts were perhaps over-preoccupied with the solution of the detailed fluid flow problems of turbomachines to the neglect of overall considerations linked to dimensional analysis. The paper by S. F. Smith (1965) was pivotal in this respect, at least to the present author, in restoring the balance of design perspectives, since it demonstrated the crucial role of dimensional analysis in relating families of systematically designed and efficient

turbomachine stages operated at their best duty points and reveals how velocity triangles and consequent blade aerodynamics are linked to this.

At the time of writing, in response to the even more rapid development of computer speed and capacity, there has been a quite different shift of emphasis away from these specific computer codes tailored to particular problems such as cascade and meridional flow analysis, towards commercial Computational Fluid Dynamic (CFD) codes of a more open ended variety. These are aimed at the direct solution of the above governing laws (1) to (4) for thermo-fluid dynamics within a widely adaptable geometrical framework to suit a broad range of engineering applications. Such codes may attempt to simulate real fluid flows including the effects of viscosity and turbulence in fully three-dimensional flows. Impressive and helpful though these are, there are two inherent dangers. Firstly the user is at the mercy of the computer code unless it is possible to maintain contact with and understanding of the core source code, its content and its interpretation, especially where choices of numerical model are involved. In view of this, educational contributions such as the prize-winning paper by Potts and Anderson (1991) are to be applauded. Secondly, and more important for turbomachinery design, there is a danger of losing sight once again of *global* parameters, such as overall dimensionless duty coefficients, and their influence upon overall turbomachinery performance. In other words CFD codes need to be used in harmony with overall dimensional analysis if a designer is to maintain the broad perspective as well as the intimate local view of his total design task.

In order to shed more light on this point it may be helpful to consider the simplified flow diagram shown in Fig. 1.2 which highlights the main stages and decision sequence in the overall design of a multi-stage axial turbine. The three main computer programs provided on the accompanying PC disc, FIPSI, CASCADE and STACK, have been written to undertake not all but enough of these design or analysis tasks to enable the user to gain a feel for the overall framework for the design and performance analysis of a multi-stage axial turbine. User instructions for these three programs are given in Appendices I, II and III and their relationship to the overall design sequence is indicated in Fig. 1.2.

The remainder of this chapter will be devoted to introduction of some of the basic equations referred to above for use in later chapters and to review some of the aspects of dimensional analysis also referred to above. Chapter 2 will explain in brief how the complex three-dimensional turbomachinery flow problem may be broken down into two equivalent and superimposed types of two-dimensional flow, namely the *blade-to-blade* or *cascade* flow and the *meridional* pseudo-axisymmetric flow referred to in Fig. 1.2. Chapter 3 will then address the background theory behind the design and performance analysis of multi-stage axial turbines, making use of dimensional analysis and related to the Rolls-Royce test stage correlation published by S. F. Smith in 1965 and to the program FIPSI. This will be extended to similar treatments for axial fans and compressors in Chapter 4. At this point a presentation of simplified meridional analysis will be developed in Chapter 5 linked to Pascal source codes also included on the PC disc. Since turbomachines function largely on vortex flow interactions, Chapter 6 will be devoted to the important mechanisms of vorticity production and their influence upon meridional flows. Following this, overall performance analysis will be presented in Chapter 7 for mixed-flow and radial turbomachines and in Chapter 8 for ducted propellers and ducted fans. Chapter 9 concludes the book with the presentation of supporting aerodynamic theoretical treatments of selected problems including background theory underlying the program CASCADE but also a number of other source codes to help students who wish to develop similar design/analysis tools.
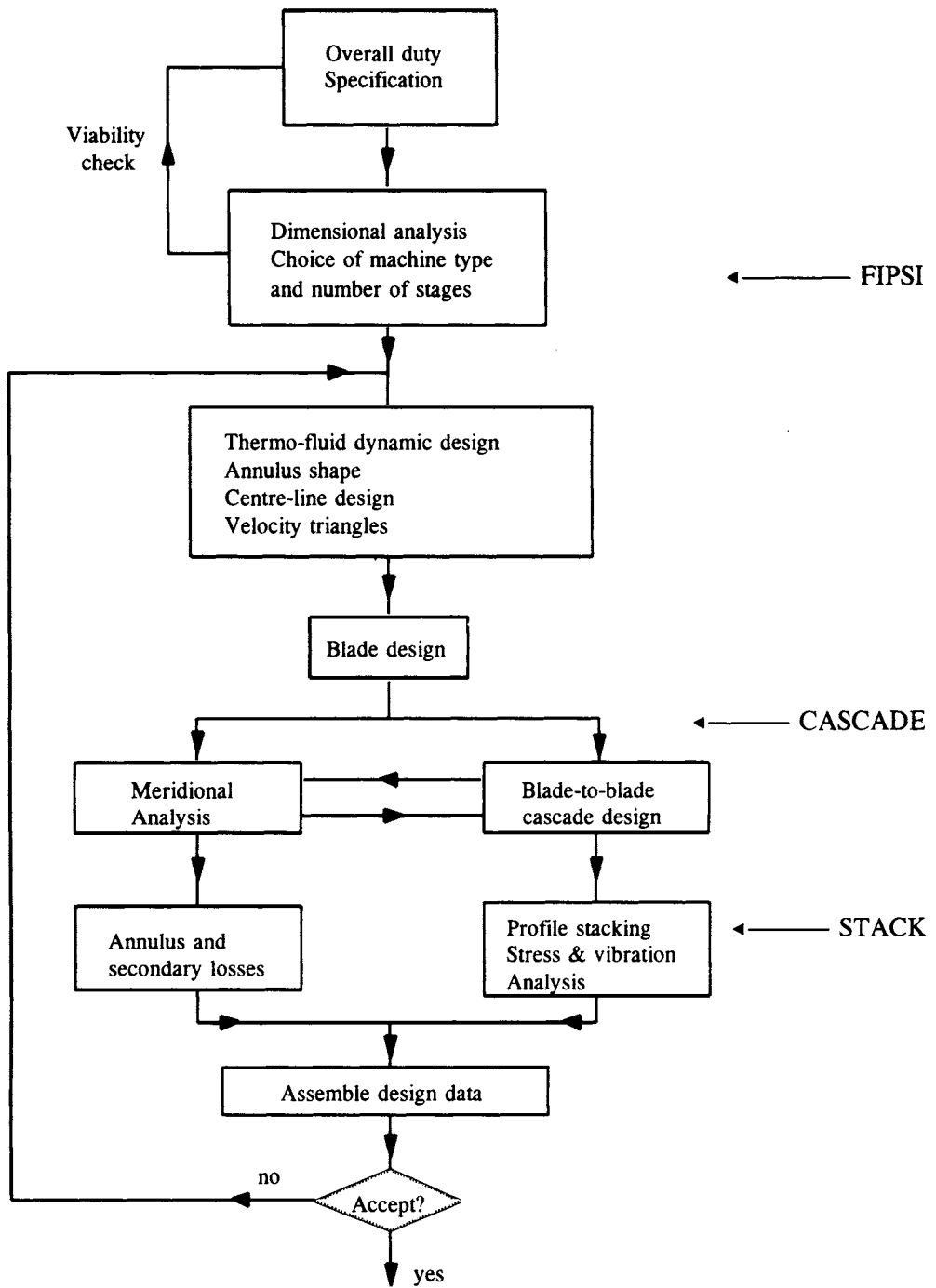
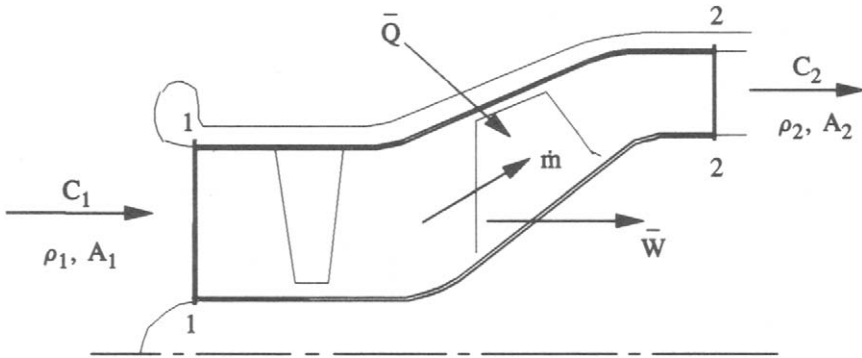**Fig. 1.2** Overall design sequence for a multi-stage axial turbine

Fig. 1.3 Control volume for a mixed-flow fan

1.1 Basic governing equations

The basic physical laws (1) to (3) listed above will now be expressed in forms suitable for turbomachinery analysis. Let us first define a control volume to suit the mixed-flow fan shown here in Fig. 1.3. We will define the inlet plane 1–1 and the exit plane 2–2 which have areas A_1 and A_2 respectively. For simplicity we will assume uniform entry and exit velocities C_1 and C_2 and also constant densities ρ_1 and ρ_2 across the planes 1–1 and 2–2.

1.1.1 Continuity equation

Assuming the mass flow rate $\dot{m} = \mathrm{d}m/\mathrm{d}t$ through the annulus to be conserved, we may express the principle of mass flow conservation through

$$\dot{m} = \rho_1 A_1 C_1 = \rho_2 A_2 C_2 \tag{1.1}$$

This is the most simple one-dimensional form of continuity equation, applicable to a system as a whole. If we wish to focus instead upon some local infinitesimal region of a system, an equivalent different form of this may be derived in any selected coordinate system. As shown by B. S. Massey (1989), and with reference to Fig. 1.4(a), the continuity equation in plane cartesian (x, y) coordinates becomes

$$\left. \begin{array}{ll} \dfrac{\partial c_x}{\partial x} + \dfrac{\partial c_y}{\partial y} = 0 & \text{for incompressible steady flow} \\[3mm] \dfrac{\partial \rho c_x}{\partial x} + \dfrac{\partial \rho c_y}{\partial y} = 0 & \text{for compressible steady flow} \end{array} \right\} \tag{1.2}$$

For the annular control volume shown in Fig. 1.3 we may adopt a more appropriate (x, r) cylindrical coordinate system instead, whereupon the equivalent compressible flow continuity equation applicable to turbomachinery meridional flows becomes

$$\frac{\partial \rho c_x}{\partial x} + \frac{\partial \rho c_r}{\partial r} + \frac{\rho c_r}{r} = 0 \tag{1.3}$$

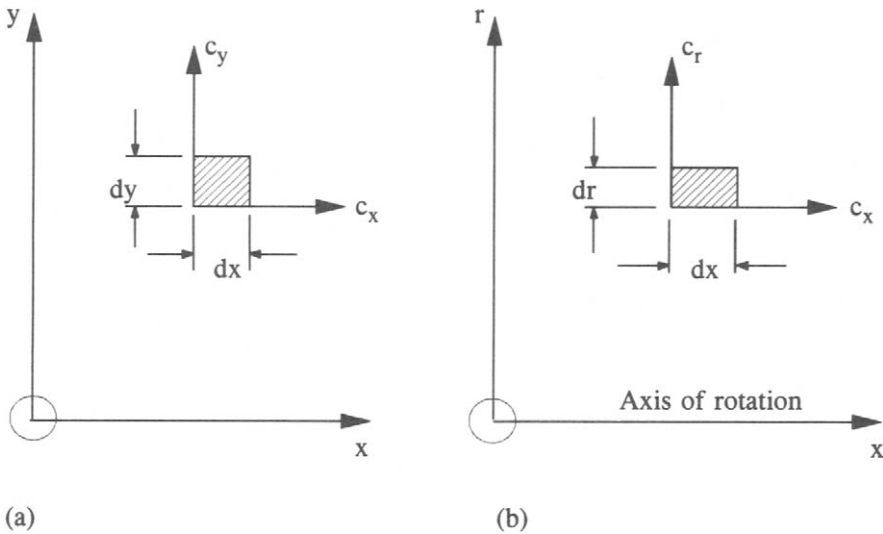and we simply delete density ρ for the incompressible case.

Fig. 1.4 Fluid elements in plane and axisymmetric flow: (a) plane flow in (x,y) cartesian coordinates; (b) axisymmetric flow in (x,r) cylindrical coordinates

1.1.2   Steady flow energy equation

If the First Law of Thermodynamics is applied to the control volume defined in Fig. 1.3 (Rogers and Mayhew, 1992), we obtain the steady flow energy equation,

$$\dot{Q} - \dot{W} = \dot{m}\{(h_2 - h_1) + \tfrac{1}{2}(c_2^2 - c_1^2) + g(z_2 - z_1)\} \tag{1.4}$$

where $\dot{Q} = \mathrm{d}Q/\mathrm{d}t$ is the rate of heat supply (if any) to the control volume and $\dot{W} = \mathrm{d}W/\mathrm{d}t$ is the power extracted. h is the specific enthalpy and z the height of the duct in the gravitational field g. Ignoring the latter potential energy effects for our axisymmetric case, Fig. 1.3, the steady flow energy equation becomes

$$\bar{Q} - \bar{W} = (h_2 + \tfrac{1}{2}c_2^2) - (h_1 + \tfrac{1}{2}c_1^2) = h_{o2} - h_{o1} \qquad \text{for compressible flow} \tag{1.5a}$$

$$= (p_2/\rho + \tfrac{1}{2}c_2^2) - (p_1/\rho + \tfrac{1}{2}c_1^2) = p_{o2} - p_{o1} \qquad \text{for incompressible flow} \tag{1.5b}$$

where we have divided throughout by $\dot{m}$ to obtain the specific (i.e. per unit mass) values of heat supply $\bar{Q}$ and work extraction $\bar{W}$. h_o is called the 'stagnation specific enthalpy', or 'stagnation enthalpy' for short, and p_o is called the 'stagnation pressure'.

1.1.3   Momentum equation – Euler pump and Euler turbine equations

Instead of the full control volume of Fig. 1.3 we consider next the flow of fluid through the elementary stream tube ψ_0 passing through the pump rotor between stations 1 and 2, Fig. 1.5. The torque τ which must be supplied through the shaft to the rotor in order to change the tangential momentum of mass m of fluid from $mc_{\theta 1}$ to $mc_{\theta 2}$ may be found by applying Newton's second law to the elementary control volume, Fig. 1.5(b). This must take the relevant form for a rotating system, namely

$$\text{Applied torque} = \text{rate of change of moment of momentum}$$
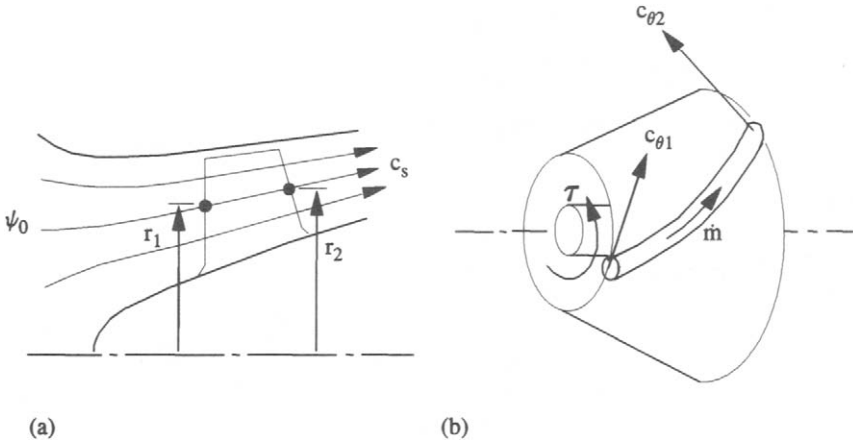
Fig. 1.5 Meridional flow through a turbomachine and flow through an elementary streamtube: (a) meridional flow through a pump or fan rotor; (b) streamtube flowing along the surface of revolution mapped out by the meridional streamline ψ_0

or expressed analytically,

$$\tau = \frac{\mathrm{d}}{\mathrm{d}t}(mrc_\theta)$$
$$= \dot{m}(r_2 c_{\theta 2} - r_1 c_{\theta 1}) \tag{1.6}$$

The power input P then follows directly through

$$\dot{P} = \dot{W} = \tau\Omega$$
$$= \dot{m}\Omega(r_2 c_{\theta 2} - r_1 c_{\theta 1}) \tag{1.7}$$
$$= \dot{m}(U_2 c_{\theta 2} - U_1 c_{\theta 1})$$

where Ω is the rotor angular velocity and $U = r\Omega$ is the so-called 'blade speed'. If we divide through by $\dot{m}$ we obtain the specific work input $\bar{W}$:

$$\bar{W} = \frac{\mathrm{d}W}{\mathrm{d}t} \bigg/ \frac{\mathrm{d}m}{\mathrm{d}t} = U_2 c_{\theta 2} - U_1 c_{\theta 1} \tag{1.8}$$

Making use of the steady flow energy equation (1.5) and neglecting the heat transfer rate into the control volume, i.e. $\bar{Q} = 0$, we obtain finally the well-known Euler pump equation for fans with compressible fluids:

$$h_{o2} - h_{o1} = U_2 c_{\theta 2} - U_1 c_{\theta 1} \quad \text{for compressible flow} \tag{1.9a}$$

For incompressible fluids, i.e. liquids or low Mach number gases, we may follow the same analysis through, using the incompressible steady flow energy equation instead, namely

$$\bar{Q} - \bar{W} = (p_2 - p_1)/\rho + (c_2^2 - c_1^2)/2 \tag{1.5b}$$

to obtain the corresponding form of the Euler pump equation, namely

$$(p_{o2} - p_{o1})/\rho = U_2 c_{\theta 2} - U_1 c_{\theta 1} \quad \text{for incompressible flow} \tag{1.9b}$$

where $p_o = p + \frac{1}{2}\rho c^2$ is the stagnation pressure.

For a turbine rotor we simply reverse suffices 1 and 2 to obtain the Euler turbine equation, namely

$$\left.\begin{aligned} h_{o1} - h_{o2} &= U_1 c_{\theta 1} - U_2 c_{\theta 2} \quad \text{for compressible flow} \\ (p_{o1} - p_{o2})/\rho &= U_1 c_{\theta 1} - U_2 c_{\theta 2} \quad \text{for incompressible flow} \end{aligned}\right\} \tag{1.10}$$

The Euler pump and turbine equations as derived here are one-dimensional equations in the sense that they are applicable to unit mass of fluid flowing along the line mapped out by the elementary streamtube illustrated in Fig. 1.5(b). The circumferential projection of such infinitely thin stream tubes onto the (x, r) plane leads to the definition of a family of so-called meridional streamlines illustrated in Fig. 1.5(a) of which the hub and casing form the boundary streamlines. It is clear that one Euler pump or turbine equation must be derived for each meridional streamline during the design phase for a turbomachine and that these equations will lead to a precise specification of the swirl velocity change from $c_{\theta 1}$ to $c_{\theta 2}$ required for a specified stagnation enthalpy change h_{o1} to h_{o2}. The Euler pump or turbine equation is thus central to the design process, combining both the energy and momentum conservation laws, and will be referred to many times throughout this book.

As with the continuity equation treatment in Section 1.1.1 above, it is possible and indeed necessary for detailed flow modelling to derive differential equations equivalent to the one-dimensional equations of this section in order to express the three-dimensional or more frequently two-dimensional axisymmetric equations of motion at any point in a turbomachine. It will be more helpful to leave this matter for fuller consideration in Chapters 6 and 7 where we will show how such equations may be used to derive the actual meridional streamline distributions such as that illustrated in Fig. 1.5(a).

All of the basic governing equations required for the time being have now been derived. Further consideration will be given to the second law of thermodynamics in later chapters as needs demand. To conclude this chapter we will now give some preliminary consideration to dimensionless groups of special significance to the turbomachinery designer.

1.2 Dimensional analysis

An indication of the primary goals of dimensional analysis was given in the introduction to this chapter. In the present section attention will be drawn to two different levels of dimensional analysis and consequent dimensionless groups, namely

(a) *global* dimensionless performance variables, and
(b) *local* dimensionless design and performance variables.

The first of these may be more familiar to the student and is concerned with the key overall or *global* performance variables of a turbomachine such as flow rate, pressure rise and efficiency in the case of a fan or pump. Such global dimensionless groups will be derived in Section 1.2.1 to illustrate the power and scope of dimensional analysis to take advantage of laboratory-scale model testing as a design and

performance predictive tool. An extension of the use of global dimensionless variables for the selection of machine type, axial, radial or mixed-flow, to best suit a given operating duty specification will be outlined in Section 1.2.2 with reference to useful published correlations.

The use of *local* dimensionless variables may be less familiar territory for the student and is the main theme of many of the subsequent chapters of this book where analytical developments will be laid out in detail for a wide range of turbomachine types. In view of this a brief outline only will be given in Section 1.2.3 to illustrate the main ideas and implications of this type of analysis, which involves selection of dimensionless performance coefficients for each meridional streamline such as ψ_0, Fig. 1.5.

1.2.1 Overall dimensional analysis and *global* dimensionless performance parameters

The fundamental basis of dimensional analysis is well covered in standard fluid-dynamic texts such as Massey (1989) or Shepherd (1965), including the use of Buckingham's π-theorem to derive dimensionless groups, and will be taken as read. For the present purpose we will approach the matter from the turbomachinery engineer's viewpoint by considering the performance analysis of a given centrifugal pump, drawing out its main key performance characteristics and showing how global dimensionless performance parameters can help to take advantage of scale model tests.

For example, let us consider the twofold purpose of the centrifugal pump illustrated in Fig. 1.6, namely

(a) to move fluid at a specified flow rate Q, and
(b) to raise the fluid pressure through $(p_2 - p_1)$,

achieving both goals with high pumping efficiency η. Alternatively we may regard the second duty requirement (b) as that of lifting the fluid through the height H in the gravitational field g, where Bernouilli's equation or the incompressible steady flow energy equation (1.5b) provides the connecting relationship

$$p_2 - p_1 = \rho g H \tag{1.11}$$

The effective 'pumping power' P (i.e. the useful power output of the pump) may then be calculated through

$$P = \dot{m}gH = \rho Q g H \tag{1.12}$$

where $\dot{m}$ is the mass flow rate and ρ the fluid density. In other words, the pumping power delivered is the product of the two specified primary design duty parameters (Q, gH) and is also proportional to g and ρ. The quantity gH is in fact the energy input to a unit mass of fluid passing through the pump and turns out to be a more useful parameter than simply H in subsequent dimensional analysis. We will term it the gravitational head. A suitable definition of overall hydraulic efficiency then follows from

$$\eta = \frac{\text{Pumping power}}{\text{Shaft input power}}$$
$$= \frac{\rho Q g H}{\tau N} \tag{1.13}$$

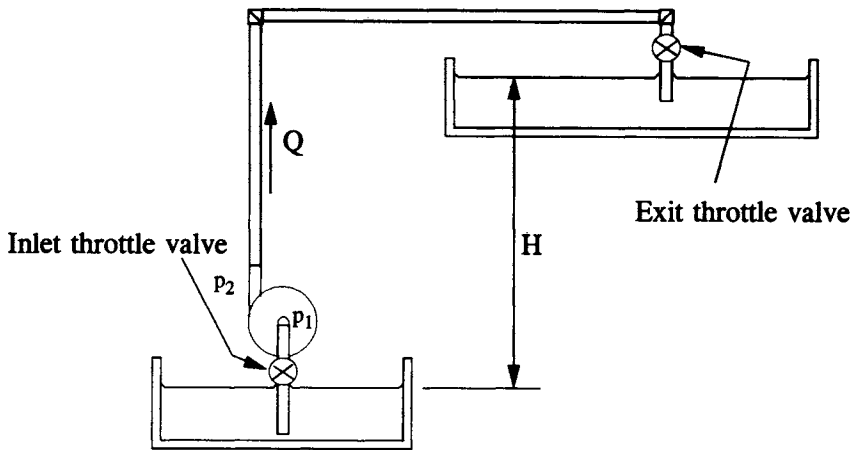where τ is the shaft input torque and N the rotational speed.

Fig. 1.6 Centrifugal pump raising fluid through head *H*

Suppose we were to set ourselves the aim of finding out by experimental test how all the various features of the pump will affect its efficiency. The variety of factors involved could be summarised as follows:

(1) The shape of each pump component such as the annulus and the blades.
(2) The duty coefficients (Q, gH).

In addition to these and of particular significance for model testing, we have

(3) The fluid density ρ.
(4) The rotational speed of the pump N.
(5) The size of the pump which may be typified by any characteristic length scale, such as its maximum diameter D.

Consistent units must obviously be used to specify all these parameters but we can continue the argument without reference to any particular system of units for the time being. The effect of all of these parameters upon the efficiency η may be expressed through the parametric equation

$$\eta = f(\underbrace{Q, gH,}_{\substack{\text{Plant duty} \\ \text{parameters}}} \quad \underbrace{\rho, N, D)}_{\substack{\text{Machine design or} \\ \text{scale variables}}} \qquad (1.14)$$

Here we have identified two groups. The first involves the design duty (Q, gH) which the pump is to provide. The second group includes the three items which the experimenter is free to vary independently on his model test facility, namely the type of fluid, categorised here through its density ρ, the speed N and size D. Clearly the one pump feature not accounted for by this parametric equation is the very one which will affect its efficiency most of all, namely its detailed shape. However, we have already stated that the present aim is to use small scale model tests to predict the performance of a full scale machine. The one feature which we must preserve if these tests are to be truly 'dynamically similar' is its shape. The model must be a true geometric scale of the prototype, in which case we can accept Eqn (1.14) as a correct representation of all the other relevant performance factors which will affect

efficiency. There could of course be other influential factors such as the fluid viscosity but we will ignore these for the moment just to keep the argument simple.

Now the most obvious choice of performance characteristics by which to express the pump's behaviour and quality are those shown in Fig. 1.7, namely curves of gH versus Q and of η versus Q. Such curves are obtained by running the pump at constant rotational speed N while varying the flow rate Q by means of a throttle valve $\otimes$ in the delivery line, Fig. 1.6. In this case characteristic curves are compared for two pumps in the author's laboratory which have geometrically similar rotors but which are different in scale and have been tested at different rotational speeds. Pump A is 0.14 m in diameter and was tested here at 2600 rev min^{-1} whereas the smaller pump B is 0.1 m in diameter but was run at the higher speed of 3000 rev min^{-1}.
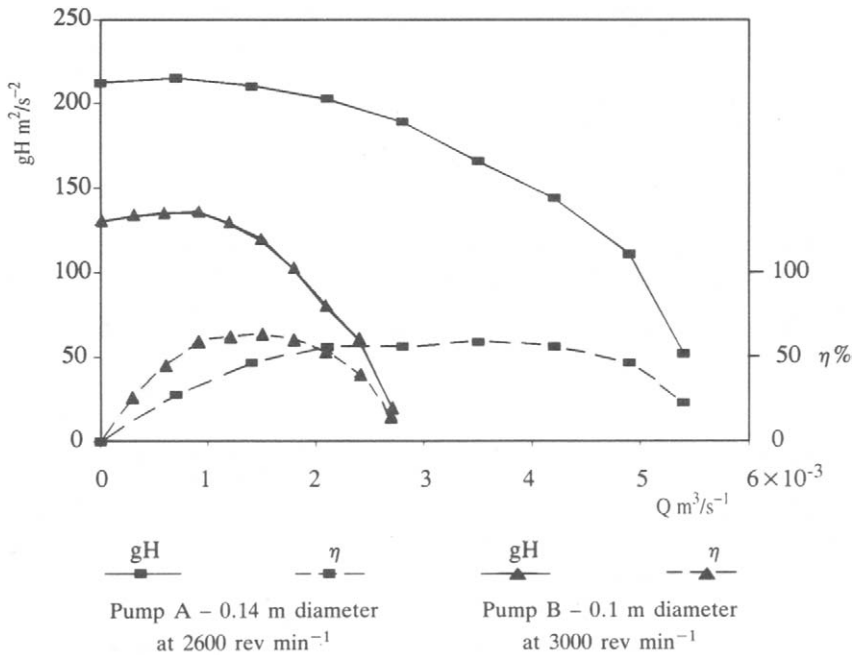
Fig. 1.7 Comparison of the characteristic curves of two pumps with similar geometry

The two sets of characteristics bear little resemblance as one might expect and at first sight it would seem unlikely that the characteristics of pump A might be able to be inferred from pump B or vice versa. Dimensional analysis provides the way forward and in the process reduces the total number of variables involved. In its present dimensional form Eqn (1.14) states that the hydraulic efficiency is a function of five independent variables. Two of these are the primary characteristic duty parameters Q and gH. The other three represent design or test variables which may be varied independently, namely ρ, N and D. Since all five parameters have dimensions formed from all or some of the three basic dimensions of mass M, length L and time T, the π-theorem states that the total number of independent parameters may be reduced from 5 to $5 - 3 = 2$ by forming dimensionless groups. Applying the method of indices, the modified parametric equation then transforms to

$$\eta = f(\Phi, \Psi) \tag{1.15}$$

where the dimensionless global duty parameters are as follows:

$$\Phi = Q/(ND^3) \qquad \text{Flow coefficient} \left.\vphantom{\begin{array}{c}a\\b\end{array}}\right\}$$
$$\Psi = gH/(N^2D^2) \qquad \text{Head coefficient} \quad\quad (1.16)$$

The efficiency is thus dependent upon only two dimensionless parameters which represent the primary duty requirements of the pump, namely the production of flow Φ and head rise Ψ.

If the test data for the two pumps previously considered are replotted as Ψ–Φ and η–Φ characteristics instead, as shown in Fig. 1.8, they are found to be remarkably similar to one another, bearing in mind of course that although the overall blade and annulus geometries are generally true to scale, there will be differences of surface finish and more importantly of tip clearance between blade and casing, a parameter which is difficult to set precisely. Despite these minor departures from true geometrical similarity, both the head and efficiency characteristics follow the same pattern over a wide range of operating duties. Thus we may conclude from this study that one set of scale model test results would have been sufficient to predict the actual characteristic of both pumps and, if required, for a very much larger prototype, resulting in a considerable reduction in effort and cost. Furthermore from the dimensionless characteristics we may select a recommended design duty point ◯ located somewhere close to the maximum efficiency.

It is essential to use a consistent set of units for D, N, Q, g and H when evaluating Φ and Ψ. All consistent sets will then deliver the same values for these truly dimensionless coefficients. We will adopt the SI system for which the dimensions and units of various useful quantities are summarised in Table 1.1.

The reader may have noticed that the fluid density ρ does not as yet feature in the dimensionless coefficients, Eqn (1.16), since it is the only one of the five variables in Eqn (1.14) to include the mass dimension M. It is normal practice, however, to plot a third dimensionless characteristic to express power P versus flow Q. According to the π-theorem any pair of dimensionless variables may be combined to form a

Table 1.1 Quantities and their dimensions and SI units

Quantity	Dimension	Unit	Symbol or combination
Length	L	metre	m
Mass	M	kilogram	kg
Time interval	T	second	s
Velocity	LT^{-1}	metres per second	$m\,s^{-1}$
Force	MLT^{-2}	newton	N or $kg\,m\,s^{-2}$
Pressure	$ML^{-1}T^{-2}$	pascal	Pa or $N\,m^{-2}$
Work, heat	ML^2T^{-2}	joule	J or $N\,m$
Power	ML^2T^{-3}	watt	W or $J\,s^{-1}$
Rotational speed	T^{-1}	radians per second	$rad\,s^{-1}$
Frequency	T^{-1}	hertz	Hz or s^{-1}
Density ρ	ML^{-3}	kilograms per metre^3	$kg\,m^{-3}$
Dynamic viscosity μ	$ML^{-1}T^{-1}$	poise	$kg\,m^{-1}\,s^{-1}$
Kinematic viscosity ν	L^2T^{-1}	stoke = $10^{-4}\,m^2\,s^{-1}$	$m^2\,s^{-1}$
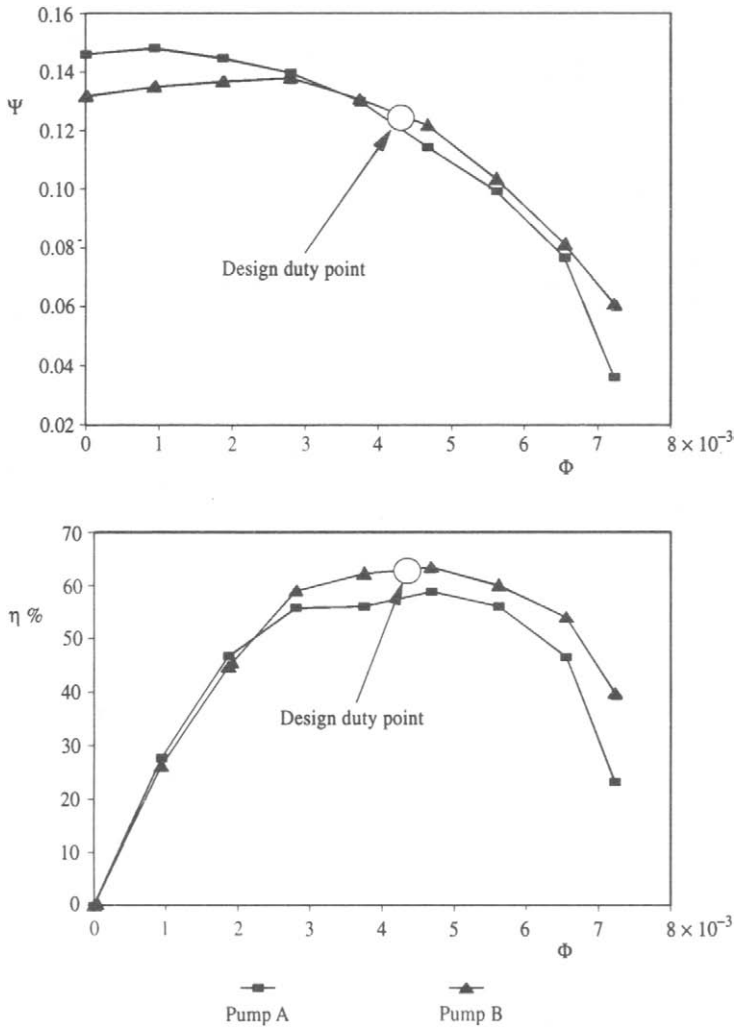
Fig. 1.8 Dimensionless characteristics for two centrifugal pumps of different scale operating at different rotational speeds

new variable. Thus if we manipulate Eqn (1.12) by dividing both sides by $\rho N^3 D^5$ we obtain the dimensionless pumping power coefficient Π:

$$\Pi = \frac{P}{\rho N^3 D^5} = \left(\frac{Q}{ND^3}\right)\left(\frac{gH}{N^2 D^2}\right) = \Phi\Psi \qquad (1.17a)$$

Making use of the definition of efficiency, Eqn (1.13), the alternative shaft power input coefficient may then also be defined:

$$\Pi_{\text{shaft}} = \Pi/\eta = \Phi\Psi/\eta \qquad (1.17b)$$

Thus the fluid density ρ is required at this point to introduce the mass dimension

M into the Π group. ρ will also be required if we wish to extend the above treatment to include viscous effects. To achieve this let us modify the parametric equation (1.14) by including also the dynamic viscosity μ:

$$\eta = f(\underbrace{Q, gH,}_{\substack{\text{Plant} \\ \text{duty}}} \quad \underbrace{\rho, \mu,}_{\substack{\text{Fluid} \\ \text{properties}}} \quad \underbrace{N, D)}_{\substack{\text{Design or scale} \\ \text{variables}}} \tag{1.18}$$

We may now identify three groups of related variables as indicated. If we apply the π-theorem to this six-parameter equation we will now obtain $6 - 3 = 3$ dimensionless groups which are as follows:

$$\eta = f(\Phi, \Psi, R_e) \tag{1.19}$$

where the new dimensionless coefficient R_e is called the machine Reynolds number and is defined as

$$R_e = \frac{ND^2}{\mu/\rho} = \frac{ND^2}{\nu} \tag{1.20}$$

where ν is the kinematic viscosity.

It is more usual to think of the Reynolds number as the ratio between dynamic action and viscous action within an actual fluid, for which dimensional analysis generates the well-known form

$$R_e = \frac{(\text{Fluid velocity}) \times (\text{Typical length})}{\nu} = \frac{cD}{\nu}$$

R_e for the overall turbomachine as stated by Eqn (1.20) can be better interpreted in relation to this if it is rearranged in the analogous form as follows:

$$R_e \approx \frac{(\text{Blade speed } ND/2) \times (\text{Typical length } D)}{\nu}$$

where tip blade speed $ND/2$ replaces fluid velocity c, and diameter D is chosen as the typical length scale.

The essential point is that true dynamic similarity will now most certainly be obtained if we ensure that the following three conditions are satisfied:

(1) True scale geometry of the model.
(2) The same dimensionless duty coefficients (Φ, Ψ).
(3) Identical Reynolds number R_e for both model and prototype.

In such cases the two characteristic curves shown in Fig. 1.8 will be identical for both prototype and scale model with incompressible fluids. Unfortunately, however, this can present a practical difficulty since we must settle upon some particular rotational speed N in order to complete the constant speed characteristic tests to obtain the raw data Q and gH. To illustrate this let us compare the machine Reynolds numbers for the two pumps A and B. From Eqn (1.20), introducing the data given in Fig.

1.7, the ratio of the Reynolds numbers for these particular tests was

$$\frac{R_{eA}}{R_{eB}} = \left(\frac{N_A}{N_B}\right)\left(\frac{D_A}{D_B}\right)^2 = 1.306\,67$$

To ensure that pump B is tested at the same Reynolds number as pumnp A, the above expression may be inverted to give the appropriate speed of rotation for pump B, namely

$$N_B = N_A\left(\frac{R_{eB}}{R_{eA}}\right)\left(\frac{D_A}{D_B}\right)^2$$
$$= N_A\left(\frac{D_A}{D_B}\right)^2$$

which for the case under consideration is $3920\,\text{rev}\,\text{min}^{-1}$.

1.2.2 Selection of a suitable pump shape to suit a given application

For the above development we happened to choose a so-called mixed-flow pump for which the annulus shape is partly axial and partly radial. The majority of pumps and fans in fact tend to be either axial or radial (centrifugal) in annulus shape. If we were to test several of each type of machine to obtain their Φ–Ψ characteristics, a comparison would show the trends illustrated by Fig. 1.9. The centrifugal machine, having a restricted inlet orifice, would tend to exhibit low Φ values but would be capable of delivering higher Ψ values due to the centrifugal effects (see Chapter 7). The axial machine is geometrically most suited to pass high flow rates and would exhibit the highest Φ values. Its head generating capacity would, however, be limited by the allowable lift coefficients of the blade aerofoils resulting in low Ψ coefficients. Mixed-flow machines would show a compromise performance between these extremes. If we were to mark out the best efficiency point for each member of this family of machines we would obtain a curve $\Phi = f(\Psi)$ similar to that shown in Fig. 1.9. In reality, if we were to test a very large number of machines and record their performance in this way, we would obtain not a thin curve but a scatter plot or banded region. A much narrower scatter band and a more distinct relationship between optimum (Φ, Ψ) duty and machine type could obviously be obtained if one individual designer were to build up a progressive family of machines on the same basis with continual reference back to this family history curve over a period of time. Such techniques enable the designer to select machine type off the shelf quite quickly based on proven experience.

A much more familiar and very long established approach to machine shape selection takes advantage of two other dimensionless groups known as the specific speed and diameter, defined as

$$N_s = \frac{NQ^{1/2}}{(gH)^{3/4}} \quad \text{specific speed} \tag{1.21}$$

$$D_s = \frac{D(gH)^{1/4}}{Q^{1/2}} \quad \text{specific diameter} \tag{1.22}$$

so called because, while both contain the two plant variables Q and gH, the specific
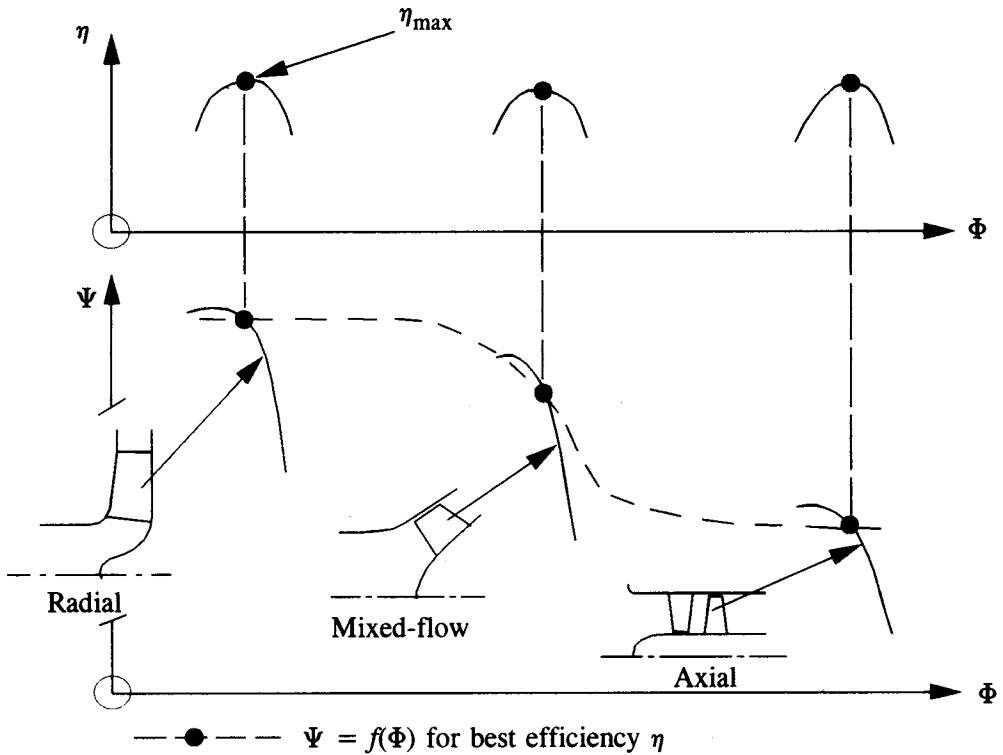
Fig. 1.9 Typical Φ–Ψ characteristics for a family of radial mixed-flow and axial fans or pumps showing relationship of best duty points

speed N_s is also proportional to the rotational speed N and the specific diameter D_s is proportional to the diameter D.

Originally due to Cordier (1953) and as given by Csanady (1964) in a useful discussion of this subject, the famous 'Cordier Diagram' is shown in Fig. 1.10, linking N_s with D_s for a wide range of pump types. The recommended ranges for pumps and fans are shown on the right-hand side. Although the plot is shown as a thin line, it is in reality a mean experience curve fitted through a scatter plot and only serves as an indication of the suitable machine type to select for a given application. In many situations it may well be possible to depart from this and to design high performance axial, mixed-flow or radial machines for the same situation, especially in the middle range of specific speed.

To illustrate this last point it is of considerable interest to note the relationships between the (Φ, Ψ) and (N_s, D_s) dimensionless groups. If we substitute Eqns (1.16) into (1.21) and (1.22) we obtain

$$N_s = \frac{\Phi^{1/2}}{\Psi^{3/4}}, \quad D_s = \frac{\Psi^{1/4}}{\Phi^{1/2}} \tag{1.23}$$

or, put the other way round,

$$\Phi = \frac{1}{N_s D_s^3}, \quad \Psi = \frac{1}{N_s^2 D_s^2} \tag{1.24}$$

Fig. 1.10 Cordier diagram showing empirical relationship between specific speed N_s and specific diameter D_s for pumps and fans

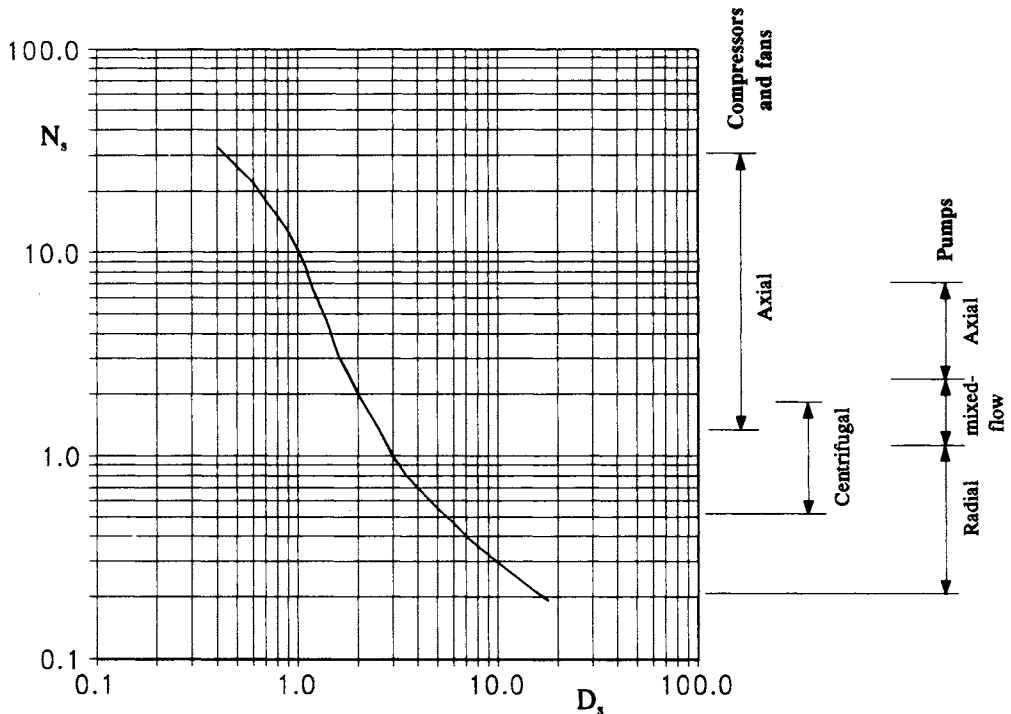If the (N_s, D_s) Cordier line data are now introduced into these expressions, most interesting perceptions follow from replotting the Cordier diagram as an equivalent (Φ, Ψ) chart, Fig. 1.11. Here we observe immediately a more definitive shape of the optimum machine selection curve which is dominated by the influences of the centrifugal and axial machines. The centrifugal machines tend to settle for a fairly constant head coefficient in the region of $\Psi = 0.1$ over a wide range of flow coefficients. The axial machines cope with a much wider range of head coefficients of roughly $\Psi = 0.005$ to 0.05 over again a fairly wide Φ range. The mixed-flow machines are sandwiched in between in a very narrow range. One would expect a much greater spread of mixed-flow machines here for a progressively designed family of pumps or fans. The reason for this is almost certainly the designer's wish to settle for either an axial or a centrifugal machine wherever possible since these tend to offer less geometrical and therefore manufacturing complexity than the mixed-flow machine which would need to be tailor-made.

Before concluding this section two points should be mentioned. Firstly most manufacturers will have their own alternatives to the 'Cordier' diagrams shown here which will reflect the features and choices of their own special approach, although the same overall principles will apply. Secondly Csanady (1964) and others often include hydraulic turbines on the same (N_s, D_s) plot and Csanady has provided the interesting bar chart shown in Fig. 1.12 linking general turbomachine type to specific speed.

A more recent review of industrial practice in expressing optimum machine selection has been given by ESDU (1980) specifically for fans. This is illustrated in
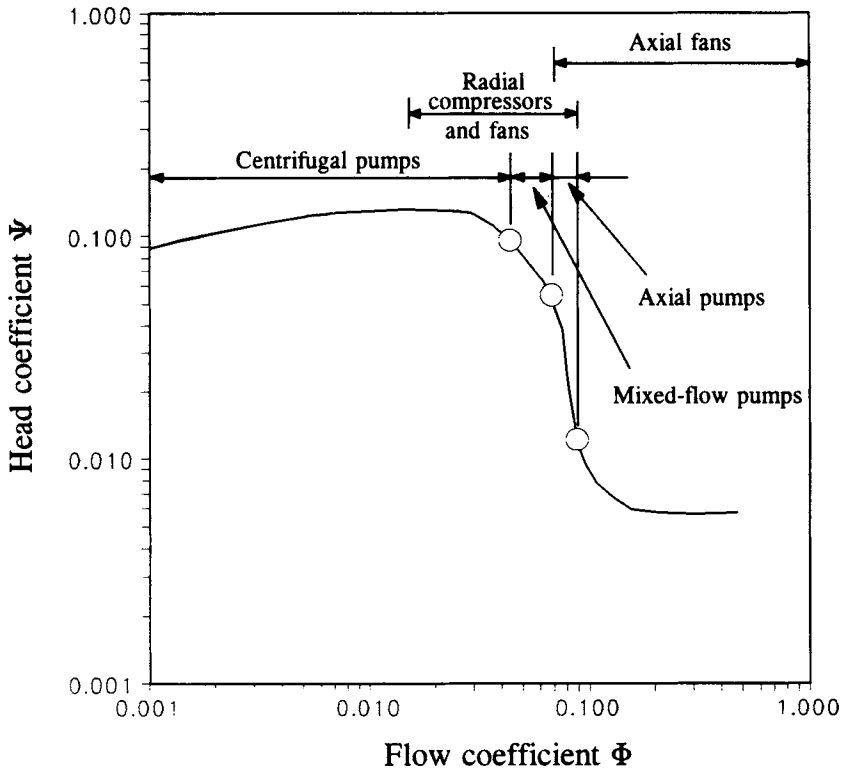
Fig. 1.11 Φ–Ψ chart for pumps and fans

Fig. 1.13 in which the empirical information covered is compared with the above Cordier curves for both D_s–N_s and Φ–Ψ plots. Referring first to the D_s–N_s chart, the recommended areas for selection of axial fans and centrifugal fans certainly confirm the Cordier curve although centrifugals depart more significantly from it in the medium specific speed range. In the last two or three decades mixed-flow fans have received more attention for applications requiring both high flow rate and fairly high pressure rises such as nuclear reactor gas circulators and hovercraft fans. Cross-flow fans are a relative newcomer, widely used in ventilation and air conditioning, and now find a place on this chart.

The Φ–Ψ plot in Fig. 1.13 illustrates well how the transformation from D_s–N_s coordinates to Φ–Ψ coordinates using Eqns (1.24) exaggerates departure of the zones of ideal machine types from the Cordier curve. This is particularly so for centrifugal machines so far as the allowable flow coefficient range Φ is concerned, while the spread of recommended head coefficients Ψ is relatively restricted.

1.2.3 *Local* dimensionless design and performance variables

As already indicated, a turbomachine may contain many and complex blade elements as illustrated by Fig. 1.1. Furthermore the flow within any single blade row may vary considerably from hub to casing, requiring detailed specification of blade profile for each meridional stream surface, Fig. 1.5. Thus it may seem optimistic to expect *global* dimensionless groups such as we have just considered to be able to do justice to such
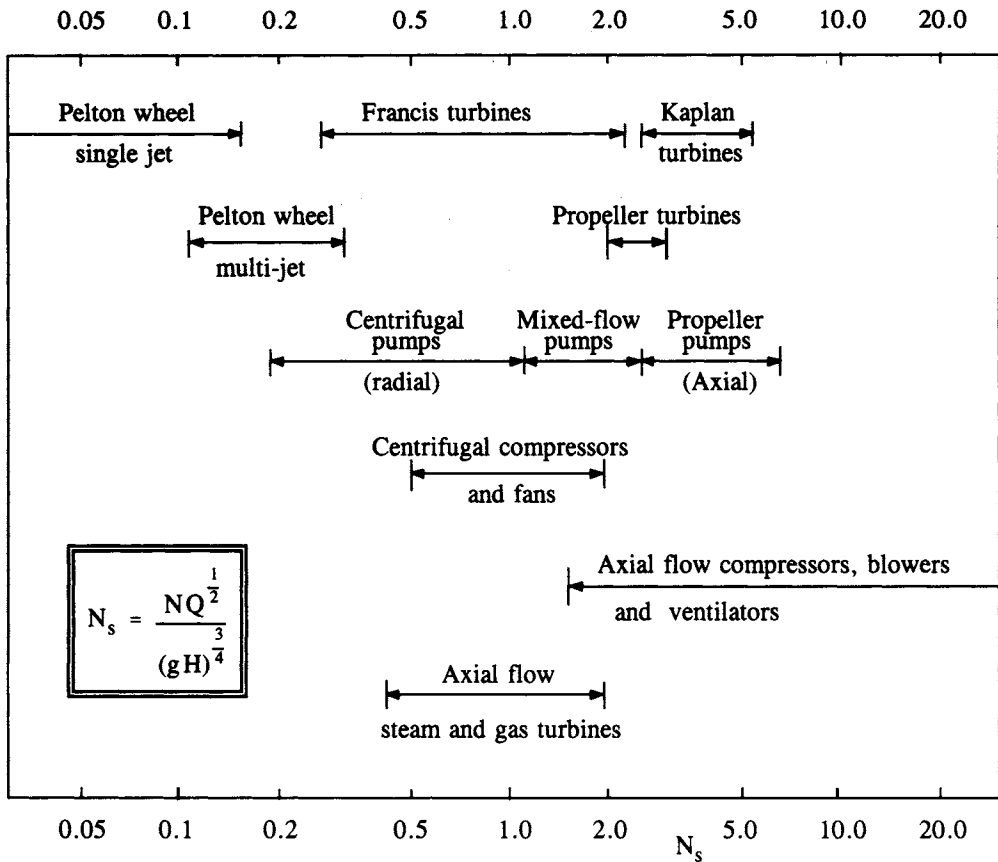
Fig. 1.12 Correlation of turbomachine type with specific speed

complex internal flows. A completely different level of dimensional analysis has therefore been developed to deal with this problem and is indeed the main theme of this book. For example, let us consider how we might deal with the blade element generated by the intersection of the central meridional stream surface ψ_0 in Fig. 1.5. Instead of applying the formal procedures of the π-theorem, designers frequently select intuitively what seem to be appropriate dimensionless groups, and the popular choice for this mixed-flow fan would be as follows:

$$\begin{aligned}\phi &= c_{s2}/U_2 && \text{flow coefficient} \\ \psi &= \Delta h_o/U_2^2 && \text{work or head coefficient}\end{aligned} \quad \Biggr\} \quad (1.25)$$

For focusing upon a particular zone of the blade we are thus interested in the relationship between the local meridional velocity c_s and the local blade speed $U = r\Omega$. Since the blade speed for a mixed-flow machine varies from inlet to exit due to radius change, Fig. 1.5, the above are referred to just one station, namely the exit station 2 at the blade trailing edge. The work coefficient likewise focuses upon the local stagnation enthalpy rise as compared with the quantity U_2^2.

All that is intended here is to draw attention to these alternative *local* dimensionless variables which have different values for each meridional streamline. In practice attention is often focused upon the central meridional streamline only for the
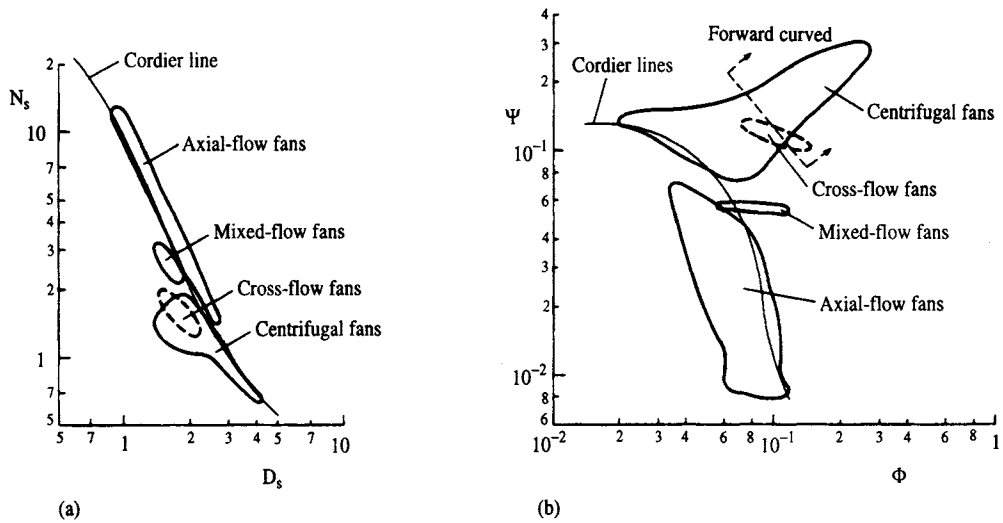
Fig. 1.13 Optimum efficiency contours for various types of fan on (a) D_s–N_s and (b) Φ–Ψ plots (by courtesy of Engineering Sciences Data Unit, ESDU, 1980)

definition of a single (ϕ, ψ) duty to typify the blade row as a whole. For the development of experimental test correlations such as those given in Chapter 3 for axial turbines, this may be a necessary practical limitation. However, it will be shown in later chapters that such local (ϕ, ψ) duty parameters are closely related to the velocity triangle shape and therefore to blade aerodynamic behaviour for each meridional streamline, thus offering much deeper insights into the detailed performance of turbomachine stages and a much more productive framework for design and performance analysis. However, it will be left until Chapters 3, 4, 7 and 8 to develop this in some detail as a primary and most valuable tool for design and performance analysis of a wide range of turbomachines.

2
Two-dimensional cascades

Introduction

From very early days in the history of axial turbines and compressors designers have treated the complex three-dimensional flow in such machines as the superposition of a number of two-dimensional flows which lead to more manageable blade design and profile selection techniques. As illustrated by Fig. 2.1, two types of flow may be identified, namely an assumed axisymmetric or so-called 'meridional flow' and a series of 'blade-to-blade' or 'cascade' flows. For example, for the axial turbomachine with cylindrical hub and casing shown here, it is quite reasonable to assume to begin with that the stream surfaces at entry to the annulus remain cylindrical as they progress through the machine. Each cylindrical meridional stream surface will then intersect the blade row to form a circumferential array of blade shapes known as a cascade. If one such cylindrical surface were unwrapped from its $(x, r\theta)$ coordinates and laid out flat onto the (x, y) plane as illustrated by Fig. 2.2, we would then obtain an infinite array of blade or aerofoil shapes stretching along the y axis. The full three-dimensional flow could then be modelled by a series of such plane two-dimensional cascades, one for each of the cylindrical meridional surfaces equally spaced between hub and casing. Six to ten sections would suffice to represent a typical steam turbine, gas turbine, compressor or fan blade row, although we will show just five here to simplify the diagrams.

The advantage of this simple approach is that the Euler pump or turbine equations (1.9) and (1.10) may then be applied to each cascade section independently to determine the inlet and outlet velocity triangles for that particular blade section. The

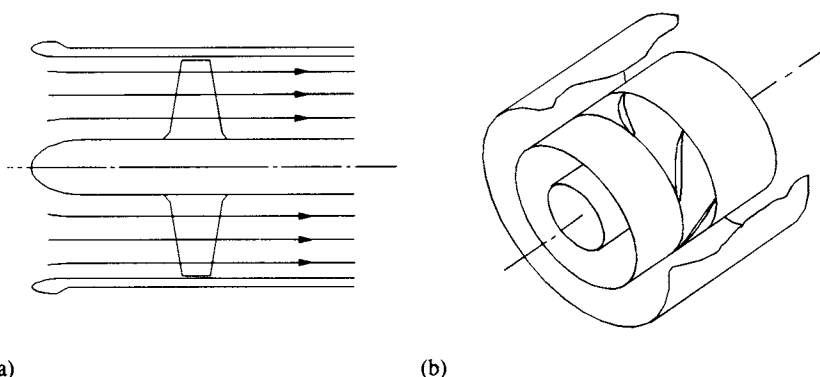(a)   (b)

Fig. 2.1 Treatment of three-dimensional flow through an axial fan as superposition of axisymmetric meridional flow and two-dimensional cascade or blade-to-blade flows: (a) meridional streamlines; (b) cascade intersection of a cylindrical stream surface with a fan rotor blade
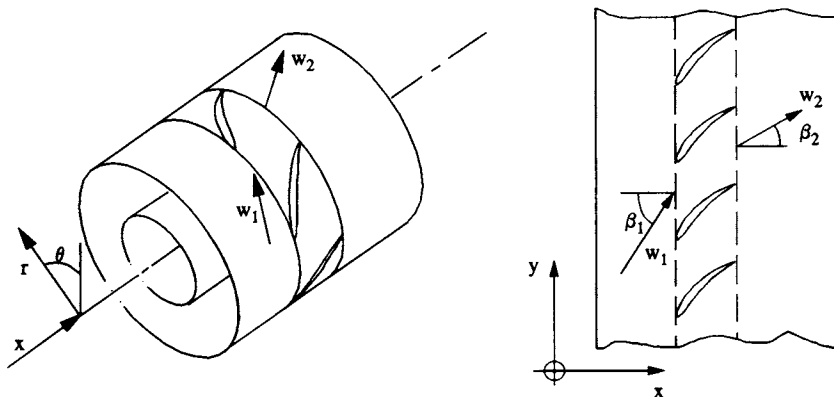
Fig. 2.2 Development of a cylindrical blade-to-blade section into an infinite rectilinear cascade in the (*x,y*) plane

designer's task is then to select a suitable blade shape to achieve the required flow deflection from the inlet angle β_1 to the outlet angle β_2, measured relative to the rotor here, and to do so with the minimum loss of energy due to fluid friction. The requirements for this are threefold. Firstly care must be taken not to aerodynamically overload the cascade blades, a matter which will be dealt with in Sections 2.2 and 2.7. Secondly the cascade must produce the correct fluid outlet angle β_2 and hence deflection $\varepsilon = \beta_1 - \beta_2$. Thirdly it must achieve the latter with smooth inlet flow around the profile leading edges. These last two matters will be dealt with in Appendix II, Section II.8, where the computer program CASCADE, provided on the accompanying PC disc, is used to select an optimum compressor cascade.

The reader will immediately see also the strategic drafting advantages of this simple two-dimensional modelling of a flow that is in truth really three-dimensional. For example the full twisted blade shape of our fan rotor, Fig. 2.3, can be generated quite simply and in a form suitable for subsequent manufacture by NC or CNC machine tools, probably with some preliminary curve fitting of the data to provide say 100 or more intermediate blade sections.

As early in the history of gas turbines as 1952, however, C. H. Wu recognised the truly three-dimensional nature of the flow in his classic paper and proposed the remarkably sophisticated computational scheme illustrated in Fig. 2.4. The fully three-dimensional flow was again treated by the superposition of a number of two-dimensional flows, but in this case located on the so-called S-1 and S-2 stream surfaces. S-2 surfaces follow the primary fluid deflection caused by the blade profile curvature and its associated aerodynamic loading. Due to the variation of static pressure between the convex surface of blade No. 1 and the concave surface of blade No. 2 the curvature of each S-2 stream surface will differ, calling for the introduction of several surfaces for adequate modelling (just three S-2 surfaces are shown here). The S-1 surfaces, also shown in Fig. 2.4, are equivalent to the meridional surfaces of revolution which we have just considered in the simpler model illustrated in Figs 2.1 and 2.2. In Wu's model, however, the S-1 surfaces are allowed to twist to accommodate the fluid movements caused by the variations of the three S-2 surfaces. The S-1 and S-2 surfaces in fact represent a selection of the true stream surfaces passing through the blade row. By solving the equations of motion for the flows on this adaptable mesh, successively improved estimates of the S-1 and S-2 surfaces may be obtained, allowing also for the fluid dynamic coupling between them. An iterative
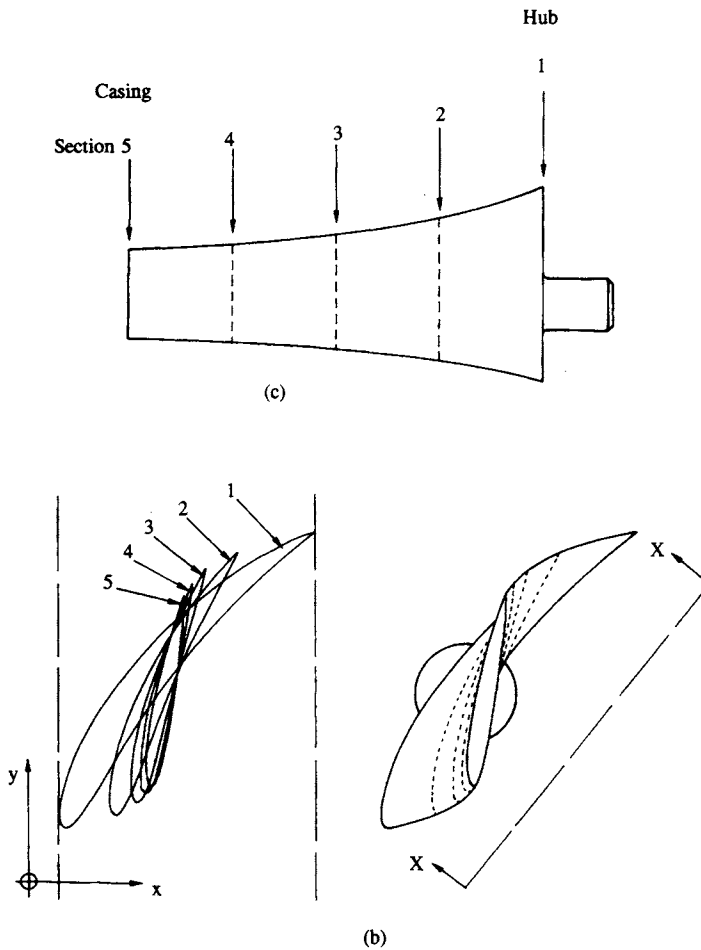
Fig. 2.3 Stacking of blade profiles designed in the (x,y) cascade plane to form a fan blade: (a) five cascade sections between hub and casing; (b) blade sections stacked to form the fan blade; (c) view on X–X

approach to achieving a good estimate of the fully three-dimensional flow was fairly comprehensively laid out by Wu (1952) in a rigorous paper which was truly 20 years ahead of its time. It still remains today as an extremely useful presentation of the basic governing equations for compressible turbomachinery flows, and a remarkable early attempt at numerical modelling prior to the widespread availability of digital computers.

The first major computational scheme based upon Wu's work was published by Marsh (1966), dealing in effect with axisymmetric meridional flow located on an average S-2 surface. Subsequently alternative formulations of the governing equations were developed, notably the time-marching method of Denton (1982), opening the door to practicable design codes for compressible three-dimensional flow analysis. However, Potts (1987, 1991) was also able to adapt the time-marching method to study the twisting of Wu S-1 stream surfaces within highly swept turbine cascades. Apart from these and many other published schemes, industrial companies have developed their own codes for meridional analysis or taken advantage of commercial
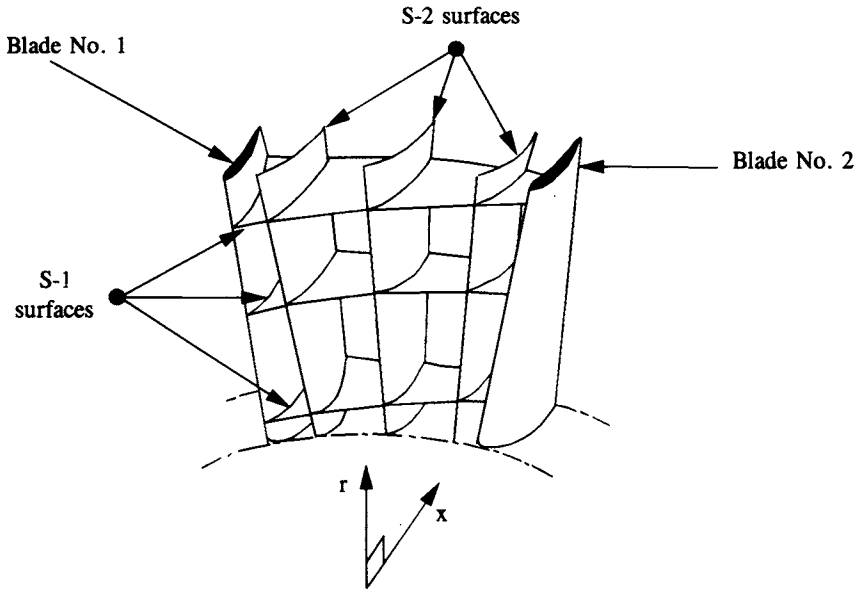
Fig. 2.4 S-1 and S-2 stream surface (after Wu, 1952)

codes. Crucial though this is for advancement of the thermo-fluid dynamic design of turbomachines, detailed review is beyond the scope of this book. Much more simplified meridional flow analysis treatments will be given in Chapter 5, followed in Chapter 6 by a detailed discussion of the mechanisms of vorticity production in turbomachines and their influence upon meridional flows.

In Section 2.1 we will develop the overall fluid dynamic analysis of two-dimensional compressor and fan cascades including the definition of key performance parameters. Section 2.2 will be concerned with the efficiency of a compressor cascade viewed as a diffuser. Design and analysis of cascades by direct and inverse methods will be discussed in Sections 2.3 to 2.5. Means for selection of optimum cascades will be dealt with in Sections 2.6 and 2.7. The chapter is concluded with methods for predicting the fluid deviation or outlet angle in Section 2.8. Illustrative use of the program CASCADE will be made where relevant and familiarisation of the reader with this would be helpful. User instructions are given in full in Appendix II.

2.1 Cascade dynamics and parameters

In order to derive equations which express the fluid dynamic effect of a blade row, let us consider flow through the control volume *abcd* surrounding one blade of a compressor cascade, Fig. 2.5. Analysis is simplified if we select sides *ab* and *dc* to coincide with equivalent streamlines through adjacent passages. Sides *ad* and *bc* will be drawn parallel to the *y* axis and equal in length to the blade pitch *t*. Generally speaking the fluid passing through the control volume will be deflected through the angle $\varepsilon = \beta_1 - \beta_2$ in reaction to the lift force *L*. In addition there will be a drag force *D* at right angles to this caused by viscous shear stresses at the blade surface, resulting in an overall loss of stagnation pressure Δp_0. Subsequent analysis will show that *L* and *D* lie in the directions normal and parallel to the vector mean velocity W_∞. As shown by the velocity triangles for the blade row, Fig. 2.5, W_∞ is defined as the vector
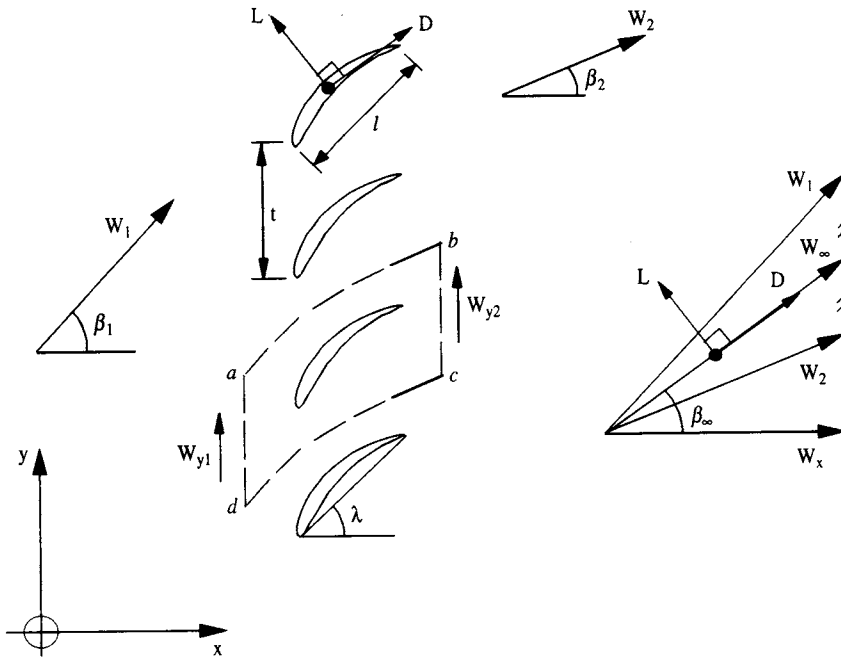
Fig. 2.5 Cascade geometry and velocity triangles

average of the inlet and outlet velocities W_1 and W_2 and is thus suitably representative of the general velocity level of the cascade. The vector mean angle β_∞ may thus be expressed in terms of the inlet and outlet flow angles β_1 and β_2 through

$$\tan \beta_\infty = \tfrac{1}{2}(\tan \beta_1 + \tan \beta_2) \tag{2.1}$$

For fans and compressors the lift coefficient C_L serves as a most important indicator of profile aerodynamic loading and may be defined, together with the drag coefficient C_D, in a form which links naturally with the established notion for isolated aerofoils, namely

$$C_L = \frac{L}{\tfrac{1}{2}\rho W_\infty^2 l}, \quad C_D = \frac{D}{\tfrac{1}{2}\rho W_\infty^2 l} \tag{2.2}$$

Here L and D are defined as the lift and drag forces acting on unit length of aerofoil in the z direction (i.e. perpendicular to the x, y plane). Hence the additional dimension (unit) length is implied in the denominators of Eqns (2.2) to ensure that C_L and C_D are dimensionless.

In order next to complete a force balance on the control volume, two alternative diagrams are shown in Fig. 2.6. Figure 2.6(a) shows the aerodynamic forces and their components X and Y acting on the compressor blade. Figure 2.6(b) on the other hand, shows the equal and opposite reaction forces acting on the control volume *abcd* and also the externally imposed pressure forces $p_1 t$ and $p_2 t$ acting on *ad* and *bc* respectively. We first note that the lift force L and drag force D may be combined into the single aerodynamic force F acting on the blade profile. F may then be resolved
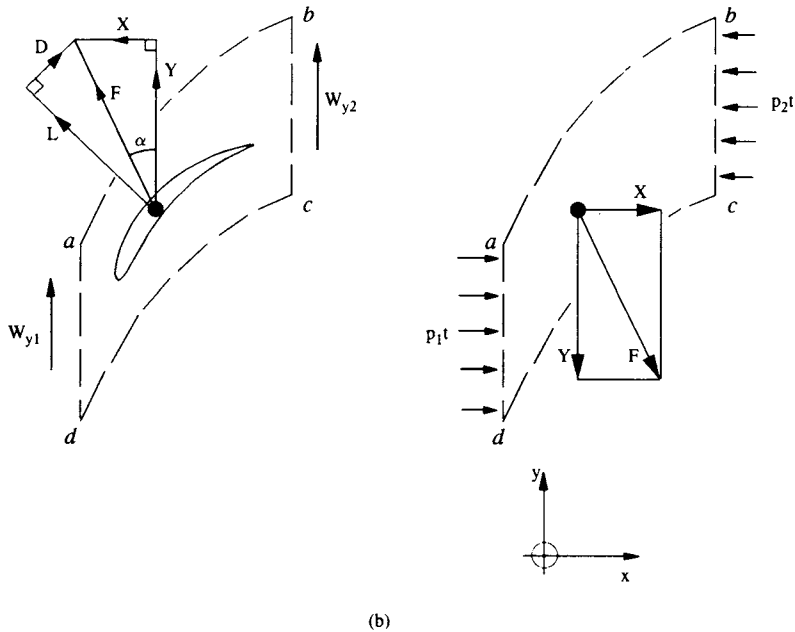
Fig. 2.6 Aerodynamic forces acting upon a compressor blade and applied forces acting on a control volume *abcd*: (a) blade force *F* and its components *L* and *D* or *X* and *Y*; (b) blade reaction force *F* and external pressure forces applied to control volume *abcd*

into its components parallel to the x and y axes, namely X and Y. A balance of forces on the control volume in the x direction may be stated as follows:

(Force X applied by + (pressure force on *ad*) − (pressure force on *bc*) = 0
   the blade profile)

We take note that the pressure forces on *ab* and *dc* are equal and opposite and may thus be ignored. Expressed analytically we thus have

$$X = (p_2 - p_1)t$$

If we define stagnation pressure

$$p_\text{o} = p + \tfrac{1}{2}\rho W^2$$

and make use of velocity triangles, Fig. 2.5, the above equation transforms into

$$
\begin{aligned}
X &= \tfrac{1}{2}\rho(W_1^2 - W_2^2)t - (p_{\text{o}1} - p_{\text{o}2})t \\
&= \tfrac{1}{2}\rho W_x^2 t\,(\tan^2\beta_1 - \tan^2\beta_2) - \Delta p_\text{o} t \\
&= \rho W_\infty^2 t \tan\beta_\infty(\tan\beta_1 - \tan\beta_2) - \Delta p_\text{o} t
\end{aligned}
\tag{2.3}
$$

where $\Delta p_\text{o} = p_{\text{o}1} - p_{\text{o}2}$ is the stagnation pressure drop across the cascade. In reality of course the stagnation pressure will vary across *bc* in passing through the blade wake. A long way downstream of the blade row, on the other hand, the wake will

have diffused across the blade pitch t sufficiently for us to regard the flow as uniform, whereupon the above analysis is valid.

An analogous expression for the y component of the blade force F may be obtained by applying Newton's Second Law to the control volume. First we observe that the mass flow rate per unit length of blade is given by $\dot{m} = \rho W_x t$. We then have

(Force applied to	(Rate of change of
control volume in $=$	momentum in y
y direction)	direction)

or

$$- Y = \dot{m}(W_{y2} - W_{y1})$$
$$= \rho W_x^2 t (\tan \beta_2 - \tan \beta_1) \qquad (2.4)$$

2.1.1 Case 1 – Frictionless flow

To isolate the effect of the lift force L let us consider first the simpler case of frictionless fluid flow, for which the stagnation pressure loss Δp_0 will be zero. Making use of Eqns (2.3) and (2.4) with $\Delta p_0 = 0$, the angle α, Fig. 2.6, then follows from

$$\tan \alpha = \frac{X}{Y} = \frac{\rho W_x^2 t \tan \beta_\infty (\tan \beta_1 - \tan \beta_2)}{\rho W_x^2 t (\tan \beta_1 - \tan \beta_2)} \qquad (2.5)$$
$$= \tan \beta_\infty$$

or $\alpha = \beta_\infty$. Thus we see from Figs 2.5 and 2.6 that the lift force L is normal to the vector mean velocity W_∞, and its components are thus

$$\left. \begin{array}{l} X = L \sin \beta_\infty \\ Y = L \cos \beta_\infty \end{array} \right\} \qquad (2.6)$$

2.1.2 Case 2 – Real cascades with fluid friction

For real fluids influenced by viscosity, however, the full X force equation (2.3) must be used including the loss term $\Delta p_0 t$. Now this may be attributed entirely to the drag force D taken in the direction normal to L. Thus making use of both Eqns (2.3) and (2.4) and resolving forces parallel to D we have

$$D = Y \sin \beta_\infty - X \cos \beta_\infty$$
$$= \Delta p_0 t \cos \beta_\infty \qquad (2.7)$$

Introducing this into the definition of C_D, Eqn (2.2b), we obtain

$$C_D = \frac{D}{\frac{1}{2}\rho W_\infty^2 l} = \left\{ \frac{\Delta p_0}{\frac{1}{2}\rho W_\infty^2} \right\} \frac{t}{l} \cos \beta_\infty$$
$$= \zeta_\infty \left(\frac{t}{l} \right) \cos \beta_\infty \qquad (2.8)$$

where the cascade loss coefficient ζ_∞ based upon vector mean velocity is defined as

$$\zeta_\infty = \frac{\Delta p_0}{\frac{1}{2}\rho W_\infty^2} \tag{2.9}$$

An expression for C_L may be derived now as follows. First we obtain the lift force L from Eqns (2.3) and (2.4):

$$L = X \sin \beta_\infty + Y \cos \beta_\infty$$
$$= \rho W_x^2 t (\tan \beta_1 - \tan \beta_2) \sin \beta_\infty - (\Delta p_0 t) \sin \beta_\infty$$
$$= \rho W_\infty^2 t (\tan \beta_1 - \tan \beta_2) \cos \beta_\infty - (\Delta p_0 t) \sin \beta_\infty$$

Hence the lift coefficient, Eqn (2.2a), becomes

$$C_L = 2 \frac{t}{l} (\tan \beta_1 - \tan \beta_2) \cos \beta_\infty - \left(\frac{\Delta p_0}{\frac{1}{2}\rho W_\infty^2} \right) \left(\frac{t}{l} \right) \sin \beta_\infty$$
$$= 2 \frac{t}{l} (\tan \beta_1 - \tan \beta_2) \cos \beta_\infty - C_D \tan \beta_\infty \tag{2.10}$$

We observe that the presence of viscous drag forces expressed through the drag coefficient C_D results in a reduction of the lift coefficient below that of C_{Li} for a frictionless fluid, namely

$$C_{Li} = 2 \frac{t}{l} (\tan \beta_1 - \tan \beta_2) \cos \beta_\infty \qquad \text{for frictionless flow} \tag{2.10a}$$

We note also that C_L is strongly affected by the term $(\tan \beta_1 - \tan \beta_2)$ which itself is closely related to fluid deflection $(\beta_1 - \beta_2)$ as we might expect. C_L is also linearly dependent on the cascade pitch/chord ratio t/l as again we would expect. t/l and the 'solidity' $\sigma = l/t$ are thus important cascade geometrical parameters through which the designer can exercise close control over blade loading.

In the case of axial fans, for which the blade spacing is often quite wide, e.g. $t/l \gg 1.0$, a rough guide to profile selection is provided by the abundance of published C_L, C_D data for isolated aerofoils such as that given by I. H. Abbott and A. E. Von Doenhoff (1959) or F. Riegels (1961). This reveals that a lift coefficient of value $C_L = 1.2$ would be close to the maximum achievable for many aerofoils. For a fan application a more conservative design value of say $C_L = 0.8$ to 1.0 would be desirable to increase the allowable stall margin. An example will help to illustrate how one might then select a suitable pitch chord ratio.

Example 2.1

Problem
Given $\beta_1 = 65°$ and $\beta_2 = 60°$ estimate t/l for a fan cascade for which $C_L = 0.8$. Given a C_L/C_D ratio of 30 calculate the loss coefficient.

Solution
From Eqn (2.1),

$$\beta_\infty = \arctan ((\tan 65° + \tan 60°)/2) = 62.71°$$
$$C_D = C_L/30 = 0.026\,67$$

From Eqn (2.10),

$$\frac{t}{l} = \frac{C_L + C_D \tan \beta_\infty}{2 (\tan \beta_1 - \tan \beta_2) \cos \beta_\infty} = 2.2519$$

From Eqn (2.8),

$$\zeta_\infty = \frac{C_D}{(t/l) \cos \beta_\infty} = 0.025\,828$$

2.2 Diffuser efficiency of a compressor cascade

While the primary role of a fan is to move large volumes of air or other gas while raising its pressure sufficiently to overcome the duct system losses, priorities are reversed for an axial compressor. In view of the requirement for a large pressure rise, the primary role of the compressor cascade is that of a diffuser. The standard definition of diffuser efficiency η_D may then be applied:

$$\eta_D = \frac{\text{Actual pressure rise}}{\text{Ideal pressure rise}} = \frac{p_2 - p_1}{\frac{1}{2}\rho(W_1^2 - W_2^2)} \qquad (2.11)$$

Application of the steady flow energy equation for incompressible flow to the control volume results in

$$p_2 - p_1 = \frac{1}{2}\rho(W_1^2 - W_2^2) - \Delta p_o$$

so that η_D may be rewritten

$$\eta_D = 1 - \frac{\Delta p_o}{\frac{1}{2}\rho(W_1^2 - W_2^2)}$$

and after substitutions from Eqns (2.8) to (2.10)

$$\eta_D = 1 - \frac{\Delta p_o}{\rho W_x^2 \tan \beta_\infty (\tan \beta_1 - \tan \beta_2)}$$

$$\qquad (2.12)$$

$$= 1 - \frac{\zeta_\infty}{\sin(2\beta_\infty)(\tan \beta_1 - \tan \beta_2)}$$

or

$$\eta_D = 1 - 2\left(\frac{C_D}{C_{Li}}\right)\frac{1}{\sin(2\beta_\infty)} \qquad (2.13)$$

As shown by Dixon (1975), quoting Howell (1945), the lift drag ratio C_{Li}/C_D varies weakly with β_∞ for efficient cascades and may be assumed constant when differentiating η_D to estimate the optimum β_∞. Thus

$$\frac{d\eta_D}{d\beta_\infty} \approx 4\left(\frac{C_D}{C_{Li}}\right)\frac{\cos(2\beta_\infty)}{\sin^2(2\beta_\infty)} = 0 \quad \text{for } (\beta_\infty)_{opt}$$

This simple analysis shows that if we regard a compressor cascade as a diffuser the optimum performance requires that $\cos(2\beta_\infty) = 0$, that is $\beta_\infty = 45°$. This provides a very simple way forward as a basic design guide but of course ignores a wide range of other factors which may influence compressor performance such as annulus wall frictional losses, secondary losses due to the impact of the annulus wall boundary layer upon the blade row, and tip clearance losses due to leakage through the gap between blade tip and casing. Some of these matters will be dealt with briefly later where pertinent, but detailed reviews have been given by Dixon (1975) and Horlock (1958, 1966).

Apart from these additional influences, closer consideration of the blade profile fluid dynamics reveals how far in practice the actual flow departs from that of an equivalent diffuser. To illustrate this the blade surface pressure distribution for a typical well-designed compressor cascade is compared in Fig. 2.7 with the pressure rise through an equivalent two-dimensional plane walled diffuser, Diffuser No. 1. For this purpose normal practice in dealing with compressor cascades is to define a dimensionless surface pressure coefficient C_{p1} based upon inlet dynamic head:

$$C_{p1} = \frac{p - p_1}{\frac{1}{2}\rho W_1^2} \tag{2.14}$$

where p is the static pressure on the blade surface and p_1 is the static pressure upstream of the cascade.

The cascade considered here was designed and analysed using the program CASCADE, in order to deliver an ideal lift coefficient $C_{Li} = 1.15$, given $t/l = 1.0$ and $\beta_\infty = 45°$. To achieve this some preliminary analysis is required to determine β_1 and β_2. Equations (2.1) and (2.10a) may be rearranged into the form

$$\left.\begin{aligned} \tan\beta_1 + \tan\beta_2 &= 2\tan\beta_\infty \\ \tan\beta_1 - \tan\beta_2 &= \frac{C_{Li}}{2\frac{t}{l}\cos\beta_\infty} \end{aligned}\right\} \tag{2.15}$$

providing a pair of simultaneous equations whose solution yields $\beta_1 = 54.59°$, $\beta_2 = 30.69°$. Making use of the design technique outlined in Appendix II, Section II.8, the cascade was designed for smooth inlet flow to deliver the required outlet angle and overall fluid deflection $\beta_1 - \beta_2 = 23.90°$.

Before making general observations about the predicted C_{p1} distribution it is of help to note the three following special values of the pressure coefficient C_{p1} if we apply its definition, Eqn (2.14), to conditions upstream and downstream of the cascade and also to the leading edge stagnation point.

Upstream of the cascade, point A:

$$(C_{p1})_{upstream} = \frac{p_1 - p_1}{\frac{1}{2}\rho W_1^2} = 0$$

Downstream of the cascade, point C:

$$(C_{p1})_{downstream} = \frac{p_2 - p_1}{\frac{1}{2}\rho W_1^2} = 1 - \left(\frac{W_2}{W_1}\right)^2$$

$$= 1 - \left(\frac{\cos\beta_1}{\cos\beta_2}\right)^2 = 0.546$$

Surface pressure distribution diagram

Compressor cascade

Equivalent diffuser No. 1
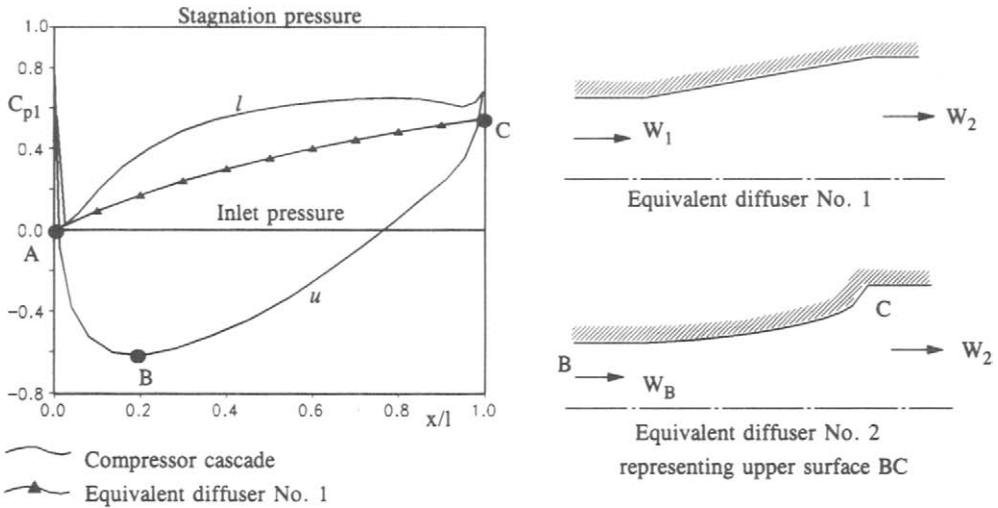
Cascade data

$t/\ell = 1.0$, $\lambda = 41.28°$, $\beta_1 = 54.59°$, $\beta_2 = 30.69°$
Circular arc camber with $\theta = 41.5°$, C4 profile

u Upper blade surface
l Lower blade surface

Fig. 2.7 Surface pressure distribution for a compressor cascade and equivalent diffusers

At the stagnation point on the blade profile leading edge where the pressure p equals the stagnation pressure p_o,

$$p - p_1 = p_o - p_1 = \tfrac{1}{2}\rho W_1^2$$

so that

$$(C_{p1})_{\text{stagnation}} = 1.0$$

Interpretation of C_{p1} plots is made much easier by this observation. As we may see from Fig. 2.7, the static pressure in general rises for both the upper (convex) surface of the blades marked u and the lower (concave) surface marked l. As we approach the leading edge ($x/l = 0$) and the trailing edge ($x/l = 1$), the averages of the upper and lower surface C_{p1} values converge towards points A and C respectively, showing that the cascade is indeed raising the static pressure overall from $C_{p1} = 0$ to $C_{p1} = 0.546$ as required.

Also shown in Fig. 2.7 is the C_{p1} curve for the equivalent plane-walled diffuser, Diffuser No. 1, connecting points A and C. It is immediately apparent just how far from this the actual compressor cascade C_{p1} departs. On the lower surface l the pressure remains a good deal higher than on the equivalent diffuser following a fairly rapid diffusion over the range $0 < x/l < 0.4$. On the blade upper surface u, on the other hand, conditions are much more demanding than those required of the equivalent diffuser. First of all the static pressure falls rapidly from the leading edge stagnation point $C_{p1} = 1.0$ to a minimum value of $C_{p1} = -0.6138$ at location B where

$x/l = 0.1656$. Following this the static pressure has to rise more than double the overall $(p_2 - p_1)$ of the cascade over the remaining upper surface section BC. Thus the upper or convex surface of a compressor cascade is subjected to extremely high diffusions, in this example more than double those of the cascade overall equivalent diffuser. In view of this S. Lieblein (1956) developed an experimental correlation linking this blade upper surface diffusion between points B and C to cascade losses and loading limits, since boundary layer growth and stability on this section of a compressor blade are known to have dominating aerodynamic effects. We will return to this matter in Section 2.7. For the present purpose it will be instructive just to consider the equivalent diffuser for the upper surface section BC, shown here as Diffuser No. 2. The aim is to select its area A as a fraction of the area A_1 at inlet with velocity W_1 such that the upper surface C_{p1} value is obtained along the diffuser. If the local velocity on the blade surface is v_s, then for incompressible flow the continuity equation gives

$$\frac{A}{A_1} = \frac{W_1}{v_s}$$

But from the definition of C_{p1}

$$C_{p1} = \frac{p - p_1}{\frac{1}{2}\rho W_1^2} = 1 - \left(\frac{v_s}{W_1}\right)^2$$

and hence for the equivalent diffuser to model the flow over the blade surface section BC,

$$\frac{A}{A_1} = \frac{1}{\sqrt{1 - C_{p1}}} \tag{2.16}$$

From this we observe two things as compared with equivalent diffuser No. 1. First, much more overall diffusion is required. Second, heavy diffusion demands are made upon the trailing edge. In practice the thickening boundary layers would tend to separate close to the trailing edge, contributing to losses and tending also to unload the blade in that region.

2.3 Specification of blade profile geometry

The foregoing discussion suggests that considerable care is needed when designing compressors or fans to select profile shapes which will produce stable diffusing flows, particularly on the vulnerable upper surface. There are two approaches to blade profile selection which are often referred to as the *direct* (analysis) and *inverse* (synthesis) methods. These may be described briefly as follows:

(1) *Direct (or analysis) method.* Blade profiles are generated by a systematic geometrical technique such as that illustrated in Fig. 2.8. Series of such cascades are then analysed either by experimental test or by theoretical analysis to identify the most efficient geometries and their detailed aerodynamic performance.

(2) *Inverse (or synthesis, PVD) methods.* This technique allows the designer to specify the surface velocity or pressure distribution along the blade surface.
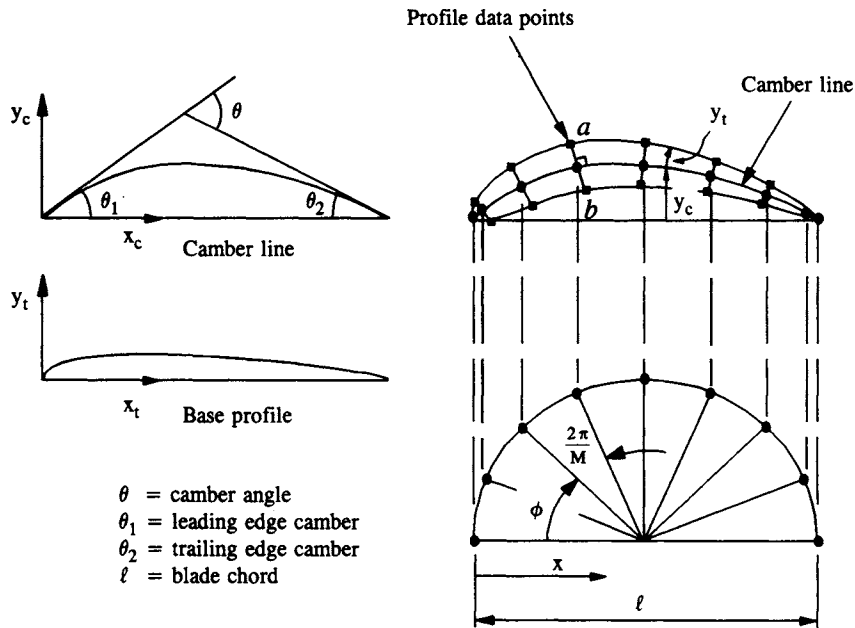
Fig. 2.8 Construction of a blade profile from a camber line and a base profile

Extremely advanced mathematical analyses are now available to find the blade profile which will generate this. Such methods are often referred to as PVD (prescribed velocity distribution) analyses.

Although *inverse* methods appear to offer the perfect solution for prescribing in advance the blade aerodynamic behaviour one would like, there are snags and we will mention these later, in Section 2.5. In engineering practice the systematic procedures of the *direct* method offer special attractions for building up experimental and theoretical data systematically for closely related families of cascades. This approach has formed the bedrock of compressor and turbine blade profile development. The geometrical method shown in Fig. 2.8 is widely used in the UK, the USA and elsewhere and follows that adopted for isolated aerofoil design. Aerofoil profiles are constructed by superimposing a standard profile half-thickness shape y_t normal to and on either side of a camber line y_c. The camber line shape is usually either a circular arc or a parabola. Thickness distributions, sometimes called 'base profiles', are tabulated in such texts as Riegels (1961) and Abbott and Von Doenhoff (1959).

2.4 Use of program CASCADE to perform the *direct* analysis

A limited number of well-known thickness distributions have been provided in the data file PROFILES for use with the program CASCADE in the standard published format. These are recorded in Table 2.1. Although they are likely to be adequate for most purposes, instructions are given in Appendix II for the inclusion of more base profiles if required.

Table 2.1 Sample of base profile thicknesses used in programs CASCADE and STACK

c4		T4		NACA 0012		NACA 0015		NACA 66-010		NGTEmod	
x_t	y_t	x_t	y_t	x_t	y_t	x_t	y_t	x_t	y_t	x_t	y_t
0.00	0.00	0.00	0.00	0.00	0.000	0.00	0.000	0.0	0.0	0.00	0.000
1.25	1.65	1.25	1.17	1.25	1.894	1.25	2.367	0.5	0.759	1.25	1.375
2.50	2.27	2.50	1.54	2.50	2.615	2.50	3.268	0.75	0.913	2.50	1.910
5.00	3.08	5.00	1.99	5.00	3.555	5.00	4.443	1.25	1.141	5.00	2.680
7.50	3.62	7.50	2.37	7.50	4.200	7.50	5.250	2.5	1.516	7.50	3.195
10.00	4.02	10.00	2.74	10.00	4.683	10.00	5.853	5.0	2.087	10.00	3.600
15.00	4.55	15.00	3.40	15.00	5.345	15.00	6.682	7.5	2.536	15.00	4.180
20.00	4.83	20.00	3.95	20.00	5.737	20.00	7.172	10.0	2.917	20.00	4.550
30.00	5.00	30.00	4.72	25.00	5.941	25.00	7.427	15.0	3.53	30.00	4.950
40.00	4.89	40.00	5.00	30.00	6.002	30.00	7.502	20.0	4.001	40.00	4.820
50.00	4.57	50.00	4.67	40.00	5.803	40.00	7.254	25.0	4.363	50.00	3.980
60.00	4.05	60.00	3.70	50.00	5.294	50.00	6.617	30.0	4.636	60.00	3.250
70.00	3.37	70.00	2.51	60.00	4.563	60.00	5.704	35.0	4.832	70.00	2.450
80.00	2.54	80.00	1.42	70.00	3.664	70.00	4.580	40.0	4.953	80.00	1.740
90.00	1.60	90.00	0.85	80.00	2.623	80.00	3.279	45.0	5.0	85.00	1.500
95.00	1.06	95.00	0.72	90.00	1.448	90.00	1.810	50.0	4.971	90.00	1.270
100.00	0.00	100.00	0.00	95.00	0.807	95.00	1.008	55.0	4.865	92.50	1.170
				100.00	0.000	100.00	0.000	60.0	4.665	95.00	1.080
								65.0	4.302	97.50	0.980
								70.0	3.787	100.00	0.000
								75.0	3.176		
								80.0	2.494		
								85.0	1.773		
								90.0	1.054		
								95.0	0.408		
								100.0	0.0		

The program CASCADE is able to construct the blade profile of your choice following the geometrical strategy shown in Fig. 2.8 which concentrates the profile data points into the leading and trailing edge region. If we first construct a semi-circle of radius $l/2$ as shown and divide it into M equal segments $\Delta\phi = 2\pi/M$, camber line x_c coordinates are then given by

$$\frac{x_c}{l} = \frac{1}{2}(1 - \cos\phi) \qquad (2.17)$$

Camber line y_c coordinates and slopes dy_c/dx_c may then be calculated. The half-thickness y_t may then be interpolated from the tabulated base profile data. The coordinates of profile points a and b on the upper and lower surface then follow from

$$\left.\begin{array}{l} x_a = x_c - y_t\sin\theta_c \quad \text{upper surface} \\ y_a = y_c + y_t\cos\theta_c \quad \ldots\ldots \end{array}\right\} \qquad (2.18a)$$

$$\left.\begin{array}{l} x_b = x_c + y_t\sin\theta_c \quad \text{lower surface} \\ y_b = y_c - y_t\cos\theta_c \quad \ldots\ldots \end{array}\right\} \qquad (2.18b)$$

where $\theta_c = \arctan(dy_c/dx_c)$ is the slope of the camber line. The camber angle θ is defined in Fig. 2.8 together with the leading and trailing edge camber angles θ_1 and θ_2.

An interesting application of the *direct* method is shown in Fig. 2.9 where three different cascade profiles have been selected to achieve the same overall design requirements as the cascade shown in Fig. 2.7, namely

(1) $t/l = 1.0$, $\beta_1 = 54.59°$, $\beta_2 = 30.69°$,
(2) shock-free inflow, and
(3) three camber line types:
    (a) Circular arc.
    (b) Parabola with position of maximum camber $x_c/l = 0.3$.
    (c) Parabola with position of maximum camber $x_c/l = 0.7$.

Fluid dynamic analysis of these three cascades illustrates the important effect which camber line shape has upon the surface pressure distribution and especially that of the upper surface u. By moving the position of maximum camber forward towards the leading edge, the blade loading $C_{p1l} - C_{p1u}$, and centre of lift are also moved forward and vice versa.

In case (b), $(x_c/l)_{max} = 0.3$, the upper surface pressure falls rapidly to a very low value $C_{p1} = -1.0$ at $x/l = 0.2$ and then diffuses steadily towards the trailing edge. On the lower surface the pressure remains almost constant over most of the chord length. This profile might exhibit better aerodynamic characteristics than profile (a) but would be less attractive for pumps where its low C_{p1u} would reduce its threshold for resisting cavitation.

Considering case (c), $(x_c/l)_{max} = 0.7$, moving the position of maximum camber towards the trailing edge has produced a fairly constant pressure over most of the upper surface $0.1 < x/l < 0.8$ followed by a dramatic diffusion. Although the latter might result in flow separation approaching the trailing edge, this profile would certainly offer better cavitation performance due to its lightly loaded leading edge and generally higher upper surface pressure distribution.

2.5   Design of a cascade by the *inverse* method

Two options are available for aerofoil or cascade design by the *inverse* method.

Option A permits the designer to specify a prescribed velocity distribution (PVD) (and therefore pressure distribution) on both upper and lower surfaces, resulting in automatic synthesis of the entire profile to meet this specification. Although this sounds attractive the procedure has its setbacks. At worst the designer may choose an impossible PVD for which there is no corresponding blade profile. At best his chosen PVD may lead to unsuitable profile thickness distributions.

In view of the latter problems, Wilkinson (1967) proposed *Option B* whereby the PVD is limited to the more aerodynamically sensitive upper surface only but a profile thickness is also prescribed. In effect the inverse method is then designing the camber line shape required to achieve the desired PVD on the upper surface. The velocity distribution on the lower surface is simply accepted to adjust freely to whatever it will.

Theoretical techniques to achieve this, often quite ingenious, have been invented by many research analysts including Ackeret (1942), Railly (1965), Wilkinson (1967), Cheng (1981) and Lewis (1982) and some of these have been reviewed by Lewis (1991) for application to aerofoils, cascades and slotted aerofoils and cascades. Cheng,
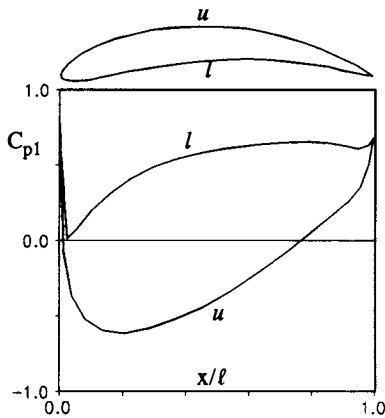
(a) Circular arc camber

$(x_c/\ell)_{max}$ $= 0.5$
θ $= 41.50°$
λ $= 41.28°$
t/ℓ $= 1.0$
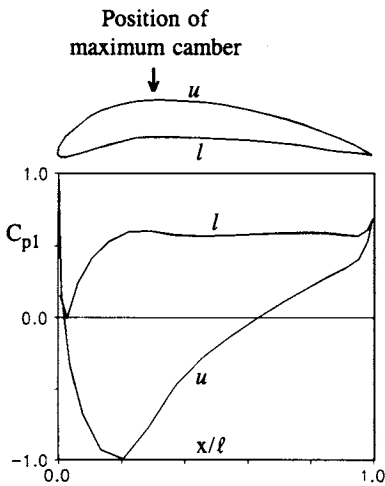
(b) Parabolic camber

$(x_c/\ell)_{max}$ $= 0.3$
θ $= 48.0°$
λ $= 39.5°$
t/ℓ $= 1.0$
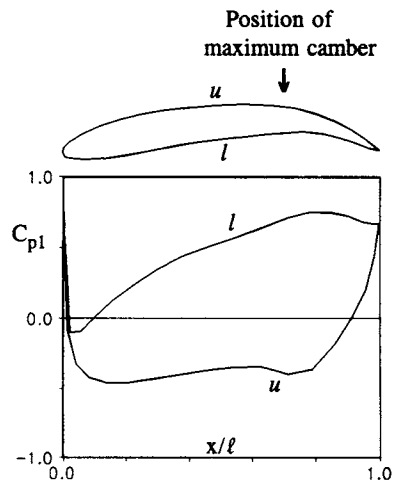
(c) Parabolic camber

$(x_c/\ell)_{max}$ $= 0.7$
θ $= 44.0°$
λ $= 44.0°$
t/ℓ $= 1.0$

Fig. 2.9 Effect of camber line shape on surface pressure distribution of a fan cascade designed for shock-free inflow with $\beta_1 = 54.59°$ and $\beta_2 = 30.69°$

applying this technique to the design of wind turbine blade sections, has shown that extremely high lift/drag ratios may be achieved.

For commercial use a high lift fan cascade was required to produce a deflection from $\beta_1 = 67.45°$ to $\beta_2 = 53.33°$. The *inverse* boundary layer method of Stratford (1959) was used to prescribe the upper surface PVD as shown in Fig. 2.10. Further details of this, and of the inverse cascade analysis employed, have been published by Lewis (1982, 1991). The surface velocity v_s/W_1 (i.e. normalised by the inlet velocity W_1) was kept constant for the first 30% of the blade surface and then diffused to
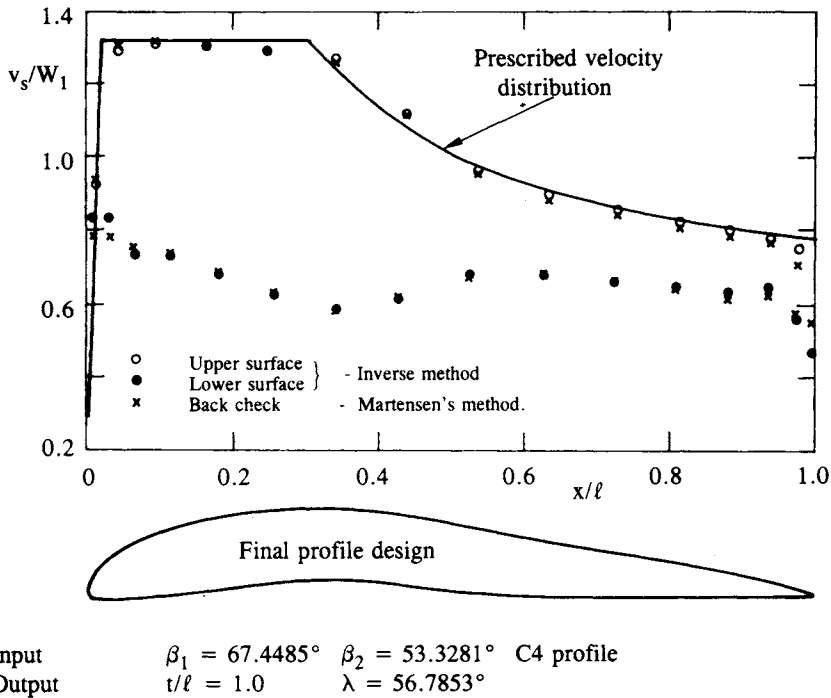
Fig. 2.10 Inverse design of a fan cascade for prescribed velocity distribution on the upper surface and with a C4 base profile thickness (reproduced by courtesy of the American Society of Mechanical Engineers)

a fairly high value of $v_s/W_2 = 1.2$ at the trailing edge. Adopting Option B, a C4 profile was selected to predetermine the profile thickness distribution. The outcome of the inverse computational procedure is shown in Fig. 2.10, namely a complete prediction of v_s for both surfaces and the consequent profile shape. Also shown is a back-check analysis of flow past the designed profile using the *analysis* program CASCADE which confirms that the required PVD was obtained. The predicted velocity on the lower surface is almost constant ($v_s \approx 0.6$) and perfectly acceptable.

2.6 'Shock-free' inflow and optimum incidence of a cascade

In Section 2.4 we referred without explanation to the so-called 'shock-free' inflow condition. This terminology is a little unfortunate since it has nothing to do with the shock waves caused by compressibility effects in high speed flow. It is instead frequently used to refer to the particular inlet angle β_1 for which the leading edge stagnation point is located precisely on the end of the profile camber line, Fig. 2.11(b). For greater or smaller inlet angles the stagnation point will move instead onto the lower or upper surface respectively as illustrated. Shock-free inlet flow thus ensures the smoothest entry conditions into the cascade and is thus likely to be close to the minimum loss situation.

Most published correlations refer not to the optimum inlet angle β_1 of a cascade but to the optimum angle of incidence i since this parameter relates more directly to profile geometry. The angle of incidence i is defined as the angle between the inlet
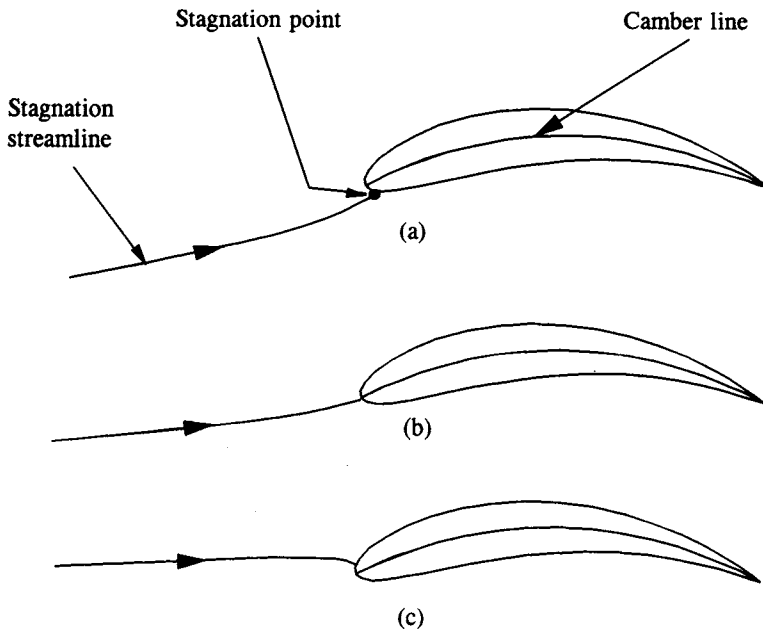
Fig. 2.11 Stagnation streamline and 'shock-free' inflow: (a) $\beta_1 >$ shock-free inlet angle; (b) shock-free inlet flow; (c) $\beta_1 <$ shock-free inlet angle
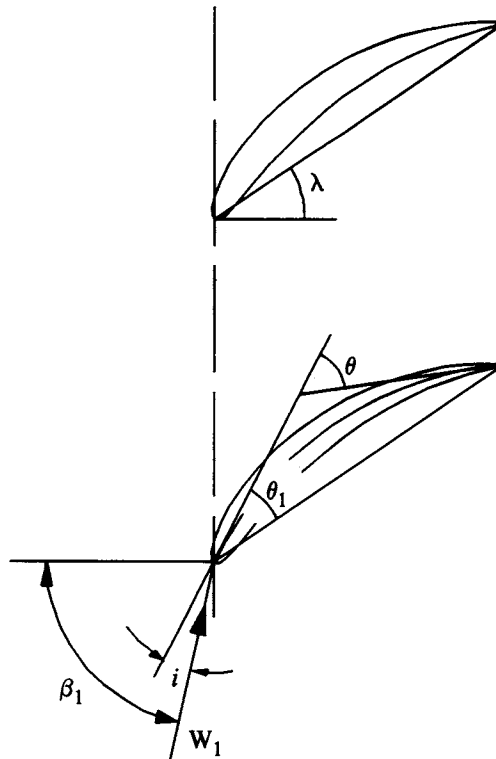
Fig. 2.12 Definition of incidence angle i
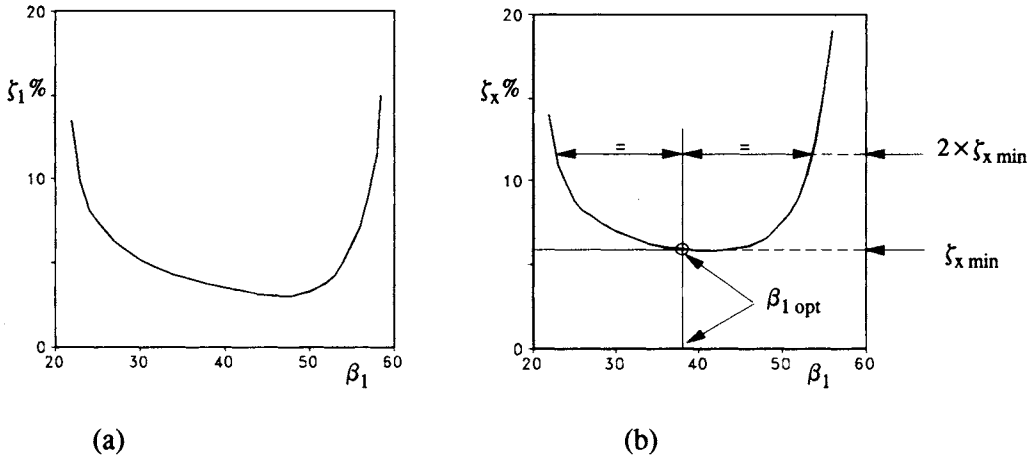
Fig. 2.13 Typical cascade loss coefficients versus inlet angle: (a) ζ_1 versus β_1; (b) ζ_x versus β_1

velocity vector W_1 and the tangent to the camber line. From Fig. 2.12 this can be related directly to β_1 through

$$i = \beta_1 - \lambda - \theta_1 \qquad (2.19)$$

In general i will not necessarily be zero but will normally be a small negative angle. For example, for case (a) shown in Fig. 2.7 designed for shock-free inflow, the shock-free incidence i_{SF} is given by

$$i_{SF} = 54.59° - 41.28° - \tfrac{1}{2} \times 41.5° = -7.44°$$

Designing for shock-free inflow is a simple matter using modern flow analyses such as the computer program CASCADE, Appendix II, Section II.8. However, the shock-free inlet angle or incidence may not necessarily coincide exactly with that for minimum loss, which will usually be one or two degrees greater (e.g. say $\beta_1 = 56.59°$, $i = -5.44°$ for the case under consideration).

For the production of experimental correlations, on the other hand, there is no need to search for the shock-free inflow condition since the cascade loss coefficient may be measured directly by means of a wake traverse. The strategies involved have been adequately outlined by Horlock (1958), Gostelow (1984) and Cumpsty (1989) and will not be repeated here. A typical presentation of loss versus inlet angle for a compressor cascade is shown in Fig. 2.13 where the loss coefficient ζ_1 is normalised by the inlet dynamic head. ζ_1 is defined as follows and may be related to ζ_∞, Eqn (2.9), through

$$\zeta_1 = \frac{\Delta p_o}{\tfrac{1}{2}\rho W_1^2} = \zeta_\infty \left(\frac{\cos\beta_1}{\cos\beta_\infty} \right)^2 \qquad (2.20)$$

Although cascade loss data are frequently plotted as ζ_1 versus β_1 or i as shown in Fig. 2.13(a), this is to some extent misleading since the presence of $\tfrac{1}{2}\rho W_1^2$ in the denominator of ζ_1 tends to distort the plot. A better approach is to plot the actual loss Δp_o instead or alternatively to define a loss coefficient based upon the velocity perpendicular to the cascade W_x, which is not a function of the inlet angle. ζ_x may thus be defined as

$$\zeta_x = \frac{\Delta p_o}{\tfrac{1}{2}\rho W_x^2} = \zeta_1/\cos^2\beta_1 \qquad (2.21)$$

As shown by Fig. 2.13(b), the resulting curve becomes roughly symmetrical about the inlet angle $\beta_1 = 38°$ which can be taken as the optimum inlet angle.

Because the loss curve $\zeta_x(\beta_1)$ is fairly flat, identification of the minimum loss point is not always easy. The technique adopted by S. Lieblein (1956), illustrated in Fig. 2.13(b), is much more definitive. At excessively high or low inlet angles the losses will suddenly begin to rise rapidly until the cascade reaches either positive or negative stall. Lieblein defined stall arbitrarily as the inlet angles or incidences for which the loss coefficient reaches twice the minimum value. The optimum inlet angle β_1 is then taken as the average of the positive and negative stalling inlet angles. Stall is in reality the condition at high positive or negative incidence for which the fluid separates catastrophically from the blade surface resulting in sudden collapse of lift and increase in drag and therefore also of loss. Lieblein's definition of $(\beta_1)_{\text{opt}}$ is thus a sensible concept since it takes stall into consideration by ensuring a good stall margin on either side of the optimum or reference inlet angle.

2.7 Diffusion factors for compressor cascades

Early on in our discussion of cascade performance in Section 2.2 we considered the idea of the compressor or fan cascade as a diffuser and postulated the concept of an equivalent diffuser in Fig. 2.7 and Eqn (2.16). Examination of the blade surface pressure distribution revealed, however, that for a typical cascade the diffusion, i.e. pressure rise, demanded of the upper surface of the blade is always much greater than the overall pressure rise. Consequently the boundary layer developed on the upper surface exerts the predominant influence upon compressor cascade aerodynamic performance. S. Lieblein (1956), based on earlier unpublished work (Lieblein *et al.*, 1953), was the first to identify this principle and to develop the 'diffusion factor' technique as a means for setting suitable aerodynamic loading limits on compressor cascades. We will refer here to two of his definitions of diffusion factor.

2.7.1 Local diffusion factor

Previously, in Fig. 2.7, we considered the surface pressure coefficient C_{p1} defined by Eqn (2.14). Lieblein instead considers the surface velocity distribution and defines the local diffusion factor as

$$D_{\text{loc}} = \frac{W_{\text{max}} - W_2}{W_{\text{max}}} \tag{2.22}$$

where W_{max} is the maximum surface velocity distribution and W_2 is the cascade outlet velocity. By experimental investigation of boundary layer behaviour, Lieblein has shown that D_{loc} should not exceed 0.5.

Now W_{max} will correspond to the minimum surface pressure point on the blade surface, namely location B in Fig. 2.7. But from Eqn (2.14), the maximum surface velocity W_{max} corresponding to local pressure p_{min} may be expressed as

$$\frac{W_{\text{max}}}{W_1} = \sqrt{1 - (C_{p1})_{\text{min}}}$$

The local diffusion factor, Eqn (2.22), may thus be expressed in the alternative form

$$D_{\text{loc}} = 1 - \left(\frac{\cos \beta_1}{\cos \beta_2}\right) \frac{1}{\sqrt{1 - (C_{p1})_{\text{min}}}} \tag{2.23}$$
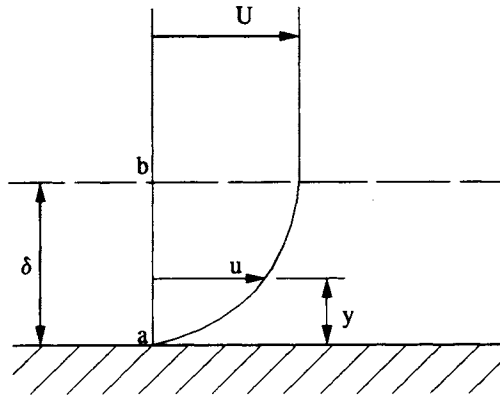
Fig. 2.14 Boundary layer past a plane wall

For our sample cascade, Fig. 2.7, $(C_{p1})_{min} = -0.62$, $\beta_1 = 54.59°$, $\beta_2 = 30.69°$, hence the predicted $D_{loc} = 0.470\,62$ lies within the acceptable limit but quite close to it.

A word should be said here about the underlying boundary layer criterion behind Lieblein's work. First we must define the concept of boundary layer momentum thickness θ with reference to the flow past a plane wall, Fig. 2.14. Due to fluid friction the velocity u parallel to the wall will decrease from the mainstream value U at the edge of the boundary layer, $y = \delta$, to zero at the wall, $y = 0$. The consequent decrement in momentum flux crossing the line ab may thus be expressed by the integral

$$\Delta M = \rho \int_0^\delta u(U - u)\,\mathrm{d}y \tag{2.24}$$

Dividing both sides by the factor ρU^2 we obtain the definition of boundary layer momentum thickness:

$$\theta = \int_0^\delta \frac{u}{U}\left(1 - \frac{u}{U}\right)\mathrm{d}y \tag{2.25}$$

Figure 2.15, given by Lieblein (1956), shows θ/l as a function of D_{loc} for the NACA-65 series of aerofoil cascades at their minimum loss incidence. From this summary of well-designed cascades it is clear that momentum thickness and therefore loss tend to increase dramatically for D_{loc} values greater than 0.5. This provides a simple limiting load criterion which can be applied to purely theoretical surface pressure predictions based upon frictionless flow methods such as the computer program CASCADE.

Before we move on to Lieblein's alternative definition of diffusion factor DF it is helpful to point out that θ/l may be related to the cascade loss coefficient ζ_1 as follows. From Fig. 2.16 the momentum flux decrement for one blade wake $\rho W_2^2(\theta_u + \theta_l)$ may be related to an equivalent pressure force $\Delta p_o t \cos \beta_2$ due to stagnation pressure loss averaged over one blade pitch viewed along the exit velocity vector W_2,

$$\Delta p_o t \cos \beta_2 = \rho W_2^2(\theta_u + \theta_l) \tag{2.26}$$
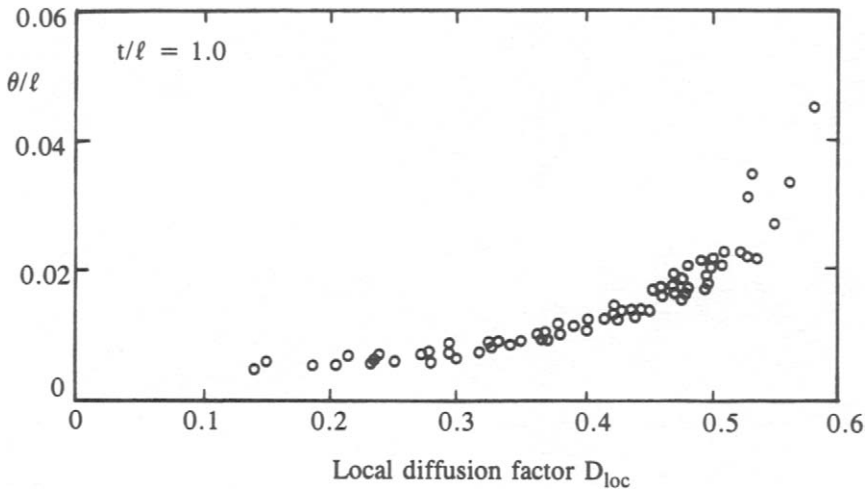
Fig. 2.15 Wake momentum thickness versus local diffusion factor for NACA-65 cascades at minimum loss incidence
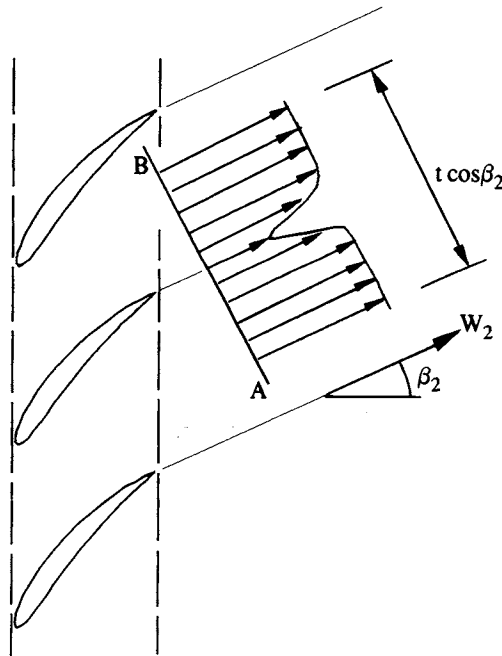
Fig. 2.16 Blade wake downstream of a cascade

where θ_u and θ_l are the momentum thicknesses of the trailing edge boundary layers. If these are absorbed into a wake momentum thickness $\theta = \theta_u + \theta_l$, Eqn (2.26) may be rearranged to give

$$\zeta_1 = \frac{\Delta p_o}{\frac{1}{2}\rho W_1^2} = 2\left(\frac{\theta}{l}\right)\frac{\sigma}{\cos\beta_2}\left(\frac{\cos\beta_1}{\cos\beta_2}\right)^2 \qquad (2.27)$$

www.semeng.ir
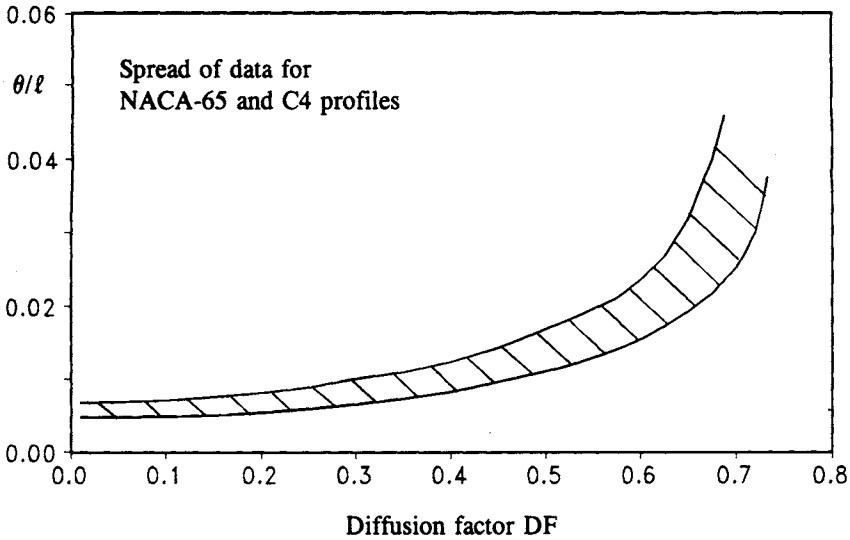
Fig. 2.17 Wake momentum thickness versus overall diffusion factor DF for NACA-65 and C4 aerofoils at minimum loss incidence

From this useful equation the reader may calculate the wake momentum thickness from the value of loss coefficient ζ_1 or vice versa.

2.7.2 Diffusion factor (earlier definition)

Prior to the advent of computational fluid dynamics it was not easy to predict the maximum surface velocity W_{max}. Lieblein *et al.* (1953) therefore developed the alternative form of diffusion factor DF based upon a postulated type of surface velocity distribution which in general resembled those measured on NACA-65 blades. Without repeating all the analysis involved, the final definition of DF is as follows:

$$DF = 1 - \frac{\cos \beta_1}{\cos \beta_2} + \frac{\cos \beta_1}{2}\left(\frac{t}{l}\right)(\tan \beta_1 - \tan \beta_2) \qquad (2.28)$$

Lieblein's plot of θ/l versus DF for the American NACA-65 and British C4 series of cascades is shown in Fig. 2.17, from which it is clear that DF = 0.6 imposes an upper limit for the allowable diffusion factors. In the case of our example cascade, Fig. 2.7, the predicted diffusion factor is thus $DF = 0.5618$.

2.7.3 Selection of optimum pitch/chord ratio for a compressor cascade

It follows from the above discussion that Eqn (2.28) may be rearranged to provide an expression for the maximum allowable pitch/chord ratio. If we introduce DF ≤ 0.6, we obtain

$$\frac{t}{l} \leq \frac{2 \cos \beta_1 / \cos \beta_2 - 0.8}{\cos \beta_1 (\tan \beta_1 - \tan \beta_2)} \qquad (2.29)$$
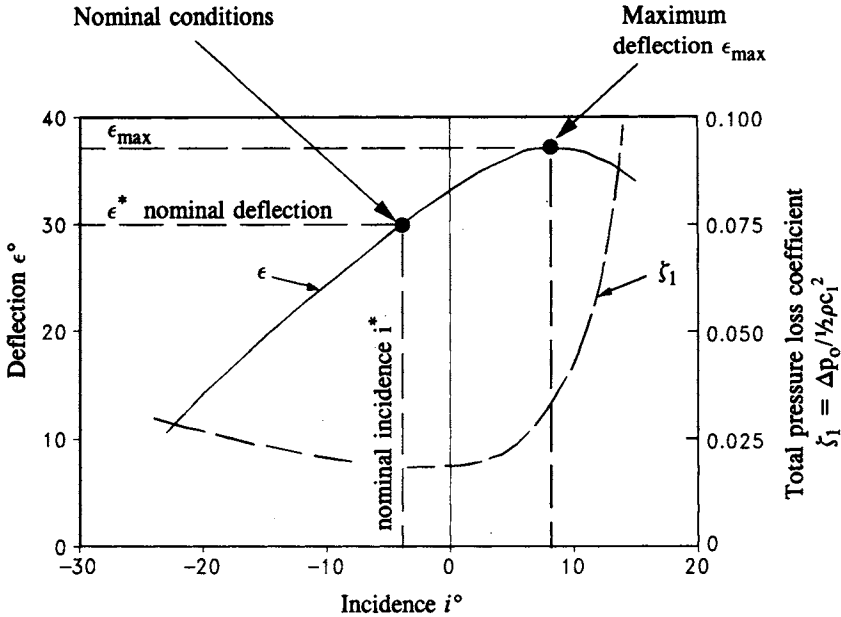
Fig. 2.18 Definition of cascade nominal conditions (from Howell (1942) by courtesy of HMSO)

For our example cascade for which we specified $\beta_1 = 54.59°$, $\beta_2 = 30.69°$, the maximum allowable pitch chord ratio is thus $t/l = 1.1623$, as compared with the more conservative value $t/l = 1.0$ previously used when predicting the pressure distribution in Fig. 2.7.

2.8 Nominal deflection and fluid deviation

2.8.1 Nominal deflection

An even simpler approach than that of Lieblein to the setting of cascade stall margins, postulated by A. R. Howell (1942, 1945) in the early days of gas turbine axial compressor development, has stood the test of time. Howell defined 'nominal' conditions for a compressor cascade as those relating to a fluid deflection $\varepsilon^* = \beta_1 - \beta_2$ equal to 80% of the stalling deflection, Fig. 2.18. Following Horlock (1958), stalling deflection could be referred to maximum attainable deflection. Alternatively we could adopt the definition of stall discussed in Section 2.6 and illustrated in Fig. 2.13, namely that incidence for which the loss is double the minimum possible value.

From experimental correlations Howell was able to obtain a relationship between ε^* and the nominal outlet angle β_2^* for a wide range of practical cascade geometries, Fig. 2.19(a), revealing the trends one would expect. Thus for a typical outlet angle, say $\beta_2^* = 30°$, the nominal deflection ε^* decreases substantially as t/l increases.

It is possible to compare this correlation with Lieblein's conceptually different diffusion factor approach outlined in Section 2.7. Equation (2.28) may be rearranged to read

$$\frac{t}{l} = 2 \left\{ \frac{\cos \beta_1 / \cos \beta_2 - 1 + \text{DF}}{\cos \beta_1 (\tan \beta_1 - \tan \beta_2)} \right\} \qquad (2.30)$$
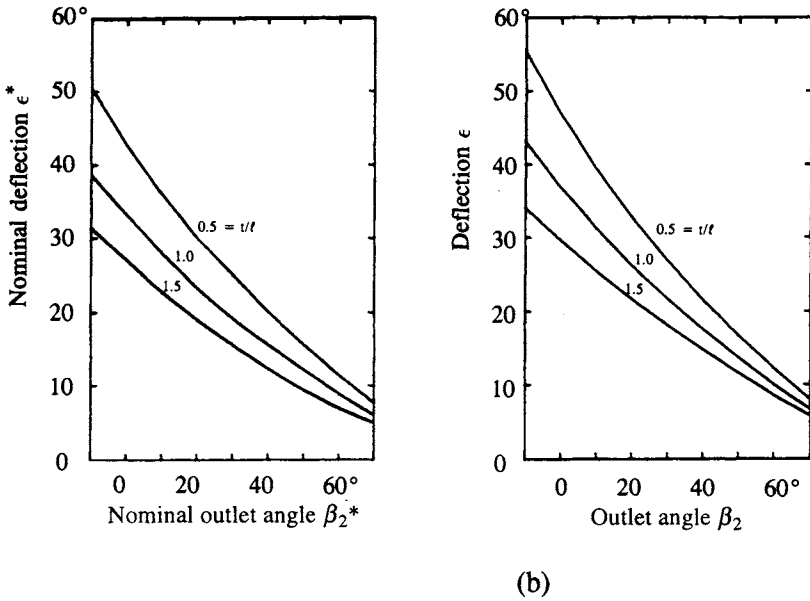
Fig. 2.19 Compressor cascade optimum deflection data, comparing A. R. Howell and S. Lieblein: (a) cascade nominal conditions (Howell, 1945) (reproduced by courtesy of the Institution of Mechanical Engineers); (b) data derived from Lieblein's method, Eqn (2.30)

Introducing a conservative diffusion factor DF = 0.5 into this equation, solutions for β_1 may be derived by an iterative procedure for prescribed values of t/l and β_2, resulting in Fig. 2.19(b). The similarity of this to Howell's data for cascades at 'nominal' conditions is quite remarkable for the extremely wide range of compressor cascades represented, Howell's correlation remaining slightly more conservative throughout (i.e. $\varepsilon_{\text{Lieblein}} > \varepsilon^*$).

2.8.2 Fluid deviation

In Section 2.6 and Fig. 2.12 we defined the incidence i as the angle between the fluid upstream velocity vector W_1 and the blade leading edge camber line. Analogous to this is the fluid deviation δ at exit from the cascade, Fig. 2.20, defined as the angle between the fluid exit velocity W_2 and the tangent to the camber line at exit. δ is thus given by

$$\delta = \beta_2 - \lambda + \theta_2 \tag{2.31}$$

and is a fine measure of departure of the fluid deflection from the blade curvature. Thus in general fluid deflection ε is less than the blade camber angle θ.

An empirical correlation relating nominal deviation δ^* to camber and pitch/chord ratio t/l has been given by Howell:

$$\delta^* = m\theta(t/l)^n \tag{2.32}$$
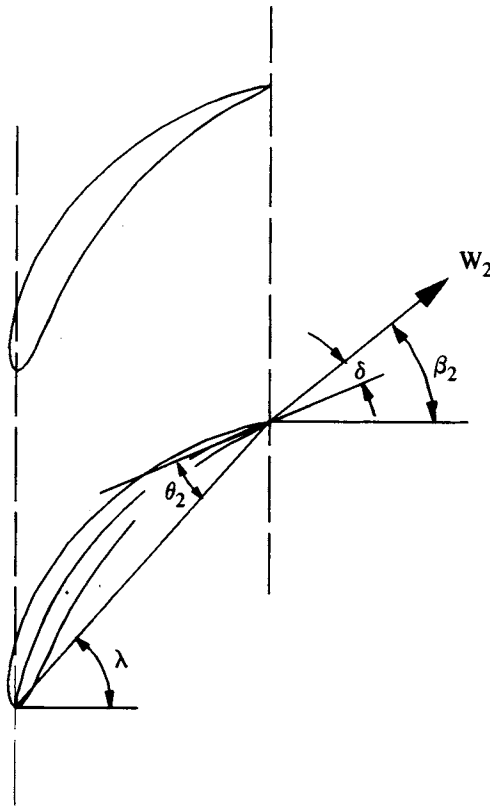
Fig. 2.20 Definition of deviation angle δ

where $n = \frac{1}{2}$ for compressor cascades and $n = 1$ for compressor inlet guide vanes, and

$$m = 0.23(2a/l)^2 + \beta_2^*/500 \tag{2.33}$$

Here a/l is the position of maximum camber from the leading edge as a fraction of blade chord and is the same as $(x_c/l)_{\text{max}}$, Section 2.4 and Fig. 2.8.

3
Principles of performance analysis for axial turbines

Introduction

Rapid progress in turbomachinery technology since the invention and development of the gas turbine during the second world war has called for conflicting requirements of both breadth, to meet manufacturing and marketing demands, and depth, to advance specialist fields such as stress and vibration analysis and turbomachinery fluid dynamics. Increasing computer power has tempted research and design engineers to focus excessively on detailed fluid flow problems without paying sufficient attention to overall factors which influence performance. In Chapter 1 we did indeed focus upon broader considerations with the help of dimensional analysis, to bring out the overall performance trends of families of related machines such as axial, mixed-flow and centrifugal pumps, Figs 1.9 to 1.12, making use of *global* dimensionless variables, Section 1.2. It is the purpose of the present chapter to show how dimensional analysis, based upon *local* dimensionless variables (see Section 1.2.3), can be used to provide a unified framework for performance analysis of axial turbines which integrates logically the three main fluid dynamic design activities, namely

(a) choice of *local* dimensionless design duty coefficients (ϕ, ψ),
(b) velocity triangle design, and
(c) fluid flow considerations (efficiency, losses, selection of blade shapes, etc.).

Methodology in this area, valuable to designer, student and teacher alike, is a scarce commodity. A pivotal paper by S. F. Smith (1965) should be acknowledged as eminent. Presented to a specialists' meeting largely concerned with advanced fluid dynamics, this paper perhaps sat uneasily and seemed to attract relatively little interest at the time. Related to unpublished theoretical studies by Hawthorne (1956) discussed by Horlock (1966), this has in fact provided a simple and rational basis linking both experimental and theoretical performance analyses for axial turbines.

The author's computer program FIPSI embodies the principles to be outlined in this chapter and enables the student to attempt the overall thermo-fluid dynamic layout of a multi-stage axial turbine. A 'screen-dump' of a typical three-stage turbine design is shown in Fig. 3.1 togeher with a summary of the input design data. To give some idea of the overall design sequence for such a machine the various steps may be related through the flow chart shown in Fig. 3.2, which is a development of the previous flow diagram Fig. 1.2 giving rather more specific detail.

The program FIPSI is concerned with the first three stages of this procedure, namely

(a) specification of overall duty requirements,
(b) derivation of the consequent *local* dimensionless performance duty coefficients (ϕ, ψ) and the checking of these against test data to decide upon the appropriate number of stages, and

Station	rhub	rtip	Press.	Temp
No.	m	m	bar	K
1	0.300	0.450	2.50	1200.0
2	0.283	0.466	1.90	1116.8
3	0.260	0.489	1.41	1033.6
4	0.229	0.520	1.02	950.5

Axis of rotation

Thermodynamics Design data Graphics File etc.

Design input data are presently as follows :-

Inlet hub radius	= 0.300 m	Input pressure	= 2.500 bar
Inlet tip radius	= 0.450 m	Outlet pressure	= 1.020 bar
Number of stages	= 3	Inlet temp. T1	= 1200.0 K
Stator aspect ratio	= 6.0	Rot. speed	= 6000.0 revs/min
Rotor aspect ratio	= 8.0	Mass flow rate	= 35.000 kg/s
		Total to total effy.	= 92%
Cp/Cv ratio gamma	= 1.40	Gas constant R	= 287.0 J/kg K

Other calculated design data for the above are:-

Outlet hub radius	= 0.229 m	Outlet temp. T2	= 950.5 K
Outlet tip radius	= 0.520 m	Flow coeff. fi	= 0.57899
Axial velocity	= 136.42 m/s	Work coeff. psi	= 1.50459
Last stage hub stator exit Mach No. M2		= 0.773	
Last stage tip rotor exit Mach No. M3 relative		= 0.626	

< <Press Alt key and first letter together to grab a menu> >
< <e.g. Alt-T pulls down the Thermodynamics menu> >

Fig. 3.1 Design of a three-stage axial turbine. Screen presentations from computer program FIPSI

(c) the detailed thermodynamic and velocity triangle design for each blade row.

We will begin by considering dimensional analysis for a single stage only in Section 3.1. These generalised results will then be related to dimensionless velocity triangles in Section 3.2. Theoretical analyses will then be developed in Section 3.3 for 50% reaction stages and in Section 3.5 for stages of arbitrary reaction. Use of a simple loss correlation will be made in Section 3.4 to facilitate the prediction of total-to-total efficiencies, based on the Rolls-Royce test data for model turbine stages published by S. F. Smith (1965). In Section 3.7 we will extend the performance analysis to model turbines with zero interstage swirl.

3.1 Dimensional analysis for a single stage

Let us consider the idealised model stage shown in Fig. 3.3 consisting of one stator and one rotor. We will make the following assumptions:

(1) Constant axial velocity c_x.
(2) Constant mean radius $r_m = \frac{1}{2}(r_h + r_t)$.
(3) Identical velocity vectors c_1 and c_3 at entry to and exit from the stage at the mean radius r_m.
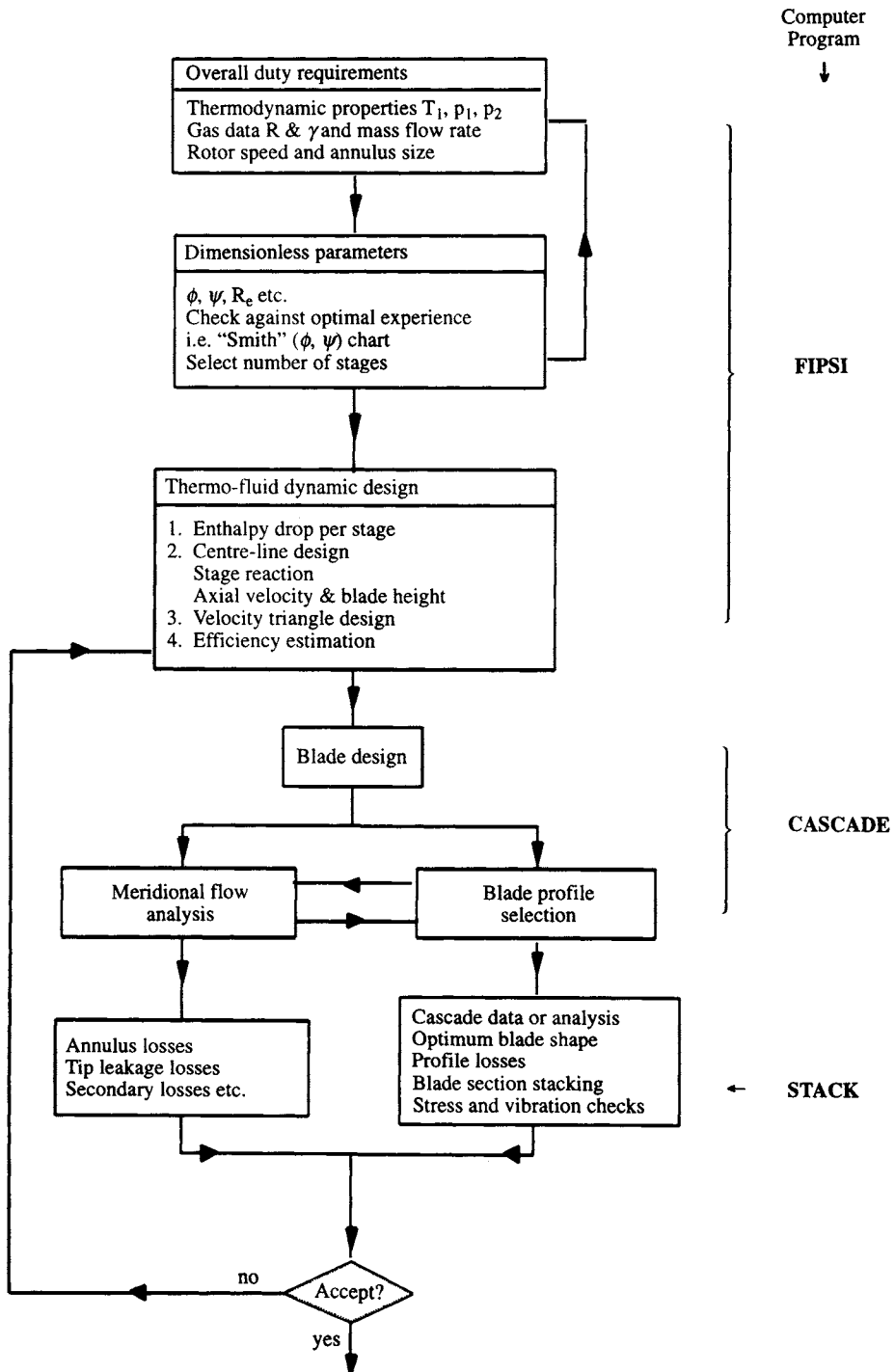
Fig. 3.2 Overall design sequence for a multi-stage axial turbine
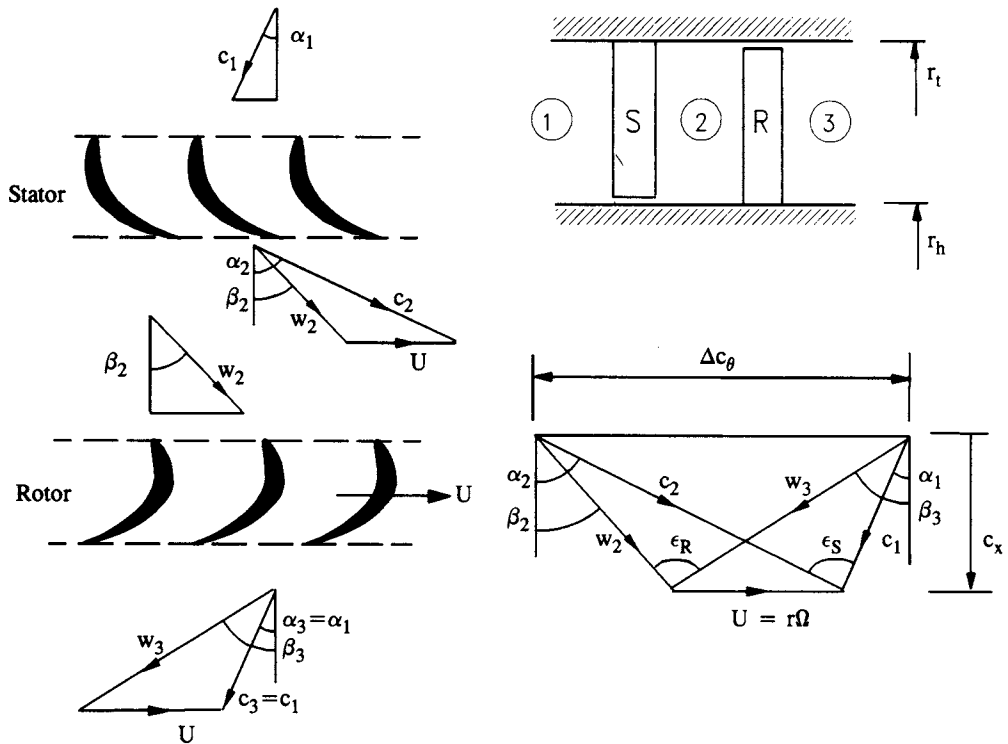
Fig. 3.3 Velocity triangles for turbine model stage

Also shown in Fig. 3.3 are the velocity triangles at entry to and exit from both blade rows. All flow angles are measured relative to the machine axial direction with the following notation:

Absolute velocity c
Absolute flow angle α
Velocity relative to rotor w
Flow angle relative to rotor β

The four velocity triangles may be assembled into one single diagram for the stage as a whole as illustrated.

Now let us focus upon the efficiency η_{TT} of this stage and make the assumption that it will be dependent upon the following variables:

$$\eta_{TT} = f(\underbrace{\Delta h_o, h_1, h_2, h_3,}_{\substack{\text{Thermodynamic} \\ \text{variables}}} \underbrace{\Omega, r_m,}_{\substack{\text{Speed} \\ \text{and size}}} \underbrace{c_x, c_2, w_3,}_{\substack{\text{Velocity} \\ \text{triangle} \\ \text{shape}}} \underbrace{a_2, a_3, \mu, \rho,}_{\substack{\text{Properties} \\ \text{of working} \\ \text{substance}}} \underbrace{\Delta p_{oS}, \Delta p_{oR}}_{\text{Losses}}) \quad (3.1)$$

There could of course be many other factors which would influence efficiency but most of these, such as flow leakage through the clearance gap between the rotor tip and the casing, can be subsumed into the losses. Here we can identify five different categories of influential factors:

(1) *Thermodynamic variables*. The stage stagnation enthalpy drop Δh_o determines

the specific work output and signifies stage loading (see Steady Flow Energy Equation (1.5), Section 1.1.2). The specific enthalpies h_1, h_2 and h_3 typify the progression in energy transfer through the stage. All four are independent design variables at the designer's disposal.

(2) *Speed and size.* Both are independent design variables.

(3) *Velocity triangles.* Four velocities are required to determine the shape of the velocity triangles, Fig. 3.3. The blade speed $U = r_m \Omega = \frac{1}{2}(r_h + r_t)\Omega$ is already covered by item (2) above. c_x must be provided as an independent variable. c_2 and w_3 then follow from (1) above as dependent variables.

(4) *Properties of working substance.* The dynamic viscosity μ, density ρ and speeds of sound a_2 and a_3 depend upon the physical and thermodynamic properties of the gas.

(5) *Losses.* We have assumed here that stator and rotor losses from all sources (profile drag, tip clearance loss, etc.) may be lumped into stagnation pressure losses Δp_{oS} and Δp_{oR} respectively in order to relate to cascade definitions such as Eqns (2.9) or (2.20).

More detailed analysis interconnecting all these terms will evolve as we proceed. As a first step we may reduce the number of variables from 16 to 13 by application of Buckingham's π-theorem. If we select Ω, r_m and ρ as repeating variables, Eqn (3.1) takes the form

$$\pi_1 = f_1(\pi_2, \pi_3, \ldots, \pi_{13}) \tag{3.2}$$

where the following dimensionless groups are formed:

$$\pi_1 = \eta_{TT} \qquad \pi_2 = \frac{\Delta h_o}{\Omega^2 r_m^2} \qquad \pi_3 = \frac{h_1}{\Omega^2 r_m^2}$$

$$\pi_4 = \frac{h_2}{\Omega^2 r_m^2} \qquad \pi_5 = \frac{h_3}{\Omega^2 r_m^2} \qquad \pi_6 = \frac{c_x}{\Omega r_m}$$

$$\pi_7 = \frac{c_2}{\Omega r_m} \qquad \pi_8 = \frac{w_3}{\Omega r_m} \qquad \pi_9 = \frac{a_2}{\Omega r_m} \tag{3.3}$$

$$\pi_{10} = \frac{a_3}{\Omega r_m} \qquad \pi_{11} = \frac{\rho r_m^2 \Omega}{\mu} \qquad \pi_{12} = \frac{\Delta p_{oS}}{\rho r_m^2 \Omega^2}$$

$$\pi_{13} = \frac{\Delta p_{oR}}{\rho r_m^2 \Omega^2}$$

Now as they stand these groups are not all particularly helpful or useful and do not match those normally used in engineering practice. In fact the π-theorem permits us to combine these basic groups to form more appropriate alternatives. At this point we need to exercise engineering judgement to achieve this end. Thus the stage reaction R as normally defined absorbs π_3, π_4 and π_5 into a single group:

$$\left. \begin{aligned} R &= \frac{\text{Specific enthalpy drop across the rotor}}{\text{Specific enthalpy drop across the stage}} \\ &= \frac{h_2 - h_3}{h_1 - h_3} = \frac{\pi_4 - \pi_5}{\pi_3 - \pi_5} \end{aligned} \right\} \tag{3.4}$$

Similarly the stator and rotor exit Mach numbers may be defined:

$$\left.\begin{array}{l} M_2 = \dfrac{c_2}{a_2} = \dfrac{\pi_7}{\pi_9} \\[2ex] M_3 = \dfrac{w_3}{a_3} = \dfrac{\pi_8}{\pi_{10}} \end{array}\right\} \tag{3.5}$$

and the loss coefficients may be expressed in terms of the exit velocities c_2 and w_3 relative to the blade rows:

$$\zeta_{S2} = \frac{\Delta p_{oS}}{\frac{1}{2}\rho c_2^2} = \frac{2\pi_{12}}{\pi_7^2} \quad \text{Stator loss coefficient} \tag{3.6a}$$

$$\zeta_{R3} = \frac{\Delta p_{oR}}{\frac{1}{2}\rho w_3^2} = \frac{2\pi_{13}}{\pi_8^2} \quad \text{Rotor loss coefficient} \tag{3.6b}$$

As we shall see later, the most influential of all the dimensionless parameters are the flow coefficient ϕ and work coefficient ψ defined as given. Introducing the blade speed $U = r_m \Omega$ we have

$$\phi = \frac{c_x}{U} = \pi_6 \quad \text{Flow coefficient} \tag{3.7}$$

$$\psi = \frac{\Delta h_o}{U^2} = \pi_2 \quad \text{Work coefficient} \tag{3.8}$$

One of the remaining groups of special importance is π_{11} which, as it stands, may be identified as the stage Reynolds number based on mean radius:

$$\mathrm{Re}_m = \frac{U r_m}{\nu} = \pi_{11} \tag{3.9}$$

where $\nu = \mu/\rho$ is the kinematic viscosity. Assembling these results, the original expression for η_{TT}, Eqn (3.1), reduces to

$$\begin{aligned} \eta_{TT} &= f\left(\frac{c_x}{U}, \frac{\Delta h_o}{U^2}, \frac{h_2 - h_3}{h_1 - h_3}, \frac{c_2}{U}, \frac{w_3}{U}, \frac{c_2}{a_2}, \frac{w_3}{a_3}, \frac{U r_m}{\nu}, \frac{\Delta p_{oS}}{\frac{1}{2}\rho c_2^2}, \frac{\Delta p_{oR}}{\frac{1}{2}\rho w_3^2} \right) \\[2ex] &= f\left(\underbrace{\phi, \quad \psi,}_{\substack{\text{Duty} \\ \text{coefficients}}} \quad \underbrace{R,}_{\substack{\uparrow \\ \text{Stage} \\ \text{reaction}}} \quad \underbrace{\frac{c_2}{U}, \frac{w_3}{U},}_{\substack{\text{Velocity} \\ \text{triangles}}} \underbrace{M_2, M_3,}_{\substack{\text{Mach} \\ \text{numbers}}} \underbrace{\mathrm{Re}_m,}_{\substack{\uparrow \\ \text{Stage} \\ \text{Reynolds} \\ \text{number}}} \underbrace{\zeta_{S2}, \quad \zeta_{R3}}_{\substack{\text{Loss} \\ \text{coefficients}}} \right) \end{aligned} \tag{3.10}$$

Thus we have now reduced the number of variables which we expect to influence the efficiency from 15 to ten and these fall into six distinct categories as indicated. Further consideration in fact enables us to remove three of these categories entirely for the following reasons:

(1) *Velocity triangles.* We will show shortly in Section 3.3 that the two velocity triangle groups c_2/U and w_3/U are not independent variables but are in fact dependent entirely upon ϕ and ψ. That is

$$\frac{c_2}{U} = f_1(\phi, \psi), \quad \frac{w_3}{U} = f_2(\phi, \psi) \tag{3.11}$$

(2) *Mach number and Reynolds number.* Furthermore, the loss coefficients ζ_{S2} and ζ_{R3} can be shown by experiment to be dependent upon the exit Mach numbers and a blade row Reynolds number. Since the losses will also depend upon the velocity triangles (e.g. exit gas velocity and fluid deflection or blade loading), we would also expect ζ_{S2} and ζ_{R3} to depend upon ϕ and ψ. These dependent relationships can be expressed through

$$\left. \begin{array}{l} \zeta_{S2} = f_3(\phi, \psi, \mathrm{Re}_2, M_2) \\ \zeta_{R3} = f_4(\phi, \psi, \mathrm{Re}_3, M_3) \end{array} \right\} \tag{3.12}$$

where blade row Reynolds numbers have been introduced based upon stator and rotor blade chords l_S and l_R:

$$\left. \begin{array}{ll} \mathrm{Re}_2 = \dfrac{c_2 l_S}{\nu} & \text{Stator Reynolds number} \\[3mm] \mathrm{Re}_3 = \dfrac{w_3 l_R}{\nu} & \text{Rotor Reynolds number} \end{array} \right\} \tag{3.13}$$

Thus finally we may reduce Eqn (3.10) to the form

$$\eta_{TT} = f(\phi, \psi, R, \zeta_{S2}, \zeta_{R3}) \tag{3.14}$$
$$\quad\; \text{i} \quad \text{i} \quad \text{i} \quad \text{d} \quad\;\; \text{d}$$

The efficiency of our turbine stage has been shown to depend upon only five dimensionless variables which are sufficient to account for all of the 15 items we began with in Eqn (3.1). Of these, just three can be varied independently (i) by the designer while two are dependent (d) variables. Once a designer has selected the stage duty (ϕ, ψ) and reaction R, the losses and thus efficiency will be determined.

The reader may wonder what practical use this equation is to the designer except as a means for planning and interpreting experimental tests to create a data base for selecting suitable (ϕ, ψ) duties for highly efficient turbines. Such a thought would be highly commendable as will be demonstrated in Section 3.4. However, by simple analysis in Section 3.5 we will show that this equation, expressed here only as a general parametric relationship, may in fact be developed into an explicit closed form which enables us to evaluate efficiencies directly for a given (ϕ, ψ), ζ_{S2} and ζ_{R3}, namely,

$$\eta_{TT} = \cfrac{1}{1 + \cfrac{1}{2\psi}\left[\left\{ \phi^2 + \left(\dfrac{\psi}{2} + 1 - R \right)^2 \right\} \zeta_{S2} + \left\{ \phi^2 + \left(\dfrac{\psi}{2} + R \right)^2 \right\} \zeta_{R3} \right]} \tag{3.15}$$
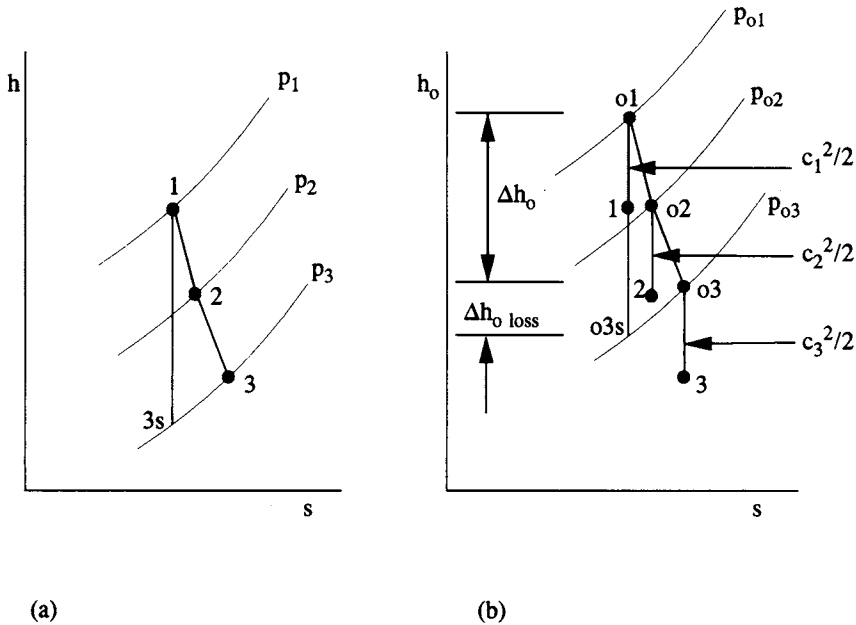
Fig. 3.4 Condition line for a gas turbine stage: (a) *h–s* condition line; (b) *h₀–s* condition line

3.2 Total-to-total efficiency η_{TT}

So far we have used total-to-total efficiency η_{TT} without formal definition. Let us now correct this by consideration of the stage thermodynamics. The condition line 1–2–3 recording the thermodynamic changes of state through the blade row can be plotted on an *h–s* diagram as illustrated in Fig. 3.4(a). Alternatively we may derive the stagnation enthalpies $h_{o1} = h_1 + c_1^2/2$ etc. and plot the h_o–*s* condition curve o1–o2–o3, Fig. 3.4(b). From this we may then more easily visualise the definition of total-to-total efficiency η_{TT}:

$$\eta_{TT} = \frac{\text{Stagnation enthalpy drop}}{\text{Ideal stagnation enthalpy drop}}$$

$$= \frac{h_{o1} - h_{o3}}{h_{o1} - h_{o3s}} \tag{3.16}$$

$h_{o1} - h_{o3s}$ represents the maximum possible stagnation enthalpy drop for isentropic flow through an ideal loss-free turbine having the same overall pressure ratio p_1/p_3. Thus we can identify the lost stagnation enthalpy $(\Delta h_o)_{\text{loss}}$ of the real turbine stage through

$$(\Delta h_o)_{\text{loss}} = h_{o3} - h_{o3s} \tag{3.17}$$

Also, since $\Delta h_o = h_{o1} - h_{o3}$, Eqn (3.16) for η_{TT} may be expressed as

$$\eta_{TT} = \frac{\Delta h_o}{\Delta h_o + (\Delta h_o)_{\text{loss}}} = \frac{1}{1 + \dfrac{(\Delta h_o)_{\text{loss}}}{\Delta h_o}} \tag{3.18}$$

Now our previous definitions of loss coefficient, Eqns (3.6), involved stagnation pressure losses Δp_{oS} and Δp_{oR} rather than stagnation enthalpy loss. To accommodate this we make use of the well-known thermodynamic relationship (Rogers and Mayhew, 1992):

$$dh = T\,ds + \frac{1}{\rho}\,dp \qquad (3.19)$$

If we apply this along the reversible path 1–3s of the perfect turbine for which $ds = 0$, we obtain

$$dh = \frac{1}{\rho}\,dp \qquad \text{(for the isentropic line 1–3s)}$$

If $(\Delta h_o)_{loss}$ is small we may thus make the assumption that

$$(\Delta h_o)_{loss} \approx \frac{1}{\rho}(\Delta p_o)_{loss}$$

where $(\Delta p_o)_{loss}$ represents the total loss of stagnation pressure for the stage. η_{TT} then approximates to

$$\eta_{TT} \approx \frac{1}{1 + \dfrac{(\Delta p_o)_{loss}}{\rho \Delta h_o}} \qquad (3.20)$$

Since $(\Delta p_o)_{loss} = \Delta p_{oS} + \Delta p_{oR}$ we may introduce the dimensionless groups from Eqns (3.6) and (3.18) to obtain finally

$$\eta_{TT} = \frac{1}{1 + \dfrac{1}{2\psi}\left[\left(\dfrac{c_2}{U}\right)^2 \zeta_{S2} + \left(\dfrac{w_3}{U}\right)^2 \zeta_{R3}\right]} \qquad (3.21)$$

To proceed further we need to derive relationships for c_2/U and w_3/U in terms of ϕ, ψ and R by reference to the velocity triangles. We will first tackle the easier case of 50% reaction stages ($R = 0.5$), Sections 3.3 and 3.4. Following this we will go on to deal with stages of arbitrary reaction, Section 3.5.

3.3 50% reaction stages

From the definition of stage reaction, Eqn (3.4), for 50% reaction we have

$$R = \frac{h_2 - h_3}{h_1 - h_3} = 0.5$$

from which we obtain

$$h_1 - h_2 = h_2 - h_3 \qquad (3.22)$$
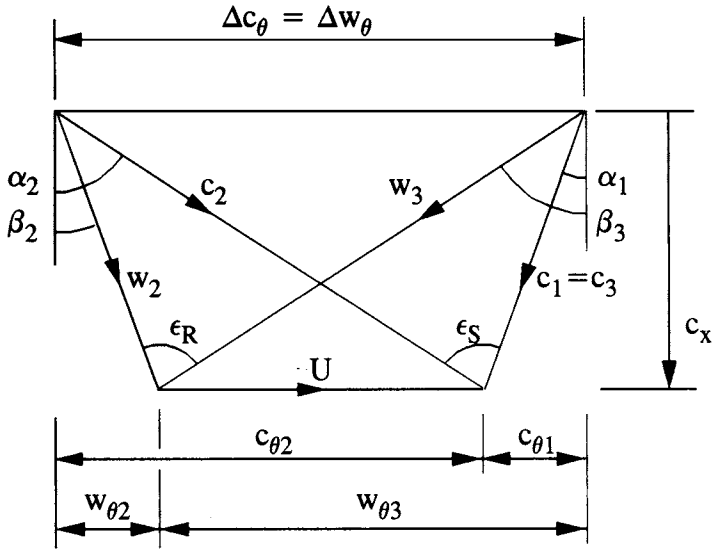
Fig. 3.5 Velocity triangles for a 50% reaction turbine stage

The specific enthalpy drop across stator and rotor are thus equal. From this we may deduce that the velocity triangles are symmetrical as shown in Fig. 3.5. To be certain of this we will prove it as follows. Since the stagnation pressure remains constant through the stator,

$$h_1 - h_2 = \tfrac{1}{2}(c_2^2 - c_1^2) \tag{3.23}$$

Similarly, relative to the rotor (see Section 7.2), the relative stagnation enthalpy remains constant, resulting in

$$h_2 - h_3 = \tfrac{1}{2}(w_3^2 - w_2^2) \tag{3.24}$$

Equating these and introducing $c_1^2 = c_x^2 + c_{\theta 1}^2$ etc.,

$$c_2^2 - c_1^2 = w_3^2 - w_2^2$$

hence

$$c_{\theta 2}^2 - c_{\theta 1}^2 = w_{\theta 3}^2 - w_{\theta 2}^2$$

and

$$(c_{\theta 2} - c_{\theta 1})(c_{\theta 2} + c_{\theta 1}) = (w_{\theta 3} - w_{\theta 2})(w_{\theta 3} + w_{\theta 2})$$

but from the velocity triangles we observe that

$$c_{\theta 2} + c_{\theta 1} = w_{\theta 3} + w_{\theta 2}$$

The previous equation then reduces to

$$c_{\theta 2} - c_{\theta 1} = w_{\theta 3} - w_{\theta 2}$$

Solving these last two equations we have finally

$$c_{\theta 1} = w_{\theta 2} \quad \text{and} \quad c_{\theta 2} = w_{\theta 3} \tag{3.25}$$

Thus for 50% reaction the velocity triangles are symmetrical as drawn in Fig. 3.5.

Example 3.1

Problem
Given the design input data of the turbine shown in Fig. 3.1, calculate ϕ and ψ assuming identical blade geometry at the mean radius for all three stages.

Solution
The calculation for ϕ is as follows.

$$r_m = \tfrac{1}{2}(r_h + r_t) = 0.375 \text{ m}$$
$$U = r_m \Omega = 0.375 \times 2\pi \times 6000/60 = 235.62 \text{ m s}^{-1}$$

From the equation of state

$$\rho = p_1/RT_1 = 2.5 \times 10^5/(287.0 \times 1200)$$
$$= 0.7259 \text{ kg m}^{-3}$$

From the continuity equation

$$\dot{m} = \rho c_x \pi (r_t^2 - r_h^2)$$

Therefore

$$c_x = 35.0/(0.7259 \times \pi(0.45^2 - 0.3^2)) = 136.42 \text{ m s}^{-1}$$

and

$$\phi = c_x/U = 0.578\,98$$

Next we calculate ψ.

$$(\Delta h_o)_{\text{total}} = h_{o1} - h_{o3} = h_1 - h_3 \qquad \text{since} \quad c_1 = c_3$$

$$= c_p(T_1 - T_3) = \frac{\gamma R}{\gamma - 1}(T_1 - T_3)$$

To find T_3,

$$\eta_{\text{TT}} = \frac{h_{o1} - h_{o3}}{h_{o1} - h_{o3s}} \approx \frac{h_1 - h_3}{h_1 - h_{3s}} = \frac{T_1 - T_3}{T_1 - T_{3s}}$$
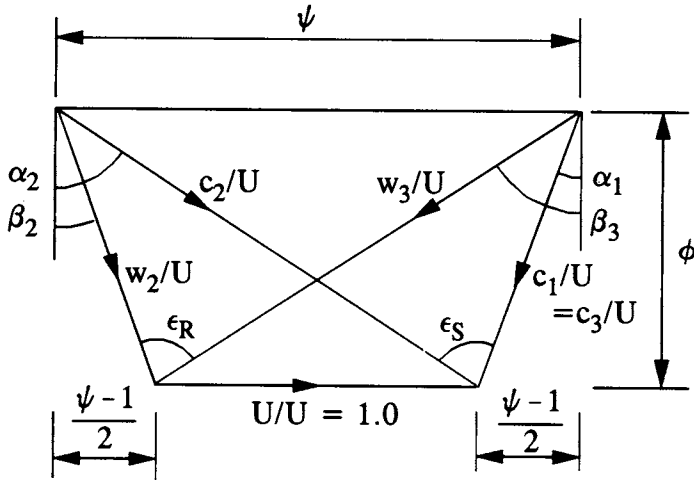
Fig. 3.6 Dimensionless velocity triangles for a 50% reaction turbine stage

Therefore

$$
\begin{aligned}
T_3 &= T_1 - \eta_{TT}(T_1 - T_{3s}) \\
&= T_1\left\{1 - \eta_{TT}\left(1 - \left(\frac{p_{3s}}{p_1}\right)^{(\gamma-1)/\gamma}\right)\right\} \\
&= 1200\{1 - 0.92(1 - (1.02/2.5)^{0.4/1.4})\} \\
&= 950.53\,K
\end{aligned}
$$

Substituting this into the equation for $(\Delta h_o)_{total}$ above,

$$
(\Delta h_o)_{total} = \frac{1.4 \times 287.0}{0.4}(1200 - 950.53) = 250\,589\,J\,kg^{-1}
$$

Hence for one stage

$$
\Delta h_o = \tfrac{1}{3} \times 250\,589 = 83\,529.7\,J\,kg^{-1}
$$

$$
\psi = \Delta h_o/U^2 = 1.504\,58
$$

3.3.1 Dimensionless velocity triangles

Let us now consider the factors which determine the general shape of the velocity triangles. By inspection of Fig. 3.5 we see that the overall shape is governed entirely by the three velocities c_x, Δc_θ and U. Now we can show that c_x and Δc_θ are uniquely related to the flow coefficient ϕ and work coefficient ψ respectively. Thus from Eqn (3.7),

$$
c_x = \phi U \tag{3.26}
$$

Also from the Euler turbine equation (1.10)

$$\Delta h_{\mathrm{o}} = U(c_{\theta 1} + c_{\theta 2}) = U\Delta c_\theta$$

where $c_{\theta 1}$ and $c_{\theta 2}$ are the absolute values as shown in Fig. 3.5 and Δc_θ is thus the change in peripheral whirl through either the stator or rotor. By definition $\Delta h_{\mathrm{o}} = \psi U^2$, Eqn (3.8), so that finally

$$\Delta c_\theta = \psi U \qquad (3.27)$$

The obvious strategy to follow at this point is to make the velocity triangles dimensionless by dividing all velocities by the blade speed U. The outcome of this is portrayed in Fig. 3.6 from which important and interesting conclusions may be drawn. We observe that the dimensionless velocity triangles and therefore the general blade shapes required to achieve them are totally determined by the stage duty coefficients ϕ and ψ. The dimensionless blade speed is of course unity. It follows also that all other angles and velocities may be expressed explicitly as functions of ϕ and ψ. These may be summarised as follows.

$$\left.\begin{aligned}
\alpha_1 = \beta_2 &= \arctan\left(\frac{\psi - 1}{2\phi}\right) \\
\alpha_2 = \beta_3 &= \arctan\left(\frac{\psi + 1}{2\phi}\right) \\
\frac{c_2}{U} = \frac{w_3}{U} &= \sqrt{\phi^2 + \frac{1}{4}(\psi + 1)^2} \\
\frac{c_1}{U} = \frac{c_3}{U} = \frac{w_2}{U} &= \sqrt{\phi^2 + \frac{1}{4}(\psi - 1)^2}
\end{aligned}\right\} \qquad (3.28)$$

The fluid deflection angles for stator and rotor thus become

$$\begin{aligned}
\varepsilon_{\mathrm{S}} = \varepsilon_{\mathrm{R}} &= \arctan(\alpha_1 + \alpha_2) \\
&= \arctan\left(\frac{\psi/\phi}{1 - \dfrac{\psi^2 - 1}{4\phi^2}}\right)
\end{aligned} \qquad (3.29)$$

It is quite clear therefore that the designer's choice of overall duty requirements and therefore of duty (ϕ, ψ), Fig. 3.2, will have a crucial effect upon the velocity triangles and thus upon blade aerodynamics. We will now go on to study some of these effects in relation to published data from experimental tests.

Example 3.2

Problem (a)
Calculate the angles and velocities identified in Fig. 3.5 for the stages considered in Example 3.1 and comment.

Solution
From solution of Example 3.1, the duty coefficients were $\phi = 0.578\,98$, $\psi = 1.504\,58$. Introducing these into Eqns (3.28) and (3.29) we have

$\alpha_1 = \beta_2 = 23.45°$ Modest interstage swirl

$\alpha_2 = \beta_3 = 76.98°$ Fairly high efflux angles from stator and rotor

$\varepsilon_S = \varepsilon_R = 88.73°$ Fairly high fluid deflections required of stator and rotor

$\dfrac{c_2}{U} = \dfrac{w_3}{U} = 1.3797$ Stator and rotor exit velocities fairly high compared with blade speed

$\dfrac{c_1}{U} = \dfrac{c_3}{U} = \dfrac{w_2}{U} = 0.631\,56$ Interstage velocities kept well below blade speed

Problem (b)
Calculate exit Mach number from the stator.

Solution
M_2 is given by

$$M_2 = \frac{c_2}{a_2} = \frac{\left(\dfrac{c_2}{U}\right)U}{\sqrt{\gamma R T_2}}$$

where a_2 = speed of sound, and T_2 = temperature at exit from stator.
   To find T_2 we can note the following. For identical stages with the same velocity levels c_x and U, the temperature drop per stage will be one-third of the overall temperature drop, namely

$$\Delta T_{\text{stage}} = \tfrac{1}{3}(1200 - 950.53) = 83.157 \text{ deg C per stage}$$

Since the stages are 50% reaction, half of this occurs through stator and half through rotor. Thus

$$T_2 = 1200 - \tfrac{1}{2} \times 83.157 = 1158.42 \text{ K}$$

Hence from the equation for M_2 above,

$$M_2 = \frac{1.3797 \times 235.62}{\sqrt{1.4 \times 287.0 \times 1158.42}} = 0.476\,49$$

3.4   An experimental correlation based on model tests

All large manufacturers of gas and steam turbines do of course undertake extensive test work on models or prototypes leading to experimental correlations which act as a vital long term data base for future design and development. Such a correlation was published by S. F. Smith (1965) based upon 70 model turbine tests related to
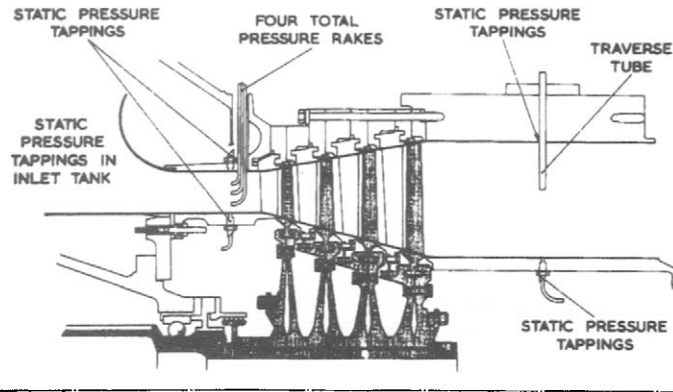
Fig. 3.7 Model turbine instrumentation (Smith, 1965) (by courtesy of the Von Karman Institute)

the post-war aircraft propulsion gas turbines of Rolls-Royce such as the Avon, Dart, Spey, Conway and others. The special model four-stage turbine test facility, illustrated in Fig. 3.7, had blade rows 15 to 20 inches (38 to 51 cm) in diameter and was supplied with air at 100 °C to 200 °C. Such low temperatures, as compared with 1000 °C or more in the prototype, not only simplified the instrumentation needed for accurate assessment but also permitted easy matching of prototype Mach numbers at the smaller model scale. An additional advantage was the small power output of 800 to 2000 bhp as compared with, for example, the 70 000 bhp produced by the Conway. Matching of Reynolds number between model and prototype is another requirement to be met, but Smith reported little influence of blade chord Reynolds number upon efficiency for the bigger engines for which Re_l tended to be in excess of 10^5.

The important outcome of this test series was the turbine efficiency correlation shown in Fig. 3.8. Each turbine was tested over a range of pressure ratios to determine its maximum efficiency point, for which ϕ and ψ were then calculated. Thus each point plotted on Fig. 3.8 represents one particular test model turbine at its best duty point (ϕ, ψ), and its efficiency is entered adjacent to that point. A pattern emerges from the data immediately, from which contours of constant efficiency can be constructed revealing very distinct trends. The following comments are worthy of note:

(1) All data points represent best efficiencies likely to be achievable. For example, a turbine designed to operate at $\phi = 0.9$, $\psi = 1.2$ might achieve at best 92% efficiency.
(2) The best turbine design duty point to aim at, if efficiency is all that matters, is in the region of $\phi = 0.6$, $\psi = 1.0$. However, it should be observed that this lies on the edge of the available test data in this correlation.
(3) The majority of test points, being related to a practical series of engines, were aimed at higher ϕ and ψ values. A designer may thus accept some reduction of efficiency in order to increase mass flow (hence engine thrust) and stage loading (hence less blade rows/weight/cost).

One important point which should be mentioned is that efficiencies were evaluated on the assumption of zero tip clearance. Losses due to flow through the clearance
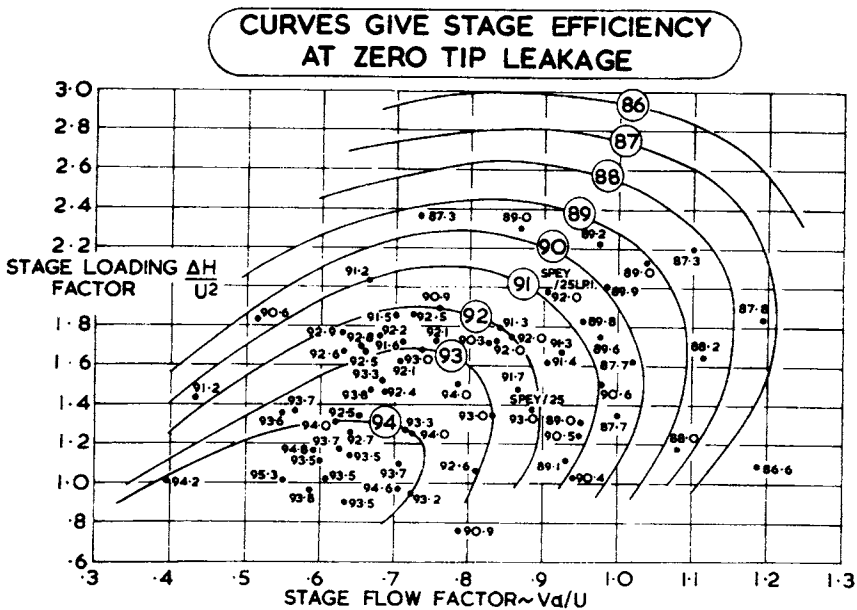
Fig. 3.8 Efficiency correlation for turbine stage (Smith, 1965) (by courtesy of the Von Karman Institute)

gap between blade end and annulus wall can be enormous compared with other losses. They can be eliminated from the correlation by repeating tests with increasing tip clearance and then extrapolating the results to simulate zero tip clearance. Alternatively, formulae analogous to those developed in Section 8.4.5 for fans can be used to estimate the tip leakage losses. These may then be subtracted from the measured stage losses before working out the total-to-total efficiency.

3.4.1 Theoretical analysis by S. F. Smith

S. F. Smith developed a most interesting theoretical analysis to explain the shape of these efficiency contours, as follows. He argued that the losses in any blade row will be proportional to the dynamic head or kinetic energy in the row. He proposed that the average kinetic energy in a blade row could be represented by $\frac{1}{2}(c_1^2 + c_2^2)$, Fig. 3.6. For his 50% reaction stages Smith therefore defined the coefficient $f_s = \Delta h_o/(c_1^2 + c_2^2)$ as the ratio of the shaft work output to the sum of the mean kinetic energies within stator + rotor. He argued that we should expect a high efficiency when this ratio of work output to kinetic energy is high and to confirm this action he proceeded to plot contours of $f_s = \Delta h_o/(c_1^2 + c_2^2)$ onto a (ϕ, ψ) chart.

It is indeed striking to compare the η_{TT} contours of Fig. 3.8 with the f_s contours of Fig. 3.9 which show a remarkable similarity, confirming Smith's hypothesis. By reference to the dimensionless velocity triangles, Fig. 3.6, we can derive an analytical expression for f_s as follows:

$$
\begin{aligned}
f_s &= \frac{\Delta h_o}{c_1^2 + c_2^2} = \frac{\Delta h_o/U^2}{(c_1/U)^2 + (c_2/U)^2} \\
&= \frac{2\psi}{4\phi^2 + \psi^2 + 1}
\end{aligned}
\tag{3.30}
$$

$$\psi_{\mathrm{opt}} = \sqrt{4\phi^2 + 1}$$

$$f_s = \frac{2\psi}{4\phi^2 + \psi^2 + 1}$$
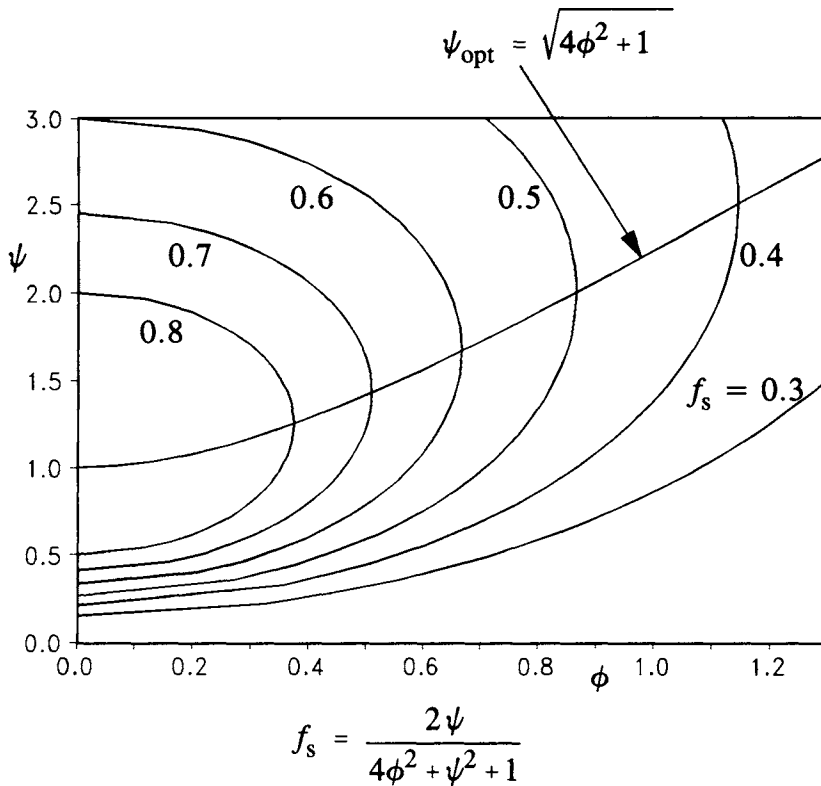
Fig. 3.9 Contours of blade row kinetic energy coefficients, after Smith (1965)

From this expression we can estimate the optimum work coefficient for a given flow coefficient and hence obtain a theoretical curve of the form $\psi = f(\phi)$ which defines the optimum desirable design duty coefficients. Thus writing

$$\frac{\partial f_s}{\partial \psi} = \frac{2(4\phi^2 - \psi^2 + 1)}{(4\phi^2 + \psi^2 + 1)^2} = 0$$

the optimum duty coefficient locus becomes

$$\psi_{\mathrm{opt}} = \sqrt{4\phi^2 + 1} \tag{3.31}$$

This is shown on Fig. 3.9 and to some extent follows the trend of optimum efficiency turbines of the Rolls-Royce correlation, Fig. 3.8. We will return to this later (see Eqn (3.35)).

3.4.2 Theoretical performance analysis by R. I. Lewis (1978)

A more rational and explicit approach which links directly with the generalised dimensional analysis of Sections 3.1 and 3.2 has been developed by the present author (Lewis, 1978). Let us pick up the argument from Eqn (3.21). For 50% reaction stages

$$\psi_{opt} = \sqrt{4\phi^2 + 1}$$

$$f_L = \frac{1}{\psi}\left[\phi^2 + \frac{1}{4}(1+\psi)^2\right]$$
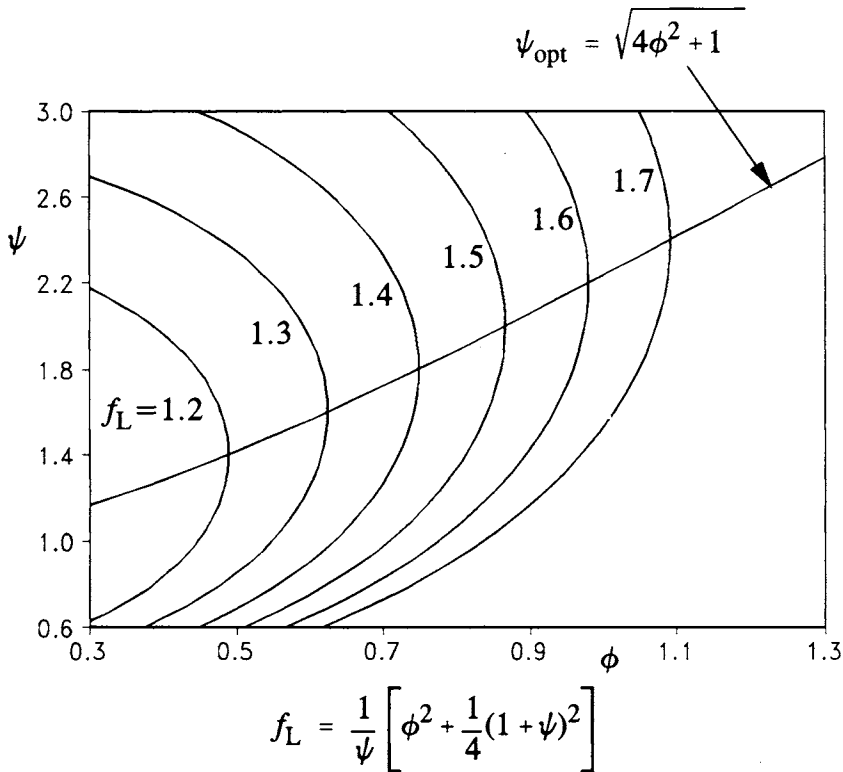
Fig. 3.10 Loss weighting coefficients for 50% axial turbine stages

since stator and rotor fluid deflection angles ε_S and ε_R are identical, Fig. 3.6, it seems reasonable to assume equal loss coefficients,

$$\zeta_{S2} \approx \zeta_{R3} \tag{3.32}$$

But from Eqns (3.28) we recall that

$$\frac{c_2}{U} = \frac{w_3}{U} = \sqrt{\phi^2 + \frac{1}{4}(\psi+1)^2}$$

Introducing these into Eqn (3.21), the efficiency of our 50% reaction stage becomes

$$\eta_{TT} = \cfrac{1}{1 + \cfrac{1}{\psi}\left(\phi^2 + \cfrac{1}{4}(\psi+1)^2\zeta_{S2}\right)} \tag{3.33a}$$

$$= \frac{1}{1 + f_L(\phi,\psi)\zeta_{S2}} = f(\phi,\psi,\zeta_{S2}) \tag{3.33b}$$

This equation thus agrees with the general result derived from dimensional analysis, Eqn (3.14), for the special case when R is fixed at 0.5 and $\zeta_{R3} = \zeta_{S2}$. However, we

have now succeeded in expressing η_{TT} in a most interesting and informative explicit form. Equation (3.33) states that the dimensionless losses and hence the efficiency are dependent upon the product of two factors different in kind:

(1) *Blade row aerodynamics.* The loss coefficient ζ_{S2} depends entirely upon the detailed blade geometry and may be derived from cascade and other model tests, namely

$$\zeta_{S2} = \frac{\Delta p_{oS}}{\frac{1}{2}\rho c_2^2} \qquad [3.6a]$$

(2) *(ϕ, ψ) duty and velocity triangles.* These losses are then scaled or 'given weight' by the parameter $f_L(\phi, \psi)$ which we will call the 'weighting coefficient':

$$f_L = \frac{1}{\psi}\left\{ \phi^2 + \frac{1}{4}(\psi + 1)^2 \right\} \qquad (3.34)$$

This coefficient represents the velocity triangle environment and therefore the magnitude of local dynamic head within which the blades are to operate. As already established, Fig. 3.6, velocity triangles are also fixed by the duty coefficients (ϕ, ψ).

Now the analytical form of f_L is different from the coefficient f_S, Eqn (3.30), implicit in Smith's analysis although their physical significance is similar. The present analysis offers the additional advantage of the explicit form for η_{TT}, Eqn (3.33a), and the separation of the two influential factors (1) and (2) discussed above. Thus to raise efficiency we may proceed as follows:

(1) First we must select a (ϕ, ψ) duty to help us minimise $f_L(\phi, \psi)$ before even choosing blade profiles.
(2) Then we may concentrate on aerodynamic design to minimise blade row losses Δp_{oS}.

If we assume for the moment that ζ_{S2} is independent of ϕ and ψ, we can repeat the procedure of Section 3.4.1 to find the optimum weighting coefficient. Thus maximum η_{TT} will correspond to minimum f_L. For a prescribed value of ϕ this follows from

$$\left\{\frac{\partial f_L}{\partial \psi}\right\}_\phi = -\frac{1}{\psi^2}\left\{ \phi^2 + \frac{1}{4}(\psi+1)^2 \right\} + \frac{1}{2\psi}(\psi+1) = 0$$

from which, perhaps surprisingly, we obtain exactly the same result as yielded by the Smith approach, namely

$$\psi_{opt} = \sqrt{4\phi^2 + 1} \qquad [3.31]$$

This curve together with contours of constant f_L are shown in Fig. 3.10. Once again there is a striking resemblance of these to the Rolls-Royce model test efficiency contours. We observe as expected that the loss weighting coefficients take on a lower

value within regions where efficiencies are found experimentally to be high and vice versa, confirming the strong influence of velocity triangle shape upon loss levels.

A curve analogous to Eqn (3.31) could be picked out from the Rolls-Royce data. This will be found to lie close to the following curve which forms a simple designers' rule of thumb for selection of the experimentally optimum ψ for a given ϕ:

$$\psi_{\text{opt.exp.}} = 0.65\sqrt{4\phi^2 + 1} \tag{3.35}$$

Example 3.3

Problem
For the stage considered in Examples 3.1 and 3.2, estimate the blade row loss coefficient ζ_{S2} given a total-to-total efficiency of 93%.

Solution
From Eqn (3.33),

$$\zeta_{S2} = \left(\frac{1}{\eta_{TT}} - 1\right)\frac{1}{f_L(\phi, \psi)}$$

But $\phi = 0.578\,98$, $\psi = 1.504\,58$ (Example 3.1) and $\eta_{TT} = 0.93$, therefore

$$f_L = \frac{1}{1.504\,58}\left\{0.578\,98^2 + \frac{1}{4}(1.504\,58 + 1)^2\right\} = 1.2651$$

Thus

$$\zeta_{S2} = \left(\frac{1}{0.93} - 1\right)\Big/1.2651 = 0.0595$$

3.4.3   Influence of fluid deflection upon losses

Shown in Fig. 3.11(a) are contours of constant fluid deflection compared with predicted contours of constant profile loss. The former follow from Eqn (3.29) for ε_S and ε_R, while the latter were computed from the simple correlation due to Soderberg (1949) which has subsequently been expressed by Hawthorne (1956) in the following form, as outlined by Horlock (1966):

$$\left.\begin{aligned}
\zeta_2 &= 0.025\left(1 + \left(\frac{\varepsilon^\circ}{90}\right)^2\right) \\
\zeta_{2\text{sec}} &= 3.2\left(\frac{b}{H}\right)\zeta_2
\end{aligned}\right\} \tag{3.36}$$

ζ_2 here accounts for profile losses only. $\zeta_{2\text{sec}}$ is the secondary loss coefficient accounting for all other losses (except tip leakage loss) and is assumed to be proportional to the profile loss ζ_2 and also to the reciprocal of the blade row aspect ratio H/b where $b = l\cos\lambda$ is the axial chord and $H = r_t - r_h$ is the blade height. Of course this is a very simple correlation which ignores other important influences such
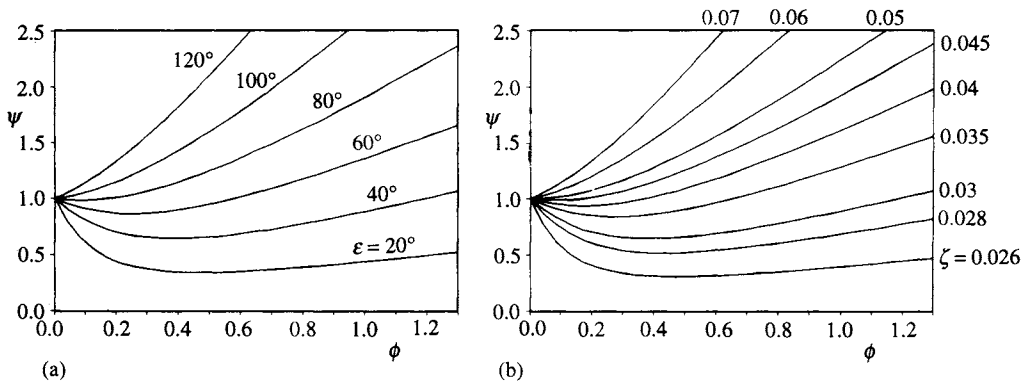
Fig. 3.11 Contours of constant deflection and loss coefficient for 50% reaction axial turbine stages: (a) contours of constant deflection; (b) contours of constant profile loss coefficient

as Reynolds number and Mach number. Nevertheless it yields quite credible results and offers the advantage of simplicity for preliminary design and performance studies. A number of observations may be made here.

(1) If we ignore the effect of aspect ratio the profile loss coefficients ζ_2 will bring out the main (ϕ, ψ) trends, Fig. 3.11(b).
(2) Fluid deflection is strongly dependent upon work coefficient ψ. Thus more highly loaded stages require greater fluid deflections and consequently generate higher losses as we would intuitively expect.
(3) The aerodynamic loss contours ζ_2 (ϕ, ψ) bear no resemblance whatsoever to the efficiency contours.

This last point is of particular interest regarding the discussion in Section 3.4.2. Clearly the duty coefficients (ϕ, ψ) and thus velocity triangles have much stronger control over the general shape of the efficiency contours than do the blade profile aerodynamics. It is clear, however, from the loss contours of Fig. 3.11(b) that $\zeta_{S2} = (\zeta_2 + \zeta_{2sec})$ will have the effect of reducing the efficiency levels at higher design values of ψ.

To conclude this section, predicted efficiency contours are shown in Fig. 3.12 based upon Soderberg's simple correlation and assuming a blade row aspect ratio of $H/b = 10.0$. These do indeed show a remarkable similarity to the Rolls-Royce efficiency contours bearing in mind (a) the wide range of (ϕ, ψ) duties covered, (b) the simplicity of the loss correlation, and (c) the probable variation of aspect ratio H/b of the test stages.

Finally, introducing Eqn (3.31) into (3.29), the fluid deflection of the theoretical optimum family of turbines would be

$$\varepsilon_S = \varepsilon_R = \arctan\left(\frac{4\phi\psi}{4\phi^2 - \psi^2 + 1}\right) = \arctan(\infty) = 90°$$

In practice Eqn (3.35) gives a better curve fit for the optimum family of turbines, resulting in the experimental optimum deflection

$$(\varepsilon_S)_{opt.exp.} = \arctan\left\{\frac{2.6\phi\sqrt{4\phi^2 + 1}}{2.31\phi^2 + 0.5775}\right\} \tag{3.37}$$
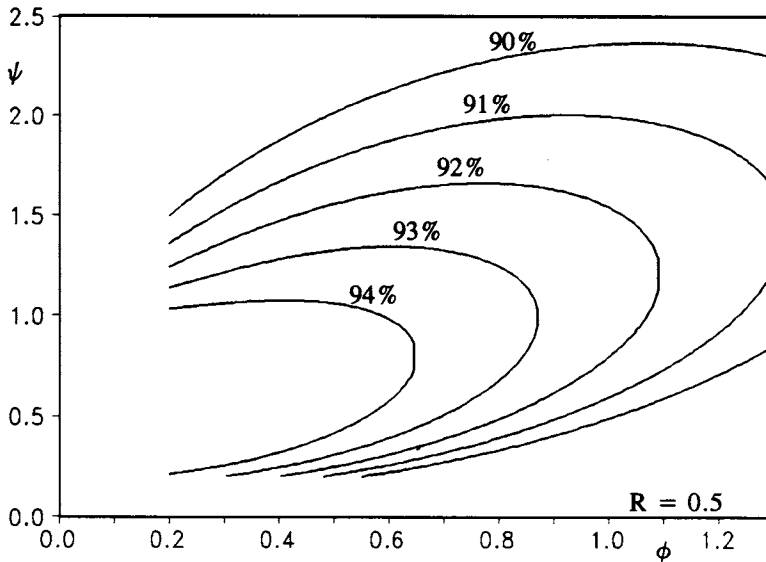
Fig. 3.12 Predicted total-to-total efficiencies for axial turbines with 50% reaction and blade aspect ratio $H/b = 10.0$

This is the region of 60° for the range of high performance turbines for which $0.5 < \phi < 0.8$ and gives a very crude rule of thumb. It is of interest to note, however, that deflection angles well in excess of 60° can be achieved with low loss in turbine cascades. The key point is that velocity triangles and thus the value of the loss weighting coefficient $f_L(\phi, \psi)$ have the overriding influence upon efficiency. Despite this, the selector of the model tests leading to Fig. 3.8 opted for many more highly loaded stages in the vicinity of $\phi = 0.7$, $\psi = 1.6$ for which the fluid deflection would be $\varepsilon_S = \varepsilon_R = 84.9°$. The benefit reaped by choosing a higher work coefficient is the requirement of fewer stages resulting in reduced weight and manufacturing costs. The consequent performance cost incurred would be a reduction of efficiency, although the consequent fluid deflections of 84.9° are aerodynamically well within reach.

3.5 Stages with arbitrary reaction *R*

Let us now generalise this analysis to stages with arbitrary reaction R, for which the velocity triangles will no longer be symmetrical, Fig. 3.3.

The dimensionless velocity triangles are shown in Fig. 3.13. Swirl velocities $w_{\theta2}/U$ and $c_{\theta2}/U$ may be related to ϕ, ψ and R as follows. We recall that

$$R = \frac{h_2 - h_3}{h_1 - h_3} \qquad [3.4]$$

But since we are assuming $c_1 = c_3$, then

$$h_1 - h_3 = h_{o1} - h_{o3} = \Delta h_o = \psi U^2$$
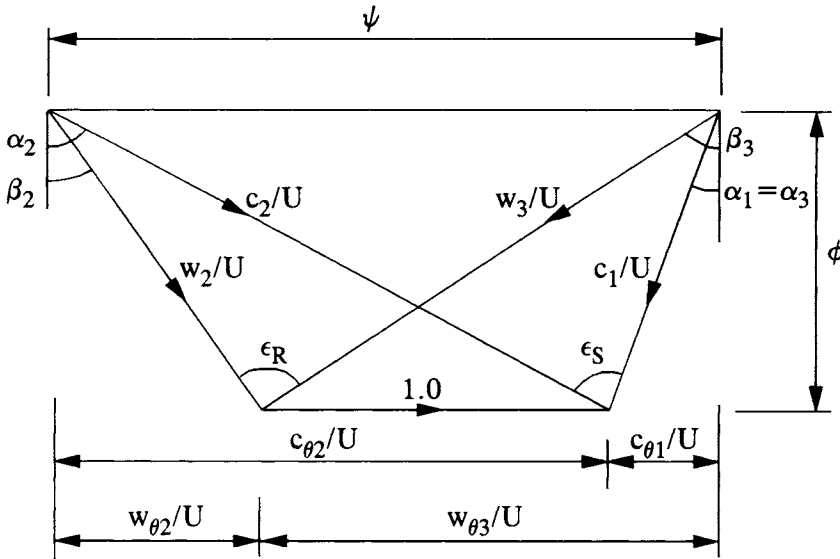
Fig. 3.13 Dimensionless velocity triangles for axial turbine stages of arbitrary reaction

Also, relative to the rotor,

$$h_2 - h_3 = \tfrac{1}{2}(w_3^2 - w_2^2)$$
$$= \tfrac{1}{2}(w_{\theta3}^2 - w_{\theta2}^2)$$

Thus Eqn (3.4) becomes

$$R = \frac{(w_{\theta3} + w_{\theta2})(w_{\theta3} - w_{\theta2})}{2\psi U^2}$$

But from the Euler turbine equation (1.10)

$$\Delta h_o = U(w_{\theta3} + w_{\theta2}) = \psi U^2$$

Introducing this into the previous equation we obtain

$$\frac{w_{\theta2}}{U} = \frac{\psi}{2} - R \qquad (3.38)$$

Also

$$\left.\begin{array}{l} \dfrac{c_{\theta2}}{U} = \dfrac{w_{\theta2} + U}{U} = \dfrac{\psi}{2} + 1 - R \\[3mm] \dfrac{w_{\theta3}}{U} = \psi - \dfrac{w_{\theta2}}{U} = \dfrac{\psi}{2} + R \end{array}\right\} \qquad (3.39)$$

and

Thus the gas exit velocities from stator and rotor become

$$\left(\frac{c_2}{U}\right)^2 = \left(\frac{c_x}{U}\right)^2 + \left(\frac{c_{\theta 2}}{U}\right)^2 = \phi^2 + \left(\frac{\psi}{2} + 1 - R\right)^2 \right\}$$
$$\left(\frac{w_3}{U}\right)^2 = \left(\frac{c_x}{U}\right)^2 + \left(\frac{w_{\theta 3}}{U}\right)^2 = \phi^2 + \left(\frac{\psi}{2} + R\right)^2 \right\}$$
(3.40)

and the total-to-total efficiency, Eqn (3.21), becomes

$$\eta_{TT} = \frac{1}{1 + \dfrac{1}{2\psi}[\{\phi^2 + (\psi/2 + 1 - R)^2\}\, \zeta_{S2} + \{\phi^2 + (\psi/2 + R)^2\}\, \zeta_{R3}]}$$
(3.41)

$$= f(\psi, \phi, R, \zeta_{S2}, \zeta_{R3})$$

η_{TT} has thus been expressed explicitly as a function of the five dimensionless variables ϕ, ψ, R, ζ_{S2} and ζ_{R3} as promised in Section 3.2. All angles and velocities in addition to Eqn (3.40) may also be expressed in terms of ϕ, ψ and R as follows:

$$\alpha_1 = \arctan\left\{\frac{\psi/2 + R - 1}{\phi}\right\} \right\}$$
$$\alpha_2 = \arctan\left\{\frac{\psi/2 - R + 1}{\phi}\right\}$$
$$\beta_2 = \arctan\left\{\frac{\psi/2 - R}{\phi}\right\}$$
$$\beta_3 = \arctan\left\{\frac{\psi/2 + R}{\phi}\right\}$$
$$\varepsilon_S = \arctan\left\{\frac{\phi\psi}{\phi^2 - \psi^2/4 + (R - 1)^2}\right\} = \alpha_1 + \alpha_2$$
$$\varepsilon_R = \arctan\left\{\frac{\phi\psi}{\phi^2 - \psi^2/4 + R^2}\right\} = \beta_2 + \beta_3$$
(3.42)

and

$$\frac{c_1}{U} = \frac{c_3}{U} = \sqrt{\phi^2 + (\psi/2 + R - 1)^2} \right\}$$
$$\frac{w_2}{U} = \sqrt{\phi^2 + (\psi/2 - R)^2}$$
(3.43)

3.5.1 Optimum reaction

For any prescribed (ϕ, ψ) duty we may now estimate the stage reaction R which will produce maximum efficiency ζ_{TT}. The easiest approach is to define the dimensionless loss L from Eqn (3.41) expressed as

$$\eta = \frac{1}{1 + L}$$

where

$$L = \frac{1}{2\psi}[\{\phi^2 + (\psi/2 + 1 - R)^2\}\zeta_{S2} + \{\phi^2 + (\psi/2 + R)^2\}\zeta_{R3}] \tag{3.44}$$

The minimum loss and therefore maximum efficiency with respect to reaction R follows from

$$\left\{\frac{\partial L}{\partial R}\right\}_{\phi,\psi} = 0 \tag{3.45}$$

where ϕ, ψ are kept constant. If we assume that the loss coefficients are weak functions of R and may be assumed constant also, Eqn (3.45) yields finally

$$R_{\text{optimum}} = \frac{\zeta_{S2} + \psi/2(\zeta_{S2} - \zeta_{R3})}{\zeta_{S2} + \zeta_{R3}} \tag{3.46}$$

One possible solution to this which is true for all values of ψ is

$$\left.\begin{array}{c} R = 0.5 \\ \zeta_{S2} = \zeta_{R3} \end{array}\right\} \tag{3.47}$$

Although the stator and rotor velocity triangles are identical for this condition of 50% reaction, there would in reality be differences in the two loss coefficients. Even so, the strong indication is that 50% reaction will be close to optimum.

3.5.2   Optimum ψ for a given ϕ and R

Alternatively we may search for the ψ value leading to minimum loss for given ϕ and R values by writing

$$\left\{\frac{\partial L}{\partial \psi}\right\}_{\phi,R} = 0$$

resulting in

$$\psi_{\text{opt}} = 2\sqrt{\phi^2 + \tfrac{1}{2} + R(R - 1)} \tag{3.48}$$

where we have also assumed that ζ_{S2} and ζ_{R3} are independent of ψ. Two stages of special interest are the 50% reaction stages which we have already considered in some detail, and the 0% reaction or 'impulse' stages. For these reactions, Eqn (3.48) becomes

$$\psi_{\text{opt}} = \sqrt{4\phi^2 + 1} \qquad \text{for } R = 0.5 \tag{3.49a}$$
$$\psi_{\text{opt}} = \sqrt{4\phi^2 + 2} \qquad \text{for } R = 0.0 \tag{3.49b}$$

We observe that the theoretical ψ_{opt} for the 50% reaction case agrees with Eqn (3.31) of Section 3.4.1.
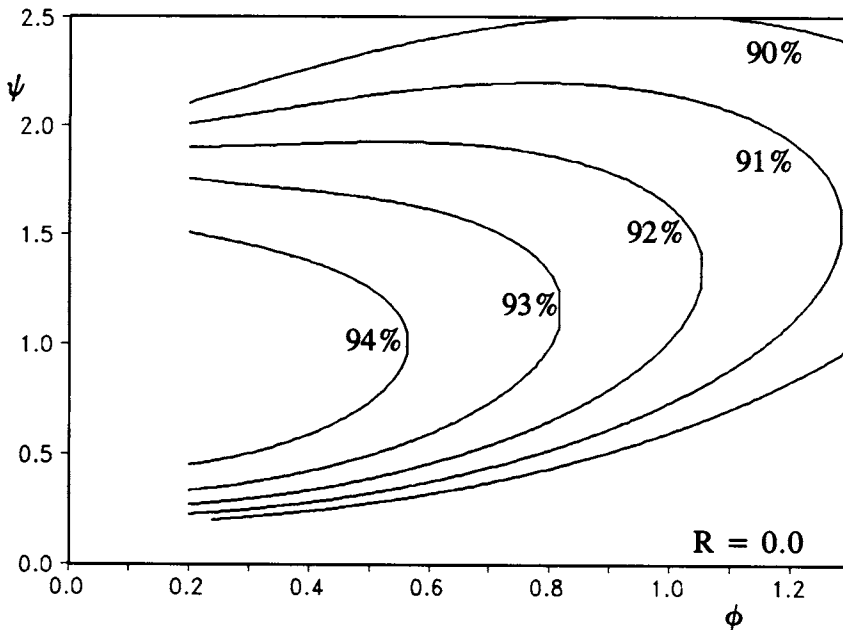
Fig. 3.14 Predicted total-to-total efficiency for axial turbines with 0% reaction (impulse stages) and blade aspect ratio $H/b = 10$

3.5.3   Zero reaction or 'impulse' stages

It is immediately apparent from Eqn (3.49b) that the theoretical optimum ψ value for an impulse stage is actually greater than that for a 50% reaction stage. This is borne out by the efficiency contours shown in Fig. 3.14 which were derived from the above analysis making use of Soderberg's loss correlation, Eqns (3.36). Comparing these with the predicted performance (ϕ, ψ) chart for 50% reaction stages, Fig. 3.12, we note the following main trends:

(1) Over a wide range of practical flow coefficients $0.4 < \phi < 1.2$ the impulse turbines will deliver a greater work coefficient ψ than the 50% reaction machines (typically about 33% greater).
(2) For low flow coefficients $\phi < 0.6$ the efficiency falls off much more rapidly with ψ for the 50% reaction stages.

3.6   Variation of reaction with radius in a free vortex turbine stage

In general a designer will introduce a variation of stage reaction R with radius. The simplest form of design is the constant loading free vortex stage for which the radial variation of R may be derived as follows.

Constant loading
If we decide to extract the same stagnation enthalpy Δh_o at all radii of our model stage, Fig. 3.3, we can relate the work coefficient ψ at any radius r to the value ψ_m at the mean radius r_m through:

$$\psi = \frac{\Delta h_o}{U^2} = \frac{\Delta h_o}{U_m^2}\left(\frac{U_m}{U}\right)^2 = \psi_m\left(\frac{r_m}{R}\right)^2 \tag{3.50}$$

Free vortex
For this type of stage (see Sections 5.1 and 6.3.4) the swirl velocities are assumed to vary with radius according to the potential flow field of a free vortex coincident with the axis. Thus the swirl velocity $c_{\theta2}$ downstream of the stator at radius r will be related to the value at r_m through

$$c_{\theta2}r = c_{\theta2m}r_m \tag{3.51}$$

Now making use of Eqn (3.39) for $c_{\theta2}/U$,

$$\frac{c_{\theta2}}{U} = 1 - R + \frac{\psi}{2} = 1 - R + \frac{\psi_m}{2}\left(\frac{r_m}{r}\right)^2$$

$$\frac{c_{\theta2m}}{U_m} = 1 - R_m + \frac{\psi_m}{2} = \frac{c_{\theta2}}{U}\left(\frac{r}{r_m}\right)^2$$

$$= (1 - R)\left(\frac{r}{r_m}\right)^2 + \frac{\psi_m}{2}$$

Thus finally R is given as a function of radius and reaction R_m at the mean radius r_m, through

$$R = 1 - (1 - R_m)\left(\frac{r_m}{r}\right)^2 \tag{3.52}$$

Applying this result to stage 3 of the turbine shown in Fig. 3.1, the radial variation reaction is given in Table 3.1.

A full ϕ, ψ, R and velocity triangle analysis is calculated for each of the three stages by the computer program FIPSI and saved onto the disc. Results for stage 3 only are shown in Table 3.1. Of particular interest in the present context is the reaction which varies from -18.4% at the hub radius r_h to 50% at r_m and 72.6% at tip r_t.

Hub section r_h
The possibility thus arises with a free vortex design that the stage reaction may actually be negative at the inner radius r_h. Furthermore a high flow coefficient ϕ will be obtained and an extremely high work coefficient ψ, in this case $\phi = 0.891$, $\psi = 3.563$. Another feature which should be drawn out of the tabulated data is the high Mach number leaving the stator hub section, $M_2 = 0.773$. Very high fluid deflections are also required at r_h for both stator and rotor, namely $\varepsilon_S = 107.12°$, $\varepsilon_R = 126.46°$. The hub section is thus subjected to extremely tough aerodynamic design requirements. Against this on the other hand are two mitigating factors:

(1) At r_h the blades are circumferentially pitched more closely, providing a narrower blade passage to facilitate fluid deflection.
(2) The mass flow rate per unit of blade height, $\Delta\dot{m}/\Delta r = \rho c_x 2\pi r$, is small at r_h so that high profile losses in that region will carry less weight.

Tip section r_t
At the tip radius r_t on the other hand the reaction is very high, $R = 0.725\,71$, while the flow and work coefficients are quite low, $\phi = 0.429$, $\psi = 0.825$. Stator deflection

Table 3.1 Design parameters for a free-vortex axial turbine stage (stage no. 3 of Fig. 3.1)

Dimensionless coefficients

Radius	Reaction	fi	psi	M2	M3
0.243 70	−0.183 93	0.891	3.563	0.773	0.453
0.269 96	0.035 20	0.804	2.903	0.698	0.464
0.296 22	0.198 68	0.733	2.411	0.638	0.477
0.322 48	0.323 87	0.673	2.035	0.589	0.492
0.348 74	0.421 86	0.623	1.740	0.549	0.508
0.375 00	0.500 00	0.579	1.505	0.515	0.526
0.401 26	0.563 30	0.541	1.314	0.486	0.545
0.427 52	0.615 30	0.508	1.158	0.461	0.564
0.453 78	0.658 54	0.478	1.028	0.440	0.584
0.480 04	0.694 88	0.452	0.918	0.421	0.605
0.506 30	0.725 71	0.429	0.825	0.404	0.626

M2 = absolute exit mach no. leaving the stator.
M3 = relative exit mach no. leaving the rotor.

Velocity triangle data

Radius	Alpha1	Alpha2	Stator deflection	Beta2	Beta3	Rotor deflection
0.244	33.843	73.276	107.119	65.613	60.849	126.462
0.270	31.186	71.590	102.777	60.411	61.589	122.000
0.296	28.883	69.937	98.819	53.949	62.438	116.387
0.322	26.872	68.317	95.189	45.844	63.342	109.186
0.349	25.106	66.734	91.839	35.737	64.266	100.003
0.375	23.545	65.187	88.731	23.545	65.187	88.731
0.401	22.158	63.677	85.835	9.829	66.087	75.916
0.428	20.918	62.206	83.124	−4.110	66.959	62.850
0.454	19.804	60.774	80.577	−16.835	67.797	50.962
0.480	18.798	59.380	78.179	−27.534	68.597	41.063
0.506	17.887	58.026	75.913	−36.125	69.358	33.233

$\varepsilon_S = 75.91°$ is less than that at the mean radius by a relatively small margin compared with rotor deflection which has the extremely small value of $\varepsilon_R = 33.23°$.

It should be pointed out that for the mean radius duty $\phi = 0.579$, $\psi = 1.505$, this stage is fairly highly loaded compared with the family of test stages shown on Fig. 3.8. However, the high reaction tip section, which is likely to have high efficiency also, passes a high mass flow rate per unit blade height and will thus play an important role in helping to raise the stage efficiency. On the debit side, however, is the crucial matter of blade tip leakage losses. Because tip reaction is high the pressure drop across the rotor tip section is also high and hence the driving effect for creating tip
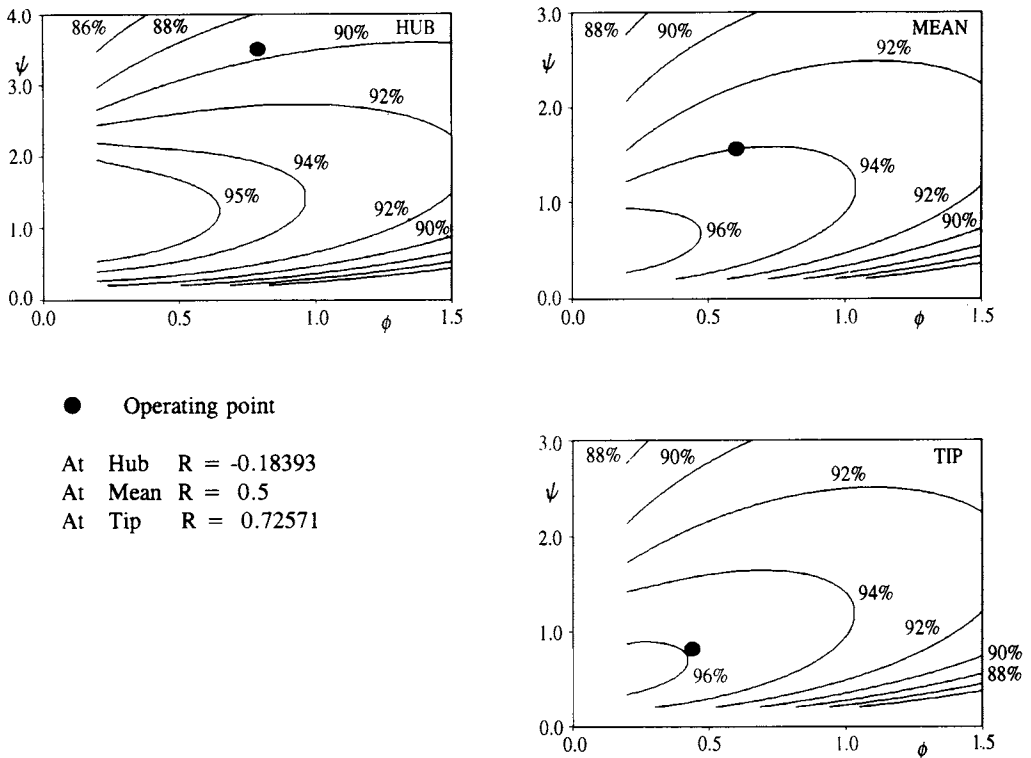
Fig. 3.15 Predicted efficiency contours for reactions *R* at hub, mean and tip radii of model turbine stage based on profile losses only, using Soderberg's correlation

clearance leakage losses. The magnitude of these will also be proportional to the mean relative dynamic head $\frac{1}{2}\rho w_\infty^2$ (based upon rotor vector mean relative velocity w_∞) which will also unfortunately be high. Thus considerable effort is made to minimise tip leakage losses either by maintaining close clearances between blade tip and casing or by the use of 'banding' strip, a popular technique in steam turbines.

3.6.1 Streamline efficiencies

In order to bring out the variation in predicted performance of blade sections from hub to casing it is helpful to produce predicted efficiency contours for selected meridional streamlines based upon profile losses only. (ϕ, ψ) charts for the hub, mean and tip sections of our model turbine are therefore shown in Fig. 3.15. From these we take note that the operating point for the stage falls closest to maximum possible efficiency at the tip section. At the mean radius, as already remarked above, the stage is quite heavily loaded, $\psi = 1.5046$, resulting in some sacrifice of local streamline efficiency. At the hub section the operating point falls excessively high on the (ϕ, ψ) chart, $\psi = 3.5626$, resulting in a predicted streamline efficiency of only 89.59%. Predicted efficiencies here were calculated by Soderberg's correlation making use of profile losses only. A summary of predicted data is given in Table 3.2.

Table 3.2 Prediction of streamtube efficiencies for a free vortex axial turbine using Soderberg's correlation

Radius	fi	psi	Reaction	e stator	e rotor	Efficiency
0.2437	0.8910	3.5626	−0.183 92	107.1191	126.4620	89.589 917
0.2700	0.8043	2.9033	0.035 21	102.7769	122.0001	90.970 849
0.2962	0.7330	2.4113	0.198 68	98.8197	116.3869	91.999 679
0.3225	0.6733	2.0346	0.323 87	95.1897	109.1860	92.813 646
0.3487	0.6226	1.7397	0.421 87	91.8397	100.0037	93.505 865
0.3750	0.5790	1.5046	0.500 00	88.7318	88.7318	94.129 091
0.4013	0.5411	1.3141	0.563 30	85.8350	75.9170	94.691 503
0.4275	0.5079	1.1576	0.615 30	83.1240	62.8503	95.166 909
0.4538	0.4785	1.0275	0.658 54	80.5779	50.9625	95.528 799
0.4800	0.4523	0.9182	0.694 88	78.1793	41.0642	95.775 830
0.5063	0.4288	0.8254	0.725 71	75.9136	33.2336	95.926 332

Mass weighted average streamtube efficiency = 94.0684%.
Stage efficiency including secondary losses = 92.3161%.

The mass weighted streamline efficiency may be defined as

$$\eta_{\text{ave}} = \frac{\displaystyle\int_{r_h}^{r_t} \rho c_x \eta_{TT} \, dr}{\displaystyle\int_{r_h}^{r_t} \rho c_x r \, dr}$$

Assuming that ρ and c_x do not vary with radius, $\eta_{\text{ave}} = 94.07\%$ for this stage which falls extremely close to the streamtube efficiency at the mean radius, $\eta_{TT} = 94.13\%$. Assuming an aspect ratio $H/b = 10$, the predicted stage efficiency including an estimate of secondary losses becomes $\eta_{TT\text{stage}} = 92.32\%$ which is slightly low compared with the published experimental correlation, Fig. 3.8.

3.7 Axial turbines with zero interstage swirl

During the period of rapid growth in steam power generation after the second world war, steam turbines were frequently designed with zero swirl velocity between the stages. The main reasons for this were:

(1) It was felt that the carry-over kinetic energy $\frac{1}{2}\rho c_3^2$ should be kept to a minimum to reduce possible 'carry-over' losses. Thus Kearton (1951) speaks of a 'carry-over' coefficient which determines the fraction of the $\frac{1}{2}\rho c_3^2$ leaving a rotor that remains available to the next stator.
(2) It was easier to manufacture diaphragm (stator) blades from formed plate if the inlet angle was zero at all radii.
(3) If $\alpha_1 = \alpha_3 = 0$, a direct relationship exists between ψ and R which speeds up desk calculations.

Although these reasons no longer apply due to greater understanding of turbo-
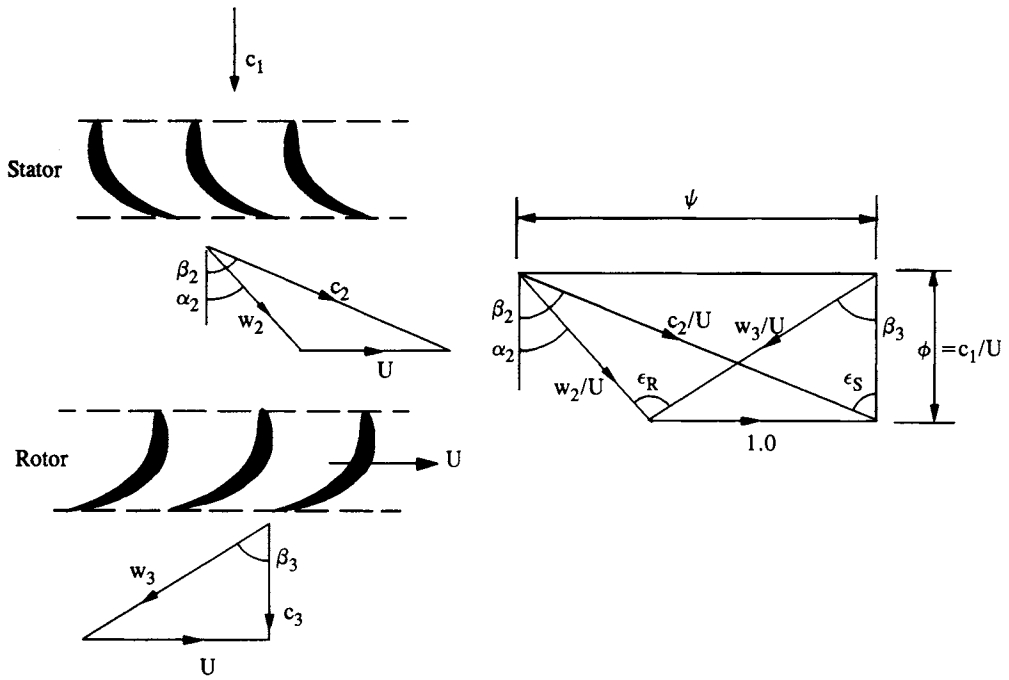
Fig. 3.16 Velocity triangles for a turbine blade row with zero interstage swirl

machinery fluid dynamics and advances in blade manufacture and computational facilities, such stages do in fact deliver very high efficiencies and are worth investigation at this point within the present performance analysis framework.

The dimensionless velocity triangles are shown in Fig. 3.16 from which we can show that the reaction R reduces to

$$R = \frac{h_2 - h_3}{h_1 - h_3} = \frac{h_2 - h_3}{h_{o1} - h_{o3}} = \frac{\frac{1}{2}(w_3^2 - w_2^2)}{\psi U^2}$$

$$= 1 - \frac{\psi}{2} \tag{3.53}$$

Now from Eqn (3.42a) for stages that *do* have interstage swirl, we can show that

$$R = 1 - \frac{\psi}{2} + \phi \tan \alpha_1 \tag{3.54}$$

Thus in general R would be a function of ϕ, ψ and α_1. The present type of stage is therefore a restricted family of turbines for which the reaction R is a function of ψ only. The design significance of this restriction can be seen if we tabulate ψ versus the interstage swirl α_1 for the typical reactions $R = 0\%$ and 50%, for a typical flow coefficient of $\phi = 0.6$.

Table 3.3 Influence of interstage swirl upon loading coefficient (assuming a flow coefficient $\phi = 0.6$)

50% reaction		0% reaction (impulse)	
$\alpha_1°$	ψ	$\alpha_1°$	ψ
0	1.000 00	0	2.000 00
10	1.211 59	10	2.211 59
20	1.436 76	20	2.436 76
30	1.692 82	30	2.692 82

As may be seen from Table 3.3, the effect of introducing swirl α_1 between the stages is to increase the work coefficient ψ, which can also be verified by comparing Figs 3.3 and 3.16. Even a modest swirl angle of $\alpha_1 = 10°$ will produce a 21% increase in work coefficient for the 50% reaction section.

3.7.1   Dimensionless velocity triangles and efficiency contours

The following useful geometrical data may be obtained from the dimensionless velocity triangles:

$$
\left.
\begin{aligned}
\alpha_2 &= \varepsilon_S = \arctan\left(\psi/\phi\right) \\[2mm]
\beta_2 &= \arctan\left(\frac{\psi - 1}{\phi}\right) \\[2mm]
\beta_3 &= \arctan\left(1/\phi\right) \\[2mm]
\varepsilon_R &= \beta_2 + \beta_3 = \arctan\left\{\frac{\phi\psi}{\phi^2 - \psi + 1}\right\}
\end{aligned}
\right\}
\tag{3.55}
$$

$$
\left.
\begin{aligned}
\frac{c_2}{U} &= \sqrt{\phi^2 + \psi^2} \\[2mm]
\frac{w_3}{U} &= \sqrt{\phi^2 + 1}
\end{aligned}
\right\}
\tag{3.56}
$$

Introducing c_2/U and w_3/U into Eqn (3.21), the total-to-total efficiency becomes

$$
\eta_{TT} = \frac{1}{1 + \dfrac{1}{2\psi}\left[(\phi^2 + \psi^2)\zeta_{S2} + (\phi^2 + 1)\zeta_{R3}\right]}
\tag{3.57}
$$

$$
= f(\phi, \psi, \zeta_{S2}, \zeta_{R3})
$$

We observe, compared with Eqn (3.41), that η_{TT} is no longer a function of reaction R as an independent variable since R is itself an explicit function of ψ, namely
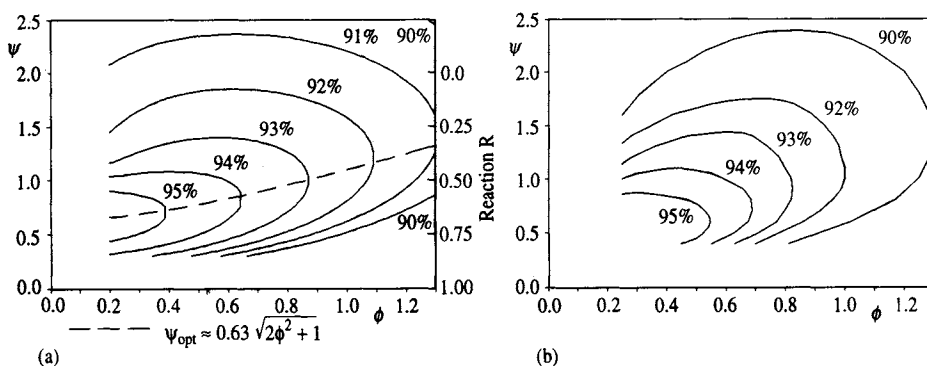
Fig. 3.17 Comparison of two performance prediction methods for axial turbines: (a) stages with zero interstage swirl $\alpha_1 = 0$ and aspect ratio $H/b = 10$ using Soderberg's correlation; (b) stages with symmetrical velocity triangles (50% reaction) (adapted from Craig and Cox, 1971)

$R = 1 - \psi/2$, Eqn (3.53). One (ϕ, ψ) chart will therefore suffice to cover all reactions. Predicted efficiency contours are shown in Fig. 3.17(a) making use of Soderberg's loss correlation.

The predicted performance map is compared in Fig. 3.17 with a performance prediction method published by Craig and Cox (1971). Although this came from within the steam turbine industry, the aim was to present a comprehensive performance prediction for both steam and gas turbines in order to provide a cross-check with the model turbine test correlation of S. F. Smith, Fig. 3.8, with which it broadly agrees. Craig and Cox's stages were reported as having symmetrical velocity triangles, which would in other words be of 50% reaction. There is indeed very good agreement between the two prediction methods for the case $\psi = 1.0$ which is encouraging, bearing in mind the simplicity of Soderberg's loss formulation as given here, Eqns (3.36). Indeed, for ψ values below 1.5 there is generally good agreement between the two prediction methods. For $\psi > 1.5$, however, the interstage swirl angle will become significant. Thus from Eqn (3.54),

$$\tan \alpha_1 = (\psi/2 - 1 + R)/\phi$$
$$= (\psi - 1)/2\phi \quad \text{for 50% reaction}$$

For this reason the efficiency values predicted by Craig and Cox fall off more rapidly for $\psi > 1.5$ and especially so at low flow coefficients.

3.7.2 Simplified theoretical analysis for optimum duty curve

Following a similar approach to that outlined in Section 3.4.2, a theoretical optimum duty curve $\psi_{\text{opt}} = f(\phi)$ may be estimated if we extract the dimensionless losses L from the expression for η_{TT}, Eqn (3.57), and minimise them:

$$L = \frac{1}{2\psi}[(\phi^2 + \psi^2)\zeta_{\text{S2}} + (\phi^2 + 1)\zeta_{\text{R3}}] \tag{3.58}$$

Thus ignoring the variation of ζ_{S2} and ζ_{R3} with ψ, for minimum losses we have

$$\frac{\partial L}{\partial \psi} = 0$$

whereupon finally we obtain

$$\psi_{opt} = \sqrt{(1 + \zeta_{R3}/\zeta_{S2})\,\phi^2 + \zeta_{R3}/\zeta_{S2}} \qquad (3.59)$$

If we assume $\zeta_{R3}/\zeta_{S2} \approx 1$ this simplifies to

$$\psi_{opt} \approx \sqrt{2\phi^2 + 1} \qquad (3.60)$$

In practice the stator and rotor loss coefficients ζ_{S2} and ζ_{R3} do vary with both ϕ and ψ and Eqn (3.59) does not fit the optimum duty curve. However, its form is reasonable if we introduce a scaling constant K, namely

$$\psi_{opt} = K\sqrt{2\phi^2 + 1} \qquad (3.61)$$

where $K = 0.626$ gives an acceptable curve fit for the contours shown in Fig. 3.17(a) for which the aspect ratio was $H/b = 10.0$. Again, in practice, the majority of stages or streamline designs would lie above this curve, accepting some reduction of efficiency in order to reduce the total number of stages required, by imposing greater stage loading ψ.

3.7.3   Blade/speed or velocity ratio

The blade/speed ratio or velocity ratio σ_{is} was a popular parameter in the early days of steam turbine development (Kearton, 1951), and is still useful for quick determination of the allowable streamline enthalpy drop Δh_o for a given blade speed U and reaction R. σ_{is} is defined as

$$\sigma_{is} = \frac{\text{Blade speed}}{\text{Gas velocity for isentropic expansion } p_1 \text{ to } p_3}$$

$$= \frac{U}{\sqrt{2(h_{o1} - h_{o3S})}} = \frac{U}{\sqrt{2\Delta h_{oS}}} \qquad (3.62)$$

But from Fig. 3.4,

$$\psi = \frac{\Delta h_o}{U^2} = \frac{\eta_{TT}\Delta h_{oS}}{U^2}$$

so that for turbine stages without swirl,

$$\sigma_{is} = \sqrt{\frac{\eta_{TT}}{2\psi}} = \frac{1}{2}\sqrt{\frac{\eta_{TT}}{1-R}} \qquad (3.63)$$

Thus for a given η_{TT}, there is a direct relationship between σ_{is} and reaction R as given in Table 3.4.

Table 3.4 Relationship between blade speed ratio and reaction for stages with zero interstage swirl

R	$\sigma_{is}/\sqrt{\eta_{TT}}$
0	0.500 00
0.1	0.527 05
0.2	0.590 20
0.3	0.597 61
0.4	0.645 50
0.5	0.707 11
0.6	0.790 57
0.7	0.912 87
0.8	1.118 03

Although less popular as a quick design aid, the following example illustrates its use.

Example 3.4

Problem
For a blade speed $U_m = 100 \, \mathrm{m\,s^{-1}}$ and reaction $R_m = 0.5$ at the mean radius r_m of a turbine with $\alpha_1 = \alpha_3 = 0$, calculate the stagnation enthalpy drop, assuming $\eta_{TT} = 0.93$. For constant load at all radii calculate the appropriate reaction at the hub radius $r_h = 0.75 r_m$.

Solution
At r_m

$$\sigma_{ism} = \frac{1}{2}\sqrt{\frac{0.93}{1 - 0.5}} = 0.681\,91$$

Therefore

$$\Delta h_{os} = \frac{1}{2}\left(\frac{U_m}{\sigma_{is}}\right)^2 = \frac{1}{2}\left(\frac{100}{0.681\,91}\right)^2 = 10.753 \, \mathrm{kJ\,kg^{-1}}$$

$$\Delta h_o = \eta_{TT}\Delta h_{os} = 0.93 \times 10.753 = 10.0 \, \mathrm{kJ\,kg^{-1}}$$

4
Performance analysis for axial compressors and fans

Introduction

We have already taken a close look at the aerodynamic performance characteristics of compressor cascades in Chapter 2, focusing in particular upon their role as diffusers. The purpose of a compressor or fan is twofold:

(1) To raise the pressure of a gas flow.
(2) To deliver a given mass or volume flow rate.

The first of these requirements thus classes compressors and fans as diffusing machines whose aim is to convert fluid kinetic energy into pressure head, mainly by aerodynamic means. In contrast with this, axial turbines, as demonstrated in Chapter 3, convert thermal energy into output power and their blade rows act as nozzles or flow-accelerating aerofoil cascades. Because of this, turbine blade rows are much more aerodynamically stable than compressor blade rows and as a general rule are easier to design. Furthermore the dimensional analysis strategy outlined in Chapter 3 for selection of stage loadings and consequent velocity triangles works extremely well since the (ϕ, ψ) contours for high performance stages, Fig. 3.8, are less subject to excessive stalling losses for a fairly wide band of flow coefficients ϕ and work coefficients ψ. Consequently theoretical performance analysis using the simple turbine loss correlation of Soderberg, Eqn (3.36), leads to a very credible framework for turbine stage selection based upon predicted (ϕ, ψ) charts such as those shown in Figs 3.12, 3.14 and 3.15.

Although we may anticipate much greater sensitivity of compressors and fans to losses and to stalling instabilities, attempts have been made to produce experimental (ϕ, ψ) performance correlations for high quality compressors. These will be introduced in Section 4.3 of this chapter within a dimensional analysis framework which helps to relate the duty coefficients ϕ and ψ to the velocity triangles. Theoretical cascade analysis developed in Chapter 2 will then be applied to link compressor aerodynamic loading parameters such as lift coefficient C_L, drag coefficient C_D and diffusion factor D_f directly with the overall performance correlation, in Sections 4.4 and 4.5. Dimensionless velocity triangles form the essential middle link in the following chain which provides a simple design rationale for selection of blade loading to achieve a prescribed duty:

(1) Selection of (ϕ, ψ) duty coefficients and number of stages to achieve the specified compressor or fan overall design flow rate and pressure rise.
(2) Velocity triangles at the mean radius are then fully determined.
(3) Blade pitch/chord ratio may then be selected to satisfy aerodynamic loading parameters such as lift coefficient and diffusion factor.
(4) Finally, detailed blade geometry can be selected to ensure smooth entry flow and the correct fluid efflux angle from each blade row.
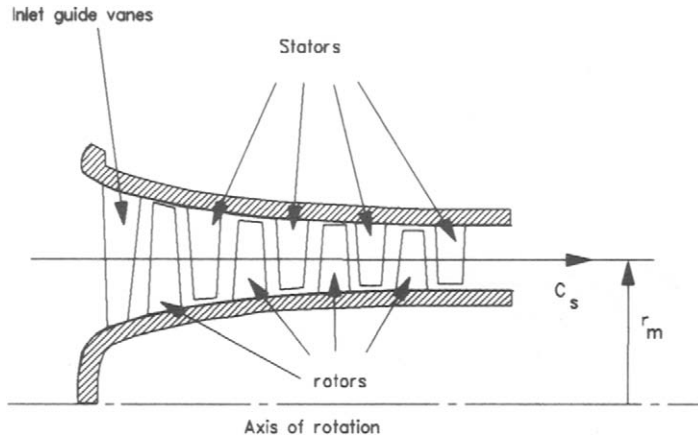
Fig. 4.1 Meridional view of a multi-stage axial compressor

   The discussion will be extended from compressors to fans in Section 4.6 although a fuller treatment of these, involving vortex design for blade sections from hub to casing, will be reserved for Chapter 5 which deals with the simple radial equilibrium model for meridional flows.

   More detailed consideration of the design process for high reaction axial fan stages will be given in Section 4.7, where use will also be made of the computer program CASCADE to illustrate a procedure for the completion of item (4) above. The present chapter will be concluded with a simple consideration of off-design performance estimation making use of theoretical predictions of outlet angle β_2 versus inlet angle β_1 derived from blade row analysis such as that provided by the computer program CASCADE.

4.1 Dimensional analysis for an axial compressor

The meridional view of a multi-stage axial compressor shown in Fig. 4.1 illustrates the main features of blading and annulus, namely:

(1) An inlet guide vane blade row to provide pre-whirl into the first stage.
(2) A set of repeating stages each comprising a rotor followed by a stator.
(3) Contraction of the annulus area to maintain constant meridional velocity c_s as the gas density ρ increases due to compression.
(4) Constant mean radius $r_m = \frac{1}{2}(r_h + r_t)$.

In practice (3) and (4) are not essential constraints and may be relaxed, but we will adopt them here since they lead to considerable simplifications. We can appreciate this by defining flow and work coefficients analogous to the turbine duty coefficients, Eqns (3.7) and (3.8), namely

$$\left. \begin{array}{ll} \phi = \dfrac{c_s}{U} & \text{Flow coefficient} \\[2em] \psi = \dfrac{\Delta h_o}{U^2} & \text{Work input coefficient} \end{array} \right\} \qquad (4.1)$$
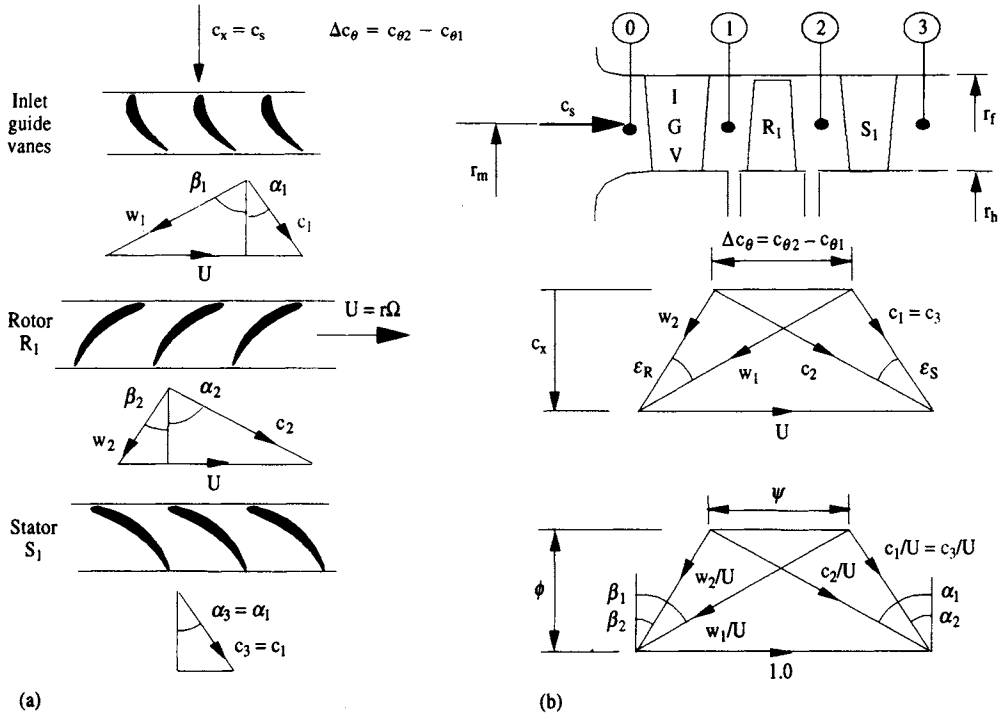
Fig. 4.2 Velocity triangles for a 50% reaction model compressor stage: (a) velocity vectors between the blade rows; (b) assembled velocity triangles for the stage

From constraints (3) and (4) above it follows that the flow coefficient ϕ will be identical for all stages. It would be logical also to provide the same specific work input and thus stagnation enthalpy rise Δh_o into each stage and therefore to select identical work input coefficients ψ for all stages. Consequently the velocity triangles and therefore blade profile design at the mean radius r_m will be identical for all stages. Apart from the reduction in aerodynamic design work, two other benefits emerge from this. Firstly we may be able to reduce the manufacturing costs if identical blade profiles are to be generated for all stators and for all rotors. Secondly and perhaps more significantly, it seems that we need only undertake model tests for the development programme on the one configuration if all stages are identical. The obvious snag is that we have enforced the identical duty (ϕ, ψ) at the mean radius only. At other radii velocity triangles will vary, demanding the introduction of blade twist. Although this will be the same for all stages, as we will show in Chapter 5, the blades will be shorter in length through the compressor, Fig. 4.1, due to the increase in fluid density. Furthermore the growth of the annulus boundary layer on the hub and casing walls soon leads to major distortion of the meridional velocity c_s from hub to tip, so that conditions become less ideal for experimental simulation by a simple model stage designed to derive performance data applicable to all stages. Despite this setback it is still important to begin our design considerations within a manageable framework and for this purpose we will define the simple idealised compressor stage illustrated in Fig. 4.2.

Since we have decided to opt for identical stage designs at the mean radius, it is useful to show here the blading and velocity triangles for stage 1 so that we can include also the inlet guide vane IGV. This is a special stator blade row at inlet to the

compressor which introduces the pre-whirl angle α_1 required at entry to the first rotor R_1 in order to establish the repeating velocity triangles. Proceeding through the rotor and then the first stator S_1 the fluid is ejected directly into stage 2 with the same entry velocity vector $c_3 = c_1$, $\alpha_3 = \alpha_1$.

The individual velocity vectors at stations 0, 1, 2 and 3 are shown in Fig. 4.2(a) and the resulting assembled stage velocity triangles in Fig. 4.2(b). Following the strategy outlined for turbines in Chapter 3, it is extremely helpful also to create dimensionless velocity triangles by normalising all velocities with the blade speed U as also shown in Fig. 4.2(b). The dimensionless axial or meridional velocity then becomes equal to the flow coefficient. That is

$$\frac{c_x}{U} = \frac{c_s}{U} = \phi \tag{4.2}$$

But from the Euler pump equation (1.9a), the stagnation enthalpy rise is given by

$$\Delta h_o = r_m \Omega (c_{\theta 2} - c_{\theta 1}) = U \Delta c_\theta \tag{4.3}$$

So that the dimensionless change in peripheral whirl through either rotor or stator becomes

$$\frac{\Delta c_\theta}{U} = \frac{\Delta w_\theta}{U} = \frac{\Delta h_o}{U^2} = \psi \tag{4.4}$$

The duty coefficients (ϕ, ψ) thus predetermine the general shape of the velocity triangles, the only other controlling design feature being the stage reaction R. By analogy with the definition for axial turbines, Eqn (3.4), the conventional definition of stage reaction for axial compressors is as follows:

$$R = \frac{\text{Specific enthalpy rise across the rotor}}{\text{Specific enthalpy rise across the stage}} \tag{4.5}$$

R represents the fraction of overall specific enthalpy rise of the stage Δh produced by the rotor. For the case illustrated in Fig. 4.2 the reaction is 50%, i.e. $R = 0.5$, so that the rotor R_1 and stator S_1 produce equal enthalpy rises. Consequently the velocity triangles are symmetrical. For axial turbines we were able to show by theoretical analysis in Section 3.5.1 that the optimum stage reaction would be close to 50%. Although some of the assumptions made there concerning stator and rotor aerodynamic loss coefficients were valid for the turbine with its accelerating cascade flow but are less valid for the diffusing cascades of axial compressors, nevertheless it is well known that 50% reaction places an axial compressor stage close to the optimum selection of velocity triangles. It is very reasonable, therefore, for our model stage to make the design selection of 50% reaction, i.e. $R = 0.5$, at the mean radius r_m. Of course at other radii, due to vortex design considerations, R will depart from this ideal value as it did for turbines, Section 3.6 and Eqn (3.52). We will return to this matter again in the next chapter within the relevant context of vortex and radial equilibrium analysis.

To conclude this section it will be helpful to draw together, as we did for turbines
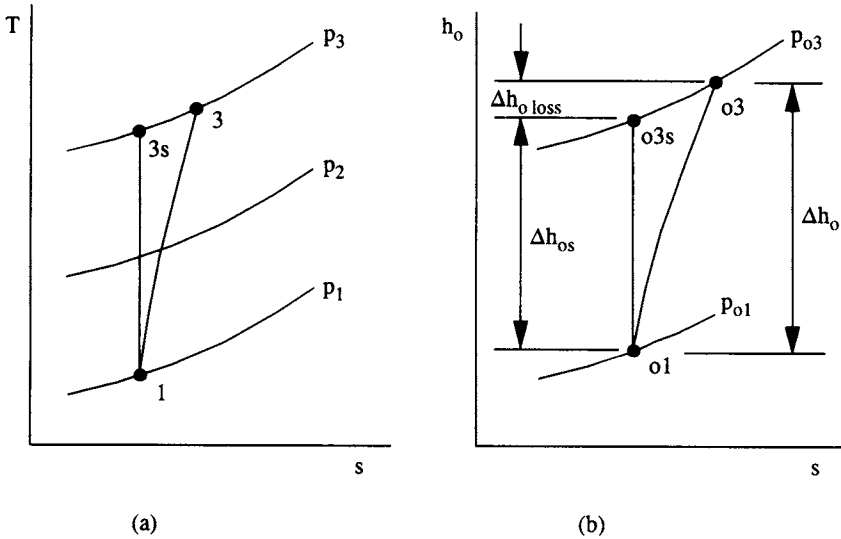
Fig. 4.3 (a) T–s and (b) h_o–s diagrams for an axial compressor stage

in Section 3.1, the various parameters considered so far which we would expect to influence the total-to-total efficiency η_{TT} of an axial compressor and then to see how these relate to the dimensionless groups which we have defined already. First of all we must define total-to-total efficiency for a compressor and we will do this for our model stage with reference to its T–s and h_o–s diagrams, Fig. 4.3.

The conventional definition of η_{TT} is as follows:

$$\eta_{TT} = \frac{\text{Stagnation enthalpy rise for an ideal (reversible) stage}}{\text{Stagnation enthalpy rise for the actual stage}}$$

$$= \frac{h_{o3s} - h_{o1}}{h_{o3} - h_{o1}} \tag{4.6}$$

where the ideal stage is operating across the same pressure ratio p_3/p_1. Due to fluid friction within the real stage, some of the ordered kinetic energy entering the blade rows is dissipated as heat during the diffusion processes which are so vulnerable to loss generation. The gas thus leaves the compressor stage at a temperature T_3 higher than that of the ideal frictionless stage T_{3s}, associated with an increase in specific entropy, $s_3 - s_1$.

Referring back now to our model stage, we could draw up the following list of variables which we would expect to have some effect upon the stage total-to-total efficiency:

$$\eta_{TT} = f(\underbrace{\Delta h_o, h_1, h_2, h_3,}_{\substack{\text{Thermodynamic} \\ \text{variables}}} \underbrace{\Omega, r_m,}_{\substack{\text{Speed and} \\ \text{size}}} \underbrace{c_x, w_1, c_2,}_{\substack{\text{Velocity} \\ \text{triangles}}} \underbrace{\mu, \rho, a_1, a_2,}_{\substack{\text{Properties of} \\ \text{working} \\ \text{substance}}} \underbrace{\Delta p_{oR}, \Delta p_{oS})}_{\substack{\text{Rotor and} \\ \text{stator} \\ \text{losses}}} \tag{4.7}$$

At this point the reader is referred to Chapter 3, Section 3.1, where similar groupings

have been presented and discussed for axial turbines. The main differences here are selections of maximum velocities w_1 and c_2 and associated local sonic velocities a_1 and a_2, now all chosen at entry to the blade rows. Following arguments from dimensional analysis similar to those in Section 3.1, this equation may be simplified to the following dimensionless form:

$$\eta_{TT} = f\{\underbrace{\phi, \psi,}_{\substack{\text{Duty} \\ \text{coefficients}}} \underbrace{R,}_{\substack{\text{Stage} \\ \text{reaction}}} \underbrace{\frac{w_1}{U}, \frac{c_2}{U},}_{\substack{\text{Velocity} \\ \text{triangles}}} \underbrace{M_1, M_2,}_{\substack{\text{Mach} \\ \text{numbers}}} \underbrace{\text{Re}_m,}_{\substack{\text{Stage} \\ \text{Reynolds} \\ \text{number}}} \underbrace{\zeta_R, \zeta_S\}}_{\substack{\text{Loss} \\ \text{coefficients}}} \qquad (4.8)$$

where ϕ, ψ and R have been defined already, and

$$\left.\begin{aligned}
M_1 &= \frac{w_1}{a_1} && \text{Rotor relative inlet Mach number} \\[2mm]
M_2 &= \frac{c_2}{a_2} && \text{Stator inlet Mach number} \\[2mm]
\text{Re}_m &= \frac{Ur_m}{\nu} && \text{Stage Reynolds number} \\[2mm]
\zeta_R &= \frac{(\Delta p_{oR})_{loss}}{\frac{1}{2}\rho w_1^2} && \text{Rotor loss coefficient} \\[2mm]
\zeta_S &= \frac{(\Delta p_{oS})_{loss}}{\frac{1}{2}\rho c_2^2} && \text{Stator loss coefficient}
\end{aligned}\right\} \qquad (4.9)$$

But from the dimensionless velocity triangles, Fig. 4.2(b), for our 50% reaction stage we can show that

$$\left.\begin{aligned}
\frac{w_1}{U} &= \frac{c_2}{U} = \sqrt{\phi^2 + \frac{1}{4}(1+\psi)^2} \\[2mm]
\frac{w_2}{U} &= \frac{c_1}{U} = \sqrt{\phi^2 + \frac{1}{4}(1-\psi)^2}
\end{aligned}\right\} \qquad (4.10)$$

so that Eqn (4.8) simplifies to

$$\eta_{TT} = f(\underset{i}{\phi}, \underset{i}{\psi}, \underset{i}{R}, \underset{d}{M_1}, \underset{d}{M_2}, \underset{d}{\text{Re}_m}, \underset{d}{\zeta_R}, \underset{d}{\zeta_S}) \qquad (4.8a)$$

where the labels i and d have been added below to indicate independent and dependent design variables respectively. Let us comment on these in turn.

Independent design variables
The designer is free at the outset to select the design duty coefficients (ϕ, ψ). As we will see later from experimental tests, the designer's choice will have a profound effect upon the stage efficiency η_{TT} attainable even with optimum aerodynamic design. The reason for this is that ϕ and ψ entirely control the shape of the velocity triangles and

therefore the flow environment within which the blades must operate. For the moment we have adopted 50% reaction for our consideration of mean radius design; but R will also exercise direct control over velocity triangle shape and hence efficiency should we depart from this (see Sections 4.3 and 4.5 later).

Dependent variables affecting η_{TT}
Experimental cascade tests show that the loss coefficients ζ_R and ζ_S are themselves dependent upon blade row Reynolds number and inlet Mach number. We would also expect loss levels to be directly influenced by the velocity triangle environment within which the blades have to operate and hence to depend directly upon ϕ, ψ and R. We can express this through

$$\left. \begin{aligned} \zeta_R &= f_1(\phi, \psi, R, Re_R, M_1) \\ \zeta_S &= f_2(\phi, \psi, R, Re_S, M_2) \end{aligned} \right\} \qquad (4.11)$$

where the blade row Reynolds numbers Re_R and Re_S are introduced based on rotor and stator blade chords l_R and l_S:

$$\left. \begin{aligned} Re_R &= \frac{w_1 l_R}{\nu} \\ Re_S &= \frac{c_2 l_S}{\nu} \end{aligned} \right\} \qquad (4.12)$$

Adopting these instead of the machine Reynolds number, Eqn (4.9c), to cater for the individual blade row frictional effects, Eqn (4.8) may be further simplified to

$$\eta_{TT} = f(\phi, \psi, R, \zeta_R, \zeta_S) \qquad (4.13)$$
$$\quad \text{i}\quad \text{i}\quad \text{i}\quad \text{d}\quad \text{d}$$

The efficiency of an axial compressor stage has thus been shown to depend upon five dimensionless parameters which are sufficient to account for all the 15 items originally listed in Eqn 4.7. Of these just three may be independently selected by the designer, namely ϕ, ψ and R. The loss coefficients themselves are also dependent upon the duty (ϕ, ψ) and reaction R but in addition are influenced by Reynolds number and Mach number.

4.2   Simple analytical formulation for the total-to-total efficiency of a compressor stage

Equations such as (4.13) in parametric form are frequently used for model testing to ensure dynamic and thermodynamic similarity. As with axial turbines, Chapter 3, we may go one stage further and convert Eqn (4.13) into a more useful analytical form. For the moment we will continue to assume the fixed reaction value $R = 0.5$. From the h_o–s diagram, Fig. 4.3(b), let us define the stagnation enthalpy loss due to irreversibilities, namely

$$(\Delta h_o)_{loss} = h_{o3} - h_{o3s} \qquad (4.14)$$

The stage stagnation enthalpy rise is given by

$$\Delta h_{\mathrm{o}} = h_{\mathrm{o}3} - h_{\mathrm{o}1} \tag{4.15}$$

Hence the total-to-total efficiency, Eqn (4.6), becomes

$$\eta_{\mathrm{TT}} = \frac{h_{\mathrm{o}3\mathrm{s}} - h_{\mathrm{o}1}}{h_{\mathrm{o}3} - h_{\mathrm{o}1}}$$

$$= 1 - \frac{(\Delta h_{\mathrm{o}})_{\mathrm{loss}}}{\Delta h_{\mathrm{o}}}$$

$$= 1 - \frac{(\Delta p_{\mathrm{o}})_{\mathrm{loss}}}{\rho \Delta h_{\mathrm{o}}} = 1 - \frac{1}{\psi}\left(\frac{(\Delta p_{\mathrm{o}})_{\mathrm{loss}}}{\rho U^2}\right) \tag{4.16}$$

The reader is referred to the full treatment given for turbines in Section 3.2 for guidance on the thermodynamic approximation leading to the use of the stage stagnation pressure loss $(\Delta p_{\mathrm{o}})_{\mathrm{loss}}$ in this last equation. Since

$$(\Delta p_{\mathrm{o}})_{\mathrm{loss}} = (\Delta p_{\mathrm{oR}})_{\mathrm{loss}} + (\Delta p_{\mathrm{oS}})_{\mathrm{loss}}$$

introduction of Eqns (4.9) and (4.10) results in the dimensionless loss

$$\frac{(\Delta p_{\mathrm{o}})_{\mathrm{loss}}}{\rho U^2} = \frac{1}{2}\zeta_{\mathrm{R}}\left(\frac{w_1}{U}\right)^2 + \frac{1}{2}\zeta_{\mathrm{S}}\left(\frac{c_2}{U}\right)^2$$

$$= \left(\frac{\zeta_{\mathrm{R}} + \zeta_{\mathrm{S}}}{2}\right)\left(\phi^2 + \frac{1}{4}(1+\psi)^2\right) \tag{4.17}$$

Finally, introducing this into Eqn (4.16), the total-to-total efficiency becomes

$$\eta_{\mathrm{TT}} = 1 - \frac{1}{2\psi}\left\{\phi^2 + \frac{1}{4}(1+\psi)^2\right\}(\zeta_{\mathrm{R}} + \zeta_{\mathrm{S}}) \tag{4.18}$$

Equation (4.18) is equivalent to the parametric equation (4.13) derived in general form from dimensional analysis for the fixed reaction $R = 0.5$, but is in the much more useful explicit form of an analytical relationship which shows exactly how η_{TT} depends upon the various dimensionless groups. From this we can make the following interpretation.

The efficiency of a 50% axial compressor stage is dependent upon two main factors:

(1) The stage duty coefficients (ϕ, ψ).
(2) The blade row loss coefficients ζ_{R} and ζ_{S} (i.e. the blade row aerodynamics).

The initial selection of the stage duty point (ϕ, ψ) is crucial. Thus we could rewrite Eqn (4.18) in the form

$$\eta_{\mathrm{TT}} = 1 - f_{\mathrm{c}}(\phi, \psi)(\zeta_{\mathrm{R}} + \zeta_{\mathrm{S}}) \tag{4.18a}$$

where the 'loss weighting coefficient' f_{c} is given by

$$f_{\mathrm{c}}(\phi, \psi) = \frac{1}{2\psi}\left\{\phi^2 + \frac{1}{4}(1+\psi)^2\right\} \tag{4.19}$$
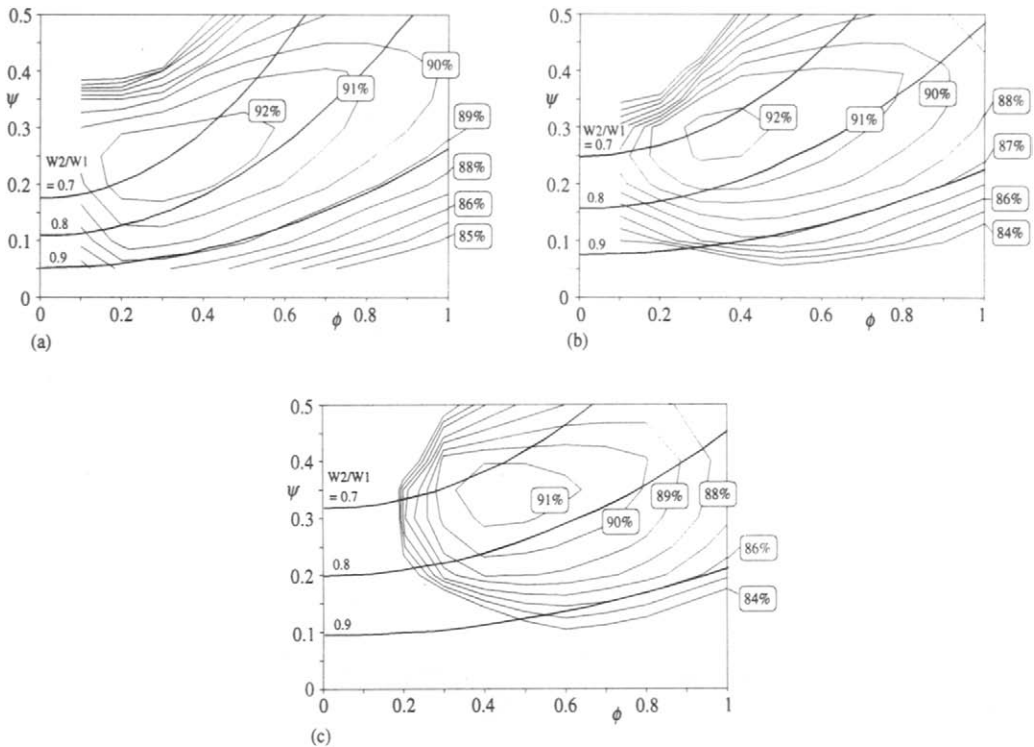
Fig. 4.4 'Smith' charts for axial compressor stages of (a) 50%, (b) 70% and (c) 90% reaction (after M. V. Casey, 1987)

ζ_R and ζ_S represent, in effect, cascade loss coefficients, since these are the loss coefficients normally used in compressor cascade model testing. For the stage, however, we would need to pin onto these all other frictional losses such as tip leakage and secondary losses related to rotor and stator. Within the present context of stage performance analysis they summarise the inherent aerodynamic loss characteristics of the blades. f_c on the other hand is dependent only upon (ϕ, ψ) and thus the velocity triangle environment into which the blades are immersed. We have called f_c a 'weighting coefficient' because it gives weight to the aerodynamic loss coefficients ζ_R and ζ_S. The latter can be minimised by very careful blade profile design, backed by wind tunnel cascade testing. This will be all in vain if the duty (ϕ, ψ) and velocity triangles are badly chosen in the first place, resulting in an excessive value of f_c.

4.3   Experimental correlation of optimum axial compressor stages – 'Smith' diagrams

M. V. Casey (1987) has published a comprehensive performance prediction method for mean radius analysis of axial compressors with identical repeating stages. In addition to this he has provided 'Smith' diagrams for optimum axial compressor stages similar in principle to the turbine charts described in Chapter 3, Fig. 3.8, and we will focus attention upon these in relation to the foregoing discussion. A (ϕ, ψ) chart for optimum 50% reaction stages is shown in Fig. 4.4 based upon model tests of a range of axial compressor stages. Any point on this diagram will indicate the optimum

Table 4.1 Comparison of optimum axial turbine and compressor stages as indicated by the 'Smith' diagrams

	ϕ	ψ	η_{TT} (%)
Axial turbines	0.6	1.0	94.5
Axial compressors	0.35	0.25	92.5

efficiency likely to be attainable from a well-designed axial compressor matched to that (ϕ, ψ) duty. Unfortunately the individual tests are not provided on this chart but efficiency contours have been curve-fitted through the test results, revealing the strong influence of both ϕ and ψ upon η_{TT}.

It is helpful to compare trends with the turbine 'Smith' diagram, Fig. 3.8. For example, the most efficient machines possible according to these two correlations would have duty coefficients as shown in Table 4.1.

The effectiveness of a compressor to fulfil its twofold task, as stated in the introduction to this chapter, may be judged

(a) by the magnitude of ϕ, typifying its capacity to move fluid,
(b) by its pressure rise coefficient ψ, typifying its pressure raising capability,
(c) and of course by its efficiency η_{TT}.

It is clear from the above comparison that the effectiveness of the optimum axial compressor stage falls far short of that of the optimum axial turbine. The optimum value of $\phi = 0.35$ is very low for practical purposes and the suggested work coefficient $\psi = 0.25$ is but a quarter of that for the optimum axial turbine stage. This is of course as expected for a turbomachine with diffusing blade rows for the reasons already discussed in the introduction to this chapter.

However, the efficiency contours of the compressor 'Smith' diagram are quite flat so that we could depart some way from the peak efficiency duty point recorded in Table 4.1 and select efficient compressor stages (e.g. $\eta_{TT} > 90\%$) for quite a wide range of (ϕ, ψ) duties. (The same is of course true for axial turbines as can be seen from Fig. 3.8 where the bulk of models tested had duty coefficients well in excess of the optimum.) Thus axial compressor stages with high efficiency and stable flow may be designed for the more practicable range $\phi = 0.5$ to 0.9 and with work coefficients as great as $\psi = 0.4$ to 0.45. We will illustrate this numerically in the next section after introducing further useful theoretical analysis. To summarise the present observations based upon Fig. 4.4, the sensible design range for axial compressor stages lies between the two curves

$$\left. \begin{array}{l} \psi_{opt} = 0.185\sqrt{4\phi^2 + 1} \\ \psi_{max} = 0.32 + 0.2\phi \end{array} \right\} \qquad (4.20)$$

4.4 Lift and drag coefficients and diffusion factor re-expressed in terms of duty coefficients

The key dimensionless parameters that indicate profile aerodynamic quality are the lift and drag coefficients C_L and C_D, Eqns (2.2). Various relationships for these were derived in Chapter 2 for compressor or fan cascades that are useful for the assessment of aerodynamic performance based upon experimental cascade tests. What matters

in practice is the aerodynamic performance of the blade profiles when located within the velocity triangle environment of the actual machine. It will be helpful therefore to re-express C_L and C_D in terms of the duty parameters (ϕ, ψ) which we have just shown to have total control over the shape of the velocity triangles. Lift coefficient for a cascade was expressed in terms of the relative inflow and outflow angles β_1 and β_2, the vector mean of these, β_∞, and the pitch to chord ratio, t/l, as follows:

$$C_{L\infty} = 2\frac{t}{l}(\tan\beta_1 - \tan\beta_2)\cos\beta_\infty - C_D\tan\beta_\infty \qquad [2.10]$$

But from the dimensionless velocity triangles, Fig. 4.2(b), we have

$$\left.\begin{array}{l} \tan\beta_1 = \dfrac{1+\psi}{2\phi} \\[4mm] \tan\beta_2 = \dfrac{1-\psi}{2\phi} \end{array}\right\} \qquad (4.21)$$

and hence

$$\tan\beta_\infty = \frac{1}{2}(\tan\beta_1 + \tan\beta_2) = \frac{1}{2\phi} \qquad (4.22)$$

Introducing these into Eqn (2.10) we thus have the alternative form for $C_{L\infty}$ involving the duty coefficients (ϕ, ψ):

$$C_{L\infty} = 2\left(\frac{t}{l}\right)\left\{\frac{2\psi}{\sqrt{4\phi^2 + 1}}\right\} - \frac{C_{D\infty}}{2\phi} \qquad (4.23)$$

Let us consider next the drag coefficient $C_{D\infty}$ as defined by Eqn (2.8):

$$C_{D\infty} = \frac{D}{\frac{1}{2}\rho W_\infty^2 l} = \zeta_\infty\left(\frac{t}{l}\right)\cos\beta_\infty \qquad [2.8]$$

where the cascade loss coefficient was based on the vector mean velocity W_∞, namely

$$\zeta_\infty = \frac{(\Delta p_o)_{loss}}{\frac{1}{2}\rho W_\infty^2} \qquad [2.9]$$

To apply this to our model compressor stage we need to convert to the form of loss coefficients based on entry velocities, Eqns (4.9d) and (4.9e). From the cascade analysis in Chapter 2 this would give

$$\begin{aligned} \zeta_1 &= \frac{(\Delta p_o)_{loss}}{\frac{1}{2}\rho W_1^2} = \zeta_\infty\left(\frac{W_\infty}{W_1}\right)^2 \\[3mm] &= \zeta_\infty\left(\frac{\cos\beta_1}{\cos\beta_\infty}\right)^2 \end{aligned} \qquad (4.24)$$
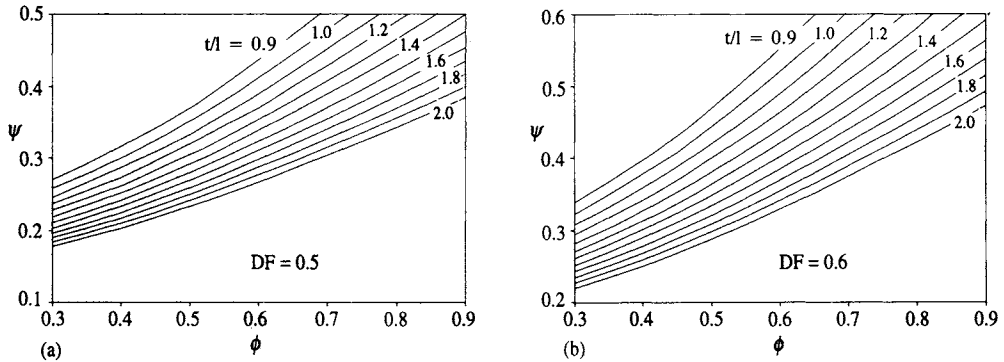
Fig. 4.5 Pitch/chord ratio as a function of ϕ and ψ for 50% reaction axial compressor stages, for diffusion factors of (a) 0.5 and (b) 0.6

so that $C_{D\infty}$ becomes, from Eqn (2.8) above,

$$
\begin{aligned}
C_{D\infty} &= \zeta_1 \left(\frac{t}{l} \right) \frac{\cos^3 \beta_\infty}{\cos^2 \beta_1} \\
&= \zeta_1 \left(\frac{t}{l} \right) \frac{2\phi(4\phi^2 + (1 + \psi)^2)}{(4\phi^2 + 1)^{3/2}}
\end{aligned}
\tag{4.25}
$$

The third aerodynamic parameter of great help for cascade selection is the Lieblein *et al.* (1953) diffusion factor dealt with in Section 2.7.2, which may also be re-expressed in terms of (ϕ, ψ) coefficients as follows. Introducing Eqns (4.20) and (4.21) into Eqn (2.28) we have

$$
\mathrm{DF} = 1 - \frac{\cos \beta_1}{\cos \beta_2} + \frac{\cos \beta_1}{2} \left(\frac{t}{l} \right) (\tan \beta_1 - \tan \beta_2)
\tag{2.28}
$$

$$
= 1 - \sqrt{\frac{4\phi^2 + (1 - \psi)^2}{4\phi^2 + (1 + \psi)^2}} + \left(\frac{t}{l} \right) \frac{\psi}{\sqrt{4\phi^2 + (1 + \psi)^2}}
\tag{4.26}
$$

which may be rearranged to provide a formulation for selection of the pitch/chord ratio to suit any specified design duty, namely

$$
\frac{t}{l} = \frac{1}{\psi} \{ \sqrt{4\phi^2 + (1 - \psi)^2} - (1 - \mathrm{DF}) \sqrt{4\phi^2 + (1 + \psi)^2} \}
\tag{4.27}
$$

As mentioned in Chapter 2 the diffusion factor should not exceed $\mathrm{DF} = 0.6$ and a more modest value of say 0.5 will suffice for an aerodynamically conservative design.

Equation (4.27) has been evaluated for a wide range of (ϕ, ψ) duties and t/l values resulting in the curves shown in Fig. 4.5 for diffusion factors of 0.5 and 0.6.

Example 4.1

Problem
In Section 2.2 a compressor cascade was designed to turn the flow from $\beta_1 = 54.59°$ to $\beta_2 = 30.69°$. Calculate the duty coefficients (ϕ, ψ) and check the efficiency of a

stage using this cascade. Compare the pitch/chord ratios and ideal lift coefficients $C_{L\infty i}$ (ignoring drag) for diffusion factors DF = 0.5 or 0.6.

Solution
From Eqn (4.22)

$$\phi = 1/(\tan\beta_1 + \tan\beta_2) = 0.5$$

From Eqn (4.21a)

$$\psi = 2\phi\tan\beta_1 - 1 = 0.406\,62$$

We note that this lies within the ψ_{max} limit suggested by Eqn (4.19). From Fig. 4.4 the expected stage efficiency is about 90.3%.

We may now evaluate Eqn (4.27) to give the recommended pitch/chord ratio for DF = 0.5 and 0.6. Then we may evaluate the ideal lift coefficient from Eqn (4.23) ignoring the drag coefficient $C_{D\infty}$, namely

$$C_{L\infty i} = 2\left(\frac{t}{l}\right)\left(\frac{2\psi}{\sqrt{4\phi^2 + 1}}\right) \tag{4.23a}$$

The outcome is as follows:

DF	t/l	$C_{L\infty i}$
0.5	0.731	0.849 72
0.6	1.162	1.336 41

It is clear from this, as we might expect, that a reduction in pitch/chord ratio t/l will result in a reduction in aerodynamic blade loading as revealed by both the diffusion factor and the lift coefficient.

Example 4.2

Problem
A compressor is to receive atmospheric air at 15 °C and raise its pressure from 1.0 bar to 3.0 bar. The mean radius is to be 0.5 m and the rotational speed 5000 rev min^{-1}. Select a suitable stage duty (ϕ, ψ) and choose a suitable number of stages. Calculate the cascade inflow and outflow angles β_1 and β_2 assuming 50% reaction and find the required pitch/chord ratio for a diffusion factor DF = 0.5.

Solution
From Fig. 4.4 we will opt for $\phi = 0.5$, $\psi = 0.35$, for which $\eta_{TT} = 91.5\%$. Next we can calculate the specific enthalpy rise per stage $\Delta h = \psi U^2$:

$$U = r_m\Omega = 0.5 \times 2\pi \times 5000/60 = 261.8 \text{ m s}^{-1}$$

Therefore

$$\Delta h = 0.35 \times 261.8^2 \times 10^{-3} = 23.99 \text{ kJ kg}^{-1}$$

Now the machine overall specific enthalpy rise is given by

$$h_{o2} - h_{o1} = \eta_{TT}(h_{o2s} - h_{o1})$$

$$= \eta_{TT} C_p T_{o1} \left[\left(\frac{p_2}{p_1} \right)^{(\gamma-1)/\gamma} - 1 \right]$$

$$= 0.915 \times 1.005 \times 288.2 \{ 3^{0.4/1.4} - 1 \}$$

$$= 97.72 \text{ kJ kg}^{-1}$$

Therefore the number of stages $\approx 97.72/23.99 = 4.0734$. Let us therefore select four stages. We now need to recalculate ψ from

$$\psi = \frac{97.72 \times 1000}{261.8^2} \times \frac{1}{4} = 0.356\,44$$

Note that the total-to-total efficiency will be slightly less than our original estimate, Fig. 4.4, but we will ignore this. From Eqns (4.21) and (4.22) the cascade inflow and outflow angles are

$$\beta_1 = \arctan \left\{ \frac{1 + 0.356\,44}{2 \times 0.5} \right\} = 53.60°$$

$$\beta_2 = \arctan \left\{ \frac{1 - 0.356\,44}{2 \times 0.5} \right\} = 32.76°$$

Substituting for $\phi = 0.5$, $\psi = 0.356\,44$, DF $= 0.5$ into Eqn (4.27), the required pitch/chord ratio for stable efficient flow is $t/l = 0.9723$.

Suppose we now decide to reduce the number of stages from four to three. The work coefficient will go up by 4/3 to $\psi = 0.475\,25$. For the same diffusion factor DF $= 0.5$ and flow coefficient $\phi = 0.5$, the required pitch/chord ratio, Eqn (4.27), now becomes $t/l = 0.501\,214$. Thus we would need almost double the number of blades to achieve the increased flow turning, in this case from $\beta_1 = 55.87°$ to $\beta_2 = 27.69°$.

4.5 Compressor stages with arbitrary reaction

So far in this chapter we have considered only 50% reaction axial compressor stages. Let us now extend the analysis to deal with repeating stages of arbitrary reaction R. The velocity triangles for these, shown in Fig. 4.6, are similar to those of the repeating 50% reaction stages illustrated in Fig. 4.2 in all but one respect, namely that they are no longer symmetrical. The dimensionless velocity triangles, Fig. 4.6(b), are now dependent upon the three variables ϕ, ψ and R where the reaction R determines the degree of asymmetry.

Let us begin by reconsidering the definition of reaction R given previously in Eqn (4.5):

$$R = \frac{\text{Specific enthalpy rise across the rotor}}{\text{Specific enthalpy rise across the stage}} = \frac{h_2 - h_1}{h_3 - h_1} \qquad [4.5]$$
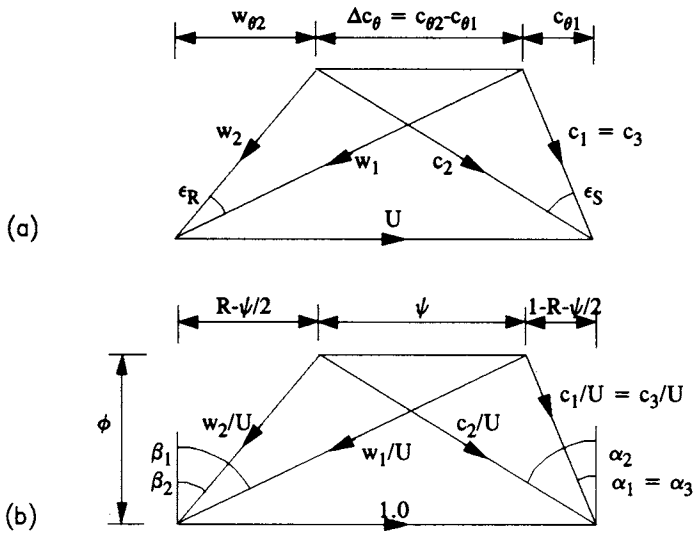
Fig. 4.6 (a) Velocity triangles and (b) dimensionless velocity triangles for repeating axial compressor stages of arbitrary reaction

Since we are limiting the analysis to repeating stages for which entry and leaving velocities are identical, $c_3 = c_1$, the denominator of Eqn (4.5) may be simplified to

$$h_3 - h_1 = \left(h_{o3} - \frac{c_3^2}{2} \right) - \left(h_{o1} - \frac{c_1^2}{2} \right) = h_{o3} - h_{o1} = \Delta h_o \qquad (4.28)$$

where Δh_o is the stage stagnation enthalpy rise. The numerator of Eqn (4.5) may be rewritten

$$h_2 - h_1 = \left(h_{o2} - \frac{c_2^2}{2} \right) - \left(h_{o1} - \frac{c_1^2}{2} \right) \qquad (4.29)$$

But since there is no work or heat input through the stator, $h_{o2} = h_{o3}$ and thus $h_{o2} - h_{o1} = \Delta h_o$. Also since the axial velocity is assumed to be constant,

$$c_2^2 - c_1^2 = (c_x^2 + c_{\theta 2}^2) - (c_x^2 + c_{\theta 1}^2)$$
$$= c_{\theta 2}^2 - c_{\theta 1}^2$$
$$= (c_{\theta 2} - c_{\theta 1})(c_{\theta 2} + c_{\theta 1})$$

From the Euler pump equation (4.3)

$$c_{\theta 2} - c_{\theta 1} = \frac{\Delta h_o}{U} = \psi U \qquad (4.30)$$

Introducing these results into Eqn (4.29) we have

$$h_2 - h_1 = \Delta h_o - \frac{\Delta h_0}{2U}(c_{\theta 2} + c_{\theta 1}) \qquad (4.29a)$$

so that the reaction R, Eqn (4.5) above, becomes

$$R = 1 - \frac{1}{2U}(c_{\theta 2} + c_{\theta 1})$$

providing a second equation for $c_{\theta 1}$ and $c_{\theta 2}$, namely

$$c_{\theta 2} + c_{\theta 1} = 2U(1 - R) \tag{4.31}$$

Solving simultaneous equations (4.30) and (4.31) we have the dimensionless swirl velocities

$$\left.\begin{aligned} \frac{c_{\theta 1}}{U} &= 1 - R - \frac{1}{2}\psi \\[1em] \frac{c_{\theta 2}}{U} &= 1 - R + \frac{1}{2}\psi \\[1em] \frac{w_{\theta 1}}{U} &= 1 - \frac{c_{\theta 1}}{U} = R + \frac{1}{2}\psi \\[1em] \frac{w_{\theta 2}}{U} &= 1 - \frac{c_{\theta 2}}{U} = R - \frac{1}{2}\psi \end{aligned}\right\} \tag{4.32}$$

and the remaining velocities also expressed in dimensionless form are thus

$$\left.\begin{aligned} \frac{w_1}{U} &= \sqrt{\phi^2 + \left(R + \frac{\psi}{2}\right)^2} && \text{Rotor relative inflow velocity} \\[1em] \frac{w_2}{U} &= \sqrt{\phi^2 + \left(R - \frac{\psi}{2}\right)^2} && \text{Rotor relative outflow velocity} \\[1em] \frac{c_1}{U} = \frac{c_3}{U} &= \sqrt{\phi^2 + \left(1 - R - \frac{\psi}{2}\right)^2} && \text{Rotor entry and stage exit velocity} \\[1em] \frac{c_2}{U} &= \sqrt{\phi^2 + \left(1 - R + \frac{\psi}{2}\right)^2} && \text{Stator inflow velocity} \end{aligned}\right\} \tag{4.33}$$

All angles of the velocity triangles can now also be expressed as functions of ϕ, ψ and R as follows: for the rotor,

$$\left.\begin{aligned} \beta_1 &= \tan^{-1}\left\{\frac{1}{\phi}\left(R + \frac{1}{2}\psi\right)\right\} && \text{Relative inflow angle} \\[1em] \beta_2 &= \tan^{-1}\left\{\frac{1}{\phi}\left(R - \frac{1}{2}\psi\right)\right\} && \text{Relative outflow angle} \\[1em] \varepsilon_R &= \tan^{-1}\left\{\frac{\phi\psi}{\phi^2 + R^2 - \frac{1}{4}\psi^2}\right\} && \text{Fluid deflection} \end{aligned}\right\} \tag{4.34}$$

and for the stator,

$$\alpha_2 = \tan^{-1}\left\{\frac{1}{\phi}\left(1 - R + \frac{1}{2}\psi\right)\right\} \qquad \text{Inflow angle}$$

$$\alpha_3 = \alpha_1 = \tan^{-1}\left\{\frac{1}{\phi}\left(1 - R - \frac{1}{2}\psi\right)\right\} \qquad \text{Outflow angle} \qquad (4.35)$$

$$\varepsilon_s = \tan^{-1}\left\{\frac{\phi\psi}{\phi^2 + (1 - R)^2 - \frac{1}{4}\psi^2}\right\} \qquad \text{Fluid deflection}$$

4.5.1   Stage losses and efficiency

The loss coefficients for rotor ζ_R and stator ζ_S have been defined by Eqn (4.9) and the total stage loss $(\Delta p_o)_{loss}$ follows from Eqn (4.17a). Introducing w_1/U and c_2/U into this we have

$$\frac{(\Delta p_o)_{loss}}{\rho U^2} = \frac{1}{2}\zeta_R\left(\frac{w_1}{U}\right)^2 + \frac{1}{2}\zeta_S\left(\frac{c_2}{U}\right)^2 \qquad (4.17a)$$

$$= \frac{1}{2}\zeta_R\left[\phi^2 + \left(R + \frac{\psi}{2}\right)^2\right] + \frac{1}{2}\zeta_S\left[\phi^2 + \left(1 - R + \frac{\psi}{2}\right)^2\right] \qquad (4.36)$$

The total-to-total efficiency then follows by substitution into Eqn (4.16), namely

$$\eta_{TT} = 1 - \frac{1}{2\psi}\left\{\zeta_R\left[\phi^2 + \left(R + \frac{\psi}{2}\right)^2\right] + \zeta_S\left[\phi^2 + \left(1 - R + \frac{\psi}{2}\right)^2\right]\right\} \qquad (4.37)$$

In Section 4.1 we were able to show from dimensional analysis using the π-theorem that η_{TT} is dependent upon the five groups ϕ, ψ, R, ζ_R and ζ_S in the general form expressed through Eqn (4.13). We have now shown that this relationship can be converted into the explicit analytical form given by Eqn (4.37) as a result of linking stage duty (ϕ, ψ) and reaction R to velocity triangles and thus to stage aerodynamics and thermodynamics. This is a most useful and extremely powerful reduction.

4.5.2   Diffusion factors and selection of pitch/chord ratio

Since the velocity triangles are no longer symmetrical for values of reaction R other than 0.5, the rotor and stator blade rows will have quite different profile geometry. In order to select suitable values of pitch/chord ratio t/l to control aerodynamic loading, it is again helpful to express the diffusion factor in terms of ϕ, ψ and R for each blade row. Introducing Eqns (4.34) and (4.35) into the expression for DF, Eqn (2.28), we thus have for the rotor

$$DF_R = 1 - \frac{\cos\beta_1}{\cos\beta_2} + \frac{\cos\beta_1}{2}\left(\frac{t}{l}\right)_R(\tan\beta_1 - \tan\beta_2)$$

$$= 1 - \sqrt{\frac{\phi^2 + (R - \psi/2)^2}{\phi^2 + (R + \psi/2)^2}} + \frac{1}{2}\left(\frac{t}{l}\right)_R\left[\frac{\psi}{\sqrt{\phi^2 + (R + \psi/2)^2}}\right] \qquad (4.38)$$

and for the stator

$$DF_S = 1 - \frac{\cos \alpha_2}{\cos \alpha_3} + \frac{\cos \alpha_2}{2}\left(\frac{t}{l}\right)_S (\tan \alpha_2 - \tan \alpha_3)$$

$$= 1 - \sqrt{\frac{\phi^2 + (1 - R - \psi/2)^2}{\phi^2 + (1 - R + \psi/2)^2}} + \frac{1}{2}\left(\frac{t}{l}\right)_S\left[\frac{\psi}{\sqrt{\phi^2 + (1 - R + \psi/2)^2}}\right] \qquad (4.39)$$

Inverting these we may obtain expressions for the pitch/chord ratios:

$$\left.\begin{array}{l}\left(\dfrac{t}{l}\right)_R = \dfrac{2}{\psi}\sqrt{\phi^2 + \left(R - \dfrac{\psi}{2}\right)^2} - \dfrac{2}{\psi}(1 - DF_R)\sqrt{\phi^2 + \left(R + \dfrac{\psi}{2}\right)^2} \\[3ex] \left(\dfrac{t}{l}\right)_S = \dfrac{2}{\psi}\sqrt{\phi^2 + \left(1 - R - \dfrac{\psi}{2}\right)^2} - \dfrac{2}{\psi}(1 - DF_S)\sqrt{\phi^2 + \left(1 - R + \dfrac{\psi}{2}\right)^2}\end{array}\right\} \qquad (4.40)$$

4.6 Selection of optimum blade profile geometry using theoretical cascade flow analysis

So far in this chapter we have considered only the selection of optimum duty coefficients ϕ, ψ for an axial compressor stage and the influence of these, together with the reaction R, upon the velocity triangles. A simple design sequence was presented in the introduction to this chapter, the final stage of which involves selection of the cascade blade profile to achieve the following:

(1) The correct fluid deflection and efflux angle β_2.
(2) Acceptable aerodynamic loading.
(3) Smooth entry flow.

The second of these design requirements has already been catered for by specifying the diffusion factor DF as considered in Section 4.4, resulting in expressions for the cascade pitch/chord ratio, Eqns (4.27) and (4.40). Requirements (1) and (3) may then be met by use of cascade analytical design techniques such as that offered by the computer program CASCADE. The design objective is to select the stagger angle λ and camber angle θ needed to achieve the correct outlet angle β_2 with 'shock-free' inlet flow. A base profile thickness (e.g. C4 profile) and type of camber line (e.g. circular arc or parabola) must also be specified.

Figure 4.7 shows curves of β_2 versus β_1 for 'shock-free' entry flow cascades made up by superimposing the C4 profile upon a circular arc camber line. (λ, θ) plots are shown for three pitch/chord ratios. The curves were derived from multiple runs of the program CASCADE which enables the user to obtain the shock-free inlet angle β_1 and its associated outlet angle β_2 for a specified stagger λ and camber θ. A set of such data may be obtained very rapidly with the help of CASCADE and provides a quick way forward for optimum cascade selection as illustrated by the following numerical example.
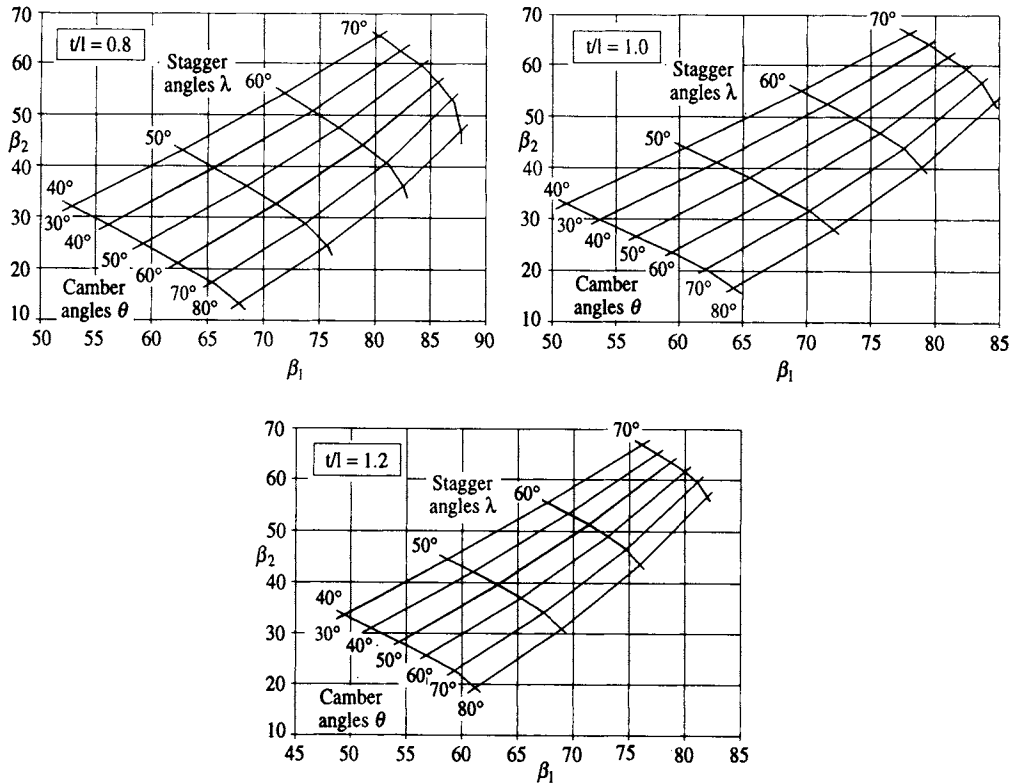
Fig. 4.7 Compressor cascades designed for 'shock-free' entry flow using computer program CASCADE

Example 4.3

Problem

For the compressor considered in Example 4.2, select a suitable blade geometry for the mean radius section. Summary of given data:

Inlet angle $\beta_1 = 53.60°$
Outlet angle $\beta_2 = 32.76°$
Diffusion factor $DF = 0.5$
Pitch/chord ratio $t/l = 0.9723$

Solution

From Fig. 4.7 we can select the stagger λ and camber θ to give smooth entry flow at the leading edge. Thus from the graph for $t/l = 1.0$ (which is close enough to the specified value of $t/l = 0.9723$ to suffice), we read off

$$\lambda \approx 41.5°$$

$$\theta \approx 35°$$

To confirm or adjust this choice we can now run the program CASCADE with this data, using the default profile thickness C4 and circular arc camber (see Appendix
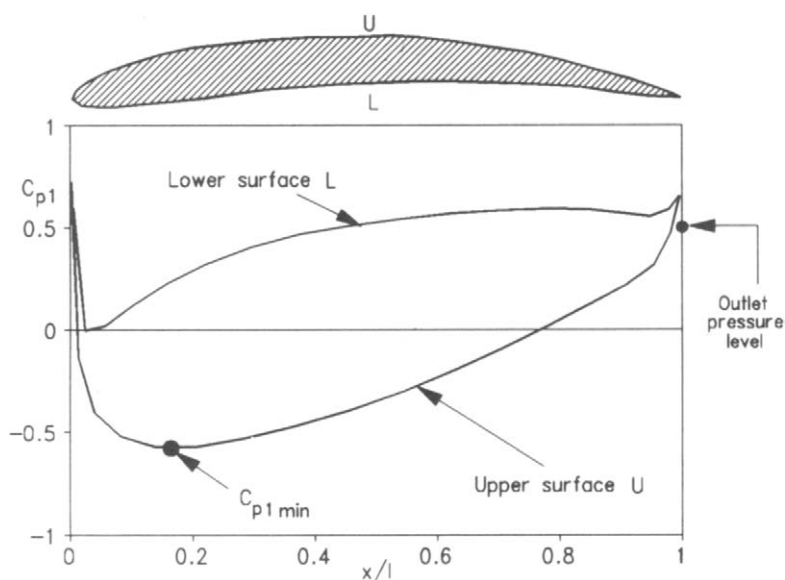
Fig. 4.8 Predicted surface pressure distribution for compressor cascade – Example 4.3

II for instructions in the use of CASCADE). We find that the predicted outlet angle is then $\beta_2 = 32.8°$ which is close enough to our design requirements, and the predicted 'shock-free' inlet angle is 54.07° which is also near enough to the design value to suffice. As proof of this we may check the surface pressure distribution, shown here as Fig. 4.8.

From this we see that the stagnation point (for which $C_{p1} = 1.0$, Eqn (2.14)) is located directly on the profile leading edge, resulting in smooth entry flow as described in Section 2.6 and illustrated by Fig. 2.11. The pressure on the upper convex surface falls rapidly to a minimum value of $(C_{p1})_{min} = -0.572$ at about $x/l = 0.16$ and then diffuses steadily towards the exit value of

$$(C_{p1})_{exit} = \frac{p_2 - p_1}{\frac{1}{2}\rho c_1^2}$$

$$= 1 - \left(\frac{c_2}{c_1}\right)^2 = 1 - \left(\frac{\cos\beta_1}{\cos\beta_2}\right)^2 = 0.502$$

[2.14]

Note that the theoretical analysis, being based upon potential flow modelling, predicts the trailing edge pressure distribution badly for $x/l > 0.96$ since there is also an implied stagnation point at the trailing edge associated with the Kutta–Joukowski condition which has to be imposed at that point. Despite this minor setback, Fig. 4.8 gives us a firm indication that we have selected an aerodynamically acceptable blade cascade geometry. Furthermore, we may use the predicted C_{p1} plot to check the upper surface stability against the later version of diffusion factor D_{loc} due to Lieblein (1956) which was defined in Section 2.7.1, Eqn (2.23). Thus

$$D_{loc} = 1 - \frac{\cos\beta_1}{\cos\beta_2} \frac{1}{\sqrt{1 - (C_{p1})_{min}}}$$

[2.23]

$$= 0.436$$
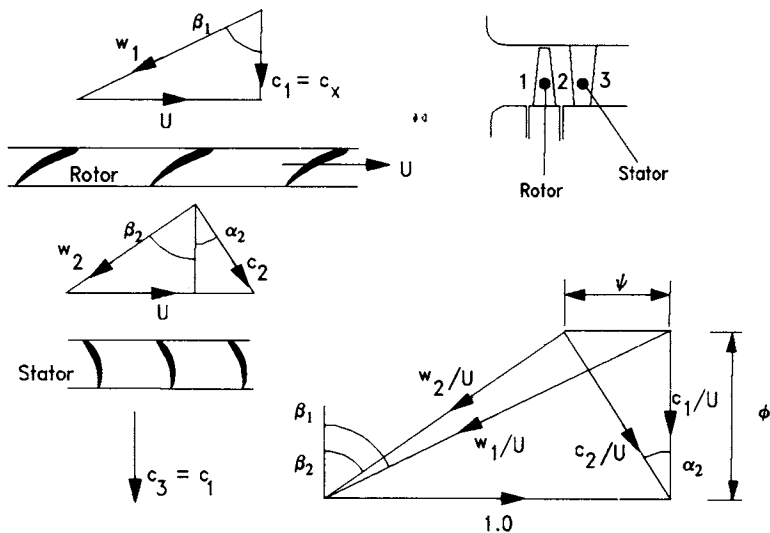
Fig. 4.9 Velocity triangles at the mean radius for an axial fan stage

According to Lieblein's experimental studies D_{loc} should be no greater than 0.5 which confirms that this cascade is conservatively designed as intended in Example 4.2.

4.7 High reaction axial fan stages

As discussed in Section 2.2 it can be argued, by considering its role as a diffusing device, that the optimum reaction of an axial compressor is in the region of 50%. Axial fans such as that illustrated in Fig. 4.9 are, on the other hand, of much higher reaction. The main aim is usually to move large volumes of gas with less emphasis on the demand for pressure rise. Many fans achieve this by means of a single rotor with no stator blade rows at all, for example for ventilation applications. Bearing in mind the definition of stage reaction for a compressor or fan, Eqn (4.5), such fans are clearly operating at 100% reaction. If the entry velocity c_1 is axial there must of course always be some swirl velocity $c_{\theta 2}$ downstream of the rotor, Fig. 4.9. If the level of this is sufficiently high then it may be advantageous to include also a downstream stator, as illustrated here, to return the flow at exit from the fan stage to the axial direction $c_3 = c_1$. We will adopt this arrangement as our model fan stage and derive next the related equations for its design and performance analysis.

The equations derived in Section 4.5 for compressor stages of arbitrary reaction are of course still applicable to our fan stage but with one restriction. There is to be zero swirl at entry, that is $c_{\theta 1} = 0$. From Fig. 4.6 and/or Eqn (4.32a) we observe that this determines the reaction R as a function of work coefficient ψ, namely

$$R = 1 - \frac{\psi}{2} \tag{4.41}$$

Thus for a fan comprising rotor plus stator without inlet guide vanes the reaction is no longer an independent variable once the design operating duty (ϕ, ψ) has been chosen. For example, if we selected the design duty $\phi = 0.5$, $\psi = 0.3$ the fan stage reaction would be $R = 0.85$. From the 'Smith' charts for experimental test axial

compressors, Fig. 4.4(c), the nearest reaction to compare with is 90% for which the proposed duty for our fan is in fact very close to optimum. The velocity triangles shown in Fig. 4.9 have been chosen to suit this prescribed duty. The blade profiles and cascade geometry shown in Fig. 4.9 have been selected by the procedures outlined in Section 4.6 for ensuring that the velocity triangles are actually delivered and with optimum aerodynamic performance setting the diffusion factor level at DF = 0.5.

   Introducing Eqn (4.41) into Eqns (4.32) to (4.40) of Section 4.5 we can now express all velocity triangle or other useful design data as functions of ϕ and ψ as follows. Dimensionless velocities are given by

$$\left.\begin{array}{l} \dfrac{w_1}{U} = \sqrt{\phi^2 + 1} \\[2mm] \dfrac{w_2}{U} = \sqrt{\phi^2 + (1 - \psi)^2} \\[2mm] \dfrac{c_1}{U} = \dfrac{c_3}{U} = \phi \\[2mm] \dfrac{c_2}{U} = \sqrt{\phi^2 + \psi^2} \end{array}\right\} \tag{4.42}$$

Flow angles are given by

$$\left.\begin{array}{l} \alpha_1 = \alpha_3 = 0 \\[2mm] \alpha_2 = \tan^{-1}(\psi/\phi) \\[2mm] \beta_1 = \tan^{-1}(1/\phi) \\[2mm] \beta_2 = \tan^{-1}\left(\dfrac{1 - \psi}{\phi}\right) \end{array}\right\} \tag{4.43}$$

The total-to-total efficiency becomes

$$\eta_{TT} = 1 - \frac{1}{2\psi}\{\zeta_R(1 + \phi^2) + \zeta_S(\phi^2 + \psi^2)\} \tag{4.44}$$

The diffusion factors, Eqns (4.38) and (4.39), become for the rotor

$$DF_R = 1 - \sqrt{\frac{\phi^2 + (1 - \psi)^2}{\phi^2 + 1}} + \frac{1}{2}\left(\frac{t}{l}\right)_R\left(\frac{\psi}{\sqrt{\phi^2 + 1}}\right) \tag{4.45}$$

and for the stator

$$DF_S = 1 - \frac{\phi}{\sqrt{\phi^2 + \psi^2}} + \frac{1}{2}\left(\frac{t}{l}\right)_S\left(\frac{\psi}{\sqrt{\phi^2 + \psi^2}}\right) \tag{4.46}$$

from which we may express the pitch/chord ratios as functions of ϕ, ψ and DF, namely

$$\left.\begin{array}{l} \left(\dfrac{t}{l}\right)_R = \dfrac{2}{\psi}[\sqrt{\phi^2 + (1 - \psi)^2} - (1 - DF_R)\sqrt{\phi^2 + 1}] \\[3mm] \left(\dfrac{t}{l}\right)_S = \dfrac{2}{\psi}[\phi - (1 - DF_S)\sqrt{\phi^2 + \psi^2}] \end{array}\right\} \tag{4.47}$$

As can be seen from Fig. 4.9 the rotor blades for this fan are both highly staggered and widely spaced. The stator on the other hand is more typical of an axial compressor blade row. The numerical example which follows invites the reader to complete the detailed design of this fan for himself.

Example 4.4

Problem
The mean radius section of an axial fan comprising rotor plus stator is to operate with duty $\phi = 0.5$, $\psi = 0.3$. Select suitable rotor and stator cascades making use of the program CASCADE. What fraction of the stage pressure rise would be lost if we dispensed with the stator?

Solution
First of all assemble velocity triangle data. From Eqns (4.43) and (4.47)

$$\alpha_2 = \tan^{-1}(0.3/0.5) = 30.964°$$

$$\alpha_3 = 0.0°$$

$$\beta_1 = \tan^{-1}(1/0.5) = 63.435°$$

$$\beta_2 = \tan^{-1}\{(1 - 0.3)/0.5\} = 54.462°$$

$$(t/l)_R = 2.0081$$

$$(t/l)_S = 1.3897$$

By trial and error use of program CASCADE the following stagger and camber angles were obtained using the C4 profile and circular arc camber for the given t/l values above:

Blade row	$\lambda°$	$\theta°$	Shock-free data	
			Inlet angle	Outlet angle
Rotor	58.2	37	63.44	54.40
Stator	14.65	57.64	30.92	0.00

The actual blade geometry for this fan is shown in Fig. 4.9 which illustrates the typical high stagger and wide spacing of the rotor. The fraction of pressure rise sacrificed if we dispense with the stator would be

$$\frac{(\Delta p_o)_{stator}}{(\Delta p_o)_{fan}} = \frac{\frac{1}{2}\rho c_{\theta 2}^2}{(\Delta p_o)_{fan}} = \frac{\frac{1}{2}(c_{\theta 2}/U)^2}{\psi} = \frac{1}{2}\psi = 0.15$$

Alternatively from the definition of reaction Eqn (4.5), using also Eqn (4.41),

$$\frac{(\Delta p_o)_{stator}}{(\Delta p_o)_{fan}} = 1 - R = 1 - (1 - \tfrac{1}{2}\psi) = 0.15$$
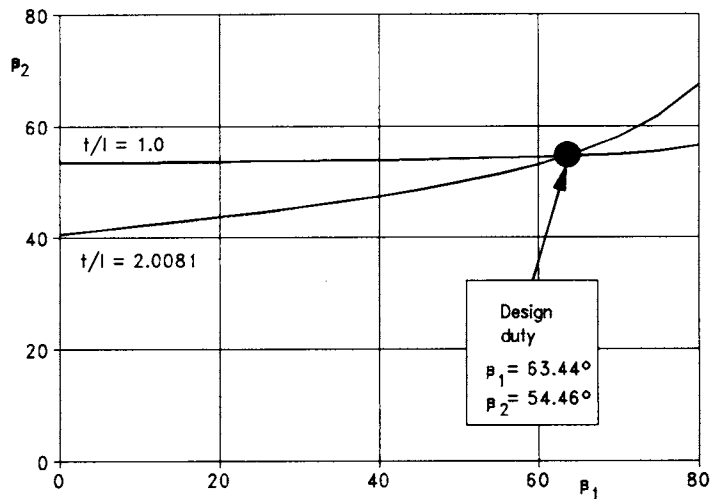
Fig. 4.10 Variation of outlet angle β_2 with inlet angle β_1 for two axial fan cascades of different pitch/chord ratios

Thus the stator accounts for 15% of the stage pressure rise, a small but significant amount.

4.8   Influence of pitch/chord ratio upon the deflection properties of cascades and upon the ϕ–ψ characteristics of an axial fan

In the example just considered the aerodynamically acceptable rotor blade spacing, corresponding to a slightly conservative diffusion factor of 0.5, was quite large, namely $t/l = 2.008$. For cascades with t/l in excess of 1.0 the variation of outlet angle β_2 with inlet angle β_1 is quite marked as illustrated by Fig. 4.10.

Curves of β_2 versus β_1 are shown here for two cascades selected to deliver the prescribed duty of Example 4.4 with shock-free inflow but with completely different pitch/chord ratios, namely $t/l = 2.008$ and $t/l = 1.0$. The first of these has the geometry previously selected and tabulated above. The cascade parameters for the second cascade have the values $t/l = 1.0$ and $\lambda = 56.7°$, again using the C4 profile thickness distributed on a circular arc camber line with $\theta = 18°$. Although one of these designs would have double the number of blades of the other and thus be aerodynamically very conservative, it would certainly do the job of matching and delivering the design duty velocity triangle requirements, $\beta_1 = 63.44°$, $\beta_2 = 54.46°$. On the other hand if we were to vary the inlet angle β_1 over some range such as that shown in Fig. 4.10 the outlet angle β_2 and fluid deflection $\varepsilon = \beta_1 - \beta_2$ would differ dramatically away from the design duty. As a simple rule of thumb it can be assumed that for $t/l < 1.0$ the outlet angle β_2 would remain almost constant over a range of β_1 values due to the fact that adjacent blades of the cascade now form distinct passages which are able to guide the fluid more strongly. For $t/l \gg 1.0$ on the other hand the blades are tending to act as separate aerofoils so widely spaced that mutual aerodynamic interference becomes less significant.

This leads us to another very important consideration in fan design, namely the off-design performance. In service conditions fans frequently have to be operated
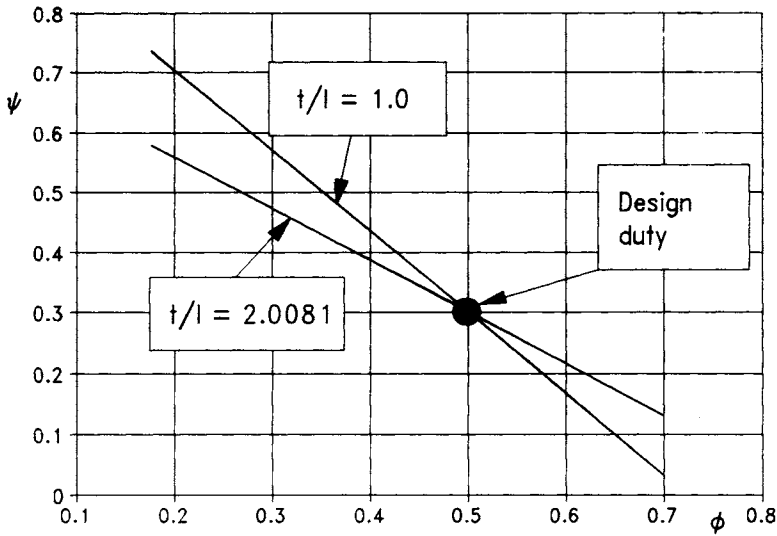
Fig. 4.11 Predicted 'frictionless' characteristics for two fan cascades with different pitch/chord ratios but the same design duty

away from the design (ϕ, ψ) duty. For example, it may be cheap and convenient for us to select a constant speed electric drive for a simple ventilation fan and there are indeed many such installations. Any change in the flow coefficient ϕ due to variations of the system resistance will then result also in a change of work coefficient ψ. To illustrate the outcome, ϕ–ψ characteristics for the two fan designs under consideration are shown in Fig. 4.11. These are styled 'frictionless' characteristics since the predictions are based on ideal frictionless fluid theory. Nevertheless, they serve to illustrate the trends related to pitch/chord ratio. For the closely pitched blade row with $t/l = 1.0$, the slope of the ϕ–ψ characteristic is very much greater due to rotor relative outflow angle being held almost constant at $\beta_2 = 54.46°$ over the whole range of flows $0.2 < \phi < 0.7$. The flatter characteristic of the more widely spaced fan, $t/l = 2.008$, is due to the relaxation of aerodynamic loading of the blades acting now as almost independent aerofoils.

Figure 4.11 has in fact been derived directly from the theoretically predicted cascade results shown in Fig. 4.10. Thus Eqns (4.43c) and (4.43d) may be rearranged to express the duty coefficients as functions of β_1 and β_2, namely

$$\phi = 1/\tan\beta_1$$
$$\psi = 1 - \frac{\tan\beta_2}{\tan\beta_1} \tag{4.48}$$

In practice as a consequence of this we would find that the fan with widely spaced blades would probably be able to operate over a wider range prior to blade stall and would tend to deliver higher pressure rises than the closely spaced fan for ϕ values greater than the design duty.

5
Simplified meridional flow analysis for axial turbomachines

Introduction

The last two chapters have been concerned with the centre-line or mean radius design of turbines, compressors and fans, enabling us to define a single design duty (ϕ, ψ) representative of the performance of a given stage. We were able to express the dimensionless velocity triangles, normalised by the blade speed $U = r\Omega$, in terms of the flow coefficient ϕ, the work coefficient ψ and the stage reaction R, leading us directly on to a rational analytic approach to blade profile design linked to stage mean duty (ϕ, ψ).

In reality of course the stage performance will be determined not just by its centre-line section but will be the average of the whole flow from hub to casing. The real flow in a turbomachine is three-dimensional and indeed extremely complex. Conditions may vary considerably from hub to casing and the blades themselves will usually be both tapered and twisted as was illustrated in the introduction to Chapter 2 and Fig. 2.3.

We move on now to consider this problem of how to analyse the three-dimensional flow in turbomachines. The starting point for this was also given in Chapter 2 where the 'cascade' and 'meridional' flow structures were introduced mainly to provide a manageable design framework. As illustrated by Fig. 2.1, the fully three-dimensional flow can be treated for practical purposes as an axisymmetric or circumferentially averaged 'meridional flow', and a series of superimposed 'cascade' flows to define blade profiles at selected sections from hub to casing.

Now so far for axial machines we have assumed that the meridional velocity c_s is constant for all meridional streamlines as illustrated for an axial fan in Fig. 5.1(a). Downstream of the rotor, however, the flow may be swirling quite considerably, resulting in an inward radial pressure gradient. This may well result in some radial shifts in the meridional streamlines as illustrated in Fig. 5.1(b). As a result of this the meridional velocity c_s will vary from hub to tip with consequent modification of the velocity triangles which must be taken into account before the blade profiles are designed.

Meridional flow analyses to handle this design problem are extremely complex. In this chapter we will content ourselves with only the simplest techniques known as radial equilibrium analysis, Sections 5.2 and 5.3, and actuator disc theory, Sections 5.4 and 5.5. Finally in Section 5.6 these analyses will be extended to deal with the design of a complete axial fan or compressor comprising several blade rows and including the meridional interference between them. Before turning to these, however, we will begin in Section 5.1 by considering the special case of free-vortex design, the simplest and most popular method for three-dimensional design of axial turbomachines.
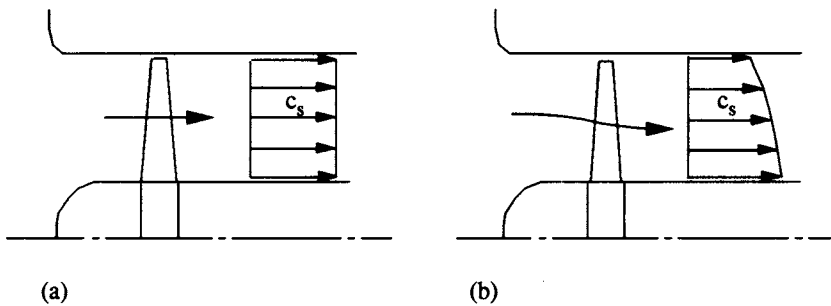
Fig. 5.1 Meridional flow through an axial fan consisting of a single rotor only: (a) free-vortex axial fan; (b) non-free-vortex axial fan

5.1 The free-vortex axial fan

In Section 4.7 we considered the mean radius design of an axial fan comprising a rotor followed by a stator, Fig. 4.9. The rational design procedure adopted to arrive at aerodynamically suitable blade profiles can be summarised as follows:

Selection of optimum duty points (ϕ, ψ) from model test data

$\downarrow$

Construction of dimensionless velocity triangles

$\downarrow$

Use of computational fluid dynamics to select suitable blade profiles which will deliver the velocity triangles with stable and low loss flow
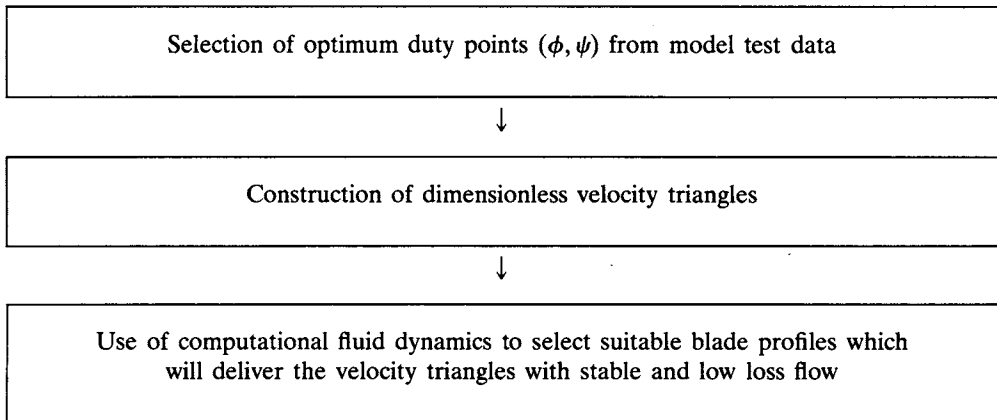
Obviously the flow conditions at the mean radius are likely to typify the general performance of the fan but we are still left with the major task of designing the rest of the rotor blade which, as we will see, will vary considerably in both duty (ϕ, ψ) and consequent blade geometry from hub to tip. We need therefore to consider carefully what aerodynamic loading can be carried by each section of the blade and whether radial variations are likely to impose extreme aerodynamic difficulties in profile selection or off-design performance.

As a first step towards the three-dimensional design of our fan rotor let us impose the reasonable constraint that the fluid should be given the same stagnation pressure rise for all meridional streamlines. For incompressible flow at radius r the Euler pump equation (1.9b), with zero pre-whirl upstream of the rotor ($c_{\theta 1} = 0$), may be written

$$\bar{W} = \frac{1}{\rho} \Delta p_{oE} = U c_{\theta 2} = r \Omega c_{\theta 2} \qquad (5.1)$$

where $\bar{W}$ is the specific work input and Δp_{oE} represents the stagnation pressure rise of a perfect (Euler) fan with frictionless loss-free flow. Thus we are actually adopting here a constant specific work input for all radii. Equating conditions at the mean radius r_m to any other radius r we thus obtain

$$r_m c_{\theta 2m} = r c_{\theta 2} = K \tag{5.2}$$

where K is a constant. The radial variation of c_θ may thus be expressed

$$c_{\theta 2} = \frac{K}{r} \tag{5.3}$$

and we see that the swirl velocity $c_{\theta 2}$ downstream of the rotor is inversely proportional to radius. This corresponds to the well-known classical flow generated by a line vortex as illustrated by Fig. 5.2. In this case we have shown the flow field in the (x, y) plane is that induced by a line vortex of strength Γ lying along the z-axis between $z = \pm\infty$, for which the induced velocity is

$$c_\theta = \frac{\Gamma}{2\pi r} \tag{5.4}$$

In consequence of this the type of fan which we have selected is called a free-vortex design. If we were to depart from the initial design constraint of equal specific work input $\bar{W}$ at all radii we could in fact select a very wide range of vortex designs and indeed we will return to this in Sections 5.4 to 5.6. For the present let us stay with 'free-vortex', 'constant specific work' design and see where this leads.

For incompressible flow the work input coefficient ψ, Eqn (4.4), may be redefined as follows for radius r:

$$\psi = \frac{\Delta p_{oE}/\rho}{U^2} = \frac{\Delta p_{oE}}{\rho r^2 \Omega^2} \tag{5.5}$$

Let us assume also that the meridional streamlines are cylindrical and the meridional velocity is thus constant and equal to C_x. The flow coefficient at radius r thus becomes

$$\phi = \frac{C_x}{U} = \frac{C_x}{r\Omega} \tag{5.6}$$

The duty coefficients at radius r may now be expressed in terms of the values (ϕ_m, ψ_m) selected at the outset for the mean radius r_m. Making use of the free-vortex Eqn (5.2) we have

$$\phi = \phi_m \left(\frac{r_m}{r}\right), \qquad \psi = \psi_m \left(\frac{r_m}{r}\right)^2 \tag{5.7}$$

and the radial variation of stage reaction R, Eqn (4.41), becomes

$$R = 1 - \frac{\psi_m}{2} \left(\frac{r_m}{r}\right)^2 \tag{5.8}$$
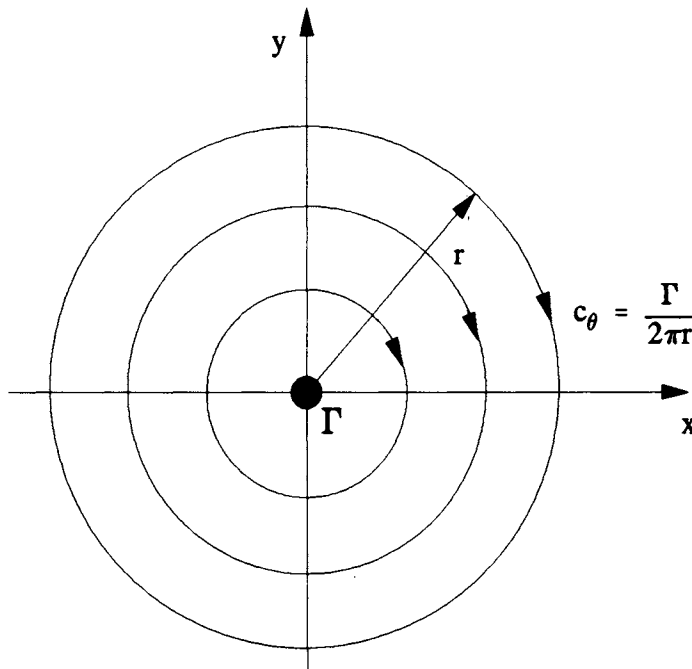
Fig. 5.2 Flow field induced in the (x,y) plane by vortex of strength Γ lying along the z-axis

At this point it will be helpful to interpret the consequences of all this by considering a numerical example.

Example 5.1

Problem
A fan is to be designed with a mean radius duty of $\phi = 0.5$, $\psi = 0.3$. If the hub/tip ratio $h = r_h/r_t$ is to be 0.3 calculate the duty coefficients and reaction at eight radial stations equally spaced between hub and casing. Calculate the velocity triangle data and pitch/chord ratio of both rotor and stator assuming a diffusion factor of 0.5.

Solution
First let us relate the mean radius r_m to the hub/tip ratio $h = r_h/r_t$. By definition $r_m = \frac{1}{2}(r_h + r_t)$ so that the ratio r/r_m needed to evaluate Eqns (5.7) and (5.8) may be expressed as

$$\frac{r}{r_m} = \frac{r}{\frac{1}{2}(r_h + r_t)} = \left(\frac{2}{1+h}\right)\left(\frac{r}{r_t}\right) = \frac{2}{1.3}\left(\frac{r}{r_t}\right)$$

It is usually more convenient numerically to use the tip radius r_t to non-dimensionalise local radius r. Now we may complete Table 5.1.

From this example we observe that the blade sections between the mean radius and blade tip, $0.65 < r/r_t < 1.0$, are lightly loaded ($0.127 < \psi < 0.3$) and also have low flow coefficients ($0.325 < \phi < 0.5$), the stage reaction lying in the range

Table 5.1 Duty coefficients and stage reaction for a free-vortex fan

r/r_t		ϕ	ψ	R
0.3	hub	1.083 33	1.408 32	0.295 84
0.4		0.812 51	0.792 20	0.603 90
0.5		0.650 00	0.507 00	0.746 50
0.6		0.541 66	0.352 08	0.823 96
0.65	mean	0.500 00	0.300 00	0.850 00
0.7		0.464 29	0.258 67	0.870 67
0.8		0.406 25	0.198 05	0.900 98
0.9		0.361 11	0.156 48	0.921 76
1.0	tip	0.325 00	0.126 75	0.936 63

Table 5.2 Velocity triangle data and pitch/chord ratios for free-vortex fan of Example 5.1

r/r_t	Rotor			Stator	
	$\beta_1°$	$\beta_2°$	$(t/l)_R$	$\alpha_2°$	$(t/l)_S$
0.300	42.7094	−20.6526	0.597 27	52.4314	0.276 83
0.400	50.9061	14.3469	0.490 84	44.2748	0.618 82
0.500	56.9761	37.1789	0.865 75	37.9542	0.938 17
0.600	61.5571	50.1039	1.567 08	33.0239	1.242 02
0.650	63.4350	54.4623	2.008 10	30.9638	1.389 68
0.700	65.0952	57.9415	2.500 86	29.1241	1.535 10
0.800	67.8906	63.1343	3.628 40	25.9892	1.820 51
0.900	70.1448	66.8242	4.933 02	23.4287	2.100 34
1.000	71.9958	69.5861	6.406 69	21.3058	2.376 00

$0.85 < R < 0.937$. According to the 'Smith' chart for 90% reaction compressor stages, Fig. 4.4(c), the tip region of the blades will tend to have a low efficiency. There is no difficulty whatsoever in designing suitable blading for the tip region but losses will necessarily be high there because of the high relative velocities.

If we consider next the inner region, $0.3 < r/r_t < 0.65$, problems of a different kind arise. We observe that ψ rises rapidly to the hub section value of 1.4 which is far in excess of what we would expect to achieve with a single stage fan, the flow coefficient $\phi = 1.083 33$ also being quite high.

Let us now make use of Eqns (4.43) to calculate the various flow angles (see Fig. 4.9). Assuming diffusion factors $D_R = D_S = 0.5$ we may also calculate appropriate pitch/chord ratios. The outcome is given in Table 5.2.

From this we observe the following about conditions at the blade root section:

(1) Excessively large fluid deflections are demanded of both rotor and stator, namely $\varepsilon_R = \beta_1 - \beta_2 = 63.362°$, $\varepsilon_S = \alpha_2 = 52.431°$.

(2) Extremely small pitch/chord ratios are required to achieve these deflections, namely $(t/l)_R = 0.597 27$, $(t/l)_S = 0.276 83$.

Although in theory we could design cascades to achieve these deflections, albeit with poor aerodynamic performance, the blades would exhibit such enormous taper that we would be hard placed to accommodate the root section of the blade, the chord of which would be over seven times greater than the chord at the mean radius r_m.

One possible solution to the dilemma posed in Example 5.1 would be to select a higher hub/tip ratio. Thus from Tables 5.1 and 5.2 we see that quite acceptable (ϕ, ψ) duties and velocity triangles are obtained for $r/r_t > 0.5$ which indicates a suitable value for h. A second solution might be to adopt a less demanding (ϕ_m, ψ_m) duty at the mean radius. The reader can make use of the simple Pascal program FVFAN, the source code of which is provided on the accompanying PC disc, to experiment with this. The most appropriate solution in practice, in order to maintain low values of hub/tip ratio and thus the maximum available annulus flow area, is to abandon our initial aim of designing for constant specific work $\bar{W}$ input at all radii. Instead we may progressively reduce $\bar{W}$ as we move radially inward from r_m to r_h and thereby reduce the pressure rise coefficient ψ to acceptable values, less than say 0.4. This will help to maintain much lighter aerodynamic loading in the blade root region but also pitch/chord ratios in excess of 1.0 and hence a wider stall-free range (see Section 4.8). Unfortunately this approach would entail a departure from free-vortex flow, resulting in a non-uniform meridional velocity profile, Fig. 5.1(b). Complex calculations are required to evaluate the variation of c_s with radius and two of the most simple analyses will now be presented in Sections 5.2 to 5.5.

5.2　Radial equilibrium analysis for axial turbomachines

Figure 5.3(a) illustrates the manner in which the meridional streamlines shift radially inward progressively under the influence of the radial pressure gradient dp/dr generated by the swirling flow downstream of a blade row (a stator is shown here). In consequence of this there will be a steady growth in the slope of the axial velocity profile c_x. Some distance downstream of the blade row at station 3 the radial velocity component c_r will approach zero, resulting in the so-called *radial equilibrium* flow. A radial momentum balance is then achieved between the radial pressure gradient dp/dr and the angular momentum of the fluid rc_θ. Our first task will be to derive this relationship by reference to the equilibrium of a small fluid element at radius r as illustrated in Fig. 5.3(b). Here we are adopting cylindrical polar coordinates (x, r, θ) where the x-axis is coincident with the axis of rotation of the turbomachine. The mass of the element, whose sides are of length dx, dr and $r\,d\theta$, is given by

$$dm = \rho\,dx \cdot dr \cdot r\,d\theta \tag{5.9}$$

If we now equate the radially inward pressure force on the faces of the element to its centrifugal acceleration, we obtain

$(p + dp)(r + dr)\,d\theta\,dx - pr\,d\theta\,dx$

$$-2\left(p + \frac{1}{2}dp\right)dr\,dx\sin\left(\frac{d\theta}{2}\right) = dm\frac{c_\theta^2}{r} \tag{5.10}$$

$$= \rho\,dx\,dr \cdot r\,d\theta\frac{c_\theta^2}{r}$$

(a)   (b)
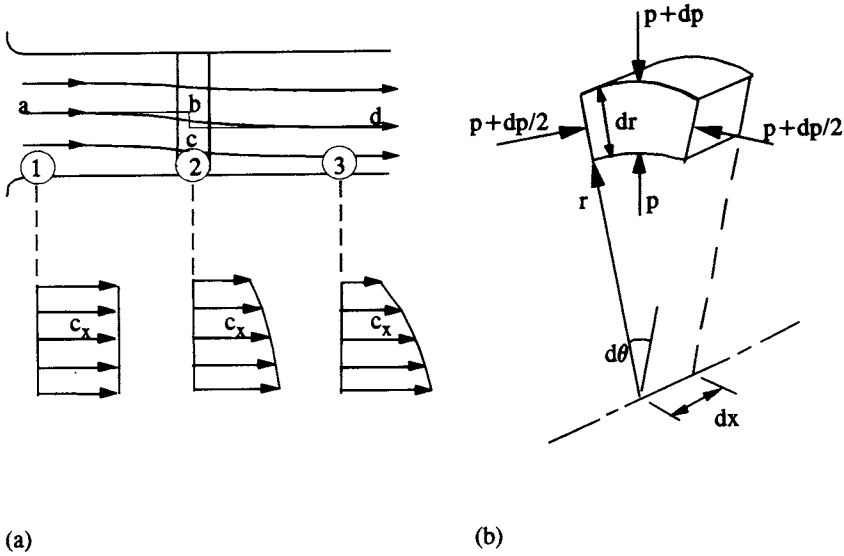
Fig. 5.3 Radial equilibrium of a small fluid element downstream of a turbomachine blade row: (a) meridional streamline shift and axial velocity profile development; (b) pressure forces on a small fluid element at station 3

which reduces to

$$\frac{1}{\rho}\frac{dp}{dr} = \frac{c_\theta^2}{r} \tag{5.11}$$

In radial equilibrium flow the radial pressure gradient is thus uniquely related to the swirl velocity c_θ irrespective of the type of vortex flow. For the special case of free-vortex flow, introducing Eqn (5.4), we note that Eqn (5.11) reduces to

$$\frac{1}{\rho}\frac{dp}{dr} = \frac{\Gamma^2}{4\pi^2 r^3} \quad \text{(free-vortex flow)} \tag{5.11a}$$

and we will later show that the axial velocity c_x is constant for this special case. For all other vortex flows, for which rc_θ is not constant, we need to relate the axial velocity c_x to c_θ and p. For simplicity let us first consider *incompressible* flow for which we may define the stagnation pressure p_0 through

$$\frac{p_0}{\rho} = \frac{p}{\rho} + \frac{c^2}{2} = \frac{p}{\rho} + \frac{c_x^2}{2} + \frac{c_r^2}{2} + \frac{c_\theta^2}{2} \tag{5.12}$$

Differentiating this equation with respect to r and putting $c_r = 0$, we have

$$\frac{1}{\rho}\frac{dp_0}{dr} = \frac{1}{\rho}\frac{dp}{dr} + c_x\frac{dc_x}{dr} + c_\theta\frac{dc_\theta}{dr} \tag{5.13}$$

Introducing dp/dr from Eqn (5.11), we have finally

$$\frac{1}{\rho}\frac{dp_0}{dr} = c_x\frac{dc_x}{dr} + \frac{c_\theta}{r}\frac{d(rc_\theta)}{dr} \tag{5.14}$$

which is known as the *radial equilibrium equation for incompressible flow*.

An equivalent equation for compressible flow can be developed by making use of the following thermodynamic relationship which links temperature T, specific entropy s and specific enthalpy h to p and ρ:

$$\left. \begin{array}{l} T\,ds = dh - \dfrac{1}{\rho}\,dp \\[2ex] \quad = dh_o - \dfrac{1}{\rho}\,dp_o \end{array} \right\} \tag{5.15}$$

where the stagnation enthalpy is defined as $h_o = h + c^2/2$. Dividing throughout by dr and substituting for $(1/\rho)(dp_o/dr)$ in Eqn (5.14), we have finally the *radial equilibrium equation for compressible flow*:

$$\frac{dh_o}{dr} - T\frac{ds}{dr} = c_x \frac{dc_x}{dr} + \frac{c_\theta}{r}\frac{d(rc_\theta)}{dr} \tag{5.16}$$

The axial velocity c_x is thus a function of the radial distribution not only of rc_θ but also of h_o and s.

5.3 Solution of the radial equilibrium equation for the inverse and direct problems

Two types of problem may be identified as follows:

(1) *The 'Inverse' or 'Design' problem.* In the design sequence outlined in Section 5.1, once the velocity triangles have been selected h_o and c_θ are known at all radii as part of the design specification. The radial distribution of specific entropy s may also be obtained from a first estimate of the losses or η_{TT} from model test data. Solution of the radial equilibrium Eqn (5.16) then yields a new estimate of the axial velocity distribution c_x and hence an updating of the velocity triangles and thus flow angles prior to blade profile selection. This is the *design problem*.
(2) *The 'Direct' or 'Analysis' problem.* We may postulate the opposite problem in which we are presented with an existing turbomachine of known blade geometry and asked to predict its fluid dynamic performance. This is the *analysis problem*.

Theoretical analysis to deal with these two rather different problems will now be presented with the help of numerical examples in Sections 5.3.1 and 5.3.2.

5.3.1 Solution of the inverse radial equilibrium problem

This is best illustrated by considering the case of a set of inlet guide vanes which are to be designed to generate a solid body swirling flow.

Example 5.2 'Solid body' swirl inlet guide vanes

Consider the case of flow through an inlet guide vane blade row, Fig. 5.3(a). In this case the swirl velocity c_θ is to be proportional to radius at station 3 a long way downstream of the blade row. We shall also assume that h_o and s are both constant

throughout the flow regime, namely

$$c_\theta = kr \quad \text{(where } k \text{ is a constant)}$$
$$h_\text{o} = \text{constant}$$
$$s = \text{constant}$$

(5.17)

Problem
Derive an analytical solution for c_x as a function of r.

Solution
In view of Eqns (5.17b) and (5.17c), the radial equilibrium Eqn (5.16) reduces to

$$0 = c_x \frac{\mathrm{d}c_x}{\mathrm{d}r} + \frac{c_\theta}{r} \frac{\mathrm{d}(rc_\theta)}{\mathrm{d}r}$$

(5.16a)

which may be rewritten

$$\frac{\mathrm{d}c_x^2}{\mathrm{d}r} = -\frac{2c_\theta}{r} \frac{\mathrm{d}(rc_\theta)}{\mathrm{d}r}$$

and hence, after integration, at radius r we have

$$c_x(r) = \sqrt{K_1 - 2 \int_{r_\text{h}}^{r} \frac{c_\theta}{r} \mathrm{d}(rc_\theta)}$$

(5.18)

Introduction of Eqn (5.17a) for the solid body rotation case then results in

$$c_x = \sqrt{K_1 - 2k^2 r^2} = \sqrt{K_1 - 2c_\theta^2}$$

(5.19)

The constant of integration K_1 can be evaluated by application of the mass flow continuity equation. Thus the mass flow $\dot{m}$ through the annulus may be expressed as

$$\dot{m} = \int_{r_\text{h}}^{r_t} \rho C_x 2\pi r \, \mathrm{d}r \quad = \quad \int_{r_\text{h}}^{r_t} \rho c_x 2\pi r \, \mathrm{d}r$$

(5.20)

station 1 – (entry)   station 3 – (exit)

where C_x is the mean axial velocity and thus $c_x = C_x$ at entry to the annulus. Assuming incompressible flow and introducing Eqn (5.19), Eqn (5.20) becomes

$$C_x(r_t^2 - r_\text{h}^2) = 2 \int_{r_\text{h}}^{r_t} r\sqrt{K_1 - 2k^2 r^2} \, \mathrm{d}r$$

$$= \frac{1}{3k^2}[(K_1 - 2k^2 r_\text{h}^2)^{3/2} - (K_1 - 2k^2 r_t^2)^{3/2}]$$

(5.21)

Because of the complexity of Eqn (5.21), K_1 cannot be evaluated explicitly and can only be derived by successive approximations. Nevertheless a reasonable approximate analytical solution may be derived as follows.

Approximate solution matching C_x at the root mean square radius r_{ms}
Let us assume that $c_x = C_x$ at the r.m.s. radius, namely $r_{ms} = \sqrt{\frac{1}{2}(r_h^2 + r_t^2)}$. Thus Eqn (5.19) yields directly an estimate for K_1, namely

$$
\begin{aligned}
K_1 &= C_x^2 + 2(c_{\theta rms})^2 \\
&= C_x^2 + 2c_{\theta t}^2(r_{ms}/r_t)^2 \\
&= C_x^2 + c_{\theta t}^2(1 + h^2)
\end{aligned}
\tag{5.22}
$$

Thus finally, at other radii r, from Eqn (5.18) we have

$$
\frac{c_x}{C_x} = \sqrt{1 + \left[1 + h^2 - 2\left(\frac{r}{r_t}\right)^2\right]\left(\frac{c_{\theta t}}{C_x}\right)^2}
\tag{5.23}
$$

Numerical solution of the inverse problem
A much more flexible approach applicable to any radial distribution of c_θ is to evaluate Eqns (5.18) and (5.20) numerically. First let us define the function

$$
f(r) = 2 \int_{r_h}^{r} \frac{c_\theta}{r} \, d(rc_\theta)
\tag{5.24}
$$

so that Eqn (5.18) becomes

$$
c_x(r) = \sqrt{K_1 - f(r)}
\tag{5.25}
$$

From the continuity equation (5.20) we may define a mass flow function

$$
\begin{aligned}
S &= \frac{\dot{m}}{2\pi\rho} \\
&= \frac{C_x}{2}(r_t^2 - r_h^2) & \text{at } -\infty \text{ upstream of blade row} \\
&= \int_{r_h}^{r_t} r\sqrt{K_1 - f(r)} \, dr & \text{at } +\infty \text{ downstream of blade row}
\end{aligned}
\left.\vphantom{\begin{aligned}&\\&\\&\end{aligned}}\right\}
\tag{5.26}
$$

For numerical analysis, the annulus may be represented by m radial steps between hub and tip radii r_h and r_t of thickness $\Delta r = (r_t - r_h)/m$. $f(r)$ may then be approximated at radius r_j by

$$
f(r_j) = 2 \sum_{i=1}^{j} \frac{c_{\theta mi}}{r_{mi}}(r_{i+1}c_{\theta i+1} - r_i c_{\theta i})
\tag{5.27}
$$

where $r_{mi} = \frac{1}{2}(r_i + r_{i+1})$ and $c_{\theta mi} = \frac{1}{2}(c_{\theta i+1} + c_{\theta i})$. The mass function S may then also be evaluated numerically if Eqn (5.26) is rewritten

$$
S_1 = \Delta r \sum_{i=1}^{m} r_{mi}\sqrt{K_1 - f(r_i)}
\tag{5.28}
$$

Since the constant K_1 is initially of unknown value, a method of successive approximations will be required. The technique adopted in the Pascal program RE-DES, provided on the accompanying PC disc, follows that of Newton. As a first estimate the value of K_1 given by the approximate analytical method of Eqn (5.22) may be used to begin the process. We may then evaluate S_1 and also the nearby value S_2 given by

$$S_2 = \Delta r \sum_{i=1}^{m} r_{mi} \sqrt{K_1 + \Delta K_1 - f(r_i)} \tag{5.29}$$

where ΔK_1 is a small increment in K_1 (e.g. $\Delta K_1/K_1 = 0.01$). A revised estimate of K_1 then follows by extrapolation from

$$(K_1)_{\text{revised}} = K_1 + \Delta K_1 \left(\frac{S - S_1}{S_2 - S_1} \right) \tag{5.30}$$

Application of this procedure to a solid body swirl with mean axial velocity $c_x = 1.0$ and tip swirl velocity $c_\theta = 1.0$ produces the solution shown in Table 5.3, which shows the precise prediction from computer program RE-DES compared with the approximate analytical solution of Eqn (5.23). To achieve numerical accuracy it is necessary to interpolate the initial (r, c_θ) data to provide many more radial steps. A Lagrangian interpolation procedure is included in RE-DES and for the above computations $m = 400$ radial divisions of the annulus were used.

Results for two other vortex flows have also been calculated using RE-DES and these are shown in Table 5.4. Let us now consider these in turn.

Example 5.3 Free-vortex flow

Since the function $f(r)$, Eqn (5.24), is zero for this case, the axial velocity must be uniform and equal to the mean velocity C_x. This is borne out by the numerical prediction as can be seen from Table 5.4.

Example 5.4 Constant swirl velocity c_θ

Problem
Following the lines of the analysis given in Example 5.2 for solid body flow, the reader is invited to derive the approximate radial equilibrium solution for the following vortex specification:

$$\left. \begin{array}{l} c_\theta = \text{constant} \\ h_o = \text{constant} \\ s = \text{constant} \end{array} \right\} \tag{5.31}$$

Solution
Matching c_x at the r.m.s. radius, the analytical solution for this flow is given by

$$\frac{c_x}{C_x} = \sqrt{1 + 2 \left(\frac{c_\theta}{C_x} \right)^2 \ln \left(\frac{r_{\text{ms}}}{r} \right)} \tag{5.32}$$

Table 5.3 Comparison of radial equilibrium axial velocity profiles for solid body swirl predicted by approximate analysis and by numerical method (computer program RE-DES)

r	c_θ	$c_{x\infty}$ Approx. method, Eqn (5.52)	$c_{x\infty}$ Numerical method, axial velocity
0.4	0.4	1.356 466	1.379 527
0.5	0.5	1.288 410	1.312 666
0.6	0.6	1.200 000	1.226 007
0.7	0.7	1.086 278	1.114 941
0.8	0.8	0.938 083	0.971 130
0.9	0.9	0.734 847	0.776 591
1.0	1.0	0.400 000	0.472 329

Table 5.4 Radial equilibrium profiles predicted by program RE-DES for free-vortex and constant swirl flows

r	Free-vortex swirl		Constant swirl velocity	
	c_θ	c_x	c_θ	c_x
0.40	2.500 00	1.000 012	1.0	1.495 487
0.45	2.222 22	1.000 008	1.0	1.414 537
0.50	2.000 00	0.999 999	1.0	1.337 981
0.55	1.818 18	1.000 005	1.0	1.264 742
0.60	1.666 67	0.999 995	1.0	1.193 965
0.65	1.538 46	1.000 003	1.0	1.124 930
0.70	1.428 57	1.000 004	1.0	1.057 002
0.75	1.333 33	1.000 005	1.0	0.989 579
0.80	1.250 00	1.000 001	1.0	0.922 057
0.85	1.176 47	1.000 001	1.0	0.853 780
0.90	1.111 11	1.000 002	1.0	0.783 979
0.95	1.052 63	1.000 002	1.0	0.711 680
1.00	1.000 00	1.000 001	1.0	0.635 532

This is found to be in reasonable agreement with the precise result obtained from the numerical procedure.

5.3.2 Solution of the radial equilibrium direct problem

We now consider the 'direct' or 'analysis' problem in which the blade geometry and hence fluid deflection is specified and we are required to calculate the resulting axial velocity profile $c_x(r)$. In reality, as illustrated previously in Fig. 5.3, radial equilibrium develops progressively as the fluid proceeds from $-\infty$ to $+\infty$. Simple radial equilibrium theory, on the other hand, assumes that equilibrium is achieved completely by the time the fluid leaves the blade trailing edge. The contour abcd,
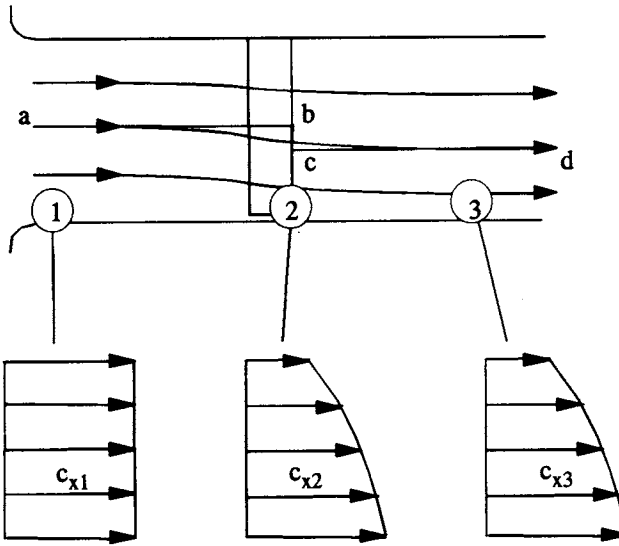
Fig. 5.4 Radial equilibrium downstream of a stator

Fig. 5.4, would then typify the consequent approximation to the meridional streamlines, implying that the swirl angle α_2 remains constant along cd. This is in fact a gross and unnecessary assumption which we will drop later when moving on to more sophisticated analysis in Section 5.4. On the other hand, it is helpful to progress analytically in stages and to look now for simple radial equilibrium solutions to the flow through a stator and a rotor on the present basis.

Radial equilibrium direct analysis for a single stator
Let us consider the simple case illustrated in Fig. 5.4 where h_o and s are both constant and the swirl angle α_2 downstream of the stator is specified as a general function of radius through

$$\tan \alpha_2 = \frac{c_{\theta 2}}{c_{x2}} = f(r) \tag{5.33}$$

The radial equilibrium equation (5.16) then becomes

$$c_{x2} \frac{dc_{x2}}{dr} + \frac{c_{x2} \tan \alpha_2}{r} \frac{d}{dr} (rc_{x2} \tan \alpha_2) = 0$$

which may be rewritten

$$\{1 + \tan^2 \alpha_2\} \frac{dc_{x2}}{dr} + \left(\frac{\tan \alpha_2}{r} \frac{d}{dr} (r \tan \alpha_2) \right) c_{x2} = 0 \tag{5.34}$$

To summarise, this may be expressed as the linear first-order differential equation

$$\frac{dc_{x2}}{dr} + R(r)c_{x2} = 0 \tag{5.35}$$

where $R(r)$ is a function of radius given by

$$R(r) = \frac{\dfrac{\tan \alpha_2}{r}\dfrac{\mathrm{d}}{\mathrm{d}r}(r \tan \alpha_2)}{1 + \tan^2 \alpha_2} \tag{5.36}$$

The general solution of Eqn (5.35) is given by

$$c_{x2} = K \exp\left(-\smallint R(r)\,\mathrm{d}r\right) \tag{5.37}$$

where the constant K must be determined from the continuity equation (5.20).

Example 5.5 Constant α_2 stator

Problem
Derive an expression for c_{x2}/C_x downstream of a stator given that $\tan \alpha_2 = $ constant.

Solution
The function $R(r)$, Eqn (5.36), now reduces to

$$R(r) = \frac{1}{r}\left(\frac{\tan^2 \alpha_2}{1 + \tan^2 \alpha_2}\right) = \frac{\sin^2 \alpha_2}{r} = \frac{p}{r}$$

where $p = \sin^2 \alpha_2$. Thus

$$\smallint R(r)\,\mathrm{d}r = \ln\left(r^p\right)$$

and

$$\exp\left(-\smallint R(r)\,\mathrm{d}r\right) = r^{-p}$$

Equation (5.37) thus yields the solution

$$c_{x2} = K r^{-p}$$

Application of the continuity equation (5.20) then results in

$$C_x \pi (r_t^2 - r_h^2) = 2\pi K \int_{r_h}^{r_t} r^{1-p}\,\mathrm{d}r$$

$$= \frac{2\pi K}{2 - p}[r_t^{2-p} - r_h^{2-p}]$$

and hence the constant K is determined through

$$K = \frac{C_x(r_t^2 - r_h^2)(1 - p/2)}{r_t^{2-p} - r_h^{2-p}}$$
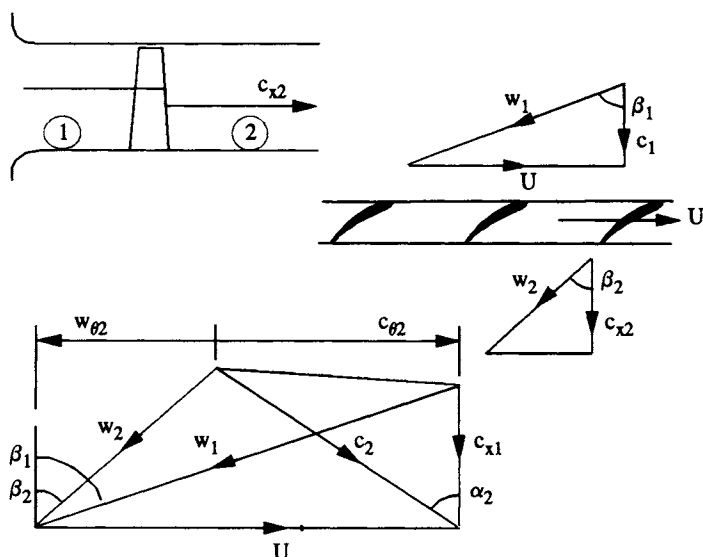
Fig. 5.5 Radial equilibrium downstream of a fan rotor

Finally, putting $h = r_h/r_t$, we have the solution

$$\frac{c_{x2}}{C_x} = \left(\frac{1-h^2}{1-h^{2-\sin^2\alpha_2}}\right)\left(1 - \frac{\sin^2\alpha_2}{2}\right)\left(\frac{r}{r_t}\right)^{-\sin^2\alpha_2} \tag{5.38}$$

Radial equilibrium direct analysis for a single rotor axial fan
Let us consider next the flow through the axial fan rotor shown in Fig. 5.5. In this case we will assume that the relative outflow angle β_2 is specified as a function of radius. For incompressible flow and zero inlet swirl $c_{\theta1}$, the Euler pump equation may be written

$$\frac{1}{\rho}(p_{o2} - p_{o1}) = r\Omega c_{\theta2} \tag{5.39}$$

If the inlet stagnation pressure p_{o1} is constant we may differentiate the above to obtain

$$\frac{1}{\rho}\frac{\mathrm{d}p_{o2}}{\mathrm{d}r} = \Omega \frac{\mathrm{d}(rc_{\theta2})}{\mathrm{d}r}$$

which may be introduced into the radial equilibrium equation (5.14) to yield

$$c_{x2}\frac{\mathrm{d}c_{x2}}{\mathrm{d}r} = \Omega \frac{\mathrm{d}(rc_{\theta2})}{\mathrm{d}r} - \frac{c_{\theta2}}{r}\frac{\mathrm{d}}{\mathrm{d}r}(rc_{\theta2}) = \left(\frac{r\Omega - c_{\theta2}}{r}\right)\frac{\mathrm{d}}{\mathrm{d}r}(rc_{\theta2}) \tag{5.40}$$

But from velocity triangles, Fig. 5.5,

$$\left.\begin{array}{l} c_{\theta2} = r\Omega - w_{\theta2} \\ w_{\theta2} = c_{x2}\tan\beta_2 \end{array}\right\} \tag{5.41}$$

Introduction of these equations into Eqn (5.40) leads finally to the following first-order linear differential equation:

$$\{1 + \tan^2 \beta_2\} \frac{dc_{x2}}{dr} + \left(\frac{\tan \beta_2}{r} \frac{d}{dr} (r \tan \beta_2) \right) c_{x2} = 2\Omega \tan \beta_2 \qquad (5.42a)$$

which may be summarised as

$$\frac{dc_{x2}}{dr} + f_1(r) c_{x2} = f_2(r) \qquad (5.42b)$$

where the two functions of radius are given by

$$\left. \begin{aligned} f_1(r) &= \left(\frac{\tan \beta_2}{r} \frac{d}{dr} (r \tan \beta_2) \right) \frac{1}{1 + \tan^2 \beta_2} \\ f_2(r) &= \frac{2\Omega \tan \beta_2}{1 + \tan^2 \beta_2} \qquad \cdot \end{aligned} \right\} \qquad (5.43)$$

The standard procedure for solution of Eqn (5.42) is to multiply throughout by $\exp(\int f_1(r) \, dr)$ and then integrate with respect to radius, resulting in

$$c_{x2} = \frac{\displaystyle\int f_2(r) \exp(\int f_1(r) \, dr) \, dr + K_1}{\exp(\int f_1(r) \, dr)} \qquad (5.44)$$

As for the previous example of the stator blade row, the constant K_1 must be determined from the continuity equation (5.20). We observe that the stator solution, Eqn (5.37), is simply a subset of the above for the case when $\Omega = 0$ and hence $f_2(r) = 0$. For the free-vortex stator, on the other hand, since $\tan \beta_2 = K_1/r$, $f_1(r)$ is also zero and Eqn (5.44) reduces as expected to $c_{x2} = K_1 = C_x$.

Numerical solution of the direct problem for a fan rotor
Although a solution has been obtained above in closed analytic form, the integrals in Eqn (5.44) would still in most cases need to be evaluated numerically. In view of this a better strategy is to solve Eqn (5.42) numerically. Thus after integration the solution may be expressed as

$$c_{x2} = L(r, c_{x2}) + K_1 \qquad (5.45)$$

where

$$\left. \begin{aligned} L(r_j, c_{x2}) &= \int_{r_h}^{r_j} \{ -c_{x2} f_1(r_j) + f_2(r_j) \} \, dr \\ &\approx \Delta r \sum_{i=1}^{j} \{ -c_{x2} f_1(r_i) + f_2(r_i) \} \end{aligned} \right\} \qquad (5.46)$$

where β_2 and thus $f_1(r_i)$ and $f_2(r_i)$ are specified at m equally spaced radii from r_h
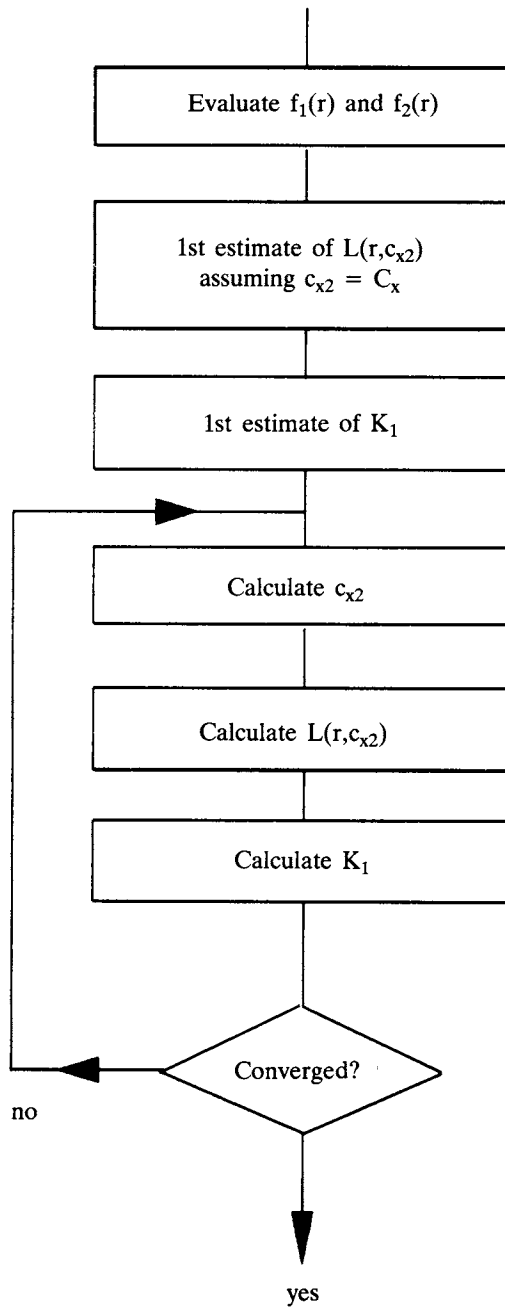
Fig. 5.6 Flow diagram for numerical solution of radial equilibrium downstream of a rotor

to r_t with $\Delta r = (r_t - r_h)/m$. The constant of integration follows from the continuity equation (5.20) which leads to

$$
\left.
\begin{aligned}
K_1 &= C_x + \frac{2}{(r_t^2 - r_h^2)} \int_{r_h}^{r_t} r L(r, c_{x2}) \, dr \\[2mm]
&\approx C_x + \frac{2\Delta r}{(r_t^2 - r_h^2)} \sum_{i=1}^{m} r_i L(r_i, c_{x2})
\end{aligned}
\right\}
\tag{5.47}
$$

However, we note that c_{x2} also appears in the expression for $L(r, c_{x2})$, Eqn (5.46), and an iterative approach is required as shown in Fig. 5.6.

The computer program RE-ANAL, the source code of which is given on the accompanying PC disc, executes this computational sequence for which sample output is given in Table 5.5.

Table 5.5 'Back to back' test using output from *design* radial equilibrium program RE-DES as input to *analysis* radial equilibrium program RE-ANAL

Initial input data to RE-DES		Output predicted by RE-DES		Final output from RE-ANAL using $\beta_{2\infty}$ values from RE-DES (column 4)	
r	$c_{\theta2}$	$c_{x\infty}$	$\beta_{2\infty}$	$c_{x\infty}$	$c_{\theta2}$
0.4	0.4	1.379 529	16.169 731	1.379 893	0.400 106
0.5	0.5	1.312 669	20.851 998	1.313 066	0.500 151
0.6	0.6	1.226 010	26.076 781	1.226 347	0.600 165
0.7	0.7	1.114 944	32.122 009	1.115 265	0.700 202
0.8	0.8	0.971 134	39.481 002	0.971 401	0.800 220
0.9	0.9	0.776 596	49.209 612	0.776 830	0.900 272
1.0	1.0	0.472 335	64.716 982	0.472 413	1.000 165

Example 5.2 of a 'solid body swirl' stator is reconsidered here where $c_{\theta2}$ is proportional to radius r, columns 1 and 2. The axial velocity $c_{x\infty}$ and consequent exit swirl angle $\beta_{2\infty}$ predicted by program RE-DES are recorded in columns 3 and 4. To check the accuracy of the two computer programs a 'back to back' test has been undertaken here in which the $\beta_{2\infty}$ values output from RE-DES were used as input to the direct analysis program RE-ANAL, setting the rotational speed $\Omega = 0$. The outcome is tabulated in columns 5 and 6 where $c_{x\infty}$ shows very close agreement with the results predicted by RE-DES, column 3. The ultimate test is the final prediction of the $c_{\theta2}$ values, column 6, which are in very close agreement with the original design data.

5.4 Actuator disc theory applied to an axial turbomachine blade row

Actuator disc theory provides a simple means for improvement to radial equilibrium analysis to allow for the progressive development of the axial velocity profile through the blade row as illustrated by Fig. 5.7. The method has been extensively documented
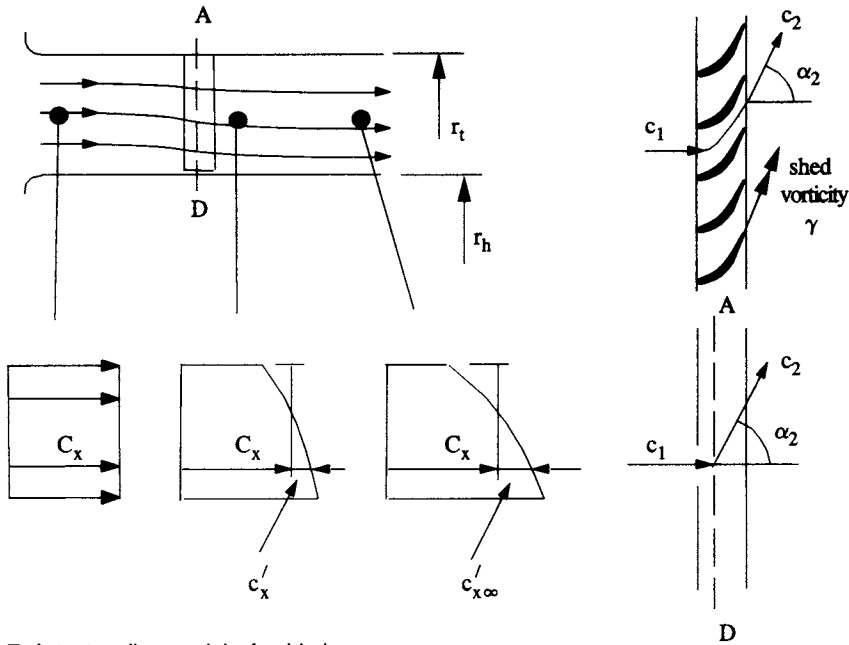
Fig. 5.7 Actuator disc model of a blade row

by Horlock (1978) and more detailed analysis will be given in Chapter 6. In this section the basic principles and final results will be presented and applied to a single blade row. In later sections the method will be extended to a series of increasingly complex design and analysis problems.

The concept of the actuator disc, borrowed from propeller theory, is illustrated in Fig. 5.7. The meridional disturbances which produce the radial shift of the streamlines are in fact caused by the shedding of vortex sheets γ from the blade trailing edges. The mechanisms underlying this will be discussed in more detail in Chapter 6. In fact the vortex shedding builds up progressively from the leading edge to the trailing edge due to any variation of the blade circulation with radius. For simplicity, however, we will assume instead that the trailing vorticity is shed discontinuously in the plane AD of the so-called *actuator disc*. An actuator disc is thus a simple mathematical model of a blade row consisting of a plane discontinuity at which the fluid deflection and associated vortex shedding are assumed to occur instantaneously.

Alternatively we could think of an actuator disc as a real blade row with the same cascade shape but with an infinite number of blades Z of infinitesimal chord l (i.e. $Z \rightarrow \infty$ as $l \rightarrow 0$). Since the actuator disc represents the centre of vortex shedding, it would seem reasonable to locate AD in the plane of the centre of bound circulation Γ of the blade profiles, i.e. at the centre of lift. The usual practice is to locate AD at the one-third blade chord position for a stator as illustrated in Fig. 5.7 and at the half chord position for a high stagger rotor. Alternatively the centre of lift could be calculated from the pressure distributions predicted by the program CASCADE. If we now express the axial velocity in the form

$$c_x = C_x + c_x' \tag{5.48}$$

r_h/r_t	k
0.3	3.2935
0.4	3.2330
0.5	3.1967
0.6	3.1731
0.7	3.1567
0.8	3.1480
0.9	3.1435
1.0	3.1416
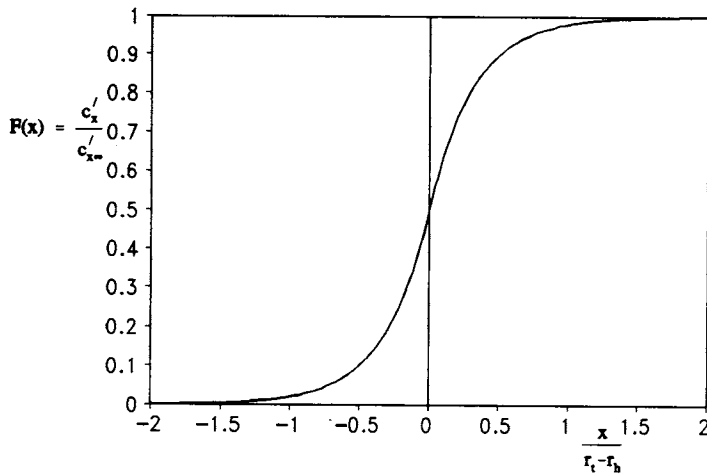
Table 5.6 Actuator disc coefficients k

Fig. 5.8 Growth of axial velocity perturbations through an actuator disc

where c_x' is a small perturbation of the mean axial velocity C_x, actuator disc analysis shows that the perturbations throughout the annulus are given by

$$
\left.
\begin{aligned}
\frac{c_x'}{c_{x\infty}'} &= \frac{1}{2}\exp\left(\frac{kx}{r_t - r_h}\right) = F(x) && \text{for } x < x_{AD} \\
&= 1 - \frac{1}{2}\exp\left(-\frac{kx}{r_t - r_h}\right) = F(x) && \text{for } x > x_{AD}
\end{aligned}
\right\}
\tag{5.49}
$$

$c_{x\infty}'$ is the radial equilibrium perturbation which obtains as $x \to \infty$, Fig. 5.7, and k is a constant, the value of which depends upon the hub/tip ratio of the annulus, Table 5.6.

The function $F(x)$ has been evaluated in Fig. 5.8 for an annulus with $r_h/r_t = 0.5$, showing how the axial velocity perturbations grow exponentially from $-\infty$ to $+\infty$. It is of particular interest to note that the perturbations c_x' reach exactly half of the radial equilibrium value $c_{x\infty}'$ at the plane of the actuator disc $x_{AD} = 0$. At any other location (x, r) the axial velocity may thus be expressed in terms of the radial equilibrium axial velocity at the same radius through

$$
c_x = C_x + c_{x\infty}' F(x - x_{AD}) = C_x + (c_{x\infty} - C_x) F(x - x_{AD})
\tag{5.50}
$$

5.5 Actuator disc analysis for a single rotor axial fan

We are now in a position to improve on the numerical scheme for direct analysis considered in the last section. Let us make the following assumptions for our actuator disc model of the single rotor fan, Fig. 5.9:

(1) The actuator disc is located at the mid-chord position x_{AD}.
(2) The blade relative outlet flow angle β_2 is determined at the trailing edge plane x_{te}.
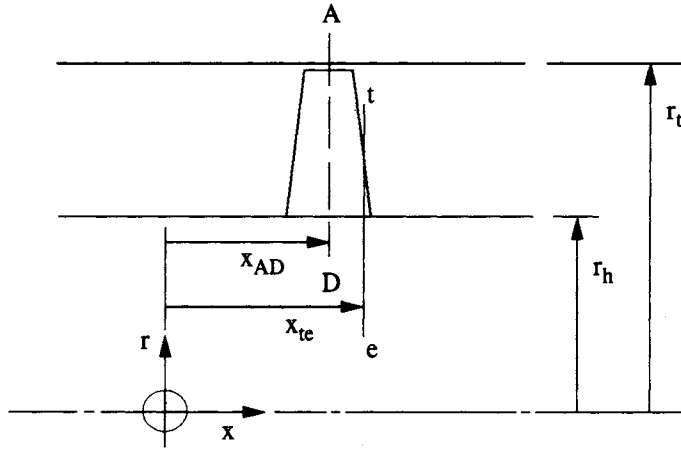
Fig. 5.9 Location of actuator disc plane (AD) and trailing edge plane (te) for axial fan

Equation (5.41) may then be rewritten

$$w_{\theta 2} = c_{x\text{te}} \tan \beta_2 \tag{5.51}$$

Thus the radial equilibrium Eqn (5.40) may be modified to read

$$
\begin{aligned}
c_{x\infty} \frac{\mathrm{d}c_{x\infty}}{\mathrm{d}r} &= \frac{w_{\theta 2}}{r} \frac{\mathrm{d}}{\mathrm{d}r}(r^2 \Omega - r w_{\theta 2}) \\
&= c_{x\text{te}} \frac{\tan \beta_2}{r} \left(2\Omega r - \frac{\mathrm{d}}{\mathrm{d}r}(c_{x\text{te}} r \tan \beta_2) \right)
\end{aligned}
\tag{5.52}
$$

If β_2 is specified as a function of radius, the above may be written in simplified form

$$\frac{\mathrm{d}c_{x\infty}}{\mathrm{d}r} = p(r, c_{x\infty}) \tag{5.53}$$

where

$$p(r, c_{x\infty}) = \frac{c_{x\text{te}}}{c_{x\infty}} \frac{\tan \beta_2}{r} \left(2\Omega r - \frac{\mathrm{d}}{\mathrm{d}r}(c_{x\text{te}} r \tan \beta_2) \right) \tag{5.54}$$

We note that $c_{x\text{te}}$ is a function of $c_{x\infty}$ through Eqn (5.50), namely

$$c_{x\text{te}} = C_x + c'_{x\infty} F(x_{\text{te}} - x_{\text{AD}}) = C_x + (c_{x\infty} - C_x) F(x_{\text{te}} - x_{\text{AD}}) \tag{5.55}$$

Equation (5.53) may now be integrated with respect to radius to provide a form of solution analogous to Eqn (5.45) suitable for iterative numerical analysis, namely

$$c_{x\infty} = L'(r, c_{x\infty}) + K_1 \tag{5.56}$$

where at radius r_j

$$
\left.
\begin{aligned}
L'(r_j, c_{x\infty}) &= \int_{r_h}^{r_j} p(r, c_{x\infty})\,\mathrm{d}r \\
&\approx \Delta r \sum_{i=1}^{j} p_i
\end{aligned}
\right\}
\tag{5.57}
$$

The previous iterative scheme, Fig. 5.6, may then be used with slight modification to achieve a numerical solution for $c_{x\infty}$ by successive approximations and hence for c_x at any other axial location in the annulus making use of Eqn (5.50).

Two computer programs are given on the accompanying PC disc which undertake actuator disc analyses for single blade rows. Program AD-ANAL solves the 'analysis' problem, predicting the flow through a blade row of prescribed efflux angle β_2. Program AD-DES solves the opposite 'design' problem, predicting the efflux angle β_2 required in order to generate a prescribed swirl velocity distribution $c_{\theta 2}$. Studies will be undertaken in the next two sections to illustrate these design and analysis problems.

5.5.1 Actuator disc design of a solid body swirl stator

To bring out the deficiencies of radial equilibrium analysis, the r–$c_{\theta 2}$ data given in Table 5.5 have been used as input into the actuator disc design program AD-DES and the results are given in Table 5.7. Although AD-DES has been written to deal with fan rotor design, a stator may also be designed by simply specifying zero speed of rotation, $\Omega = 0$.

Two solutions are illustrated here as follows:

(1) The *radial equilibrium solution*, obtained by placing the actuator disc artificially a very long way upstream of the blade row ($x_{AD} = -1000$ was used here).
(2) The *actuator disc solution* with the following locations:
   Leading edge located at $x_{LE} = 0.0$
   Actuator disc located at $x_{AD} = 0.1$
   Trailing edge located at $x_{TE} = 0.2$

Our design aim here is to predict the blade efflux angle β_2 distribution which would generate the specified swirl velocity $c_{\theta 2}$ given in column 2 with a mean axial velocity $C_x = 1.0$. Two observations may be made:

(a) Solution (1) is in close agreement with the previous radial equilibrium solution shown in Table 5.5.
(b) The true blade trailing edge efflux angles β_2 according to actuator disc analysis, solution (2), differ significantly from the $\beta_{2\infty}$ values a long way downstream delivered by radial equilibrium analysis.

5.5.2 Actuator disc design and analysis of a single stage rotor axial fan

For our second study let us reconsider the axial fan illustrated in Fig. 5.5 which comprises a single rotor only. Our aim will be to generate velocity triangle design data from an initial specification of $c_{\theta 2}$ versus radius, including also meridional flow analysis by actuator disc theory. Program AD-DES will then be used to demonstrate

Table 5.7 Design of a solid rotation swirl stator blade row: comparison of radial equilibrium and actuator disc methods

Initial input data		Solution 1 Radial equilibrium method $x_{AD} \to -\infty$		Solution 2 Actuator disc method $x_{LE} = 0.0$, $x_{AD} = 0.1$, $x_{TE} = 0.2$	
r	$c_{\theta 2}$	c_{xTE}	$\beta_{2\infty}$	c_{xTE}	β_2
0.4	0.4	1.379 52	16.169 82	1.268 81	17.497 78
0.5	0.5	1.312 66	20.852 20	1.221 45	22.261 73
0.6	0.6	1.225 99	26.077 20	1.160 06	27.348 60
0.7	0.7	1.114 91	32.122 79	1.081 39	32.915 60
0.8	0.8	0.971 09	39.482 26	0.979 52	39.239 32
0.9	0.9	0.776 57	49.210 37	0.841 75	46.915 40
1.0	1.0	0.472 86	64.692 23	0.626 64	57.927 32

how competitive designs may be postulated for different types of vortex flow $c_{\theta 2}(r)$ and in particular we will compare the free-vortex design method expounded fully in Section 5.1 with non-free-vortex swirl distributions. A suitable approach towards the latter would be to adopt a mixed-vortex which combines the two vortex types already considered, namely the free-vortex and the forced-vortex or solid-body swirl. Thus let us specify

$$c_{\theta 2} = \frac{a}{r} + br \qquad (5.58)$$

Control over the vortex mix and thus the radial distribution of loading may be exercised by careful selection of the constants a and b. However, a much better design strategy would be to consider instead the work coefficient ψ, which may be expressed as

$$\psi = \frac{\Delta p_o}{\rho U^2} = \frac{c_{\theta 2}}{U} = \frac{1}{\Omega}\left(\frac{a}{r^2} + b\right) \qquad (5.59)$$

By specifying the work coefficient ψ_m at the mean radius r_m and ψ_0 at any other radius r_0, Eqn (5.59) may be solved for the coefficients a and b to yield the following equation for $\psi(r)$:

$$\psi = \psi_m + (\psi_0 - \psi_m)\left(\frac{1/r^2 - 1/r_m^2}{1/r_0^2 - 1/r_m^2}\right) \qquad (5.60)$$

If we elect to specify the fan duty (ϕ_m, ψ_m) at the mean radius, the swirl velocity distribution, from Eqn (5.59), becomes

$$\frac{c_{\theta 2}}{C_x} = \frac{\psi}{\phi_m}\frac{U}{U_m} = \frac{\psi}{\phi_m}\frac{r}{r_m}$$

$$= \frac{1}{\phi_m}\frac{r}{r_m}\left\{\psi_m + (\psi_0 - \psi_m)\left(\frac{1/r^2 - 1/r_m^2}{1/r_0^2 - 1/r_m^2}\right)\right\} \qquad (5.61)$$

where C_x is the mean axial velocity. Close inspection confirms that this equation conforms with the original mixture of free-vortex and forced-vortex, Eqn (5.58), but instead makes use of much more helpful initial design data. Thus $c_{\theta 2}$ is now determined in terms of the design duty (ϕ_m, ψ_m) at r_m, and for a prescribed work coefficient ψ_0 at any chosen reference radius r_0.

At this point attention might usefully be directed to the following two special vortex cases.

(1) *Free-vortex swirl (b = 0)*. A free-vortex swirl distribution is obtained if we specify that

$$\frac{c_{\theta 20}}{c_{\theta 2m}} = \frac{r_m}{r_0}$$

and hence ψ_0 must be given the value

$$\psi_0 = \psi_m \left(\frac{r_m}{r_0}\right)^2 \tag{5.62}$$

As shown in Section 4.7 for zero inlet swirl, the reaction of such a rotor-only fan becomes

$$R = 1 - \frac{\psi}{2}$$

$$= 1 - \frac{\psi_m}{2}\left(\frac{r_m}{r}\right)^2 \quad \text{for the free-vortex fan} \tag{4.41}$$

Thus the radial variation of both work coefficient ψ and reaction will be very considerable for a free-vortex fan, as was shown in Table 5.1.

(2) *Forced-vortex or constant reaction fan rotor*. A pure solid-body swirl or forced-vortex will be delivered by Eqn (5.61) by specifying $\psi_0 = \psi_m$ at the reference radius r_0. In this case Eqns (5.60) and (5.61) reduce to

$$\psi = \psi_m \tag{5.60a}$$

$$\frac{c_{\theta 2}}{C_x} = \frac{\psi_m}{\phi_m}\frac{r}{r_m} \tag{5.61a}$$

Thus a fan rotor designed to generate a forced-vortex exit swirl $c_{\theta 2}$ will have the same work coefficient at all radii. From Eqn (4.41) we see that the reaction R will also be constant at all radii and equal to $R = 1 - \psi_m/2$.

Two fan designs have been completed on this basis using the program AD-DES for the common data specification given at the head of Table 5.8. For these designs a hub/tip ratio $h = 0.4$ was chosen and r_m was set at the r.m.s. radius. At r_m the selected duty coefficients were $\phi_m = 0.5$ and $\psi_m = 0.3$. The hub section was chosen for the representative radius r_0 at which the work coefficient was set at $\psi_0 = 1.0875$ for the free-vortex fan (see Eqn (5.62)) and at 0.5 for the mixed-vortex fan.

Table 5.8 Vortex and loading specifications for two alternative fan designs

Common design data:

Hub/tip ratio $h = r_h/r_t$	$= 0.4$	Leading edge location x_{le}/r_t $= 0.0$
r_m/r_t (r.m.s. radius)	$= 0.761\,577$	Trailing edge location x_{te}/r_t $= 0.2$
Duty coefficients at r_m:	$\phi_m = 0.5$	Actuator disc location $x_{AD}/r_t = 0.1$
	$\psi_m = 0.3$	Reference radius r_0 $= 0.4$

	Free-vortex design			Mixed-vortex design		
r/r_t	$c_{\theta2}/C_x$	ψ	R	$c_{\theta2}/C_x$	ψ	R
0.40	1.142 37	$\psi_0 = 1.0875$	0.456 25	0.630 27	$\psi_0 = 0.600\,00$	0.700 00
0.45	1.015 44	0.859 259	0.570 37	0.606 30	0.513 05	0.743 48
0.50	0.913 89	0.696 000	0.652 00	0.592 00	0.450 86	0.774 57
0.55	0.830 81	0.575 207	0.712 40	0.584 74	0.404 84	0.797 58
0.60	0.761 58	0.483 333	0.758 33	0.582 75	0.369 84	0.815 08
0.65	0.702 99	0.411 834	0.794 08	0.584 82	0.342 60	0.828 70
0.70	0.652 78	0.355 102	0.822 45	0.590 08	0.320 99	0.839 50
0.75	0.609 26	0.309 333	0.845 33	0.597 88	0.303 56	0.848 22
0.80	0.571 18	0.271 875	0.864 06	0.607 76	0.289 29	0.855 36
0.85	0.537 58	0.240 830	0.879 59	0.619 35	0.277 46	0.861 27
0.90	0.507 72	0.214 815	0.892 59	0.632 35	0.267 55	0.866 23
0.95	0.481 00	0.192 798	0.903 60	0.646 56	0.259 16	0.870 42
1.00	0.456 95	0.174 000	0.913 00	0.661 78	0.252 00	0.874 00

From Table 5.8 it can be seen that there is considerable radial variation of ψ and reaction R for the free-vortex design as expected. On the other hand the mixed-vortex design exhibits only modest radial variation of R and reduced spread of the work coefficient ψ. Indeed, the objective of the mixed-vortex fan design here is to shift aerodynamic loading towards the blade tips by imposing greater work coefficients, at the same time unloading the blade root region. These competing fan designs make an interesting comparison, as illustrated by Table 5.9, giving an insight into the designer's art.

The predicted velocity triangle data for these two designs are presented in Table 5.9. From these data the pitch/chord ratio t/l was also calculated assuming a diffusion factor of $DF = 0.5$ and using Eqn (2.28). A blade chord scale was then obtained according to the following definition: chord scale = (chord at r)/(chord at r_h). The following items of comparison between the two designs may be drawn out from the detailed design data in Table 5.9:

(1) The axial velocity profile c_{xte} at the trailing edge plane for the free-vortex fan is constant as we would expect for this constant work input design. For the mixed-vortex fan, on the other hand, c_{xte} varies enormously from only 0.723 18 at the hub to 1.245 07 at the tip. This is the consequence of the increase of specific work input from hub to tip for the mixed-vortex design introduced by the forced vortex component of the specified swirl $c_{\theta2}$, Table 5.8.
(2) We notice considerable variation of the relative outlet angle β_2 for the free-vortex design, which has a dramatic effect upon the rotor deflection ε_R.

Table 5.9 Comparison of free-vortex and mixed-vortex fan designs

Free-vortex design

r/r_t	c_{xte}/C_x	$c_{x\infty}/C_x$	β_1	β_2	α_2
0.4	1.0	1.0	46.410	−5.252	48.802
0.5	1.0	1.0	52.708	21.761	42.424
0.6	1.0	1.0	57.599	39.149	37.292
0.7	1.0	1.0	61.455	49.852	33.136
0.8	1.0	1.0	64.546	56.827	29.734
0.9	1.0	1.0	67.067	61.682	26.918
1.0	1.0	1.0	69.154	65.250	24.558

r/r_t	ε_R	ϕ_{te}	ψ	t/l	Chord scale
0.4	51.661	0.951 97	1.087 50	0.4886	1.0000
0.5	30.947	0.761 58	0.696 00	0.5503	1.1097
0.6	18.450	0.634 65	0.483 33	0.9359	0.7830
0.7	11.603	0.543 98	0.355 10	1.5460	0.5530
0.8	7.719	0.475 99	0.271 87	2.3257	0.4201
0.9	5.385	0.423 10	0.214 81	3.2494	0.3383
1.0	3.904	0.380 79	0.174 00	4.3049	0.2837

Mixed-vortex design

r/r_t	c_{xte}/C_x	$c_{x\infty}/C_x$	β_1	β_2	α_2
0.4	0.723 18	0.609 17	49.854	30.157	45.975
0.5	0.783 91	0.694 91	55.247	42.609	40.428
0.6	0.862 89	0.806 42	59.086	49.008	35.853
0.7	0.952 01	0.932 24	61.932	52.667	32.332
0.8	1.046 82	1.066 11	64.119	54.996	29.686
0.9	1.144 95	1.204 65	65.851	56.520	27.696
1.0	1.245 07	1.346 01	67.255	57.632	26.182

r/r_t	ε_R	ϕ_{te}	ψ	t/l	Chord scale
0.4	19.697	0.688 45	0.600 00	1.2604	1.0000
0.5	12.638	0.597 01	0.450 86	1.8468	0.8531
0.6	10.078	0.547 63	0.369 84	2.1231	0.8905
0.7	9.265	0.517 88	0.320 99	2.0783	1.0613
0.8	9.153	0.498 27	0.289 29	1.8794	1.3413
0.9	9.330	0.484 43	0.267 55	1.6444	1.7246
1.0	9.623	0.474 11	0.252 00	1.4230	2.2142

Thus the cost of demanding constant specific work at all radii is that ε_R must vary from a mere 3.904° at the tip section to an unrealistically high value of 51.661° at the hub. To achieve such high deflection from a diffusing cascade would in fact be very difficult and would be associated with high losses. The mixed-vortex fan, on the other hand, exhibits much more modest aerodynamic requirements with a much more uniform deflection ε_R in the range of 10° to 20°.

(3) The deflection levels are reflected to some extent in the recommended t/l values for the two fans and in the consequent values of chord scale. The latter show that the free-vortex fan blade will taper considerably from hub to tip which is obviously advantageous for carrying centrifugal stresses. For the mixed-vortex fan, on the other hand, the blade chords actually increase with radius in order to accommodate the greater specific work and its associated aerodynamic loading.

(4) Because the specific work input increases towards the outer radii of the mixed-vortex fan, the greater outlet stagnation pressure produces two effects. Firstly the axial velocity profile increases in the tip region. Secondly, and consequently, the mass weighted power input is greater for the mixed-vortex design. Thus integrating from hub to tip, the average specific work inputs for the two designs are as follows:

Specific work input, free-vortex design $= 1.20 \, \text{W kg}^{-1}$
Specific work input, mixed-vortex design $= 1.2473 \, \text{W kg}^{-1}$

The mixed-vortex fan is thus capable of transmitting more pumping power into the fluid, although unlike the free-vortex it will not be uniformly distributed but will be concentrated more towards the outer radii.

The blade profiles at hub, arithmetic mean and tip sections for these two fans have been designed by means of the program CASCADE, resulting in the camber and stagger angles shown in Table 5.10 which are required to achieve the correct outlet angle β_2 with shock-free inflow.

The resulting blade profiles are shown in Fig. 5.10, which reveals the marked difference in aerodynamic design requirements for these two types of fan vortex design. In particular the free-vortex fan blade is both strongly twisted and tapered, while the mixed-vortex fan blade has minimal twist and in fact increased blade chord at the tip section.

5.6 Actuator disc theory applied to multiple blade rows – the design problem

So far we have considered the meridional flow induced by a single blade row only, such as the inlet guide vanes shown in Fig. 5.7 or the axial fan rotor, Fig. 5.9. For these simple configurations the vortex flow created by the blade row is convected unhindered downstream and will grow progressively towards the radial equilibrium state as $x \to \infty$ in the manner illustrated by Figs 5.7 and 5.8. More frequently an axial turbomachine will comprise several blade rows each designed to develop a new vortex swirl $c_\theta = f(r)$ in order to control the energy transfer between blades and fluid. Horlock (1958, 1978) demonstrated the use of multiple actuator discs to model the consequential blade row interference and to predict the complex meridional flow for the whole assembly.

A suitable actuator disc model to simulate a two-stage axial fan is shown in Fig.
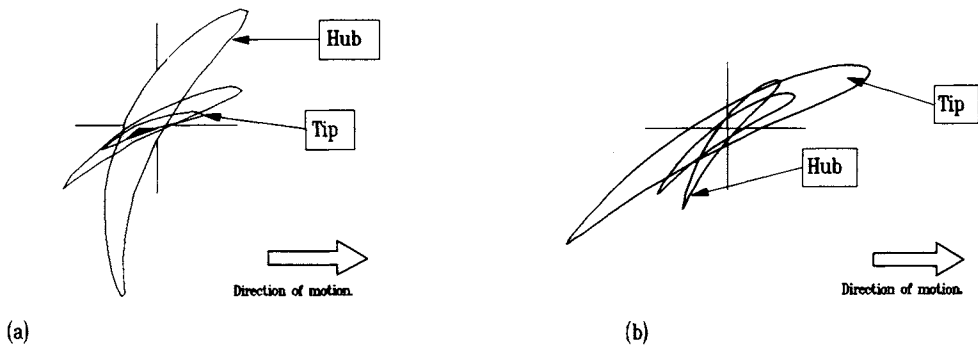
(a)　　　　　　　　　　　　　　　　　　　　(b)

Fig. 5.10 Comparison of fan rotor blade geometries for (a) free-vortex and (b) mixed-vortex designs

Table 5.10 Cascade design parameters for free-vortex and mixed-vortex fan rotor design selected to achieve shock-free inflow, using the C4 profile and circular arc camber θ

Design	Section	r/r_t	t/l	λ	θ
Free-vortex	Hub	0.4	0.4886	18.44	58
	Mean	0.7	1.5460	54.2	32
	Tip	1.0	4.3049	65.0	40
Mixed-vortex	Hub	0.4	1.2604	38.5	38
	Mean	0.7	2.0783	55.62	34
	Tip	1.0	1.4230	61.4	30

5.11 and we will consider here the *design* problem, which may be stated as follows:

(1) The swirl distributions $c_{\theta1}$, $c_{\theta2}$ etc. generated by each blade row are prescribed as functions of radius and are assumed to be created at the actuator disc planes AD1, AD2 etc.
(2) The resulting axial velocity profiles and swirl angles are then to be calculated for the leading and trailing edge planes of the blade rows, x_{le} and x_{te}.

We observe from Fig. 5.11 that the vortex field emanating from each actuator disc is in effect terminated by the next actuator disc and replaced by a new vortex field. To simplify matters at this stage let us consider first the single vortex field bounded by just the first two actuator discs, Fig. 5.12.

As illustrated above, the vortex field bounded by actuator discs AD1 and AD2 may be treated as the superposition of vortex fields for two isolated actuator discs both extending to $x = \infty$. The vortex field emanating from AD2 here is the negative of the vortex field emanating from AD1. Thus the first task required for solution of the meridional flow is calculation of the radial equilibrium solution for the vortex field created by AD1, yielding the axial velocity $c_{x\infty1} = C_x + c'_{x\infty1}$. The axial velocity
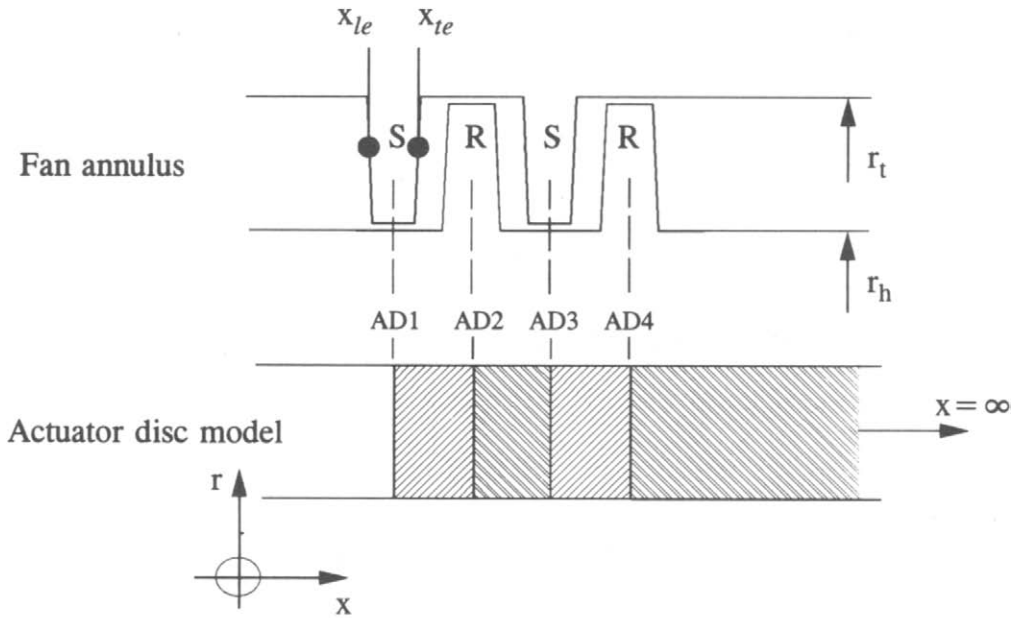
Fig. 5.11 Actuator disc model for a two-stage fan
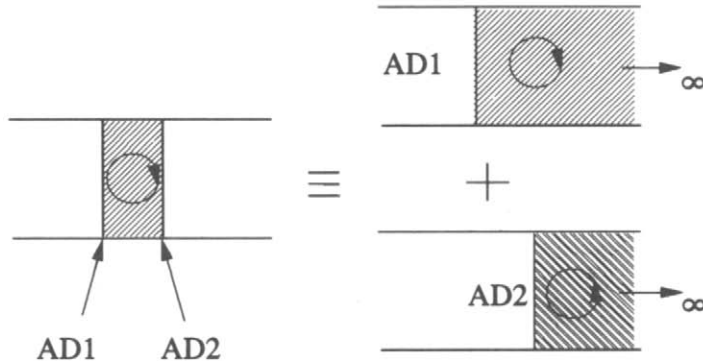
Fig. 5.12 Vortex field between two actuator discs

at any other location x in the annulus then follows from the actuator disc equation (5.55), applied to AD1 and AD2, namely

$$c'_x = c'_{x\infty 1} F(x - x_{AD1}) - c'_{x\infty 1} F(x - x_{AD2})$$
$$= c'_{x\infty 1}[F(x - x_{AD1}) - F(x - x_{AD2})] \qquad (5.63)$$

Applying this to the entire set of four blade rows illustrated in Fig. 5.11, the axial velocity c_x at any location x becomes

$$c_x = C_x + c'_x$$
$$= \sum_{i=1}^{3} c'_{x\infty i}[F(x - x_{ADi}) - F(x - x_{ADi+1})]$$
$$+ c'_{x\infty 4} F(x - x_{AD4}) \qquad (5.64)$$

The last term accounts for the vortex field created at the last actuator disc AD4 which is assumed to extend to $x = \infty$. From this discussion we may set out the simple flow diagram given in Fig. 5.13 to summarise the various stages required of the design process. The computer program MULTI has been written to perform this design sequence which will now be illustrated by considering the design of a two-stage axial fan.

Specify annulus geometry r_h, r_t, Ω, C_x and for each blade row x_{le}, x_{te}, x_{AD}

Specify c_θ as a function of radius downstream of each blade row

Solve the radial equilibrium equation for region downstream of each blade row

Calculate the axial velocity profiles at le and te locations, Eqn (5.64)

Calculate velocity triangle data and also ϕ, ψ, t/l etc. versus radius for each blade row
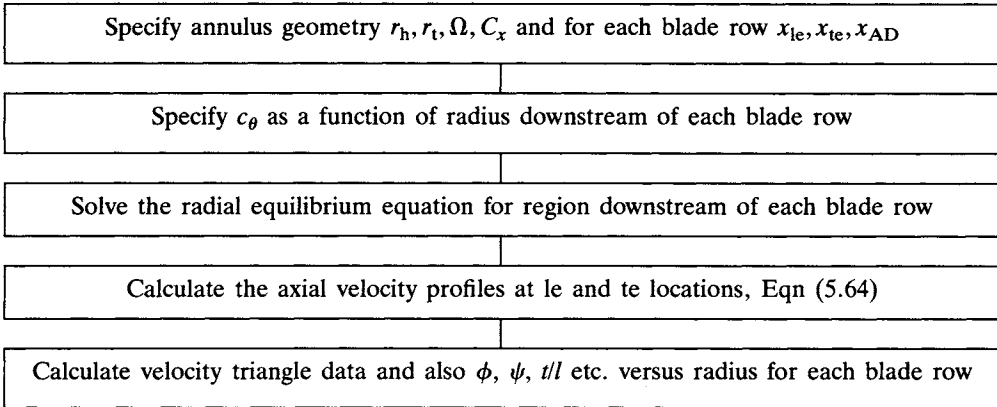
Fig. 5.13 Flow diagram for meridional analysis and design of multi-stage fan by actuator disc theory

5.6.1 Theory for constant specific work multi-stage axial fans

In Section 5.5.2 analysis was developed for a single rotor axial fan for which the downstream vortex field was formed of a mixture of free-vortex and forced-vortex swirl, Eqn (5.58). This strategy may be extended to multi-stage axial fans or compressors by specifying the swirl downstream of the stators and rotors through

$$
\left.
\begin{aligned}
c_{\theta 1} &= -\frac{a}{r} + br \quad \text{downstream of a stator} \\[2mm]
c_{\theta 2} &= \frac{a}{r} + br \quad \text{downstream of a rotor}
\end{aligned}
\right\}
\tag{5.65}
$$

Application of this to the two-stage fan illustrated in Fig. 5.11 will result in identical stages, each absorbing constant specific work at all radii. Thus from the Euler pump equation for compressible flow, Eqn (4.3), the specific work input of one stage at radius r is given by

$$
\begin{aligned}
\bar{W}(\text{J kg}^{-1}) &= \Delta h_o = U(c_{\theta 2} - c_{\theta 1}) \\
&= 2a\Omega = \text{constant}
\end{aligned}
\tag{5.66}
$$

Thus the fan will deliver the same stagnation enthalpy rise Δh_o for all meridional streamlines from hub to casing, thereby preventing the possible accumulation of radial

strong gradients dh_o/dr and thus strong variations in the axial velocity profile at exit from the fan. This style of vortex design clearly offers great attractions although there are other limitations as we shall see. The constant a may be evaluated in terms of a specified duty (ϕ_m, ψ_m) at the mean or r.m.s. radius r_m since

$$\psi_m = \frac{\Delta h_o}{U_m^2} = \frac{2a\Omega}{U_m^2} = \frac{2a}{C_x}\frac{\phi_m}{r_m}$$

and thus

$$\frac{a}{C_x} = \frac{r_m}{2}\frac{\psi_m}{\phi_m} \tag{5.67}$$

The constant b may also be expressed in terms of useful initial design input variables by reference to the velocity triangles at the mean radius, Fig. 4.6. Thus adding Eqns (5.65) we obtain for the mean radius r_m,

$$\frac{b}{C_x} = \frac{c_{\theta 1} + c_{\theta 2}}{2C_x r_m} = \frac{1 - R_m}{\phi_m r_m} \tag{5.68}$$

The dimensionless swirl velocities c_θ/C_x are now prescribed at all other radii by introducing these results into Eqn (5.65), resulting in

$$\frac{c_\theta}{C_x} = (\pm)\frac{\psi_m}{2\phi_m}\left(\frac{r_m}{r}\right) + \frac{1 - R_m}{\phi_m}\left(\frac{r}{r_m}\right) \tag{5.69}$$

with $(-)$ for stators and $(+)$ for rotors. The vortex field is thus determined entirely by the selection of the key overall design duty variables at the r.m.s. radius r_m, namely ϕ_m, ψ_m and the reaction R_m.

5.6.2 Sample design of a two-stage constant specific work axial fan

To illustrate the above analysis, a two-stage fan will be designed for the following overall specification:

Hub radius r_h = 0.6
Tip radius r_t = 1.0
r.m.s. radius $r_m = \sqrt{(r_h^2 + r_t^2)/2}$ = 0.824 62
At r_m, ϕ_m = 0.5
$\quad\quad \psi_m$ = 0.25
$\quad\quad R_m$ = 0.6

The axial locations of leading edge, trailing edge and actuator discs for the four blade rows are specified as in Table 5.11 for a fairly tightly packed machine with a good deal of meridional interaction between the blade rows.

The resulting design swirl distributions for stators and rotors as calculated with the Pascal program CONSTWK, given on the accompanying PC disc, are shown in Fig. 5.14.

Thus a fairly modest swirl c_θ/C_x is introduced in the direction of rotation by the
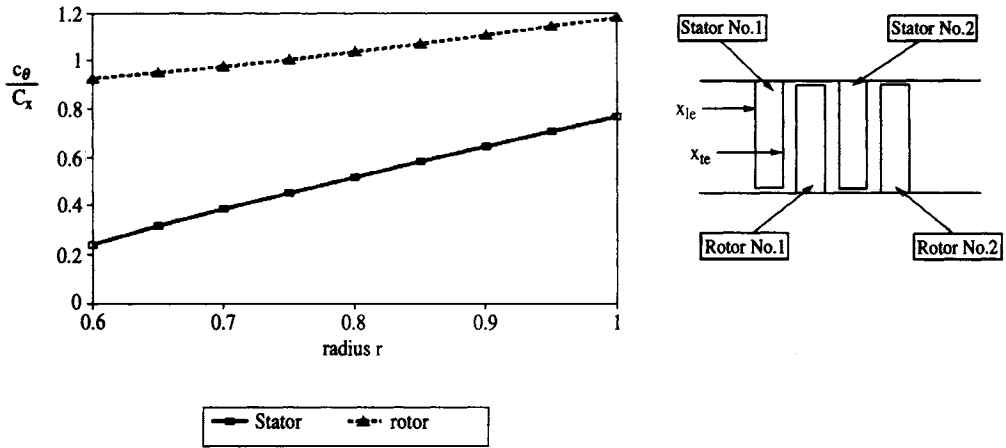
Fig. 5.14 Design swirl distributions downstream of example two-stage axial fan stator and rotor blade rows

Table 5.11 Axial location of two-stage fan blade rows and equivalent actuator discs

Item	Stator No. 1	Rotor No. 1	Stator No. 2	Rotor No. 2
Leading edge x_{le}	0.0	0.15	0.3	0.45
Trailing edge x_{te}	0.1	0.25	0.4	0.55
Actuator disc x_{AD}	0.05	0.2	0.35	0.5

first stator to precondition the entry flow to the first rotor. On the other hand, fairly substantial swirl velocities of the order $c_\theta/C_x \approx 1.0$ emanate from Rotor No. 1 and the pattern is repeated for the second stage. The axial velocity profiles predicted by actuator disc theory, using computer program MULTI, are shown in Fig. 5.15 for the leading and trailing edge planes, together with the radial equilibrium profiles.
   The following observations may be made from these results.

(1) The radial equilibrium axial velocity profiles are identical for the regimes downstream of stators 1 and 2 and downstream of rotors 1 and 2 as one would expect for identical prescribed swirl distributions.

(2) The radial equilibrium profiles slope much more heavily downstream of the rotors due to the stronger vortex flows.

(3) The actuator disc smoothing effect tends to reduce the leading and trailing edge profile slopes for the rotors well below the radial equilibrium values.

(4) The reverse is true for stator 2. Being sandwiched between two rotors, its axial velocity profile slope is greater even than that of its own radial equilibrium profile.

(5) Stator 1, being subject to less mutual blade row interference, exhibits only modest profile slopes at x_{le} and x_{te}.

(6) The radial equilibrium solutions alone would give a quite inaccurate prediction of the meridional flow which is clearly strongly influenced by mutual interference between the blade rows.
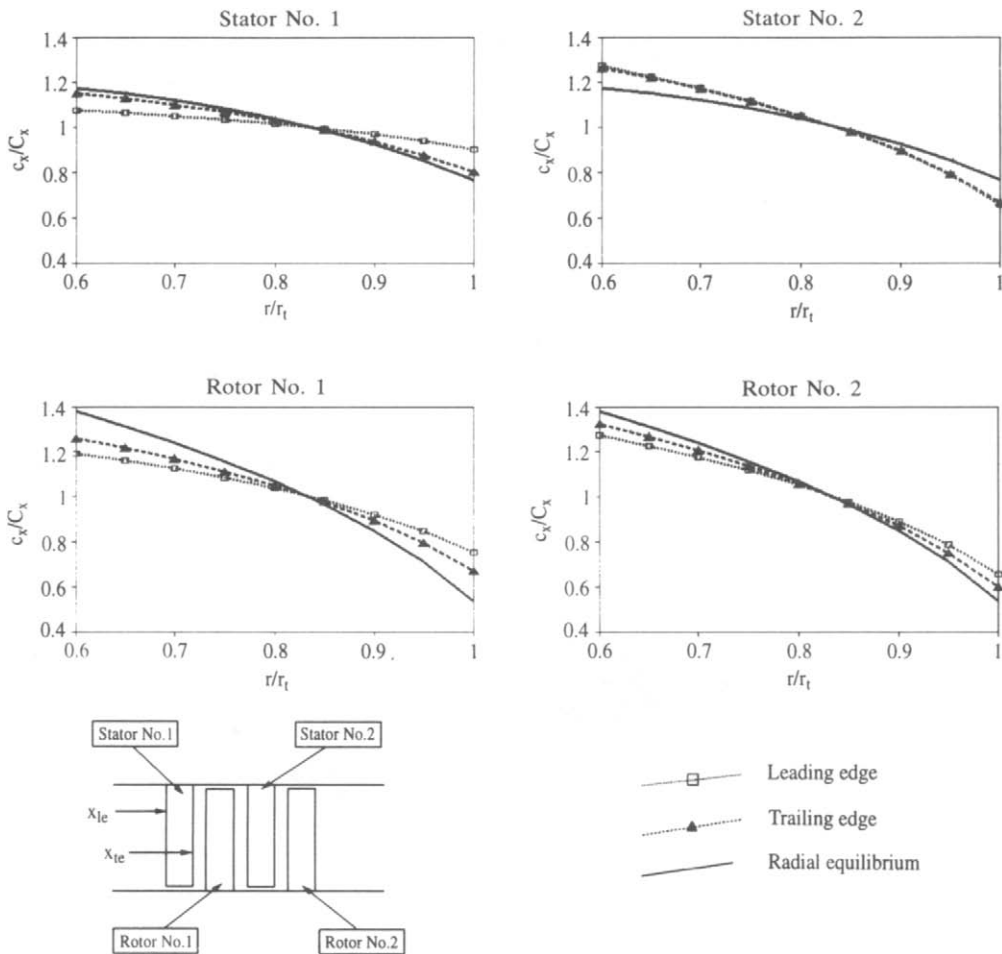
Fig. 5.15 Axial velocity profiles at various locations in a two-stage fan

Now we would expect the two stator designs to be quite different since stator 1 receives zero swirl at inlet while stator 2 has to absorb the strong swirling flow emerging from rotor 1. On the other hand the two rotors receive and eject identical swirl velocities $c_{\theta 1}$ and $c_{\theta 2}$ and we would hope therefore to be able to adopt identical blade profile geometry. Unfortunately, however, as shown by Fig. 5.15, the axial velocity profiles for the two rotors do in fact differ, resulting in slightly different velocity triangles. This is borne out by the tabulation of predicted relative inflow and outflow angles given in Table 5.12.

5.6.3   Meridional flow reversals due to excessive vortex swirl

As already explained with reference to the radial equilibrium equation (5.14) and as illustrated in Example 5.3, Section 5.3.1, the axial velocity c_x is constant for a free-vortex flow whatever the vortex strength, which makes it a very attractive design option, especially for turbines. For non-free-vortex flows, on the other hand, excessively high swirl distributions may produce such strong meridional disturbances

Table 5.12 Relative flow angles predicted for the two-stage fan rotors

r/r_t	Rotor No. 1		Rotor No. 2	
	$\beta_1°$	$\beta_2°$	$\beta_1°$	$\beta_2°$
0.6	45.69	22.82	43.77	21.84
0.7	49.44	31.83	48.18	31.02
0.8	53.88	40.82	53.50	40.55
0.9	59.06	50.35	59.95	51.11
1.0	65.49	61.69	68.44	64.41

that the axial velocity could become negative at the hub or the casing depending on the vortex type. In such situations the real flow would break down and reverse. Consequently no solution to the radial equilibrium equation would be possible. For example, the approximate solution for solid body swirl, Eqn (5.23), indicates that $c_{x_t}/C_x = 0$ at the tip radius r_t if the tip swirl velocity is set at $c_{\theta t}/C_x = 1.091\,089$ with a hub/tip ratio $h = 0.4$.

This problem represents a real physical limit on practical design which can be detected during numerical analysis but is quite difficult to predetermine. For example, for the fan duty specified in Section 5.6.2 a design is impossible for a hub tip ratio $h < 0.5$ and the program MULTI has difficulty coping with such a specification and cannot compute c_x values in reversed flow regions. It is thus essential to avoid such flow regimes and there are two options available to the designer:

(1) Prescribe a less powerful vortex type.
(2) Increase the hub/tip ratio.

We will now pursue the first of these two options.

5.6.4   Power law vortex flows for low hub/tip ratio axial fans and compressors

Although there are many possible types of vortex flow available, a wider range of constant specific work flows may be considered if Eqns (5.65) are modified as follows:

$$\left. \begin{aligned} c_{\theta 1} &= -\frac{a}{r} + br^p \quad \text{downstream of a stator} \\ c_{\theta 2} &= \frac{a}{r} + br^p \quad\;\; \text{downstream of a rotor} \end{aligned} \right\} \tag{5.70}$$

Following the same strategy as that outlined in Section 5.6.1 for multi-stage fans and compressors, the coefficients a and b may be expressed in terms of overall design parameters ϕ_m, ψ_m and R_m specified at the r.m.s. radius r_m, resulting in the vortex specification

$$\frac{c_\theta}{C_x} = (\pm)\frac{\psi_m}{2\phi_m}\left(\frac{r_m}{r}\right)^p + \frac{1-R_m}{\phi_m}\left(\frac{r}{r_m}\right)^p \tag{5.71}$$
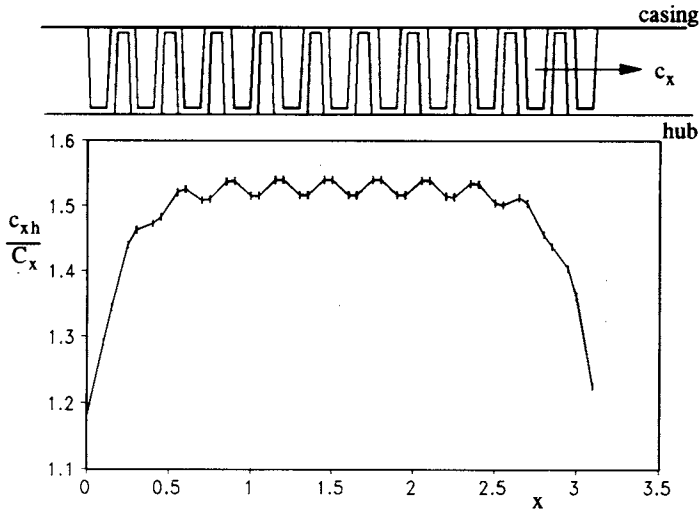
Fig. 5.16 Axial velocity c_{xh}/C_x at the hub radius of a ten-stage axial compressor predicted by actuator disc theory assuming incompressible flow
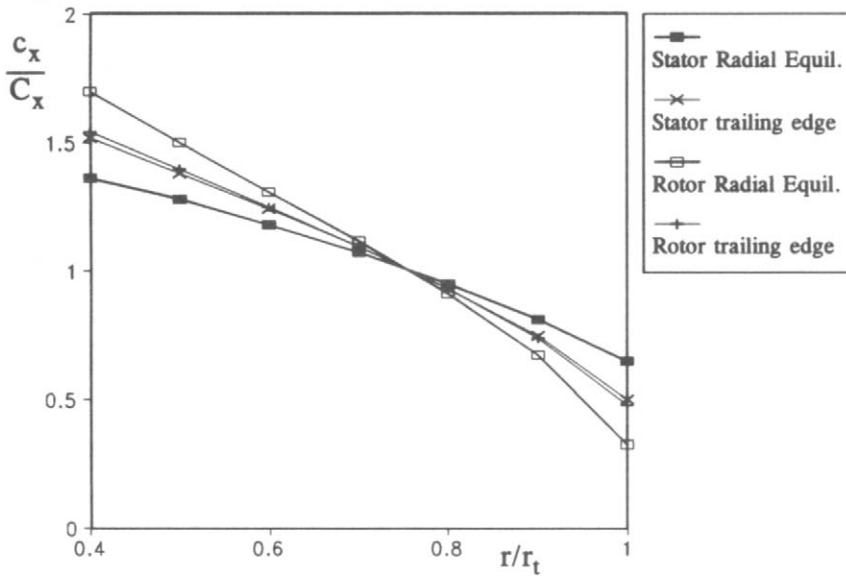
Fig. 5.17 Axial velocity profiles compared with radial equilibrium profiles for ten-stage axial compressor

with ($-$) for stators and ($+$) for rotors. $p = 1.0$ obviously corresponds to the special case of the forced vortex for the second term. More modest values of $p < 1.0$ will thus result in reduced meridional disturbances and axial velocity profile slopes and permit the designer to select a smaller value of hub/tip ratio if so desired. To illustrate this and to conclude this chapter the actuator disc solution has been undertaken using program MULTI for a ten-stage compressor with the following overall design

specification with $p = 0.25$:

Hub/tip ratio r_h/r_t	$= 0.4$
r.m.s. radius r_m/r_t	$= 0.812\,40$
At r_m, ϕ_m	$= 0.5$
ψ_m	$= 0.25$
R_m	$= 0.5$
Vortex power coefficient p	$= 0.25$

Figure 5.16 illustrates how the meridional velocity at the hub radius builds up rapidly during the first two stages and settles down into a small periodic variation from stator to rotor around a value in the region of $c_{x_h}/C_x = 1.52$. The predicted axial velocity profiles at the stator and rotor trailing edge planes for stage 5 are compared in Fig. 5.17 with the related radial equilibrium solutions.

From these studies two conclusions may be drawn. Firstly, the meridional flow tends to settle down fairly quickly to a regular pattern such that identical blade geometry could be adopted for all stages except the first and last. Secondly, the trailing edge axial velocity profiles for stator and rotor are almost identical and lie roughly half-way between the two radial equilibrium solutions for stator and rotor. It should be pointed out that an extra stator has been provided here downstream of the last stage to remove the exit swirl.

A final and most important observation to make is that in practice for a gas compressor the area should be reduced progressively proceeding through the stages to maintain constant axial velocity c_x as the density increases. Introduction of compressibility into actuator disc analysis to handle this problem will be dealt with in the next chapter.

6
Vorticity production in turbomachines and its influence upon meridional flows

Introduction

The title of this chapter has been chosen with good reason, for turbomachines operate, as the Latin *turbo* suggests, by creating a whirling motion or *vortex* (again, Latin for whirlpool). Vorticity production is the prime mechanism for both the development of blade lift, as we have shown in Chapter 2, and energy transfer between fluid and rotating shaft, Chapters 1 and 5. In the last chapter free-vortex machines, for which the swirl velocity obeys the law $c_\theta r$ = constant, were shown to exhibit very simple meridional flow characteristics. Thus for incompressible flow through axial turbomachines with cylindrical hub and casing the axial velocity c_x and stagnation pressure p_0 are then constant, satisfying the radial equilibrium equation (5.14) for cylindrical flow. On the other hand a designer may prefer to specify some other swirl and/or stagnation pressure distributions. Radial equilibrium and actuator disc theory have been presented in Chapter 5 as two means for prediction of the consequent meridional disturbances.

Similar design problems arise in non-cylindrical or 'mixed-flow' turbomachines as illustrated by Fig. 6.1. If the blades of a mixed-flow fan are designed to generate equal stagnation pressure rise $p_{o2} - p_{o1}$ for all meridional streamlines, the swirl velocity $c_{\theta 2}$ will obey the free-vortex law $c_{\theta 2}r$ = constant. In this case, as for cylindrical machines, the meridional flow (defined as the circumferential average or equivalent axisymmetric flow) and streamline pattern will be uninfluenced by the presence of the blades, Fig. 6.1(a). Should the designer depart from free-vortex swirl, on the other hand, the blades will produce tangential vorticity ω_θ which will cause meridional flow disturbances as illustrated by Fig. 6.1(b).
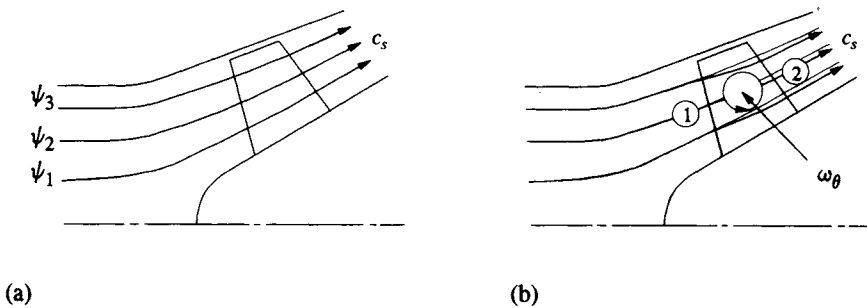

Fig. 6.1 Meridional streamlines in a mixed-flow fan: (a) meridional flow through empty annulus or with free-vortex blading; (b) meridional flow disturbances caused by non-free-vortex blading

The principal aims of this chapter are

(a) to develop the meridional equations for axial and mixed-flow turbomachines, and
(b) to show the underlying vortex production mechanisms linking two types of vorticity generated by turbomachinery blade rows, namely *streamwise vorticity* and *smoke-ring vorticity*.

These matters will be dealt with in Sections 6.1 to 6.4, including a full derivation of the equations of motion for axisymmetric flow and the reduction of these to form a set of governing equations for turbomachinery meridional flows. The origin of the classical actuator disc solution for cylindrical annuli as already used in Chapter 5 will then be presented briefly in Section 6.5. To conclude this chapter, solutions will be developed for compressible flow through actuator discs, Section 6.5, including recent extensions of this to include annulus area changes needed to accommodate density decrease in multi-stage axial turbines.

(a)   (b)
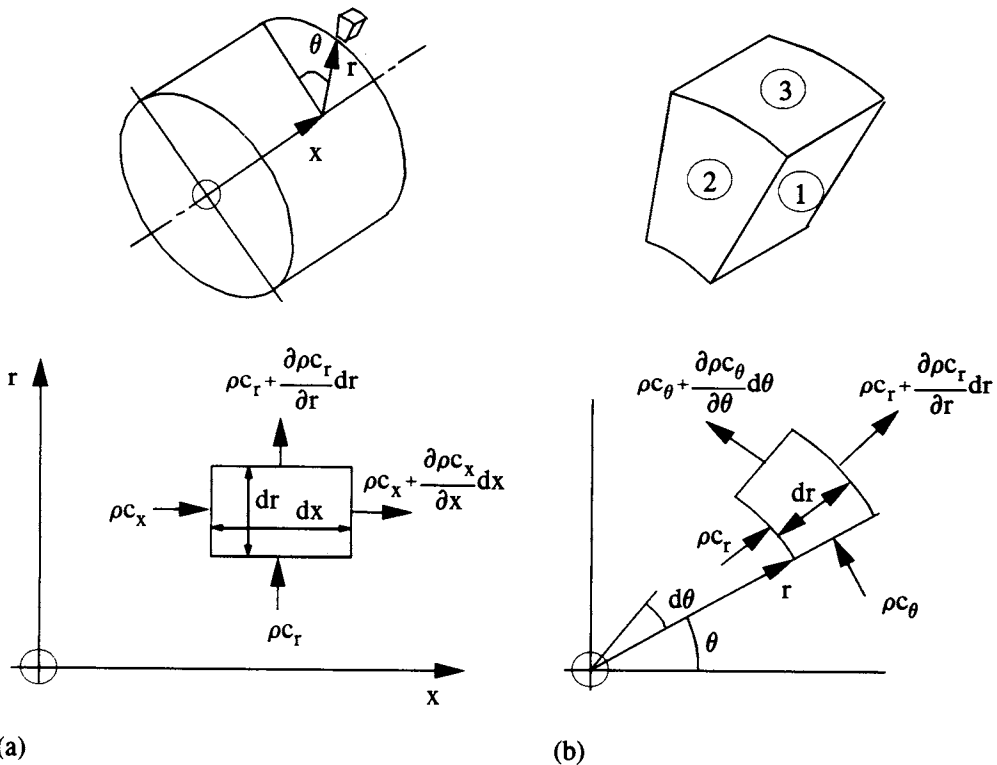
Fig. 6.2 Elementary control volume ($dv = dx.dr.rd\theta$) in cylindrical coordinates: (a) view on face 1 in the x,r plane; (b) view on face 2 in the r,θ plane

6.1 Equations of motion for axisymmetric flow

In order to derive a set of governing equations for turbomachinery meridional flow we must first state the equations of motion for axisymmetric flow. These comprise:

(a) the continuity equation, which invokes the physical principle of the conservation of matter, and

(b) the momentum equations, which invoke Newton's second law as applied to a fluid.

These will be dealt with in turn in the following subsections, adopting cylindrical polar coordinates, (x, r, θ), Fig. 6.2.

6.1.1 The continuity equation

Applying the principle of conservation of matter to the elementary control volume $dV = dx \cdot dr \cdot rd\theta$, Fig. 6.2, the net mass flux leaving the control volume must be equated to zero. For axisymmetric flow all derivatives in the θ direction such as $\partial(\rho c_\theta)/\partial\theta$ must be zero. Accounting for the mass flux through opposite pairs of faces of the element we thus obtain

$$\left. \begin{array}{l} \text{(faces 2)} \ \{\rho c_x + \dfrac{\partial \rho c_x}{\partial x}\,dx - \rho c_x\}\, r\, d\theta\, dr \\[2ex] \text{(faces 3)} \ \{\rho c_r + \dfrac{\partial \rho c_r}{\partial r}\,dr\}\,(r + dr)\, d\theta\, dx - \rho c_r r\, d\theta\, dx = 0 \end{array} \right\} \tag{6.1}$$

Neglecting terms of second order of smallness, this equation reduces to the continuity equation for axisymmetric steady compressible flow:

$$\frac{\partial \rho c_x}{\partial x} + \frac{\partial \rho c_r}{\partial r} + \frac{\rho c_r}{r} = 0 \qquad \text{compressible flow} \tag{6.2}$$

For incompressible flow the density ρ is constant, resulting in the simpler form

$$\frac{\partial c_x}{\partial x} + \frac{\partial c_r}{\partial r} + \frac{c_r}{r} = 0 \qquad \text{incompressible flow} \tag{6.3}$$

Alternatively the continuity equation may be expressed in vector form through

$$\left. \begin{array}{ll} \text{div}\,\rho\hat{q} = 0 & \text{compressible flow} \\ \text{div}\,\hat{q} = 0 & \text{incompressible flow} \end{array} \right\} \tag{6.4}$$

Several important analytical derivations pertinent to meridional flows can be made from the continuity equation and we will return to this matter again in Sections 6.3 and 6.6. At this point, on the other hand, it will be more helpful to introduce the momentum equations.

6.1.2 The momentum equations for axisymmetric flow in Eulerian form

If Newton's second law is applied to the elementary control volume, Fig. 6.3, then for any specified direction

$$\begin{pmatrix} \text{Applied forces on} \\ \text{the control volume} \end{pmatrix} = \begin{pmatrix} \text{Rate of change of momentum of} \\ \text{the fluid crossing the boundary} \end{pmatrix}$$
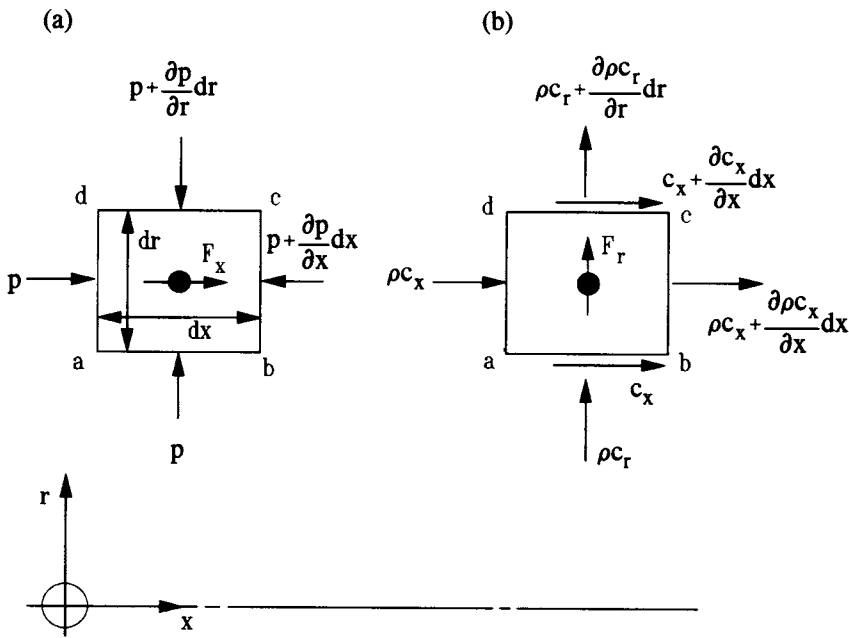
Fig. 6.3 (a) Pressure forces on element; (b) momentum flux

Thus for the x direction we have the following.

(1) *Applied forces in x direction.* These are given by:

Applied forces in x direction

$$= F_x \rho\, dx \cdot dr \cdot r\, d\theta + p\, dr \cdot r\, d\theta - \left(p + \frac{\partial p}{\partial x} dx \right) dr \cdot r\, d\theta$$

$$= \rho\, dx \cdot dr \cdot r\, d\theta \left(F_x - \frac{1}{\rho}\, \frac{\partial p}{\partial x} \right) \tag{6.5}$$

where F_x is defined as the distributed body force per unit mass of fluid at point (x, r, θ). Distributed body forces can be introduced into a fluid by externally applied potential fields such as electrostatic, electromagnetic or gravitational force fields. In turbomachines body forces from such sources are rarely significant and real body forces such as lift and drag are applied at the blade surfaces and not throughout the fluid. On the other hand, in some meridional analyses, because of the assumption of an equivalent axisymmetric flow, it is helpful to smear the blade forces throughout the regions occupied by the blade rows and to include their influence upon the meridional flow as distributed body forces.

(2) *Momentum flux in x direction through ad and bc.* The momentum flux through element faces ad and bc which are normal to the x direction is given by

$$dM_{xx} = \left(\left(\rho c_x + \frac{\partial \rho c_x}{\partial x}\, dx \right) \left(c_x + \frac{\partial c_x}{\partial x}\, dx \right) - \rho c_x c_x \right) dr \cdot r\, d\theta$$

$$= \left(c_x \frac{\partial \rho c_x}{\partial x} + \rho c_x \frac{\partial c_x}{\partial x} \right) dx \cdot dr \cdot r\, d\theta \tag{6.6}$$

where the term involving the product $(\partial\rho c_x/\partial x)(\partial c_x/\partial x)\,\mathrm{d}x^2$ has been neglected, being of second order of smallness.

(3) *Momentum flux in x direction through ab and cd.* It is perhaps less obvious that fluid is convected through the element sides ab and cd even though they are parallel to the x direction, due to the radial velocity component c_r. Such momentum flux can be expressed through

$$\mathrm{d}M_{xr} = \left(\rho c_r + \frac{\partial\rho c_r}{\partial r}\,\mathrm{d}r \right)\left(c_x + \frac{\partial c_x}{\partial r}\,\mathrm{d}r \right)(r+\mathrm{d}r)\,\mathrm{d}\theta\,\mathrm{d}x - \rho c_r c_x r\,\mathrm{d}\theta\,\mathrm{d}x$$

$$= \left(c_r\frac{\partial c_x}{\partial r} + \frac{c_x}{\rho}\frac{\partial\rho c_r}{\partial r} + \frac{c_r c_x}{r} \right)\rho r\,\mathrm{d}\theta\,\mathrm{d}x\,\mathrm{d}r \tag{6.7}$$

where once again second-order terms have been neglected. Combining Eqns (6.5a) to (6.7) the momentum equation in the x direction becomes

$$F_x - \frac{1}{\rho}\frac{\partial p}{\partial x} = \frac{c_x}{\rho}\left\{ \frac{\partial\rho c_x}{\partial x} + \frac{\partial\rho c_r}{\partial r} + \frac{\rho c_r}{r} \right\} + c_x\frac{\partial c_x}{\partial x} + c_r\frac{\partial c_x}{\partial r}$$

But from the continuity equation (6.2) the term in braces {} is zero.

Applying the same derivation procedure in the r and θ directions the full set of momentum equations for axisymmetric flow may be obtained, namely

$$\left.\begin{aligned}
F_x - \frac{1}{\rho}\frac{\partial p}{\partial x} &= c_x\frac{\partial c_x}{\partial x} + c_r\frac{\partial c_x}{\partial_r} \\[2mm]
F_r - \frac{1}{\rho}\frac{\partial p}{\partial r} &= c_x\frac{\partial c_r}{\partial x} + c_r\frac{\partial c_r}{\partial r} - \frac{c_\theta^2}{r} \\[2mm]
F_\theta &= c_x\frac{\partial c_\theta}{\partial x} + c_r\frac{\partial c_\theta}{\partial r} + \frac{c_\theta c_r}{r}
\end{aligned}\right\} \tag{6.8}$$

Together with the continuity equation (6.2) or (6.3), these form the equations of motion or Eulerian equations for axisymmetric inviscid (frictionless) fluid flow.

6.1.3   Alternative form of momentum equations in terms of stagnation pressure and vorticity

The momentum equations may be expressed in terms of the stagnation pressure p_0 if we introduce the definition

$$\frac{p_0}{\rho} = \frac{p}{\rho} + \frac{c_x^2}{2} + \frac{c_r^2}{2} + \frac{c_\theta^2}{2}$$

Thus, differentiating these partially with respect to x and r, for *incompressible flow* we have the expressions

$$\frac{1}{\rho}\frac{\partial p}{\partial x} = \frac{1}{\rho}\frac{\partial p_0}{\partial x} - c_x\frac{\partial c_x}{\partial x} - c_r\frac{\partial c_r}{\partial x} - c_\theta\frac{\partial c_\theta}{\partial x}$$

$$\frac{1}{\rho}\frac{\partial p}{\partial r} = \frac{1}{\rho}\frac{\partial p_0}{\partial r} - c_x\frac{\partial c_x}{\partial r} - c_r\frac{\partial c_r}{\partial r} - c_\theta\frac{\partial c_\theta}{\partial r}$$

so that Eqns (6.8) transform to

$$\left.\begin{aligned}
F_x - \frac{1}{\rho}\frac{\partial p_o}{\partial x} &= \quad c_r\left(\frac{\partial c_x}{\partial r} - \frac{\partial c_r}{\partial x}\right) - c_\theta\frac{\partial c_\theta}{\partial x} \\
F_r - \frac{1}{\rho}\frac{\partial p_o}{\partial r} &= -c_x\left(\frac{\partial c_x}{\partial r} - \frac{\partial c_r}{\partial x}\right) - \frac{c_\theta}{r}\frac{\partial r c_\theta}{\partial r} \\
F_\theta &= c_x\frac{\partial c_\theta}{\partial x} + \frac{c_r}{r}\frac{\partial r c_\theta}{\partial r}
\end{aligned}\right\} \qquad (6.9)$$

At this point it is helpful to introduce vorticity which in vectors is defined as $\hat{\omega} = \mathrm{curl}\,\hat{q}$. Expressed in cylindrical polar coordinates the three components of vorticity, Lamb (1945), become

$$\left.\begin{aligned}
\omega_x &= \frac{1}{r}\frac{\partial c_\theta r}{\partial r} - \frac{1}{r}\frac{\partial c_r}{\partial \theta} \\
\omega_r &= \frac{1}{r}\frac{\partial c_x}{\partial \theta} - \frac{\partial c_\theta}{\partial x} \\
\omega_\theta &= \frac{\partial c_r}{\partial x} - \frac{\partial c_x}{\partial r}
\end{aligned}\right\} \qquad (6.10)$$

For axisymmetric flows, since $\partial/\partial\theta = 0$, these reduce to

$$\left.\begin{aligned}
\omega_x &= \frac{1}{r}\frac{\partial c_\theta r}{\partial r} \\
\omega_r &= -\frac{\partial c_\theta}{\partial x} \\
\omega_\theta &= \frac{\partial c_r}{\partial x} - \frac{\partial c_x}{\partial r}
\end{aligned}\right\} \qquad (6.11)$$

and we see immediately that the momentum equations (6.9) simplify to

$$\left.\begin{aligned}
\frac{1}{\rho}\frac{\partial p_o}{\partial x} - F_x &= c_r\omega_\theta - c_\theta\omega_r \\
\frac{1}{\rho}\frac{\partial p_o}{\partial r} - F_r &= c_\theta\omega_x - c_x\omega_\theta \\
-F_\theta &= c_x\omega_r - c_r\omega_x
\end{aligned}\right\} \qquad (6.12)$$

In vector notation this may be stated as

$$\frac{1}{\rho}\mathrm{grad}\,p_o - \hat{F} = \hat{q}\times\hat{\omega} = \hat{q}\times\nabla\times\hat{q} \qquad (6.13)$$

In this form the momentum equations tell us that the presence of stagnation pressure gradients or distributed body forces within a fluid in motion are associated with distributed vorticity $\hat{\omega}$ with vector direction normal to the local velocity $\hat{q}$. In axisymmetric flow since $\partial p_o/\partial\theta = 0$ then the $\mathrm{grad}\,p_o$ vector lies in the (x, r) meridional

plane. Thus the tangential vorticity component ω_θ, which is normal to the meridional velocity c_s, Fig. 6.1, will play the major role in controlling the meridional flow.

Turbomachinery blade rows are designed to control and manipulate the swirl velocity c_θ in order deliberately to produce changes of stagnation pressure p_o or enthalpy h_o in exchange for shaft work. Thus blade rows are in essence the producers of vorticity and later in Section 6.3 we will return to this important subject of vorticity production in turbomachines which is the key mechanism at the heart of meridional flow analysis. Before proceeding with this it will be helpful to reconsider briefly the radial equilibrium analysis of Chapter 5 in the light of the radial equation of motion.

6.2 Comparison of the radial equilibrium equation with the true radial momentum equation

The radial momentum equation (6.9b), in the absence of body forces, may be rewritten

$$\frac{1}{\rho}\frac{\partial p_o}{\partial r} = c_x \frac{\partial c_x}{\partial r} + \frac{c_\theta}{r}\frac{\partial r c_\theta}{\partial r} - c_x \frac{\partial c_r}{\partial x}$$

Now as shown in Chapter 5 the radial equilibrium equation (5.14) is given by

$$\frac{1}{\rho}\frac{\mathrm{d} p_o}{\mathrm{d} r} = c_x \frac{\mathrm{d} c_x}{\mathrm{d} r} + \frac{c_\theta}{r}\frac{\mathrm{d} r c_\theta}{\mathrm{d} r}$$

Radial velocity components c_r are assumed to be zero in radial equilibrium analysis and we see that these equations are identical apart from the last term, $c_x(\partial c_r/\partial x)$.

Let us pause briefly to examine this assumption of radial equilibrium theory by reference to Fig. 6.4 which illustrates the behaviour of c_r and thus $\partial c_r/\partial x$ in the neighbourhood of a single blade row. The meridional streamline radial shifts required to accommodate the build-up of the axial velocity profile c_x to its radial equilibrium value $c_{x\infty}$ imply a growth and decay of c_r symmetrically about $x = 0$ as illustrated. Taking the differential of this curve, Fig. 6.4(b), we see that $\partial c_r/\partial x \to 0$ as $x \to \pm\infty$ as expected for radial equilibrium at a long distance from the blade row. It is of interest to note that surprisingly $\partial c_r/\partial x$ will also vanish at $x = 0$, for example in the plane of an equivalent actuator disc (see Section 5.4). Curiously, in this plane the equation of motion momentarily reduces to the radial equilibrium equation even though c_r itself is non-zero. More important, however, are the regions A and B just upstream and downstream of the blade row where maximum meridional disturbances occur, of special importance should they interfere with neighbouring blade rows. Actuator disc theory as outlined in Chapter 5 provides a very good estimate of these meridional disturbances and associated mutual blade row interference for multi-stage cylindrical turbomachines. Here we observe that they are due to radial redistributions of mass flow caused by radial velocities c_r. These effects are vortical in nature and caused by the tangential vorticity ω_θ produced by the blade row, which provides the fluid dynamic link between velocity components c_x and c_r through its definition, Eqn (6.10c), namely

$$\omega_\theta = \frac{\partial c_r}{\partial x} - \frac{\partial c_x}{\partial r}$$

(a)

(b)
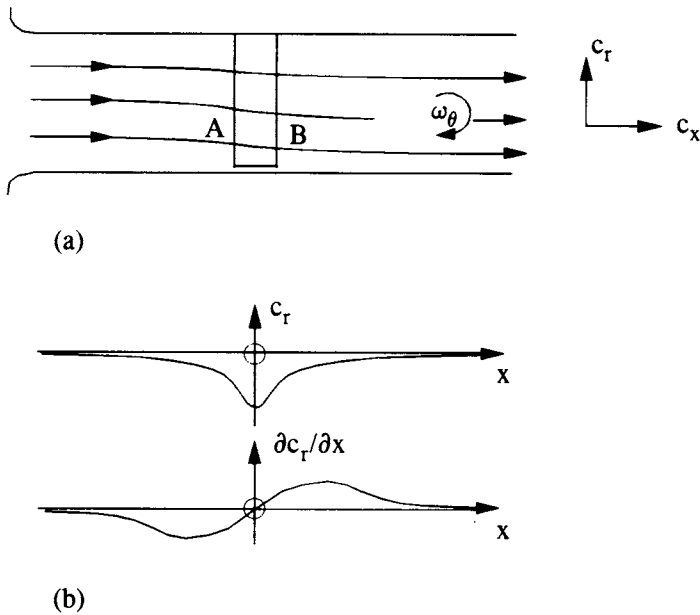
Fig. 6.4 Meridional disturbances due to tangential vorticity ω_θ created by a blade row: (a) meridional streamline shift; (b) axial variation of c_r and $\partial c_r/\partial x$

6.3   Stokes' stream function and the governing equations for meridional flow

In order to convert the above equations of motion into a set of governing equations suitable for meridional analysis it is helpful first to derive Stokes' stream function. To achieve this the continuity equation (6.2) may be rearranged to read as follows:

$$\frac{\partial(\rho r c_x)}{\partial x} + \frac{\partial(\rho r c_r)}{\partial r} = 0 \tag{6.14}$$

By observation we can postulate that a function $\psi(x,r)$ exists such that

$$\left. \begin{aligned} c_x &= \frac{1}{\rho r}\frac{\partial \psi}{\partial r} \\[2mm] c_r &= -\frac{1}{\rho r}\frac{\partial \psi}{\partial x} \end{aligned} \right\} \quad \text{for compressible flow} \tag{6.15}$$

The truth of this can be checked by back substitution, and ψ is known as Stokes' stream function. For incompressible flow ρ vanishes from the continuity equation and Eqns (6.15) become

$$\left. \begin{aligned} c_x &= \frac{1}{r}\frac{\partial \psi}{\partial r} \\[2mm] c_r &= -\frac{1}{r}\frac{\partial \psi}{\partial x} \end{aligned} \right\} \quad \text{for incompressible flow} \tag{6.16}$$

6.3.1 Properties of the stream function – incompressible flow

Stokes' stream function has the characteristics of a potential whose derivative in a given direction multiplied by $1/r$ gives the velocity component at right-angles clockwise. Its other more significant property is that contours $\psi = $ constant define the meridional streamlines. To confirm this, since ψ is a function of both x and r its derivative is given by

$$
\begin{aligned}
\mathrm{d}\psi &= \frac{\partial\psi}{\partial x}\,\mathrm{d}x + \frac{\partial\psi}{\partial r}\,\mathrm{d}r \\
&= r(-c_r\,\mathrm{d}x + c_x\,\mathrm{d}r)
\end{aligned}
\tag{6.17}
$$

where use has been made of Eqn (6.16).

Now the slope α of a meridional streamline, Fig. 6.5, is given by

$$
\left.\begin{aligned}
\tan\alpha &= \frac{c_r}{c_x} = \frac{\mathrm{d}r}{\mathrm{d}x} \\
\text{or} -c_r\,\mathrm{d}x &+ c_x\,\mathrm{d}r = 0
\end{aligned}\right\}
\tag{6.18}
$$

Introducing this into Eqn (6.17) we see that along a meridional streamline

$$
\left.\begin{aligned}
\mathrm{d}\psi &= 0 \\
\text{or}\quad \psi &= \text{constant}
\end{aligned}\right\}
\tag{6.19}
$$

Introducing Eqn (6.18) back into (6.17) the following useful result is obtained:

$$
c_x\frac{\partial\psi}{\partial x} + c_r\frac{\partial\psi}{\partial r} = 0
\tag{6.20a}
$$

In vector notation this becomes

$$
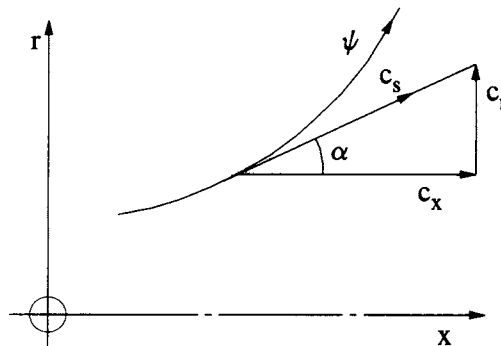\hat{q}\cdot\operatorname{grad}\psi = 0
\tag{6.20b}
$$

Fig. 6.5 Slope of a meridional streamline ψ

In other words the gradient (derivative) of ψ in the direction of the local meridional velocity $\hat{q}$ is zero. That is, ψ is constant along the meridional streamlines and hence its title *stream function*.

6.3.2   Governing equation in Stokes' stream function – incompressible flow

If we now eliminate c_x and c_r from the third vorticity component ω_θ, Eqn (6.10c), by introducing Eqns (6.16), then

$$\omega_\theta = \frac{\partial c_r}{\partial x} - \frac{\partial c_x}{\partial r} = \frac{\partial}{\partial x}\left\{-\frac{1}{r}\frac{\partial \psi}{\partial x}\right\} - \frac{\partial}{\partial r}\left\{\frac{1}{r}\frac{\partial \psi}{\partial r}\right\}$$

and finally we have Stokes' equation for incompressible rotational axisymmetric flow:

$$\frac{\partial^2 \psi}{\partial x^2} - \frac{1}{r}\frac{\partial \psi}{\partial r} + \frac{\partial^2 \psi}{\partial r^2} = -\omega_\theta r \tag{6.21}$$

This is now our principal governing equation for incompressible meridional flow and its solution ψ yields the meridional streamline distribution for an annular space containing a specified spatial distribution of tangential vorticity ω_θ. Although the numerical solution of this equation seems straightforward enough, subject to annulus wall boundary conditions $\psi = \psi_h$ and $\psi = \psi_t$ along hub and casing respectively, one big problem remains, namely the spatial distribution of ω_θ. This requires the derivation of an auxiliary equation linking ω_θ to the swirl velocity c_θ and the stagnation pressure p_o. Further analysis to accomplish this will be undertaken in the next two subsections.

6.3.3   Convection of stagnation pressure and angular momentum in axisymmetric flows

In the absence of body forces the momentum equations (6.12) become

$$\left.\begin{array}{r} \dfrac{1}{\rho}\dfrac{\partial p_o}{\partial x} = c_r\omega_\theta - c_\theta\omega_r \\[2mm] \dfrac{1}{\rho}\dfrac{\partial p_o}{\partial r} = c_\theta\omega_x - c_x\omega_\theta \\[2mm] 0 = c_x\omega_r - c_r\omega_x \end{array}\right\} \tag{6.22}$$

If the first two are combined to eliminate ω_θ we obtain

$$c_x\frac{\partial p_o}{\partial x} + c_r\frac{\partial p_o}{\partial r} = \rho c_\theta(c_r\omega_x - c_x\omega_r)$$

and introducing the third equation we have finally

or

$$\left.\begin{array}{r} c_x\dfrac{\partial p_o}{\partial x} + c_r\dfrac{\partial p_o}{\partial r} = 0 \\[3mm] \hat{q}\cdot\operatorname{grad}p_o = 0 \end{array}\right\} \tag{6.23}$$

Comparing this result with Eqn (6.20) we see that p_o, like the stream function ψ, remains constant along the meridional streamlines. Thus, as might be expected, the stagnation pressure p_o is conserved along the meridional streamlines. Now the third momentum equation (6.22), introducing the vorticity definitions for ω_x and ω_r from Eqns (6.11), may be expressed in similar format, namely

or

$$\left.\begin{aligned} c_x \frac{\partial rc_\theta}{\partial x} + c_r \frac{\partial rc_\theta}{\partial r} &= 0 \\[2mm] \hat{q} \cdot \mathrm{grad}\,(rc_\theta) &= 0 \end{aligned}\right\} \tag{6.24}$$

Thus we see that angular momentum rc_θ is also proven to be conserved along the meridional streamlines. These conservation laws may be summarised as follows:

$$\left.\begin{aligned} c_\theta r &= f_1(\psi) \\ p_o &= f_2(\psi) \end{aligned}\right\} \tag{6.25}$$

and the quantities p_o and $c_\theta r$ are unique functions of ψ.

6.3.4 Auxiliary equation for ω_θ

We may now bring together all of these analytical/physical results to obtain an auxiliary equation linking p_o and $c_\theta r$ to the tangential vorticity ω_θ. Thus since $p_o = f_2(\psi)$, Eqn (6.25), while $\psi = f(x,r)$ (Section 6.3), the total derivative of p_o with respect to ψ may be expressed as

$$\frac{1}{\rho}\frac{\mathrm{d}p_o}{\mathrm{d}\psi} = \frac{1}{\rho}\frac{\partial p_o}{\partial x}\frac{\mathrm{d}x}{\mathrm{d}\psi} + \frac{1}{\rho}\frac{\partial p_o}{\partial r}\frac{\mathrm{d}r}{\mathrm{d}\psi}$$

Introducing Eqns (6.22a) and (6.22b), this becomes

$$\frac{1}{\rho}\frac{\mathrm{d}p_o}{\mathrm{d}\psi} = \omega_\theta \left(c_r \frac{\mathrm{d}x}{\mathrm{d}\psi} - c_x \frac{\mathrm{d}r}{\mathrm{d}\psi} \right) + c_\theta \left(\omega_x \frac{\mathrm{d}r}{\mathrm{d}\psi} - \omega_r \frac{\mathrm{d}x}{\mathrm{d}\psi} \right) \tag{6.26}$$

However, from Eqn (6.17) the first bracketed expression on the right-hand side reduces to $-1/r$. The second bracketed expression on the right-hand side may also be simplified if we use Eqn (6.25a) to obtain the total derivative of $c_\theta r$ with respect to ψ, namely

$$\frac{\mathrm{d}c_\theta r}{\mathrm{d}\psi} = \frac{\partial c_\theta r}{\partial x}\frac{\mathrm{d}x}{\mathrm{d}\psi} + \frac{\partial c_\theta r}{\partial r}\frac{\mathrm{d}r}{\mathrm{d}\psi}$$

and from the definitions of vorticity, Eqns (6.11a) and (6.11b),

$$\frac{\mathrm{d}c_\theta r}{\mathrm{d}\psi} = r \left\{ -\omega_r \frac{\mathrm{d}x}{\mathrm{d}\psi} + \omega_x \frac{\mathrm{d}r}{\mathrm{d}\psi} \right\}$$

Introducing these results into Eqn (6.26) and rearranging, we have finally an auxiliary equation for ω_θ as follows:

$$\omega_\theta = c_\theta \frac{\mathrm{d}(c_\theta r)}{\mathrm{d}\psi} - \frac{r}{\rho}\frac{\mathrm{d}p_o}{\mathrm{d}\psi} \tag{6.27}$$

The tangential vorticity ω_θ has thus been found to depend entirely upon the distributions of the two key physical design quantities $(c_\theta r)$, the angular momentum and p_o, or the stagnation pressure. These are independently conserved along streamlines as proved in Section 6.3.3 for the annular regions between blade rows. The levels of $c_\theta r$ and p_o may of course be changed at a blade row as determined by the Euler pump or Euler turbine equations (1.9) and (1.10), Chapter 1. The actual vorticity ω_θ thus created, however, will depend only upon the gradient of $c_\theta r$ or p_o across the meridional streamlines $\mathrm{d}(c_\theta r)/\mathrm{d}\psi$ and $\mathrm{d}p_o/\mathrm{d}\psi$. For the classic free-vortex case as discussed in Section 5.1, Eqn (6.27) reduces to

$$\left.\begin{array}{c} c_\theta r = \text{constant} \\ p_o = \text{constant} \end{array}\right\} \text{ free-vortex flow } \left.\begin{array}{c} \\ \\ \\ \\ \end{array}\right\} \tag{6.28}$$

and hence $\quad\quad\quad \omega_\theta = 0$

Thus for free-vortex turbomachines the governing equation reduces to

$$\frac{\partial^2\psi}{\partial x^2} - \frac{1}{r}\frac{\partial\psi}{\partial r} + \frac{\partial^2\psi}{\partial r^2} = 0 \tag{6.29}$$

In all other cases the meridional flow for incompressible turbomachines is described by the combined governing and auxiliary equation (6.21) and (6.27), namely

$$\frac{\partial^2\psi}{\partial x^2} - \frac{1}{r}\frac{\partial\psi}{\partial r} + \frac{\partial^2\psi}{\partial r^2} = -\omega_\theta r = -c_\theta r\frac{\mathrm{d}(c_\theta r)}{\mathrm{d}\psi} + \frac{r^2}{\rho}\frac{\mathrm{d}p_o}{\mathrm{d}\psi} \tag{6.30}$$

6.4 Streamwise and smoke-ring vorticity

As revealed by Eqn (6.27) the tangential vorticity ω_θ has two independent components, one produced by gradients of angular momentum $\mathrm{d}(c_\theta r)/\mathrm{d}\psi$ and the other by gradients of stagnation pressure $\mathrm{d}p_o/\mathrm{d}\psi$. These have quite different physical origins which are illustrated in Fig. 6.6 and consequently have completely different properties which lead to their respective titles *streamwise* and *smoke-ring* vorticities. Let us deal with these in turn.

6.4.1 Streamwise vorticity – constant stagnation pressure flows

For constant stagnation pressure flows the equations of motion (6.22) reduce to

$$\frac{\omega_x}{c_x} = \frac{\omega_r}{c_r} = \frac{\omega_\theta}{c_\theta} = \frac{\hat{\omega}}{\hat{c}} \tag{6.31}$$

Blade bound Vortex Γ

Meridional streamline ψ_1

Shed streamwise
vorticity γ_{shed}

δA
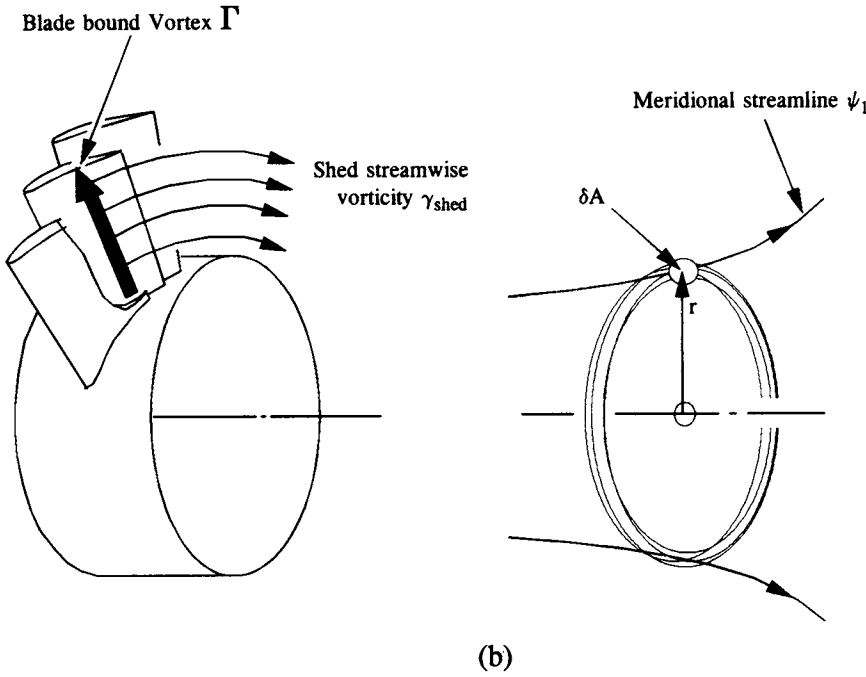
r

(a)   (b)

Fig. 6.6 Streamwise and smoke-ring vorticity in turbomachine meridional flows: (a) streamwise vorticity shed from a turbomachine blade; (b) smoke-ring vorticity due to presence of grad p_0

In this case the local vorticity vector $\hat{\omega}$ lies parallel to the velocity vector $\hat{c}$, a condition which can be defined as 'streamwise vorticity'. By analogy with the trailing vortex systems downstream of an aircraft wing, a vortex sheet γ_{shed} will be shed from the trailing edge of a non-free-vortex turbomachine blade, Fig. 6.6(a), which will spiral downstream following the swirling flow created by the blade row. For this situation the tangential vorticity, Eqn (6.27), reduces to

$$\omega_\theta = c_\theta \frac{d(c_\theta r)}{d\psi} \tag{6.32}$$

where ω_θ is the tangential component of the shed vortex sheet γ_{shed}, which is assumed to be smeared circumferentially across the blade pitch as a distributed swirling vorticity $\hat{\omega}$.

Bearing in mind that $c_\theta r = f_1(\psi)$ as previously proved, Eqn (6.25a), the streamwise vorticity equation (6.32) becomes

$$\omega_\theta = \frac{1}{r} f_1(\psi) \frac{df_1(\psi)}{d\psi} = \frac{1}{r} F_1(\psi) \tag{6.33}$$

where $F_1(\psi)$ is a function of ψ. This equation shows that the tangential component of streamwise vorticity in turbomachines obeys the convection law $\omega_\theta r = F_1(\psi)$ and is thus constant along a given meridional streamline ψ. Thus if the streamline radius changes, as in mixed-flow machines, ω_θ will also change in strength inversely with radius.

6.4.2   Smoke-ring vorticity – free-vortex or non-swirling flows

If either $c_\theta = 0$ or $c_\theta r$ = constant, the streamwise vorticity is zero and the first term of Eqn (6.27) vanishes, reducing the tangential vorticity to

$$\omega_\theta = -\frac{r}{\rho}\frac{dp_o}{d\psi} \qquad (6.34)$$

Recalling the conservation law for stagnation pressure from Eqn (6.25b), namely that $p_o = f_2(\psi)$, the above equation becomes

$$\omega_\theta = -\frac{r}{\rho}\frac{df_2(\psi)}{d\psi} = -rF_2(\psi) \qquad (6.35)$$

where $F_2(\psi)$ is a function of ψ. In this case the tangential vorticity obeys a quite different convection law, namely that $\omega_\theta/r = -F(\psi)$, and is thus constant along a given meridional streamline ψ. From the definitions of vorticity components, Eqn (6.11), it is clear that ω_x and ω_r are both zero for the flows presently under consideration. As the only vorticity component present in the fluid, ω_θ takes the form of smoke-ring vorticity concentric with the x-axis as illustrated in Fig. 6.6(b).

   As a check upon Eqn (6.35) we can apply the circulation theorem of Kelvin, devised in 1869, to this elementary smoke-ring vortex tube of cross-sectional area δA. As proved by Kelvin the circulation around the perimeter of δA, $\oint q \cdot ds$, which is defined as the strength of the vortex tube, remains constant as it convects with the fluid. As previously proved by Helmholtz in 1858, the strength of a vortex tube also equals the total vorticity flux through its cross-sectional area, in this case $\omega_\theta \delta A$. Thus by Kelvin's theorem

$$\omega_\theta \delta A = \text{constant} \qquad (6.36)$$

These laws apply only to a control mass that contains the same fluid making up an actual vortex tube. Thus we can also state for incompressible flow that the vortex tube volume remains constant, namely

$$2\pi r \delta A = \text{constant} \qquad (6.37)$$

Dividing Eqns (6.36) by (6.37) it follows that ω_θ/r = constant along the drift path ψ_1 of the vortex tube in agreement with Eqn (6.35).

6.4.3   Axisymmetric flows involving a mixture of both streamwise and smoke-ring type vorticity components

In general, gradients of both $c_\theta r$ and p_o will be present in turbomachines and the associated complex vortex motion will comprise both streamwise and smoke-ring type vorticities. The governing equations for the general turbomachine will then reduce to

$$\frac{\partial\psi^2}{\partial x^2} - \frac{1}{r}\frac{\partial\psi}{\partial r} + \frac{\partial^2\psi}{\partial r^2} = F_1(\psi) + r^2 F_2(\psi) \qquad (6.38)$$
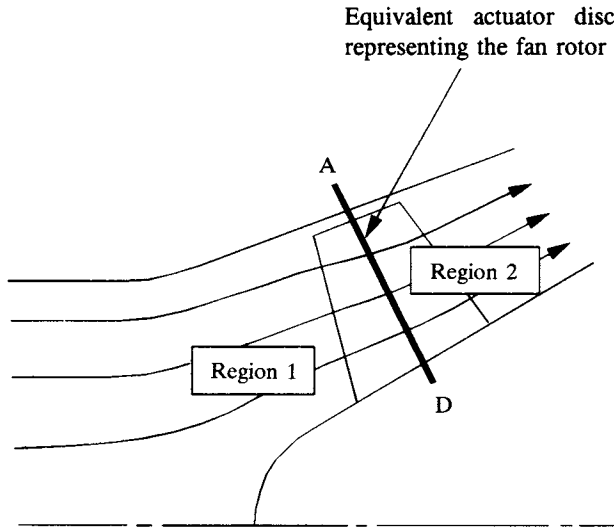
Equivalent actuator disc
representing the fan rotor

Fig. 6.7 Representation of a mixed-flow fan rotor by an equivalent actuator disc

where

$$F_1(\psi) = c_\theta r \frac{\mathrm{d}c_\theta r}{\mathrm{d}\psi}$$
$$F_2(\psi) = \frac{1}{\rho}\frac{\mathrm{d}p_\mathrm{o}}{\mathrm{d}\psi}$$

$$\left.\begin{array}{c} \\ \\ \end{array}\right\} \qquad (6.39)$$

Thus the solution of an incompressible meridional flow field via Eqn (6.38) is possible provided the functions $F_1(\psi)$ and $F_2(\psi)$ are fully determined. This is the case once $(c_\theta r)$ and p_o have been specified as functions of ψ.

6.4.4 Example of the mixed-flow fan

The foregoing equations were derived in the absence of distributed blade forces (see Section 6.3.3) and are thus only applicable in blade-free spaces. A suitable strategy for analysis of the mixed-flow fan illustrated in Fig. 6.1 would be to represent the blade row by an equivalent actuator disc, the blade lift forces being assumed to be concentrated in its plane AD, Fig. 6.7.

In region 1 upstream of the rotor the entry flow is irrotational so that $F_1(\psi)$ and $F_2(\psi)$ are both zero. In region 2 downstream of the rotor we have

$$F_1(\psi) = c_{\theta 2}r \frac{\mathrm{d}c_{\theta 2}r}{\mathrm{d}\psi} \,, \quad F_2 = \frac{1}{\rho}\frac{\mathrm{d}p_{\mathrm{o}2}}{\mathrm{d}\psi}$$

But the Euler pump equation (1.9b) for this situation, with zero pre-whirl, becomes

$$\frac{1}{\rho}(p_{\mathrm{o}2} - p_{\mathrm{o}1}) = \Omega r c_{\theta 2} \qquad [1.9\mathrm{b}]$$

ω_θ assumed to be convected along the cylindrical streamlines of the unperturbed flow (i.e. the meridional flow with the blades removed)
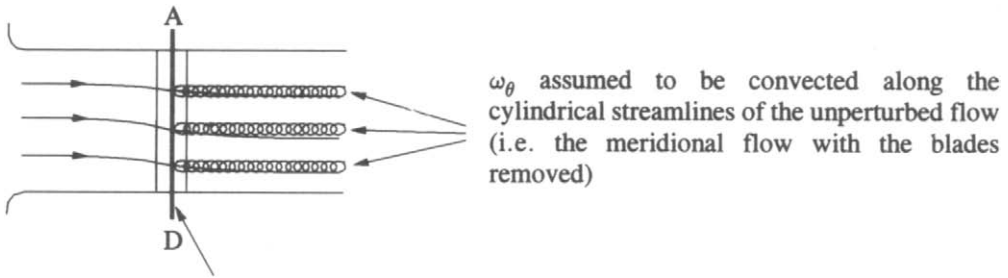
Equivalent actuator disc AD

Fig. 6.8 Physical assumption of linearised actuator disc theory

Thus finally the governing equation for the fan problem may be fully stated in terms of p_{o2} only through

$$\left.\begin{array}{l} \dfrac{\partial^2 \psi}{\partial r^2} - \dfrac{1}{r}\dfrac{\partial \psi}{\partial r} + \dfrac{\partial^2 \psi}{\partial r^2} = 0 \qquad\qquad\text{Region 1} \\[4mm] \qquad = \left(\dfrac{(p_{o2}-p_{o1})/\rho}{\Omega^2} + r^2 \right)\dfrac{1}{\rho}\dfrac{\mathrm{d}p_{o2}}{\mathrm{d}\psi} \quad\text{Region 2} \end{array}\right\} \qquad (6.40)$$

6.5 Analytical solution for linearised cylindrical actuator disc theory

Early in the history of meridional flow analyses exact solutions to Eqns (6.30) were obtained by Bragg and Hawthorne (1950) and these have been discussed in full by Horlock (1978) in his extensive text on actuator disc theory. These solutions formed a most important benchmark in this subject and the genesis of many of the physical concepts presented in this chapter. They were, however, restricted to certain classes of flow and were succeeded by more generally applicable linearised analyses such as that adopted in the last chapter. The aim in this section is to derive the cylindrical actuator disc solution from the governing equations (6.38) and (6.39) in linearised form for flow through a single blade row with the following assumptions:

(1) The blade row is represented by a plane actuator disc at which the vorticity ω_θ is created discontinuously.
(2) The vorticity ω_θ is assumed to be convected downstream of the actuator disc along the undisturbed streamlines.

The terms on the right-hand side of Eqn (6.38) being non-linear presented difficulties for numerical reduction in the 1950s and assumption (2) provided, in effect, a linearisation of those terms since the vorticity ω_θ could now be approximated as follows. From Eqn (6.38)

$$\left.\begin{array}{l} r\omega_\theta = F_1(\psi) + r^2 F_2(\psi) \\[2mm] \qquad \approx F_1(r) + r^2 F_2(r) \\[2mm] \qquad \approx F(r) \end{array}\right\} \qquad (6.41)$$

For the single blade row depicted in Fig. 6.8 the governing equation (6.36) simplifies to

$$\left. \begin{array}{ll} \dfrac{\partial^2 \psi}{\partial x^2} - \dfrac{1}{r}\dfrac{\partial \psi}{\partial r} + \dfrac{\partial^2 \psi}{\partial x^2} = -F(r) & \text{for } x > 0 \\[3mm] \qquad\qquad\qquad\quad = 0 & \text{for } x < 0 \end{array} \right\} \tag{6.42}$$

Since this equation is linear its solution can be compounded from three components:

$$\psi = \underset{\text{(a)}}{\Psi(r)} + \underset{\text{(b)}}{\psi'_\infty(r)} + \underset{\text{(c)}}{\psi'(x, r)} \tag{6.43}$$

where term (a) represents the uniform stream C_x at entry to the duct $x = -\infty$, (b) represents the radial equilibrium flow at exit $x = \infty$, and (c) is a smoothing function which merges the flow progressively between these two extremes. Equation (6.42) may now be replaced by three independent equations as follows:

$$-\frac{1}{r}\frac{\partial \Psi}{\partial r} + \frac{\partial^2 \Psi}{\partial r^2} = 0 \qquad\qquad \text{Uniform stream } -\infty < x < \infty \tag{6.44}$$

$$-\frac{1}{r}\frac{\partial \psi_\infty}{\partial r} + \frac{\partial^2 \psi_\infty}{\partial r^2} = -F(r) \qquad \begin{array}{l}\text{Radial equilibrium} \\ \text{perturbation for } x > 0\end{array} \tag{6.45}$$

$$\qquad\qquad\qquad\qquad = -\omega_\theta r$$

$$\frac{\partial^2 \psi'}{\partial x^2} - \frac{1}{r}\frac{\partial \psi'}{\partial r} + \frac{\partial^2 \psi'}{\partial r^2} = 0 \qquad \begin{array}{l}\text{Irrotational smoothing} \\ \text{perturbation for } -\infty < x < \infty\end{array} \tag{6.46}$$

Bearing in mind the definition of stream function, Eqn (6.16a), the first equation may be integrated once to yield

$$C_x = \frac{1}{r}\frac{\partial \Psi}{\partial r} = \text{constant} \tag{6.47}$$

The second equation (6.45) likewise may be integrated once to give the radial equilibrium velocity perturbation directly from the specified vorticity ω_θ:

$$c'_{x\infty} = \frac{1}{r}\frac{\partial \psi'_\infty}{\partial r} = -\int_{r_h}^{r_t} \omega_\theta \, dr + K \tag{6.48}$$

where the constant K is chosen such that the velocity perturbation $c'_{x\infty}$ provides no contribution to mass flow through the annulus, that is

$$\int_{r_h}^{r_t} \rho c'_{x\infty} 2\pi r \, dr = 0$$

or

$$K = \frac{2}{r_t^2 - r_h^2} \int_{r_h}^{r_t} r \int_{r_h}^{r} \omega_\theta \, dr \, dr \tag{6.49}$$

Thus solutions to Eqns (6.44) and (6.45) have been obtained explicitly in terms of the specified mean axial velocity C_x and tangential vorticity ω_θ respectively. The solution of Eqn (6.46) may be obtained by separation of variables, Hildebrand (1956), as an infinite series of the following form:

$$\psi' = r \sum_{n=1}^{\infty} A_n \{ J_1(k_n r) + \nu_n Y_1(k_n r) \} e^{\pm k_n x} \qquad (6.50)$$

where $J_1(k_n r)$ and $Y_1(k_n r)$ are Bessel functions of the first and second kind of first order and A_n, ν_n are arbitrary constants. The coefficients k_n are determined by specification of zero radial velocity perturbation c_r'. Thus from Eqn (6.16b)

$$c_r' = -\frac{1}{r} \frac{\partial \psi'}{\partial x} = -(\pm) \sum_{n=1}^{\infty} k_n A_n \{ J_1(k_n r) + \nu_n Y_1(k_n r) \} e^{(\pm) k_n x} = 0$$

Application of this at hub and tip radii r_h and r_t for the nth term results in

$$J_1(k_n r_h) + \nu_n Y_1(k_n r_h) = 0$$
$$J_1(k_n r_t) + \nu_n Y_1(k_n r_t) = 0$$

and eliminating ν_n we have

$$J_1(k_n r_h) Y_1(k_n r_t) - J_1(k_n r_t) Y_1(k_n r_h) = 0 \qquad (6.51)$$

Solutions of this equation for the coefficients k_n are given in Table 5.6, Section 5.4, for hub/tip ratios in the range $0.3 < r_h/r_t < 1.0$. The remaining boundary conditions to be satisfied are as follows.

(1) *Boundary conditions at entry and exit.* For the smoothing perturbation to vanish at $\pm\infty$ let us propose separate solutions upstream and downstream of the blade row with the appropriate sign convention as follows:

$$\psi_1' = r \sum_{n=1}^{\infty} A_{n1} \{ J_1(k_n r) + \nu_n Y_1(k_n r) \} e^{k_n x} \qquad x < 0$$

$$\psi_2' = r \sum_{n=1}^{\infty} A_{n2} \{ J_1(k_n r) + \nu_n Y_1(k_n r) \} e^{-k_n x} \qquad x > 0$$

$$(6.52)$$

(2) *Smooth matching of c_r' at $x = 0$.* In reality the vorticity ω_θ is shed progressively by the blades from leading edge to trailing edge. For mathematical simplicity, however, we will replace the blade row by a plane discontinuity at $x = 0$ or *actuator disc* at which ω_θ is shed discontinuously. However, although this implies that swirl velocities c_θ also change discontinuously at the actuator disc, the meridional velocity components c_x and c_r in the (x, r) plane develop smoothly over $-\infty < x < \infty$. This will be achieved if the two solutions, Eqns (6.52), are matched at the actuator disc. Since $c_r' = -(1/r)(\partial \psi / \partial x)$ we have

$$c'_{r1} = -\sum_{n=1}^{\infty} k_n A_{n1}\{J_1(k_n r) + \nu_n Y_1(k_n r)\}\, e^{k_n x} \qquad x \le 0$$

$$c'_{r2} = \sum_{n=1}^{\infty} k_n A_{n2}\{J_1(k_n r) + \nu_n Y_1(k_n r)\}\, e^{-k_n x} \qquad x \ge 0$$

Matching these two solutions at $x = 0$ we have

$$-\sum_{n=1}^{\infty} k_n A_{n1}\{J_1(k_n r) + \nu_n Y_1(k_n r)\} = \sum_{n=1}^{\infty} k_n A_{n2}\{J_1(k_n r) + \nu_n Y_1(k_n r)\}$$

This condition is satisfied if, term by term,

$$A_{n1} = -A_{n2} = A_n$$

whereupon we have finally the solution

$$\psi' = (\pm)r \sum_{n=1}^{\infty} A_n\{J_1(k_n r) + \nu_n Y_1(k_n r)\}\, e^{(\pm)k_n x} \tag{6.53}$$

with $(+)$ for $x < 0$ and $(-)$ for $x > 0$.

(3) *Smooth matching of c_x at $x = 0$.* The axial velocity c_x may now be expressed as

$$\left.\begin{aligned}
c_{x1} &= C_x + \sum_{n=1}^{\infty} A_n \frac{\partial}{\partial r}\{J_1(k_n r) + \nu_n Y_1(k_n r)\}\, e^{k_n x} && \text{for } x \le 0 \\[2mm]
c_{x2} &= C_x + c'_{x\infty} - \sum_{n=1}^{\infty} A_n \frac{\partial}{\partial r}\{J_1(k_n r) + \nu_n Y_1(k_n r)\}\, e^{-k_n x} && \text{for } x \ge 0
\end{aligned}\right\} \tag{6.54}$$

Thus matching the upstream and downstream axial velocity solutions at $x = 0$, by stating $c_{x1} = c_{x2}$, we have

$$\sum_{n=1}^{\infty} A_n\{J'_1(k_n r) + \nu_n Y'_1(k_n r)\} = \frac{1}{2} c'_{x\infty} \tag{6.55}$$

Since $c'_{x\infty}$ is a known function of radius once ω_θ is prescribed, Eqn (6.48), the coefficients A_n, ν_n may be derived by Fourier–Bessel analysis term by term.

6.5.1 Simplified actuator disc solution

To avoid the complexity of Fourier–Bessel analysis simple results follow if we assume that the first term of the Bessel series in Eqns (6.55) predominates. Neglecting all terms except $n = 1$ we could approximate Eqn (6.55) as

$$A_1\{J'_1(k_1 r) + \nu_1 Y'_1(k_1 r)\} \approx c'_{xd} = \tfrac{1}{2}c'_{x\infty}$$

and thus the solution for c_x, Eqns (6.54), reduces to the simple actuator disc formulation used in Chapter 5, Eqns (5.49) and (5.50):

$$
\left.
\begin{aligned}
c_x &= C_x + \tfrac{1}{2}c'_{x\infty}e^{k_1 x} && \text{for } x < 0 \\
&= C_x + c'_{x\infty}(1 - \tfrac{1}{2}e^{-k_1 x}) && \text{for } x > 0
\end{aligned}
\right\}
\tag{6.56}
$$

where the coefficient k_1 is related to the k values listed in Table 5.6 through $k_1 = k/(r_t - r_h)$.

6.6 Compressible flow actuator disc theory

The first attempt to extend actuator disc theory to compressible flows was published by Hawthorne and Ringrose (1963). This was followed by a broader-ranging paper by Lewis and Horlock (1969) which was mainly concerned with the influence upon meridional flows of blockage due to blade thickness, linking this to compressibility effects. Appendix 1 of the latter reference contains the basis of a compressible flow linearised actuator disc theory similar to that to be presented here. Let us begin with the continuity equation (6.14) for compressible flow and the consequent definition of Stokes' stream function:

$$
\left.
\begin{aligned}
c_x &= \frac{1}{\rho r}\frac{\partial \psi}{\partial r} \\[2mm]
c_r &= -\frac{1}{\rho r}\frac{\partial \psi}{\partial x}
\end{aligned}
\right\}
\tag{6.15}
$$

Introduction of these expressions into the tangential vorticity component ω_θ, Eqn (6.11), results in

$$
\begin{aligned}
\omega_\theta &= \frac{\partial c_r}{\partial x} - \frac{\partial c_x}{\partial r} \\[2mm]
&= -\frac{\partial}{\partial x}\left(\frac{1}{\rho r}\frac{\partial \psi}{\partial x}\right) - \frac{\partial}{\partial r}\left(\frac{1}{\rho r}\frac{\partial \psi}{\partial r}\right)
\end{aligned}
$$

Expanding the partial derivatives, this can be rearranged to read as follows:

$$
\frac{\partial^2 \psi}{\partial x^2} - \frac{1}{r}\frac{\partial \psi}{\partial r} + \frac{\partial^2 \psi}{\partial r^2} = -\rho r \omega_\theta - r c_r \frac{\partial \rho}{\partial x} + r c_x \frac{\partial \rho}{\partial r}
\tag{6.57}
$$

The strategy adopted here has been to separate the Stokes' operator onto the left-hand side of the equation and to consign all terms involving the density ρ to the right-hand side. These include the following:

(1) Disturbances due to the presence of tangential vorticity ω_θ (we note that these are now weighted by the density ρ for this case of compressible flow).
(2) Disturbances due to the density gradients $\partial \rho/\partial r$ and $\partial \rho/\partial x$. We will consider these in more detail in the next section.
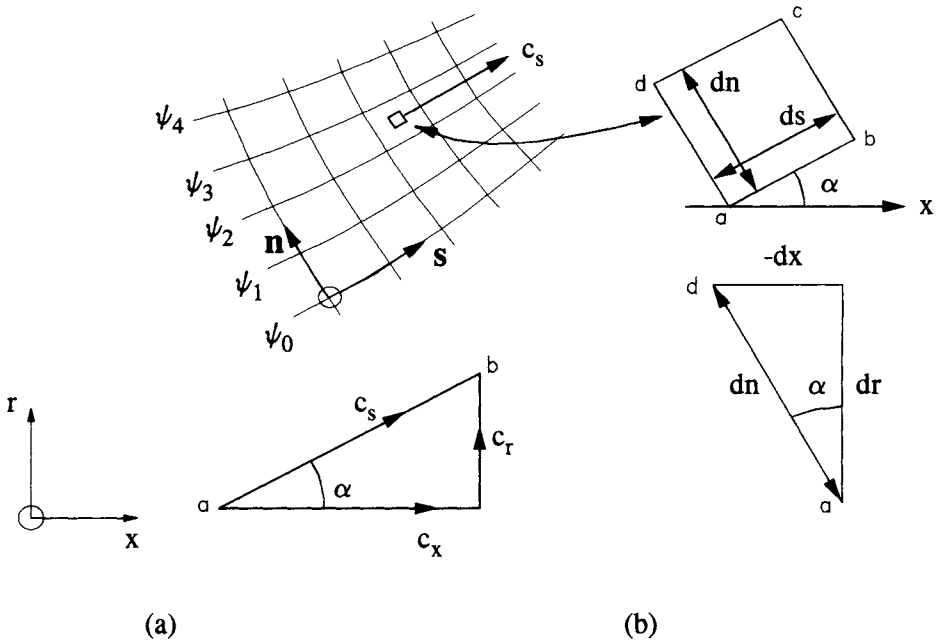
Fig. 6.9 Curvilinear grid (s,n) in the meridional plane – and small element abcd: (a) meridional velocity components; (b) resolution of elementary normal dn

6.6.1 Curvilinear coordinates (s, n) in meridional flow

A useful way forward at this point, leading to a better interpretation of the density gradient terms in Eqn (6.57), is to introduce the curvilinear coordinates (s,n) illustrated in Fig. 6.9 for general mixed-flow turbomachines. Coordinate s lies along the local meridional velocity vector c_s and is thus coincident with the contours ψ = constant which map out the meridional streamlines. Coordinate n is defined as normal to s thus creating a curvilinear (s,n) grid. Let us consider the small element abcd located at (s,n) where the meridional velocity c_s makes the angle α with the x-axis, Fig. 6.9(a). The side ad of the element is of length dn and is normal to c_s, Fig. 6.9(b). From these two triangles, we have the relationships

$$\left.\begin{array}{c} \cos\alpha = \dfrac{c_x}{c_s} = \dfrac{\mathrm{d}r}{\mathrm{d}n} \\[2mm] \sin\alpha = \dfrac{c_r}{c_s} = -\dfrac{\mathrm{d}x}{\mathrm{d}n} \end{array}\right\} \tag{6.58}$$

Now density will in general be a function of x and r, say $\rho = \rho(x,r)$, and a very useful result follows if we take its total derivative normal to the meridional streamlines dρ/dn. Thus

$$\frac{\mathrm{d}\rho}{\mathrm{d}n} = \frac{\partial\rho}{\partial x}\frac{\mathrm{d}x}{\mathrm{d}n} + \frac{\partial\rho}{\partial r}\frac{\mathrm{d}r}{\mathrm{d}n}$$

and introducing Eqns (6.58)

$$\frac{\mathrm{d}\rho}{\mathrm{d}n} = -\frac{c_r}{c_s}\frac{\partial\rho}{\partial x} + \frac{c_x}{c_s}\frac{\partial\rho}{\partial r}$$

Thus finally, the compressibility terms on the right-hand side of the governing equation (6.57) become

$$-c_r\frac{\partial\rho}{\partial x} + c_x\frac{\partial\rho}{\partial r} = c_s\frac{\mathrm{d}\rho}{\mathrm{d}n}$$

It is useful to note here that the operator $-c_r(\partial/\partial x) + c_x(\partial/\partial r)$ performs the differential of a quantity normal to the meridional streamlines $\mathrm{d}/\mathrm{d}n$ multiplied by the meridional velocity c_s. The governing equation (6.57) for compressible meridional flow now becomes

$$\frac{\partial^2\psi}{\partial x^2} - \frac{1}{r}\frac{\partial\psi}{\partial r} + \frac{\partial^2\psi}{\partial r^2} = -\rho r\omega_\theta + rc_s\frac{\mathrm{d}\rho}{\mathrm{d}n} \tag{6.59}$$

Another important result follows from a reconsideration of Eqn (6.17) for compressible flow. Thus

$$\mathrm{d}\psi = \frac{\partial\psi}{\partial x}\mathrm{d}x + \frac{\partial\psi}{\partial r}\mathrm{d}r$$
$$= -\rho r c_r\mathrm{d}x + \rho r c_x\mathrm{d}r$$

Introducing Eqns (6.58) this transforms into

$$\mathrm{d}\psi = \rho r c_s(-\mathrm{d}x\sin\alpha + \mathrm{d}r\cos\alpha)$$
$$= \rho r c_s(\mathrm{d}n\sin^2\alpha + \mathrm{d}n\cos^2\alpha) = \rho r c_s\,\mathrm{d}n$$

Thus finally the meridional velocity c_s is given by

$$c_s = \frac{1}{\rho r}\frac{\mathrm{d}\psi}{\mathrm{d}n} \tag{6.60}$$

For numerical computation Eqn (6.59) could be rewritten more conveniently

$$\frac{\partial^2\psi}{\partial x^2} - \frac{1}{r}\frac{\partial\psi}{\partial r} + \frac{\partial^2\psi}{\partial r^2} = -\rho r\omega_\theta + \frac{\mathrm{d}\psi}{\mathrm{d}n}\frac{1}{\rho}\frac{\mathrm{d}\rho}{\mathrm{d}n} \tag{6.61}$$

A full numerical analysis would thus require an iterative process such as that illustrated in Fig. 6.10. Alternatively for cylindrical annuli we could make the linearising assumption that the compressible term in Eqn (6.59) may be approximated to

$$r c_s\frac{\mathrm{d}\rho}{\mathrm{d}n} \approx r C_x\frac{\mathrm{d}\rho}{\mathrm{d}r} \tag{6.62}$$
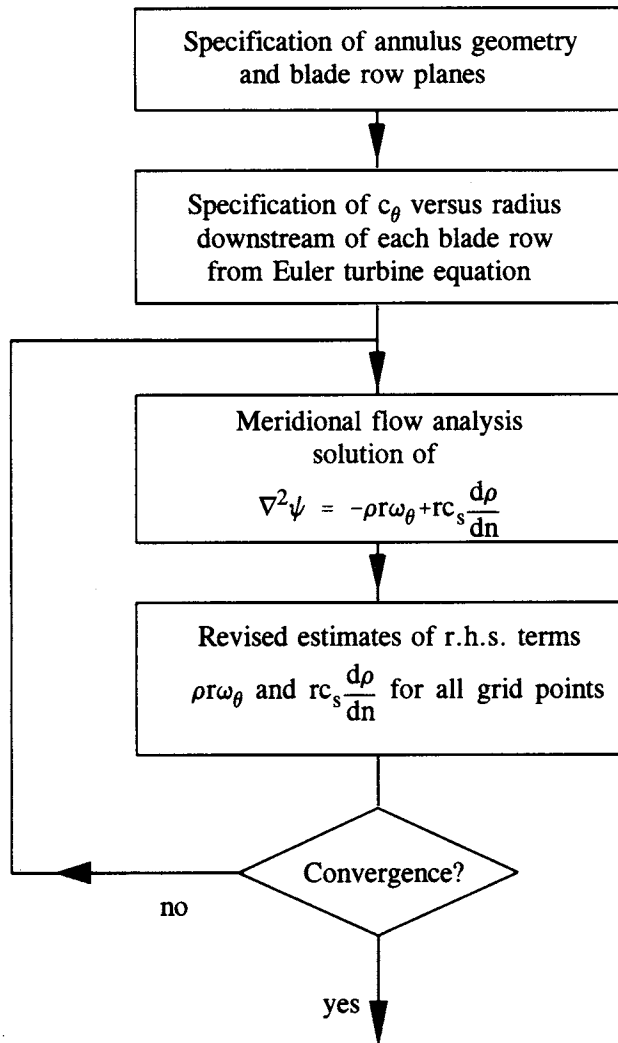
Fig. 6.10 Flow diagram for turbomachinery compressible meridional flow analysis

Inherent in this is the assumption that ρ is a function of radius only and thus the governing equation (6.59) approximates to

$$\frac{\partial^2 \psi}{\partial r^2} - \frac{1}{r}\frac{\partial \psi}{\partial r} + \frac{\partial^2 \psi}{\partial x^2} \approx -\rho r \omega_\theta + rC_x\frac{\mathrm{d}\rho}{\mathrm{d}r} \qquad (6.63)$$

$$= F_1(r) + F_2(r)$$

where $F_1(r)$ covers the rotational meridional flow disturbances leading to the actuator disc solution via Eqns (6.42) through to (6.55), and $F_2(r)$ covers the compressible flow disturbances. Since both are functions of radius only we would expect to be able to adopt the actuator disc solution equations (6.55) directly to handle the compres-

sible flow problem. Although this is possible, a more direct analysis, offering also deeper perception of the physical nature of compressible flows, follows from adoption of the velocity potential instead of the stream function. This will be introduced in the next section.

6.6.2   Analogy between compressible flows and incompressible flows with source distributions

The continuity equation in vector form has already been stated as follows:

$$\left. \begin{array}{ll} \operatorname{div} \rho \hat{q} = 0 & \text{Compressible flow} \\ \operatorname{div} \hat{q} = 0 & \text{Incompressible flow} \end{array} \right\} \qquad [6.4]$$

The equation for incompressible flow may be further developed to accommodate spatial distributions of source strength S, defined as fluid created at any point per unit volume per unit time. Equation (6.4b) then becomes

$$\operatorname{div} \hat{q} = S \qquad (6.64)$$

An analogy with compressible flow follows if the vector derivative of Eqn (6.4a) is expanded, namely

$$\operatorname{div} \rho \hat{q} = \rho \operatorname{div} \hat{q} + \hat{q} \cdot \operatorname{grad} \rho = 0$$

Rearranging this, the compressible flow continuity equation may be expressed as

$$\begin{aligned} \operatorname{div} \hat{q} &= -\frac{1}{\rho} \hat{q} \cdot \operatorname{grad} \rho \\ &= \sigma \end{aligned} \qquad (6.65)$$

The quantity on the right-hand side, $-(1/\rho)\hat{q} \cdot \operatorname{grad} \rho$, which absorbs all of the compressibility effects could be treated analytically as an equivalent distributed source density σ in incompressible flow; thus Eqns (6.64) and (6.65) are identical in form. In the one case the Poisson term S is due to distributed source strength. In the other case the Poisson term σ is caused by local gradients of fluid density.

Let us now apply this idea to the free-vortex turbine stator illustrated in Fig. 6.11(a), modelled by an actuator disc AD. In this *free-vortex* case the flow is irrotational and there is no tangential vorticity ω_θ shed from the blade row. Instead the fluid is assumed to undergo a sudden drop in density in the plane of the actuator disc, or in other words a sudden rise in specific volume. As shown by Lewis and Horlock (1969) this is physically analogous to the incompressible flow through a source actuator disc, Fig. 6.11(b), the streamline shifts and velocity distributions being the same. These authors have presented a full exposition, the main outline of which will be given here. Since ω_θ is to be zero, Eqn (6.11c) becomes

$$\omega_\theta = \frac{\partial c_r}{\partial x} - \frac{\partial c_x}{\partial r} = 0$$
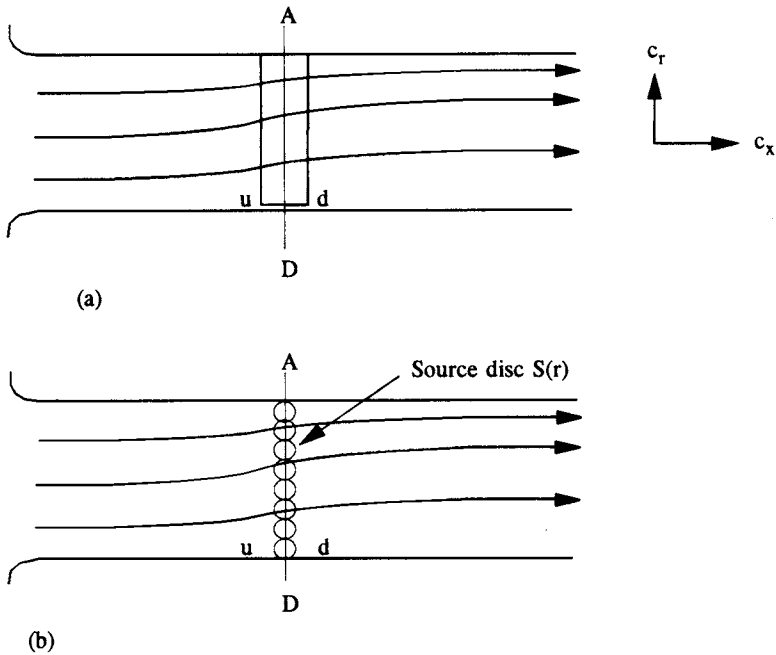
Fig. 6.11 Analogy between (a) compressible irrotational meridional flow through an axial turbine free-vortex stator and (b) flow through an equivalent source actuator disc AD

which implies the existence of the velocity potential function $\phi(x,r)$ such that

$$c_x = \frac{\partial \phi}{\partial x} \quad \text{and} \quad c_r = \frac{\partial \phi}{\partial r} \tag{6.66}$$

The continuity equation (6.65) then becomes

$$\operatorname{div} \operatorname{grad} \phi = \sigma = -\frac{1}{\rho} \hat{q} \cdot \operatorname{grad} \rho$$

or for axisymmetric flow

$$\frac{\partial^2 \phi}{\partial x^2} + \frac{1}{r} \frac{\partial \phi}{\partial r} + \frac{\partial^2 \phi}{\partial r^2} = -\frac{c_x}{\rho} \frac{\partial \rho}{\partial x} - \frac{c_r}{\rho} \frac{\partial \rho}{\partial r}$$

$$= -\frac{c_s}{\rho} \frac{\mathrm{d}\rho}{\mathrm{d}s} \equiv S(x,r) \tag{6.67}$$

where use has been made of Fig. 6.9 to establish the operator on the right-hand side, $c_s(\mathrm{d}\rho/\mathrm{d}s) = c_x(\partial\rho/\partial x) + c_r(\partial\rho/\partial r)$. $S(x,r)$ is the distributed source strength of the equivalent incompressible flow. The physical meaning of this is that the compressible flow disturbances are caused when the density changes along the direction of the meridional velocity c_s. For a turbine $\mathrm{d}\rho/\mathrm{d}s$ will assume large values due to flow acceleration within the blade row. Elsewhere upstream and downstream of the stator

under consideration, Fig. 6.11(a), $c_s(\mathrm{d}\rho/\mathrm{d}s)$ is likely to be negligible by comparison. It is thus plausible to replace the blade row by a source actuator disc $S(r)$ as illustrated in Fig. 6.11(b) in which the source strength generated within the blade row is assumed to be created instantaneously. For all values of x except $x = x_{\mathrm{AD}}$, Eqn (6.67) then reduces to

$$\frac{\partial^2 \phi}{\partial x^2} + \frac{1}{r}\frac{\partial \phi}{\partial r} + \frac{\partial^2 \phi}{\partial r^2} = 0 \tag{6.68}$$

As shown by Lewis and Horlock (1969) the general source distribution $S(r)$ may be expanded as the Bessel series

$$S(r) = S_{\mathrm{m}} - 2\sum_{n=1}^{\infty} a_n k_n \{J_0(k_n r) + \nu_n Y_0(k_n r)\}$$

$$= S_{\mathrm{m}} - 2\sum_{n=1}^{\infty} a_n k_n Z_0(k_n r) \tag{6.69}$$

where $Z_0(k_n r)$ is a combination of Bessel functions of zero order of the first and second kind and S_{m} is the mean disc source strength defined by

$$S_{\mathrm{m}} = \frac{2\displaystyle\int_{r_{\mathrm{h}}}^{r_{\mathrm{t}}} S(r) r\,\mathrm{d}r}{r_{\mathrm{t}}^2 - r_{\mathrm{h}}^2} \tag{6.70}$$

For the time being let us consider the flow field induced by the disc source alone in the absence of net throughflow as illustrated by Fig. 6.12. The general solution of Eqn (6.68) for a disc source $S(r)$ located at $x = 0$ is then as follows:

$$\left. \begin{aligned}
\phi &= (\pm)x\tfrac{1}{2}S_{\mathrm{m}} + \sum_{n=1}^{\infty} a_n Z_0(k_n r)\,\mathrm{e}^{-(\pm)k_n x} \\[2mm]
c_x' &= (\pm)\tfrac{1}{2}S_{\mathrm{m}} - (\pm)\sum_{n=1}^{\infty} a_n k_n Z_0(k_n r)\,\mathrm{e}^{-(\pm)k_n x} \\[2mm]
c_r' &= -\sum_{n=1}^{\infty} a_n k_n Z_1(k_n r)\,\mathrm{e}^{-(\pm)k_n x}
\end{aligned} \right\} \tag{6.71}$$

with the sign convention $(+)$ for $x > 0$, $(-)$ for $x < 0$. The coefficients a_n follow directly from Fourier–Bessel analysis, namely

$$a_n = \frac{\displaystyle\int_{r_{\mathrm{h}}}^{r_{\mathrm{t}}} rS(r) Z_0(k_n r)\,\mathrm{d}r}{k_n\{[r_{\mathrm{h}} Z_0(k_n r_{\mathrm{h}})]^2 - [r_{\mathrm{t}} Z_0(k_n r_{\mathrm{t}})]^2\}} \tag{6.72}$$
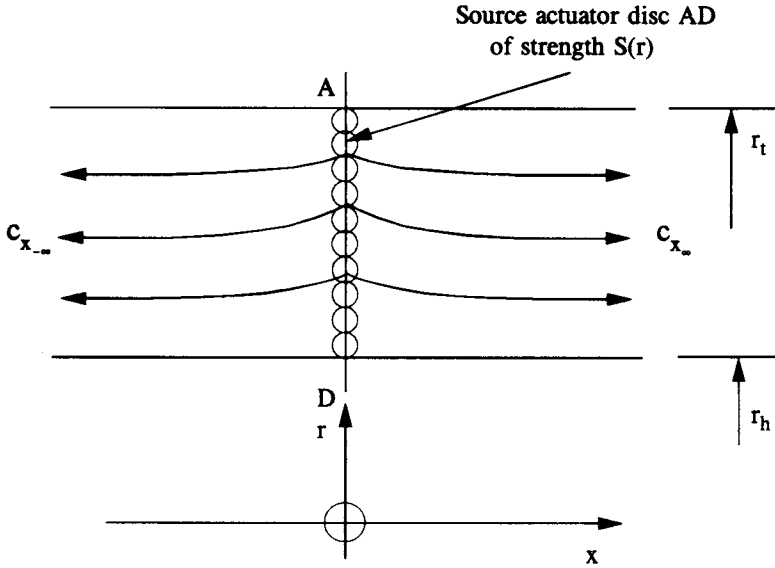
Source actuator disc AD
of strength S(r)

Fig. 6.12 Flow generated by a source disc of non-uniform strength $S(r)$ in a cylindrical annulus

A simple approximate solution can be derived with assumptions analogous to vortex actuator disc analysis. If for example the first eigenvalue only of the Bessel series is present, the velocity perturbations close to the actuator disc with $x > 0$ but $x \rightarrow 0$ are

$$c'_{xd} = \tfrac{1}{2}S_m - a_1 k_1 Z_0(k_1 r) = \tfrac{1}{2}S(r)$$

$$c'_{rd} = -a_1 k_1 Z_1(k_1 r) = \frac{1}{2k_1} \frac{dS(r)}{dr} \qquad (6.73)$$

Elsewhere in the duct we then have

$$\left. \begin{aligned} c'_x &= (\pm)\tfrac{1}{2}S_m - (\pm)(c'_{xd} - \tfrac{1}{2}S_m)\,e^{-(\pm)k_1 x} = (\pm)\tfrac{1}{2}[S_m + (S(r) - S_m)\,e^{-(\pm)k_1 x}] \\ c'_r &= c'_{rd}\,e^{-(\pm)k_1 x} = \frac{1}{2k_1}\frac{dS(r)}{dr}\,e^{-(\pm)k_1 x} \end{aligned} \right\} \qquad (6.74)$$

6.6.3 Solution for compressible flow through a turbomachine actuator disc

So far the only influence introduced into the flow field is the source disc $S(r)$. Equation (6.71) shows that this emits a net flux $S_m \pi (r_t^2 - r_h^2)$ and Eqn (6.74) shows that this leaves the duct at $\pm\infty$ with a uniform velocity $c_{x\pm\infty} = (\pm)\tfrac{1}{2}S_m$. To simulate compressible flow through a turbomachine blade row let us first superimpose a uniform stream C_x. The axial velocity distribution combining both $S(r)$ and C_x then becomes

$$\left. \begin{aligned} c_x &= C_x - \tfrac{1}{2}S_m - \tfrac{1}{2}(S(r) - S_m)\,e^{k_1 x} && \text{for } x < 0 \\ c_x &= C_x + \tfrac{1}{2}S_m + \tfrac{1}{2}(S(r) - S_m)\,e^{-k_1 x} && \text{for } x > 0 \end{aligned} \right\} \qquad (6.75)$$
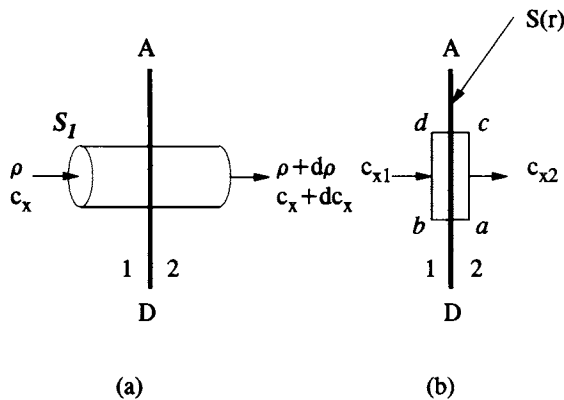
Fig. 6.13 Flow through streamtube with sudden change in density ρ and axial velocity C_x across a compressible flow actuator disc AD: (a) streamtube through compressible actuator disc; (b) equivalent source disc

where the duct entry and exit velocities are thus

$$\left.\begin{array}{ll} C_{x1} = C_x - \frac{1}{2}S_m & \text{at } x = -\infty \\ C_{x2} = C_x + \frac{1}{2}S_m & \text{at } x = +\infty \end{array}\right\} \tag{6.76}$$

We need now to relate the source strength $S(r)$ of the incompressible flow so far considered to the density change across the actuator disc in the equivalent compressible flow problem. For the stream tube S_1 crossing the actuator disc plane AD, Fig. 6.13(a), both ρ and c_x will change discontinuously at x_{AD} but the mass flow per unit area ρc_x will be conserved. Thus in crossing the plane AD

$$\text{d}(\rho c_x) = \rho\text{d}c_x + c_x\,\text{d}\rho = 0$$

For finite changes in density $\Delta\rho$ across the actuator disc the jump in axial velocity Δc_x may be approximated by

$$\Delta c_x \approx - C_x \frac{\Delta\rho}{\rho_m} \approx \frac{1}{2}(C_{x1} + C_{x2}) \frac{\rho_1 - \rho_2}{\frac{1}{2}(\rho_1 + \rho_2)} \tag{6.77}$$

ρ_m is the average of upstream and downstream densities ρ_1 and ρ_2 at radius r. C_{x1} and C_{x2} are the mean velocities upstream and downstream, already related to S_m through Eqn (6.76). For the equivalent incompressible source disc of strength (Sr), chosen to produce the same axial velocity jump Δc_x the continuity equation may be applied to the small control volume abcd, Fig. 6.13(b), namely

Rate of creation of fluid internally = volume flow across boundary abcd

or

$$S(r) = \Delta c_x \approx \frac{1}{2}(C_{x1} + C_{x2})\frac{\rho_1 - \rho_2}{\rho_m} \tag{6.78}$$

Now the mean axial velocities upstream and downstream can be related to one another by application of the mass flow continuity equation at $\pm\infty$, namely

$$\dot{m} = \int_{r_\mathrm{h}}^{r_\mathrm{t}} C_{x1}\rho_1 2\pi r\, \mathrm{d}r = \int_{r_\mathrm{h}}^{r_\mathrm{t}} C_{x2}\rho_2 2\pi r\, \mathrm{d}r \qquad (6.79)$$

For the single stator blade row under consideration here, ρ_1 is constant and the above equation thus yields the ratio C_{x2}/C_{x1}:

$$\frac{C_{x2}}{C_{x1}} = \frac{\displaystyle\int_{r_\mathrm{h}}^{r_\mathrm{t}} \rho_1 r\, \mathrm{d}r}{\displaystyle\int_{r_\mathrm{h}}^{r_\mathrm{t}} \rho_2 r\, \mathrm{d}r}$$

$$= \frac{\rho_1(r_\mathrm{t}^2 - r_\mathrm{h}^2)}{2\displaystyle\int_{r_\mathrm{h}}^{r_\mathrm{t}} \rho_2 r\, \mathrm{d}r} \quad \text{(if } \rho_1 = \text{constant as for case of a single stator)} \quad (6.80)$$

The previous solution for incompressible flow through a source disc, Eqn (6.75), now transforms to that for compressible flow:

$$c_x = C_{x1} + \frac{(\rho_2 C_{x2} - \rho_1 C_{x1})}{\rho_\mathrm{m}} \frac{1}{2} e^{k_1 x} \quad \text{for } x < 0$$

$$c_x = C_{x2} - \frac{(\rho_2 C_{x2} - \rho_1 C_{x1})}{\rho_\mathrm{m}} \frac{1}{2} e^{-k_1 x} \quad \text{for } x > 0 \qquad (6.81)$$

The original actuator disc analysis due to Hawthorne and Ringrose (1963) resulted in the following alternative solution including extra terms involving the axial Mach numbers M_{x1} and M_{x2}:

$$c_x = C_{x1} + \frac{(\rho_2 C_{x2} - \rho_1 C_{x1})(1 - M_{x1}^2)^{1/2}}{(1 - M_{x1}^2)^{1/2}\rho_1 + (1 - M_{x2}^2)^{1/2}\rho_2} e^{k_1 x/(1 - M_{x1}^2)^{1/2}} \quad \text{for } x < 0$$

$$c_x = C_{x2} - \frac{(\rho_2 C_{x2} - \rho_1 C_{x1})(1 - M_{x2}^2)^{1/2}}{(1 - M_{x1}^2)^{1/2}\rho_1 + (1 - M_{x2}^2)^{1/2}\rho_2} e^{-k_1 x/(1 - M_{x2}^2)^{1/2}} \quad \text{for } x > 0 \qquad (6.82)$$

For small axial Mach numbers the terms $(1 - M_{x1}^2)$ and $(1 - M_{x2}^2)$ approximate to unity and the two solutions are then identical, justifying the simpler formulation given by Eqn (6.81).

Example 6.1

The main features of such flows are illustrated by Figs 6.14 and 6.15 for the stator belonging to a turbine stage with the overall specification shown in Table 6.1.

Table 6.1 Specification for model turbine stage

Hub/tip ratio r_h/r_t $= 0.6$
At r.m.s. radius:
    Flow coefficient ϕ_m $= 0.5$
    Work coefficient ψ_m $= 1.0$
Exit Mach no. at r_h, M_{2h} $= 1.0$
Total to total efficiency η_{TT} $= 92\%$
Zero swirl upstream of stator
Free-vortex swirl distribution downstream of stator
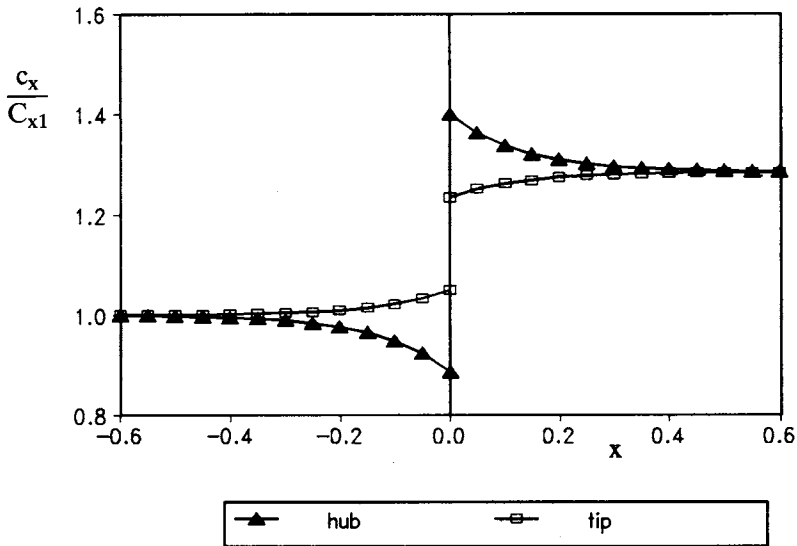Perfect gas assumed with the properties of air

Fig. 6.14 Growth of axial velocity at hub and tip radii of an axial turbine by compressible actuator disc theory

The development of the axial velocity expressed as c_x/C_{x1} at hub and tip radii are shown in Fig. 6.14 over the range $-0.6 < x < 0.6$. The following features are worthy of note:

(1) Due to the overall decrease in gas density the mean axial velocity increases overall by the ratio $C_{x2}/C_{x1} = 1.2853$.
(2) Since the local gas density drop $(\rho_1 - \rho_2)$ is greater at the hub than at the tip, the consequent axial velocity jump Δc_x across the actuator disc is likewise greater.
(3) In view of (2), c_x/C_{x1} at the hub and tip radii follow the pattern shown in Fig. 6.14 upstream and downstream of the blade row.

The consequent axial velocity profiles from hub to tip are shown in Fig. 6.15, limited here to the annulus entry and exit planes $x = \pm 1.0$ and the planes just upstream and downstream of the actuator disc at $x = 0$. The radial variation of density
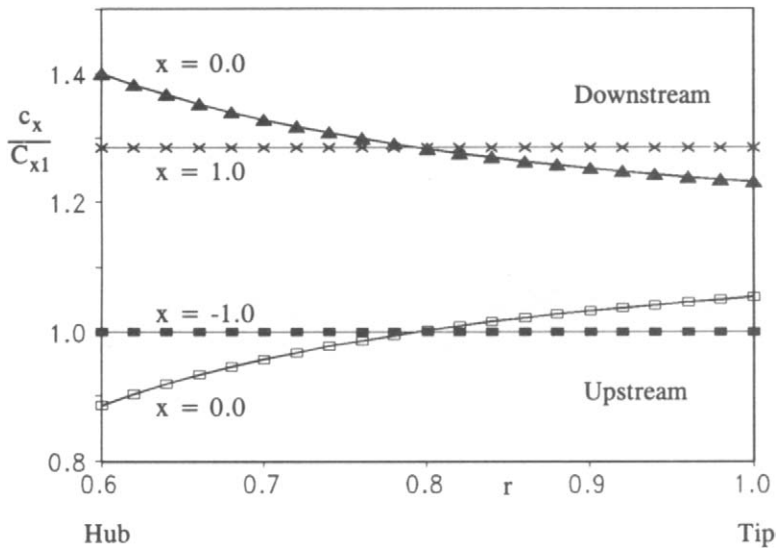
Fig. 6.15 Axial velocity profile development through an axial turbine stator predicted by compressible actuator disc theory

$\rho_2(r)$ is thus responsible for maximum axial velocity disturbances as great as 10% close to the blade row. For this stator, which is typical of practical gas or steam turbine stage loadings, there are thus significant flow disturbances induced by the large density gradients as the gas expands through the blade row. These result in large increases of c_x in the axial direction and also smaller but significant variations of c_x in the radial direction. On the other hand, in practice the cylindrical annulus assumed here, Fig. 6.11, would be replaced by a conical expanding annulus chosen to maintain constant mean axial velocity C_x, thus requiring an annulus area ratio for the blade row of $A_2/A_1 = C_{x2}/C_{x1}$.

Analysis to determine ρ_2/ρ_1
To complete the above computations it is necessary to evaluate ρ_2/ρ_1 in terms of the specified data. To begin with, ρ_2/ρ_1 may be related to T_2/T_1 following Example 3.1 of Chapter 3:

$$\frac{\rho_2}{\rho_1} = \frac{T_1}{T_2}\left\{1 - \frac{1}{\eta_{TT}}\left(1 - \frac{T_2}{T_1}\right)\right\}^{\gamma/(\gamma-1)} \tag{6.83}$$

T_1 and T_2 may also be related through the enthalpy drop across the stator at any radius r:

$$\Delta h = c_p(T_1 - T_2) = \tfrac{1}{2}(c_2^2 - c_1^2) = \frac{\psi^2 U^2}{2}$$

and thus

$$T_1 - T_2 = \frac{U^2 \psi^2}{2c_p} \tag{6.84}$$

Applying this equation at the hub radius r_h:

$$T_1 - T_{2h} = \frac{U_h^2 \psi_h^2}{2c_p} \tag{6.84a}$$

Dividing the last two equations results finally in

$$\frac{T_2}{T_1} = 1 - \left(1 - \frac{T_{2h}}{T_1}\right)\left(\frac{r_h}{r}\right)^2 \tag{6.85}$$

Now the exit temperature at the hub T_{2h} can be expressed in terms of the given Mach number M_{2h}. Thus

$$M_{2h} = \frac{c_{2h}}{a_{2h}} = \frac{c_{2h}}{\sqrt{\gamma R T_{2h}}}$$

where a_{2h} is the local speed of sound, or

$$T_{2h} = \frac{c_{2h}^2}{\gamma R M_{2h}^2} = \frac{U_h^2(\phi_h^2 + \psi_h^2)}{(\gamma - 1)c_p M_{2h}^2} \tag{6.86}$$

where $\phi_h = \phi_m(r/r_h)$ and $\psi_h = \psi_m(r/r_h)^2$. Combining Eqns (6.84a) and (6.86) we then have finally

$$\frac{T_{2h}}{T_1} = \frac{1}{1 + \dfrac{\gamma - 1}{2}M_{2h}^2\left(\dfrac{\psi_h^2}{\phi_h^2 + \psi_h^2}\right)} \tag{6.87}$$

The density ratio across the stator blade row at any radius is thus now fully specified in terms of the given data r_h/r_t, ϕ_m, ψ_m, M_{2h} and η_{TT} through Eqns (6.83), (6.85) and (6.87).

6.6.4 Compressible meridional flow through a turbine stage

The previous analysis may be extended with little difficulty to model a complete turbine stage by the introduction of a second actuator disc to represent the rotor. Assuming that there is no swirl at entry to and at exit from the stage and that $c_{x3} \approx c_{x1}$, the overall enthalpy drop may be expressed as

$$\psi U^2 = h_{01} - h_{03} \approx h_1 - h_3 = C_p(T_1 - T_3)$$

If $h_{01} - h_{03}$ is to be equal at all radii,

$$T_3 = T_{3h} = T_1 - \frac{\psi_h U_h^2}{C_p}$$
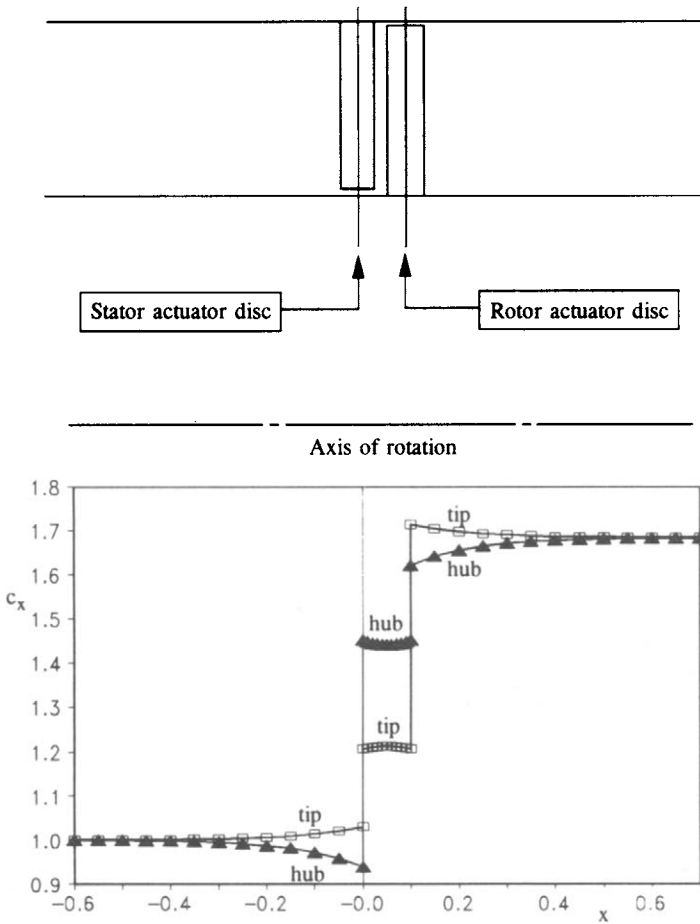
Fig. 6.16 Compressible flow through a turbine stage in a cylindrical annulus predicted by actuator disc theory

and introducing Eqn (6.86) to eliminate U_h^2/C_p

$$\frac{T_3}{T_1} = 1 - (\gamma - 1) M_{2h}^2 \left(\frac{\psi_h}{\phi_h^2 + \psi_h^2} \right) \frac{T_{2h}}{T_1} \tag{6.88}$$

By analogy with Eqn (6.83), the density at exit from the stage then becomes

$$\rho_3 = \rho_1 \frac{T_1}{T_3} \left\{ 1 - \frac{1}{\eta_{TT}} \left(1 - \frac{T_3}{T_1} \right) \right\}^{\gamma/(\gamma-1)} \tag{6.89}$$

The previous compressible actuator disc analysis may then be applied to account for the radial distribution of density jump $\rho_3 - \rho_2$ across the rotor actuator disc, resulting in the solution shown in Fig. 6.16. The blade row annulus geometry selected

Fig. 6.17 Compressible flow through turbine stage with gap of 0.5 between stator and rotor (blade height = 0.4)

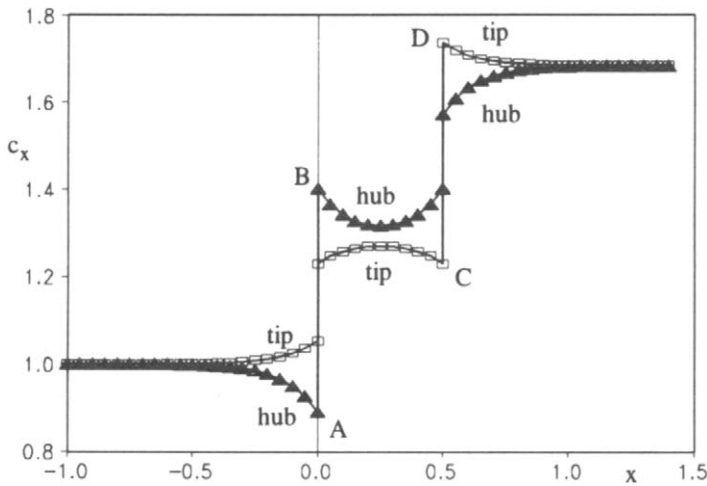here represents a tightly packed stage with blade aspect ratios of 5.0 and with a typical gas turbine stage loading as specified in Table 6.1.

The main features to note here are as follows:

(1) The mean velocity jumps from $C_{x1} = 1.0$ at inlet to $C_{x2} = 1.3$ between the blade rows and then to $C_{x3} = 1.65$ at exit from the stage.
(2) The greater density drop across the rotor tip produces the reverse behaviour of the upstream and downstream perturbations as compared with the stator.
(3) Interference between the stator and rotor increases the level of the axial velocity perturbations in between the blade rows to variations of $\pm 7.5\%$ from the mean.
(4) The reverse is true in the regions upstream and downstream of the stage where the disturbances are less than those of the individual blade rows.

Features (3) and (4) are brought out by Fig. 6.17 which shows the velocity perturbations at hub and tip for a blade row spacing of 0.5, which is sufficiently wide to minimise blade row interference. The individual behaviour of stator and rotor is clearer from this example from which it can be seen that they produce opposite trends at hub and tip. Thus the highest velocity jump Δc_x across the stator occurs at the hub, AB, and for the rotor at the tip, CD.

Comparing Fig. 6.17 with Fig. 6.16 it is clear that the velocity disturbances upstream and downstream of the stage are reduced for the closely packed blade rows, whereas the disturbances between stator and rotor are substantially increased by blade row interference in close proximity.

As mentioned previously it is not usual practice to adopt a cylindrical annulus. A better strategy to maintain similar velocity triangles and (ϕ, ψ) duty at the mean radius r_m is to expand the annulus area to try to maintain constant mean axial velocity C_x. Figure 6.18 illustrates an attempt to achieve this by simply adapting the cylindrical actuator disc solution to fit a suitably flared annulus. The blade row region was first chosen as illustrated to represent the confines of the stage. Conical hub and casing contours were then chosen with overall area ratio to enforce equal entry and exit
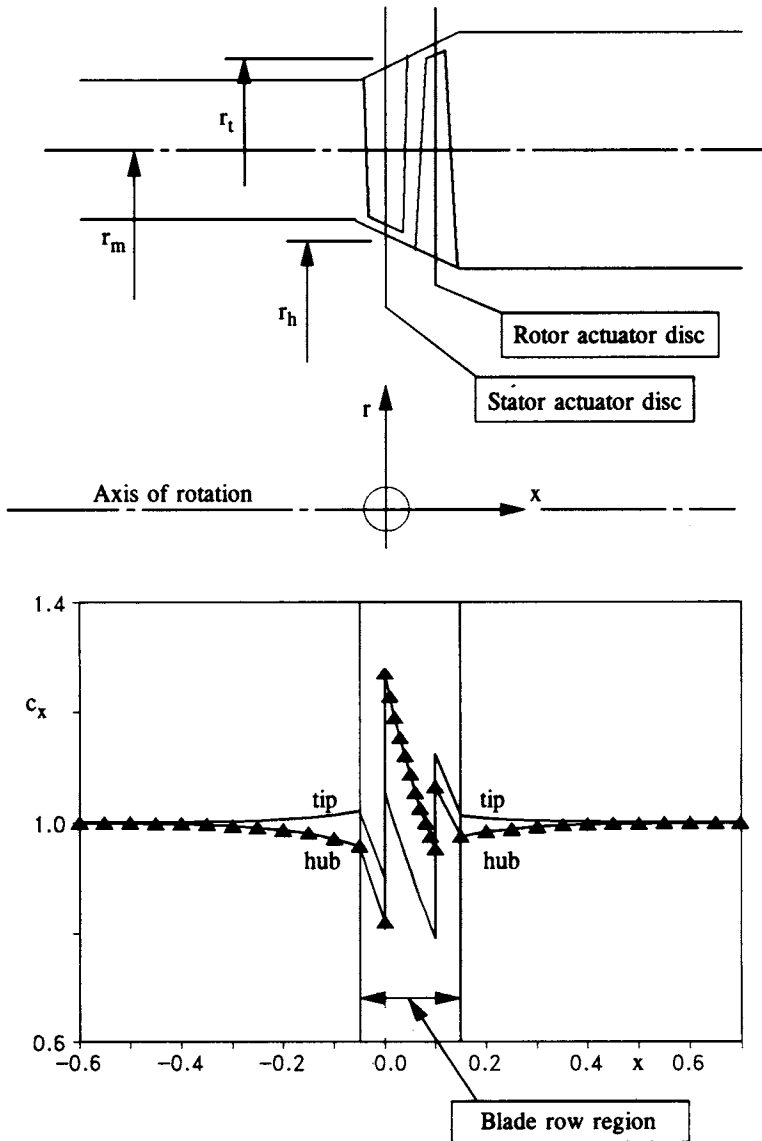
Fig. 6.18 Compressible flow through annulus with area increase to maintain constant mean axial velocity

mean axial velocities $C_x = 1.0$. For all other x locations the c_x values shown in Fig. 6.17 were simply scaled to satisfy mass flow continuity. While this cannot be justified rigorously from a fluid-dynamic point of view, it does at least offer a simple design approach leading to a first-order assessment of meridional disturbances due to compressibility. From Fig. 6.18 one can conclude that these disturbances will in general be small outside the confines of the stage. Within the stage, however, where the density gradient 'action' is taking place, there will be much more significant variations in c_x which need the attention of a more advanced analysis. The plane
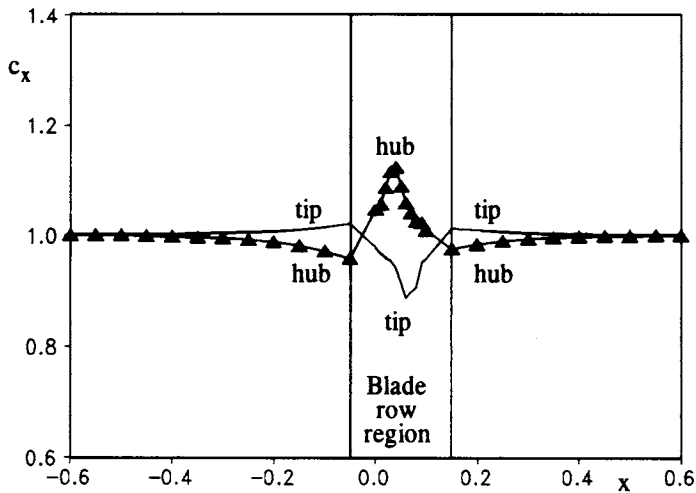
Fig. 6.19 Compressible flow through model stage with smeared actuator disc representation of stator and rotor

actuator disc model over-exaggerates these effects by concentrating the fluid divergence into the two actuator disc planes. The paper by Lewis and Horlock (1969) outlined a method for smearing source and vortex actuator discs across the blade region and this has been extended to compressible actuator discs recently by Lewis (1995). This leads to improved estimations of the activity within the blade row region as illustrated by Fig. 6.19 in which the density gradients were assumed to be evenly distributed between leading edge and trailing edge for both stator and rotor. Although considerable velocity disturbances are still predicted, they are much reduced in amplitude. Modern throughflow and time-marching numerical methods should provide much better resolution of these problems but are beyond the scope of the present discussion.

7
Mixed-flow and radial turbomachines

Introduction

In the early days of the development of the aircraft gas turbine engine there was fair competition between the multi-stage axial compressor and the centrifugal compressor as contenders for the same task, namely the delivery of large volume flow rates of air to the engine with fairly high pressure ratios. Competition was fair in the sense that these quite different devices have their own particular advantages and disadvantages. As illustrated by Fig. 7.1(a) and the data shown in Figs 1.11 and 1.13 and the related discussion in Section 1.2.2 of Chapter 1, several stages of an axial compressor would be required to deliver the same pressure ratio as that which can be produced by a single stage centrifugal compressor.

On the other hand, for the same inlet area and meridional inlet velocity c_{s1}, the centrifugal compressor presents two inconvenient geometrical features. Firstly the exit diameter must be much greater than the inlet diameter to obtain the centrifugal effect and consequent high head rise. Secondly the flow path is turned radially outwards, delivering the air unhelpfully in the radial direction and requiring an exit volute. The axial compressor, on the other hand, while presenting the expense of its many blade rows, is geometrically ideally suited to the general throughflow requirements of a modern aircraft gas turbine engine which will comprise an axial turbine and an axial bypass fan in addition to the multi-stage axial compressor.

For more general applications fans fall into the three categories illustrated in Fig. 7.1(b), namely axial, mixed-flow and radial (or centrifugal). These configurations and their general characteristics have been very helpfully reviewed by ESDU (1980) to assist the non-specialist with fan selection and with tender appraisal, including the presentation of Fig. 1.13. Regions for optimum efficiency of each category of fan are plotted first against axes of specific diameter D_s versus specific speed N_s and secondly against axes of Φ versus Ψ where these coefficients are defined as in Eqns (1.16) and (1.23), namely

$$\left.\begin{aligned} \Phi &= \frac{Q}{ND^3} \\[2mm] \Psi &= \frac{gH}{N^2 D^2} \end{aligned}\right\} \qquad [1.16]$$

$$\left.\begin{aligned} N_s &= \frac{\Phi^{1/2}}{\Psi^{3/4}} \quad \text{Specific speed} \\[2mm] D_s &= \frac{\Psi^{1/4}}{\Phi^{1/2}} \quad \text{Specific diameter} \end{aligned}\right\} \qquad [1.23]$$
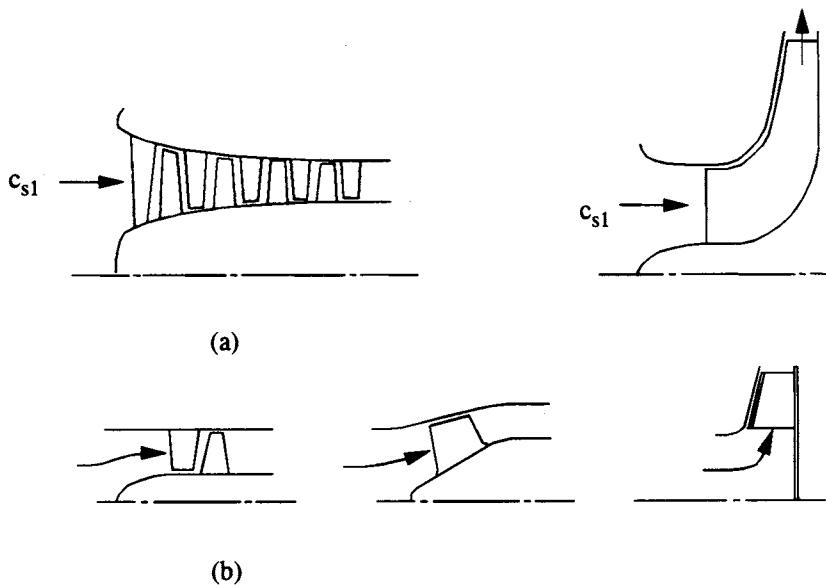
Fig. 7.1 Meridional flow through (a) axial and centrifugal compressors and (b) axial, mixed-flow and radial fans

The spread of 'practice' recorded in Fig. 1.13(a) is generally quite close to the well-known curve of Cordier (1953) and marks out axial fans as suited to *high specific speeds* while centrifugals are the appropriate choice for *low specific speeds*. To summarise, the selection ranges suggested by Fig. 1.13(a) are given in Table 7.1.

Table 7.1 Recommended selection ranges for axial, mixed-flow and radial fans

Specific speed N_s range	Fan type
0.5 to 2.0	Radial
2.1 to 3.2	Mixed-flow
1.4 to 13.0	Axial

These data suggest quite wide ranges of N_s appropriate for axial and centrifugal or radial fans even with a measure for possible overlap in the middle range, $1.4 < N_s < 2.0$. Alternatively in this range it may be just as appropriate to select instead a mixed-flow fan, so named because its configuration is a mixture of both the axial and the radial machines, Fig. 7.1(b). Such fans have fulfilled a crucial role in high technology applications such as gas-cooled nuclear reactor circulators and hovercraft lift fans for which a combination is required of high mass flow rate and fairly high pressure ratio (i.e. more than that capable of a single stage axial) at high efficiency. The range of applications suggested by Table 7.1 and Fig. 1.13 is, however, unnecessarily restricted and simply reflects the limits set by 'practice'. It would be perfectly possible for mixed-flow fans to serve a much wider range of specific speeds than the above data suggest, offering perhaps the advantages of fewer stages than an axial fan or the more suitable throughflow annulus shape as compared with a radial fan.
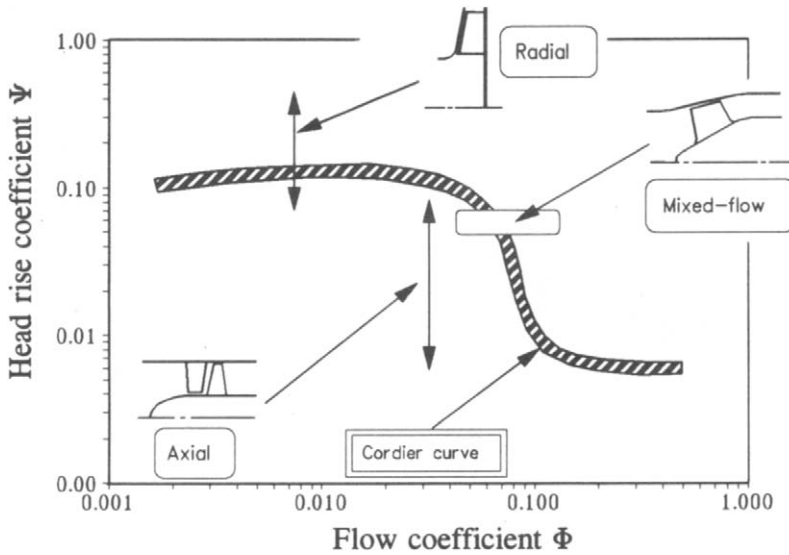
Fig. 7.2 Cordier diagram for fans replotted on (Φ, Ψ) axes

Much more revealing is the re-presentation of the same *optimum fan* data against the axes Φ and Ψ, Fig. 7.2, where use has been made of Eqns (1.24) to transform the data to a form more given to physical interpretation. According to this format axial fans stand out as suitable for low pressure rise applications and centrifugal fans for high pressure rise. Mixed-flow practice here has obviously been quite narrowly restricted to the intermediate Ψ range. The guidelines are given in Table 7.2.

Table 7.2 Recommended selected ranges for axial, mixed-flow and radial fans

Range for $\Psi = gh/N^2 D^2$	Fan type
0.006 to 0.09	Axial
0.04　to 0.06	Mixed-flow
0.07　to 0.4	Radial

Although there is an enormous spread of Ψ here over the range $0.006 < \Psi < 0.4$, calling for selection of an appropriate fan type to ensure high efficiency, there is no similar obvious link between Φ and machine type observable from Figs 1.13(b) and 7.2. All three fan types offer a fairly wide spread of possible design flow coefficients which will provide an efficient machine for a specified Ψ with a good deal of overlap. This is an important observation in support of the use of Φ, Ψ axes for presentation of optimum test data for machine selection rather than N_s, D_s axes.

In the present context these data highlight the different performance patterns progressing through from axial to mixed-flow and on to radial fans or pumps, calling for a physical explanation. With this in mind we will begin in Section 7.1 by reconsidering the Euler pump equation and the origins of work input and energy transfer to the fluid in the general mixed-flow turbomachine. This will lead on to the

derivation of the property *rothalpy* relevant to energy transfer in rotating systems with radial flow, Section 7.2. Dimensionless velocity triangles will then be considered in Section 7.3 to link stage duty based on *local* dimensionless variables (ϕ, ψ), machine overall radius ratio (r_2/r_1) and annulus area ratio (A_2/A_1) with expressions for stage efficiency to link with the performance philosophy developed in Chapters 3 and 4 for axial turbines and compressors.

The handling of the general three-dimensional design problem of a mixed-flow turbomachine by the combination of an axisymmetric meridional flow and a series of mixed-flow cascades will be introduced in Section 7.4. To conclude the chapter, Section 7.5 will be given to the problems of the *relative eddy* and the related *slip* which occur in radial and mixed-flow pumps and fans and appropriate correlations for their estimation.

7.1 Origins of specific work input in mixed-flow fans and pumps

The potential ability of radial and mixed-flow fans and pumps to deliver higher head rise coefficients than axial machines is revealed if the Euler pump equation is re-expressed relative to the rotor. As shown in Chapter 1, Eqn (1.9a) and Fig. 1.5, the Euler pump equation for a mixed-flow fan may be expressed as

$$\bar{W} = h_{o2} - h_{o1} = U_2 c_{\theta 2} - U_1 c_{\theta 1} \tag{7.1}$$

where $\bar{W}$ is the specific work input (J kg^{-1}), $U = r\Omega$ is the local blade speed and c_θ is the absolute swirl velocity. Now c_θ is related to the swirl velocity w_θ measured relative to the rotor at any point at radius r within the rotor, through

$$c_\theta = U + w_\theta = r\Omega + w_\theta \tag{7.2}$$

where c_θ and w_θ are defined as positive in the direction of the rotor blade velocity U. Introduction of this into Eqn (7.1) results in the following alternative and revealing form of the Euler pump equation:

$$\left.\begin{aligned} \bar{W} = h_{o2} - h_{o1} &= U_2 w_{\theta 2} - U_1 w_{\theta 1} + U_2^2 - U_1^2 \\ &= \Omega(r_2 w_{\theta 2} - r_1 w_{\theta 1}) + \Omega^2(r_2^2 - r_1^2) \\ &= \left(\begin{array}{c} \text{Specific work input} \\ \text{due to aerodynamic} \\ \text{forces} \end{array}\right) + \left(\begin{array}{c} \text{Specific work input} \\ \text{due to Coriolis} \\ \text{forces} \end{array}\right) \end{aligned}\right\} \tag{7.3}$$

For axial machines, since $r = $ constant, this reduces to

$$\bar{W} = \Omega r_1(w_{\theta 2} - w_{\theta 1}) \tag{7.3a}$$

In this special case all the specific work input derives from the blade aerodynamic forces set up in reaction to the fluid deflection $\varepsilon = \beta_1 - \beta_2$, Fig. 7.3. For the case of the mixed-flow fan, on the other hand, we are able to identify two separate sources of work input as stated by Eqn (7.3). These are as follows:

(1) Specific work input due to aerodynamic forces results from the change in angular momentum of the flow viewed relative to the rotor, $|r_2 w_{\theta 2} - r_1 w_{\theta 1}|$.
(2) A second specific work contribution completely *independent* of blade profile
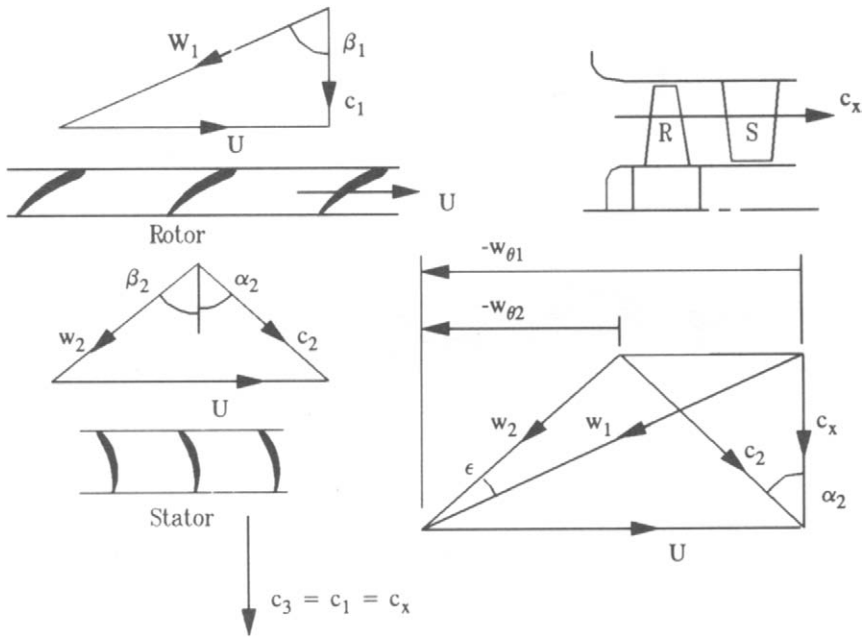
Fig. 7.3 Velocity triangles for an axial fan
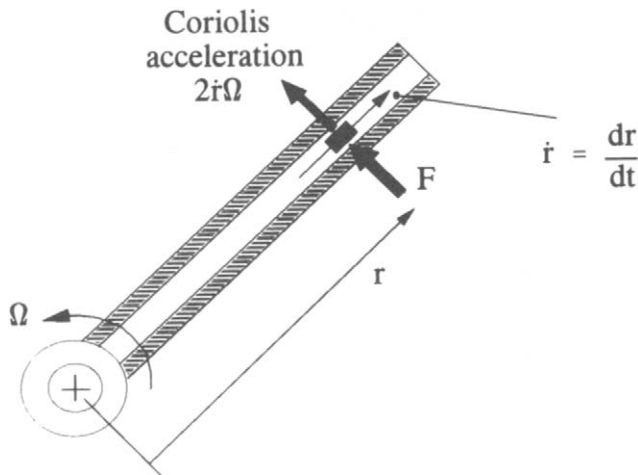
Fig. 7.4 Coriolis acceleration and force on a particle of mass m in a rotating slider

shape and therefore of aerodynamics and entirely dependent upon *meridional streamline radial shift* between inlet r_1 and exit r_2, Fig. 7.4, namely $\Omega^2(r_2^2 - r_1^2)$. This can be identified as originating from the Coriolis forces exerted on the fluid by the rotor by virtue of their radial component of velocity c_r. To confirm this let us consider the simpler but analogous situation of a solid particle of mass m being propelled radially outwards with velocity $\dot{r} = dr/dt$ in a rotating radial slider, Fig. 7.4. The Coriolis acceleration
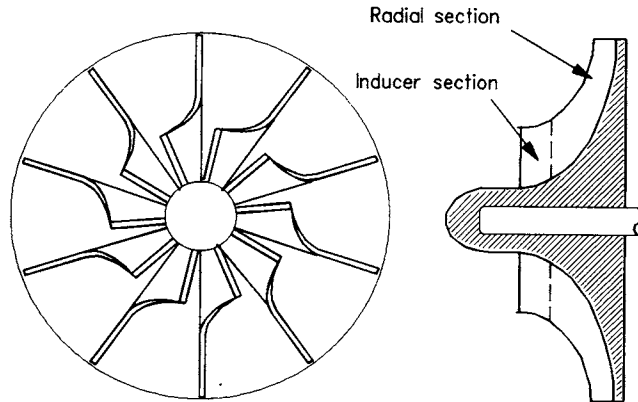
Fig. 7.5 Centrifugal compressor rotor showing inducer and radial sections

of the particle will be $2\dot{r}\Omega$, resulting in the Coriolis force normal to r of $F = 2m\dot{r}\Omega$. The shaft power input is thus

$$\frac{dW}{dt} = Fr\Omega = 2mr\frac{dr}{dt}\Omega^2 \tag{7.4}$$

Integrating between r_1 and r_2 the specific work done on the particle is thus

$$\bar{W} = \frac{W}{m} = \int_{r_1}^{r_2} 2\Omega^2 r\, dr = \Omega^2(r_2^2 - r_1^2) \tag{7.5}$$

which is identical to the second term on the right-hand side of Eqn (7.3).

This observation is of considerable importance. Apparently energy may be transferred from rotor to fluid in large measure simply by imposing meridional streamline radially outward shift. In other words the annulus design for mixed-flow turbomachines becomes as crucial to the specification of work input and hence enthalpy or head rise as the selection of blade profile shapes is for axial machines, Chapter 2. Furthermore it is obvious from Eqn (7.3) that a very large head rise will result from the specification of a large radius ratio r_2/r_1.

Another appropriate design technique might be to maximise the work input and consequent head rise due to aerodynamic forces by attempting to set $w_{\theta 2} = 0$ by adopting radial blading.

The typical centrifugal compressor rotor depicted in Fig. 7.5 meets all of these objectives. First of all the flow enters an inducer section which in many respects is like an axial compressor blade row. The task of the inducer is to turn the flow from its relative inlet angle β_1 towards the axial direction before it begins its large radius change from r_1 to r_2. The fluid then enters the main radial section of the impeller where it is first turned from the axial direction to the radially outward direction. All of the relative swirl $w_{\theta 1}$ at inlet has now been absorbed and the aim is to eject the fluid at the blade tips with zero relative swirl velocity $w_{\theta 2} = 0$. In practice this proves impossible with purely radial blades at exit as illustrated in Fig. 7.5 due to 'relative eddy' and its related 'slip', matters to which we will return later in Section 7.5.

7.2 Stagnation enthalpy relative to a rotor and *rothalpy*

As shown in Section 1.1.2 the steady flow energy equation for a turbomachine may be expressed as

$$\bar{Q} - \bar{W} = (h_2 + \tfrac{1}{2}c_2^2) - (h_1 + \tfrac{1}{2}c_1^2) \qquad [1.5]$$
$$= h_{o2} - h_{o1}$$

where stagnation enthalpy is defined as

$$h_o = h + \frac{c^2}{2} \qquad (7.6)$$

The heat transferred into the system per unit mass $\bar{Q}$ will normally be negligible. For a *stator* the specific work input $\bar{W}$ will also be zero so that

or
$$\left.\begin{array}{c} h_{o2} = h_{o1} \\ h_o = \text{constant} \end{array}\right\} \quad \text{for a stator} \qquad (7.7)$$

Thus stagnation enthalpy is conserved through a stationary blade row, even if there are frictional losses.

For a *rotor*, on the other hand, the specific work $\bar{W}$ is non-zero so that the steady flow energy equation becomes

$$h_{o2} - h_{o1} = -\bar{W} \qquad (7.8)$$

Suppose, however, that we were to sit on the rotor and observe the relative flow. In such a rotating laboratory the turbomachine rotor would now appear to us to be stationary and thus we might justifiably expect the stagnation enthalpy measured relative to our observer's framework to be conserved. To test this let us define relative stagnation enthalpy as we did for the non-rotating reference frame, Eqn (7.6), namely

$$(h_o)_{\text{rel}} = h + \frac{w^2}{2} \qquad (7.9)$$

where h is the specific enthalpy and w is the fluid velocity which we observe relative to our rotating framework. Adopting cylindrical polar coordinates (x, r, θ) the absolute velocity components c_x, c_r and c_θ at radius r may be related to the velocity components viewed relative to the rotor w_x, w_r and w_θ through

$$\left.\begin{array}{l} c_x = w_x \\ c_r = w_r \\ c_\theta = r\Omega + w_\theta \end{array}\right\} \qquad (7.10)$$

Rotation obviously has no effect upon axial and radial velocity components but only upon the θ component as already stated by Eqn (7.2). The stagnation enthalpy h_o may now be related to $(h_o)_{\text{rel}}$ at the point P within the mixed-flow fan or pump rotor
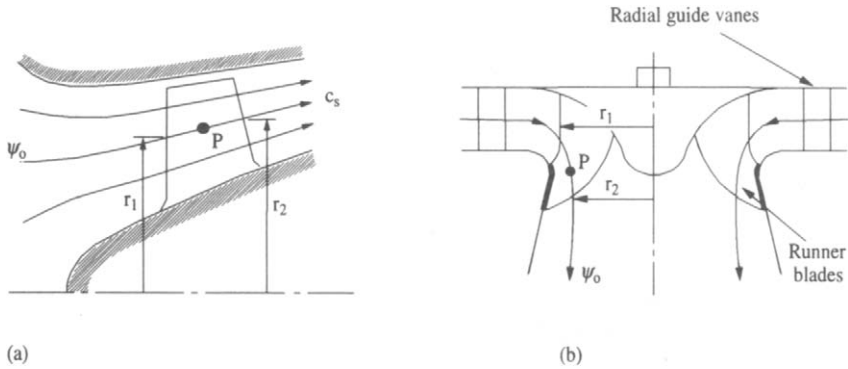
Fig. 7.6 Meridional flow through mixed-flow turbomachines: (a) mixed-flow pump or fan rotor; (b) Francis turbine

depicted in Fig. 7.6, as follows:

$$
\left.
\begin{aligned}
h_{\mathrm{o}} &= h + \tfrac{1}{2}c_x^2 + \tfrac{1}{2}c_r^2 + \tfrac{1}{2}c_\theta^2 \\
&= h + \tfrac{1}{2}w_x^2 + \tfrac{1}{2}w_r^2 + \tfrac{1}{2}(r\Omega + w_\theta)^2 \\
&= h + \tfrac{1}{2}w_x^2 + \tfrac{1}{2}w_r^2 + \tfrac{1}{2}w_\theta^2 + \tfrac{1}{2}r^2\Omega^2 + r\Omega w_\theta \\
&= (h_{\mathrm{o}})_{\mathrm{rel}} + r\Omega w_\theta + \frac{U^2}{2}
\end{aligned}
\right\}
\tag{7.11}
$$

At rotor inlet

$$
h_{\mathrm{o}1} = (h_{\mathrm{o}1})_{\mathrm{rel}} + r_1\Omega w_{\theta 1} + \frac{U_1^2}{2}
\tag{7.12}
$$

If these equations are subtracted, then at any point P within the rotor

$$
h_{\mathrm{o}} - h_{\mathrm{o}1} = (h_{\mathrm{o}})_{\mathrm{rel}} - (h_{\mathrm{o}1})_{\mathrm{rel}} + \Omega(rw_\theta - r_1 w_{\theta 1}) + \frac{U^2}{2} - \frac{U_1^2}{2}
$$

But for a location such as that of P on a meridional streamline within the rotor, the Euler pump equation (7.3) may be adapted to give the local value of h_{o}, namely

$$
h_{\mathrm{o}} - h_{\mathrm{o}1} = \Omega(rw_\theta - r_1 w_{\theta 1}) + U^2 - U_1^2
\tag{7.3a}
$$

Subtracting the last two equations we have finally the steady flow energy equation expressed relative to the rotor, whether it be a turbine, pump, compressor or fan:

$$
\left.
\begin{aligned}
(h_{\mathrm{o}})_{\mathrm{rel}} - \frac{U^2}{2} &= (h_{\mathrm{o}1})_{\mathrm{rel}} - \frac{U_1^2}{2} \\
&= I = \text{constant along a meridional streamline}
\end{aligned}
\right\}
\tag{7.13}
$$

The quantity $I = (h_{\mathrm{o}})_{\mathrm{rel}} - U^2/2$ is called the *rothalpy* and the energy conservation law

applicable to rotating fluid systems is that the rothalpy I remains constant along a meridional streamline passing through the rotor. We note also that in non-rotating systems such as stators, since $U = 0$ the rothalpy is equal in value to the stagnation enthalpy, $I = h_o$.

It follows immediately from the above that turbomachines designed to operate in a non-rotating framework may move off design performance if located in a spinning environment. Thus even in earth-bound laboratories the stagnation enthalpy will not be conserved precisely due to the earth's rotation, although the errors involved in assuming this are trivial since the variation of $U = r\Omega$ from bottom to top of the turbomachine is negligible. The same may not be true for turbomachines installed on space platforms spun to generate artificial gravity, which could be subject to more significant departure from intended duty if such rotational effects were not carefully considered at the design stage.

7.3 Dimensionless performance parameters for mixed-flow fans and pumps

Following similar arguments to those which led to a rational performance analysis for axial turbines (Chapter 3) and axial compressors and fans (Chapter 4), we would expect the general performance of a mixed-flow fan or pump to depend upon a number of leading geometrical or fluid-dynamic design variables, some independent and some dependent. Thus we might anticipate that the total-to-total efficiency η_{TT} would be influenced by the following minimal selection of 11 likely design variables:

$$\eta_{TT} = f(\underbrace{c_{s2}, w_\infty, U_2,}_{\substack{\text{Velocity} \\ \text{triangles}}} \quad \underbrace{r_1, r_2, A_1, A_2,}_{\substack{\text{Annulus} \\ \text{geometry}}} \quad \underbrace{\Delta h_o, (\Delta p_{oR})_{\text{loss}},}_{\substack{\text{Head} \\ \text{rise}}} \quad \underbrace{\rho, \mu)}_{\substack{\text{Fluid} \\ \text{physical} \\ \text{properties}}} \qquad (7.14)$$

Velocity triangles and annulus geometrical data are shown in Fig. 7.7 where attention is focused on the mean meridional streamline ψ_o as representative of the average stage performance from hub to casing. c_{s2} and U_2 are the meridional and blade velocities applicable at the rotor trailing edge flow exit point P_2. w_∞ is the vector mean velocity relative to the fan rotor, that is the vector average of w_1 and w_2, typifying velocity levels relative to the rotor blades. r_1 and r_2 are as defined in Fig. 7.7(a)
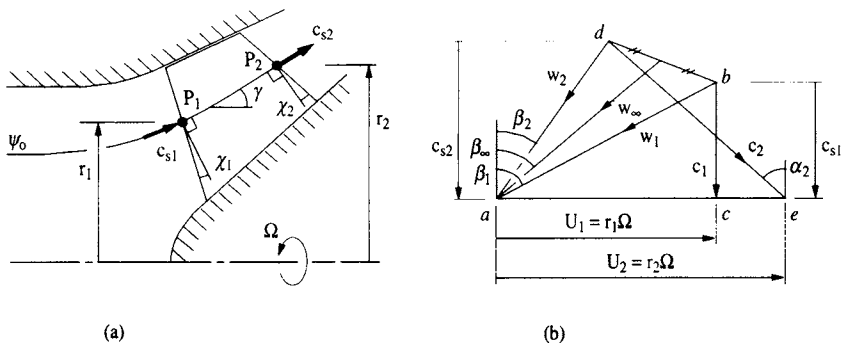

Fig. 7.7 (a) Meridional annulus geometry and (b) velocity triangles for a mixed-flow fan

and A_1 and A_2 are the annulus areas at the leading and trailing edge planes viewed along the directions of c_{s1} and c_{s2}, which may be approximated as follows:

$$\left. \begin{array}{l} A_1 = \pi(r_{t1}^2 - r_{h1}^2)/\cos\chi_1 \\ A_2 = \pi(r_{t2}^2 - r_{h2}^2)/\cos\chi_2 \end{array} \right\} \tag{7.15}$$

Here χ_1 and χ_2 are the leading and trailing edge 'lean' angles as defined in Fig. 7.7(a) and (r_{h1}, r_{t1}) and (r_{h2}, r_{t2}) are the hub and tip radii of the rotor leading and trailing edges. Selecting suitable dimensionless groups, η_{TT} may be expressed alternatively as follows:

$$\eta_{TT} = f\left(\phi, \psi, \frac{r_2}{r_1}, \frac{A_2}{A_1}, \zeta_\infty, R_{e2}\right) \tag{7.16}$$

with the following definitions

$$\left. \begin{array}{ll} \phi = c_{s2}/U_2 & \text{Flow coefficient} \\ \psi = \Delta h_o/U_2^2 & \text{Work input or head coefficient} \\ r_2/r_1 & \text{Annulus radius ratio} \\ A_2/A_1 & \text{Annulus area ratio} \\ \zeta_\infty = \dfrac{(\Delta p_{oR})_{\text{loss}}}{\frac{1}{2}\rho w_\infty^2} & \text{Rotor loss coefficient} \\ R_{e2} = \dfrac{2r_2 U_2}{\mu/\rho} & \text{Machine Reynolds number} \end{array} \right\} \tag{7.17}$$

Although Eqn (7.16) provides immediate guidelines for data reduction and selection of suitable correlation formats for systematic model tests (e.g. ϕ, ψ) charts for specified ranges of r_2/r_1 and A_2/A_1), it is in parametric form only and gives no indication of the likely dependency of η_{TT} on the six dimensionless variables. It is possible to move towards a more rational analytical equivalent equation to do just that with the help of the velocity triangles, Fig. 7.7(b). Let us consider the case of an incompressible fluid for which η_{TT} is defined as

$$\left. \begin{array}{l} \eta_{TT} = \dfrac{\text{Actual stagnation pressure rise}}{\text{Frictionless ideal stagnation pressure rise}} \\[2mm] \quad = \dfrac{\Delta p_o - (\Delta p_o)_{\text{loss}}}{\Delta p_o} \\[2mm] \quad = 1 - \dfrac{1}{2}\left(\dfrac{(\Delta p_o)_{\text{loss}}}{\frac{1}{2}\rho w_\infty^2}\right)\left(\dfrac{U_2^2}{\Delta p_o/\rho}\right)\left(\dfrac{w_\infty}{U_2}\right)^2 \\[2mm] \quad = 1 - \dfrac{\zeta}{2\psi}\left(\dfrac{w_\infty}{U_2}\right)^2 \end{array} \right\} \tag{7.18}$$

From velocity triangles, Fig. 7.7(b),

$$w_\infty^2 = \left(\frac{c_{s1} + c_{s2}}{2}\right)^2 + \left(\frac{w_{\theta 1} + w_{\theta 2}}{2}\right)^2 = \frac{1}{4}\left\{ c_{s2}^2\left(1 + \frac{A_2}{A_1}\right)^2 + (U_1 + U_2 - c_{\theta 2})^2 \right\}$$
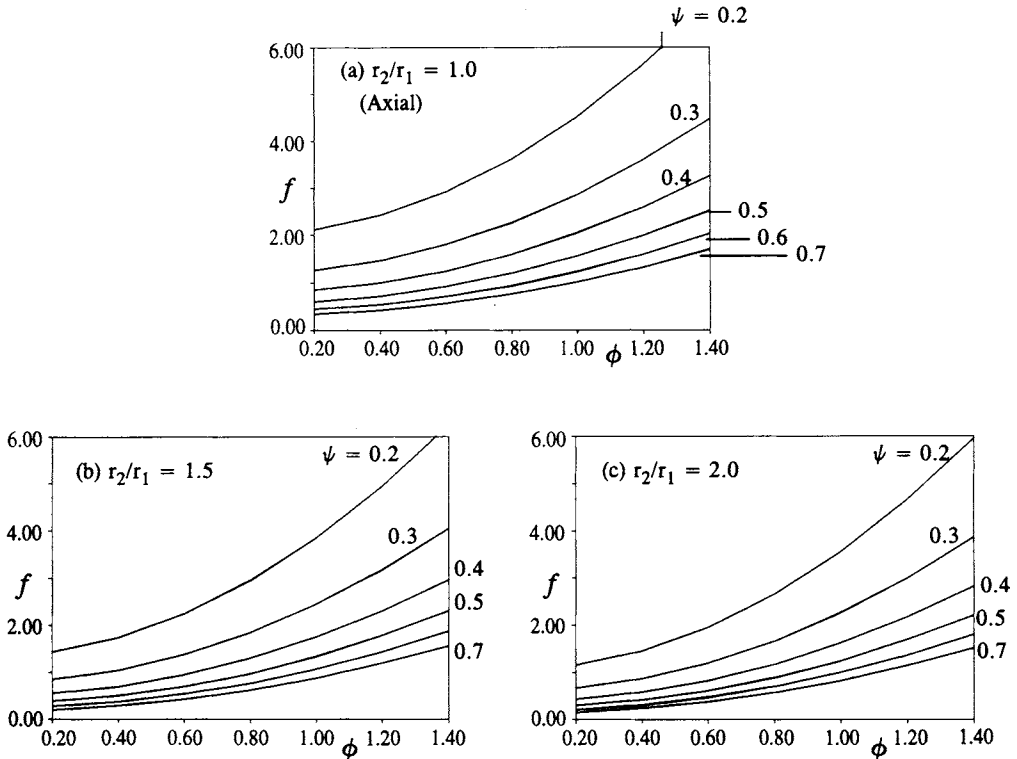
Fig. 7.8 Loss weighting coefficients for mixed-flow fans for three different radius ratios r_2/r_1 with constant annulus area ratio $A_2/A_1 = 1.0$

But from the definition of flow coefficient, $c_{s2} = \phi U_2$, and from the Euler pump equation (1.9a), with zero inlet swirl $c_{\theta1} = 0$, $\Delta h_o = U_2 c_{\theta2} = \psi U_2^2$ and thus $c_{\theta2} = \psi U_2$. The previous equation then becomes

$$\left(\frac{w_\infty}{U_2}\right)^2 = \frac{1}{4}\left\{\phi^2\left(1 + \frac{A_2}{A_1}\right)^2 + \left(\frac{r_1}{r_2} + 1 - \psi\right)^2\right\} \tag{7.19}$$

Finally the total-to-total efficiency of the fan or pump may be expressed in the following closed analytical form:

$$\left.\begin{aligned} \eta_{TT} &= 1 - \frac{\zeta_\infty}{8\psi}\left\{\phi^2\left(1 + \frac{A_2}{A_1}\right)^2 + \left(\frac{r_1}{r_2} + 1 - \psi\right)^2\right\} \\ &= 1 - f(\phi, \psi, r_1/r_2, A_2/A_1)\,\zeta_\infty \end{aligned}\right\} \tag{7.20}$$

The losses are thus the product of the profile loss coefficient ζ_∞ and the loss weighting coefficient f.

To summarise:

(1) The loss coefficient ζ_∞ is dependent upon the blade profile shape and the consequent boundary layer development. It will also be dependent upon the

Reynolds number R_{e2}, accounting for the last dimensionless variable listed in Eqn (7.17).

(2) The magnitude of the weighting coefficient f is a unique analytical function of the selected duty (ϕ, ψ) and the annulus geometry through (r_1/r_2) and (A_1/A_2), namely

$$f = \frac{1}{8\psi}\left\{ \phi^2 \left(1 + \frac{A_2}{A_1}\right)^2 + \left(\frac{r_1}{r_2} + 1 - \psi\right)^2 \right\} \qquad (7.21)$$

This powerful method of analysis thus brings out quite clearly the primary influence which the dimensionless groups will exercise over the expected efficiency of a mixed-flow fan. Irrespective of the detailed profile aerodynamic characteristics as represented here by ζ_∞, the rotor losses will depend directly upon the weighting coefficient f which is itself governed by the selected duty loading (ϕ, ψ) and the annulus geometry $(r_2/r_1, A_2/A_1)$. To illustrate these dependencies f has been evaluated in Fig. 7.8 for a wide range of (ϕ, ψ) duties and for $r_2/r_1 = 1.0, 1.5$ and 2.0 with constant annulus area $A_2/A_1 = 1.0$. Figure 7.8(a) represents the limiting case of an axial machine $(r_2/r_1 = 1)$ for which the loss weighting coefficients exhibit the highest values. As might be expected the duty coefficients ϕ and ψ exercise the strongest influence over f, but for a typical (ϕ, ψ) duty the radius ratio r_2/r_1 will produce significant changes in predicted efficiency as illustrated by the following example.

Example 7.1

Problem
Assuming a rotor loss coefficient $\zeta_\infty = 0.08$, estimate and compare the mean streamline efficiency of mixed-flow fans of varying r_2/r_1 for a prescribed duty of $\phi = 0.6$, $\psi = 0.35$.

Solution
Making use of Eqns (7.20) and (7.21), the data tabulated in Table 7.3 may be obtained. According to this simple example, gains in rotor efficiency are indicated for increasing radius ratio r_2/r_1, with the important reservation that we have assumed the same loss coefficient ζ_∞ for all four designs. Bearing in mind, however, that the (ϕ, ψ) duty loading is the same for all four machines, this may not be too unreasonable an assumption for this simple study aimed merely at revealing trends.

To conclude this section the weighting coefficients are shown in Fig. 7.9 for two mixed-flow fans of radius ratio $r_2/r_1 = 2.0$, but with different area ratios, one diffusing

Table 7.3 Predicted efficiency of mixed-flow fans as a function of radius ratio r_2/r_1

r_2/r_1	f	ζ_∞	$\eta_{TT} = 1 - f\zeta_\infty$ (%)
1.0	1.436 46	0.08	88.51
1.5	1.083 29	0.08	91.33
2.0	0.936 46	0.08	92.51
2.5	0.857 89	0.08	93.14
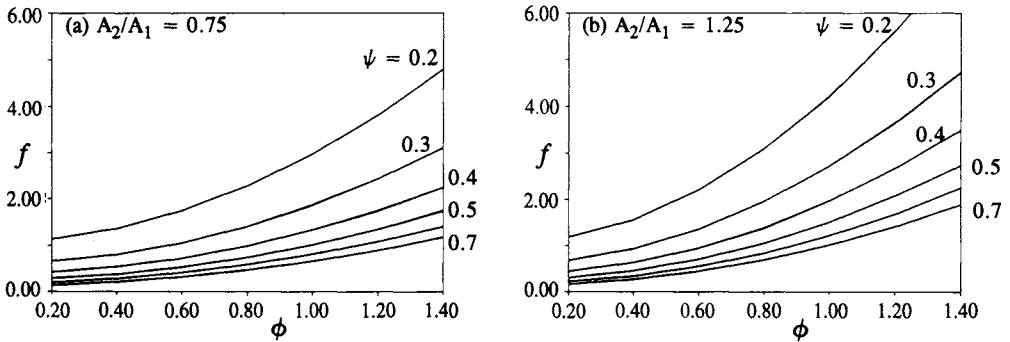
Fig. 7.9 Effect of annulus area ratio A_2/A_1 upon loss weighting coefficients for a mixed-flow fan with radius ratio $r_2/r_1 = 2.0$
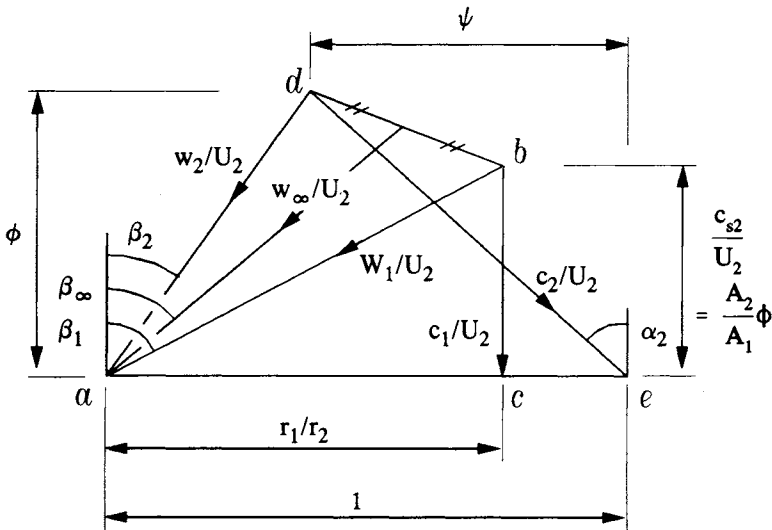
Fig. 7.10 Dimensionless velocity triangles for a mixed-flow fan

$(A_2/A_1 = 1.25)$ and the other accelerating $(A_2/A_1 = 0.75)$. There is clearly a gain in rotor efficiency offered by the accelerating annulus, although of course this would impose additional demands on the downstream diffusing requirements of the exit stator or volute.

7.3.1 Dimensionless velocity triangle relationships

Dimensionless velocity triangles may be constructed if all velocities in Fig. 7.7(b) are divided by the rotor exit blade speed U_2. The outcome of this is shown in Fig. 7.10.

The various flow angles can now be expressed in terms of the chosen dimensionless groups as follows. The absolute exit swirl angle is given by

$$\alpha_2 = \tan^{-1}(\psi/\phi) \tag{7.22}$$

and the relative swirl angles are given by

$$
\left.
\begin{array}{l}
\beta_1 = \tan^{-1}\left\{ \dfrac{1}{\phi}\left(\dfrac{r_1}{r_2}\right)\left(\dfrac{A_1}{A_2}\right) \right\} \\[3mm]
\beta_2 = \tan^{-1}\left\{ \dfrac{1}{\phi}(1-\psi) \right\} \\[3mm]
\beta_\infty = \tan^{-1}\left\{ \dfrac{1 - \psi + \dfrac{r_1}{r_2}}{\phi\left(1 + \dfrac{A_2}{A_1}\right)} \right\}
\end{array}
\right\}
\qquad (7.23)
$$

The fluid deflection relative to the rotor then follows from

$$
\left.
\begin{array}{l}
\varepsilon_r = \beta_1 - \beta_2 \\[4mm]
\quad = \tan^{-1}\left\{ \dfrac{\phi\left(\dfrac{r_1 A_1}{r_2 A_2} - 1 + \psi\right)}{\phi^2 + (1-\psi)\left(\dfrac{r_1 A_1}{r_2 A_2}\right)} \right\}
\end{array}
\right\}
\qquad (7.24)
$$

Table 7.4 Velocity triangle data for a range of mixed-flow fans

Prescribed duty $\phi = 0.6$, $\psi = 0.35$			$A_2/A_1 = 1.0$			$A_2/A_1 = 0.75$		
r_2/r_1	α_2	β_2	β_1	β_∞	ε_R	β_1	β_∞	ε_R
1.00	30.256	47.291	59.036	53.973	11.746	65.772	57.529	18.482
1.25	30.256	47.291	53.130	50.389	5.839	60.642	54.090	13.352
1.50	30.256	47.291	48.013	47.654	0.722	55.981	51.429	8.690
1.75	30.256	47.291	43.603	45.507	−3.688	51.780	49.316	4.489
2.00	30.256	47.291	39.806	43.781	−7.485	48.013	47.603	0.722

The above equations have been evaluated for a family of mixed-flow fans to illustrate the influence of r_2/r_1 and A_2/A_1 upon the velocity triangles, Table 7.4. The following observations may be made from these data:

(1) *Exit flow*. As can be seen from Eqns (7.22) and (7.23b) the absolute and relative exit swirl angles α_2 and β_2 are in fact dependent only upon the fan duty (ϕ, ψ) and are thus the same for all of the fans considered here.
(2) $A_2/A_1 = 1.0$. It is of special interest to note that the rotor deflection angle ε_R decreases as the design value for r_2/r_1 is increased. Indeed, if $r_2/r_1 > 1.538$, then $\beta_2 > \beta_1$ and the blade profiles must be those of an accelerating (turbine) cascade rather than those of a diffuser. Surprisingly, ε_R is then negative.

(3) $A_2/A_1 = 0.75$. With this modest contraction of the annulus area, significantly greater fluid deflections ε_R are required to deliver the same duty ψ and ε_R then remains positive (i.e. diffusing) for all radius ratios r_2/r_1.

Item (2) illustrates rather dramatically the discussion already presented in Section 7.1 regarding the two origins of specific work and hence work coefficient ψ in mixed-flow turbomachines, namely

(a) Coriolis forces, and
(b) aerodynamic (Newtonian reaction) forces.

For large radius ratios the specific work input due to Coriolis forces is simply too great and therefore negative specific work must be supplied by the aerodynamic forces for delivery of the specified work coefficient ψ. To illustrate this further we could express the work coefficient as the sum of these two contributions thus:

$$\psi = \psi_{\text{Aero.}} + \psi_{\text{Cor.}} \tag{7.25}$$

From the Euler pump equation (7.3), dividing through by U_2^2 we then have

$$\left.\begin{aligned} \psi_{\text{Cor.}} &= 1 - \left(\frac{r_1}{r_2}\right)^2 \\ \psi_{\text{Aero.}} &= \psi - 1 + \left(\frac{r_1}{r_2}\right)^2 \end{aligned}\right\} \tag{7.26}$$

From the second of these equations it follows that the blade profile aerodynamics will be those of a turbine rather than a compressor unless

$$\frac{r_2}{r_1} < \frac{1}{\sqrt{1-\psi}} \qquad \begin{array}{l}\text{Limits of } r_2/r_1 \text{ for positive} \\ \text{aerodynamic specific work input}\end{array} \tag{7.27}$$

However, some caution is needed at this point, since this limit does not actually coincide with that of zero deflection. Thus from Eqn (7.24) we see that ε_R is positive only if

$$\frac{r_1}{r_2} < \frac{A_1}{A_2}\left(\frac{1}{1-\psi}\right) \qquad \begin{array}{l}\text{Limits of } r_2/r_1 \text{ for positive} \\ \text{deflection } \varepsilon_R\end{array} \tag{7.28}$$

The explanation for this is subtle and not of easy perception. From the Euler pump equation (7.3) we see that the specific work input from blade profile aerodynamics may be expressed as

$$\bar{W}_{\text{Aero.}} = \Omega(r_2 w_{\theta 2} - r_1 w_{\theta 1}) \tag{7.29}$$

For zero deflection the relative swirl velocities are equal, namely $w_{\theta 1} = w_{\theta 2}$, whereas in Eqn (7.29) for zero specific work we must have the condition of equal relative angular momentum $r_1 w_{\theta 1} = r_2 w_{\theta 2}$. Thus the radial shift r_1 to r_2 does in fact influence also the aerodynamic work input and it would seem that a small measure of negative rotor deflection can still produce some pumping effect.

7.4   Geometrical techniques for dealing with design and analysis of mixed-flow cascades

As already discussed in the introduction to Chapter 2, the fully three-dimensional flow through axial turbomachines can be modelled with sufficient accuracy in most cases by a series of two-dimensional *blade-to-blade* or *cascade* flows superimposed upon a circumferentially averaged axisymmetric meridional flow. This strategy was illustrated in Fig. 2.1 for an axial fan located within a cylindrical annulus. The intersection of a cylindrical meridional stream surface with the blades then generates a cylindrical cascade which can be developed into an infinite rectilinear or *straight* cascade in the flat (x,y) plane, Fig. 2.2, by simply unwrapping the cylinder and laying it flat on the (x,y) plane.

Figure 7.11 illustrates the equivalent quasi-two-dimensional modelling of the much more complex three-dimensional flow through a mixed-flow turbomachine, in this case the Francis turbine previously considered in Section 7.2, Fig. 7.6(b). The circumferentially averaged meridional flow for this machine forms a series of coaxial stream surfaces of revolution between hub and shroud (casing), Fig. 7.11(a), which enter the inlet guide vanes radially and leave downstream of the runner axially. The annulus is designed to turn the flow from radial to axial in the zone occupied by the turbine runner, resulting in a wide range of geometries of the so-called elementary turbines located on each surface of revolution. Thus along the shroud meridional surface a–a the flow is predominantly that of an axial turbine. Along the hub stream surface b–b, on the other hand, the elementary turbine b–b is subject to a very large radial shift from r_1 to r_2 resulting in large loading contributions due to Coriolis forces.

A typical stream surface ψ_o somewhere in between the hub and shroud will intersect the guide-vanes and runner blades as illustrated in Fig. 7.11(b). The guide-vane blade profiles then form on this axisymmetric surface what is usually referred to as a radial (or circular) cascade, stationary in space. The runner blades, on the other hand, form a mixed-flow (sometimes called radial–axial) cascade rotating on the surface of revolution.

The geometrical complexity at first sight seems gross by comparison with the axial machine for which the equivalent two-dimensional cascade model in the (x,y) plane was so easily obtained, Fig. 2.2. In fact relatively simple geometrical transformations can be found to convert the radial or mixed-flow blade-to-blade geometry into equivalent straight cascades and the related procedures required to achieve this will

(a)   (b)
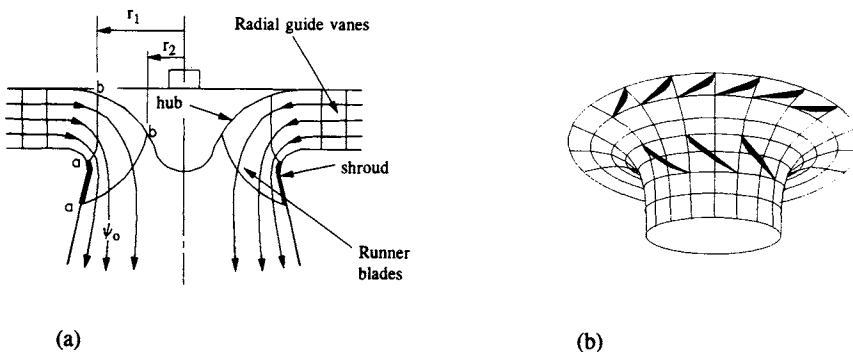
Fig. 7.11 Intersection of a meridional surface of revolution with the blade rows of a Francis turbine: (a) meridional streamlines; (b) surface of revolution for meridional streamline ψ_o

1. Selection of annulus geometry
Hub and casing shapes.
Leading and trailing edges of
blade rows (e.g. a–b in Fig. 7.11(a))

2. Meridional flow
Flow analysis resulting in
surfaces of revolution

3. Geometrical transformation
of each surface of revolution
into a flat plane with flow angles

4. Selection of straight cascades
in the flat planes to deliver
required flow angles and loading

5. Reverse transformation
of cascade geometry and flow data
back to the blade-to-blade intersections
on the surfaces of revolution

6. Recalculation of
meridional axisymmetric flow for
convergence check

no

convergence?

yes

Fig. 7.12 Flow diagram of overall design/selection of mixed-flow turbomachine blading

Fig. 7.13 Transformation of a mixed-flow cascade into an equivalent straight cascade: (a) mixed-flow cascade in the z-plane; (b) straight cascade in the ζ-plane

be derived in the next two subsections. Before moving on to consider these it may be helpful to summarise the overall design strategy needed for developing the blade geometry of mixed-flow turbines, pumps or fans, which is presented as a flow diagram in Fig. 7.12.

The key fluid-dynamic elements in any such complex iterative scheme are:

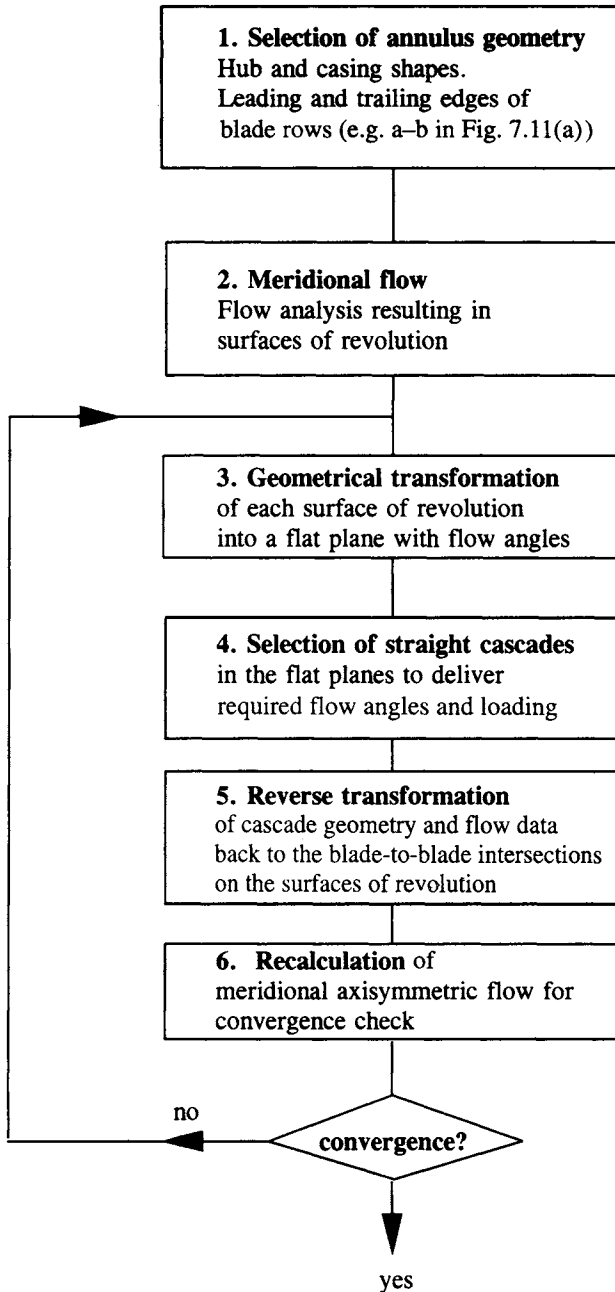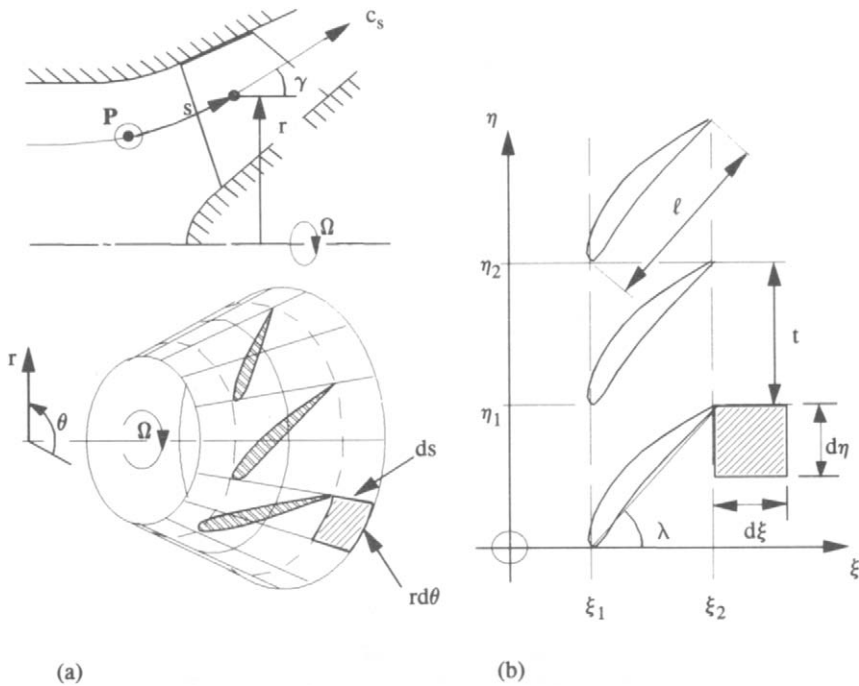(1) The design and analysis of mixed-flow cascades (boxes 3 to 5). This involves the handling of both the complex geometrical problem and the fluid flow analysis to ensure the correct aerodynamic performance, especially the fluid turning angle and consequent loading.
(2) Meridional flow analysis to determine the shapes of the surfaces of revolution and the distribution of the meridional velocity c_s.

The geometrical content of item (1) will be dealt with next, followed in Section 7.5 by an initial consideration of the fluid flow aspects of mixed-flow cascades. Full details of a theoretical fluid-dynamic design and analysis method for mixed-flow cascades have been given by the author elsewhere (Lewis, 1991). This technique is based on boundary integral modelling by the surface vorticity method, the foundations of which are developed in Chapter 9 for aerofoils and cascades and also for axisymmetric flows past bodies and ducts. Regarding item (2), some important fundamentals and governing equations for meridional flow have already been given in Chapters 5 and 6.

7.4.1   Conformal transformation of a mixed-flow cascade into an equivalent straight cascade

Figure 7.13 illustrates the transformation of a typical meridional stream surface of revolution (in the z-plane) into an infinite straight cascade (in the ζ-plane) for the case of a mixed-flow fan or pump. The equivalent axes in the two planes are as follows:

(1) Distance s measured along the meridional streamline from some datum P in the z-plane is equivalent to coordinate ξ in the ζ-plane.
(2) Circumferential distance $r\theta$ is equivalent to coordinate η.

If the complex variable $\zeta = \xi + i\eta$ is an analytic function $\zeta = f(z)$ of the complex variable $z = s + ir\theta$, not only the blade geometry but also the flow field in the z-plane may be transformed across to the ζ-plane or vice versa. The reader is referred to advanced fluid-dynamics texts such as Batchelor (1970) for a full treatment of conformal transformation. For the present purpose the condition of conformality may be described quite simply by reference to the two equivalent elementary areas $ds \cdot rd\theta$ and $d\xi \cdot d\eta$ shown in Fig. 7.13. For the transformation to be *conformal* these elements must be geometrically similar, that is

(1) The corner angles should be the same.
(2) Equivalent sides (such as ds and $d\xi$ or $rd\theta$ and $d\eta$) should bear a fixed ratio.

In both planes all corner angles are $\pi/2$ satisfying condition (1). Condition (2) may be stated as follows:

$$\frac{d\xi}{d\eta} \equiv \frac{ds}{rd\theta} \quad \text{(for conformality)} \tag{7.30}$$

Following Young (1958), this may be achieved by the separate coordinate transformations

$$\left.\begin{array}{l} d\xi = \dfrac{ds}{r} = \dfrac{1}{r\sin\gamma}\,dr \\[2mm] d\eta = d\theta \end{array}\right\} \tag{7.31}$$

where $\gamma = \sin^{-1}(dr/ds)$ is the local cone angle of the meridional streamline, Fig. 7.13. Integration of these equations gives us the direct coordinate transformations:

$$\left.\begin{array}{l} \xi = \displaystyle\int \dfrac{1}{r}\,ds = \int \dfrac{1}{r\sin\gamma}\,dr \\[2mm] \eta = \theta \end{array}\right\} \tag{7.32}$$

From the second of these equations it is clear that the mixed-flow cascade of say Z blades transforms into an infinite straight cascade in the ζ plane stretching between $\eta = \pm\infty$ and of pitch

$$t = \frac{2\pi}{Z} \tag{7.33}$$

Equation (7.32a) may be integrated numerically if γ is specified as a function of r. On the other hand for true conical surfaces with angle $\gamma = $ constant, Eqn (7.32) becomes

$$\left.\begin{array}{l} \xi = \dfrac{1}{\sin \gamma} \ln (r) \\[3mm] \eta = \theta \end{array}\right\} \tag{7.34}$$

7.4.2 Pitch/chord ratio and stagger of a mixed-flow cascade

At first sight the awkward geometry of a mixed-flow cascade would seem to rule out the definition of representative pitch/chord ratio and stagger, Fig. 7.13(a). This problem is resolved by the transformation method. Thus in the transformed ζ-plane, Fig. 7.13(b), the blade chord is given by $l = (\xi_2 - \xi_1)/\cos\lambda$, and making use also of Eqn (7.33), the pitch/chord ratio becomes

$$\left.\begin{array}{l} \dfrac{t}{l} = \dfrac{2\pi \cos \lambda}{Z(\xi_2 - \xi_1)} \\[4mm] \quad = \dfrac{2\pi \cos \lambda \sin \gamma}{Z \ln (r_2/r_1)} \end{array}\right\} \tag{7.35}$$

The stagger angle λ can be calculated from the given leading and trailing edge coordinates of the mixed-flow blade row (r_1, θ_1) and (r_2, θ_2) by reference again to the transformed cascade in the ζ-plane:

$$\tan \lambda = \frac{\eta_2 - \eta_1}{\xi_2 - \xi_1} = \frac{(\theta_2 - \theta_1) \sin \gamma}{\ln (r_2/r_1)} \tag{7.36}$$

Example 7.2

Problem
Calculate λ and t/l for a mixed-flow cascade given the following data, as in Fig. 7.13:

Number of blades $Z = 8$, $\gamma = 30°$

$$
\begin{array}{lll}
r_1 = 50 \text{ mm} & \theta_1 = 0 & \text{(leading edge coordinates)} \\
r_2 = 75 \text{ mm} & \theta_2 = 45° & \text{(trailing edge coordinates)}
\end{array}
$$

Solution
From Eqn (7.36)

$$\lambda = \tan^{-1}\left\{\frac{45 \times \dfrac{\pi}{180} \times \sin 30°}{\ln(75/50)}\right\} = 44.084°$$

From Eqn (7.35)

$$\frac{t}{l} = 0.6957$$

7.4.3 Axial and radial blade rows

Axial and radial blade rows are special cases of the mixed-flow cascade for which the cone angle γ is equal to zero and $\pi/2$ respectively.

Axial blade rows
Thus for an axial blade row, since the stream surface is cylindrical, $r = $ constant, the transformation Eqns (7.32) reduce to

$$\xi = \frac{x}{r}, \quad \eta = \frac{(r\theta)}{r} \tag{7.37}$$

As illustrated by Fig. 2.2 and discussed already in Chapter 2, this is equivalent to simply unwrapping and flattening out the cylindrical meridional surface, generating identical blade profile geometry in the ζ-plane.

Radial guide vanes
For radial cascades, on the other hand, Eqns (7.34) are applicable and setting $\gamma = \pi/2$ we obtain

$$\xi = \ln(r), \quad \eta = \theta \tag{7.38}$$

The analytical relationship between the complex coordinates $\zeta = f(z)$ may now be determined since

$$\begin{aligned} \zeta &= \xi + i\eta = \ln r + i\theta = \ln(r\, e^{i\theta}) \\ &= \ln z \end{aligned} \tag{7.39}$$

which is a very well-known conformal transformation between Cartesian and polar coordinate systems.

The application of this log transformation to a straight cascade of turbine blades is shown in Fig. 7.14. In this case the fluid flows from right to left in the ζ-plane in order to simulate a set of radial inflow guide vanes such as might be used at entry to the Francis turbine previously shown in Fig. 7.11. The straight cascade shown here was designed using the program STACK with a stagger of $\lambda = 45°$, a circular arc camber with angle $\theta = 30°$ and pitch/chord ratio $t/l = 1.0$. The circular cascade was transformed from this by embedding the above coordinate transformations into a Quattro Pro spreadsheet.

Velocity transformation
For *stator* cascades such as this inlet guide-vane blade row, it is also possible to transform the complex velocity in the ζ-plane $q_\zeta = u_\zeta + iv_\zeta$ from the straight cascade to its value $q_z = u_z + iv_z$ at the equivalent point in the z-plane. By introducing the complex potential $\omega = \phi + i\psi$ the following general relationship is then applicable (Batchelor, 1970):

$$\begin{aligned} u_z - iv_z &= \frac{d\omega}{dz} = \frac{d\omega}{d\zeta}\frac{d\zeta}{dz} \\ &= (u_\zeta - iv_\zeta)\frac{d\zeta}{dz} \end{aligned} \tag{7.40}$$
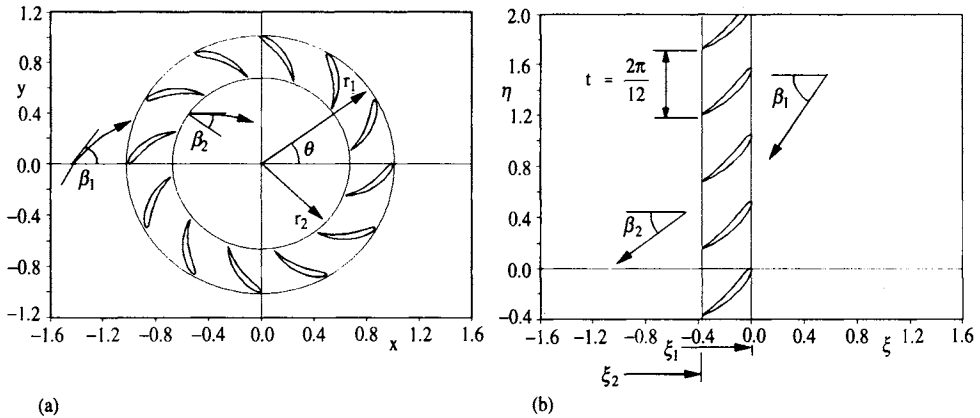
Fig. 7.14 Transformation of a set of radial inflow guide vanes into an equivalent straight cascade (a) radial guide vanes in the z-plane; (b) transformed straight cascade in the ζ-plane

But from Eqn (7.39) $d\zeta/dz = 1/z$, and the last equation then reduces to

$$q_z = \frac{1}{r} q_\zeta \tag{7.41}$$

Thus velocities calculated by straight cascade analysis in the ζ-plane can be transformed across to the radial cascade simply scaled by $1/r$.

For *rotors*, on the other hand, an allowance must be made for the 'relative rotation' in fluid dynamic analyses. This matter is too complex to be dealt with here but has been discussed in detail by Lewis (1966, 1991) and is handled by the author's software MIXEQU. The physical nature of the 'relative eddy' or 'slip' flow will be discussed next.

7.5 Relative eddy and slip flow in radial and mixed-flow turbomachines

As early as 1928 Busemann published his classic paper on prediction of the flow through centrifugal pump rotors with logarithmic spiral blades, using conformal transformation theory. It was already fully realised that the flow viewed relative to a centrifugal pump or fan is strongly influenced by the so-called 'relative eddy' which is introduced when transforming from stationary coordinates to a system which rotates with the rotor. For example, consider the simple radial bladed centrifugal impeller illustrated in Fig. 7.15.

Let us assume that the flow enters without swirl, $c_{\theta 1} = 0$, and is thus irrotational, Fig. 7.15(a). Adopting polar coordinates (x, r, θ) which are stationary relative to the laboratory, the vorticity ω will be zero. From its definition, Eqn (6.10a), we then have

$$\omega = \frac{\partial c_\theta}{\partial r} + \frac{c_\theta}{r} - \frac{1}{r}\frac{\partial c_r}{\partial \theta} = 0 \tag{7.42}$$

with the sign convention that both ω and the rotor angular velocity Ω are defined as anticlockwise positive.
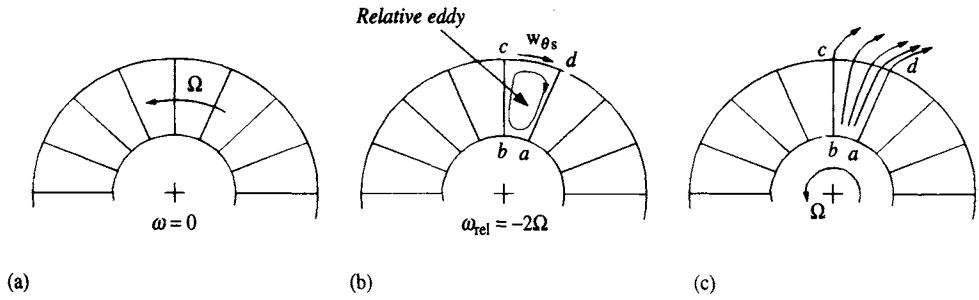
Fig. 7.15 Relative eddy and slip flow in a radial bladed pump impeller: (a) zero vorticity ω in stationary coordinates; (b) vorticity ω_{rel} in rotating coordinates and relative eddy; (c) streamline flow relative to blade passage *abcd*

Let us now consider the flow as viewed by an observer sitting on and travelling with the rotor. The velocity components (w_r, w_θ) relative to his coordinate system which rotates with the rotor are related to those in the stationary coordinates (c_r, c_θ) through Eqns (7.10b) and (7.10c). Introducing these into Eqns (7.42) results in the following expression for the relative vorticity ω_{rel} as seen by the observer:

$$\omega_{\text{rel}} = \frac{\partial w_\theta}{\partial r} + \frac{w_\theta}{r} - \frac{1}{r}\frac{\partial w_r}{\partial \theta} = -2\Omega \tag{7.43}$$

Thus viewed relative to the rotor the entire flow field is filled with vorticity ω_{rel} of strength 2Ω, i.e. double the rotor angular velocity Ω but clockwise in direction. Because of this, the packet of fluid contained within any blade passage such as *abcd*, Fig. 7.15(b), being temporarily cut off from fluid in neighbouring blade passages, tends to rotate in the clockwise sense as illustrated, producing the slip velocity $w_{\theta s}$ along the exit line *cd*. Superimposing the throughflow on top of this the streamline pattern of the relative flow will be similar to that illustrated in Fig. 7.15(c). Instead of leaving radially parallel to the blades, the flow slips backwards in the direction opposite to rotation, resulting in a reduction in the anticipated head rise. To account for this the slip factor may be defined as follows:

$$\sigma = \frac{\text{Actual swirl velocity at rotor exit } c_{\theta 2}}{\text{Swirl velocity with perfect guidance by the blades } c'_{\theta 2}} \tag{7.44}$$

where $c'_{\theta 2}$ is based on the ideal machine in which the relative flow at exit follows the blade direction exactly. Thus for radially bladed machines $c'_{\theta 2} = U_2 = r_2 \Omega$ and the slip factor becomes

$$\sigma = \frac{U_2 - w_{\theta s}}{U_2} = 1 - \frac{w_{\theta s}}{U_2} \tag{7.45}$$

The slip factor will thus always be less than unity and provides a simple basis for implementing the relative eddy slip flow correction. Thus from the Euler pump equation (7.1) the predicted frictionless head rise becomes

$$h_{o2} - h_{o1} = U_2 c_{\theta 2} = \sigma U_2 c'_{\theta 2} \tag{7.46}$$

where $c'_{\theta 2}$ assumes *perfect guidance by the blades* at exit from the rotor.
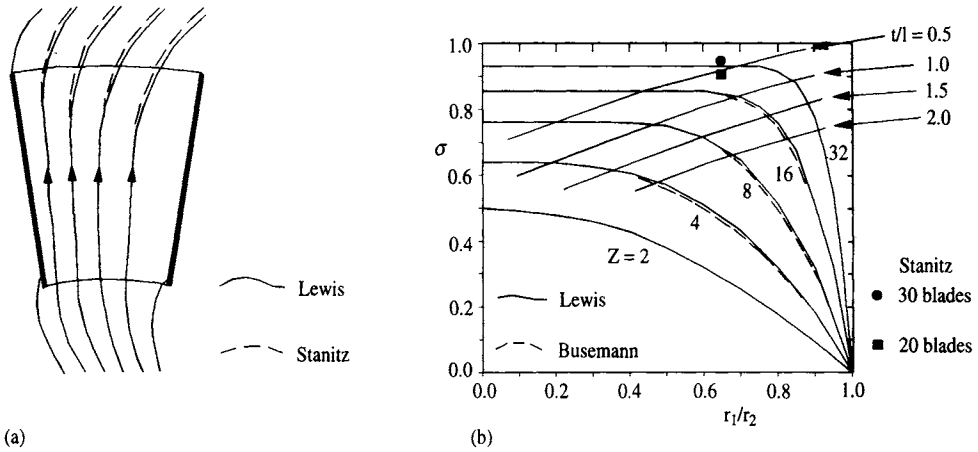
Fig. 7.16 Typical streamline pattern for a radial bladed centrifugal impeller and predictions of slip factor for a wide range of geometries and blade numbers: (a) streamline pattern with 20 blades; (b) slip factors for range of geometries

7.5.1 Predicted slip factors for radial bladed centrifugal machines

Theoretical analyses of radial bladed rotors were undertaken by Stanitz (1952) using finite difference methods and by Lewis (1966) by conformal transformations, both methods permitting the prediction of streamline patterns. Results are compared in Fig. 7.16 for a 20-bladed rotor with radius ratio $r_1/r_2 = 0.65$. Stanitz imposed a boundary condition of radial entry flow at r_1. Lewis's method, on the other hand, modelled the entry flow also and Fig. 7.16(a) shows the predicted flow with prewhirl put equal to the blade speed, $c_{\theta 1} = r_1 \Omega$. The methods are in good agreement and reveal strong slip flow at the rotor exit. Predicted slip factors according to Lewis's theory are compared with the results of Busemann (1928) in Fig. 7.16(b) for a very wide range of radial bladed impellers but with zero prewhirl, $c_{\theta 1} = 0$, showing excellent agreement. Two cases calculated by Stanitz are also shown and are found to be in good agreement. Although Stanitz assumed the presence of prewhirl $c_{\theta 1} = r_1 \Omega$ for these cases, the blades are sufficiently tightly packed for the entry flow at r_1 to exercise almost insignificant influence over the exit flow at r_2.

Of special interest in relation to this last point are the contours of constant pitch/chord ratio superimposed upon Fig. 7.16(b). These were obtained from Eqn (7.35), introducing $\gamma = \pi$ (for radial meridional flow) and $\lambda = 0$ (zero stagger for radial blades). For $t/l < 1.0$ the slip factor σ is almost constant for a given number of blades as r_1/r_2 is reduced. For $t/l > 1.0$, on the other hand, the slip factor falls off considerably as either (a) the number of blades is reduced or (b) r_1/r_2 is increased. This behaviour pattern is much in line with that of axial cascades as discussed in Chapter 4, Section 4.8 in relation to fans. As a general rule it is advisable to select the blade number Z and the radius ratio r_1/r_2 such that $t/l < 1.0$ in order to maintain high slip factors and thus high head rise. For radial bladed machines this design constraint can be fed into Eqn (7.36) to give recommended minimum blade numbers, namely

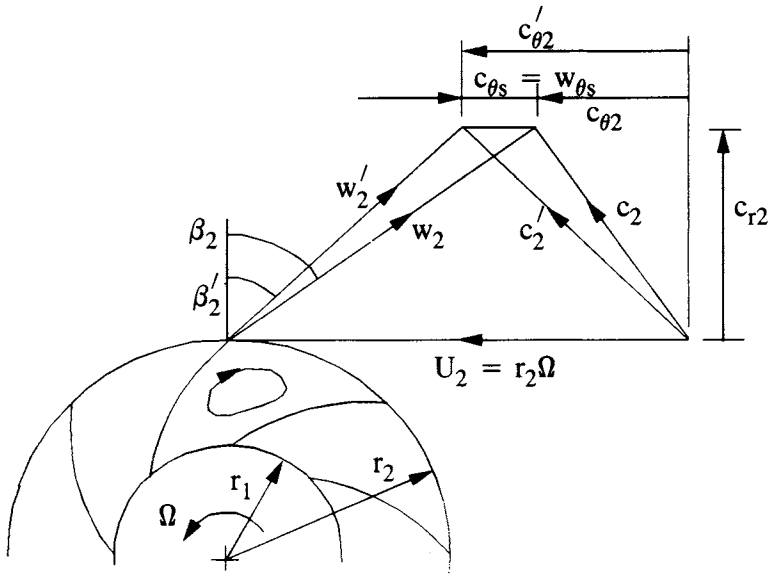$$Z > \frac{2\pi}{\ln(r_2/r_1)} \quad \text{(for } t/l < 1.0) \tag{7.47}$$

Fig. 7.17 Velocity triangles for a swept-back centrifugal impeller with blade angle β_2'

7.5.2 Slip factors for swept-back centrifugal impellers

A typical centrifugal pump impeller and its exit velocity triangles are shown in Fig. 7.17 with blade exit angle β_2' leaning backwards in the opposite direction to rotation Ω. Due to the influence of the relative eddy, however, the actual efflux angle β_2 will be greater than β_2'. Constructing the velocity triangles the effect of slip is to reduce the exit swirl by the slip velocity $c_{\theta s}$. The previous definition of slip factor, Eqn (7.44), is still valid and for swept-back impellers it becomes

$$
\left.
\begin{aligned}
\sigma = \frac{c_{\theta 2}}{c_{\theta 2}'} &= 1 - \frac{c_{\theta s}}{c_{\theta 2}'} = 1 - \frac{c_{\theta s}}{U_2 - c_{r2}\tan\beta_2'} \\
&= 1 - \frac{c_{\theta s}/U_2}{1 - \phi\tan\beta_2'}
\end{aligned}
\right\}
\tag{7.48}
$$

The slip factor is thus generally dependent upon two parameters, namely

(1) The dimensionless slip velocity $c_{\theta s}/U_2$ – that is, the slip velocity as a fraction of the tip blade speed U_2.
(2) The flow coefficient $\phi = c_{r2}/U_2$ based on exit radial velocity c_{r2}.

First we should take notice that item (2) does not apply for radially bladed rotors since β_2' is then zero and Eqn (7.48) reduces to

$$
\sigma = 1 - \frac{c_{\theta s}}{U_2} \quad \text{(for radial blades only)}
\tag{7.49}
$$

In this case Busemann's theoretically predicted σ values, Fig. 7.16(b), are applicable irrespective of the flow coefficient ϕ.
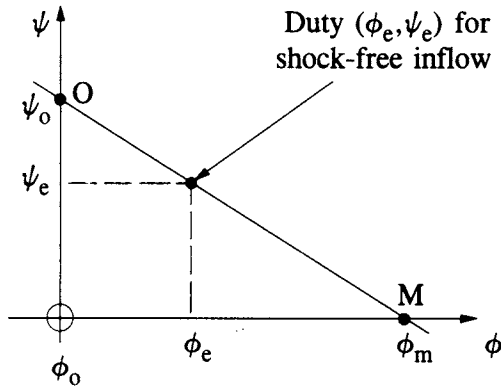
Fig. 7.18 Dimensionless head-flow characteristic for a backward-swept centrifugal rotor

Secondly, we can deduce from the earlier discussion of the physical origin of relative eddy flows that the magnitude of the slip velocity $c_{\theta 2} = w_{\theta s}$ is dependent mainly upon the relative vorticity 2Ω and the blade passage shape, Section 7.5.[1] Thus for a constant speed characteristic $\phi = c_{r2}/U_2$ versus $\psi = gh/U_2^2$, since Ω is constant the dimensionless slip factor $c_{\theta s}/U_2$ can be determined from any convenient duty (ϕ, ψ). The obvious choice of duty to make is the 'shut-off' head h_o for which the flow coefficient is zero, $\phi_o = 0$. From Eqn (7.49) we then have

$$\frac{c_{\theta s}}{U_2} = 1 - \sigma_o \qquad (7.50)$$

where σ_o is the slip factor for zero mass flow. Introducing this into Eqn (7.48), the slip factor for any other flow rate ϕ becomes

$$\sigma = \frac{\sigma_o - \phi \tan \beta_2'}{1 - \phi \tan \beta_2'} \qquad (7.51)$$

The dimensionless characteristic (ϕ, ψ) curve for the impeller is illustrated in Fig. 7.18, in which point O is the shut-off head duty $\phi = 0$, $\psi = \psi_o$. Its equation follows from the Euler pump equation since

$$\psi = \frac{gh}{U_2^2} = \frac{c_{\theta 2}}{U_2} \quad \text{(for zero prewhirl machines)}$$

$$= \frac{\sigma c_{\theta 2}'}{U_2} = \sigma \left(1 - \frac{w_{\theta 2}'}{U_2} \right) = \sigma(1 - \phi \tan \beta_2') \qquad (7.52)$$

Introducing Eqn (7.51) into this, we have finally the alternative expression for the constant speed characteristic curve in terms of the shut-off head slip factor σ_o:

$$\psi = \sigma_o - \phi \tan \beta_2' \qquad (7.53)$$

---

[1]We will return to this assumption later at the end of Section 7.5.3.

Z = number of blades	Vane angle β is measured from radial direction
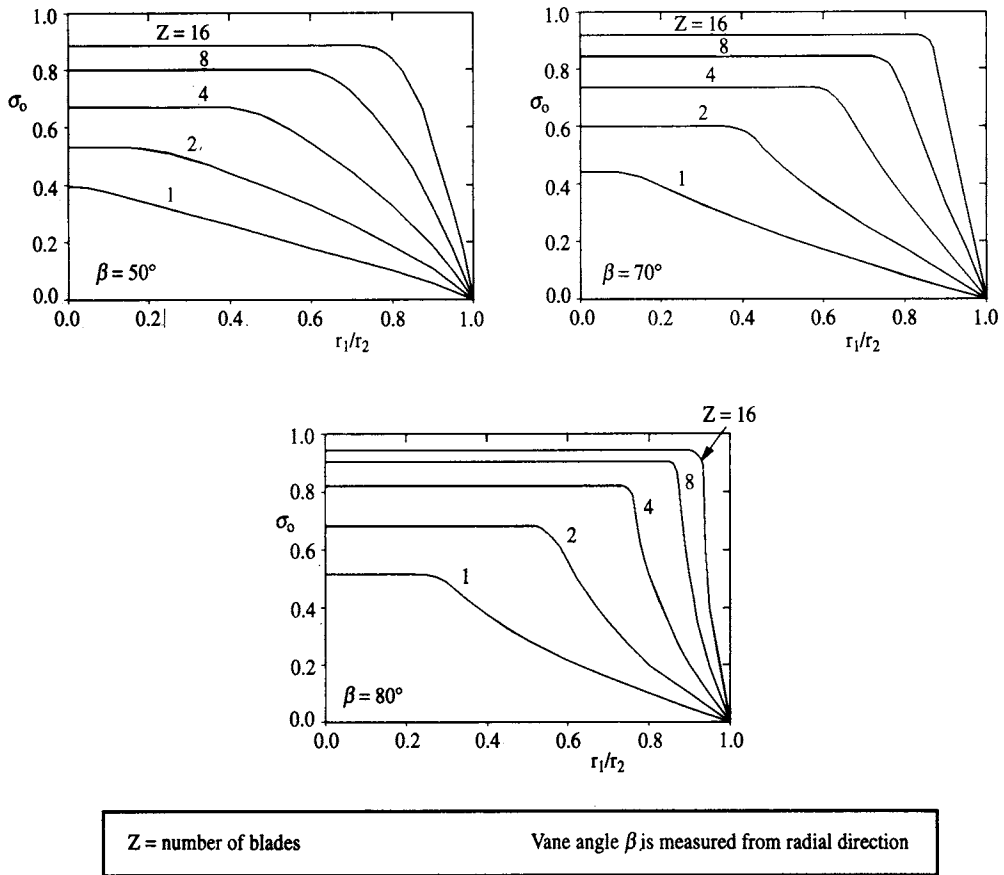
Fig. 7.19 Predicted shut-off head slip factors σ_o for swept-back centrifugal impellers, after Busemann (1928)

Thus the theoretical frictionless characteristic (losses have been ignored here) is linear and is determined by the vane angle β_2' and the shut-off head coefficient ψ_o, which, from Eqn (7.53), is given by $\psi_o = \sigma_o$.

The maximum flow which can be delivered at point M on the characteristic, Fig. 7.18, is thus for the condition $\psi = 0$, namely

$$\phi_M = \sigma_o/\tan \beta_2' \qquad (7.54)$$

Busemann (1928), in his comprehensive foundation paper on this subject, gave shut-off head slip factors for a wide range of vane angles for centrifugal impellers with logarithmic-spiralled blades (i.e. with constant vane angle $\beta = \beta_2'$ from leading edge to trailing edge). Figure 7.16(b) shows Busemann's results for the special case $\beta = 0°$ for radial blades. A selection of his predicted data for vane angles in the useful range for swept-back rotors is shown in Fig. 7.19 for $\beta = 10°$, 20° and 40°. Busemann's classical model as given was restricted to infinitely thin log-spiral blades. It is possible to extend his method to a family of blades with finite profile thickness and camber as shown by Fisher and Lewis (1972) for the case of radial blades, but these are of

Z = number of blades	Vane angle β is measured from radial direction
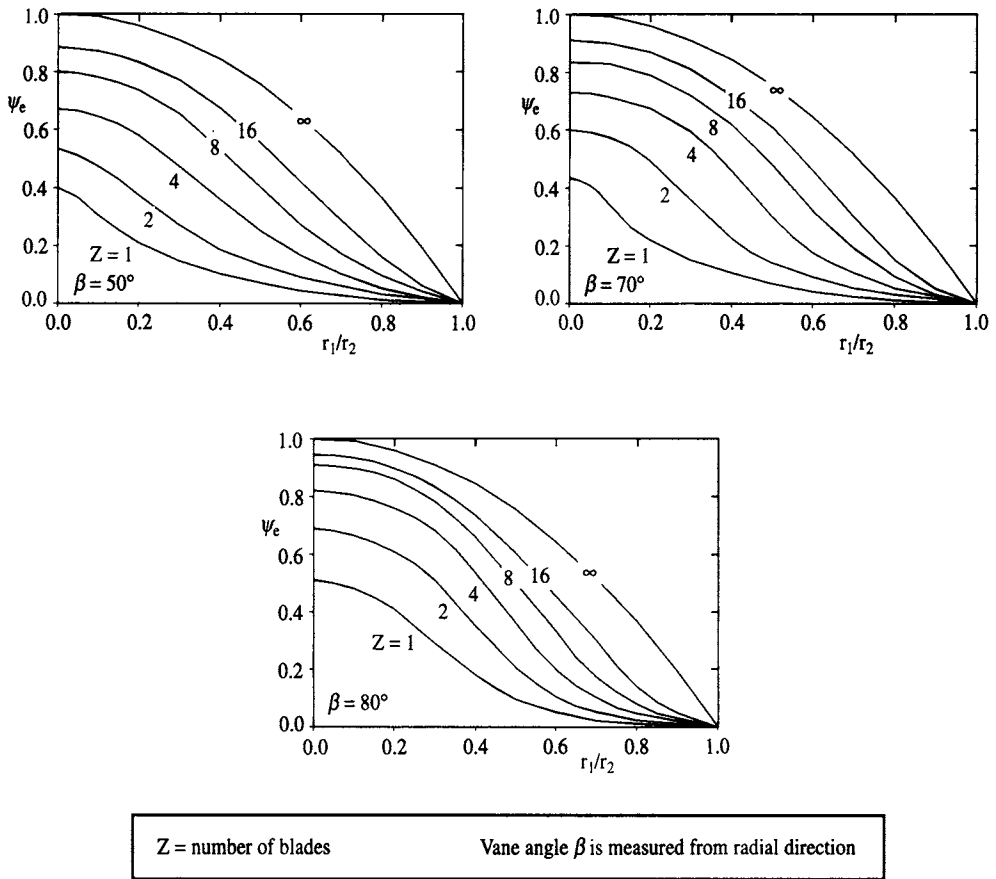
Fig. 7.20 Predicted work coefficients for swept-back centrifugal impellers with shock-free inflow, after Busemann (1928)

limited scope. An alternative, extremely powerful and flexible numerical method for dealing with radial or mixed flow rotors of arbitrary profile shape was published in full by Fisher (1975) and reviewed in brief by Lewis, Fisher and Saviolakis (Lewis *et al.*, 1972). This method, which employs boundary integral modelling techniques, includes the influence of relative eddy and slip flow and has been validated against exact solutions and experimental test. The author has more recently reviewed this in depth (Lewis, 1991) and developed PC software for design and analysis of arbitrary mixed flow turbomachines including a simple meridional analysis.

7.5.3 Shock-free inflow data for swept-back centrifugal impellers

As explained already in Section 2.6, the term 'shock-free inflow' refers to the optimum inlet angle β_1 at entry to a blade row for which the stagnation point is located exactly on the leading edge resulting in smooth entry flow and hence low losses. This will correspond to some duty point (ϕ_e, ψ_e), Fig. 7.18, for which the entry aerodynamics are optimum and the efficiency is therefore likely to be close to its maximum value. (ϕ_e, ψ_e) would thus be a sensible choice for design duty. To help

with design duty selection Busemann used his theoretical analysis to produce the curves shown in Fig. 7.20.

For a given vane angle β, number of blades Z and radius ratio r_1/r_2, the work coefficient for shock free inflow ψ_e has a unique value available from these curves. The corresponding flow coefficient ϕ_e then follows from the characteristic curve, Eqn 7.53, namely

$$\phi_e = (\sigma_o - \psi_e)/\tan \beta_2' \qquad (7.55)$$

As already stated, Busemann's data, both Figs 7.19 and 7.20, are applicable only to rotors with thin backward-swept log-spiral blades and with zero prewhirl, $c_{\theta 1} = 0$. Numerical methods such as the author's MIXEQU computer code are able to lift these restrictions totally and provide accurate (although only frictionless) design/analysis facilities for the whole range of radial or mixed-flow fans or turbines, usually with incompressible flow. An example will help to illustrate the use of the above analysis.

Example 7.3

Problem
A centrifugal pump has eight log-spiral blades with vane angle $\beta = 70°$ and radius ratio $r_1/r_2 = 0.6$. Use the above data and analysis to estimate the following:
(1) The shut-off work coefficient ψ_o.
(2) The maximum flow coefficient ϕ_M.
(3) The shock-free duty (ϕ_e, ψ_e).
For shock-free flow calculate the relative inlet and outlet angles, β_1 and β_2, and the slip factor σ_e.

Solution
(1) From Fig. 7.19, $\sigma_o = 0.85$.
(2) From Eqn (7.54),

$$\phi_M = \sigma_o/\tan \beta_2' = 0.85/\tan 70° = 0.309\,37$$

(3) From Fig. 7.20, $\psi_e = 0.33$, and thus from Eqn (7.53) (the characteristic curve),

$$\phi_e = (\sigma_o - \psi_e)/\tan \beta_2' = 0.1893$$

Calculation of β_1

$$\tan \beta_1 = \frac{r_1 \Omega}{c_{r1}} = \frac{r_2 \Omega}{c_{r2}} \times \frac{c_{r2}}{c_{r1}} \times \frac{r_1}{r_2} = \frac{1}{\phi}\left(\frac{r_1}{r_2}\right)^2$$

Hence $\beta_1 = 62.26°$.
Calculation of β_2

$$\tan \beta_2 = \frac{w_{\theta 2}}{c_{r2}} = \frac{U_2 - c_{\theta 2}}{c_{r2}} = \frac{U_2 - \psi U_2}{c_{r2}} = \frac{1 - \psi}{\phi}$$

Hence $\beta_2 = 74.22°$.

Note that the relative eddy increases β_2 but decreases β_1 as compared with the vane angle β for the case of shock-free inflow.

From Eqn (7.51) the slip factor for shock-free inflow is

$$\sigma_e = \frac{0.85 - 0.1893 \tan 70°}{1 - 0.1893 \tan 70°} = 0.6874$$

Reconsideration of the assumption regarding $c_{\theta s}$

In Section 7.5.2 a crucial assumption was made regarding the slip velocity $c_{\theta s}$ that led to simplifications, namely that the slip velocity 'is dependent mainly upon the relative vorticity 2Ω and the blade passage shape'. Now c_θ is vectorially equal to $w_2 - w_2'$, Fig. 7.17. Thus the slip velocity represents the departure of the actual exit velocity relative to the rotor from the actual blade exit angle. Clearly this is influenced by the relative eddy 2Ω but also by any variation of the inflow angle β_1 at different flow coefficients. As was shown in Chapter 2 for straight cascades, the outlet angle β_2 will depend upon the inlet angle β_1 (in this case with no relative eddy for the straight cascade), but significantly so only if the pitch/chord ratio is greater than unity. Applying this to centrifugal machines, the foregoing analysis and use of Busemann's data is therefore valid provided $t/l < 1$. From Eqn (7.35) this is satisfied for log-spiral blades if

$$\frac{2\pi \cos \beta}{Z \ln(r_2/r_1)} < 1.0 \tag{7.56}$$

In most practical designs t/l will be less than unity and the above procedures are then justified. The full Busemann analysis does not in fact require this assumption but is rather more complex and difficult to apply.

7.6 Some other slip factor formulations for radial and mixed-flow fans and pumps

One of the earliest slip factor formulations was proposed by Stodola (1927) based upon the assumption which was qualified in the last paragraph. Referring to Fig. 7.21, Stodola assumes that the slip velocity $c_{\theta s}$ is approximately equal to the circulation velocity around the throat circle C of diameter d due to the relative eddy. Thus

$$\text{Circulation} \approx (\text{vorticity inside circle}) \times \text{area}$$

or
$$c_{\theta s} \pi d \approx 2\Omega \pi \frac{d^2}{4}$$

The diameter d may also be approximated by

$$d \approx t_2 \cos \beta_2' \approx \frac{2\pi r_2}{Z} \cos \beta_2'$$

where t_2 is the circumferential pitch at radius r_2. Combining these equations we have finally

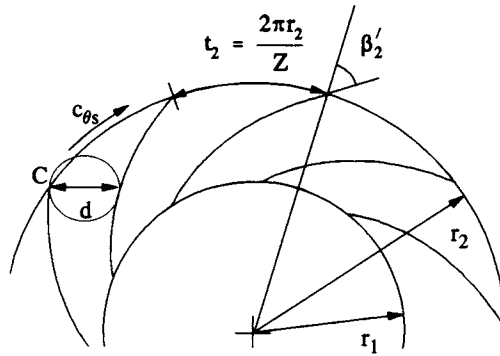$$c_{\theta s} = \frac{\pi r_2 \Omega \cos \beta_2'}{Z}$$

Fig. 7.21 Throat section of swept-back impeller

and from Eqn (7.48) the slip factor approximates to

$$\sigma = 1 - \frac{(\pi/Z)\cos\beta_2'}{1 - \phi\tan\beta_2'} \qquad \text{(Stodola)} \quad (7.57)$$

Stanitz (1952) undertook a remarkably thorough and penetrating theoretical study of centrifugal and mixed-flow compressors by finite difference modelling, concentrating mainly on radially bladed machines but including some studies with modest sweep-back angles β of 26.56° and 45°. In addition to slip factors his analysis delivered detailed streamline predictions, such as that shown already in Fig. 7.16(a), for various flow coefficients and also blade surface velocity distributions indicating the presence of a standing eddy with reversed flow at low ϕ values and the special influence of compressibility. According to his findings the slip velocity $c_{\theta s}$ was dependent upon blade number Z only, and the earlier expression of Stanitz and Ellis (1950) was justified irrespective of vane angle β, namely

$$c_{\theta s} = 0.63 r_2 \Omega \pi/Z$$

so that the slip factor, Eqn (7.48), can then be expressed as

$$\sigma = 1 - \frac{0.63\pi/Z}{1 - \phi_2\tan\beta_2'} \qquad \text{(Stanitz)} \quad (7.58)$$

Although compressibility was found to influence his predicted streamline patterns within the blade passage, Stanitz found its influence upon slip factor to be negligible for the cases considered.

7.6.1 Slip factors for mixed-flow fans and pumps

Lewis (1966) derived exact conformal transformation solutions for mixed-flow turbomachines with straight blades of zero stagger. This analysis was later extended by Fisher and Lewis (1972) to profiled symmetrical or cambered blades. Although there is a lack of data on slip factors for mixed-flow machines, these analyses have established that a correct estimate of σ for a mixed-flow fan or pump with cone angle

γ, Fig. 7.13, is given by that for an equivalent radial machine with M blades where

$$M = \frac{Z}{\sin \gamma} \tag{7.59}$$

This follows directly from the conformal transformation theory outlined in Section 7.4.1, although in this case transforming the mixed-flow cascade into an equivalent radial (rather than straight) cascade. The analysis of Stanitz (1952) confirms this approach. Thus all of the foregoing formulations may be applied directly to mixed-flow pumps and fans.

8
Ducted propellers and fans

Introduction

The main function required of the various turbomachines considered so far is the rotodynamic transfer of energy between an impeller and the fluid passing through a carefully prescribed constraining annulus such as that of the mixed-flow fan illustrated in Fig. 8.1(a). In the case of a pump or fan the requirement is to move a given volume flow rate of fluid while at the same time increasing its stagnation pressure or enthalpy, these two tasks being typified by the related duty coefficients (ϕ, ψ) as defined by Eqns (4.2) and (4.4).

The ship or aircraft propeller is no less a rotodynamic pumping device by means of which shaft input work may be converted into energy increase of the through-flow fluid. As illustrated by Fig. 8.1(b), however, the operational requirements of a propeller are usually quite different from those of an axial or mixed-flow fan, even though the blade shapes and the aerodynamic/rotodynamic mechanisms are very similar. Firstly propellers operate in 'open water' so that the energised fluid is finally delivered at ambient pressure p_∞. Secondly the main purpose of a propeller is usually the production of thrust for the purpose of propulsion. This is achieved in reaction to the momentum developed by the jet exit velocity V_j as a result of the energy transferred to the fluid. The basic principles underlying this will be elaborated in Section 8.1 including a suitable definition of propulsive efficiency.

The ducted propeller or fan illustrated in Fig. 8.2(a) sits half-way between these two extremes. Firstly, such devices are required to operate in the 'open water' situation and to deliver thrust in reaction to a fluid jet V_j delivered finally at ambient pressure. On the other hand the propeller is now located within a duct of short length. Although the duct in a sense fulfils the role of the turbomachine annulus casing in guiding the fluid through the blade space, its primary duty is much more important
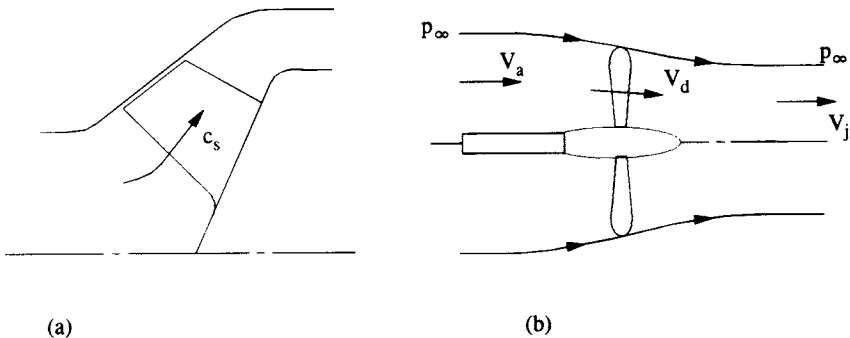

Fig. 8.1 Turbomachine and propeller configurations: (a) mixed-flow fan; (b) open propeller
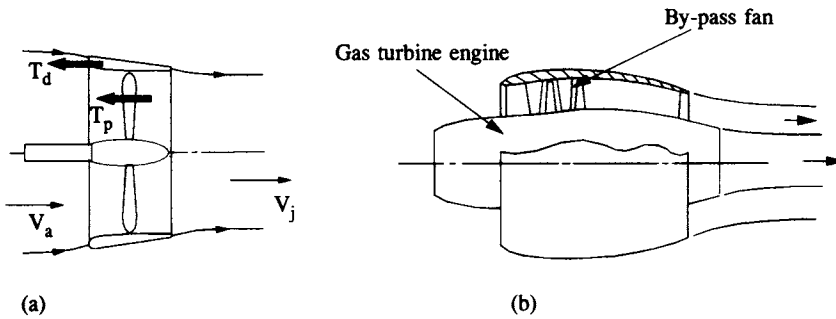
Fig. 8.2 Ducted propeller and by-pass fan configurations: (a) ducted propeller or fan; (b) by-pass engine

and complex than this. For ducted propulsors the total forward thrust T is shared between the propeller T_p and the duct T_d. Typically in a highly loaded unit the duct may actually supply as much as 30% of the total thrust. The benefit of this feature is twofold, namely (a) an increase in the total possible achievable thrust for a given propeller diameter and (b) an increase in propulsive efficiency. The basic principles underlying this will be explained in Section 8.2. A design and performance analysis will be developed in Sections 8.3 and 8.4 including a discussion of the main fluid dynamic loss mechanisms and related analysis. A simple method for prediction of the off-design performance characteristics will be developed in Section 8.5.

8.1   One-dimensional actuator disc performance analysis for open propellers

Figure 8.3 depicts the flow viewed relative to a propeller and illustrates the slipstream contraction associated with the progressive rise of the through-flow velocity from V_a a long way upstream to V_{jo} in the downstream jet. For simplicity we shall assume here that the specific work input and consequent stagnation enthalpy (compressible fluids) or stagnation pressure (incompressible fluids) is the same for all streamlines passing through the area swept out by the propeller and that the through-flow velocity rises to V_{po} in the plane of the propeller. Applying Newton's second law, the propeller thrust is then given by

$$T_p = \dot{m}(V_{jo} - V_a) \tag{8.1}$$

where the mass flow rate $\dot{m}$ through the propeller is given by

$$\dot{m} = \rho \frac{\pi D^2}{4} V_{po} \tag{8.2}$$

and where for simplicity we are neglecting the area occupied by the propeller hub. Thus

$$T_p = \rho \frac{\pi D^2}{4} V_{po}(V_{jo} - V_a) \tag{8.3}$$
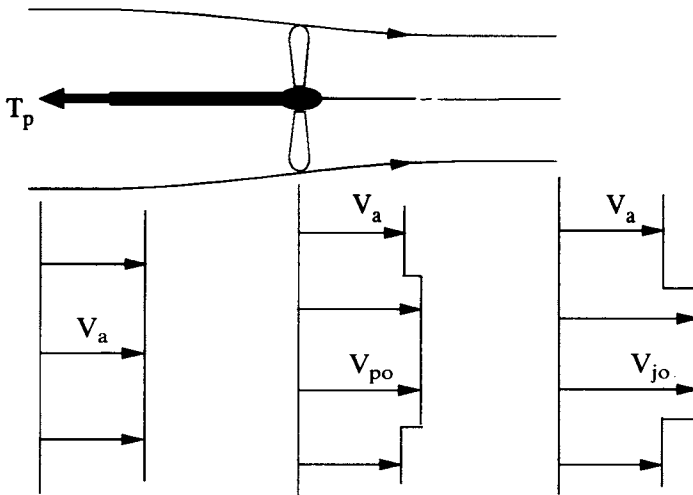
Fig. 8.3 Development of an open propeller jet flow

Alternatively we may obtain an equally valid but different expression for thrust in terms of the pressure rise $p_2 - p_1$ across the propeller. At this point it is appropriate to model the propeller by an equivalent actuator disc as illustrated in Fig. 8.3 and as discussed in Section 5.4 in relation to axial fans. The pressure force acting on the disc is then given by

$$T_p = (p_2 - p_1)\frac{\pi D^2}{4} \qquad (8.4)$$

Let us consider the case of inviscid incompressible flow. In many propeller applications the swirl velocity in the wake will also be small compared with V_{jo}, whereupon we may appeal to the energy equation in the form of Bernoulli's equation, from which

$$p_2 - p_1 = \tfrac{1}{2}\rho(V_{jo}^2 - V_a^2) \qquad (8.5)$$

In other words the pressure rise introduced by the actuator disc is finally converted into increased kinetic energy in the wake. Combining Eqns (8.4) and (8.5)

$$\begin{aligned} T_p &= \frac{\rho\pi D^2}{8}(V_{jo}^2 - V_a^2) \\ &= \frac{\rho\pi D^2}{8}(V_{jo} - V_a)(V_{jo} + V_a) \end{aligned} \qquad (8.6)$$

Eliminating T_p from Eqns (8.3) and (8.6), the following result is obtained for flow through an open propeller actuator disc:

$$V_{po} = \tfrac{1}{2}(V_a + V_{jo}) \qquad (8.7)$$

and thus we see that the relative through-flow velocity V_{po} in the plane of the actuator disc is the average of the relative velocities V_a and V_{jo} at $x = \pm\infty$.

Various dimensionless parameters have been defined for handling propeller performance analysis but of particular importance are the *thrust coefficient* C_{To} and the *propulsive efficiency* η_{p}. C_{To} is defined as

$$C_{\text{To}} = \frac{T_{\text{p}}}{\frac{1}{2}\rho V_{\text{a}}^2 \dfrac{\pi D^2}{4}} \tag{8.8}$$

which, through Eqn (8.6), is given in terms of the dimensionless jet velocity $V_{\text{jo}}/V_{\text{a}}$ by

$$C_{\text{To}} = \left(\frac{V_{\text{jo}}}{V_{\text{a}}}\right)^2 - 1 = a^2 - 1 \tag{8.9}$$

where

$$\frac{V_{\text{jo}}}{V_{\text{a}}} = a \tag{8.10}$$

A suitable definition of propulsive efficiency may be expressed as

$$\eta_{\text{p}} = \frac{\text{Propulsive power delivered to vehicle, } P}{\text{Shaft input power, } P_{\text{s}}}$$

$$= \frac{P}{P + E_{\text{w}}} \tag{8.11}$$

Thus the shaft input P_{s} has to provide both the useful propulsive power P and the kinetic energy losses E_{w} dissipated ultimately by the jet wake, which may be expressed as follows. Firstly the propulsive power P delivered to the vehicle may be expressed through

$$P = T_{\text{p}} V_{\text{a}} = \text{Thrust} \times \text{speed of vehicle}$$

$$= \frac{\rho \pi D^2}{8} (V_{\text{jo}}^2 - V_{\text{a}}^2) V_{\text{a}}$$

$$= \frac{\rho \pi D^2 V_{\text{a}}^3}{8} (a^2 - 1) \tag{8.12}$$

Secondly the wake kinetic energy loss due to mixing of the jet finally at $x = \infty$ is

$$E_{\text{w}} = \tfrac{1}{2}\dot{m}(V_{\text{jo}} - V_{\text{a}})^2$$

and making use of Eqns (8.2) and (8.7)

$$E_{\text{w}} = \frac{\rho \pi D^2}{16} (V_{\text{jo}} - V_{\text{a}})^2 (V_{\text{a}} + V_{\text{jo}})$$

$$= \frac{\rho \pi D^2 V_{\text{a}}^3}{16} (a - 1)^2 (a + 1) \tag{8.13}$$
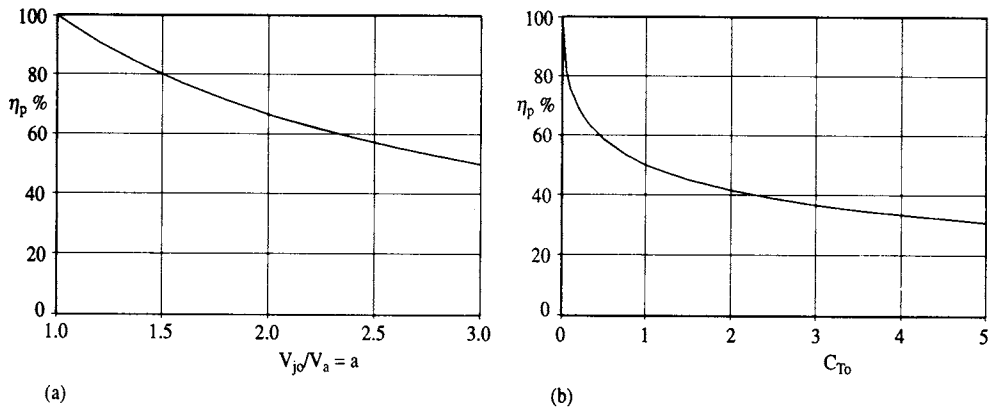
Fig. 8.4 Open propeller propulsive efficiency versus V_{jo}/V_a and C_{To}: (a) effect of jet velocity upon η_p; (b) effect of thrust coefficient upon η_p

Introducing these results into Eqns (8.11), the propulsive efficiency may be expressed directly in terms of V_{jo}/V_a through

$$\eta_p = \frac{2}{1 + V_{jo}/V_a} = \frac{2}{1 + a} \tag{8.14}$$

Alternatively, eliminating V_{jo}/V_a from Eqn (8.9), η_p may be expressed as a unique function of the thrust coefficient only, namely

$$\eta_p = \frac{2}{1 + \sqrt{1 + C_{To}}} \tag{8.15}$$

Graphs portraying these important and very interesting functional relationships are shown in Fig. 8.4. As the jet velocity ratio V_{jo}/V_a is increased to raise the design choice of thrust coefficient C_{To}, so the kinetic energy dissipated in the propeller wake will also increase, resulting in a progressive reduction of propulsive efficiency, Fig. 8.4(a).

This is also borne out by Fig. 8.4(b) which reveals a very rapid reduction of η_p as the selected design value of C_{To} is increased for lightly loaded propellers in the range $0 < C_{To} < 1.0$ and a progressive reduction of η_p for higher values of C_{To}. To obtain a feel for likely practical levels of C_{To} it is necessary to consider the propeller blade hydrodynamic or aerodynamic loading and this we will undertake in the next section in relation to the earlier consideration of axial fans in Chapter 4.

8.1.1 Velocity triangles and duty coefficients for open propellers

Inlet and outlet velocity triangles for flow at some reference radius such as the r.m.s. or mean radius of the propeller are shown in Fig. 8.5. Dimensionless velocity triangles have also been assembled from these by normalising all velocities with the blade speed U. Adapting the duty coefficients (ϕ, ψ) defined for fans and compressors, Section
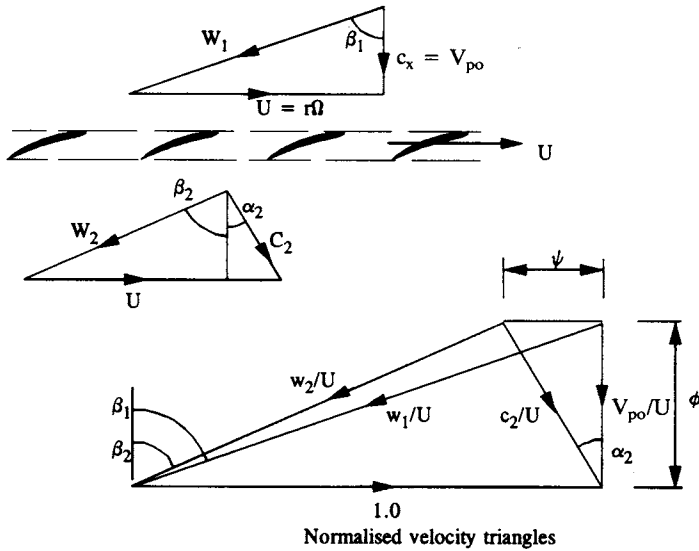
Fig. 8.5 Velocity triangles for a propeller.

4.1, for the propeller in incompressible flow, we then have

$$\left.\begin{aligned}\phi &= \frac{V_{po}}{U} \\ \psi &= \frac{\Delta p_o}{\rho U^2}\end{aligned}\right\} \tag{8.16}$$

where flow coefficient ϕ relates to the axial velocity V_{po} in the plane of the propeller. Combining Eqns (8.4), (8.8) and (8.7) the thrust coefficient may be developed as follows:

$$\begin{aligned}C_{To} &= \frac{p_2 - p_1}{\frac{1}{2}\rho V_a^2} = \frac{\frac{1}{2}\rho(w_1^2 - w_2^2)}{\frac{1}{2}\rho V_{po}^2}\left(\frac{V_{po}}{V_a}\right)^2 \\ &= \frac{w_1^2 - w_2^2}{U^2 \phi^2} \times \frac{(1+a)^2}{4}\end{aligned}$$

But from the dimensionless velocity triangles

$$\begin{aligned}\left(\frac{w_1}{U}\right)^2 - \left(\frac{w_2}{U}\right)^2 &= [1 + \phi^2] - [(1-\psi)^2 + \phi^2] \\ &= \psi(2 - \psi)\end{aligned}$$

so that C_{To} is related to the duty coefficients ϕ and ψ and the jet velocity ratio a through

$$C_{To} = \frac{\psi(2 - \psi)(1+a)^2}{4\phi^2}$$
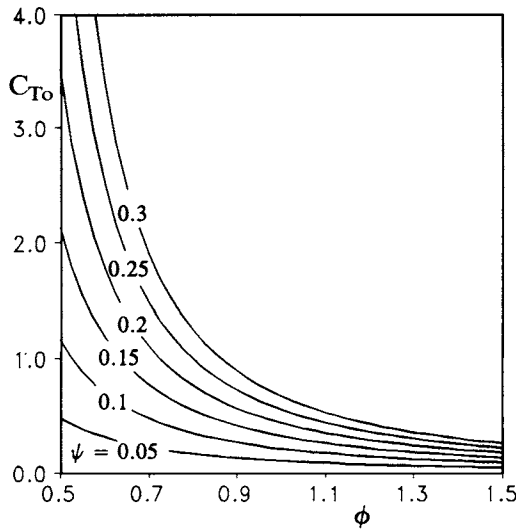
Fig. 8.6 Thrust coefficient versus duty coefficients (ϕ, ψ) at the r.m.s. radius of an open propeller

Eliminating a by means of Eqn (8.9) we have finally an identity relating ϕ, ψ and C_{To}, namely

$$C_{\text{To}} = \frac{\psi(2 - \psi)(1 + \sqrt{1 + C_{\text{To}}})^2}{4\phi^2} \tag{8.17}$$

For a specified propeller blade (ϕ, ψ) duty (i.e. loading) at the r.m.s. radius, this equation may be solved for C_{To} by successive approximations resulting in the functional relationship plotted in Fig. 8.6. C_{To} values are shown here for the practical range of work coefficients applicable to axial fans, $0 < \psi < 0.3$, and for a very wide range of flow coefficients, $0.5 < \phi < 1.5$. Although in the field of propellers the thrust coefficient C_{To} presents itself as an obvious primary design/selection variable typifying the propeller's main duty as a thrusting device, data maps such as Fig. 8.6 provide an essential link to aero/hydrodynamic constraints on the permissible blade loading expressed through the duty coefficients (ϕ, ψ). This link extends yet further to the velocity triangles and thus to the operating environment of the blading as illustrated already by Fig. 8.5.

Example 8.1

Problem
Determine the thrust coefficient, the relative flow angles β_1 and β_2 and the pitch/chord ratio for a propeller with specified blading duty $\phi = 0.55$, $\psi = 0.15$ at the r.m.s. reference radius. Assume a conservative diffusion factor of DF $= 0.4$.

Solution
From Fig. 8.6 a first estimate of $C_{\text{To}} = 1.55$ may be obtained. Refining this by successive solution of Eqn (8.17) results finally in the solution

$$C_{\text{To}} = 1.5446$$

From velocity triangles we then have

$$\beta_1 = \arctan\,(1/\phi) \qquad = \arctan\,(1/0.55) = 61.189°$$

$$\beta_2 = \arctan\left(\frac{1-\psi}{\phi}\right) = \arctan\left(\frac{0.85}{0.55}\right) = 57.095°$$

From Section 4.7, Eqn (4.47a), by analogy with a high reaction axial fan, the pitch/chord ratio is given by

$$\frac{t}{l} = \frac{2}{\psi}\,\{\sqrt{\phi^2 + (1-\psi)^2} - (1-\mathrm{DF})\sqrt{\phi^2 + 1}\}$$
$$= 4.369$$

As might be expected, for this lightly loaded propeller ($\psi = 0.15$), the pitch/chord ratio is much higher than would be expected for a typical axial fan (see Example 4.4) p. 104. We need to bear in mind that an open propeller does not have the benefit of a surrounding duct or annulus which enables axial fan blades to generate lift from hub to tip. Propeller blades must be designed to unload their aerodynamic lift forces progressively to zero at the blade tips resulting in the shedding of helical vortices in the tip region which also lead to additional induced drag. Some discussion of this will be given in Section 8.4.1 but it is outside the present objectives and scope to provide specific details of these complex fluid-dynamic design problems and their solution. A wide variety of propeller blade design and profile selection methods to handle this are covered in the literature, ranging from lifting line and lifting surface theories (Glover, 1970; Pien, 1961; Kerwin and Lee, 1978; Weissinger and Maass, 1968) to the cascade strip method which is followed here in Chapters 2 and 4 based on turbomachinery thinking. The objective at this point will be to turn our attention instead to a class of propulsors much more akin to fans and pumps for which turbomachinery methodology is more certainly applicable, namely ducted propeller systems.

8.2   Kort Nozzle and Pump Jet ducted propellers

The operating environment of a propeller may be modified considerably by locating it within a surrounding annular duct which itself becomes an important component of the propulsive system. As illustrated in Fig. 8.7 there are two types of ducted propulsor which have been widely used, namely the *Kort Nozzle* and the *Pump Jet*. These have quite different performance features and applications which are as follows.

The Kort Nozzle propulsor (Fig. 8.7(a)) has an accelerating duct designed to increase the mass flow swallowing capacity of the propeller by raising the velocity V_{p} in the propeller plane and therefore the jet momentum $\dot{m}V_{\mathrm{j}}$ and total thrust. The duct itself can provide a considerable proportion T_{d} of the total thrust $T = T_{\mathrm{p}} + T_{\mathrm{d}}$ of such propulsors, typically 25–30%. As will be shown later, an additional important advantage of a Kort Nozzle propulsor is its capacity to develop much higher propulsive efficiency than an open propeller of the same total thrust and to achieve this with a smaller propeller diameter. Kort Nozzles are thus very attractive for the propulsion of heavily loaded vehicles requiring good fuel economy and have consequently been widely used for the propulsion of trawlers and tugs at the small scale and also for supertankers and bulk carriers at the large scale where draft imposes severe upper limits on propeller diameter. They also offer attractions for light
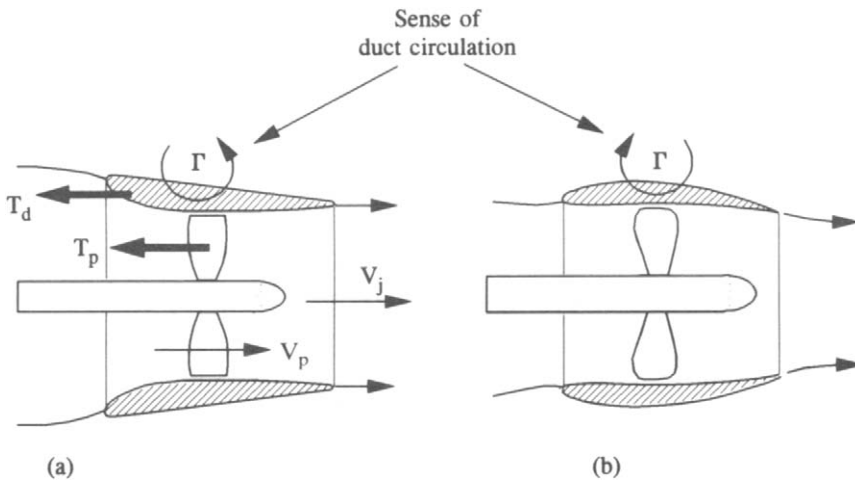
Fig. 8.7 (a) Kort Nozzle (accelerating duct) and (b) Pump Jet (decelerating duct) ducted propellers

low-speed aircraft and hovercraft and for submersibles and other ocean survey vehicles for which the possibility of a steerable duct provides the advantages of additional vector thrust.

The Pump Jet propulsor, on the other hand, has a diffusing duct as illustrated by Fig. 8.7(b), designed to reduce the velocity V_p and to raise the 'ambient' pressure in the propeller plane. The advantages of this are twofold. Firstly the propeller will be more resistant to cavitation. Secondly, as a consequence of this and also of the reduced levels of velocity relative to the propeller blades, the noise propagation may be significantly reduced. Such features could be advantageous for fairly high speed vessels operating close to the free surface with low submergence, where cavitation in particular is a distinct possibility. Military applications are thus pertinent here. Function must override propulsive efficiency η_p as the governing factor over design choice since in general for such devices η_p will prove to be less than that of an open propeller of the same total thrust while the propeller diameter will be greater.

Also indicated on Fig. 8.7 is the sense of the duct circulation. Thus the duct may be thought of as an annular aerofoil generating a bound circulation Γ and consequent lift. In general we would expect the sense of the circulation to match that of the camber. Thus the negative camber of the Kort Nozzle duct profile will generate an anticlockwise circulation Γ (Fig. 8.7(a)) and an associated radially inward 'lift' force on the duct. Conversely the positive camber of the Pump Jet duct will generate clockwise circulation Γ resulting in radially outward duct thrust. If we think of the duct circulation Γ as a ring vortex, it is evident that it will induce additional mass flux through the propeller plane for the Kort Nozzle and reduced mass flux (and hence a diffusing effect) for the Pump Jet. Duct shape is thus crucial for the proper functioning of a ducted propulsor and has been the subject of considerable theoretical and experimental research. Crucial though such fluid dynamic techniques are for the design and development of high performance ducted propulsors with correctly matched duct and propeller geometries, they must be based upon an initial sound overall dimensional analysis capable of revealing the various interactions between suitably defined overall dimensionless design/performance parameters. The development of such an analysis will be the main purpose of the next two sections.

8.3   Dimensional analysis for ducted propellers

Following similar arguments the analysis in Section 8.1 may be extended to ducted propellers for which the total thrust may be expressed as

$$T = \rho \frac{\pi D^2}{4} V_p (V_j - V_a)$$

$$= T_p + T_d$$

(8.18)

In this case it is convenient to define an additional dimensionless variable to account for the duct thrust, namely the thrust ratio τ:

$$\tau = \frac{\text{Propeller thrust}}{\text{Total thrust}} = \frac{T_p}{T}$$

(8.19)

As before, Eqn (8.4), the propeller thrust T_p may be related to jet velocity V_j by applying Bernoulli's equation to yield

$$T_p = (p_2 - p_1) \frac{\pi D^2}{4} = \frac{\rho \pi D^2}{8} (V_j^2 - V_a^2)$$

$$= \tau T$$

(8.20)

Eliminating T from Eqns (8.18) and (8.20) results in the following expression for the velocity V_p in the propeller plane:

$$V_p = \frac{V_a + V_j}{2\tau}$$

(8.21)

Comparing this with the analogous result for open propellers, Eqn (8.7), we note that the thrust ratio τ influences V_p as shown in Table 8.1.

Table 8.1 Effect of duct thrust on velocity V_p in the plane of a ducted propeller

Duct thrust T_p	Thrust ratio τ	Type of ducted propeller	Comparison with equivalent open propeller
Positive	$\tau < 1.0$	Kort Nozzle	$V_p > V_{po}$
Zero	$\tau = 1.0$	Open propeller	$V_p = V_{po}$
Negative	$\tau > 1.0$	Pump Jet	$V_p < V_{po}$

The thrust ratio τ thus has a profound effect upon the velocity level in the propeller plane and unequivocally determines whether a ducted propulsor is a Kort Nozzle ($\tau < 1.0$) or a Pump Jet ($\tau > 1.0$).

The propulsive efficiency for an open propeller was shown to be a function of the thrust coefficient C_{To} only, Eqn (8.15). For a ducted propulsor, on the other hand,

adopting the same basic definition of propulsive efficiency, Eqn (8.11), we would expect η_p to exhibit the following general form of relationship:

$$\eta_p = f(C_T, \tau) \tag{8.22}$$

where both C_T and τ can now be regarded as the available overall independent design variables. By analysis similar to that in Section 8.1 this general equation may be transformed into an explicit form which determines quite definitively the influence of both C_T and τ upon η_p. To achieve this the thrust coefficient may first be expressed as

$$C_T = \frac{T_p + T_d}{\frac{1}{2}\rho V_a^2 \frac{\pi D^2}{4}} = \frac{1}{\tau}\left\{ \frac{T_p}{\frac{1}{2}\rho V_a^2 \frac{\pi D^2}{4}} \right\} \tag{8.23}$$

Introducing T_p from Eqn (8.20) then yields

$$C_T = \frac{1}{\tau}\left\{ \left(\frac{V_j}{V_a}\right)^2 - 1 \right\}$$

which may be inverted to reveal the dependency of the jet velocity V_j/V_a upon the independent design variables C_T and τ, namely

$$\frac{V_j}{V_a} = \sqrt{1 + \tau C_T} \tag{8.24}$$

Now as already suggested, the previous definition of propulsive efficiency for open propellers, Eqn (8.11), is no less valid here for ducted propellers, namely

$$\eta_p = \frac{\text{Propulsive power delivered to vehicle, } P}{\text{Shaft input power, } P_s} = \frac{P}{P + E_w} \tag{8.11}$$

where, making use of Eqn (8.20), the propulsive power P is given by

$$\begin{aligned} P = \text{Thrust} \times \text{vehicle speed} &= TV_a \\ &= \frac{\rho \pi D^2}{8\tau}(V_j^2 - V_a^2)V_a \end{aligned} \tag{8.25}$$

The wake kinetic energy loss E_w, making use also of Eqns (8.2) and (8.21), becomes

$$\begin{aligned} E_w = \frac{1}{2}\dot{m}(V_j - V_a)^2 &= \frac{1}{2}\rho\frac{\pi D^2}{4}V_p(V_j - V_a)^2 \\ &= \frac{\rho \pi D^2}{16\tau}(V_j - V_a)^2(V_a + V_j) \end{aligned} \tag{8.26}$$
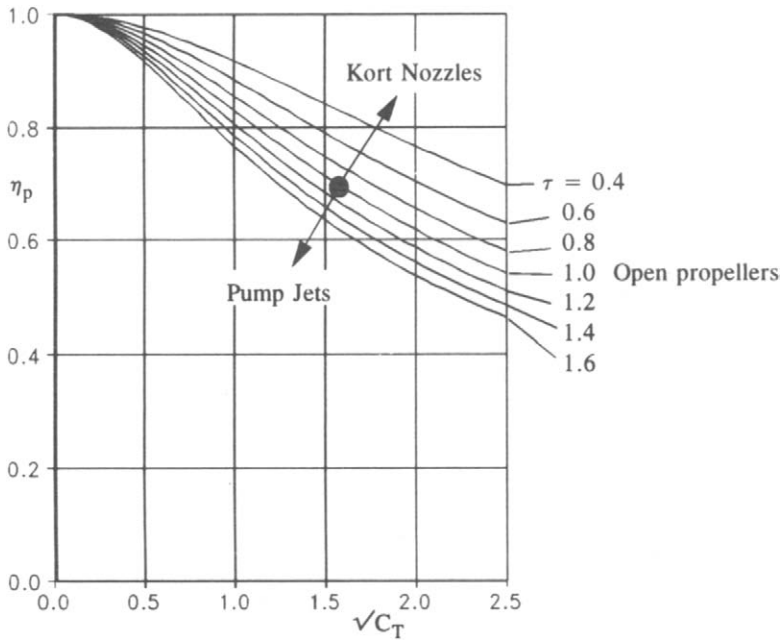
Fig. 8.8 Propulsive efficiency for ducted propellers as a function of C_T and τ

Introducing P and E_w into Eqn (8.11) above, results finally in

$$\eta_p = \frac{2}{1 + V_j/V_a}$$

which is identical to the result obtained for open propellers, Eqn (8.14), as might be expected. However, if V_j/V_a is replaced by substitution from Eqn (8.24), propulsive efficiency η_p is finally expressed as an explicit function of C_T and τ. Thus Eqn (8.22) transforms to

$$\eta_p = \frac{2}{1 + \sqrt{1 + \tau C_T}} \tag{8.27}$$

and from Eqns (8.21) and (8.24) the velocity in the propeller plane is given by

$$\frac{V_p}{V_a} = \frac{1}{2\tau}\left(1 + \frac{V_j}{V_a}\right) = \frac{1}{2\tau}(1 + \sqrt{1 + \tau C_T}) \tag{8.28}$$

The evaluation of Eqn (8.27) is displayed in Fig. 8.8 as a series of curves of η_p versus C_T for a range of τ values covering a large spread of design duties. The following conclusions may be drawn:

(1) Propulsive efficiency η_p decreases always with propulsor thrust coefficient C_T

as would be expected due to the increased jet velocity V_j and the consequent wake kinetic energy dissipation E_w.

(2) For a given design choice of C_T the propulsive efficiency will be increased by selection of thrust ratio in the range $\tau < 1.0$, corresponding to a Kort Nozzle.

(3) Conversely, for a given design choice of C_T, the propulsive efficiency will be reduced if a Pump Jet duct is chosen for which $\tau > 1.0$.

(4) The open propeller corresponds to the situation $\tau = 1.0$ for which there would be zero duct thrust so that there would be little point in retaining the duct.

Example 8.2

Problem

A propulsor is to be chosen to deliver a thrust coefficient $C_T = 2.0$. Compare three designs for which $\tau = 0.7$, 1.0 and 1.3 respectively.

Solution

By substitution into Eqns (8.27) and (8.28), the following table may be completed:

Design no.	C_T	τ	Type	V_p/V_a	η_p
1	2.0	0.7	Kort Nozzle	1.820 85	0.784 56
2	2.0	1.0	Open propeller	1.366 03	0.732 05
3	2.0	1.3	Pump Jet	1.114 37	0.690 28

If we regard Design No. 2 as the open propeller standard for comparison, the following conclusions may be drawn:

(1) *Design No. 1.* Selection of a Kort Nozzle with this fairly typical value of $\tau = 0.7$ will result in a 5.2% gain in propulsive efficiency. However, the velocity V_p in the propeller plane will then be about 33% greater than that of the equivalent open propeller. This will result in lower static pressure levels thus raising the cavitation threshold.

(2) *Design No. 2.* Selection of the Pump Jet will result in a lower V_p value, thus raising the static pressure level in the propeller plane, which will help to reduce the possibility of cavitation. However, the cost of this gain will be a reduction in propulsive efficiency η_p by 4.2% by comparison with the equivalent open propeller.

Following the analyses of Van Manen and Oosterveld (1966) and Lewis (1972), Eqn (8.28) may be used to derive the ratio of V_p to V_{po} for an open propeller of the same thrust coefficient C_T, namely

$$\frac{V_p}{V_{po}} = \frac{1}{\tau}\left\{\frac{1 + \sqrt{1 + \tau C_T}}{1 + \sqrt{1 + C_T}}\right\} \tag{8.29}$$

This relationship is shown graphically in Fig. 8.9 for the practical range of ducted propellers and provides a useful quick visual reference for design use and discussions such as Example 8.2.
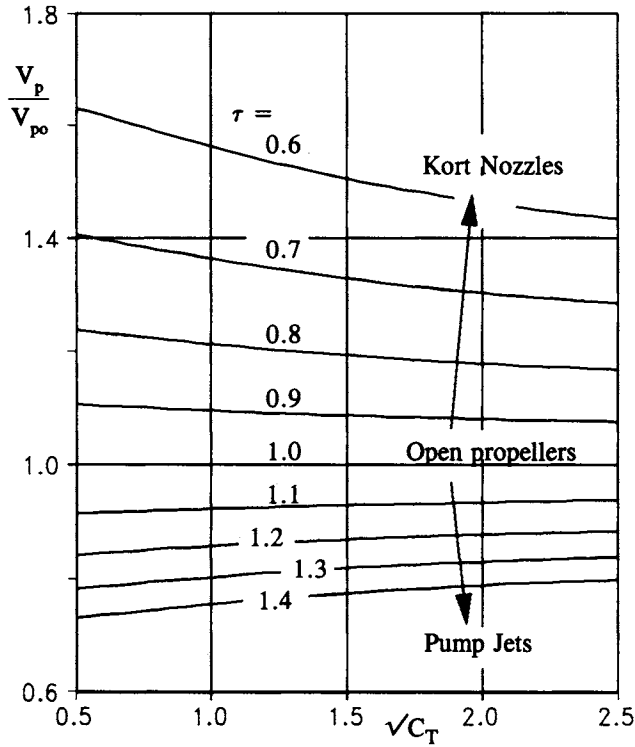
Fig. 8.9 Comparison of velocity in the plane of open and ducted propellers

One more extremely important matter which impinges upon design choice is the effect of the duct upon propeller size. From the definition of thrust coefficient, Eqn (8.23),

$$T = \frac{1}{2}\rho V_a^2 \frac{\pi D^2}{4} C_T \qquad (8.30)$$

Thus for a ducted propeller of diameter D and an open propeller of diameter D_o but with the same total thrust T,

$$\frac{D}{D_o} = \sqrt{\frac{C_{To}}{C_T}} = \sqrt{\tau \frac{C_{po}}{C_p}} \qquad (8.31)$$

where the propeller thrust coefficient C_p is defined as

$$C_p = \frac{T_p}{\frac{1}{2}\rho V_a^2 \frac{\pi D^2}{4}} \qquad (8.32)$$

Making use of Eqn (8.20) this transforms to

$$C_p = \frac{p_2 - p_1}{\frac{1}{2}\rho V_a^2} \qquad (8.33)$$
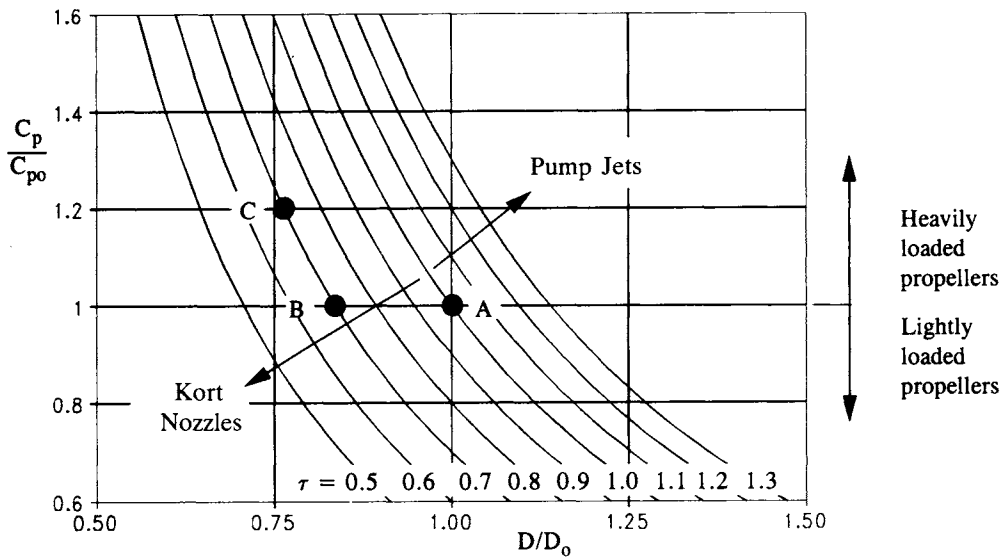
Fig. 8.10 Diameter ratio of ducted and open propellers of equal total thrust

C_p is thus the dimensionless pressure rise produced by the propeller and is indicative of propeller loading.

Equation (8.31) is shown graphically in Fig. 8.10 from which the following conclusions may be drawn:

(1) The diameter ratio D/D_o reduces for Kort Nozzles ($\tau < 1.0$) and increases for Pump Jets ($\tau > 1.0$).
(2) Thus considering an open propeller, point A, and a ducted propeller with the same thrust T but with $\tau = 0.7$, point B, the propeller diameter is reduced to 83.67% as a result of transferring 30% of the thrust onto the duct. In this case the pressure coefficients of both the propellers have been assumed equal, $C_p = C_{po}$.
(3) One attraction of a Kort Nozzle is that provided close tip clearance is maintained, the propeller blades may be loaded more heavily towards the tip region, permitting higher total propeller thrust coefficients. Point C on Fig. 8.10 illustrates the case of a modest increase by 20% of the propeller loading while retaining a thrust ratio $\tau = 0.7$, resulting in a reduced diameter compared with the open equivalent propeller of $D/D_o = 0.763\,74$. At the same time, recalling Fig. 8.8, the propulsive efficiency will be increased. These factors confirm the multiple advantages of the use of Kort Nozzles where there are constraints on propeller diameter and where fuel economy is important.

8.4 More detailed performance analysis for ducted propellers

The foregoing analysis is extremely powerful for displaying the influence of the primary design variables C_T and τ upon propulsive efficiency η_p, but is based upon the premise that the only significant losses are those of the wake jet kinetic energy

dissipation E_w. Replacing the shaft input power by $P = TV_a$, Eqn (8.12), the propulsive efficiency, Eqn (8.11), may then be written in the approximate form

$$\eta_p = \cfrac{1}{1 + \cfrac{\text{jet KE losses}}{\text{shaft power}}} = \cfrac{1}{1 + \cfrac{E_w}{TV_a}} \tag{8.34}$$

As shown by Lewis (1972) in a comprehensive paper on ducted propeller performance analysis as seen from a turbomachine viewpoint, the last equation should be expanded to include losses from four other sources:

$$\eta_p = \cfrac{1}{1 + \cfrac{E_w}{TV_a} + \cfrac{S_w}{TV_a} + \cfrac{F_p}{TV_a} + \cfrac{F_d}{TV_a} + \cfrac{\text{TL}}{TV_a}} \tag{8.35}$$

E_w and S_w now cover kinetic energy losses due to both axial and swirl velocities in the downstream jet, F_p and F_d account for propeller and duct frictional losses, and TL accounts for the tip leakage losses at the propeller blade tips. Each loss is normalised here by the thrust power TV_a. In order to derive expressions for these in terms of design variables, some considerations of dimensional analysis are necessary at this point.

8.4.1   Detailed dimensional analysis for ducted propellers

The losses and hence the propulsive efficiency depend upon a large number of operational and geometric variables, most of which are at the outset independent design variables. η_p may thus be expressed as a function of these variables grouped as follows:

$$\eta_p = f(\underbrace{T, V_a, n,}_{\substack{\text{System} \\ \text{variables}}} \underbrace{\tau, D, r_h, l_d, l_p, Z, \delta,}_{\substack{\text{Machine} \\ \text{design} \\ \text{variables}}} \underbrace{C_{Dd}, C_{Dp})}_{\substack{\text{Frictional} \\ \text{coefficients}}} \tag{8.36}$$

where n is rotational speed (rev s^{-1}), r_h is hub radius, l_d is duct length, l_p is propeller chord, Z is the number of blades and δ is the tip clearance. *System variables* would normally be prescribed for the designer in the initial specification. *Frictional coefficients* C_{Dd} for the duct and C_{Dp} for the propeller will depend upon both the machine shape and the operating conditions and thus, like η_p, are dependent variables.

By formation of conventionally accepted dimensionless groupings, the number of variables may be reduced spontaneously from 12 to nine, resulting in

$$\eta_p = f(\underbrace{C_T, J,}_{\substack{\text{System} \\ \text{variables}}} \underbrace{\tau, h, l_d/D, t/l_p, \delta/D,}_{\substack{\text{Machine} \\ \text{design} \\ \text{variables}}} \underbrace{C_{Dd}, C_{Dp})}_{\substack{\text{Frictional} \\ \text{coefficients}}} \tag{8.37}$$

where in addition to previous definitions of C_T and τ,

$$J = \frac{V_a}{nD} \qquad \text{(advance coefficient)} \qquad (8.38)$$

$$h = \frac{r_h}{D/2} \qquad \text{(hub/tip ratio)} \qquad (8.39)$$

$$\frac{t}{l_p} = \frac{\pi D}{Z l_p} \qquad \text{(propeller tip pitch/chord ratio)} \qquad (8.40)$$

A number of alternative system parameters are frequently used in the propeller literature. Although not strictly pertinent to the present analysis they will be listed here for completeness, namely,

$$K_T = \frac{T}{\rho n^2 D^4} = \frac{\pi}{8} C_T J^2 \qquad \text{(thrust coefficient)} \qquad (8.41)$$

$$K_Q = \frac{Q}{\rho n^2 D^5} \qquad \text{(torque coefficient)} \qquad (8.42)$$

$$B_p = \frac{N P^{1/2}}{V_a^{5/2}} = 33.08 \left(\frac{K_Q}{J^5} \right)^{1/2} \qquad \text{(loading coefficient)} \qquad (8.43)$$

$$\delta_v = \frac{ND}{V_a} = \frac{101.27}{J} \qquad \text{(velocity coefficient)} \qquad (8.44)$$

In the last two items the speed of rotation N is expressed in rev min^{-1}, D in feet, V_a in knots and P in horse power.

All the appropriate dimensionless groups involving independent variables have now been defined and we may proceed to express the various losses in Section 8.4 in terms of these.

8.4.2 Axial and swirl jet kinetic energy losses

The dimensionless jet axial kinetic energy loss follows from Eqns (8.24) to (8.26), namely

$$\frac{E_w}{TV_a} = \frac{1}{2} (\sqrt{1 + \tau C_T} - 1) \qquad (8.45)$$

where the assumption is retained that V_p and V_j are constant at all radii. This would indeed be the case for a free-vortex propeller, which combines uniform loading $\Delta p_o = p_{o2} - p_{o1}$ with a free-vortex swirl $c_{\theta 2} r$ = constant, Section 5.1. These are also related through the Euler pump equation

$$\frac{\Delta p_o}{\rho} = c_{\theta 2} r \Omega$$

$$= \text{constant for free-vortex swirl} \qquad (8.46)$$

Now the swirl kinetic energy created at the propeller plane may be expressed as

$$S_w = \int_{r_h}^{r_t} \frac{c_{\theta 2}^2}{2} \rho V_p 2\pi r \, dr = \rho V_p \pi \int_{r_h}^{r_t} c_{\theta 2}^2 r \, dr$$

Substituting for V_p from Eqn (8.28), this becomes

$$S_w = \frac{\rho \pi V_a}{2\tau} (1 + \sqrt{1 + \tau C_T}) I \tag{8.47}$$

Making use of the Euler pump equation (8.46), the integral I may be evaluated for free-vortex propellers as follows:

$$\begin{aligned}
I &= \int_{r_h}^{r_t} c_{\theta 2}^2 r \, dr = \int_{r_h}^{r_t} \left(\frac{\Delta p_o}{\rho \Omega}\right)^2 \frac{1}{r} \, dr \\
&= \frac{\Delta p_o^2}{4\rho^2 \pi^2 n^2} \ln(1/h) = \frac{C_{p_o t}^2 V_a^4}{16\pi^2 n^2} \ln(1/h)
\end{aligned} \tag{8.48}$$

where the propeller tip loading coefficient $C_{p_o t}$ is defined as

$$C_{p_o t} = \frac{\Delta p_{ot}}{\frac{1}{2}\rho V_a^2} \tag{8.49}$$

Now from the definition of thrust coefficient C_T, Eqn (8.23),

$$TV_a = C_T \tfrac{1}{2}\rho V_a^2 \frac{\pi D^2}{4} V_a$$

Thus finally, the dimensionless swirl loss of a free-vortex ducted propeller becomes

$$\begin{aligned}
\frac{S_w}{TV_a} &= \frac{C_{p_o t}^2 V_a^2}{4\pi^2 \tau C_T n^2 D^2} (1 + \sqrt{1 + \tau C_T}) \ln(1/h) \\
&= \frac{C_{p_o t}^2 J^2}{4\pi^2 \tau C_T} (1 + \sqrt{1 + \tau C_T}) \ln(1/h)
\end{aligned} \tag{8.50}$$

Lewis (1972, Appendix II) has shown that the tip loading coefficient $C_{p_o t}$ may be expressed for free-vortex ducted propellers through

$$C_{p_o t} = \frac{\pi^2(1 - h^2)}{J^2 \ln(1/h)} \left\{ 1 - \sqrt{1 - \frac{2\tau C_T J^2 \ln(1/h)}{\pi^2(1 - h^2)^2}} \right\} \tag{8.51}$$

so that the swirl loss S_w/TV_a is known explicitly as a function of all the independent design variables τ, C_T, J and h.
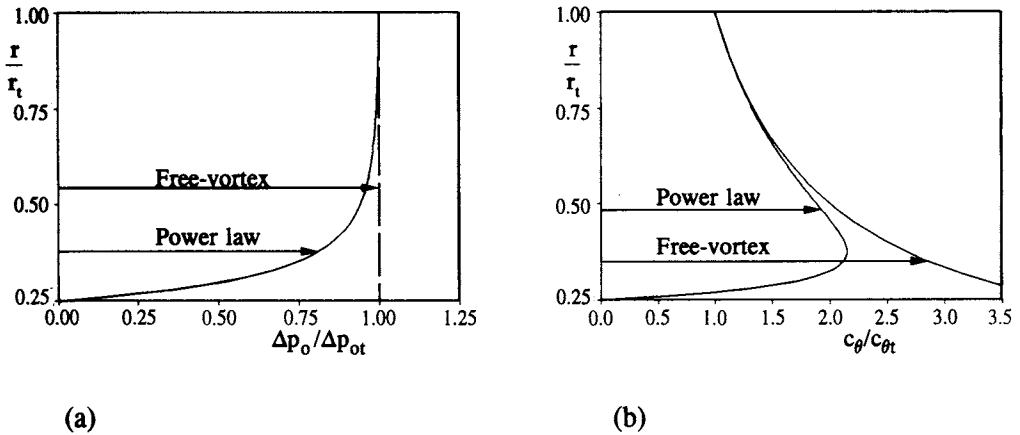
Fig. 8.11 Radial distributions of propeller loading and swirl velocity for free-vortex and fourth-order power law designs of ducted propeller for hub/tip ratio $h = 0.25$: (a) propeller loading; (b) downstream swirl

Power law loading

Free-vortex design has simplicity as its main advantage but results in unrealisable hub loadings for low hub/tip ratio propellers and bad downstream flow at the hub where swirl velocities are high. As a remedy for this Lewis (1972) postulated a near-free-vortex design with swirl velocities and thus blade loadings which taper rapidly to zero in the hub region as illustrated by Fig. 8.11. This is achieved by imposing a power law loading defined as follows:

$$\frac{\Delta p_o}{\Delta p_{ot}} = \frac{1 - \left(h\dfrac{r_t}{r}\right)^m}{1 - h^m} \tag{8.52}$$

where m is an integer. From the Euler pump equation (8.46a) the corresponding swirl velocity is given by

$$\frac{c_{\theta 2}}{c_{\theta 2t}} = \frac{r_t}{r}\left\{\frac{1 - \left(h\dfrac{r_t}{r}\right)^m}{1 - h^m}\right\} \tag{8.53}$$

Figure 8.11 provides a comparison of the propeller loading and swirl distributions produced by the power law design (for $m = 4$) with the free-vortex design for a low hub/tip ratio $h = 0.25$ and illustrates how the excessive swirl velocities in the hub region are removed by this technique. The previous analysis for S_w culminating in Eqn (8.47) remains valid. In this case evaluation of the integral I, substituting Eqn (8.52) into Eqn (8.48), results finally in

$$\frac{S_w}{TV_a} = \frac{C_{p_{ot}}^2 J^2}{4\pi^2 \tau C_T}(1 + \sqrt{1 + \tau C_T})A(h) \tag{8.54}$$
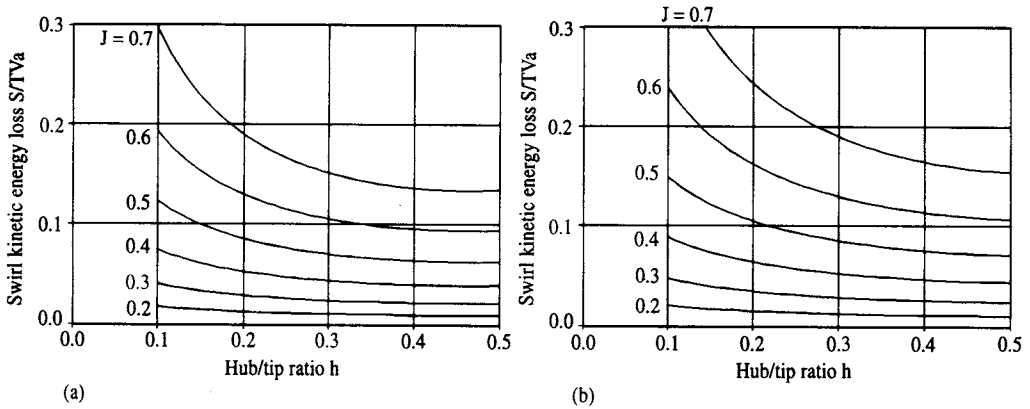
Fig. 8.12 Influence of hub/tip ratio h and advance coefficient J upon jet swirl losses for a Kort Nozzle propulsor with $C_T = 4.0$ and $\tau = 0.7$: (a) fourth-order power law loading; (b) free-vortex loading

where the loading coefficient $C_{p_{\mathrm{o}t}}$ is given by

$$C_{p_{\mathrm{o}t}} = \frac{\pi^2 B(h)}{J^2 A(h)} \left\{ 1 - \sqrt{1 - \frac{2\tau C_T J^2 A(h)}{\pi^2 B(h)}} \right\} \tag{8.55}$$

and the functions $A(h)$ and $B(h)$ are given by

$$A(h) = \frac{\ln(1 - h) - \dfrac{2}{m}(1 - h^m) + \dfrac{1}{2m}(1 - h^{2m})}{(1 - h^m)^2} \tag{8.56}$$

$$B(h) = \frac{(1 - h^2) - \left(\dfrac{2h^2}{m - 2}\right)(1 - h^{m-2})}{1 - h^m} \tag{8.57}$$

Figure 8.12 illustrates the dependency of the swirl losses S/TV_a upon the hub/tip ratio for a specified typical duty of $C_T = 4.0$, $\tau = 0.7$ and for a wide range of advance coefficients J. As might be expected the losses are generally higher for the free-vortex design than for the power law vortex. The losses are strongly dependent upon the advance coefficient J and increase rapidly for $J > 0.4$. On the other hand, the losses are a fairly weak function of hub/tip ratio above practical values of, say, $h > 0.2$.

Examination of Eqns (8.45) for E_w/TV_a and of Eqns (8.47) to (8.55) for S_w/TV_a reveals that both the axial and swirl kinetic energy loss coefficients are functions of τC_T, the propeller thrust coefficient. These losses are shown graphically in Fig. 8.13 for free vortex design with a hub/tip ratio $h = 0.25$, covering the practical range of Kort Nozzle propulsors. While both losses increase with rising τC_T it is clear that the swirl losses do so much more rapidly and begin to escalate for very highly loaded propellers with large advance coefficients J. For a typical design value $J = 0.5$, on the other hand, jet kinetic energy losses due to swirl are less than half of those due to axial velocities but of course are still significant.
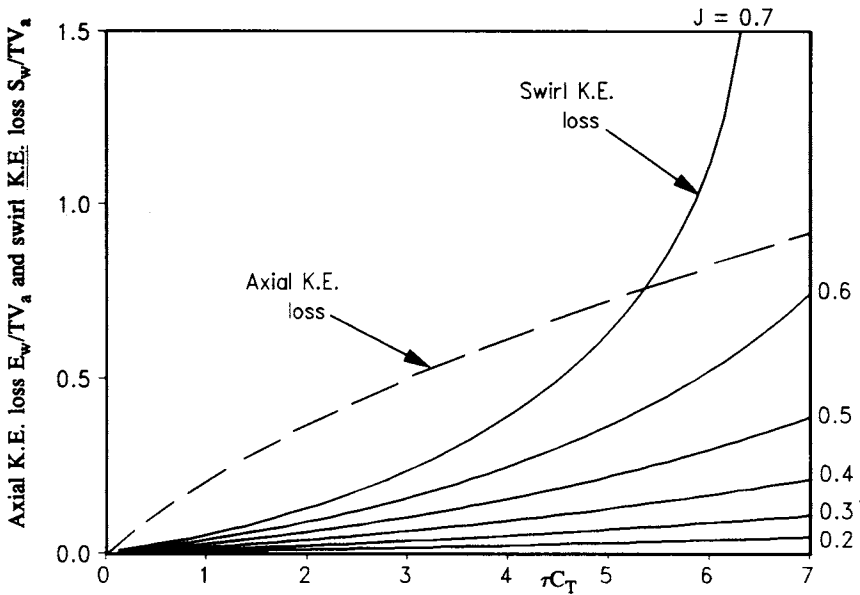
Fig. 8.13 Jet kinetic energy loss coefficients for a range of propeller thrust coefficients τC_T and advance coefficients J ($h = 0.25$)

8.4.3 Propeller frictional losses F_p/TV_a

If the stagnation pressure loss $(\Delta p_o)_{\text{loss}}$ due to blade profile drag is assumed equal for all meridional streamlines, the total power loss from this source will be

$$F_p = \frac{\pi D^2}{4}(1 - h^2) V_p (\Delta p_o)_{\text{loss}}$$

Making use of Eqns (8.23) and (8.28), the dimensionless loss then becomes

$$\frac{F_p}{TV_a} = \frac{1 - h^2}{2\tau C_T}\{1 + \sqrt{1 + \tau C_T}\}\frac{(\Delta p_o)_{\text{loss}}}{\frac{1}{2}\rho V_a^2} \tag{8.58}$$

The most obvious way of dealing with the last term, $(\Delta p_o)_{\text{loss}}/\frac{1}{2}\rho V_a^2$, is to consider the blades in relation to cascade analysis. As shown in Chapter 2, Eqn (2.9), the most appropriate definition of cascade loss coefficient applicable here is that based on vector mean relative velocity W_∞:

$$\zeta_\infty = \frac{(\Delta p_o)_{\text{loss}}}{\frac{1}{2}\rho W_\infty^2} \tag{2.9}$$

Now from velocity triangles, Fig. 8.5,

$$\left(\frac{W_\infty}{U}\right)^2 = \phi^2 + \left(1 - \frac{\psi}{2}\right)^2 \tag{8.59}$$

Combining these results,

$$\frac{(\Delta p_o)_{\text{loss}}}{\frac{1}{2}\rho V_a^2} = \left(\frac{U}{V_a}\right)^2 \left\{\phi^2 + \left(1 - \frac{\psi}{2}\right)^2\right\} \zeta_\infty$$

If this is now applied to the propeller tip radius $D/2$, making use of the definition of advance coefficient J and introducing the rotational speed $\Omega = 2\pi n$,

$$J = \frac{V_a}{nD} = \frac{\pi V_a}{\Omega D/2} = \pi\left(\frac{V_a}{U}\right) \qquad (8.60)$$

The previous equation then becomes

$$\frac{(\Delta p_o)_{\text{loss}}}{\frac{1}{2}\rho V_a^2} = \left(\frac{\pi}{J}\right)^2 \left\{\phi_t^2 + \left(1 - \frac{\psi_t}{2}\right)^2\right\} \zeta_\infty$$

Substitution of this result into Eqn (8.58) yields finally

$$\frac{F_p}{TV_a} = \frac{1 - h^2}{2\tau C_T}\{1 + \sqrt{1 + \tau C_T}\}\left(\frac{\pi}{J}\right)^2 \left\{\phi_t^2 + \left(1 - \frac{\psi_t}{2}\right)^2\right\} \zeta_\infty \qquad (8.61)$$

$$= f(\tau, C_T, J, h, \phi_t, \psi_t, \zeta_\infty)$$

The propeller profile losses have thus been expressed as an explicit function of six independent design variables plus the loss coefficient ζ_∞. Losses will thus depend upon two main groups of design variables:

(1) The overall propulsor duty specification C_T, τ and J.
(2) The blade row duty (ϕ_t, ψ_t) which has been stated here for the tip section.

As shown in Chapter 2, Eqn (2.8), the cascade loss coefficient ζ_∞ can be expressed in terms of the profile drag coefficient C_{Dp} through

$$\zeta_\infty = \frac{l}{t} C_{Dp} \sec \beta_\infty$$

$$= \frac{l}{t} C_{Dp} \frac{1}{\phi_t} \sqrt{\phi_t^2 + \left(1 - \frac{\psi_t}{2}\right)^2}$$

$$= f(t/l, C_{Dp}, \phi_t, \psi_t) \qquad (8.62)$$

Introducing this into Eqn (8.61) we have finally the more useful form

$$\frac{F_p}{TV_a} = \frac{1 - h^2}{2\tau C_T}\{1 + \sqrt{1 + \tau C_T}\}\frac{1}{\phi_t}\left\{\phi_t^2 + \left(1 - \frac{\psi_t}{2}\right)^2\right\}^{3/2}\left(\frac{\pi}{J}\right)^2\left(\frac{l}{t}\right)C_{Dp} \qquad (8.63)$$

$$= f(\underbrace{\tau, C_T, J,}_{\substack{\text{Propulsor} \\ \text{duty}}} \underbrace{\phi_t, \psi_t,}_{\substack{\text{Propeller} \\ \text{duty}}} \underbrace{h, t/l,}_{\substack{\text{Machine} \\ \text{geometry}}} \underbrace{C_{Dp})}_{\substack{\text{Cascade} \\ \text{drag coefficient}}}$$

Although it is helpful to bring out the dependency upon propeller tip duty (ϕ_t, ψ_t) in these expressions, these coefficients themselves may also be expressed in terms of the propulsor duty (τ, C_T, J) as follows:

$$\phi_t = \frac{V_p}{\pi n D} = \frac{J}{\pi}\frac{V_p}{V_a} = \frac{J}{2\pi\tau}\{1 + \sqrt{1 + \tau C_T}\} \tag{8.64}$$

and

$$\psi_t = \frac{\Delta p_{ot}}{\rho(\pi n D)^2} = \frac{1}{2}\left(\frac{\Delta p_{ot}}{\frac{1}{2}\rho V_a^2}\right)\left(\frac{J}{\pi}\right)^2 = \frac{Cp_{ot}}{2}\left(\frac{J}{\pi}\right)^2$$

$$= \frac{1 - h^2}{2\ln(1/h)}\left\{1 - \sqrt{1 - \frac{2\tau C_T J^2 \ln(1/h)}{\pi^2(1 - h^2)^2}}\right\} \quad \text{for free-vortex loading}$$

$$= \frac{B(h)}{2A(h)}\left\{1 - \sqrt{1 - \frac{2\tau C_T J^2 A(h)}{\pi^2 B(h)^2}}\right\} \quad \text{for power-law loading} \tag{8.65}$$

where $A(h)$ and $B(h)$ have already been given as Eqns (8.56) and (8.57) respectively.

8.4.4 Duct frictional losses F_d/TV_a

The usual method for defining a suitable drag coefficient is to regard the duct as an annular aerofoil located in open water of velocity V_a. Adopting the conventional definition of C_d for aerofoils, C_{Dd} is then defined as

$$C_{Dd} = \frac{\text{Drag in open water}}{\frac{1}{2}\rho V_a^2 \pi D l_d} \tag{8.66}$$

When combined with a propeller, on the other hand, the high velocity on the inner surface will tend to generate dominating losses and it would seem reasonable to assume that the duct drag D_d is that corresponding to a uniform stream V_p, namely

$$D_d = C_{Dd}\tfrac{1}{2}\rho V_p^2 \pi D l_d$$

The power losses due to duct drag are then

$$\frac{F_d}{TV_a} = \frac{D_d V_a}{TV_a} = \frac{4}{C_T}\frac{l_d}{D}\left(\frac{V_p}{V_a}\right)^2 C_{Dd}$$

$$= \frac{1}{\tau^2 C_T}(1 + \sqrt{1 + \tau C_T})^2\left(\frac{l_d}{D}\right)C_{Dd} \tag{8.67}$$

which may be expressed in the general form

$$\frac{F_d}{TV_a} = f_d\left(\frac{l_d}{D}\right)C_{Dd} \tag{8.68}$$
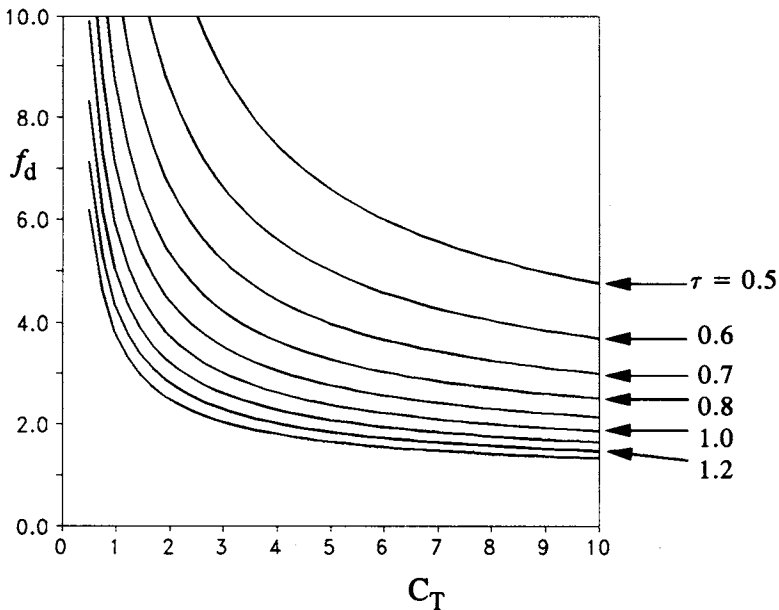
Fig. 8.14 Duct loss weighting coefficient f_d as a function of C_T and τ

where the weighting coefficient f_d is a function of the propulsor duty (τ, C_T) only, namely

$$f_d = \frac{1}{\tau^2 C_T}(1 + \sqrt{1 + \tau C_T})^2 \tag{8.69}$$

The duct losses are thus a function of three dimensionless design variables:

(1) Duct profile shape which will determine its drag coefficient C_{Dd}.
(2) Duct aspect ratio l_d/D where l_d is the duct chord length.
(3) Propeller duty (τ, C_T) which determines f_d.

Weighting coefficients are shown in Fig. 8.14 for the practical range of propulsor duties, revealing that duct losses will tend to grow in significance as either thrust ratio τ or propulsor thrust coefficient C_T is reduced.

8.4.5   Tip leakage losses TL/TV_a

In some applications a conventional propeller with rounded blades may be used, in which case the blade lift reduces progressively to zero approaching the blade tips, Fig. 8.15(a), with associated shedding of a vortex sheet. Calculation of the corresponding energy loss is an integral part of conventional propeller design methods. In the present turbomachinery context, on the other hand, our concern is with Kaplan-type propeller blades which attempt to retain substantial blade loading as close as possible to the tip region. Inevitably, due to the practical necessity of retaining a small but finite clearance δ_t between the blade tip and the duct,
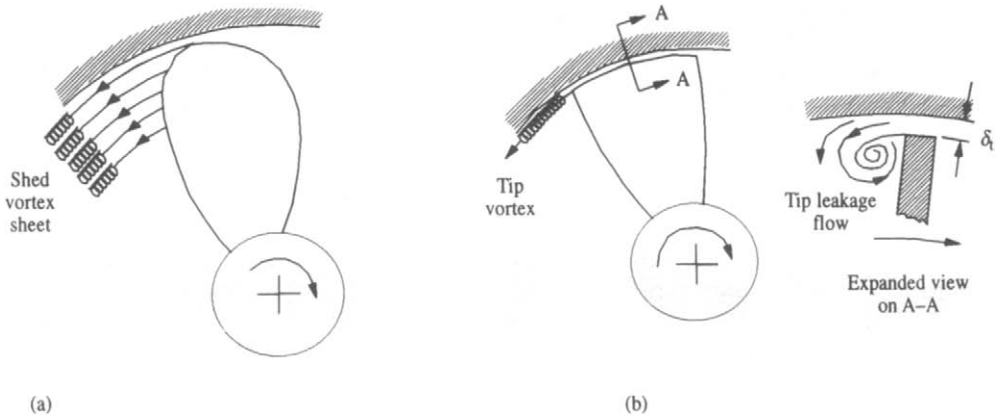
Fig. 8.15 Vortex shedding from ducted propeller blade tips: (a) open propeller type with rounded blade tips; (b) Kaplan-type propeller with loaded blade tips

the blade loading will ultimately reduce rapidly to zero in a region of the order of δ_t, with the shedding of an associated concentrated tip vortex as illustrated in Fig. 8.15(b). Adopting the analysis of Hesselgreaves (1969) for axial fans, Lewis (1972) has shown that the loss due to the consequent 'tip leakage' flow may be approximated by

$$\frac{TL}{TV_a} = \frac{16\sqrt{2}}{5} \left(\frac{\delta_t}{D}\right) \left(\frac{l_p}{t}\right) \frac{C_{L\infty}^{3/2}}{C_T} \left(\frac{W_\infty}{V_a}\right)^3 \tag{8.70}$$

Now from Chapter 2, Eqn (2.10), the lift coefficient is given by

$$C_{L\infty} = 2 \frac{t}{l_p} (\tan\beta_1 - \tan\beta_2) \cos\beta_\infty - C_D \tan\beta_\infty \tag{2.10}$$

where, from velocity triangles (Fig. 8.5),

$$\tan\beta_1 = \frac{1}{\phi}, \qquad \tan\beta_2 = \frac{1-\psi}{\phi} \tag{8.71}$$

Neglecting the effect of C_D the tip section lift coefficient may thus be approximated in terms of the blade duty (ϕ_t, ψ_t) through

$$C_{L\infty} \approx 2 \frac{t}{l_p} \frac{\psi_t}{\sqrt{\phi_t^2 + (1 - \psi_t/2)^2}}$$

Making use of Eqns (8.59) and (8.60),

$$\frac{w_\infty}{V_a} = \frac{\pi}{J} \sqrt{\{\phi_t^2 + (1 - \psi_t/2)^2\}}$$

so that finally the tip leakage loss, Eqn (8.70), becomes

$$
\begin{aligned}
\frac{TL}{TV_a} &= \frac{64}{5}\frac{\delta_t}{D}\left(\frac{t}{l_p}\right)^{1/2}\frac{\pi^3}{C_T J^3}\;\psi_t^{3/2}\left\{\phi_t^2+\left(1-\frac{\psi_t}{2}\right)^2\right\}^{3/4}\\
&= f_{tl}\left(\frac{\delta_t}{D}\right)\left(\frac{t}{l_p}\right)^{1/2}
\end{aligned}
\tag{8.72}
$$

The tip leakage losses are thus a function of the dimensionless tip clearance δ_t/D, the tip section pitch/chord ratio t/l_p and a loss weighting coefficient f_{tl} dependent upon the propulsor duty (τ,C_T,J) and the propeller tip section duty (ϕ_t,ψ_t), namely

$$
f_{tl}=\frac{64}{5}\frac{\pi^3}{C_T J^3}\psi_t^{3/2}\left\{\phi_t^2+\left(1-\frac{\psi_t}{2}\right)^2\right\}^{3/4}
\tag{8.73}
$$

Example 8.3

A breakdown of the predicted losses based on the above formulations is shown here in Table 8.2 including the consequent predicted propulsive efficiency η_p for a typical Kort Nozzle ducted propeller for a wide range of duties. The performance characteristic (C_T,τ,J) data have been derived by Lewis (1972) from the published experimental results of Van Manen and Oosterveld (1966), and values of other design data have been assumed as follows:

Tip section t/l_p = 1.82
Duct aspect ratio l_d/D = 0.5
Propeller drag coefficient C_{Dp} = 0.006 (based on NACA 64-008)
Duct drag coefficient C_{Dd} = 0.02 (pessimistic value to include hub)

The following points are worthy of note:

(1) To obtain the above characteristic data a suitable approach would be to keep the propulsor forward velocity V_a constant and to vary the propeller speed of rotation n in order to change the advance coefficient $J = V_a/nD$ over the given range $0.372 < J < 0.610$.
(2) Over this range of J the thrust coefficient C_T varies enormously from 2.7 to 7.57.
(3) Curiously, however, the propeller duty at the tip radius varies very little from the central design duty $\phi_t = 0.31687$, $\psi_t = 0.04101$. Furthermore the vector mean flow angle relative to the blade tips β_∞ also varies by only 2° over the operating range, demonstrating a remarkable advantageous feature of ducted propellers. The effect of the duct in augmenting the velocity V_p in the propeller plane is such that, if the propeller rotational speed is increased, V_p also increases, the outcome being that the angle of attack β_1 and the vector mean angle β_∞ remain almost unchanged over $2.7 < C_T < 7.57$. Thus the duct provides the optimum hydrodynamic environment for the propeller blades, enabling typical Kort Nozzle propulsors to operate over a very wide range of thrust coefficients C_T.
(4) The predominant loss is that contributed by the jet axial kinetic energy E_w/TV_a. Next in line is the propeller profile loss F_p/TV_a. Together these provide about 78% of the total losses at the lowest C_T rising to 86.3% at the

Table 8.2 Predicted loss coefficients for Van Manen Screw Series B4-55 with Nozzle No. 19A

C_T		2.7	3.5	4.5	6.0	7.57
τ	Van Manen and	0.785	0.751	0.725	0.7	0.675
J	Oosterveld (1966)	0.610	0.525	0.471	0.410	0.372
ϕ_t	Propeller duty	0.342 11	0.323 20	0.316 87	0.305 79	0.304 52
ψ_t	at tip radius	0.045 02	0.041 06	0.041 01	0.039 93	0.040 00
β_∞		70.71°	71.74°	72.07°	72.67°	72.74°
E_w/TV_a		0.383 11	0.452 43	0.532 29	0.640 18	0.735 90
S_w/TV_a		0.112 90	0.107 37	0.113 14	0.117 68	0.124 77
F_p/TV_a		0.177 85	0.212 60	0.227 70	0.256 77	0.272 15
F_d/TV_a		0.045 99	0.042 75	0.039 71	0.036 60	0.034 95
Total loss		0.719 85	0.815 14	0.912 84	1.051 22	1.167 75
Predicted propulsive efficiency η_p (%)		58.14	55.09	52.28	48.75	46.13

highest C_T, both varying considerably over the operating range. Swirl losses S_w/TV_a are small by comparison but by no means insignificant. On the other hand, the thrust losses due to duct drag are trivial by comparison.

8.5 Prediction of Kort Nozzle ducted propeller characteristic curves

Each set of (C_T, τ, J) data given at the top of Table 8.2 were derived from experimental tests. Thus for a given forward speed V_a in open water $J = V_a/nD$ can be varied simply by changing the propeller rotational speed n. The above measured data are then usually expressed by two characteristic curves of the form τ versus C_T and J versus C_T. In the following sections simple theoretical analyses will be presented which produce remarkably good predictions of off-design characteristics $\tau(C_T)$ and $J(C_T)$ for Kort Nozzle propulsors given a prescribed central design duty (C_{To}, τ_o, J_o).

8.5.1 The $\tau(C_T)$ characteristic

Lewis (1973) developed the following method for predicting the $\tau(C_T)$ characteristic beginning with the hypothesis that the duct *forward* thrust T_d is proportional to the square of the radially inward *downwash* velocity induced by the jet wake, Fig. 8.16.

To establish the relationship between T_d and the wake shed vorticity Γ_w let us consider first the analogy with the flat plate aerofoil shown in Fig. 8.17. The lift generated as a result of its total bound vorticity Γ is given by the Magnus law, $L = \rho W \Gamma$. But from the theory for the flat plate aerofoil (Batchelor, 1970), the magnitude of Γ is given by

$$\Gamma = \pi l W \sin \alpha$$

where l is the chord length, W the mainstream velocity and α its angle of attack
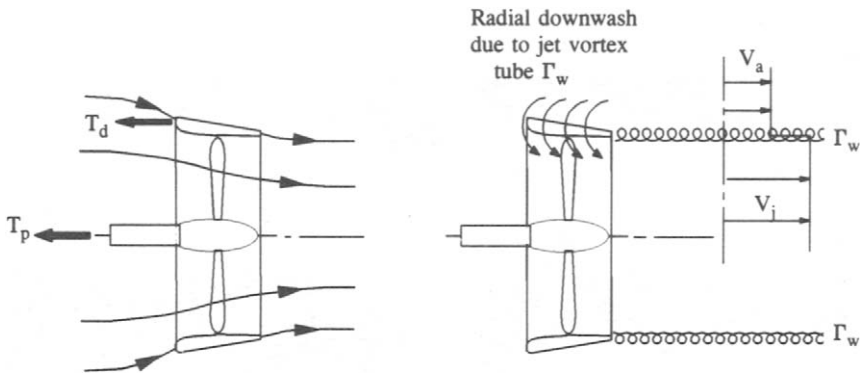
Fig. 8.16 Radially inward downwash velocities induced by Kort Nozzle wake
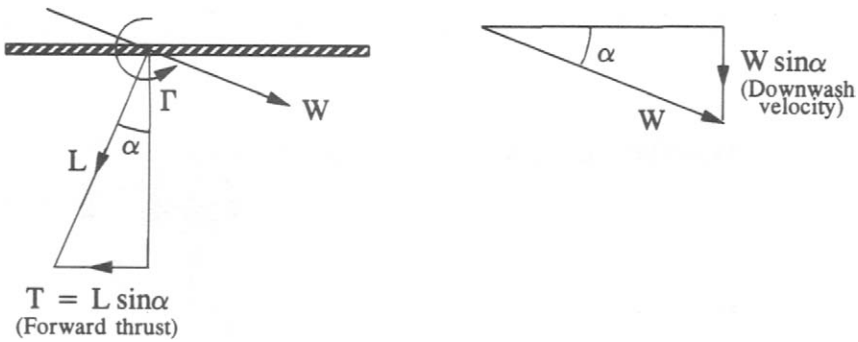
Fig. 8.17 Forward thrust *T* on a flat plate aerofoil at negative incidence

(negative here). Thus the forward component of the lift L, i.e. the forward thrust T, is given by

$$T = L \sin \alpha = \rho \pi l (W \sin \alpha)^2$$

$$\propto (\text{downwash velocity})^2$$

For any other profiled aerofoil with zero lift at zero incidence the same result may be argued qualitatively. Extending this argument now to an annular aerofoil when used to shroud a propeller, Fig. 8.16, the radial inward *downwash* velocity experienced by the duct is caused by the tubular vortex sheet Γ_w sandwiched between the high velocity jet V_j and the outer advance velocity flow V_a. As argued by Lewis (1973), the downwash velocity is proportional to the strength Γ_w of the vortex tube, so that the previous equation may be applied here to give an expression for the consequent duct thrust, namely

$$T_d \propto \Gamma_w^2 \tag{8.74}$$

where the vortex strength Γ_w (see Chapter 9, Section 9.5.3) is given by

$$\Gamma_w = -(V_j - V_a) \tag{8.75}$$

Improving slightly upon Eqn (8.20) by subtracting the hub area from the propeller swept area, the propeller thrust becomes

$$T_p = (p_2 - p_1)\frac{\pi D^2}{4}(1 - h^2) = \rho V_a^2 \left\{ \left(\frac{V_j}{V_a}\right)^2 - 1 \right\} \frac{\pi D^2}{8}(1 - h^2)$$
$$= \tau T = \tau C_T \frac{1}{2}\rho V_a^2 \frac{\pi D^2}{4} \tag{8.76}$$

which reduces to the following, slightly more accurate, development of Eqn (8.24):

$$\frac{V_j}{V_a} = \sqrt{1 + \frac{\tau C_T}{1 - h^2}} \tag{8.76a}$$

Finally the jet bounding vorticity is related to (τ, C_T) through

$$\frac{\Gamma_w}{V_a} = \sqrt{1 + \frac{\tau C_T}{1 - h^2}} - 1 \tag{8.77}$$

Now the duct forward thrust T_d may also be expressed as

$$T_d = (1 - \tau)T = (1 - \tau)C_T \frac{1}{2}V_a^2 \frac{\pi D^2}{4} \tag{8.78}$$

Introducing the last two results into the *downwash* equation (8.74) we have the proportionality

$$(1 - \tau)C_T \propto \left\{ \sqrt{1 + \frac{\tau C_T}{1 - h^2}} - 1 \right\}^2$$

Recalling our hypothesis that this condition is true for all thrust coefficients, it may be applied also to the central design duty (C_{To}, τ_o), resulting in the following identity:

$$\frac{(1 - \tau)C_T}{(1 - \tau_o)C_{To}} \equiv \left\{ \frac{\sqrt{1 + \dfrac{\tau C_T}{1 - h^2}} - 1}{\sqrt{1 + \dfrac{\tau_o C_{To}}{1 - h^2}} - 1} \right\}^2$$

or, rearranging to isolate τ,

$$\tau \equiv 1 - (1 - \tau_o)\left\{ \frac{\sqrt{1 + \dfrac{\tau C_T}{1 - h^2}} - 1}{\sqrt{1 + \dfrac{\tau_o C_{To}}{1 - h^2}} - 1} \right\}^2 \frac{C_{To}}{C_T} \tag{8.79}$$

which has the general form of the required performance characteristic $\tau = f(C_T)$. However, τ cannot be completely isolated but does also appear on the right-hand side of Eqn (8.79). Its solution must therefore be obtained by successive approximation, with each improved estimate of τ being reintroduced into the right-hand side. Convergence is found to be rapid.

8.5.2 The $J(C_T, \tau)$ characteristic

The $J(C_T, \tau)$ characteristic represents the relationship between speed of rotation and thrust. Since thrust is dependent upon blade loading and velocity triangles, which differ for each radius, we shall assume that conditions at the r.m.s. radius r_{ms} are representative of the integrated effect of the whole propeller, defining

$$r_{ms} = \sqrt{\tfrac{1}{2}(r_h^2 + r_t^2)} \qquad (8.80)$$

At this radius the cascade static pressure rise coefficient C_{pm} follows directly from velocity triangles, Fig. 8.5:

$$C_{pm} = \frac{p_2 - p_1}{\frac{1}{2}\rho V_p^2} = \tan^2 \beta_{1m} - \tan^2 \beta_{2m} \qquad (8.81)$$

It can be shown that for cascades with pitch/chord ratio greater than 1.0, the fluid deflection $\varepsilon = \beta_1 - \beta_2$ remains almost constant for small variations of β_1 such as were shown to occur in Kort Nozzle propulsors in the previous section. Thus we may assert the following assumption for the off-design duty:

$$\varepsilon = \beta_{1m} - \beta_{2m} = \varepsilon_o = \beta_{1mo} - \beta_{2mo} \qquad (8.82)$$

Now from Eqn (8.76) C_{pm} may be derived from another direction:

$$C_{pm} = \frac{\tau C_T}{1 - h^2}\left(\frac{V_a}{V_p}\right)^2$$

Introducing Eqn (8.76a) into (8.28a),

$$\frac{V_a}{V_p} = \frac{2\tau}{(1 + \sqrt{1 + \tau C_T/(1 - h^2)})} = \frac{2(1 - h^2)}{C_T}\left(\sqrt{1 + \frac{\tau C_T}{1 - h^2}} - 1\right) \qquad (8.83)$$

so that C_{pm} becomes

$$C_{pm} = \frac{4(1 - h^2)\tau}{C_T}\left(\sqrt{1 + \frac{\tau C_T}{1 - h^2}} - 1\right)^2 \qquad (8.84)$$

Finally we may eliminate β_{1m} from Eqn (8.82) to produce a system of equations involving J, C_T, τ and β_{2m}. Thus β_{1m} may be expressed as

$$\tan \beta_{1m} = \frac{U_m}{V_p} = \frac{2\pi n r_{ms}}{V_a}\frac{V_a}{V_p}$$

$$= \frac{2\pi}{JC_T}(1 - h^2)\sqrt{\frac{(1 + h^2)}{2}}\left(\sqrt{1 + \frac{\tau C_T}{1 - h^2}} - 1\right) \qquad (8.85)$$
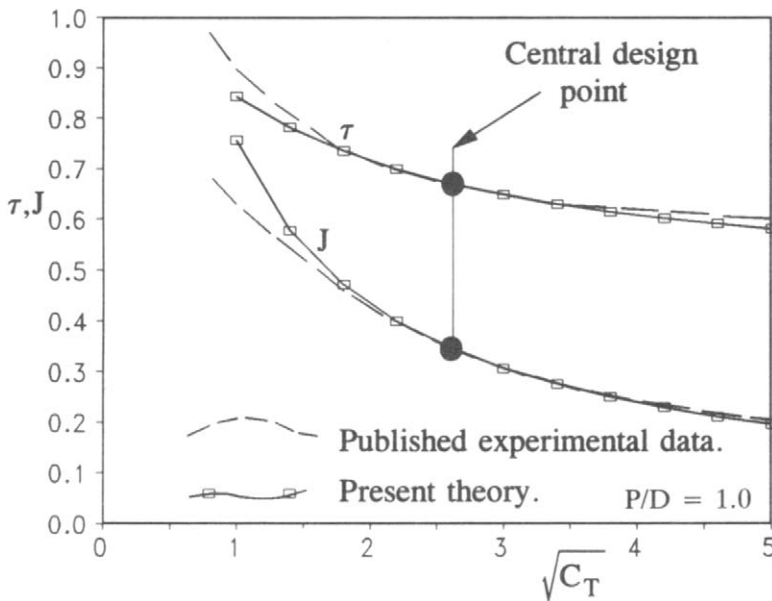
Fig. 8.18 Ka 4-55 propeller in 19A duct – predicted and measured characteristics

The computational procedure is then as follows:

(1) For the given design duty (C_{To}, τ_o, J_o), first calculate τ as directed in Section 8.5.1 for the stated off-design value of C_T.
(2) Derive the cascade pressure coefficient C_{pm} from Eqn (8.83).
(3) Make a first guess at the off-design advance coefficient J.
(4) Hence derive β_{2m} from Eqn (8.81) and calculate the fluid deflection at r_{ms}, namely $\varepsilon = \beta_{1m} - \beta_{2m}$.
(5) Obtain a new estimate of J by scaling the previous one to enforce constant fluid deflection, namely $J' = (\varepsilon/\varepsilon_o)J$.
(6) Damp the solution, e.g. by replacing J with $0.9 \times J + 0.1 \times J'$.
(7) Repeat from (1) to (6) until convergence is obtained.

As can be seen from Fig. 8.18, remarkably accurate predictions were obtained by the application of this simple analysis to the N.S.M.B. propeller Ka 4-55 located within duct 19A taking a central design duty of $C_{To} = 6.25$ for which $\tau_o = 0.677$ and $J_o = 0.358$. Theory agrees with experiment quite closely over most of the extremely wide range of duties, namely $1 < C_T < 25$. The experimental curves shown here were derived from the N.S.M.B. data published by Van Manen (1962). Data from this source are given in terms of the alternative dimensionless coefficient K_T both for the system and for the duct. From Eqn (8.41) conversion to C_T is given by $C_T = (8/\pi) . K_T/J^2$.

The predicted propulsive efficiency likewise agrees extremely well with measured results abstracted from Van Manen (1962) as shown by Fig. 8.19, the only region of substantial disagreement being at very low thrust coefficients $C_T < 1.2$. Perhaps the main reason for this excellent agreement is the fortunate fact that for typical Kort Nozzle propulsors the jet wake remains almost constant in diameter for a wide range of operation. To establish the truth of this an expression for jet diameter/propeller
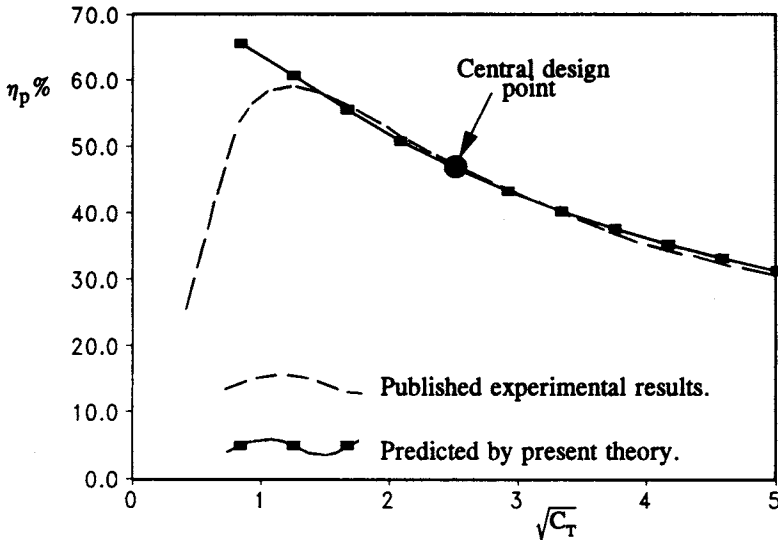
Fig. 8.19 Propulsive efficiency of N.S.M.B. Ka 4-55 propeller in Nozzle 19A for *P/D* = 1.0
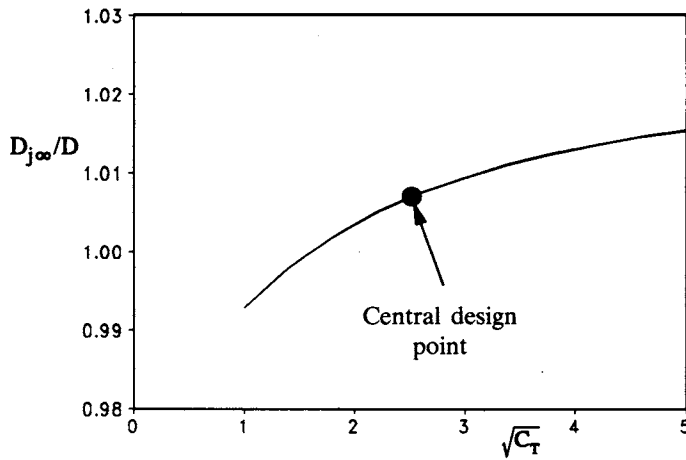
Fig. 8.20 Predicted jet diameter contraction ratio for N.S.M.B. Ka 4-55 propeller in Nozzle 19A

diameter may be obtained as follows. From mass flow continuity we have

$$V_p \frac{\pi D^2}{4} (1 - h^2) = V_{j\infty} \frac{\pi D_{j\infty}^2}{4}$$

(propeller plane)   (downstream jet)

from which

$$\left(\frac{D}{D_{j\infty}}\right)^2 = \frac{V_{j\infty}}{V_a} \frac{V_a}{V_p} \frac{1}{(1 - h^2)}$$
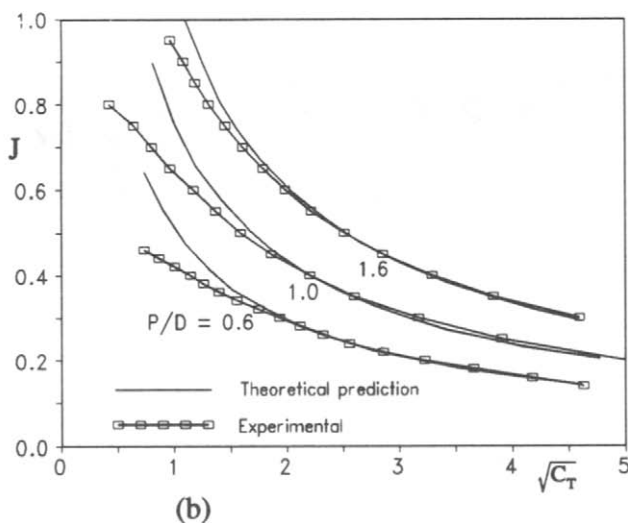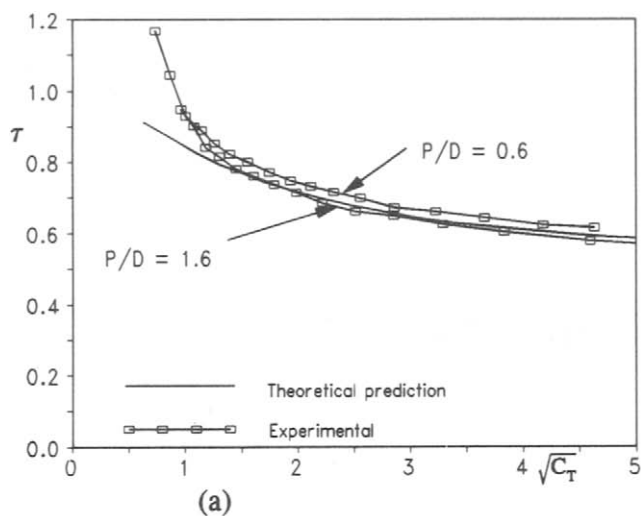
Fig. 8.21 Predicted and measured characteristic performance curves for N.S.M.B. propeller Ka 4-55 in 19A duct at *P/D* ratios of 0.6, 1.0 and 1.6: (a) $\tau(C_T)$ characteristics; (b) $J(C_T,\tau)$ characteristics

After substitution from Eqns (8.76a) and (8.83), we have finally

$$\frac{D_{j\infty}}{D} = \left\{ \frac{2}{C_T}\left(\sqrt{1 + \frac{\tau C_T}{1 - h^2}} - 1 \right) \sqrt{1 + \frac{\tau C_T}{1 - h^2}} \right\}^{-1} \qquad (8.86)$$

Figure 8.20 shows that the downstream jet wake remains almost exactly cylindrical over the whole operating range of the ducted propulsor under consideration, validating the use of the downwash condition which led to the $\tau(C_T)$ characteristic equation (8.79).
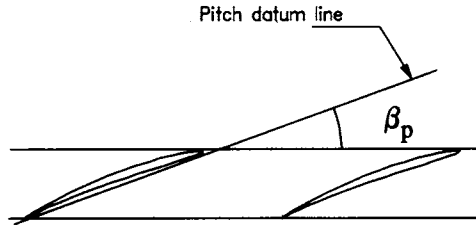
Fig. 8.22 Definition of blade pitch angle β_p

As we have seen already from Eqn (8.79), the predicted thrust ratio τ can be expressed as a function of C_T only irrespective of propeller blade geometry. This is borne out by Fig. 8.21(a) which compares the predicted $\tau(C_T)$ characteristic with experimental results adapted from the experimental data published by Van Manen (1962) for the additional pitch ratios $P/D = 0.6$ and 1.6. Results for $P/D = 1.0$ have already been shown in Fig. 8.18 and have been omitted here to emphasise the negligible influence of the pitch change. Blade geometric pitch P at any radius r is defined as

$$P = 2\pi r \tan \beta_p \qquad (8.87)$$

where β_p is the geometric pitch angle marked out by the pitch datum line, Fig. 8.22, tangential to the pressure side of the propeller blade. The geometric pitch P is frequently constant for sections at all radii of a given propeller, but should P actually vary, the value at 70% of tip radius is adopted as the geometric mean pitch. The Ka 4-55 propeller considered above is designed for a uniform pitch ratio $P/D = 1.0$.

The results shown in Figs 8.18 and 8.21 correspond to blade setting angles β_p of 10.81°, 17.66° and 26.99° respectively and in effect represent the characteristics of three completely different propellers operating within the same N.S.M.B. 19A duct. The three related experimental $\tau(C_T)$ conform closely to the single theoretical characteristic predicted by Eqn (8.79) and thus demonstrate dramatically the almost total control over the thrust ratio τ imposed by the duct geometry.

On the other hand, quite different $J(C_T, \tau)$ characteristics are obtained for the three blade settings, demonstrating, as expected, the close relationship between advance coefficient $J = V_a/nD$ and blade geometric pitch ratio P/D. Once again the curves predicted by the simple theory presented above agree with experimental tests remarkably well, with significant errors to be found only at very low thrust coefficients. Balabaskaran (1982) undertook extensive aerodynamic investigations of this particular ducted propeller, confirming both the towing tank experimentation of Van Manen (1962) and the above fairly modest performance prediction method. He was able to improve upon this by using cascade theory such as that forthcoming from the program CASCADE provided with this book, enabling him to remove the assumption adopted in Section 8.5.2 of constant fluid deflection ε.

9
Selected supporting fluid dynamic analysis

Introduction

An overview of the overall design and performance analysis for a multi-stage axial turbine was presented in Chapter 3, Fig. 3.2, which put into context the three computer programs FIPSI, CASCADE and STACK provided with this book. Table 9.1 summarises the main stages of this overall design sequence.

Table 9.1 Main stages of the overall design sequence for turbomachines

	Task	Program
I	(a) Initial duty specification. (b) Use of dimensionless parameters (e.g. ϕ, ψ data) for overall design choices and performance analysis. (c) Detailed thermodynamic design leading to the definition of velocity triangles.	FIPSI
II	(d) Detailed fluid dynamic design to generate blade shapes which will produce the required velocity triangles. This involves: (i) Cascade analysis. (ii) Meridional analysis.	CASCADE
III	(e) Mechanical design: (i) Generation of blade shapes and stacking of profiles to form a complete blade. (ii) Stress and vibration analyses.	STACK

The main thrust of this book so far has been to provide an analytical framework which links items (a), (b) and (c) for axial turbines (Chapter 3), axial compressors and fans (Chapter 4), mixed-flow and radial turbomachines (Chapter 7), and ducted propellers and fans (Chapter 8). For example, the computer program FIPSI enables the reader to complete a full thermodynamic layout for a multi-stage gas turbine with cross-checks on selection of stage duty coefficients (ϕ, ψ) and related stage efficiency, hub reaction and Mach number levels. FIPSI delivers a complete specification of velocity triangles from hub to casing as input to stage (d), aerodynamic design.

The main purpose of the present chapter is to provide the theoretical basis underlying the program CASCADE, which executes the double task of creating blade geometry as described in Section 2.4 followed by fluid flow analysis to predict outlet angle β_2 for the given inlet angle β_1, and the related blade surface pressure
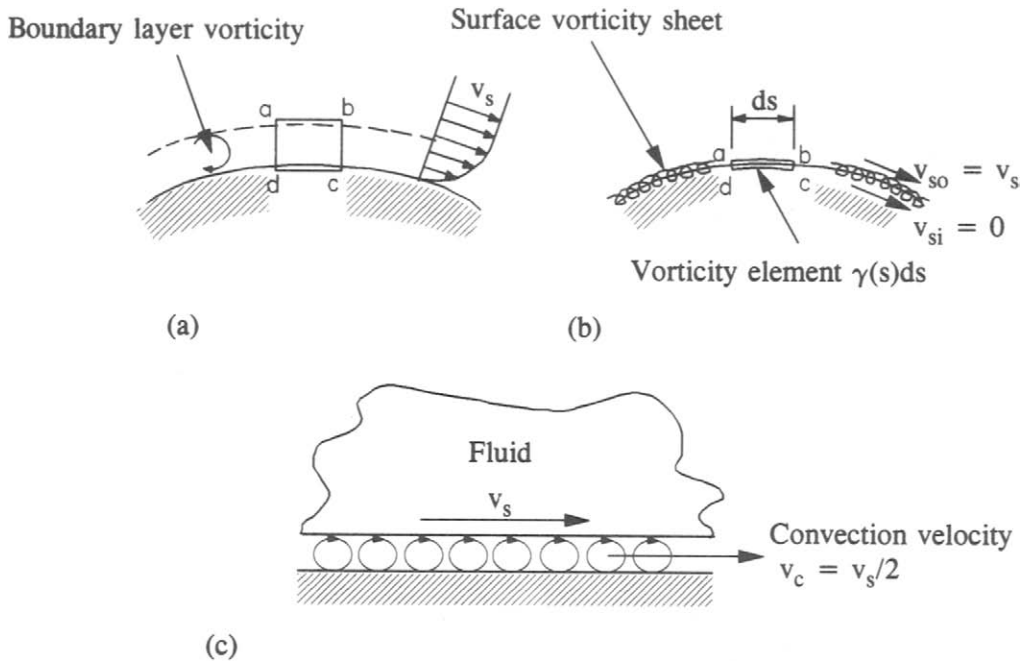
Fig. 9.1 (a) Boundary layer and (b) surface vorticity equivalent for potential flow modelling; (c) self-convection of a surface vorticity sheet

distribution. CASCADE thus enables the reader to design blade profiles which will produce the specified velocity triangles and also to predict off-design performance of the chosen blading. This will be covered in Sections 9.1 to 9.4. The particular type of analysis adopted here is the vortex element boundary integral method which is relatively simple to commit to computer code and economic to run. Although viscous constraints and aerodynamic loading indices such as diffusion factors have been discussed in Chapter 2, the present treatment will be limited only to incompressible inviscid flows. In his research monograph *Vortex Element Methods for Fluid Dynamic Analysis of Engineering Systems* (Lewis, 1991), the present author has extensively reviewed and expounded the fundamentals of this powerful and flexible flow analysis technique with applications to a wide range of turbomachinery configurations including extensions to vortex cloud simulation of viscous fluid flows. The only applications additional to cascades to be summarised in this chapter will be the extension of surface vorticity modelling to axisymmetric flow past bodies of revolution, ducts and ducted propellers, Section 9.5.

9.1 The physical basis of surface vorticity modelling

In all real fluid flows a boundary shear layer exists adjacent to any solid surface, Fig. 9.1(a), containing sufficient vorticity to reduce the fluid velocity from v_s at the outer edge a–b of the shear layer to zero on the wall c–d just inside the shear layer. The vorticity is continuously convected downstream and replenished by convection from upstream and by the creation of more vorticity in the slip-flow or sub-layer adjacent to the wall. This new vorticity is then diffused away from the wall by the fluid
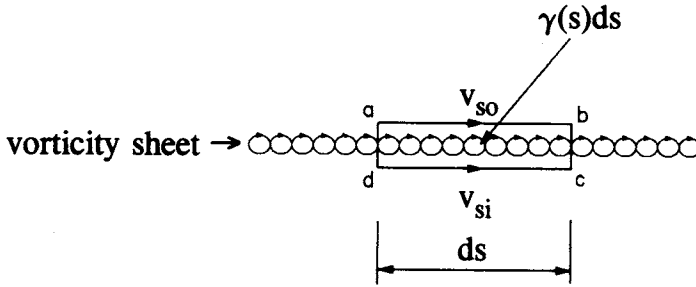
Fig. 9.2 Enlarged view of surface vorticity element

viscosity, thus maintaining the shear profile of the boundary layer. Motion within the boundary layer therefore involves a balance between dynamic normal stresses due to convection and tangential shear stresses due to viscous action. The Reynolds number Re represents the ratio between these stresses. Let us define Re in terms of a representative body length l, namely $Re = (v_s l)/\nu$. If Re is increased by progressively reducing the kinematic viscosity ν, the diminishing influence of viscous diffusion will result in a thinner boundary layer. As $Re \to \infty$ so the boundary layer transforms into an infinitely thin vorticity sheet as illustrated by Fig. 9.1(b) and this concept forms the basis of the physical model underlying the surface vorticity method of potential flow analysis. Thus in inviscid 'potential' flows the bounding surface of any body may be represented by a surface vorticity sheet of strength $\gamma(s)$ per unit length at point s on the surface. Two observations may be made at this point:

(1) The velocity jumps discontinuously from zero below the vorticity sheet at points actually on the body surface to v_s just outside the vorticity sheet.
(2) The vorticity sheet convects itself along the surface with velocity $v_c = \frac{1}{2}v_s$, implying that vorticity must be supplied from upstream, Fig. 9.1(c).

Item (1) suggests a suitable boundary condition to impose at the body surface later for fluid flow modelling, namely that the velocity v_{si} just inside the vorticity sheet and parallel to the surface is to be zero:

$$v_{si} = 0 \qquad (9.1)$$

Let us now define the contour abcd surrounding a small element ds of the surface vorticity sheet, Fig. 9.2, where ab and dc are parallel to the streamlines while da and bc are vanishingly small. The circulation around abcd, defined clockwise positive, may be equated to the total amount of vorticity enclosed by the contour, that is

$$(v_{so} - v_{si})\, \mathrm{d}s = \gamma(s)\, \mathrm{d}s \qquad (9.2)$$

Introducing Eqn (9.1), this reduces to

$$\gamma(s) = v_{so} = v_s \qquad (9.3)$$

In other words the local vortex sheet strength $\gamma(s)$ is exactly equal to the surface velocity v_s in potential flow past a body. Equations (9.1) and (9.3) thus provide the key to surface vorticity modelling of potential flows as originally propounded by E.
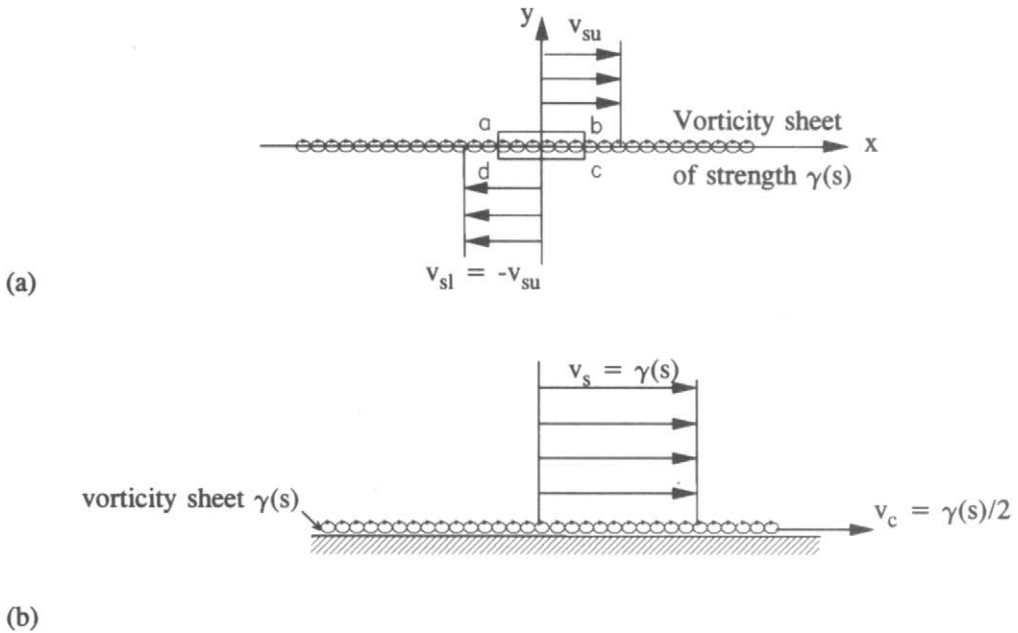
Fig. 9.3 Surface vorticity model to simulate flow of a uniform stream v_s past a plane wall: (a) infinite vortex sheet $\gamma(s)$ between $x = \pm\infty$; (b) vortex sheet $\gamma(s)$ plus uniform stream $\gamma(s)/2$

Martensen (1959), often referred to as the *Martensen method*. The procedure may be summarised as follows:

(1) The body surface is covered by a surface vorticity sheet of initially unknown strength $\gamma(s)$.
(2) A surface boundary condition $v_{si} = 0$ is imposed on the inner surface of the sheet. This is stated in the form of an integral equation to be derived in the next section.
(3) The integral equation is solved for a selection of discrete surface vortex elements at surface locations s_n resulting in the required $\gamma(s_n)$ values.
(4) The local surface velocity v_{sn} follows directly from Eqn (9.3) since
$v_{sn} = \gamma(s_n)$.

9.1.1 Surface vorticity simulation of flow past a plane wall

A simple example of surface vorticity modelling which helps to bring out the essential features is illustrated in Fig. 9.3, namely flow past a plane wall. Let us consider first the velocity field induced by a vortex sheet of strength $\gamma(s)$ lying along the x-axis between $\pm\infty$, Fig. 9.3(a). The vorticity will induce uniform velocity fields parallel to the x-axis but in opposite directions above and below the sheet as illustrated, $v_{sl} = -v_{su}$. By taking the circulation around the element abcd as before, for this case we obtain

$$\gamma(s)\,ds = v_{su}\,ds - v_{sl}\,ds = 2v_{su}\,ds$$

Surface vorticity element $\gamma(s_n)ds_n$

s_m

β_m

r_{mn}

$dq_{mn} = \dfrac{\gamma(s_n)ds_n}{2\pi r_{mn}}$

ϕ_{mn}

s_n

W_∞

V_∞

α_∞

U_∞
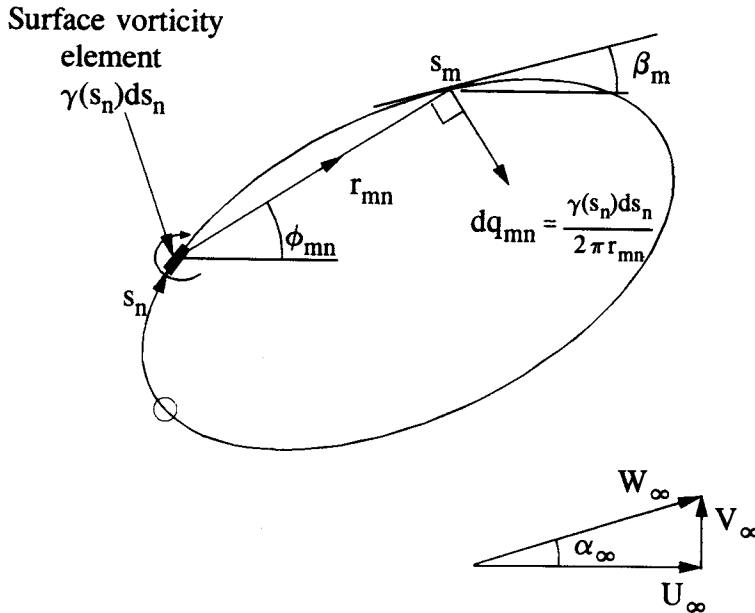
Fig. 9.4 Surface vorticity model for flow past a two-dimensional body in a uniform stream W_∞

resulting in

$$v_{su} = -v_{sl} = \tfrac{1}{2}\gamma(s) \qquad\qquad (9.4)$$

If we now superimpose a uniform stream of strength v_{su} parallel to the x-axis over the whole flow field, the outcome will be as illustrated in Fig. 9.3(b). Above the x-axis the velocity will be that of a uniform stream of strength $v_s = \gamma(s)$. Below the x-axis the velocity will be zero, so that we may replace this by a solid boundary. It follows also from this argument that the vortex sheet of the real flow convects itself parallel to the body surface with velocity $v_c = v_{su} = \gamma(s)/2$.

9.1.2   Martensen's boundary integral equation

We consider next the flow past a two-dimensional body immersed in a uniform stream W_∞ inclined to the x-axis at an angle α_∞, Fig. 9.4. Applying the principles just outlined, the flow may be modelled by clothing the body surface with a vorticity sheet of appropriate strength $\gamma(s)$ where s is measured clockwise around the body perimeter from some zero datum O such as the leading edge in the case of an aerofoil. Now the velocity dq_{mn} at some surface location s_m induced by the vortex element $\gamma(s_n)\,ds_n$ at location s_n will be normal to the radial vector r_{mn} and will be of magnitude

$$dq_{mn} = \frac{\gamma(s_n)\,ds_n}{2\pi r_{mn}} \qquad\qquad (9.5)$$

In order to state the surface boundary condition, Eqn (9.1), dq_{mn} needs to be resolved parallel to the body surface at s_m, namely

$$dv_{smn} = dq_{mn} \cos\left(\beta_m + \frac{\pi}{2} - \phi_{mn}\right) = \frac{\cos\left(\beta_m + \dfrac{\pi}{2} - \phi_{mn}\right)}{2\pi r_{mn}} \gamma(s_n) ds_n \qquad (9.6)$$

where β_m is the body profile slope at s_m. For computational purposes it proves more convenient to first express the components of dq_{mn} parallel to the x- and y-axes in terms of the (x, y) coordinates of points s_m and s_n. Thus

$$\left.\begin{aligned}
dU_{mn} &= \frac{\gamma(s_n) ds_n}{2\pi r_{mn}} \sin\phi_{mn} = \left(\frac{y_m - y_n}{2\pi r_{mn}^2}\right) \gamma(s_n) ds_n \\
dV_{mn} &= -\frac{\gamma(s_n) ds_n}{2\pi r_{mn}} \cos\phi_{mn} = -\left(\frac{x_m - x_n}{2\pi r_{mn}^2}\right) \gamma(s_n) ds_n
\end{aligned}\right\} \qquad (9.7)$$

Resolving dU_{mn} and dV_{mn} parallel to the surface at s_m and adding them we obtain

$$\left.\begin{aligned}
dv_{cmn} &= dU_{mn} \cos\beta_m + dV_{mn} \sin\beta_m \\
&= \frac{1}{2\pi}\left\{\frac{(y_m - y_n)\cos\beta_m - (x_m - x_n)\sin\beta_m}{(x_m - x_n)^2 + (y_m - y_n)^2}\right\} \gamma(s_n) ds_n
\end{aligned}\right\} \qquad (9.8)$$

The self-convection velocity v_{cm} parallel to s_m due to the entire sheet can now be obtained by integration of Eqn (9.8) to yield

$$v_{cm} = \oint dv_{cmn} = \oint k(s_m, s_n)\, \gamma(s_n) ds_n \qquad (9.9)$$

where the coupling coefficient $k(s_m, s_n)$ linking points s_m and s_n is given by

$$k(s_m, s_n) = \frac{1}{2\pi}\left\{\frac{(y_m - y_n)\cos\beta_m - (x_m - x_n)\sin\beta_m}{(x_m - x_n)^2 + (y_m - y_n)^2}\right\} \qquad (9.10)$$

Now the contour integral in Eqn (9.9) actually runs through the centre of the sheet and gives us the convection velocity equivalent to v_c. Fig. 9.3. As indicated in the previous section we must therefore subtract $\gamma(s_n)/2$ to obtain the velocity just inside the sheet, namely

$$v_{smi} = -\tfrac{1}{2}\gamma(s_m) + \oint k(s_m, s_n)\, \gamma(s_n) ds_n \qquad (9.11)$$

In addition to this we must account for the component of the uniform stream resolved parallel to the surface at s_m, namely

$$\begin{aligned}
W_{sm} &= U_\infty \cos\beta_m + V_\infty \sin\beta_m \\
&= W_\infty(\cos\alpha_\infty \cos\beta_m + \sin\alpha_\infty \sin\beta_m)
\end{aligned} \qquad (9.12)$$
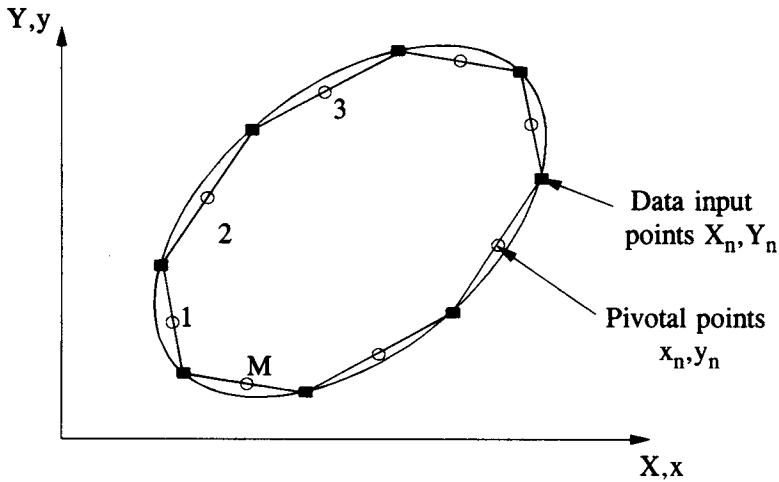
Fig. 9.5 Representation of body surface by straight line elements

Combining the last two equations to cover all contributions to v_{si}, the boundary condition at s_m, Eqn (9.1), may be expressed as

$$-\tfrac{1}{2}\gamma(s_m) + \oint k(s_m, s_n)\,\gamma(s_n)\,\mathrm{d}s_n + W_\infty(\cos\alpha_\infty \cos\beta_m + \sin\alpha_\infty \sin\beta_m) = 0 \quad (9.13)$$

9.1.3 Numerical representation of Martensen's boundary integral equation

For satisfaction of the boundary condition of parallel flow at the body surface, Eqn (9.13) is to be obeyed at all locations s_m. A practical approach which approximates to this with good accuracy in practice involves selection of a finite number M of so-called 'pivotal' points representative of the body surface, Fig. 9.5.

This can be achieved most simply if the surface is represented by M straight line elements of length Δs_n with pivotal points (x_n, y_n) located at the centre. The continuous vorticity sheet is then replaced by M finite vortex elements of strength $\gamma(s_n)\Delta s_n$ and Eqn (9.13) transorms into the linear equation

$$\sum_{n=1}^{M} K(s_m, s_n)\,\gamma(s_n) = -U_\infty \cos\beta_m - V_\infty \sin\beta_m \quad (9.14)$$

where the modified coupling coefficients $K(s_m, s_n)$ are given by

$$K(s_m, s_n) = k(s_m, s_n)\Delta s_n = \frac{\Delta s_n}{2\pi}\left\{\frac{(y_m - y_n)\cos\beta_m - (x_m - x_n)\sin\beta_m}{(x_m - x_n)^2 + (y_m - y_n)^2}\right\} \quad (9.15)$$

Several comments are needed at this point. Firstly, the summation in Eqn (9.14) is equivalent to evaluation of the contour integral of Eqn (9.13) by the trapezium rule. Secondly, one such equation must be written for each pivotal point (x_m, y_m) resulting in a set of M linear equations for the M initially unknown surface vorticity values $\gamma(s_1), \gamma(s_2), \ldots, \gamma(s_M)$. Thirdly, the term $\tfrac{1}{2}\gamma(s_m)$ of Eqn (9.13) has been absorbed into
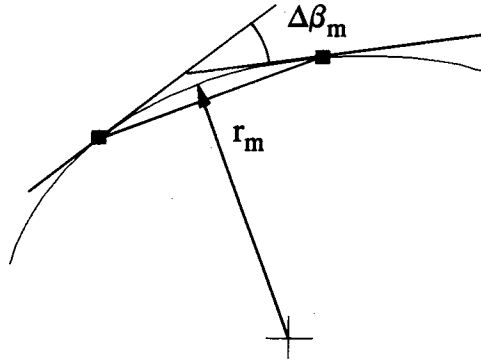
Fig. 9.6 Curvature of element m

the coupling coefficient $K(s_m, s_m)$ which is also indeterminate, a problem to be dealt with in the next section.

9.1.4 The self-inducing coupling coefficient $K(s_m, s_m)$

Following up this last point, the coupling coefficient $K(s_m, s_m)$ may be expressed as

$$K(s_m, s_m) = -\tfrac{1}{2} + K'_{mm} \qquad (9.16)$$

where, from Eqn (9.15), K'_{mm} is given by

$$K'_{mm} = \frac{\Delta s_m}{2\pi} \lim_{s_m \to s_n} \left\{ \frac{(y_m - y_n)\cos\beta_m - (x_m - x_n)\sin\beta_m}{(x_m - x_n)^2 + (y_m - y_n)^2} \right\} \qquad (9.17)$$

Since both numerator and denominator approach zero as $s_m \to s_n$ this expression is finite but indeterminate. As shown in full by Lewis (1991, page 23), application of L'Hospital's rule twice over results in

$$\left. \begin{aligned}
K'_{mm} &= \frac{\Delta s_m}{2\pi} \left\{ \frac{-\,\mathrm{d}^2 y_m/\mathrm{d}x_m^2}{[1 + (\mathrm{d}y_m/\mathrm{d}x_m)^2]^{3/2}} \right\} \\[2mm]
&= \frac{\Delta s_m}{4\pi r_m} \approx -\frac{\Delta\beta_m}{4\pi}
\end{aligned} \right\} \qquad (9.18)$$

where r_m is the internal radius of curvature of element m and $\Delta\beta_m$ is the change in profile slope from one end of the element to the other, Fig. 9.6.

Thus the so-called 'self-inducing' coupling coefficient $K(s_m, s_m)$, which represents the velocity induced parallel to the surface at s_m by element Δs_m itself, may be expressed with good approximation by

$$\begin{aligned}
K(s_m, s_m) &= -\frac{1}{2} - \frac{\Delta\beta_m}{4\pi} \\[2mm]
&\approx -\frac{1}{2} - \frac{\beta_{m+1} - \beta_{m-1}}{8\pi}
\end{aligned} \qquad (9.19)$$

where $\Delta\beta_m$ is evaluated as half the change in slope of the neighbouring elements s_{m-1} and s_{m+1}, namely $\frac{1}{2}(\beta_{m+1} - \beta_{m-1})$.

9.2 Computational scheme for flow past a body in a uniform stream

The linear equations (9.14) have the matrix form

$$
\begin{vmatrix}
K_{11} & K_{12} & K_{13} & \cdots & K_{1M} \\
K_{21} & K_{22} & K_{23} & \cdots & K_{2M} \\
K_{31} & K_{32} & K_{33} & \cdots & K_{3M} \\
\vdots & \vdots & \vdots & \cdots & \vdots \\
K_{M1} & K_{M2} & K_{M3} & \cdots & K_{MM}
\end{vmatrix}
\begin{vmatrix}
\gamma(s_1) \\
\gamma(s_2) \\
\gamma(s_3) \\
\vdots \\
\gamma(s_M)
\end{vmatrix}
=
\begin{vmatrix}
\text{rhs}_1 \\
\text{rhs}_2 \\
\text{rhs}_3 \\
\vdots \\
\text{rhs}_M
\end{vmatrix}
\qquad (9.20)
$$

(Coupling coefficient matrix)　　　Vorticity　　rhs
　　　　　　　　　　　　　　　　　　　　　vector　　　vector

with the simplified coupling coefficient notation $K_{mn} \equiv K(s_m, s_n)$ and the right-hand sides

$$\text{rhs}_m = -U_\infty \cos\beta_m - V_\infty \sin\beta_m \qquad (9.21)$$

Generally speaking the dominant coefficients of the coupling coefficient matrix will be those lying on the leading diagonal K_{11}, K_{22}, etc., and solution of the equations by matrix inversion is appropriate. A suitable numerical sequence is then as follows:

(1) Input $M + 1$ sets of raw body profile data coordinates (X_n, Y_n) as illustrated in Fig. 9.5. Note that for profile closure $X_{M+1} = X_1$ and $Y_{M+1} = Y_1$.
(2) Define the pivotal points (x_n, y_n) and element slopes β_n, namely

$$x_n = \tfrac{1}{2}(X_n + X_{n+1}), \quad y_n = \tfrac{1}{2}(Y_n + Y_{n+1}) \qquad (9.22)$$

$$\beta_n = \arctan\left(\frac{y_{n+1} - y_n}{x_{n+1} - x_n}\right) \qquad (9.23)$$

(3) Set up the coupling coefficient matrix using Eqns (9.15) and (9.19).
(4) Evaluate the rhs vector using Eqn (9.21).
(5) Invert the coupling coefficient matrix.
(6) Multiply the rhs vector by the inverted matrix to obtain the solution $\gamma(s_n) = v_{sn}$.

Example 9.1 Flow past a circular cylinder

The exact solution for the flow of a uniform stream U_∞ past a circular cylinder is well known (Batchelor, 1970), the surface velocity being given by

$$v_s = 2U_\infty \cos\phi \qquad (9.24)$$

Fig. 9.7 Profile data specification for a circular cylinder
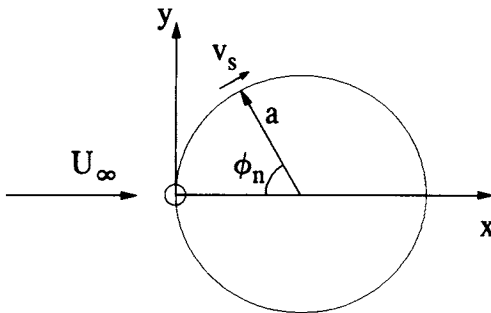
Coordinates of circle

$$X_n = a(1-\cos\phi_n)$$
$$Y_n = a \cdot \sin\phi_n$$
$$\phi_n = \left(\frac{n-1}{M}\right)2\pi \qquad n = 1...M$$

Table 9.2 Flow of a uniform stream $U_\infty = 1.0$ past a circle

Element number	Surface vorticity method v_s	Exact solution v_s
1	0.444 495	0.445 042
2	1.245 450	1.246 980
3	1.799 734	1.801 938
4	1.997 553	2.000 000
5	1.799 734	1.801 938
6	1.245 456	1.246 980
7	0.444 498	0.445 042
8	−0.444 498	−0.445 042
9	−1.245 458	−1.246 980
10	−1.799 740	−1.801 938
11	−1.997 558	−2.000 000
12	−1.799 737	−1.801 938
13	−1.245 459	−1.246 980
14	−0.444 501	−0.445 042

where ϕ is defined in Fig. 9.7 together with expressions for the data points (X_n, Y_n). A Pascal code CYLINDER.PAS which implements the above procedure is provided on the accompanying PC disc, output from which is shown in Table 9.2.

For a simple representation of the cylinder by as few as 14 elements the prediction of v_s by the surface vorticity method agrees with the exact solution to within 0.1%.

9.2.1 The problems of the singular matrix and leakage flux

Before moving on to extend this analysis to lifting aerofoils and cascades let us consider one important property of the coupling coefficient matrix.

The arrows shown in Fig. 9.8 represent the coupling coefficients in column n, in other words the velocities v_{smn} parallel to each element m induced by a vortex of
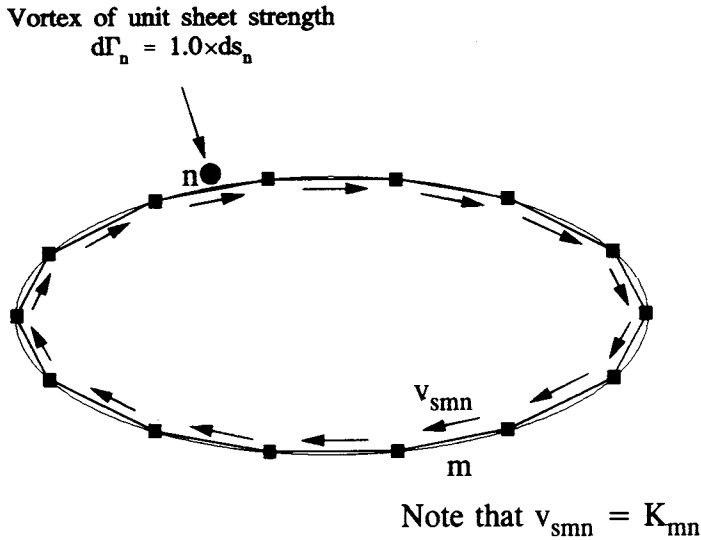
Fig. 9.8 Circulation around profile interior induced by element of unit sheet strength at *n*

unit sheet strength $d\Gamma_n = 1.0 \times ds_n$ located on element *n*. If we now take the sum of the products $K_{mn}\Delta s_m$ for column *n*, Eqn (9.20), we thus obtain

$$K_{1n}\Delta s_1 + K_{2n}\Delta s_2 + \ldots + K_{Mn}\Delta s_M = \sum_{m=1}^{M} K_{mn}\Delta s_m$$

$$\equiv \oint v_{smn}\,ds_m \tag{9.25}$$

$$= C, \text{ circulation around profile interior}$$

For each column *n* this represents the circulation around the profile interior due to the vorticity on element *n*. Since the vorticity sheet is just outside the body surface, the circulation *C* must be zero. Thus this summation for each column should ideally be zero. In practice due to numerical approximation *C* will be very small but not quite zero, implying the presence in the above solution of some leakage flux through the surface to accommodate the apparent tiny residual internal circulation.

If, on the other hand, the sums of all columns were identically zero, the matrix would be singular and without the specification of some further constraints no solution would be forthcoming. The necessity to impose a trailing edge Kutta–Joukowski condition solves this dilemma for lifting bodies which we will consider next.

9.3 Lifting aerofoils

Simulation of the flow past aerofoils introduces two new problems. Firstly, for thin body profiles, coupling coefficients on the back-diagonal are inaccurate. Secondly there is the need to impose the trailing edge Kutta–Joukowski condition related to the generation of lift. These matters will be dealt with in the next two subsections.

$$
\begin{matrix}
K_{11} & K_{12} & K_{13} & K_{14} & K_{15} & K_{16} \\
K_{21} & K_{22} & K_{23} & K_{24} & K_{25} & K_{26} \\
K_{31} & K_{32} & K_{33} & K_{34} & K_{35} & K_{36} \\
K_{41} & K_{42} & K_{43} & K_{44} & K_{45} & K_{46} \\
K_{51} & K_{52} & K_{53} & K_{54} & K_{55} & K_{56} \\
K_{61} & K_{62} & K_{63} & K_{64} & K_{65} & K_{66}
\end{matrix}
$$
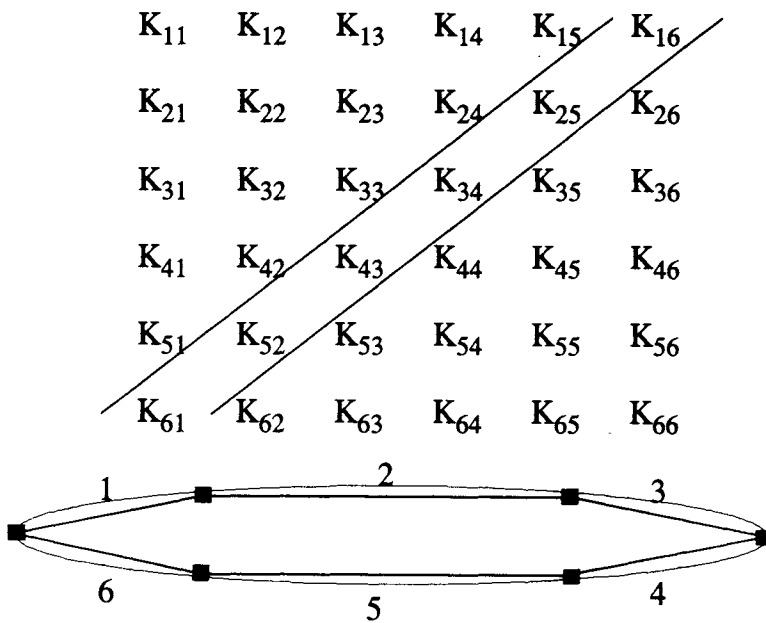
Fig. 9.9 Back-diagonal coupling coefficients linking opposite body profile points

9.3.1 Back-diagonal correction

To illustrate this problem the full matrix is shown in Fig. 9.9 for a thin profile, adopting just six elements for simplicity.

Coefficients on the back-diagonal represent the mutual influence of vortex elements directly opposite one another, namely K_{16} and K_{61}, K_{25} and K_{52}, K_{34} and K_{43}. As shown in detail by the present author (Lewis, 1991), for very thin bodies such as aerofoils these coupling coefficients become both large and inaccurate, resulting in considerable residual circulation C, Eqn (9.25). The recommended procedure to correct for this, first advocated by Jacob and Riegels (1963), is to enforce zero internal circulation $C = 0$ for each column. To illustrate this, application of Eqn (9.25) to column 4 of Fig. 9.9 results in

$$
K_{34} = -\frac{1}{\Delta s_3}(K_{14}\Delta s_1 + K_{24}\Delta s_2 + K_{44}\Delta s_4 + K_{54}\Delta s_5 + K_{64}\Delta s_6) \tag{9.26}
$$

If this estimate for K_{34} and all the other back diagonal coefficients is used instead of the normal value as given by Eqn (9.15), 'numerical leakage flux' is eliminated, ensuring that the body profile is a true streamline of the flow. However, the matrix will then be singular and insoluble without further actions such as those to be considered next.

9.3.2 Introduction of bound circulation

The most obvious way of making the matrix non-singular is to impose also a value for the circulation $\Gamma = \oint v_s \, ds$ around the outside of the body profile. Γ is called the
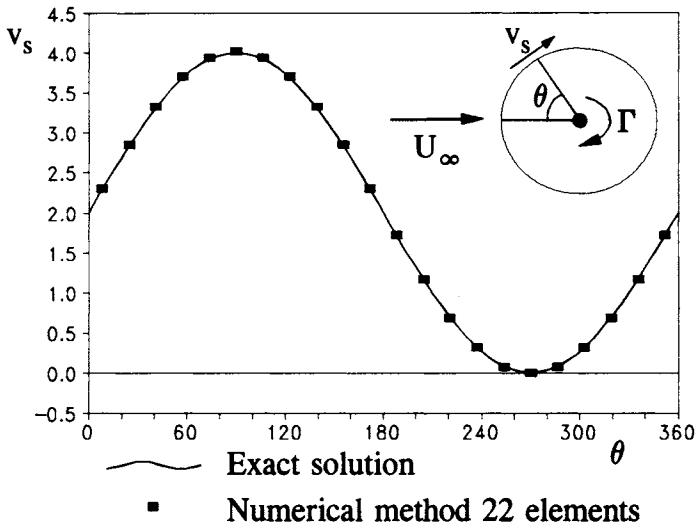
Fig. 9.10 Flow past a circular cylinder with circulation of strength $\Gamma = 4\pi a U_\infty$

bound circulation and is thus given by the total net vorticity on the body surface, namely

$$\Gamma = \oint v_s \, \mathrm{d}s = \oint \gamma(s) \, \mathrm{d}s = \sum_{n=1}^{M} \gamma(s_n) \Delta s_n$$

or in more detail

$$\gamma(s_1)\Delta s_1 + \gamma(s_2)\Delta s_2 + \gamma(s_3)\Delta s_3 + \ldots + \gamma(s_M)\Delta s_M = \Gamma \qquad (9.27)$$

If this equation is added to any one of the Martensen equations (9.20), the matrix will become non-singular and will deliver a solution for the flow with prescribed bound vorticity Γ. Better practice is the addition of Eqn (9.27) to every equation of the matrix. The mth equation (9.14) then becomes

$$\sum_{n=1}^{M} (K(s_m, s_n) + \Delta s_n) \gamma(s_n) = - U_\infty \cos \beta_m - V_\infty \sin \beta_m + \Gamma \qquad (9.28)$$

A Pascal source code MAGNUS.PAS which applies this strategy to the flow past a circular cylinder with prescribed circulation Γ is included on the accompanying PC disc. Output is shown in Fig. 9.10 for a 22-element simulation in comparison with the exact solution (Batchelor, 1970), namely

$$v_s = 2U_\infty \sin \theta + \frac{\Gamma}{2\pi a} \qquad \text{(exact solution, Fig. 9.10)} \qquad (9.29)$$

where a is the radius of the cylinder. The chosen circulation for this example was of value $\Gamma = 4\pi a U_\infty$, which is just sufficient to reduce the velocity to zero at $\theta = 3\pi/2$
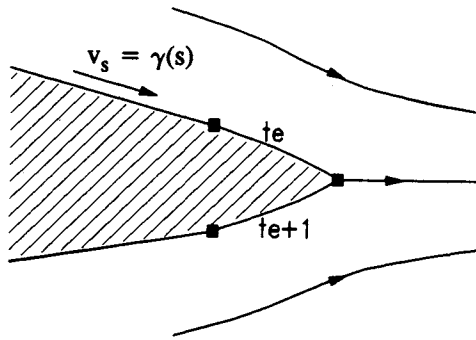
Fig. 9.11 Trailing edge flow and the Kutta–Joukowski condition

at the centre of the bottom surface as can be checked from the exact solution above.

9.3.3   Trailing edge Kutta–Joukowski condition

In reality we are unable to prescribe the bound vorticity Γ which, for aerofoils, will be strongly controlled by flow in the trailing edge region. As illustrated by Fig. 9.11 the flow direction on both upper and lower surfaces will be from left to right approaching the trailing edge. The sign of the local surface velocity and associated vorticity, $v_s = \gamma(s)$, are defined as clockwise $+^{ve}$. Thus a suitable statement of the Kutta–Joukowski trailing edge condition would be achieved by imposing the constraint of equal and opposite vorticity strengths of the two surface elements te and te + 1 which form the trailing edge, namely

$$\gamma(s_{te}) = -\gamma(s_{te+1}) \tag{9.30}$$

One way to proceed is to replace Γ by a unit bound vortex so that Eqn (9.28) becomes

$$\sum_{n=1}^{M} (K(s_m, s_n) + \Delta s_n)\gamma(s_n) = -(U_\infty \cos\beta_m + V_\infty \sin\beta_m) + 1$$

Since the right-hand side has two independent components, we may break this linear equation into separate equations for W_∞ and Γ, namely

$$\left. \begin{aligned} \sum_{n=1}^{M} (K(s_m, s_n) + \Delta s_n)\gamma_1(s_n) &= -(U_\infty \cos\beta_m + V_\infty \sin\beta_m) \\[2mm] \sum_{n=1}^{M} (K(s_m, s_n) + \Delta s_n)\gamma_2(s_n) &= 1 \end{aligned} \right\} \tag{9.31}$$

which deliver separate solutions for $\gamma_1(s)$ and $\gamma_2(s)$. Since these use the same coupling coefficient matrix this procedure demands no additional major computing requirements. Now for any particular bound vortex Γ the final solution may be expressed by recombining the separate solutions through

$$v_{sn} = \gamma(s_n) = \gamma_1(s_n) + \Gamma\gamma_2(s_n) \tag{9.32}$$

Introducing this expression into the trailing edge equation (9.30) we may then obtain the following solution for the aerofoil bound vorticity:

$$\Gamma = -\frac{\gamma_1(s_{te}) + \gamma_1(s_{te+1})}{\gamma_2(s_{te}) + \gamma_2(s_{te+1})} \tag{9.33}$$

As it stands the solution of Eqn (9.31) is required for each mainstream velocity specification $(W_\infty, \alpha_\infty)$. A further simplification is obtained if Eqn (9.31a) is broken down yet again into two separate equations for unit uniform streams $U_\infty = 1$ and $V_\infty = 1$ in the x and y directions, resulting in the following three independent *unit* equations:

$$\left.\begin{array}{ll} \displaystyle\sum_{n=1}^{M} (K(s_m, s_n) + \Delta s_n)\gamma_u(s_n) = -\cos\beta_m & \text{for } U_\infty = 1, \ V_\infty = 0 \\[2em] \displaystyle\sum_{n=1}^{M} (K(s_m, s_n) + \Delta s_n)\gamma_v(s_n) = -\sin\beta_m & \text{for } U_\infty = 0, \ V_\infty = 1 \\[2em] \displaystyle\sum_{n=1}^{M} (K(s_m, s_n) + \Delta s_n)\gamma_\Gamma(s_n) = 1 & \text{for } \Gamma = 1 \end{array}\right\} \tag{9.34}$$

These may be solved once and for all and the results recombined for any desired values of U_∞, V_∞ in the following manner. First apply the Kutta condition, Eqn (9.33), to the two unit uniform stream solutions to give the unit bound vortex strengths Γ_u and Γ_v, namely

$$\left.\begin{array}{l} \Gamma_u = -\dfrac{\gamma_u(s_{te}) + \gamma_u(s_{te+1})}{\gamma_\Gamma(s_{te}) + \gamma_\Gamma(s_{te+1})} \\[1.5em] \Gamma_v = -\dfrac{\gamma_v(s_{te}) + \gamma_v(s_{te+1})}{\gamma_\Gamma(s_{te}) + \gamma_\Gamma(s_{te+1})} \end{array}\right\} \tag{9.35}$$

The solution for any specified values of U_∞ and V_∞ then becomes

$$v_{sn} = U_\infty[\gamma_u(s_n) + \Gamma_u\gamma_\Gamma(s_n)] + V_\infty[\gamma_v(s_n) + \Gamma_v\gamma_\Gamma(s_n)] \tag{9.36}$$

and the total bound vorticity is given by

$$\Gamma = U_\infty\Gamma_u + V_\infty\Gamma_v \tag{9.37}$$

Example 9.2 Flow past an aerofoil

The program AEROFOIL.PAS (source code given on accompanying PC disc) completes this computation, an example of which is shown in Fig. 9.12 for profile NACA0012 with a circular arc camber line and angle $\theta = 30°$. Either of the programs CASCADE or STACK may be used to generate the profile coordinates following the standard geometrical specification explained in Section 2.3, the data being
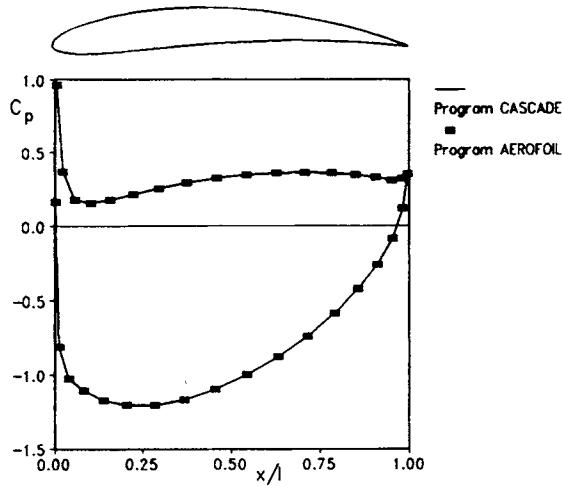
Profile – NACA0012   Circular arc camber $\theta = 30°$

$W_\infty = 1.0$, $\alpha_\infty = 2°$, ($t/l = 100$ for CASCADE calculation)

Fig. 9.12 Comparison of surface pressure distribution predicted by programs CASCADE and AEROFOIL

recorded in the file RAWDATA. The predicted distribution of surface pressure coefficient C_p, as defined by Eqn (2.14), is compared here with that predicted by the program CASCADE, for which an extremely wide blade pitch $t/l = 100$ was introduced to simulate the isolated profile. The two programs are in close agreement.

9.3.4 Computational flow sequence for programs AEROFOIL.PAS and BLADEROW.PAS

To conclude this section the overall computational flow sequence for prediction of the flow past an aerofoil is illustrated in Fig. 9.13. All the procedures up to and including calculation of the unit solutions are totally independent of the mainstream velocity W_∞ and are calculated once and for all for the given aerofoil profile. The program then permits the selection of successive values of W_∞ and α_∞ as required. The reader is referred to the source code AEROFOIL.PAS for further details.

This same computational sequence is appropriate for surface vorticity analysis of turbomachine cascade flows which will be considered in the next section.

9.4 Turbomachine cascades

The previous analysis may be extended quite easily to deal with turbomachine aerofoil or blade cascades by introduction of an alternative coupling coefficient $K(s_m, s_n)$ which automatically accounts for the complete array of blades located between $y = \pm\infty$, Fig. 9.14(a). To derive an expression for $K(s_m, s_n)$ consider first the infinite array of point vortices of strength Γ, Fig. 9.14(b). As shown by Traupel (1945) and

```
┌─────────────────────────┐
│    Read $X_n$, $Y_n$ profile    │
│       coordinates       │
│        from file        │
└─────────────────────────┘
             │
             ▼
┌─────────────────────────┐
│    Data preparation.    │
│ Pivotal points and $\beta_m$ values │
└─────────────────────────┘
             │
             ▼
┌─────────────────────────┐
│     Calculation of      │
│   coupling coefficients │
│   and right-hand sides  │
└─────────────────────────┘
             │
             ▼
┌─────────────────────────┐
│      Back-diagonal      │
│        correction       │
└─────────────────────────┘
             │
             ▼
┌─────────────────────────┐
│     Add on unit vortex  │
│  (Eqn (9.27) with $\Gamma = 1$) │
└─────────────────────────┘
             │
             ▼
┌─────────────────────────┐
│     Invert matrix and   │
│   calculate unit solutions │
└─────────────────────────┘
             │
             ▼
┌─────────────────────────┐
│  Input uniform stream data │
│     $W_\infty$ and $\alpha_\infty$   │
└─────────────────────────┘
             │
             ▼
┌─────────────────────────┐
│ Solution for $\gamma(s) = v_s$ and │
│ hence $C_p$ distribution and $C_L$ │
└─────────────────────────┘
             │
             ▼
        ◇ New case? ◇ ── yes
             │
             ▼
            no
```
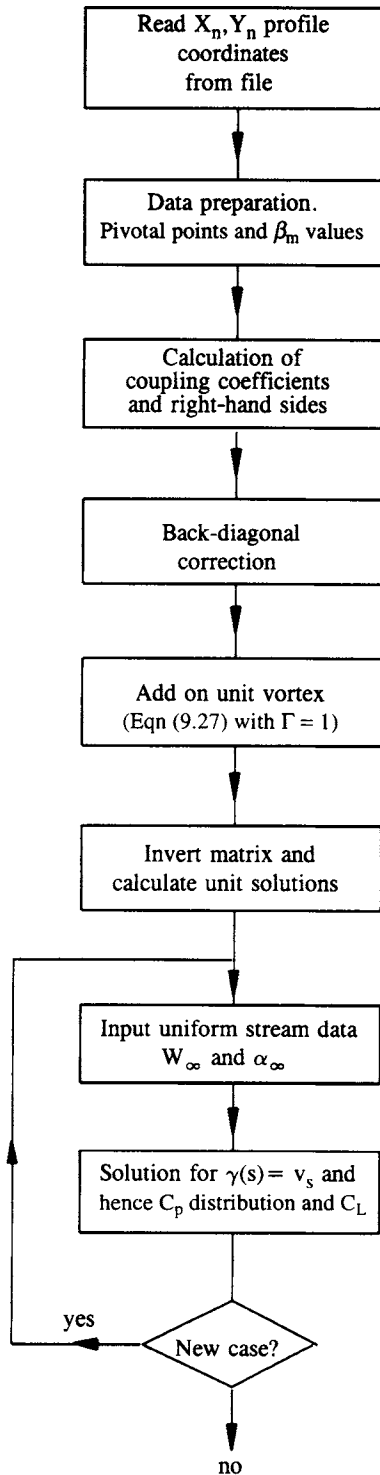
Fig. 9.13 Computational sequence for programs AEROFOIL and BLADEROW
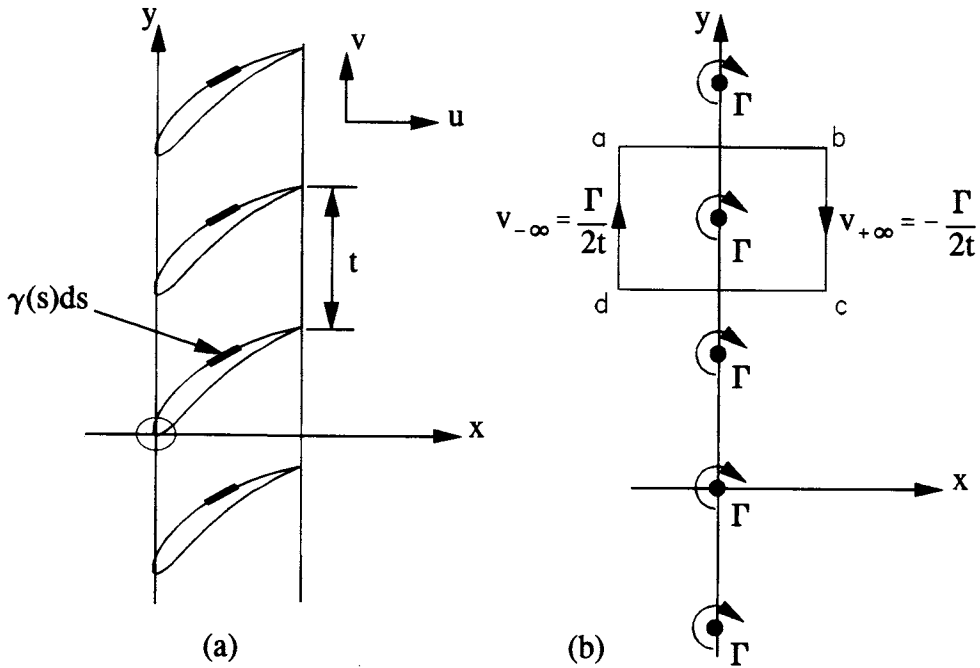
Fig. 9.14 (a) Turbomachine cascade and (b) equivalent infinite array of point vortices

developed in detail by Lewis (1991), the complex conjugate velocity induced by the infinite vortex array may be expressed as

$$u - iv = \frac{i\Gamma}{2t} \cosh \left(\frac{z}{2}\right) = \frac{i\Gamma}{2t}\left(\frac{e^z + 1}{e^z - 1}\right) \tag{9.38a}$$

$$= \frac{i\Gamma}{2t}\left(\frac{\sinh x - i \sin y}{\cosh x - \cos y}\right) \tag{9.38b}$$

Most cascade treatments transform this to normalised coordinates of the following form:

$$u - iv = \frac{i\Gamma}{2t}\left(\frac{\sinh \dfrac{2\pi x}{t} - i \sin \dfrac{2\pi y}{t}}{\cosh \dfrac{2\pi x}{t} - \cos \dfrac{2\pi y}{t}}\right)$$

Separating the real and imaginary parts, the (u, v) velocity components are thus

$$\left. \begin{array}{l} u = \dfrac{\Gamma}{2t} \dfrac{\sin \dfrac{2\pi y}{t}}{\cosh \dfrac{2\pi x}{t} - \cos \dfrac{2\pi y}{t}} \\[4em] v = -\dfrac{\Gamma}{2t} \dfrac{\sinh \dfrac{2\pi x}{t}}{\cosh \dfrac{2\pi x}{t} - \cos \dfrac{2\pi y}{t}} \end{array} \right\} \tag{9.39}$$
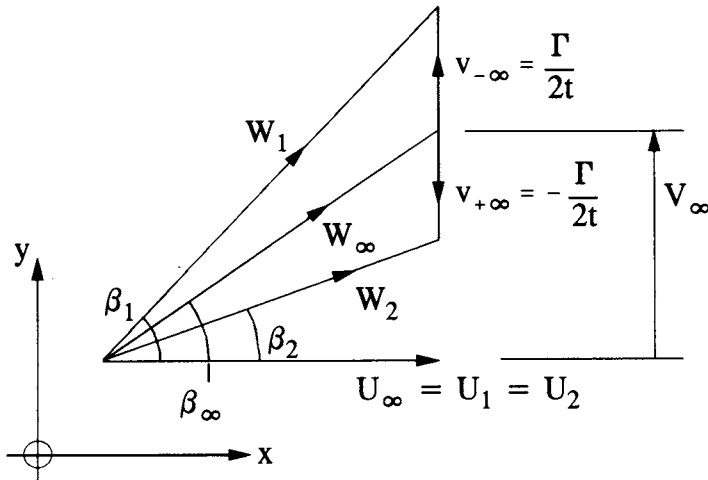
Fig. 9.15 Velocity triangles for a compressor cascade

Applying this to the cascade surface elements $\gamma(s_n)\,\mathrm{d}s_n$, Fig. 9.14(a), the cascade coupling coefficient, following the previous strategy for single bodies and aerofoils, Eqns (9.8) and (9.15), become

$$K(s_m, s_n) = u_{mn} \cos\beta_m + v_{mn} \sin\beta_m$$

$$= \frac{\Delta s_n}{2t} \left\{ \frac{\sin\dfrac{2\pi}{t}(y_m - y_n)\cos\beta_m - \sinh\dfrac{2\pi}{t}(x_m - x_n)\sin\beta_m}{\cosh\dfrac{2\pi}{t}(x_m - x_n) - \cos\dfrac{2\pi}{t}(y_m - y_n)} \right\} \tag{9.39a}$$

This equation is applicable for $m \neq n$. For the case $m = n$, it can be shown that the self-inducing coupling coefficient $K(s_m, s_m)$ is in fact identical to that for the single aerofoil, Eqn (9.19).

9.4.1 Solution of the *direct* or *analysis* problem for a cascade

The function of a turbomachine cascade is to produce fluid deflection from the uniform stream W_1 at $x = -\infty$ to W_2 at $x = +\infty$. This is accomplished by the bound vorticity Γ developed by the blades. Thus, as illustrated by Fig. 9.14(b), the Γ array produces a change in velocity v parallel to the line of the cascade from $v_{-\infty}$ upstream to $v_{+\infty}$ downstream. By taking the circulation around the contour abcd it follows that

$$v_{-\infty} = \frac{\Gamma}{2t}, \quad v_{+\infty} = -\frac{\Gamma}{2t} \tag{9.40}$$

If a uniform stream W_∞ is now superimposed onto the vortex array identical to that in the cascade plane, the overall velocity triangles will be identical to those of the actual blade row and are shown in Fig. 9.15, which may be compared with Fig. 2.5

of Chapter 2. In real applications, however, it is hardly practicable to specify the vector mean flow (W_∞, β_∞). Let us consider instead the solution of the more realistic *direct* problem in which the cascade geometry is already fully specified and we wish to predict its fluid-dynamic behaviour for a prescribed inflow (W_1, β_1).

From Fig. 9.15, making use also of Eqn (9.37), the upstream and downstream velocities in the y direction are thus

$$\left. \begin{aligned} V_1 &= V_\infty + \frac{\Gamma}{2t} = V_\infty + U_\infty \frac{\Gamma_u}{2t} + V_\infty \frac{\Gamma_v}{2t} \\ V_2 &= V_\infty - \frac{\Gamma}{2t} = V_\infty - U_\infty \frac{\Gamma_u}{2t} - V_\infty \frac{\Gamma_v}{2t} \end{aligned} \right\} \tag{9.41}$$

Since $U_1 = U_2 = U_\infty$, dividing this equation throughout by U_∞ results in

$$\left. \begin{aligned} \tan\beta_1 &= \tan\beta_\infty + \frac{\Gamma_u}{2t} + \frac{\Gamma_v}{2t}\tan\beta_\infty \\ \tan\beta_2 &= \tan\beta_\infty - \frac{\Gamma_u}{2t} - \frac{\Gamma_v}{2t}\tan\beta_\infty \end{aligned} \right\} \tag{9.42}$$

Adding these equations results in the expression for β_∞ derived in Chapter 2, namely

$$\tan\beta_\infty = \tfrac{1}{2}(\tan\beta_1 + \tan\beta_2) \tag{2.1}$$

Subtracting Eqns (9.42) and using the last expression to eliminate β_∞ results finally in

$$\beta_2 = \arctan\left[\left(\frac{1 - \Gamma_v/2t}{1 + \Gamma_v/2t}\right)\tan\beta_1 - \left(\frac{2}{1 + \Gamma_v/2t}\right)\frac{\Gamma_u}{2t}\right] \tag{9.43}$$

Thus for any chosen inlet angle β_1, the outlet angle β_2 is immediately calculable from the two unit solutions which deliver the unique values of Γ_u and Γ_v, Eqns (9.35), derived in the previous section for the single aerofoil but equally applicable for the cascade.

9.4.2   Shock-free inflow conditions

As already discussed in Section 2.6 and illustrated by Fig. 9.16, shock-free inflow is the fluid-dynamic ideal to achieve minimum profile losses. The stagnation point will then be located directly on the leading edge of the profile. By analogy with the Kutta–Joukowski trailing edge condition, Section 9.3.3, smooth leading edge flow will occur when the surface velocities v_s on elements 1 and M closest to the leading edge are equal and opposite (remembering the convention that v_s is $+^{ve}$ when clockwise). Thus, by analogy with Eqn (9.30), for shock-free inflow we will have

$$v_{s_1} = -v_{s_M} \quad \text{or} \quad \gamma(s_1) = -\gamma(s_M) \tag{9.44}$$
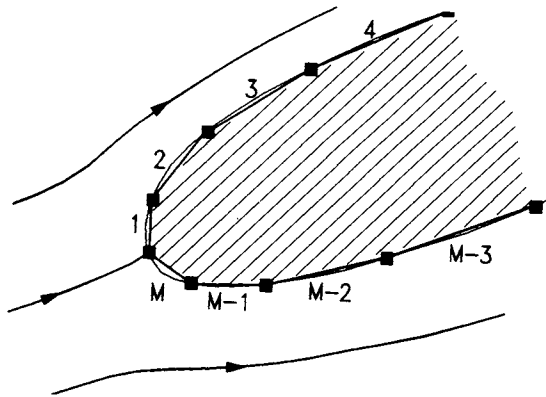
Fig. 9.16 Shock-free inflow conditions

Substituting from Eqn (9.36) and rearranging, the vector mean angle for shock-free inflow is thus

$$\beta_{\infty SF} = - \arctan\left(\frac{\gamma_u(s_1) + \gamma_u(s_M) + \Gamma_u(\gamma_\Gamma(s_1) + \gamma_\Gamma(s_M))}{\gamma_v(s_1) + \gamma_v(s_M) + \Gamma_v(\gamma_\Gamma(s_1) + \gamma_\Gamma(s_M))} \right) \qquad (9.45)$$

The shock-free inflow angle then follows from Eqn (9.42a), namely

$$\beta_{1SF} = \arctan\left\{ \frac{\Gamma_u}{2t} + \tan\beta_\infty \left(1 + \frac{\Gamma_v}{2t} \right) \right\} \qquad (9.46)$$

Example 9.3 Flow past a compressor cascade

The source code for a simple PASCAL program BLADEROW is provided on the accompanying disc to show how the above cascade analysis can be converted into computer code. BLADEROW receives as input (x,y) profile coordinate data generated by the blade design program STACK which is stored in the file RAWDATA. The more advanced program CASCADE performs both profile design and flow analysis (user instructions are given in Appendix II) and also stores the raw profile coordinates in the file RAWDATA. A comparison of predicted surface pressure distributions from both CASCADE and BLADEROW is shown in Fig. 9.17 for the default cascade geometry, which the user will find presented when undertaking a new run of program CASCADE, but with the modified inlet angle $\beta_{1SF} = 63.706°$ corresponding to shock-free inlet flow. The surface pressure coefficient C_{p1} is that defined by Eqn (2.14) and the two programs are found to be in good agreement including also the predicted outlet angle $\beta_2 = 29.161°$.

9.5   Axisymmetric bodies, ducts and ducted propellers

The previous analysis may be extended with relative ease to simulate axisymmetric flows. This will now be developed progressively beginning with flow past a body of revolution, Section 9.5.1, proceeding to flow past an annular aerofoil or duct, Section 9.5.2, and concluding with simulation of a complete ducted propeller, Section 9.5.3.
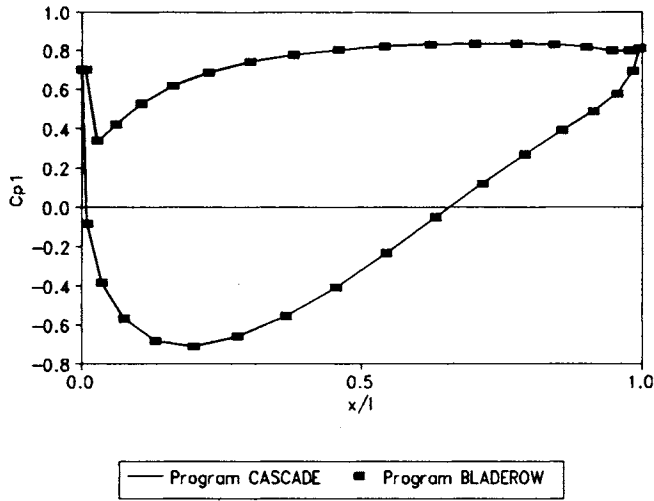
C4 profile   circular arc camber $\theta = 60°$

$\lambda = 45°$ $t/l = 1.0$ $\beta_1 = 63.706°$ (i.e. shock-free)

$\beta_2 = 29.161°$ (predicted)

Fig. 9.17 Comparison of surface pressure distributions predicted by programs CASCADE and BLADEROW for a compressor cascade designed for shock-free inflow
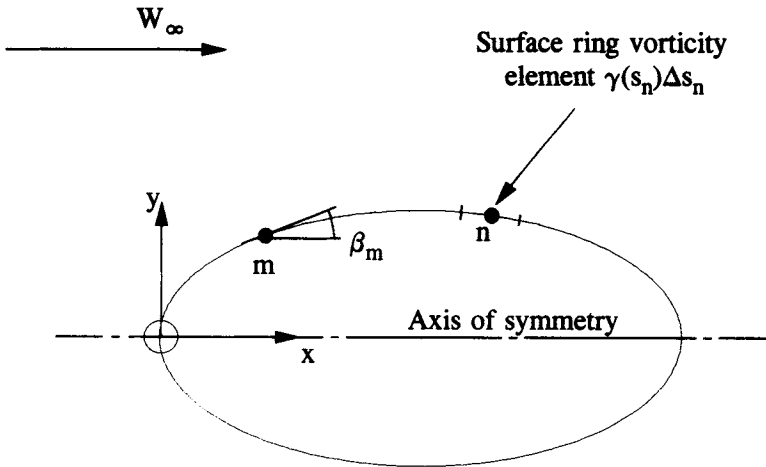
Fig. 9.18 Axisymmetric surface vorticity model for body of revolution

The aim will be to develop surface vorticity boundary integral models capable of predicting the detailed incompressible inviscid fluid flow.

9.5.1   Flow past a body of revolution

The flow past a body of revolution located in a uniform stream W_∞ parallel to the x-axis, Fig. 9.18, may be modelled by the introduction of a sheet of ring vorticity
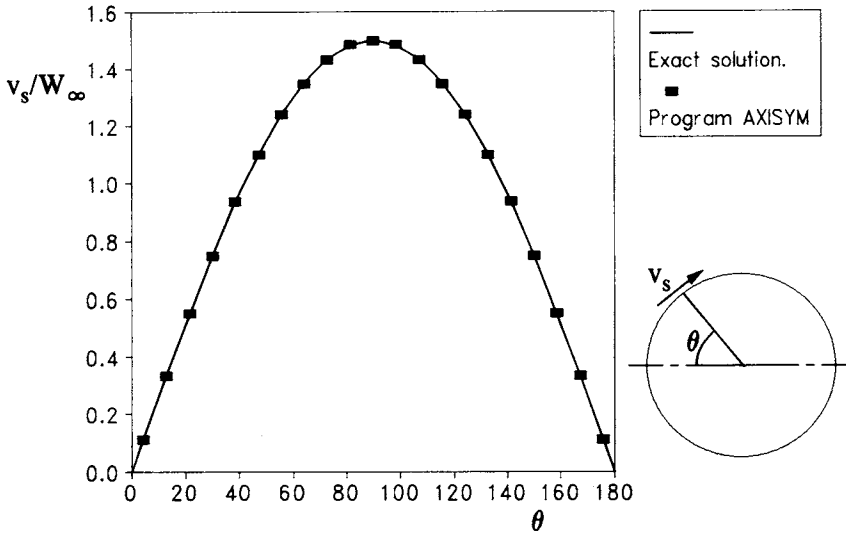
Fig. 9.19 Flow past a sphere modelled with 21 surface elements

located on the body surface and of strength $\gamma(s) = v_s$. Martensen's integral equation (9.13) for this situation becomes

$$-\tfrac{1}{2}\gamma(s_m) + \oint \overline{K}(s_m, s_n)\,\gamma(s_n)\,\mathrm{d}s_n + W_\infty \cos\beta_m = 0 \qquad (9.47)$$

where the coupling coefficient may be expressed as

$$\overline{K}(s_m, s_n) = u_{mn}\cos\beta_m + v_{mn}\sin\beta_m \qquad (9.48)$$

where (u_{mn}, v_{mn}) are the velocity components induced at surface point m due to a unit ring vortex at n. Gibson (1972) has shown that these may be expressed as follows:

$$\left.\begin{array}{l} u_{mn} = -\dfrac{1}{2\pi r_n \sqrt{x^2 + (r+1)^2}}\left(K(k) - \left[1 + \dfrac{2(r-1)}{x^2 + (r-1)^2}\right]E(k) \right) \\[4mm] v_{mn} = \dfrac{x/r}{2\pi r_n \sqrt{x^2 + (r+1)^2}}\left(K(k) - \left[1 + \dfrac{2r}{x^2 + (r-1)^2}\right]E(k) \right) \end{array}\right\} \qquad (9.49)$$

$K(k)$ and $E(k)$ are complete elliptic integrals of the first and second kind and k is given by

$$k = \sqrt{\dfrac{4r}{x^2 + (r+1)^2}} = \sin\phi \qquad (9.50)$$

where the dimensionless coordinates (x, r) linking body surface locations m and n are defined as

$$x = \dfrac{x_m - x_n}{r_n}\,, \; r = \dfrac{r_m}{r_n} \qquad (9.51)$$
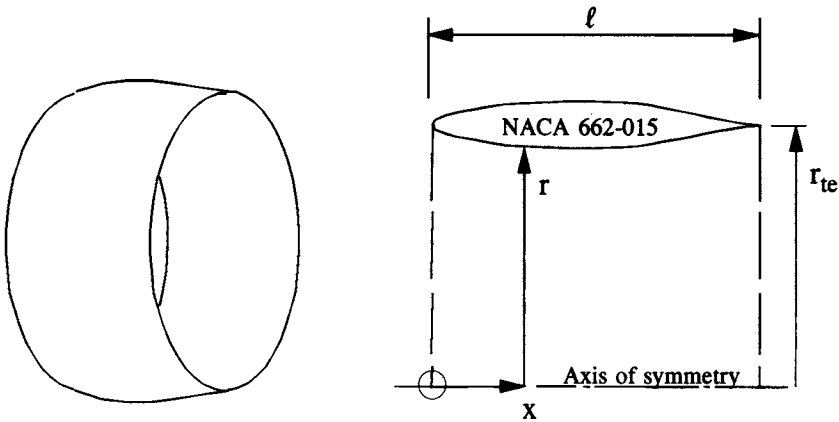
Fig. 9.20 Annular aerofoil or ducted propeller duct

A method for evaluation of $K(k)$ and $E(k)$ by use of 'look-up' tables has been documented in full by the present author (Lewis, 1991), together with relevant computer code, and this technique has been implemented in the program AXISYM.PAS for which the source code is provided on the accompanying PC disc. A full derivation for the self-inducing coupling coefficient is also given, namely

$$\bar{K}(s_m, s_m) = -\frac{1}{2} - \frac{\Delta\beta_m}{4\pi} - \frac{\Delta s_m}{4\pi r_m}\left(\ln\frac{8\pi r_m}{\Delta s_m} - \frac{1}{4}\right)\cos\beta_m \qquad (9.52)$$

The first two terms on the right-hand side are identical to those for the plane aerofoil and cascade flows, Eqn (9.19). The extra third term accounts for the self-propagation velocity of the ring vortex element Δs_m of unit sheet strength at m and is analogous to the well-known property of a smoke-ring vortex. A formulation for the latter was given by Lamb (1945) from which the above expression was adapted by Ryan (1970) and by Lewis and Ryan (1972). A full explanation and derivation has been given by Lewis (1991, pp. 154–157).

A comparison is shown in Fig. 9.19 between the surface velocity distribution v_s/W_∞ predicted by program AXISYM and the exact solution for the flow past a sphere, namely

$$\frac{v_s}{W_\infty} = \frac{3}{2}\sin\phi \qquad (9.53)$$

Precise prediction is obtained for this or any other more complex body shape, examples of which have been given by Lewis (1991), including comparisons with experimental test.

9.5.2 Annular aerofoils or engine cowls

As the first step towards the modelling of a complete ducted propeller or fan we consider next the flow past an axisymmetric duct or engine cowl located in a uniform stream W_∞. Such a device may be perceived alternatively as an annular aerofoil such
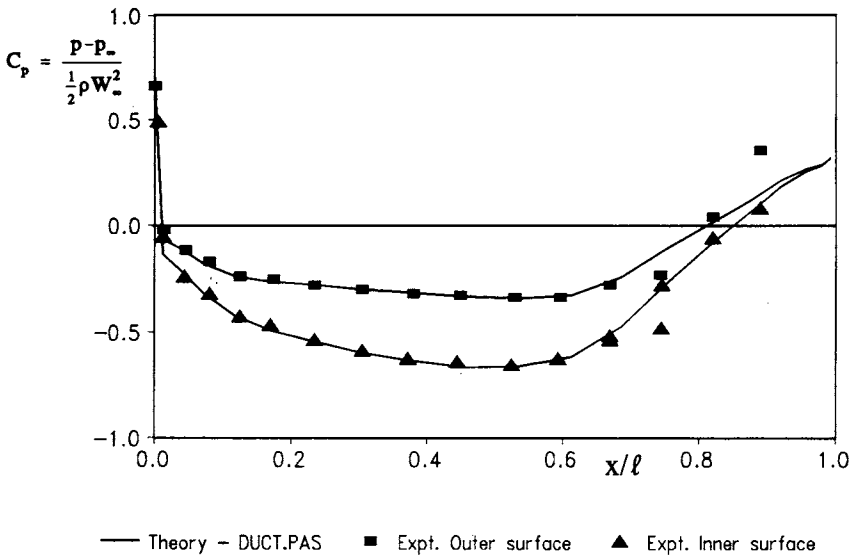
Fig. 9.21 Surface pressure distribution on annular aerofoil NACA 662-015. Comparison of program DUCT.PAS prediction with experimental tests by Hill (1975, 1978)

as that illustrated by Fig. 9.20 for the aerofoil NACA 662-015. Duct aspect ratio is defined as (trailing edge radius r_{te})/(chord l), which for this example is set at $r_{te}/l = 0.835$. The previous computational sequence specified in Fig. 9.13 is again completely appropriate and the plane aerofoil analysis of Section 9.3 may be adapted quite easily by simply replacing the coupling coefficients $K(s_m, s_n)$, Eqns (9.15) and (9.19), by the ring vortex equivalents just derived for the body of revolution, Eqns (9.48), (9.49) and (9.52). Being in effect an annular or ring aerofoil, however, the duct will generate a bound circulation Γ and a consequent radial thrust (equivalent to the lift of a two-dimensional aerofoil). Thus unlike the body of revolution it is necessary to impose the trailing edge Kutta–Joukowski condition exactly as explained in Section 9.3.3.

All of these features have been built into the computer program DUCT.PAS for which the source code is included on the accompanying PC disc. The predicted surface pressure distribution, expressed as a dimensionless pressure coefficient $C_p = (p - p_\infty)/\frac{1}{2}\rho W_\infty^2$, is compared with experimental aerodynamic test data in Fig. 9.21, for the aerofoil NACA 662-015, showing good agreement. It is of interest to note that although this profile is symmetrical and the mainstream velocity W_∞ is parallel to its chord line, the pressure on the inner surface is actually lower than that on the outer surface. Since v_s will behave in the reverse manner it is clear that this duct, despite having zero camber, will in fact develop anti-clockwise circulation Γ resulting in a slight increase of mass flux through the space occupied by the duct.

V. P. Hill (1975, 1978) constructed this duct with considerable precision to obtain a really reliable experimental benchmark for testing annular aerofoil theories, including also flows with incidence in the range $0° < \alpha_\infty < 15°$. He also extended surface vorticity modelling to deal with incidence effects. A fairly extensive literature covers earlier work based on linearised aerofoil theory which was ably reviewed by Weissinger and Maass (1968). Although source panel methods were well established

in the 1960s, e.g. Smith and Hess (1966), surface vorticity modelling was still undeveloped for duct flows until the publication by Ryan (1970) out of which the work of Hill and others developed.

9.5.3   Ducted propellers

A complete ducted propeller system may be modelled in the manner illustrated in Fig. 9.22. First of all the body of revolution and annular aerofoil solutions of Sections 9.5.1 and 9.5.2 may be combined for simulation of the propeller boss and surrounding duct. Secondly the discontinuity across the edge of the downstream jet wake from the jet velocity V_j to the mainstream advance velocity V_a may be modelled by a semi-infinite vortex tube Γ_w. Here we will consider only the free-vortex propeller and its circumferentially averaged effect. In reality the blade bound vortices would be shed from the blade tips as a structure of helical vortices extending downstream to $x = \infty$. The circumferential model of this comprises a vortex tube emanating from the blade tips in the form of a helically spiralling vortex sheet. The tangential or 'ring' vorticity component of this sheet, which forms a tube, is of special importance here since it induces velocity components (u_w, v_w) due to the propeller and its infinite wake which must be accounted for in the flow simulation model. We will return to this matter again shortly, having first considered the overall structure of the boundary integral equations and their consequent matrix form for simulation of this problem, namely

$$
\left(\begin{bmatrix} M_{11} \\ \text{Effect of} \\ \text{hub upon} \\ \text{itself} \end{bmatrix} \begin{bmatrix} M_{12} \\ \text{Effect of} \\ \text{duct upon} \\ \text{hub} \end{bmatrix} \\ \begin{bmatrix} M_{21} \\ \text{Effect of} \\ \text{hub upon} \\ \text{duct} \end{bmatrix} \begin{bmatrix} M_{22} \\ \text{Effect of} \\ \text{duct upon} \\ \text{itself} \end{bmatrix}\right) \begin{pmatrix} \gamma(s_1) \\ \gamma(s_2) \\ \gamma(s_3) \\ \vdots \\ \gamma(s_M) \end{pmatrix} = \begin{pmatrix} \text{rhs}_1 \\ \text{rhs}_2 \\ \text{rhs}_3 \\ \vdots \\ \text{rhs}_M \end{pmatrix} \tag{9.54}
$$

Since two bodies are to be represented, the coupling coefficient matrix may be partitioned as shown in Eqn (9.54). Sub-matrices M_{11} and M_{22} will be identical to the coupling coefficient matrices for the isolated hub and duct as given in Sections 9.5.1 and 9.5.2, accounting for the effect of each body upon itself. Sub-matrices M_{12} and M_{21} on the other hand introduce the mutual interference effects between hub and duct.

Initially the coupling coefficient matrix may be set up in the usual manner just as if hub and duct were a single body. Following this, as recommended for the annular aerofoil in Section 9.5.2, back-diagonal correction must then be applied to the elements in sub-matrix M_{22} followed by imposition of the trailing edge Kutta–Joukowski condition. These matters are too complex for further explanation here but have been dealt with in more detail by Ryan and Glover (1972), Gibson (1972), Gibson and Lewis (1973) and Lewis (1991). Appropriate procedures are embedded in the computer program DUCTPROP.PAS included on the accompanying PC disc.

The actual Martensen equation for this ducted propeller simulation may be developed from Eqn (9.47) as follows:

$$
-\tfrac{1}{2}\gamma(s_m) + \oint \bar{K}(s_m, s_n)\gamma(s_n)\,\mathrm{d}s_n = -(V_a + u_w)\cos\beta_m - v_w\sin\beta_m \tag{9.55}
$$

19A duct – Van Manen and Oosterveld (1966)
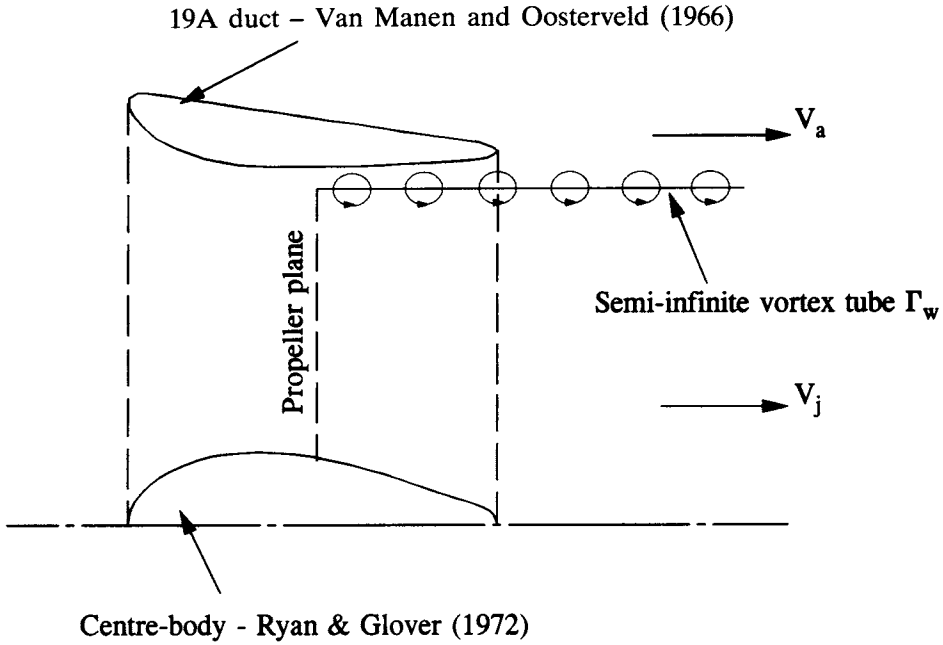
Fig. 9.22 Free-vortex ducted propeller model applied to N.S.M.B. 19A duct with centre-body

where V_a is the vehicle advance velocity and (u_w, v_w) are the velocity components induced by the propeller and wake. As shown by Gibson (1972) and fully explained by Lewis (1991), these may be expressed analytically as follows:

$$
\left.
\begin{aligned}
u_w &= \frac{\Gamma_w}{2\pi}\left(A + \frac{x}{\sqrt{x^2 + (r+1)^2}}\left[K(k) - \left(\frac{r-1}{r+1}\right)\Pi(n,k) \right] \right) \\
v_w &= \frac{2\Gamma_w}{\pi k^2\sqrt{x^2 + (r+1)^2}}\left[E(k) - \left(1 - \frac{k^2}{2}\right)K(k) \right]
\end{aligned}
\right\}
\tag{9.56}
$$

where (x, r) are the dimensionless coordinates defined by Eqns (9.51), Γ_w is the strength of the ring vortex tube which extends from $x = 0$ to $x = \infty$ and the constant A is given by

$$
\begin{aligned}
A &= \pi && \text{if } r < 1 \\
&= \pi/2 && \text{if } r = 1 \\
&= 0 && \text{if } r > 1
\end{aligned}
\tag{9.57}
$$

$\Pi(n,k)$ is the complete elliptic integral of the third kind given by Dwight (1963) as

$$
\Pi(n,k) = \int_0^{\pi/2} \frac{d\alpha}{(1 - n\sin^2\alpha)\sqrt{1 - k^2\sin^2\alpha}}
\tag{9.58}
$$

(a) J = 0.224

(b) J = 0.36

(c) J = 0.551

—Theory– DUCTPROP ■ Inner surface – Exp × Outer surface – Exp
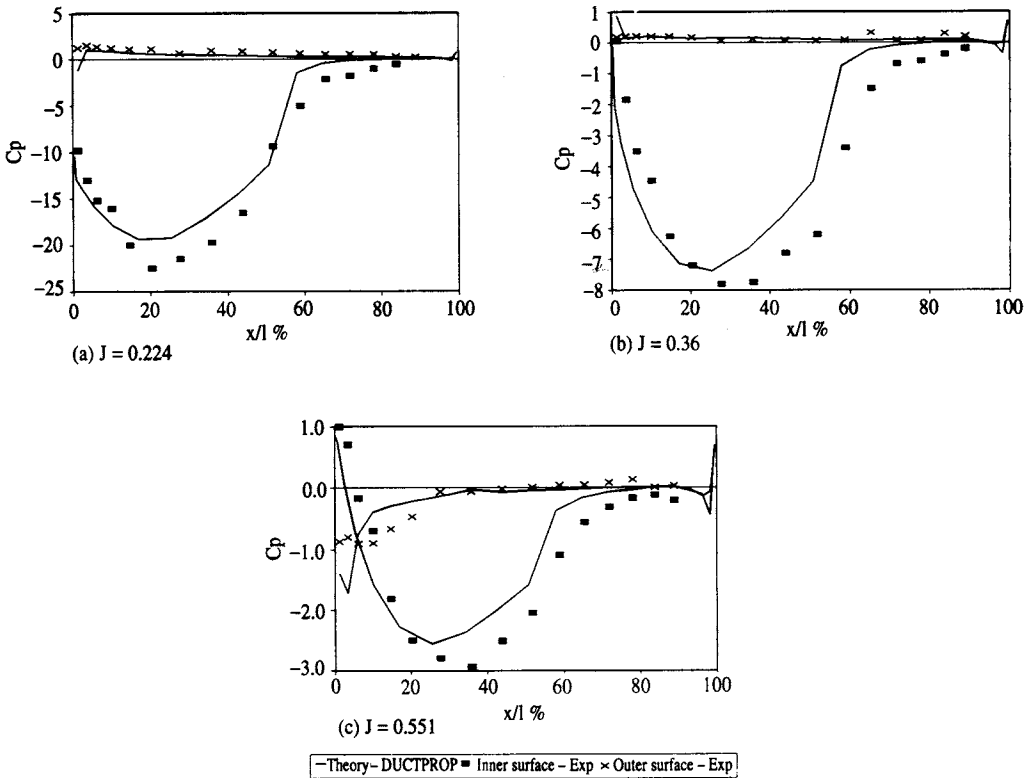
Fig. 9.23 Surface pressure distributions for 19A duct with Ka 4-55 N.S.M.B. propeller

where the parameter n is defined as

$$n = \frac{4r}{(1+r)^2} \tag{9.59}$$

The evaluation of all of these equations is completed by the program DUCTPROP.PAS and the reader is referred to the source code for further detail. The only remaining item needing further action is the allocation of a value to the vortex tube strength Γ_w. This may be related directly to the wake jet velocity V_j since

$$\Gamma_w = -(V_j - V_a) \qquad \text{(clockwise $+^{ve}$)} \tag{9.60}$$

Hence as shown in Chapter 8, Eqn (8.24), Γ_w may be expressed as a function of propeller thrust coefficient τC_T through

$$\frac{\Gamma_w}{V_a} = 1 - \sqrt{1 + \tau C_T} \tag{9.61a}$$

As shown by Lewis (1991, p. 201), this may be modified to allow for hub blockage, giving

$$\frac{\Gamma_w}{V_a} = 1 - \sqrt{1 + \frac{\tau C_T}{1 - h^2}} \tag{9.61b}$$

Duct surface pressure distributions predicted by the program DUCTPROP.PAS
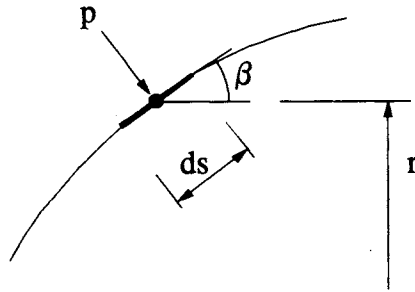
Fig. 9.24 Pressure on duct surface element

are compared in Fig. 9.23 with experimental results obtained by aerodynamic model tests (Balabaskaran, 1982; Lewis and Balabaskaran, 1983). The 19A duct (Van Manen and Oosterveld, 1966) was combined with the Netherlands Ship Model Basin Ka 4-55 propeller located in the mid-plane as illustrated in Fig. 9.22. For the theoretical calculations a tip clearance of 2% of the propeller diameter was assumed with the propeller plane located at 55% of the duct chord. Test results are shown in Fig. 9.23 for a very wide range of advance coefficients $J = 0.224$, 0.36 and 0.551, resulting in enormous variation of pressure coefficient C_p, defined as

$$C_p = \frac{p - p_\infty}{\frac{1}{2}\rho V_a^2} \tag{9.62}$$

The surface vorticity modelling of program DUCTPROP.PAS and its axisymmetric simplifying assumptions have delivered remarkably good predictions. This computer code is intended only for the simulation of accelerating Kort Nozzles for which it clearly forms a powerful design/analysis tool. It would, however, be a relatively simple matter to adapt the code to handle Pump Jets or even by-pass fan configurations. The pressure distributions shown here typify Kort Nozzle characteristics of very low suction pressures on the duct inner surface upstream of the propeller followed by a rapid pressure rise through the propeller plane. The pressure distribution on the duct outer surface tends towards ambient conditions $C_p \to 0.0$, as also does C_p on the inner surface downstream of the propeller.

Once the surface pressure distribution is known the duct thrust T_p may be obtained by integration. Thus for the surface element ds of slope β at radius r on the duct (Fig. 9.24), the forward horizontal component of thrust dT may be expressed as

$$dT_d = -p \cdot 2\pi r \, ds \cdot \sin\beta \tag{9.63}$$

Introducing the gauge pressure $p - p_\infty$ for convenience, the total duct thrust is then

$$T_d = -\oint (p - p_\infty) 2\pi r \sin\beta \, ds$$

$$= -\pi\rho V_a^2 \oint C_p \sin\beta \, r \, ds \tag{9.64}$$

The duct thrust coefficient, Eqns (8.8) and (8.23), then becomes

$$C_{Td} = \frac{T_d}{\frac{1}{2}\rho V_a^2 \frac{\pi d^2}{4}}$$

$$= -\frac{8}{D^2} \oint C_p \sin\beta \, r \, ds \tag{9.65}$$
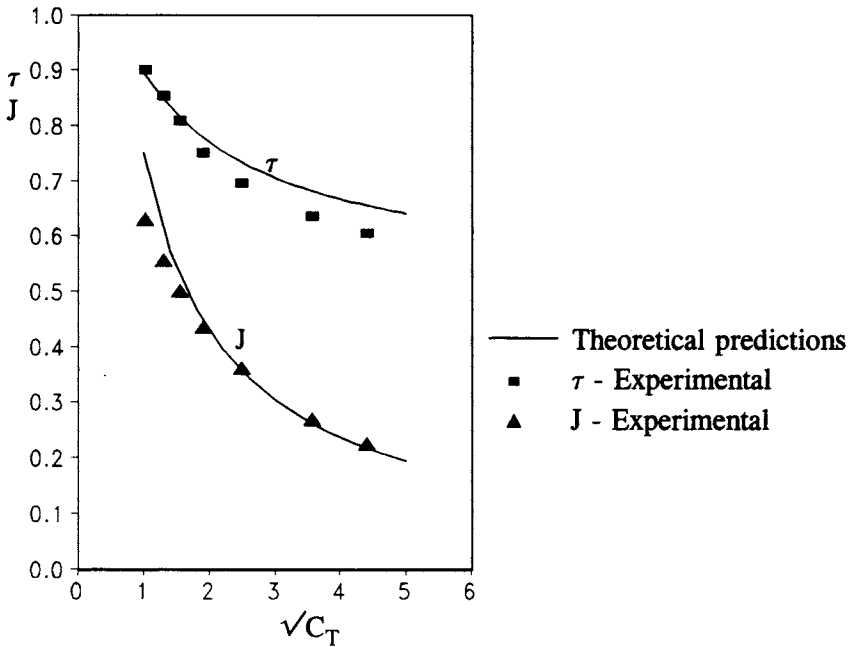
Fig. 9.25 Comparison of predicted and experimental characteristics for Ka 4-55 propeller located in 19A duct

The program DUCTPROP.PAS performs this calculation for specified input values of propeller thrust coefficient C_{Tp} providing a prediction of the overall propeller characteristic parameters $C_T = C_{Tp} + C_{Td}$ and $\tau = C_{Tp}/C_T$.

The τ–C_T characteristic predicted by DUCTPROP.PAS for the selected Kort Nozzle propulsor is compared with the experiments of Balabaskaran (1982) in Fig. 9.25. Also included there is the J–C_T characteristic predicted by the simple one-dimensional analysis given in Chapter 8, Section 8.5.2, and embodied in the computer code TAWCT.PAS. These two analyses and computer codes provide a comprehensive design and analysis toolkit for ducted propellers which is able to predict both overall performance characteristics and detailed fluid-dynamic behaviour.

Appendix I

'FIPSI'

A computer program for selection and performance analysis of axial turbine stages

I.1 Introduction and overview

'FIPSI' is a computer program for the design of multi-stage axial turbines. The underlying concepts, attributed originally to S. F. Smith (1965), have been further developed by Lewis (1978a,b) for teaching purposes. Smith published experimental data (ϕ,ψ charts) for an assembly of Rolls-Royce model turbines, each recorded at its optimum efficiency point. The outcome was a series of efficiency contours plotted on a (ϕ,ψ) chart as shown below in Fig. I.6. The dimensionless coefficients ϕ and ψ are defined as follows:

$$\phi = \frac{c_x}{U} \quad \text{Flow coefficient (shown as fi on screen)}$$

$$\psi = \frac{\Delta h_o}{U^2} \quad \text{Work coefficient (shown as psi on screen)}$$

where c_x is the axial velocity, U the blade speed and Δh_o the stagnation enthalpy drop across one stage. The (ϕ,ψ) chart is based upon values at the mean radius r_m, defined as

$$r_m = \tfrac{1}{2}(r_{hub} + r_{tip})$$

FIPSI enables you to complete the velocity triangle design of a multi-stage gas turbine with facility to check the stage centre-line design duty (ϕ,ψ) against the performance chart. The program goes on to undertake a complete three-dimensional design based upon 11 sections between hub and casing with the following assumptions:

(1) The centre-line radius r_m is the same for all stages.
(2) The axial velocity is also constant.
(3) The centre-line design is the same for all stages and has 50% reaction.
(4) Free-vortex design is adopted with equal work done at all radii.

Various other visual checks are available to present your design data graphically on the monitor. These include:

(a) a view of the annulus geometry, and
(b) details of velocity triangle data, stage reaction and exit Mach numbers from hub to casing.

These will be explained with the help of 'screen-dumps' in the next section.

```
┌─────────────────────────────────────────────────────────────────────┐
│  Thermodynamics   Design data   Graphics   File etc.                  │
├─────────────────────────────────────────────────────────────────────┤
│  Design input data are presently as follows :-                        │
│                                                                       │
│    Inlet hub radius      =  0.300 m      Input pressure   =  2.500 bar │
│    Inlet tip radius      =  0.450 m      Outlet pressure  =  1.020 bar │
│    Number of stages      =  3            Inlet temp. T1   =  1200.0 K  │
│    Stator aspect ratio   =  6.0          Rot. speed       =  6000.0 revs/min │
│    Rotor aspect ratio    =  8.0          Mass flow rate   =  35.000 kg/s │
│                                          Total to total effy. = 92%   │
│    Cp/Cv ratio gamma  =  1.40            Gas constant R   =  287.0 J/kg K │
├─────────────────────────────────────────────────────────────────────┤
│  Other calculated design data for the above are:-                     │
│    Outlet hub radius     =  0.229 m      Outlet temp. T2  =  950.5 K   │
│    Outlet tip radius     =  0.520 m      Flow coeff. fi   =  0.57899   │
│    Axial velocity        =  136.42 m/s   Work coeff. psi  =  1.50459   │
│    Last stage hub stator exit Mach No. M2          =  0.773           │
│    Last stage tip rotor exit Mach No. M3 relative  =  0.626           │
├─────────────────────────────────────────────────────────────────────┤
│      < <Press Alt key and first letter together to grab a menu> >     │
│      < <e.g.  Alt-T pulls down the Thermodynamics menu> >             │
└─────────────────────────────────────────────────────────────────────┘
```

Fig. I.1 Bar menu and default design data

I.2 Main bar menu and default turbine design

All the various design or viewing options are available from the main bar menu as shown in Fig. I.1. To get started type the program name **fipsi** at the keyboard and press the <ENTER> or <RETURN> key. A title page will be presented with the instruction to press <ENTER> once more in order to proceed. Having done this the monitor screen will appear as shown in Fig. I.1. A bar menu offering a selection of four options is spread across the top of the page. Below this a page full of detailed data is presented for the default design already embedded into the program.

The strategy for using FIPSI is to edit these data using the bar menu as many times as you wish until you have accomplished the turbine design of your choice. To access the bar menu simply hold down the ALT key while pressing the first letter of the menu item which you wish to select. This same instruction is also written at the bottom of the screen, Fig. I.1. The program is in fact menu driven and all you have to do is to obey the instructions which appear on the screen.

Just to summarise, the role of the four bar menu selections is as follows:

Thermodynamics	To edit the thermodynamic design data such as pressures and temperatures.
Design data	To edit other machine design data such as speed and size.

Graphics

To view the present status of your design on the fi-psi chart, to check velocity triangles and to view the annulus geometry.

File etc.

To enable you to save your work, quit, go temporarily into DOS or reverse the video presentation.

The first two options are thus editing menus and the third menu provides detailed viewing of the design in its present state.

I.3   Pull-down menus

When you access the bar menu with, for example, ALT-T, you will automatically enter a pull-down menu, in this case the one shown in Fig. I.2. All of the four pull-down menus are shown in Figs I.2 to I.5 and are self-explanatory. The arrow keys on the keyboard will enable you to switch to a different pull-down menu using $\leftarrow \rightarrow$ or $\uparrow \downarrow$ to select the required highlighted item on a given pull-down menu. There is no need for further explanation – just try it for yourself.

Once you have selected the item of your choice just press <ENTER> and obey all the instructions presented to you at the screen. Any changes to the [Thermodynamics] or [Design data] will then appear as an update on the design data sheet of the main menu.

```
┌───────────────────────────────────────────────────────────────┐
│ ▌Thermodynamics▐ Design data  Graphics   File etc.             │
│ ┌────────────────────┐esently as follows :-                     │
│ │▌Inlet Temp. T1    ▐│                                          │
│ │ Inlet press.  p1   │= 0.300 m     Input pressure   = 2.500 bar│
│ │ Outlet press. p2   │= 0.450 m     Outlet pressure  = 1.020 bar│
│ │ Efficiency tot. to tot.│= 3        Inlet temp. T1    = 1200.0 K │
│ │ Gas properties     │= 6.0         Rot. speed       = 6000.0 revs/min│
│    Rotor aspect ratio   = 8.0       Mass flow rate   = 35.000 kg/s │
│                                     Total to total effy. = 92%   │
│    Cp/Cv ratio gamma  = 1.40        Gas constant R   = 287.0 J/kg K│
│                                                                 │
│  Other calculated design data for the above are:-               │
│     Outlet hub radius    = 0.229 m    Outlet temp. T2  = 950.5 K │
│     Outlet tip radius    = 0.520 m    Flow coeff. fi   = 0.57899 │
│     Axial velocity       = 136.42 m/s Work coeff. psi  = 1.50459 │
│     Last stage hub stator exit Mach No. M2       = 0.773        │
│     Last stage tip rotor  exit Mach No. M3 relative  = 0.626    │
│                                                                 │
│        < <Press Alt key and first letter together to grab a menu> >│
│        < <e.g.  Alt-T pulls down the Thermodynamics menu> >     │
└───────────────────────────────────────────────────────────────┘
```

Fig. I.2 Thermodynamics pull-down menu

Design input data a...
  Mass flow rate
  Inlet hub radius   Rotational speed   ...put pressure   = 2.500 bar
  Inlet tip radius   Inlet tip radius rtin   ...tlet pressure   = 1.020 bar
  Number of stage   Inlet hub radius rhin   ...let temp. T1   = 1200.0 K
  Stator aspect rat   Number of stages   ...t. speed   = 6000.0 revs/min
  Rotor aspect rat   Blade aspect ratio   ...ass flow rate   = 35.000 kg/s
                            Total to total effy.   = 92%

  Cp/Cv ratio gamma = 1.40   Gas constant R   = 287.0 J/kg K

Other calculated design data for the above are:-
  Outlet hub radius   = 0.229 m   Outlet temp. T2   = 950.5 K
  Outlet tip radius   = 0.520 m   Flow coeff. fi   = 0.57899
  Axial velocity   = 136.42 m/s   Work coeff. psi   = 1.50459
  Last stage hub stator exit Mach No. M2   = 0.773
  Last stage tip rotor exit Mach No. M3 relative   = 0.626

<<Press Alt key and first letter together to grab a menu>>
<<e.g. Alt-T pulls down the Thermodynamics menu>>

Fig. I.3 Machine overall design pull-down menu

Design input data are presently
  Fi/psi chart
  Inlet hub radius   = 0.30... View annulus   ...sure   = 2.500 bar
  Inlet tip radius   = 0.45... View stage data   ...ssure   = 1.020 bar
  Number of stages   = 3   Inlet temp. T1   = 1200.0 K
  Stator aspect ratio   = 6.0   Rot. speed   = 6000.0 revs/min
  Rotor aspect ratio   = 8.0   Mass flow rate   = 35.000 kg/s
                            Total to total effy.   = 92%

  Cp/Cv ratio gamma = 1.40   Gas constant R   = 287.0 J/kg K

Other calculated design data for the above are:-
  Outlet hub radius   = 0.229 m   Outlet temp. T2   = 950.5 K
  Outlet tip radius   = 0.520 m   Flow coeff. fi   = 0.57899
  Axial velocity   = 136.42 m/s   Work coeff. psi   = 1.50459
  Last stage hub stator exit Mach No. M2   = 0.773
  Last stage tip rotor exit Mach No. M3 relative   = 0.626

<<Press Alt key and first letter together to grab a menu>>
<<e.g. Alt-T pulls down the Thermodynamics menu>>

Fig. I.4 Graphics presentation pull-down menu

Fig. 1.5 File etc. pull-down menu

Thermodynamics Design data Graphics File etc.

Design input data are presently as follows | Save and exit

Inlet hub radius = 0.300 m | I Quit | 2.500 bar
Inlet tip radius = 0.450 m | O Read data from file | 1.020 bar
Number of stages = 3 | I File design data | 1200.0 K
Stator aspect ratio = 6.0 | R Go to DOS | 6000.0 revs/min
Rotor aspect ratio = 8.0 | M Reverse video | 35.000 kg/s

Cp/Cv ratio gamma = 1.40 | Total to total effy. = 92%
Gas constant R = 287.0 J/kg K

Other calculated design data for the above are:-
Outlet hub radius = 0.229 m   Outlet temp. T2 = 950.5 K
Outlet tip radius = 0.520 m   Flow coeff. fi = 0.57899
Axial velocity = 136.42 m/s   Work coeff. psi = 1.50459
Last stage hub stator exit Mach No. M2 = 0.773
Last stage tip rotor exit Mach No. M3 relative = 0.626

<<Press Alt key and first letter together to grab a menu>>
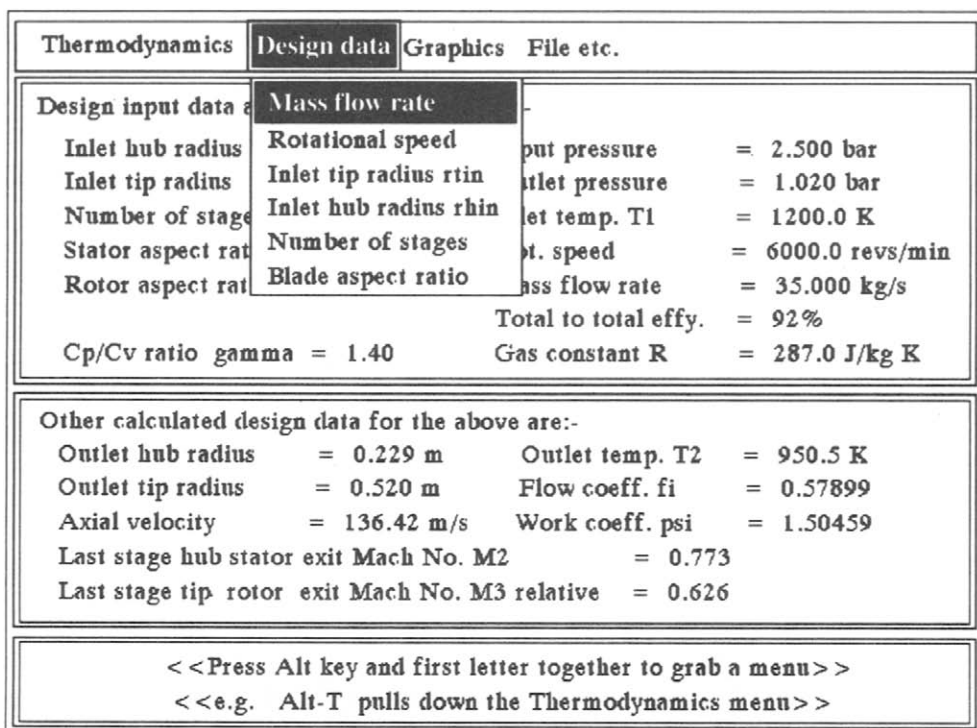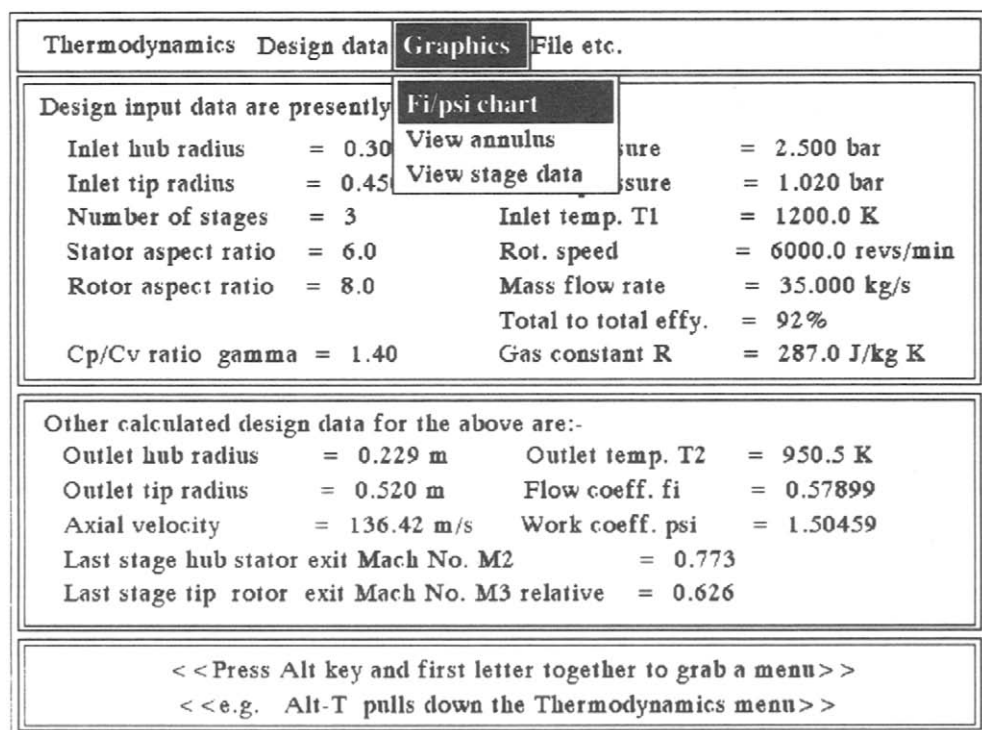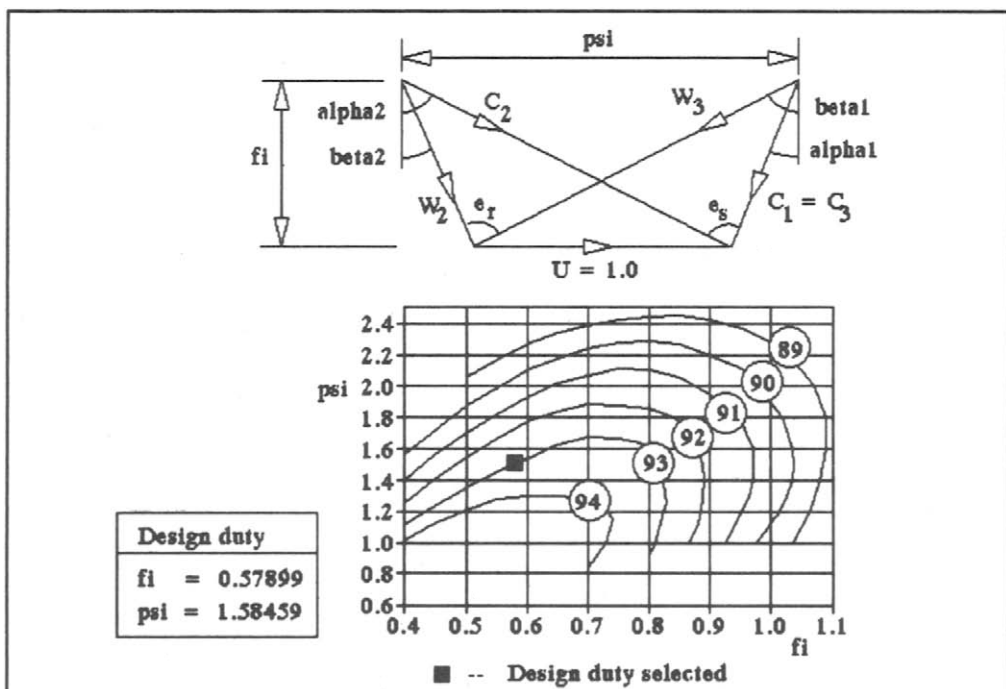<<e.g. Alt-T pulls down the Thermodynamics menu>>

Fig. 1.6 FIPSI chart and velocity triangles

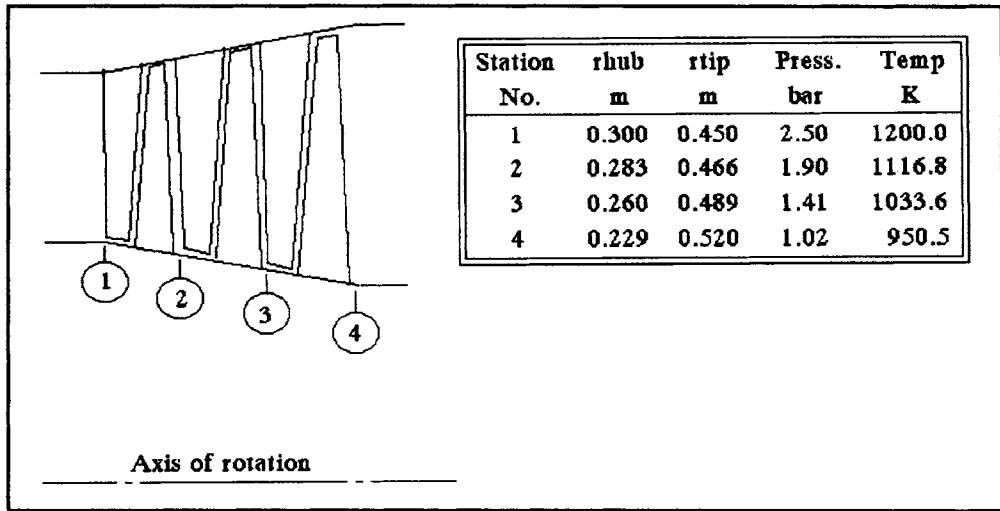| Station | rhub | rtip | Press. | Temp |
No.	m	m	bar	K
1	0.300	0.450	2.50	1200.0
2	0.283	0.466	1.90	1116.8
3	0.260	0.489	1.41	1033.6
4	0.229	0.520	1.02	950.5

Axis of rotation

Fig. I.7 Overall annulus geometry and thermodynamic data

I.4 Viewing options

Three possibilities are available from the [Graphics] pull-down menu, Fig. I.4, as follows:

(1) If the [Fi/psi chart] option is selected and entered the screen presentation will be similar to that shown in Fig. I.6. The centre-line velocity triangles, which are the same for all stages, are shown in dimensionless form (i.e. all velocities are divided by the blade speed $U_m = r_m\Omega$). Below this is shown the standard (ϕ,ψ) duty chart for the ideal model test stages with contours of constant efficiency. Your own design is plotted on this as a square marker ■ and your selected design duty coefficients are also recorded to the left. By returning to the main menu you can then change the design data to adjust or improve your design in relation to the optimum test stages. Incidentally you can also first read off the efficiency value from the chart (e.g. $\eta = 93\%$ for the default turbine) and update your estimate of this with the menu sequence [Thermodynamics] [Efficiency tot. to tot.]. For example, the default turbine has a fairly heavy loading coefficient $\psi = 1.5045$ which can be reduced if you select four stages instead of the default number of three, using the menu sequence [Design data] [Number of stages].

(2) Selection of the [View annulus] option results in the presentation shown in Fig. I.7. Overall annulus geometry (i.e. hub and tip radii) and thermodynamic data (i.e. temperature and pressure) are tabulated at entry, station 1, and after each stage, namely 2, 3, etc.

(3) Selection of the [View stage data] option results in the presentations shown in Figs I.8 and I.9, namely detailed stage design data. Whenever you update the main menu, the program goes on to undertake a detailed design for all stages for 11 sections from the hub radius to the tip radius. It assumes a free-vortex design for simplicity and consequently a constant 'work done' and axial velocity. Thermodynamic properties and full velocity triangle data are
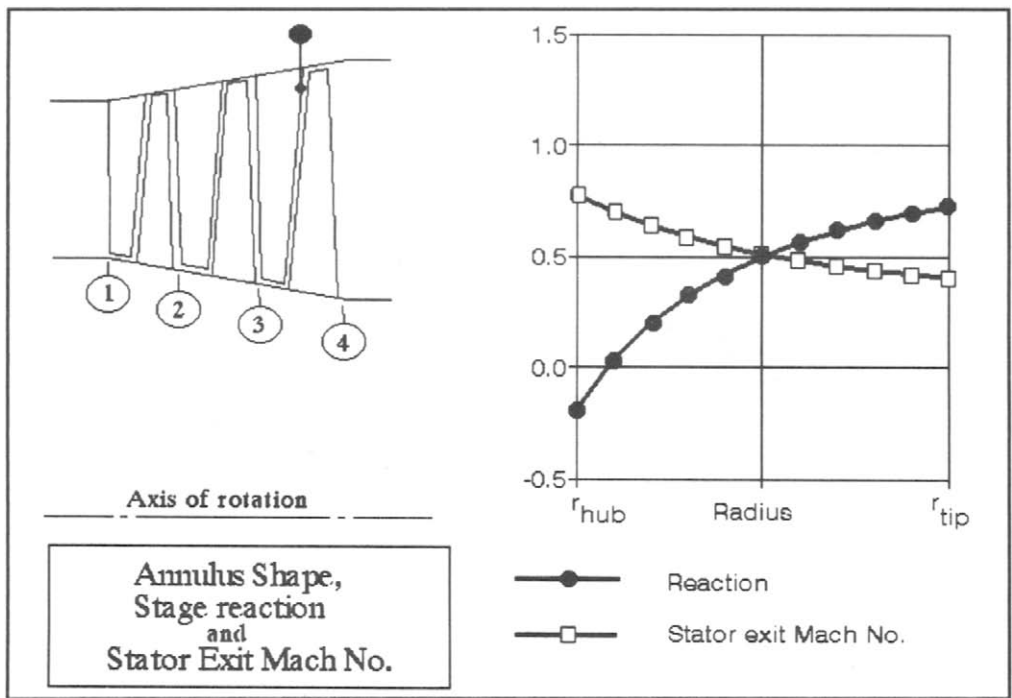
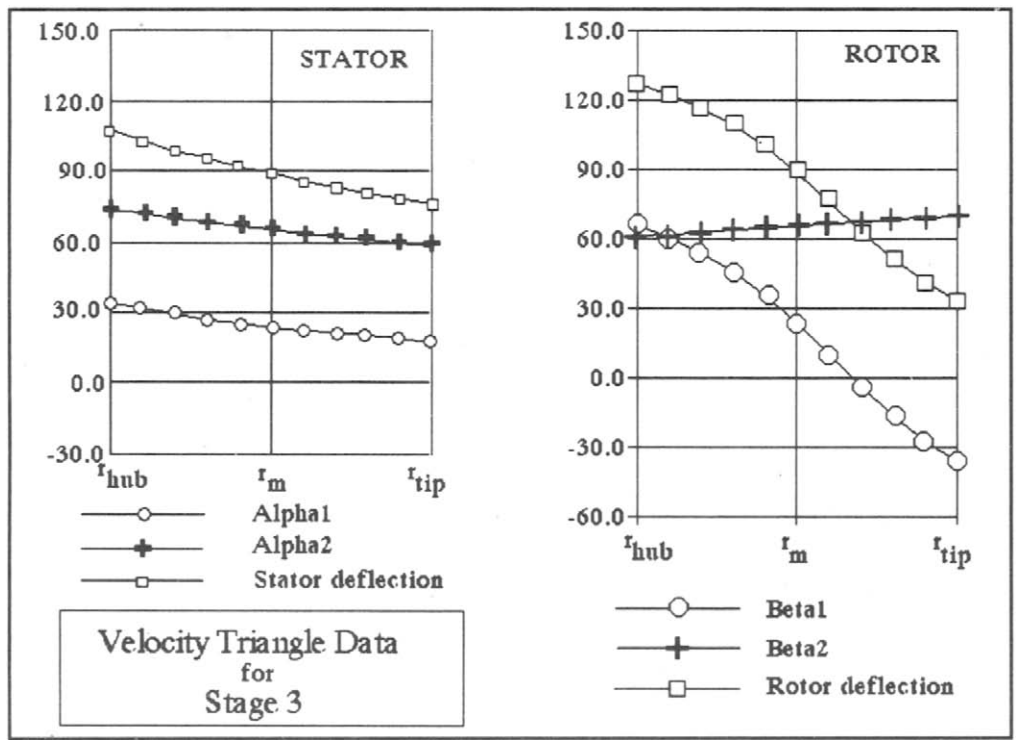**Fig. I.8** Overall data for selected stage

Fig. I.9 Detailed velocity triangle data and exit Mach no. data for selected stage

all evaluated. Many of these data are presented in Figs I.8 and I.9 for visual checking. First of all you will be asked to select a particular stage for viewing such as stage 3 as shown in Fig. I.8. It is quite helpful just to check quickly the stage reaction from hub to tip and the level of highest likely Mach number. Thus for the default design we have slightly negative reaction at the hub section which is not disastrous but just at the sensible limit here. Mach numbers at the stator exit are of more concern but here reach no more than about 0.76 at the hub section. If you now hit any key on the keyboard you will be presented with Fig. I.9, which shows detailed velocity triangle and exit Mach numbers relative to both stator and rotor of your selected stage. Thus we see here that fluid deflections of about 126° are required of the rotor hub section due to the slightly negative reaction found there, and fairly large stator deflections too. These heavy aerodynamic demands may be lightened by selecting four stages rather than three as already suggested for this default design.

I.5   [File etc.] option

The last bar menu item [File etc.], Fig. I.5, offers the following series of tools to organise files or to switch settings:

(1) [Save and exit] enables you to record your data into a text file which you will be invited to name (see Section I.7).
(2) [Quit]. If you select this option you will simply quit the session without saving your work.
(3) [Read data from file] enables you to pick up from where you left off last time, assuming that you remembered to use item (4) below before quitting.
(4) [File design data] enables you to save your present design data into a file named TURBINE.DAT. If you wish to resume the work at a later date, it is essential to use this option before using [Quit] or [Save and exit].
(5) [Go to DOS] enables you to leave FIPSI temporarily and enter DOS in order to carry out some other work. To leave DOS and return back to FIPSI simply enter 'exit' at the DOS prompt.
(6) [Reverse video] simply reverses paper and ink colours for the graphics presentations. If you wish to do screen dumps, slightly better quality may be obtained with reverse video. To obtain a screen dump:
   (a) Enter DOS.
   (b) Type the DOS graphics command appropriate to your printer.
   (c) Return to FIPSI and select one of the [Graphics] viewing options.
   (d) Hit the Print Screen key.

I.6   Disc file FIPSI.DAT

The experimental test data which forms the basis of the (ϕ,ψ) performance chart are stored in file FIPSI.DAT and must be available on the working disc. A printout of this is given in Section I.8, annotated to indicate the various items. It would be perfectly possible to replace this with your own set of test data if you so wished provided you retain the same format.

I.7 Contents of output data file JUNK for the default turbine design

***** OVERALL DESIGN DATA *****

Inlet hub radius	= 0.300 m	Inlet pressure	= 2.500 bar
Inlet tip radius	= 0.450 m	Outlet pressure	= 1.020 bar
Outlet hub radius	= 0.229 m	Inlet temp. T1	= 1200.0 K
Outlet tip radius	= 0.520 m	Outlet temp. T2	= 950.5 K
Stator aspect ratio	= 6.0	Rotor aspect ratio	= 8.0
Number of stages	= 3		
Rotational speed	= 6000.0 revs/min		
Mass flow rate	= 35.000 kg/s		
Axial velocity	= 136.42 m/s		
Cp/Cv ratio gamma	= 1.40		
Gas constant R	= 287.0 J/kg K		
Flow coeff. fi	= 0.57899		
Work coeff. psi	= 1.50459		
Tot. to tot. efficiency	= 92.0%		

```
*****        ANNULUS GEOMETRY        *****
*****             AND                *****
*****      THERMODYNAMIC DATA        *****
```

Station	x m	r hub m	r tip m	Press. bar	Temp. K
1	0.000	0.300	0.450	2.500	1200.0
2	0.072	0.283	0.467	1.901	1116.8
3	0.161	0.261	0.489	1.412	1033.7
4	0.272	0.229	0.521	1.020	950.5

```
*****      DETAILED STAGE DESIGN      *****
*****             AND                 *****
*****   PERFORMANCE ANALYSIS DATA     *****
```

Stage No. 1
DIMENSIONLESS COEFFICIENTS

Radius	Reaction	fi	psi	M2	M3
0.29081	0.16861	0.74661	2.50179	0.600	0.437
0.30765	0.25713	0.70575	2.23544	0.569	0.446
0.32449	0.33222	0.66913	2.00948	0.542	0.455
0.34133	0.39648	0.63612	1.81611	0.517	0.465
0.35816	0.45189	0.60622	1.64938	0.496	0.475
0.37500	0.50000	0.57900	1.50459	0.476	0.485
0.39184	0.54205	0.55412	1.37806	0.459	0.496
0.40867	0.57900	0.53129	1.26685	0.443	0.507
0.42551	0.61166	0.51027	1.16858	0.429	0.519
0.44235	0.64066	0.49084	1.08131	0.416	0.531
0.45919	0.66653	0.47285	1.00347	0.403	0.543

M2 = absolute exit Mach No. leaving the stator
M3 = relative exit Mach No. leaving the rotor

VELOCITY TRIANGLE DATA

Radius	Alpha1	Alpha2	Stator deflection	Beta2	Beta3	Rotor deflection
0.29081	29.331	70.275	99.606	55.400	62.257	117.657
0.30765	27.974	69.228	97.202	50.646	62.827	113.473
0.32449	26.729	68.195	94.924	45.145	63.413	108.557
0.34133	25.582	67.177	92.759	38.807	64.005	102.812
0.35816	24.524	66.174	90.698	31.590	64.598	96.188
0.37500	23.545	65.187	88.731	23.545	65.187	88.731
0.39184	22.637	64.214	86.852	14.856	65.767	80.623
0.40867	21.793	63.258	85.051	5.849	66.337	72.185
0.42551	21.008	62.317	83.325	−3.071	66.894	63.823
0.44235	20.274	61.393	81.667	−11.516	67.437	55.921
0.45919	19.588	60.484	80.072	−19.215	67.965	48.750

Stage No. 2

DIMENSIONLESS COEFFICIENTS

Radius	Reaction	fi	psi	M2	M3
0.27089	0.04184	0.80152	2.88328	0.667	0.445
0.29171	0.17374	0.74431	2.48637	0.621	0.455
0.31254	0.28016	0.69472	2.16612	0.582	0.466
0.33336	0.36728	0.65133	1.90398	0.549	0.478
0.35418	0.43948	0.61304	1.68670	0.520	0.491
0.37500	0.50000	0.57900	1.50459	0.495	0.504
0.39582	0.55122	0.54854	1.35046	0.472	0.518
0.41664	0.59495	0.52113	1.21886	0.453	0.533
0.43746	0.63259	0.49633	1.10559	0.435	0.548
0.45829	0.66522	0.47378	1.00741	0.419	0.564
0.47911	0.69369	0.45319	0.92175	0.405	0.579

M2 = absolute exit Mach No. leaving the stator
M3 = relative exit Mach No. leaving the rotor

VELOCITY TRIANGLE DATA

Radius	Alpha1	Alpha2	Stator deflection	Beta2	Beta3	Rotor deflection
0.27089	31.099	71.531	102.630	60.205	61.618	121.823
0.29171	29.255	70.218	99.474	55.163	62.287	117.450
0.31254	27.602	68.927	96.529	49.131	62.996	112.127
0.33336	26.113	67.657	93.770	41.915	63.724	105.639
0.35418	24.767	66.410	91.177	33.377	64.458	97.834
0.37500	23.545	65.187	88.731	23.545	65.187	88.731
0.39582	22.432	63.987	86.419	12.739	65.903	78.642
0.41664	21.415	62.811	84.225	1.591	66.602	68.193
0.43746	20.482	61.659	82.141	−9.134	67.281	58.147
0.45829	19.624	60.532	80.156	−18.825	67.937	49.112
0.47911	18.832	59.429	78.262	−27.190	68.569	41.379

Stage No. 3
DIMENSIONLESS COEFFICIENTS

Radius	Reaction	fi	psi	M2	M3
0.24370	−0.18393	0.89096	3.56267	0.773	0.453
0.26996	0.03520	0.80429	2.90326	0.698	0.464
0.29622	0.19868	0.73299	2.41132	0.638	0.477
0.32248	0.32387	0.67330	2.03459	0.589	0.492
0.34874	0.42186	0.62260	1.73972	0.549	0.508
0.37500	0.50000	0.57900	1.50459	0.515	0.526
0.40126	0.56330	0.54111	1.31410	0.486	0.545
0.42752	0.61530	0.50787	1.15762	0.461	0.564
0.45378	0.65854	0.47848	1.02752	0.440	0.584
0.48004	0.69488	0.45230	0.91817	0.421	0.605
0.50630	0.72571	0.42884	0.82540	0.404	0.626

M2 = absolute exit Mach No. leaving the stator
M3 = relative exit Mach No. leaving the rotor

VELOCITY TRIANGLE DATA

Radius	Alpha1	Alpha2	Stator deflection	Beta2	Beta3	Rotor deflection
0.24370	33.843	73.276	107.119	65.613	60.849	126.462
0.26996	31.186	71.590	102.777	60.411	61.589	122.000
0.29622	28.883	69.937	98.819	53.949	62.438	116.387
0.32248	26.872	68.317	95.189	45.844	63.342	109.186
0.34874	25.106	66.734	91.839	35.737	64.266	100.003
0.37500	23.545	65.187	88.731	23.545	65.187	88.731
0.40126	22.158	63.677	85.835	9.829	66.087	75.916
0.42752	20.918	62.206	83.124	−4.110	66.959	62.850
0.45378	19.804	60.774	80.577	−16.835	67.797	50.962
0.48004	18.798	59.380	78.179	−27.534	68.597	41.063
0.50630	17.887	58.026	75.913	−36.125	69.358	33.233

I.8 Contents of the φ, ψ data file FIPSI.DAT

6			{Number of constant efficiency contours}
11			{Number of fi,psi data in first contour}
94.0			{Value of total to total efficiency}
	0.4	1.02	
	0.45	1.13	
	0.5	1.21	
	0.55	1.28	
	0.6	1.3	
	0.65	1.3	{Eleven fi,psi values for this contour}
	0.7	1.28	
	0.72	1.25	
	0.74	1.15	
	0.73	1	
	0.7	0.84	

16
93.0

0.4	1.12	{Same format for remaining five contours}
0.45	1.24	
0.5	1.35	
0.55	1.45	
0.6	1.54	
0.65	1.63	
0.7	1.68	
0.75	1.67	{Efficiency contour No. 2}
0.785	1.64	
0.8	1.6	
0.81	1.57	
0.82	1.5	
0.83	1.25	
0.825	1.2	
0.81	1	
0.8	0.92	

19
92.0

0.4	1.26	
0.45	1.41	
0.5	1.545	
0.55	1.66	
0.6	1.77	
0.65	1.84	
0.7	1.89	
0.75	1.88	
0.8	1.86	
0.84	1.8	{Efficiency contour No. 3}
0.86	1.75	
0.87	1.7	
0.88	1.6	
0.887	1.5	
0.89	1.4	
0.888	1.3	
0.885	1.2	
0.88	1.1	
0.865	1	

19
91.0

0.4	1.4	
0.45	1.57	
0.5	1.7	
0.55	1.82	
0.6	1.93	
0.65	2.02	
0.7	2.27	
0.75	2.11	
0.8	2.1	{Efficiency contour No. 4}

```
        0.85    2.06
        0.9     1.95
        0.95    1.78
        0.96    1.7
        0.97    1.6
        0.972   1.5
        0.97    1.4
        0.965   1.3
        0.95    1.2
        0.925   1
18
90.0
        0.4     1.57
        0.5     1.87
        0.6     2.1
        0.65    2.18
        0.7     2.24
        0.75    2.28
        0.8     2.29
        0.85    2.27
        0.9     2.2              {Efficiency contour No. 5}
        0.95    2.12
        1       1.89
        1.018   1.8
        1.035   1.6
        1.037   1.5
        1.035   1.4
        1.027   1.3
        1.015   1.2
        0.975   1
18
89.0
        0.5     2.06
        0.55    2.17
        0.6     2.27
        0.65    2.34
        0.7     2.39
        0.75    2.42
        0.8     2.44
        0.85    2.45
        0.9     2.43            {Efficiency contour No. 6}
        0.95    2.37
        1       2.28
        1.03    2.2
        1.07    2
        1.09    1.8
        1.09    1.6
        1.08    1.4
        1.065   1.2
        1.035   1
```

Appendix II

'CASCADE'

A computer program for design and analysis of turbomachine cascades

II.1 Introduction and overview

CASCADE is a computer program for the fluid dynamic design and analysis of turbomachine cascades. Blade profile geometry is generated by superimposing a profile thickness distribution normal to a camber or mean line which can be either a circular arc or a parabola, as described in Section 2.3. Alternatively the program will accept 'raw data', namely a set of (x,y) profile coordinates as explained in Section II.2.2. Once the blade row geometry has been selected the program undertakes a fluid flow analysis based on the surface vorticity cascade method outlined in Chapter 9, Section 9.4, to predict the outlet flow angle β_2 and surface pressure distribution

```
 Profile  Camber line   Stagger,t/1  Inlet angle   Design/analyse  Quit/DOS/File

                  ********* "Design Mode" **********
           Cascade data are presently as follows:-

           Profile thickness is the C4 profile
           Profile thickness scale = 1.0

           Camber line type is circular arc
           x/1 of maximum camber = 0.5
           Camber angle theta  = 60.0

           Stagger angle lamda  = 45.0

           Pitch/chord ratio = 1.0

           Fluid inlet angle beta1 = 60.0

             <<Press Alt key and first letter together to grab a menu>>
                 <<e.g.  Alt-C pulls down the Camber menu>>
```

Fig. II.1 Main bar menu
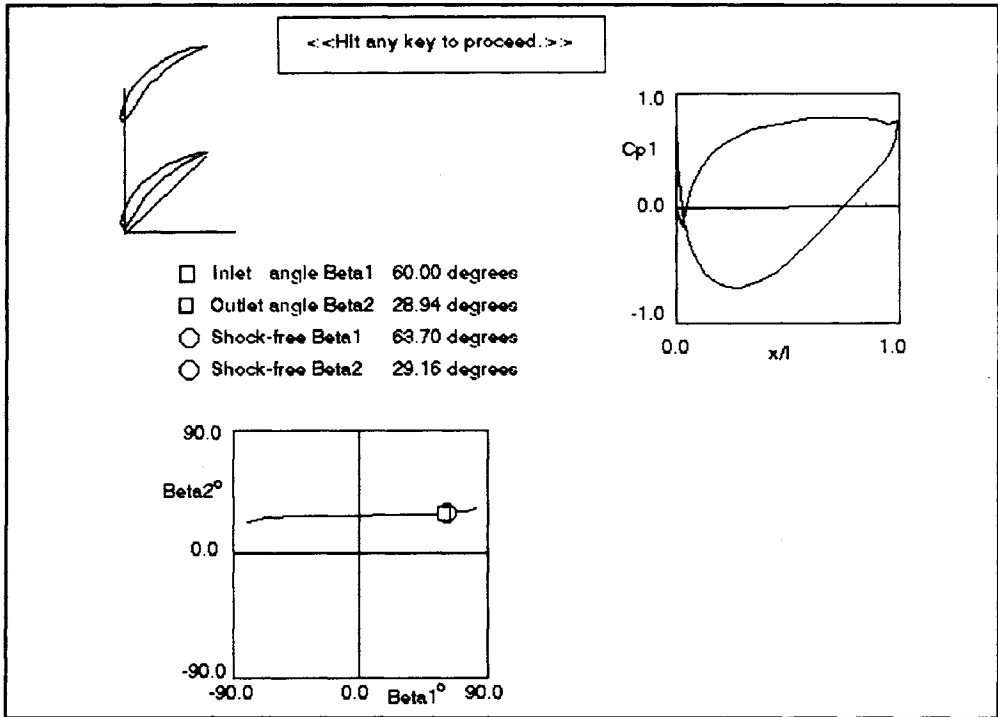
Fig. II.2 Graphical output for default cascade

C_{p1} or C_{p2} for a specified inlet angle β_1. All of these data are presented graphically at the screen and filed onto the hard disc in tabular form. To provide a quick overview it will be helpful to illustrate the two main screen presentations at this point, namely the main bar menu, Fig. II.1, and the predicted output, Fig. II.2.

The program is managed by a bar menu system with pull-down menus and is for use on IBM-compatible PCs with either mono or colour graphics. The use of each menu is explained in Sections II.2 to II.7. Below the bar menu there is a presentation of the current design data. Initially when the program is run a default design is set up automatically and comprises the data shown in Fig. II.1. Use may then be made of the bar menu to change any of these data in order to select whatever cascade geometry is of interest to the user.

Whenever the user so wishes, the current cascade data may be converted into an actual design and subjected to fluid flow analysis by accessing the Design/analyse option in the bar menu. The output is then presented graphically at the computer terminal. Figure II.2 shows the output for the default cascade data recorded in Fig. II.1.

Three graphs are presented here as follows:

(1) *Cascade geometry*. A small picture is presented showing the shape of the cascade to provide a quick visual check.
(2) *Output angle versus inlet angle*. A graph is plotted of the predicted fluid outlet angle β_2 for a very wide range of fluid inlet angles β_1.
(3) *Surface pressure distribution*. A graph is presented showing the predicted

surface pressure coefficient C_{p1} or C_{p2} versus fractional distance along the chord line x/l. The surface pressure coefficients are defined as follows:

$$C_{p1} = \frac{p - p_1}{\frac{1}{2}\rho W_1^2} \qquad \text{for a compressor} \qquad \text{(II.1)}$$

$$C_{p2} = \frac{p - p_2}{\frac{1}{2}\rho W_2^2} \qquad \text{for a turbine} \qquad \text{(II.2)}$$

The default design illustrated in Fig. II.2 is a compressor cascade for which the stagger is positive, $+45°$. A turbine cascade is selected by simply specifying a negative stagger value, e.g. $-60°$. The program then automatically selects either C_{p1} or C_{p2} as defined above.

II.1.1 How to run the program

Before running the program CASCADE it is essential to have the file **profiles** available in the current directory. The contents of this are given in Section II.9 and may be extended to include other profile thicknesses by following the given format. To run the program simply enter its name **cascade** at the keyboard. The title page which is then presented at the screen can be removed by hitting any key, whereupon the main bar menu and default design data, Fig. II.1, will then appear at the screen. To access any item in the bar menu simply press down the **Alt** key while hitting the first character of the keyword as explained at the bottom of the screen.

II.1.2 Main bar menu

Referring back to Fig. II.1, there are six keywords in the main bar menu which perform the following functions:

Profile	To select the profile base thickness distribution.
Camber line	To select the camber angle and type of curvature.
Stagger,t/l	To select the cascade geometrical parameter stagger and pitch/chord ratio.
Inlet angle	To select the inflow angle β_1.
Design/analyse	To convert the above design data into a cascade and calculate its fluid-dynamic performance.
Quit/DOS/File	To enable you to quit, to go temporarily into DOS, to file your current work or to read the previous work from file, or to reverse the video presentation.

We will now deal with these in more detail in the following six sections.

II.2 Profile menu

Before we consider use of the profile menu it will be helpful to explain the method used here to create turbomachine blade profiles as illustrated in Fig. II.3. This follows the standard gas turbine convention of superimposing a base profile thickness (x_t, y_t) either side of a camber line (x_c, y_c).

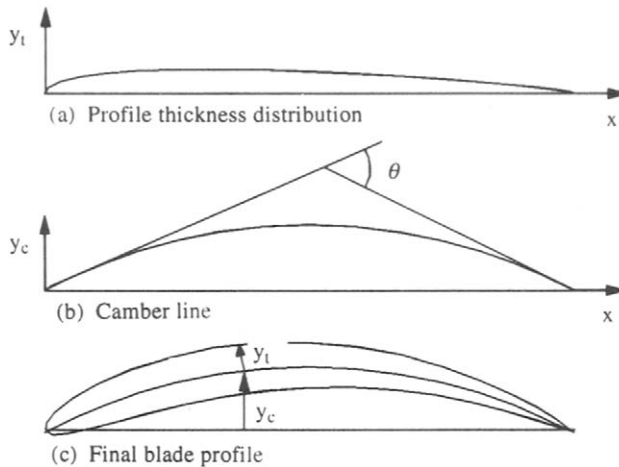If we now access the **Profile** menu by entering **Alt-p** we obtain the pull-down menu shown in Fig. II.4.

(a) Profile thickness distribution

(b) Camber line

(c) Final blade profile

Fig. II.3 Method of construction of a turbomachine blade profile

Profile Camber line Stagger, t/l Inlet angle   Design/analyse Quit/DOS/File

Profile -- C4
Profile -- T4
Profile -- NACA 0012
Profile -- NACA 0015
Profile -- Naca66-010
Profile -- NGTEmod
Raw data from file

** "Design Mode" *********

ntly as follows:-

c4 profile
= 1.0

cular arc
r = 0.5

Camber angle theta = 60.0

Stagger angle lamda = 45.0

Pitch/chord ratio = 1.0

Fluid inlet angle beta1 = 60.0

< < Press Alt key and first letter together to grab a menu > >
< < e.g. Alt-C pulls down the Camber menu > >

Fig. II.4 The **Profile** pull-down menu

II.2.1 Selection of a base profile thickness

The ↑ ↓ arrow keys enable us to highlight the profile of our choice, which may then be accepted by pressing <Enter>. Thus in Fig. II.4 the axial compressor **Profile – C4** had been selected. Following this the user is invited to specify the profile thickness scale. If the value 1.0 is entered then the standard profile thickness shape will be used to generate the y_t values, Fig. II.3, otherwise some other value may be used to thicken or thin the profile. The first six items on this pull-down menu provide a range of typical profile thicknesses to suit many turbomachine applications.

```
┌────────────────────────────────────────────────────────────────┐
│ Profile  Camber line  Stagger,t/l  Inlet angle  Design/analyse  Quit/DOS/File │
├────────────────────────────────────────────────────────────────┤
│         ********** "Raw Data" Mode **********                    │
│                                                                  │
│  Profile x,y coordinates have been read from disc file RAWDATA   │
│  The following bar menu item is disabled with this option        │
│                                                                  │
│              Camber line                                         │
│                                                                  │
│  The remaining bar menu items are accessible                     │
│                                                                  │
│         Profile        * * *   to resume "Design" mode           │
│         Stagger,t/l     * * *   to select new cascade geometry   │
│         Inlet angle     * * *   to select a new betal value      │
│         Design/quit    * * *   to proceed with the design/analysis │
│         Quit/DOS/file   * * *   to quit or organise files        │
│                                                                  │
│  Present status of cascade is as follows                         │
│         Stagger    = 45.0 deg                                    │
│         t/l ratio  = 1.0                                         │
│         inlet angle = 60.0 deg                                   │
│                                                                  │
└────────────────────────────────────────────────────────────────┘
```

Fig. II.5 Raw data option

```
┌────────────────────────────────────────────────────────────────┐
│ Profile │Camber line│Stagger,t/l  Inlet angle  Design/analyse  Quit/DOS/File │
├─────────┼───────────┴───────────────────────────────────────────┤
│         │ Camber angle │    "Design Mode" **********             │
│         ├──────────────┤  y as follows:-                         │
│         │ Circular arc type │                                    │
│         │ Parabolic type │                                       │
│         Profile thickness is the C4 profile                      │
│         Profile thickness scale = 1.0                            │
│                                                                  │
│         Camber line type is circular arc                         │
│         x/l of maximum camber = 0.5                              │
│         Camber angle theta = 60.0                                │
│                                                                  │
│         Stagger angle lamda = 45.0                               │
│                                                                  │
│         Pitch/chord ratio = 1.0                                  │
│                                                                  │
│         Fluid inlet angle betal = 60.0                           │
│                                                                  │
│      < <Press Alt key and first letter together to grab a menu> > │
│         < <e.g.  Alt-C pulls down the Camber menu> >             │
└────────────────────────────────────────────────────────────────┘
```

Fig. II.6 Camber line menu

II.2.2   Raw data option

The last item, however, is quite different in function, enabling us to adopt a profile already expressed in *x,y* profile coordinates and stored in file **rawdata**. If we select the **Raw data** pull-down menu then a new screen presentation is displayed as illustrated in Fig. II.5. The procedure is explained on screen, involving the suspension
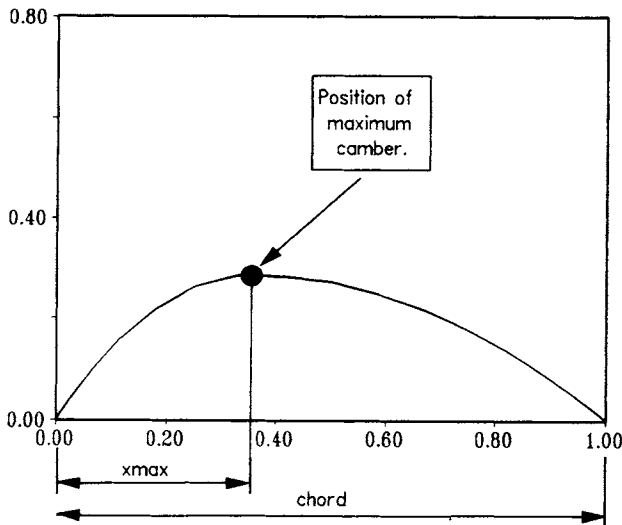
Fig. II.7 Parabolic camber line
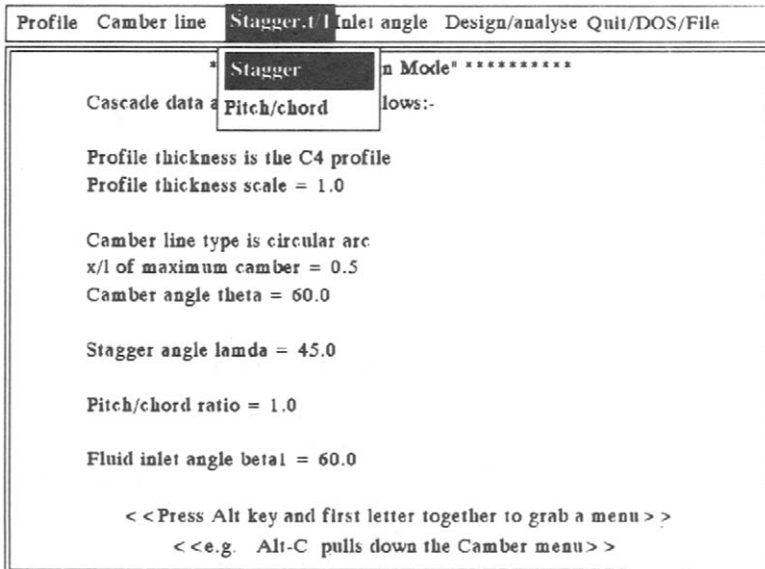
Fig. II.8 Menu for selecting cascade geometry

of the **Camber line** pull-down menu. With this option the given profile shape read from **rawdata** can be set at your own choice of stagger and camber and a flow analysis undertaken at any chosen flow inlet angle β_1. The format for data in file **rawdata** is as illustrated in Section II.10, and the author's other program STACK, for geometrical design and stacking of turbomachine blade profiles, saves its output into a file of the same name, **rawdata**, which can contain up to eleven different profiles.
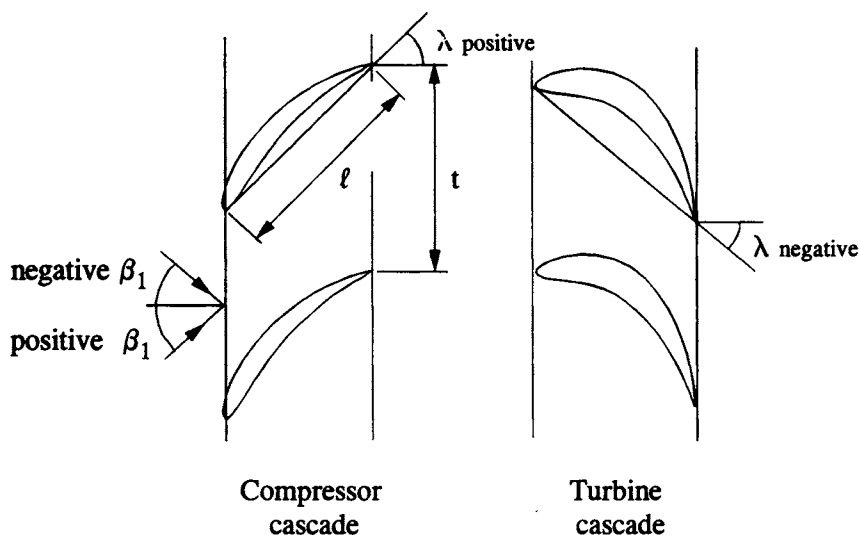
Fig. II.9 Definition of cascade geometry

II.3 Camber line menu

The **Camber line** pull-down menu has three options as shown in Fig. II.6. These have the following functions:

Camber angle   For editing the value of the camber angle θ, Fig. II.3.
Circular arc type For specifying a circular arc camber line shape.
Parabolic type   For specifying a parabolic camber line shape. If this option is selected, the user is invited to specify the position of maximum camber, xmax/chord, Fig. II.7.

II.4 Cascade geometry – Stagger,t/l menu

The **Stagger,t/l** menu (Fig. II.8) has two options permitting the selection of the two items which determine the cascade geometry, namely the stagger angle λ and the pitch/chord ratio t/l. These are defined in Fig. II.9 which illustrates two cascades. For the compressor or fan cascade the stagger angle is defined as positive and for the turbine cascade as negative as illustrated.

II.5 Inlet angle menu

This menu (Fig. II.10) enables the user to change the flow angle β_1 at entry to the cascade. The sign convention for β_1 is defined in Fig. II.9 and the sign convention for the outlet flow angle β_2 is the same, namely $+^{ve}$ above the x-axis and $-^{ve}$ below.

II.6 Design/analyse menu

This menu is shown in Fig. II.11.

```
 Profile   Camber line   Stagger,t/l   Inlet angle   Design/analyse   Quit/DOS/File

                    * * * * * * * * *   Inlet angle   * * * * * * * *

          Cascade data are presently as follows:-

          Profile thickness is the C4 profile
          Profile thickness scale = 1.0

          Camber line type is circular arc
          x/l of maximum camber = 0.5
          Camber angle theta = 60.0

          Stagger angle lamda = 45.0

          Pitch/chord ratio = 1.0

          Fluid inlet angle beta1 = 60.0

             < < Press Alt key and first letter together to grab a menu > >
                 < <e.g.  Alt-C pulls down the Camber menu> >
```

Fig. II.10 Inlet angle menu


```
 Profile   Camber line   Stagger,t/l   Inlet angle   Design/analyse   Quit/DOS/File

                    * * * * * * * * *  "Design Mod    Design & draw

          Cascade data are presently as follows:-    Flow analysis

          Profile thickness is the C4 profile
          Profile thickness scale = 1.0

          Camber line type is circular arc
          x/l of maximum camber = 0.5
          Camber angle theta = 60.0

          Stagger angle lamda – 45.0

          Pitch/chord ratio = 1.0

          Fluid inlet angle beta1 = 60.0

             < < Press Alt key and first letter together to grab a menu > >
                 < <e.g.  Alt-C pulls down the Camber menu> >
```

Fig. II.11 Menu for cascade design, drawing and flow analysis

II.6.1 The Design & draw option

When the designer wishes to assess the current state of a design, two options are made available from this menu. The **Design & draw** option constructs the cascade geometry from the profile and cascade data which has been selected and then presents it on screen as illustrated by Fig. II.12. This provides a visual check that there have been no serious errors in selecting the various variables, for example the wrong sign

www.semeng.ir
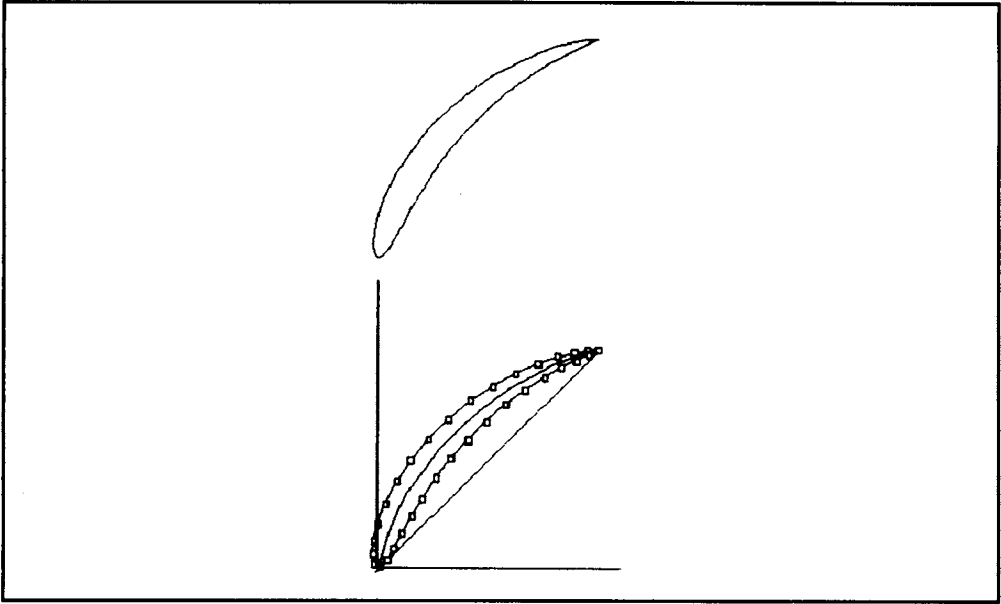
Fig. II.12 Cascade geometry presented on-screen

for the stagger λ. The geometry shown in Fig. II.12 is that of the default design which is a compressor cascade.

II.6.2 The Flow analysis option

Alternatively a prediction of the fluid flow behaviour may be obtained for the present design of cascade by selecting the second pull-down menu, **Flow analysis**. First of all the geometry shown in Fig. II.12 will be presented, followed by the flow data shown in Fig. II.13, which is in fact the same as that already illustrated in Fig. II.2 in the introduction, Section II.1, where an overview has already been given. To assist the design optimisation process graphs are plotted of the blade surface pressure distribution as defined in Eqns (II.1) and (II.2) and the deflection data β_1 versus β_2.

Selection of optimum inlet angle
A table is presented giving the predicted outlet angle β_2 for the selected inlet angle β_1, marked also by $\square$ on the graph. In addition to this, the shock-free inlet angle and its associated outlet angle are also presented to provide the designer with an estimate of the optimum inflow angle for his chosen cascade geometry. Shock-free inflow is defined as the β_1 value for which the stagnation point coincides precisely with the blade leading edge position. This condition is also plotted as point $\bigcirc$ on the graph. In practice this will be quite close to the inlet angle for minimum profile loss. Also shown at the top of the screen is the instruction:

$$\boxed{<< \text{Hit any key to proceed.} >>}$$
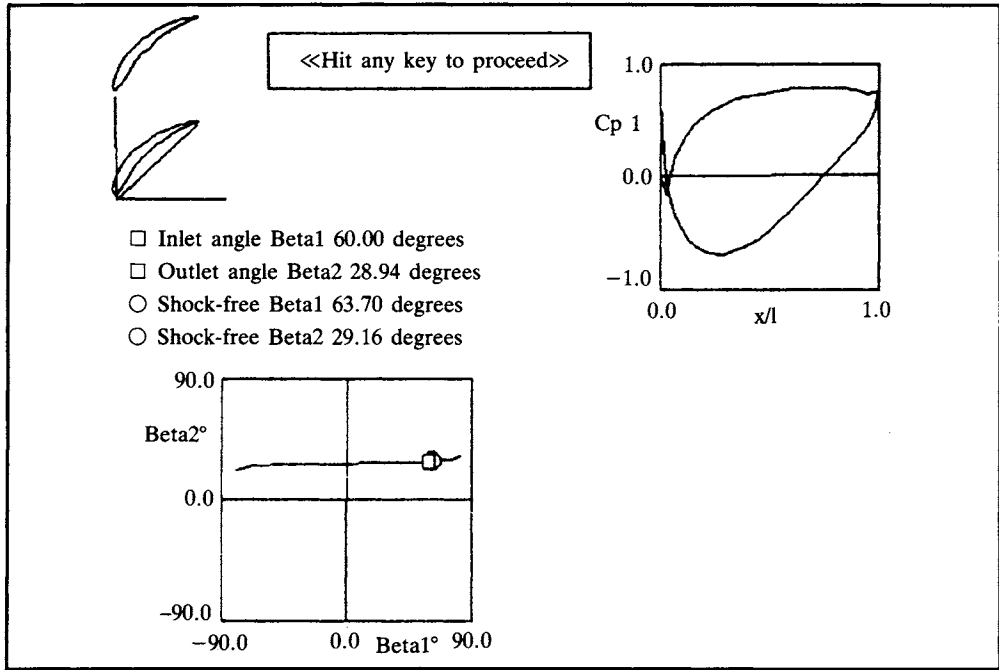
Fig. II.13 Graphical output from **Flow analysis** option

Hitting any key then results in the following presentation:

Do you wish to select a new inflow angle?
Enter y or n ***

Entering **y** in answer to this results in an invitation to enter a new value for the inflow angle β_1,

Enter new value of Beta1

after which the flow will be recalculated and a new version of Fig. II.13 presented. This enables the designer to experiment with the choice of inflow angle in order, for example, to select the optimum cascade shape for the job in hand. Thus if the shock-free value of $\beta_1 = 63.7°$ is entered the resulting pressure distribution will be much smoother in the leading edge region.

II.7 Quit/DOS/File menu

This pull-down menu (Fig. II.14) offers a variety of management tools as follows:

Quit   This menu brings the session to an end, resulting in the recording of data into the following files:

```
 Profile  Camber line  Stagger,t/1 Inlet angle  Design/analyse  Quit DOS File
┌──────────────────────────────────────────────────────────┬────────────────┐
│          ********** 'Design Mode' **********              │ Quit           │
│                                                           │ Go to DOS      │
│      Cascade data are presently as follows:-             │ File this design│
│                                                           │ Design from file│
│      Profile thickness is the C4 profile                 │ Reverse video  │
│      Profile thickness scale = 1.0                       │                │
│                                                          └────────────────┘
│      Camber line type is circular arc
│      x/l of maximum camber = 0.5
│      Camber angle theta = 60.0

│      Stagger angle lamda = 45.0

│      Pitch/chord ratio = 1.0

│      Fluid inlet angle beta1 = 60.0

│        < <Press Alt key and first letter together to grab a menu> >
│           < <e.g.  Alt-C pulls down the Camber menu> >
└─────────────────────────────────────────────────────────────────────────┘
```

Fig. II.14 Menu for handling files and other tools

	rawdata	This file contains (x,y) coordinates of the last blade profile but set at zero stagger. Sample data for the default design, Fig. II.14, are given in Section II.10.
	testdata	This file contains a record of all the work undertaken using the **Design/analyse** bar menu, Section II.11.
Go to DOS		This menu enables the user to leave the program temporarily and enter DOS to undertake other work. To re-enter program CASCADE and resume work where you left off, just enter 'exit' at the DOS prompt.
File this design		To save the current design parameters in order later to pick up the work where you are now leaving it.
Design from file		To resume from where you left off after using the previous menu **File this design**.
Reverse video		To reverse the ink and paper colours for the graphical presentations. These are initially set with black ink on white paper. Use of this menu reverses this to white ink on black paper. The main benefit of this is for screen dumping for which the reverse video usually gives a better result. Use of this menu a second time causes the screen presentation to revert back to normal.

II.7.1   Screen dumping of results

Hard copies of graphical presentations such as Figs II.12 and II.13 may be obtained by screen-dumping. To achieve this enter the [Graphics] command (using the appropriate option for your printer) before running the CASCADE program. Alternatively, if you forgot to do this before beginning the session, use the **Go to DOS** pull-down menu to go temporarily into DOS and then use the [Graphics]

command before returning to CASCADE. Then press the Print Screen key whenever you wish to dump the graphical presentations to the printer.

II.8 Example – design of an optimum compressor cascade

To illustrate the use of the program CASCADE let us consider the selection of optimum profile geometry to meet prescribed aerodynamic requirements which are to be as follows:

Design requirements
We will adopt the case considered in Chapter 2, Fig. 2.7, where we are given $\beta_1 = 54.59°$, $\beta_2 = 30.69°$, C4 profile, circular arc camber-line. Let us also specify that the loading must be conservative compared with the maximum allowable diffusion factor of DF = 0.6.

The first task is to estimate a suitable value for the pitch/chord ratio t/l. Substituting the above data into Eqn (2.30) for DF = 0.6 gives the maximum allowable value $t/l = 1.1623$. Since we are asked to produce a conservative design let us adopt the slightly smaller value $t/l = 1.0$. Back-substitution into Eqn (2.28) then yields a conservative diffusion factor of DF = 0.5618.

Now we can proceed to use the program CASCADE to find the camber θ and stagger λ values to deliver the required β_2 with shock-free inflow β_1. There are two practical approaches as follows.

Solution – first method, **interpolation**
For a first crude estimate of cascade geometry we could guess that the stagger might approximate to the average of β_1 and β_2 (see Fig. 2.5 for a perception of this). On the other hand we might expect the camber angle to be rather bigger than the fluid deflection, say $1.5 \times (\beta_1 - \beta_2)$. Thus our first estimation will be as follows:

$$\lambda \approx \tfrac{1}{2}(54.59° + 30.69°) = 42.64° \approx 43°$$
$$\theta \approx 1.5 \times (54.59° - 30.69°) = 35.85° \approx 36°$$

The strategy to be followed now is to study four test cascades around these values using the program CASCADE in order to predict their shock-free performance, and then to interpolate to estimate the required stagger and camber. The four test cases chosen for illustration are shown in Table II.1.

Table II.1 Test cases for program CASCADE

Case no.	$\lambda°$	$\theta°$	Shock-free inlet and outlet angles from CASCADE program	
			$\beta_{1opt}°$	$\beta_{2opt}°$
1	40	35	52.37	31.32
2	40	45	55.22	28.23
3	45	35	57.09	36.82
4	45	45	59.79	33.80
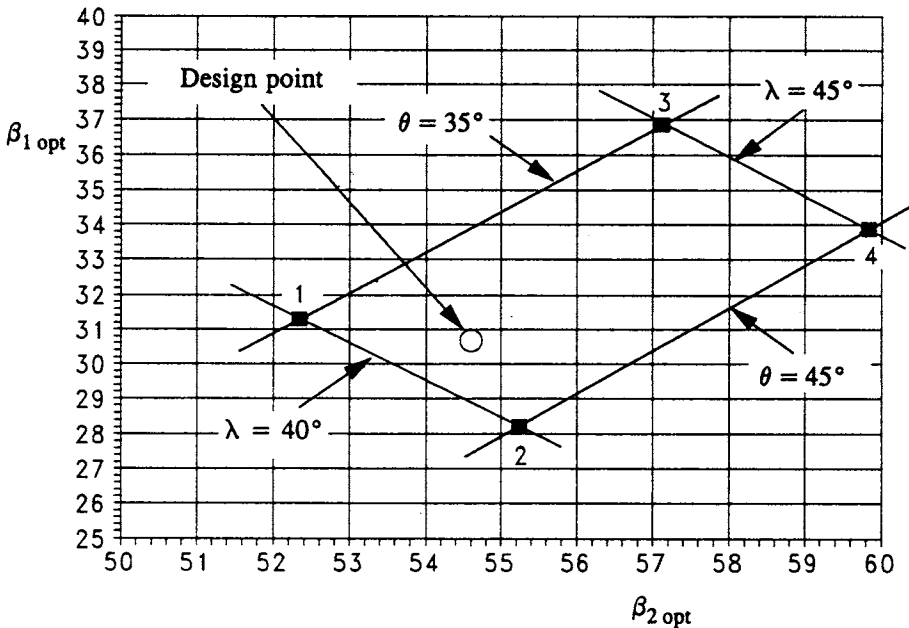
Fig. II.15 Plot of trial cascades 1 to 4 for interpolation of required λ and θ values to achieve specified design point with shock-free inflow

The four shock-free 'ideal' test cases are plotted ■ in Fig. II.15 together with the required design point ○. From this plot the estimated stagger and camber, interpolating by eye, are as follows:

$$\lambda \approx 40.8°, \; \theta \approx 40° \; \textit{Solution by interpolation}$$

A re-run of CASCADE using these values confirms that this is an excellent choice which will deliver the required outlet angle β_2 with almost precisely shock-free inflow.

*Solution – second method, **trial and error***
Alternatively λ and θ may be estimated by trial and error starting from the same first guesses as before. The following *cause-and-effect* relationships are of some help in this otherwise rather more random approach to design:

(1) Outlet angle β_2 is strongly controlled by λ for $t/l \leqslant 1.0$.
(2) Deflection increases with camber angle θ. Consequently β_2 will then decrease for a compressor cascade and increase for a turbine.
(3) Increase in either stagger or camber will increase the shock-free inflow angle for a compressor cascade, the reverse being true for a turbine, although care is needed over the signs of β_1 for the turbine case.

Table II.2 provides an example of arriving at a reasonable solution after six iterations of this rather subjective approach.

Although the final design is slightly different from method 1 it is very close to the ideal cascade required.

Table II.2 Design of a shock-free compressor cascade by trial and error selection of stagger and camber angles

Iteration	$\lambda°$	$\theta°$	Target design values		$\beta^°_{1opt}$	$\beta^°_{2opt}$
			54.59° $\beta_1°$	30.69° $\beta_2°$		
1	43	36	54.59	34.26	55.49	34.31
2	40	36	54.59	31.10	52.66	31.02
3	40	38	54.59	30.46	53.23	30.40
4	40.2	38	54.59	30.67	53.42	30.62
5	40.7	39	54.59	30.88	54.18	30.86
6	40.5	39	54.59°	30.67°	53.99	30.64
			Final design		Shock-free angles	

II.9 Contents of data file profiles

The file **profiles** contains a selection of base profile thickness coordinates with the following format:

```
C4                              Profile name
    17                          Number of (xt,yt) coordinates
        0.000000    0.000000
        1.250000    1.650000
        2.500000    2.270000
        5.000000    3.080000
        7.500000    3.620000
       10.000000    4.020000
       15.000000    4.550000
       20.000000    4.830000
       30.000000    5.000000    17 (xt,yt) pairs for this profile.
       40.000000    4.890000
       50.000000    4.570000
       60.000000    4.050000
       70.000000    3.370000
       80.000000    2.540000
       90.000000    1.600000
       95.000000    1.060000
      100.000000    0.000000
T4
    17
        0.000000    0.000000
        1.250000    1.170000
        2.500000    1.540000
        5.000000    1.990000
        7.500000    2.370000
       10.000000    2.740000
```

15.000000	3.400000
20.000000	3.950000
30.000000	4.720000
40.000000	5.000000
50.000000	4.670000
60.000000	3.700000
70.000000	2.510000
80.000000	1.420000
90.000000	0.850000
95.000000	0.720000
100.000000	0.000000

NACA 0012

18

0.000000	0.000000
1.250000	1.894000
2.500000	2.615000
5.000000	3.555000
7.500000	4.200000
10.000000	4.683000
15.000000	5.345000
20.000000	5.737000
25.000000	5.941000
30.000000	6.002000
40.000000	5.803000
50.000000	5.294000
60.000000	4.563000
70.000000	3.664000
80.000000	2.623000
90.000000	1.448000
95.000000	0.807000
100.000000	0.000000

NACA 0015

18

0.000000	0.000000
1.250000	2.367000
2.500000	3.268000
5.000000	4.443000
7.500000	5.250000
10.000000	5.853000
15.000000	6.682000
20.000000	7.172000
25.000000	7.427000
30.000000	7.502000
40.000000	7.254000
50.000000	6.617000
60.000000	5.704000
70.000000	4.580000
80.000000	3.279000
90.000000	1.810000
95.000000	1.008000
100.000000	0.000000

In addition to, or as an alternative to the six profile thicknesses tabulated here, the designer may edit the file **profiles** to suit his own requirements. Simply follow the above format for each profile thickness.

```
Naca66-010
    26
        0.0      0.0
        0.5      0.759
        0.75     0.913
        1.25     1.141
        2.5      1.516
        5.0      2.087
        7.5      2.536
       10.0      2.917
       15.0      3.53
       20.0      4.001
       25.0      4.363
       30.0      4.636
       35.0      4.832
       40.0      4.953
       45.0      5.0
       50.0      4.971
       55.0      4.865
       60.0      4.665
       65.0      4.302
       70.0      3.787
       75.0      3.176
       80.0      2.494
       85.0      1.773
       90.0      1.054
       95.0      0.408
      100.0      0.0
NGTEmod
20
        0.000000     0.000000
        1.250000     1.375000
        2.500000     1.910000
        5.000000     2.680000
        7.500000     3.195000
       10.000000     3.600000
       15.000000     4.180000
       20.000000     4.550000
       30.000000     4.950000
       40.000000     4.820000
       50.000000     3.980000
       60.000000     3.250000
       70.000000     2.450000
       80.000000     1.740000
       85.000000     1.500000
       90.000000     1.270000
       92.500000     1.170000
       95.000000     1.080000
       97.500000     0.980000
      100.000000     0.000000
```

II.10   Contents of data file rawdata

1		Number of profiles
37		Number of (x,y) profile coordinates
0.000000	0.000000	
0.001263	0.015536	
0.018483	0.038649	
0.051934	0.066698	
0.100736	0.096883	
0.163370	0.125813	
0.237550	0.150439	
0.320445	0.168477	
0.408956	0.178613	
0.500000	0.179675	
0.590410	0.171342	
0.677138	0.154552	
0.757434	0.131014	
0.828941	0.103156	
0.889792	0.074039	
0.938420	0.046618	
0.973142	0.022915	
0.993362	0.006035	
1.000000	0.000000	37 (x,y) coordinates
0.991446	0.002648	
0.966550	0.010530	
0.927606	0.024107	
0.876253	0.041388	
0.813847	0.058684	
0.742566	0.073427	
0.664882	0.083936	
0.583238	0.089055	
0.500000	0.088275	
0.417395	0.081783	
0.337535	0.070011	
0.262450	0.054002	
0.193843	0.036027	
0.133219	0.018544	
0.082040	0.004027	
0.041824	−0.005204	
0.013930	−0.006854	
0.000000	0.000000	

This file contains final profile coordinates recorded clockwise around the blade perimeter, beginning and ending at the leading edge. The profile is set at zero stagger as illustrated in Fig. II.3(c).

It is also possible to create the file **rawdata** by using the blade design and stacking program STACK. In this case up to ten profiles may be designed and the first parameter in the above data set accordingly followed by that number of (x,y) data sets. CASCADE may then be used to flow-analyse any of these. Simply follow the instructions presented on the screen.

II.11 Sample contents of output file testdata for the default design

The following contents of the output file **testdata** were obtained by running the program CASCADE and then using the menu sequence Design/analyse . . . Flow analysis to complete the blade design and fluid flow calculation for the unaltered default cascade.

This file contains a complete record of all the work which is undertaken in a given sitting before finally quitting and is thus very valuable for later review of your intermediate stages in developing a cascade design. If you wish to keep it for later use, *remember to copy it into another file for safe keeping*! Each time you start a new run of CASCADE the file **testdata** is closed and re-opened!

```
          ***** Record of Design Work *****

       New Case
              ***** Camber Line and Half Thickness *****

                  x/l              yc/l            half yt/l
               0.007596         0.004341          0.012862
               0.030154         0.016723          0.024839
               0.066987         0.035362          0.034763
               0.116978         0.057714          0.042403
               0.178606         0.080920          0.047408
               0.250000         0.102220          0.049800
               0.328990         0.119244          0.049969
               0.413176         0.130198          0.048598
               0.500000         0.133975          0.045700
               0.586824         0.130198          0.041300
               0.671010         0.119244          0.035836
               0.750000         0.102220          0.029737
               0.821394         0.080920          0.023481
               0.883022         0.057714          0.017673
               0.933013         0.035362          0.012487
               0.969846         0.016723          0.007015
               0.992404         0.004341          0.001945


                  ***** Design Parameters *****

           Profile thickness is the C4 base profile
           Profile thickness scale   = 1.0
           Camber line type is circular arc
           x/l of maximum camber= 0.5
           Camber angle theta       = 60.0
           Stagger angle lamda      = 45.0
           Pitch/chord ratio t/l    = 1.0
           Fluid inlet angle beta1  = 60.0
```

***** Blade Profile *****

x	y
0.000631	0.007768
0.009873	0.027093
0.035209	0.052673
0.076335	0.081790
0.132053	0.111348
0.200460	0.138126
0.278997	0.159458
0.364701	0.173545
0.454478	0.179144
0.545205	0.175508
0.633774	0.162947
0.717286	0.142783
0.793188	0.117085
0.859366	0.088598
0.914106	0.060329
0.955781	0.034767
0.983252	0.014475
0.996681	0.003017
0.995723	0.001324
0.978998	0.006589
0.947078	0.017319
0.901929	0.032747
0.845050	0.050036
0.778206	0.066056
0.703724	0.078681
0.624060	0.086495
0.541619	0.088665
0.458698	0.085029
0.377465	0.075897
0.299993	0.062006
0.228146	0.045015
0.163531	0.027286
0.107630	0.011286
0.061932	−0.000588
0.027877	−0.006029
0.006965	−0.003427

***** Fluid Flow Analysis Output *****

beta1	beta2	betainf
60.000002	28.944236	48.806297

Cl inf	Shockfree inlet angle *** outlet angle
1.553013	63.71	29.16

x/l	vel/cl	cp1	cp2
0.000631	0.089072	0.992066	0.975698
0.009873	0.810870	0.342490	−1.014044
0.035209	1.043871	−0.089666	−2.337798
0.076335	1.172848	−0.375574	−3.213572
0.132053	1.252750	−0.569383	−3.807236
0.200460	1.292715	−0.671113	−4.118851
0.278997	1.298880	−0.687089	−4.167787
0.364701	1.280432	−0.639506	−4.022034
0.454478	1.241971	−0.542493	−3.724869
0.545205	1.182944	−0.399358	−3.286426
0.633774	1.109494	−0.230976	−2.770651
0.717286	1.029374	−0.059611	−2.245734
0.793188	0.947414	0.102407	−1.749451
0.859366	0.869248	0.244409	−1.314481
0.914106	0.800752	0.358797	−0.964094
0.955781	0.728572	0.469183	−0.625965
0.983252	0.622611	0.612355	−0.187410
0.996681	0.490643	0.759270	0.262609
0.995723	−0.490643	0.759269	0.262609
0.978998	−0.504801	0.745176	0.219438
0.947078	−0.505936	0.744029	0.215924
0.901929	−0.483908	0.765833	0.282715
0.845050	−0.464630	0.784119	0.338727
0.778206	−0.457655	0.790551	0.358430
0.703724	−0.459038	0.789284	0.354547
0.624060	−0.467292	0.781638	0.331127
0.541619	−0.483094	0.766620	0.285125
0.458698	−0.506257	0.743703	0.214928
0.377465	−0.537967	0.710591	0.113502
0.299993	−0.583639	0.659365	−0.043412
0.228146	−0.645510	0.583316	−0.276360
0.163531	−0.722467	0.478042	−0.598830
0.107630	−0.816200	0.333818	−1.040609
0.061932	−0.934111	0.127436	−1.672785
0.027877	−1.077991	−0.162066	−2.559568
0.006965	−1.020543	−0.041507	−2.190282

***** Outlet Angle versus Inlet Angle *****

Beta1	Beta2
−80.000	23.137
−75.000	24.713
−70.000	25.499
−65.000	25.975
−60.000	26.299
−55.000	26.536
−50.000	26.720
−45.000	26.868
−40.000	26.993
−35.000	27.100
−30.000	27.195
−25.000	27.280
−20.000	27.359
−15.000	27.432
−10.000	27.503
−5.000	27.571
0.000	27.637
5.000	27.704
10.000	27.772
15.000	27.842
20.000	27.915
25.000	27.992
30.000	28.077
35.000	28.170
40.000	28.275
45.000	28.396
50.000	28.540
55.000	28.717
60.000	28.944
65.000	29.251
70.000	29.695
75.000	30.413
80.000	31.797

Appendix III

'STACK'

A computer program for geometrical design
and analysis of turbomachine cascade blades

III.1 Introduction and overview

STACK is a computer program for undertaking the geometrical design of turbo-machine blade profiles or aerofoils based upon the method outlined in Chapter 2, Section 2.4, Fig. 2.8. Blade profile coordinates are thus generated by superimposing a 'base profile' thickness normal to a mean camber line which can be either a circular arc or a parabola. In this respect it undertakes profile design tasks which are identical to those of the flow analysis program CASCADE. On the other hand its functions are entirely geometrical and its main role is that of blade stacking. In other words, and as illustrated by Fig. III.1, the designer may specify several sections from hub to casing of a turbomachine from his previous aerodynamic design work and stack
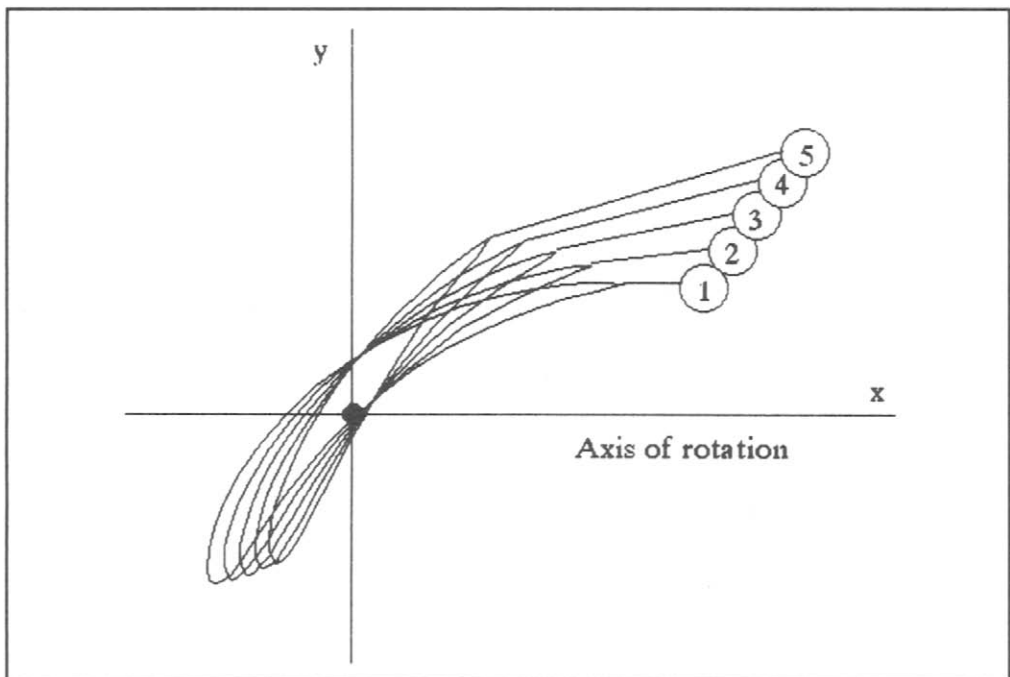
Fig. III.1 Output from program STACK

```
 Profile    Camber line    Geometry    Display    Section    Quit/save/DOS
┌─────────────────────────────────────────────────────────────────────────┐
│                   ******  Section No.1  ******                            │
│                                                                           │
│       Profile data are presently as follows :-                            │
│                                                                           │
│       Profile thickness is the C4 base profile                            │
│       Profile thickness scale = 1.0                                       │
│                                                                           │
│       Camber line type is circular arc                                    │
│       x/l of maximum camber = 0.5                                         │
│       Camber angle          = 0.0deg                                      │
│       Stagger angle         = 0.0deg                                      │
│       Chord length          = 100.0mms                                    │
│       Stacking line x        = 0.0mms                                     │
│       Stacking line v        = 0.0mms                                     │
│                                                                           │
│           < <Press Alt key and first letter together to grab a menu>>     │
│              < <e.g.  Alt-T pulls down the Thermodynamics menu>>          │
└─────────────────────────────────────────────────────────────────────────┘
```
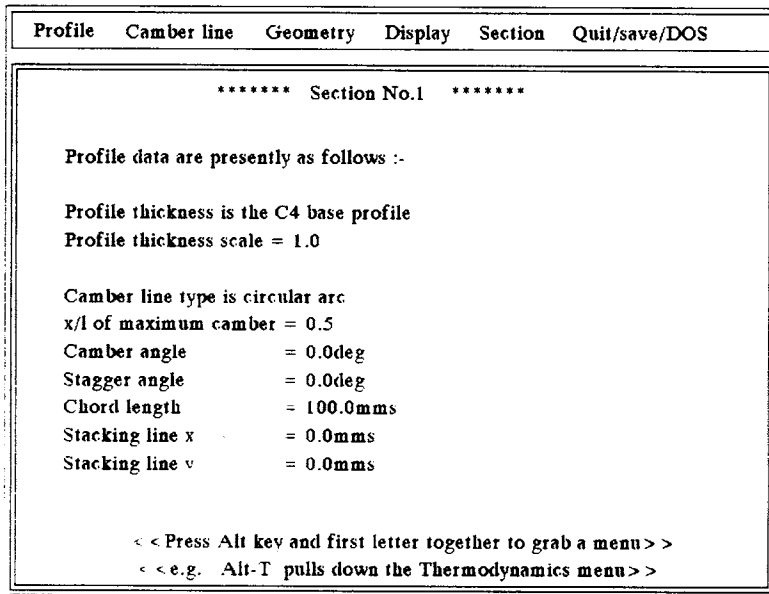
Fig. III.2 Main bar menu for program STACK

these on top of one another in some appropriate manner. For example, the five sections shown here are stacked upon their centres of gravity so that in the case of a rotor there would then be no centrifugal bending stresses. Section properties such as area, centre of gravity, principal axes and second moments of area are calculated for each section designed and recorded on file on exit from the program. Simple instruction for getting started will now be given, including an introduction to the main bar edit menu.

III.1.1 How to run the program STACK

Before running the program STACK it is essential to have the file **profiles** available in the current directory. This is the same file as that used for the program CASCADE and contains a range of base profile thicknesses entered according to the format presented in Section II.9 of Appendix II. To run the program simply enter its name **stack** at the keyboard. The title page which then appears at the screen can be removed by hitting any key, whereupon the main bar menu will be presented.

III.1.2 Main bar menu

Figure III.2 shows the main menu for STACK consisting of the top bar menu for design and display, below which the current design data are recorded for the given section, in this case Section No. 1. There are six keywords in the main bar menu which enable the user to perform the following activities:

Profile   To select the profile base thickness.
Camber line   To select the camber angle and type of camber-line curvature.
Geometry   To select profile stagger angle and scale and various options to fix the blade stacking line.
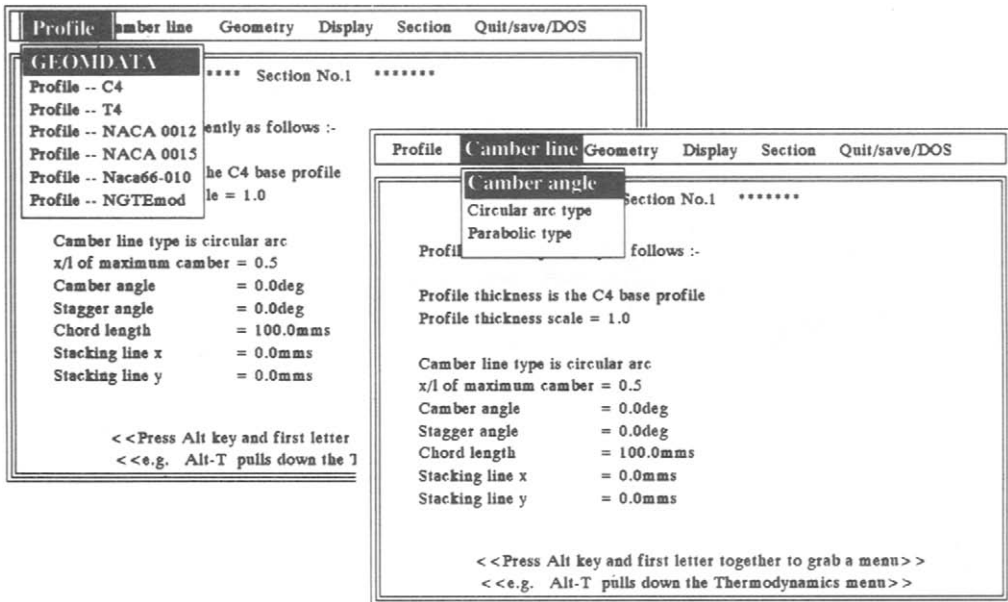
Fig. III.3 Profile geometry pull-down menus

Display   For visual presentation of the single section during design or the complete set of stacked profiles.

Section   To select a given section for further design work or display out of a possible total of eleven sections.

Quit/save/DOS   To enable the user to quit the session, to save the current work or to exit to DOS.

We will now deal with these in more detail in the following sections.

III.2   Menus for editing blade profile geometry

The first two pull-down menus, shown in Fig. III.3, enable the user to select the profile shape, namely the base profile thickness and the camber line. To access these simply enter **Alt-P** or **Alt-C** as instructed by the comment at the bottom of the screen. Since the procedures involved in using these pull-down menus are identical to those undertaken by the program CASCADE, no further instructions will be given here and the reader is referred to Appendix II where full details have been presented. The only significant difference is that of the first **profile** pull-down menu **GEOMDATA** which enables the user to recover previous work from a file of that name. Further comments about this will be made later in Section III.6.

III.3   The Geometry menu

The third bar menu **Geometry** (Fig. III.4) and its pull-down menus provide the remaining tools for blade design which are as follows:

Stagger   For setting the blade stagger angle λ which will be $+^{ve}$ for a compressor and $-^{ve}$ for a turbine.
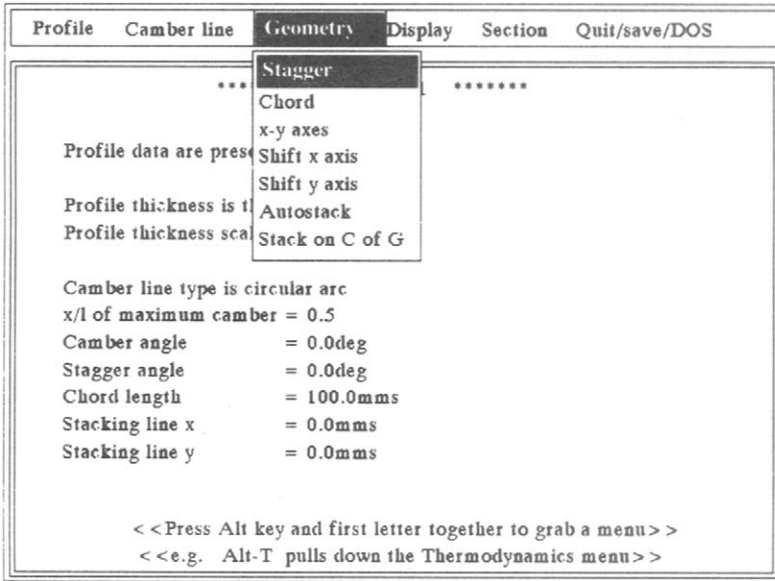
Fig. III.4 The **Geometry** pull-down menu

Chord	For choosing the blade chord length in mm.
x-y axes	
Shift x axis	
Shift y axis	Tools for blade stacking.
Autostack	
Stack on C of G	

The first two of these complete the design of the actual blade shape. The remainder can then be used to shift the position of the blade profile in the (x,y) plane in a variety of ways. Let us consider these in turn.

III.3.1 Completion of a blade design

To illustrate this we will begin by prescribing the basic blade profile parameters for the five sections shown in Fig. III.1, which are shown in Table III.1.

Table III.1 Example test case with five sections

Section no.	Base profile	Camber $\theta°$		Stagger $\lambda°$	Chord l (mm)	Location of stacking line
		Type	Value			
1	NACA0012	Circ. arc	70	40	100	C. of G.
2	NACA0012	Circ. arc	60	45	95	C. of G.
3	NACA0012	Circ. arc	50	50	90	C. of G.
4	NACA0012	Circ. arc	40	55	85	C. of G.
5	NACA0012	Circ. arc	30	60	80	C. of G.
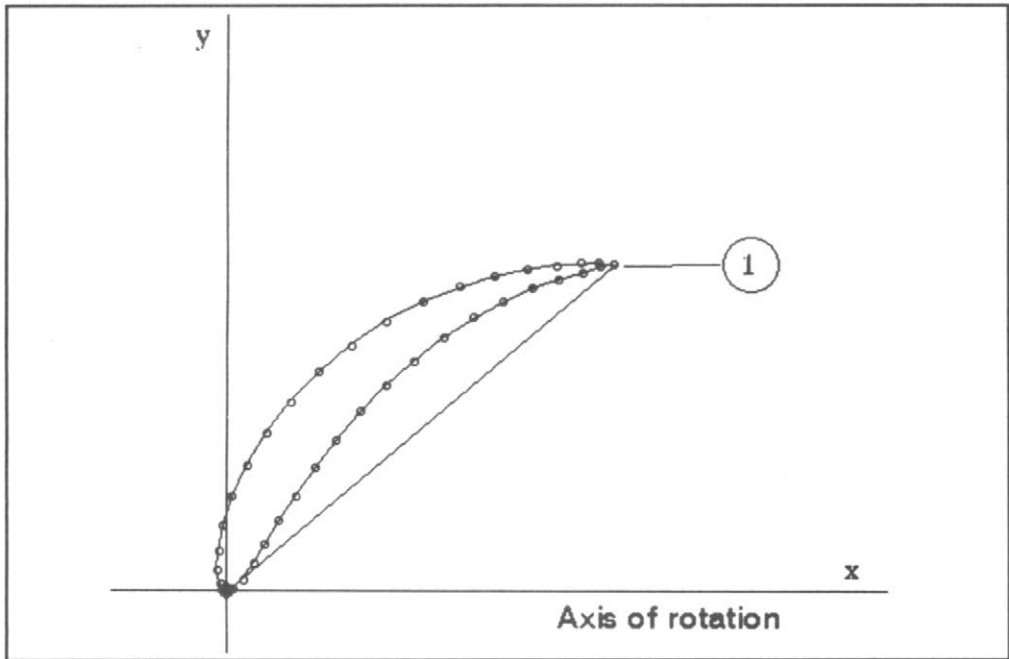
Fig. III.5 Section No. 1 of test case stacked on the leading edge

First use the **Profile** menu to select the base profile NACA0012 in place of the default profile C4. When making this selection the user is asked to specify the profile thickness, which we will set here as 1.0. By entering some other value the base profile may be thickened or thinned as required.

Next use the **Camber line** menu to select a camber angle of 700° for 8ction No. 1 instead of the default value of 0°. We note from Fig. III.3 that the default camber line is already a circular arc, so that no change in that parameter is required.

Finally access the **Geometry** menu and then select **Stagger** from the pull-down menu to reset the stagger angle to the required value for Section No. 1 of $\lambda = 40°$. By using the **Display** bar menu the outcome of these choices may be presented graphically at the screen as shown by Fig. III.5.

III.3.2   Tools for blade stacking

As can be seen from this example, any such new blade profile design will be stacked on its leading edge unless subsequent use is made of the various stacking tools listed in Section III.3 and shown in Fig. III.4. The first three of these pull-down menus enable the user to reposition the (x,y) axes (menu **x-y axes**), or to shift them independently (menus **Shift x axis** and **Shift y axis**), and the reader is invited to experiment with these.

The pull-down menu **Autostack**, on the other hand, enables the designer to stack the blade profile relative to position along and perpendicular to the chord line in answer to the following questions presented on the screen:

x/chord for stacking line?--->   <enter value>
y/(max.camber)?--->   <enter value>
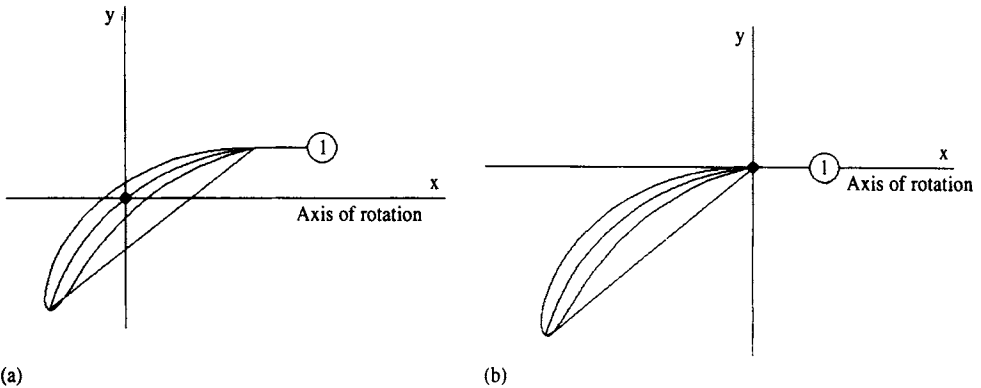
Fig. III.6 Two examples of the use of pull-down menu **Autostack**: (a) stacking on the camber line; (b) stacking on the trailing edge
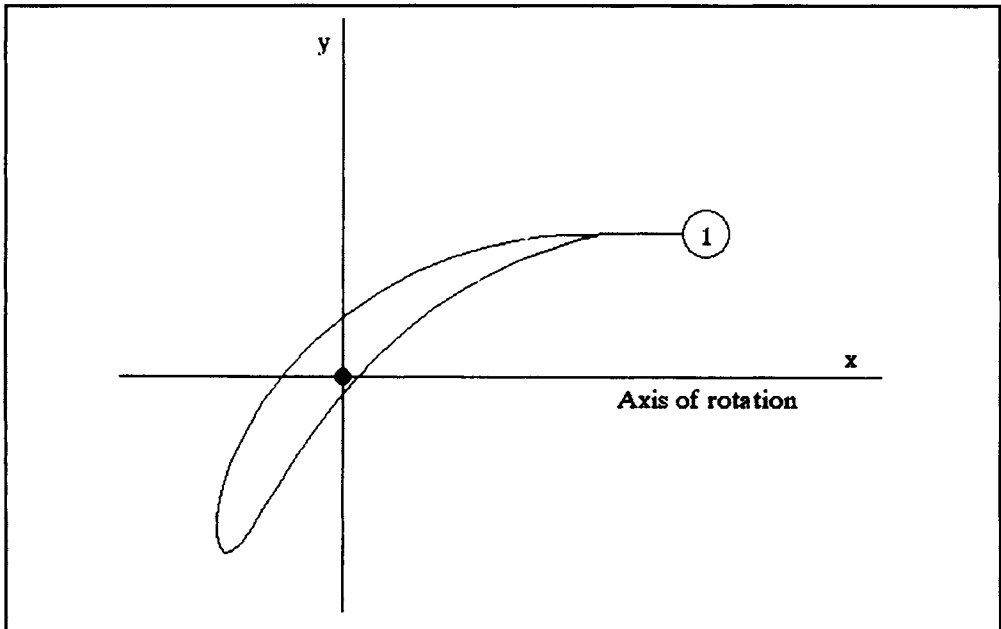
Fig. III.7 Section No. 1 stacked on its centre of gravity

For example, if the values x/chord = 0.5 and y/(max.camber) = 1.0 are entered, for this blade based on a circular arc camber, the profile will be stacked on the actual camber line at mid-chord as illustrated by Fig. III.6(a). If, on the other hand, the values entered are x/chord = 1.0 and y/(max.camber) = 0.0, the profile will be stacked on its trailing edge as illustrated by Fig. III.6(b). Try x/chord = 0.0, y/(max.camber) = 0.0!

The last of the stacking tools, **Stack on C of G**, is of obvious value for the design of rotors for which it is important to stack the sections on their centres of gravity, thereby eliminating bending stresses due to centrifugal force. If this menu is accessed all of the blade profile sections that have been designed will be thus stacked automatically. The program STACK does in fact calculate the profile section areas,
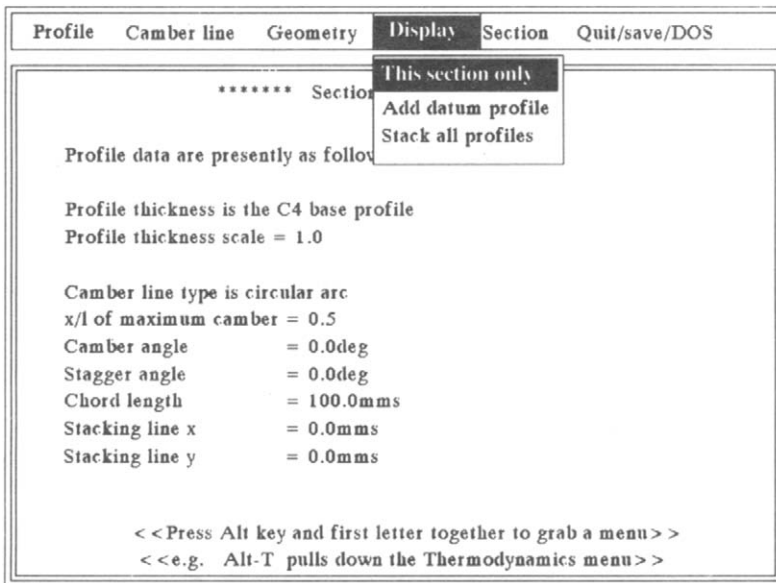
Fig. III.8 The **Display** pull-down menu

centres of gravity, principal axes and second moments of area about the principal axes and deposits these data in the file **section.dat**.

Application of this procedure to Section No. 1 is presented in Fig. III.7 which shows the first step towards generating the full set of five blade profiles as previously shown in Fig. III.1. Sample output for the full test case of five sections as specified in Table III.1 and as recorded in the file **section.dat** is included in Section III.8 and we will now deal with the remaining pull-down menus required to achieve this.

III.4 The Display menu

Three options are available with the **Display** menu. Figure III.8 provides an example of the use of the first pull-down menu **This section only**. *It is important to mention that when designing a new section it is not accepted and cannot be saved onto file until it has been displayed using either the* **This section only** *menu or the* **Add datum profile** *menu.*

The next pull-down menu, **Add datum profile**, has the effect of displaying both the section presently being designed and Section No. 1. The idea behind this feature is that Section No. 1 will normally be the blade root section. When designing a section at some other radius of a blade row it can be helpful to see how this relates geometrically to that at the hub radius. An example of this will be presented in the next section.

The third pull-down menu, **Stack all profiles**, does as it says and Fig. III.1 provides an example of its use.

III.5 The Section menu

The pull-down menu for choosing a given section is shown in Fig. III.9 from which it can be seen that eleven possible sections are available for design. For example,

```
 Profile    Camber line    Geometry    Display   [Section]  Quit/save/DOS
┌──────────────────────────────────────────────┬─────────────────────┐
│                                               │[ Section No. 1 ]    │
│               ****** Section No.1  *          │  Section No. 2      │
│                                               │  Section No. 3      │
│      Profile data are presently as follows :- │  Section No. 4      │
│                                               │  Section No. 5      │
│      Profile thickness is the C4 base profile │  Section No. 6      │
│      Profile thickness scale = 1.0            │  Section No. 7      │
│                                               │  Section No. 8      │
│      Camber line type is circular arc         │  Section No. 9      │
│      x/l of maximum camber = 0.5              │  Section No. 10     │
│      Camber angle        = 0.0deg             │  Section No. 11     │
│      Stagger angle       = 0.0deg             │  Delete section     │
│      Chord length        = 100.0mms           └─────────────────────┘
│      Stacking line x     = 0.0mms
│      Stacking line y     = 0.0mms
│
│
│        << Press Alt key and first letter together to grab a menu >>
│        << e.g.  Alt-T  pulls down the Thermodynamics menu >>
└──────────────────────────────────────────────────────────────────────┘
```

Fig. III.9 The **Section** selection pull-down menu

```
 Profile    Camber line    Geometry    Display    Section    Quit/save/DOS
┌──────────────────────────────────────────────────────────────────────┐
│              ****** Section No.2  ******                               │
│                                                                       │
│      Profile data are presently as follows :-                         │
│                                                                       │
│      Profile thickness is the NACA0012 base profile                   │
│      Profile thickness scale = 1.0                                    │
│                                                                       │
│      Camber line type is circular arc                                 │
│      x/l of maximum camber = 0.5                                      │
│      Camber angle        = 60.0deg                                    │
│      Stagger angle       = 45.0deg                                    │
│      Chord length        = 95.0mms                                    │
│      Stacking line x     = 0.0mms                                     │
│      Stacking line y     = 0.0mms                                     │
│                                                                       │
│                                                                       │
│        << Press Alt key and first letter together to grab a menu >>   │
│        << e.g.  Alt-T  pulls down the Thermodynamics menu >>          │
└──────────────────────────────────────────────────────────────────────┘
```

Fig. III.10 Design data entered for Section No. 2

to proceed with the design of Section No. 2 move the cursor down with the ↓ arrow key and once the correct section has been highlighted hit the <Enter> key. When you have entered in all the relevant data from Table III.1, Section No. 2, the screen data presentation will be as illustrated in Fig. III.10.

Making use of the **Display** bar menu and the **Add datum profile** pull-down menu option, the resulting screen presentation is as shown in Fig. III.11. Section No. 2
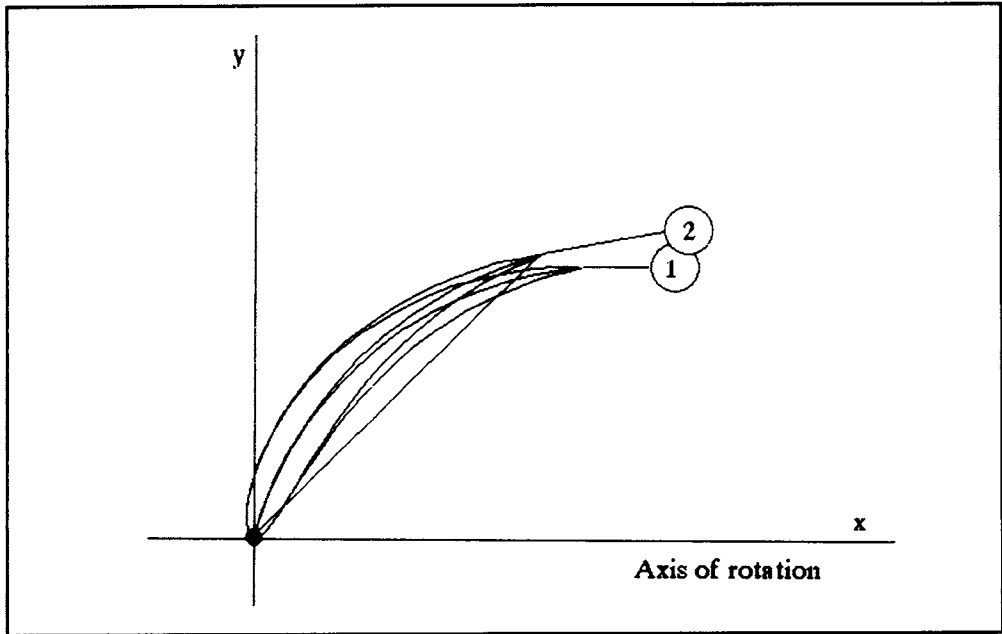
Fig. III.11 Section No. 2 using **Add datum profile** menu

is presented together with the datum Section No. 1. The assumption made here is that neither section has as yet been subjected to the restacking options so that both are stacked as entered, namely on their leading edges. Thus the reader could now use the **Stack on C of G** option to check the general appearance for this mode of stacking and, for example, its implications for machining of the final twisted blade.

The reader is now in a position to complete all of the five section designs as prescribed in Table III.1 and stack them as required, for example on their centres of gravity as illustrated by Fig. III.1.

III.6   The Quit/save/DOS menu

The final menu is that illustrated in Fig. III.12, which enables the completion of various administrative tasks now to be described.

Quit   This menu enables the user to end the session. Note that any work not saved before quitting will be lost.

Save & resume   This menu may be used at any time during design work and enables the user to deposit data on file as follows:

     geomdata   Contains the basic parameters of the current design to enable the user to resume work on a later occasion.

     rawdata   Contains the actual profile (x,y) coordinates for those profiles currently designed.

     section.dat Contains a record of all of the properties of the profiles currently designed including C. of G., area, principal axes and second moments of area.

Profile	Camber line	Geometry	Display	Section	Quite/save/DOS

```
                                                          Quit
                  ******* Section No.1  *******          Save & resume
                                                         Go to DOS
          Profile data are presently as follows :-       Reverse video


          Profile thickness is the C4 base profile
          Profile thickness scale = 1.0


          Camber line type is circular arc
          x/l of maximum camber = 0.5
          Camber angle        = 0.0deg
          Stagger angle       = 0.0deg
          Chord length        = 100.0mms
          Stacking line x      = 0.0mms
          Stacking line y      = 0.0mms


              < <Press Alt key and first letter together to grab a menu> >
              < <e.g.  Alt-T pulls down the Thermodynamics menu> >
```
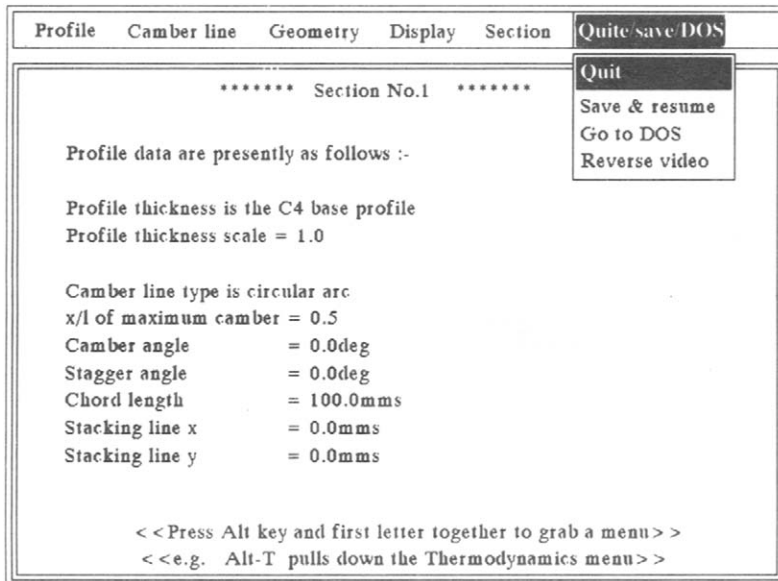
Fig. III.12 The **Quit/save/DOS** menu

<table>
<tr><td></td><td>(Alternatively new file names may be chosen in response to invitations presented at the screen to avoid overwriting previous work.)</td></tr>
<tr><td>Go to DOS</td><td>This menu enables the user to leave the program temporarily and enter DOS to undertake other work. To re-enter the program STACK and resume work where you left off, just enter 'exit' at the DOS prompt.</td></tr>
<tr><td>Reverse video</td><td>Use of this menu reverses paper and ink colours for the graphical presentation. The main reason for this is to provide an alternative and better quality of screen-dump to printer of the graphical presentations. Use of this menu a second time causes the screen presentation to revert back to normal.</td></tr>
</table>

III.7   Screen dumping of results

Hard copies of graphical presentations such as Fig. III.1 may be obtained by screen-dumping. To achieve this enter the [Graphics] command (using the appropriate option for your printer) before running STACK. Alternatively, if you omitted to do this before starting the session, use the **Go to DOS** pull-down menu to go temporarily into DOS and then use the [Graphics] command before returning to STACK. Subsequently just press the Print Screen key whenever you wish to dump a graphical presentation.

III.8   Contents of file section.dat

******* Section Geometrical Data *******

Section No.	Profile	Thickness	Camber	Type	xmax/chord	Stagger
1	NACA 0012	1.0000	70.00000	circular arc	0.50000	40.00000
2	NACA 0012	1.0000	60.00000	circular arc	0.50000	45.00000
3	NACA 0012	1.0000	50.00000	circular arc	0.50000	50.00000
4	NACA 0012	1.0000	40.00000	circular arc	0.50000	55.00000
5	NACA 0012	1.0000	30.00000	circular arc	0.50000	60.00000

******* Section data based on axes through the C. of G. *******
X and Y axes are taken parallel and normal to the chord line

Section No.	Area sqr mms	Centre of gravity X mms	Y mms	Ixx mms^4	Iyy mms^4	Ixy mms^4
		from the leading edge				
1	8.6002E+02	4.1587E+01	1.1997E+01	1.9709E+04	4.9329E+05	2.8043E+04
2	7.6692E+02	3.9622E+01	9.6859E+00	1.3046E+04	3.9247E+05	1.8962E+04
3	6.8140E+02	3.7623E+01	7.5935E+00	8.5588E+03	3.1000E+05	1.2377E+04
4	6.0279E+02	3.5597E+01	5.7040E+00	5.6017E+03	2.4274E+05	7.7184E+03
5	5.3052E+02	3.3550E+01	4.0085E+00	3.6831E+03	1.8811E+05	4.4692E+03

******* Data for principal axes *******
******* Angle of Iu axis is relative to cascade x axis. *******

Section No.	stagger degrees	Angle of Iu axis degrees	Iu mms^4	Iv mms^4
1	40.00000	43.37708	1.8054E+04	4.9494E+05
2	45.00000	47.85391	1.2101E+04	3.9342E+05
3	50.00000	52.34723	8.0515E+03	3.1050E+05
4	55.00000	56.86224	5.3508E+03	2.4299E+05
5	60.00000	61.38738	3.5749E+03	1.8821E+05

References

Abbott, I. H. and Von Doenhoff, A. E. 1959: *Theory of wing sections*. New York: Dover Publications, Inc.

Ackeret, J. 1942: Zum enwurf Dichtstehendes Schaufelgitter Schweiz. *Bauzeitung*, **120**, No. 9. Also available as: The design of closely spaced blade grids, Min. of Aviation Translation RTP 2007.

Balabaskaran, V. 1982: *Aerodynamic investigations of a ducted propeller*. Ph.D. Thesis, Indian Institute of Technology, Madras.

Batchelor, G. K. 1970: *An introduction to fluid dynamics*. Cambridge: Cambridge University Press.

Bragg, S. L. and Hawthorne, W. R. 1950: Some exact solutions of the flow through annular cascade actuator discs. *J. Aero. Sci.*, **17**, 243–249.

Busemann, A. 1928: Das Förderhöhenverhältnis radialer Kreiselpumpen mit logarithmisch-spiraligen Schaufeln, *Z. angew. Math. Mech.*, **8**(5), 372–384. Also available as: Lift-ratio of radial-flow centrifugal pumps with logarithmic-spiral blades, D.S.I.R. translation 621.671.22, Reg. File Ref. D.S.I.R./8082/CT, Feb. 1952.

Carter, A. D. S. 1964: *Blade loadings for radial flow fans*. Royal College of Military Science report.

Casey, M. V. 1987: A mean line prediction method for estimating the performance characteristics of an axial compressor stage. *Proc. Inst. Mech. Engrs.*, International Conference on Turbomachinery – Efficiency Prediction and Improvement, Paper C 264/87.

Cheng, K. Y. 1981: *Horizontal axis wind turbine and profile aerodynamics*. Ph.D. Thesis, University of Newcastle upon Tyne.

Cordier, O. 1953: *Brennstoff-Wärme-Kraft*, **5**, 337.

Craig, H. R. M. and Cox, H. J. A. 1971: Performance estimation of axial flow turbines. *Proc. Inst. Mech. Engrs.*, **185**, 32.

Csanady, G. T. 1964: *Theory of turbomachines*, McGraw-Hill.

Cumpsty, N. 1989: *Compressor aerodynamics*, Longman Scientific & Technical.

Denton, J. D. 1982: An improved time-marching method for turbomachinery flow calculation. ASME Int. Gas Turbine Conf., Wembley, England, Paper 82-GT-239.

Dixon, S. L. 1975: *Fluid mechanics, thermodynamics of turbomachinery*. Oxford: Pergamon Press.

Dwight, H. B. 1963: *Tables of integrals and other mathematical data*. New York: Macmillan.

ESDU 1980: *A guide to fan selection and performance*. ESDU Item No. 79037.

Fisher, E. H. 1975: *Performance of mixed-flow pumps and fans*. Ph.D. Thesis, University of Newcastle upon Tyne.

Fisher, E. H. and Lewis, R. I. 1972: *Exact solutions for conical mixed-flow rotors*. N.E.L. Report No. 498.

Frost, T. H. 1967: Private communications and lecture notes.

Gibson, I. S. 1972: *Application of vortex singularities to ducted propellers*. Ph.D. Thesis, University of Newcastle upon Tyne.

Gibson, I. S. and Lewis, R. I. 1973: Ducted propeller analysis by surface vorticity and actuator disc theory. Symposium on Ducted Propellers, R.I.N.A., Paper No. 1.

Glover, E. J. 1970: *Slipstream deformation and its influence on marine propeller design*. Ph.D. Thesis, University of Newcastle upon Tyne.

Gostelow, J. P. 1984: *Cascade Aerodynamics*, Pergamon Press.

Hawthorne, W. R. 1956: Thermodynamics of cooled turbines, Part I – The turbine stage, *Trans. ASME*, **78**, 1765; Part II – The multi-stage turbine, *Trans. ASME*, **78**, 1781.

Hawthorne, W. R. 1957: *Elements of turbine and compressor theory*, Gas Turbine Laboratory Note, M.I.T. (unpublished).

Hawthorne, W. R. and Ringrose, J. 1963: Actuator disc theory of the compressible flow in free-vortex turbomachinery. *Proc. Inst. Mech. Engrs.*, **178**, 3, I(ii), 1–13.

Hesselgreaves, J. E. 1969: *A correlation of tip-clearance/efficiency measurements on mixed-flow and axial flow turbomachines*. N.E.L. Report No. 423.

Hildebrand, F. B. 1956: *Advanced calculus for engineers*, Prentice Hall, Inc.

Hill, V. P. 1975: *Surface vorticity techniques applied to the annular aerofoil in non-axisymmetric flow*. Ph.D. Thesis, University of Newcastle upon Tyne.

Hill, V. P. 1978: A surface vorticity theory for propeller ducts and turbofan engine cowls in non-axisymmetric incompressible flow. *I. Mech. E., J. Mech. Eng. Sci.*, **20**, No. 4.

Horlock, J. H. 1958: *Axial flow compressors. Fluid mechanics and thermodynamics*, Butterworth.

Horlock, J. H. 1966: *Axial flow turbines. Fluid mechanics and thermodynamics*, Butterworth.

Horlock, J. H. 1978: *Actuator disk theory. Discontinuities in thermo-fluid dynamics*, McGraw-Hill.

Howell, A. R. 1942: The present basis of axial flow compressor design: Part I – Cascade theory and performance. *A.R.C., R. & M.*, No. 2095.

Howell, A. R. 1945: Fluid dynamics of axial compressors. *Proc. Instn. Mech. Engrs.*, **153**.

Jacob, K. and Riegels, F. W. 1963: The calculation of the pressure distributions over aerofoil sections of finite thickness with and without flaps and slats. *Z. Flugwiss*, **11**(9), 357–367. Available as R.A.E. Library Translation No. 1101, 1965.

Kearton, W. J. 1951: *Steam turbine theory and practice*, Pitman.

Kerwin, J. E. and Lee, Chang-Sup 1978: Prediction of steady and unsteady marine propeller performance by numerical lifting-surface theory. S.N.A.M.E., Annual Meeting, Paper No. 8.

Lamb, H. 1945: *Hydrodynamics*, Cambridge University Press.

Lewis, R. I. 1966: The mechanism of relative eddy flows in mixed-flow turbomachines. Thermodynamics and Fluid Mechanics Convention. *Proc. I. Mech. E.*, **180**, Part 3J, 54–65.

Lewis, R. I. and Horlock, J. H. 1969: Flow disturbances due to blade thickness in turbomachines. *J. Mech. Eng. Sci.*, **11**, 88–108.

Lewis, R. I. 1972: Fluid dynamic design and performance analysis of ducted propellers. *N.E.C.I., Trans.*, **88**, 91–112.

Lewis, R. I. and Ryan, P. G. 1972: Surface vorticity theory for axisymmetric potential flow past annular aerofoils and bodies of revolution with application to ducted propellers and cowls. *J. Mech. Eng. Sci.*, **14**, No. 4.

Lewis, R. I., Fisher, E. H. and Saviolakis, A. 1972: Analysis of mixed-flow rotor cascades. *A.R.C. R. & M.*, No. 3703.

Lewis, R. I. 1973: Theory for prediction of off-design performance of Kort nozzle ducted propellers. *International Shipbuilding Progress*, **20**, No. 224.

Lewis, R. I. and Yeung, E. H. C. 1977: Vortex shedding mechanisms in relation to tip clearance flows and losses in axial fans. *A.R.C. R. & M.*, No. 3829.

Lewis, R. I. 1978a: The interrelationship between fluid dynamics and dimensional analysis of turbomachines for degree teaching. 8th National Conference on Fluid Mechanics and Fluid Power, PSG College of Technology, Coimbatore, India.

Lewis, R. I. 1978b: Teaching of the fluid mechanics of turbomachines. ASME Paper 78-GT-161.

Lewis, R. I. 1982: A method for inverse aerofoil and cascade design by surface vorticity. ASME Paper 82-GT-154.

Lewis, R. I. and Balabaskaran, V. 1983: Aerodynamic investigations of a Kort nozzle ducted propeller. *Proc. 7th Conf. on Fluid Machinery*, Akademiai Kiado, Budapest.

Lewis, R. I. 1991: *Vortex Element Methods for Fluid Dynamic Analysis of Engineering Systems*. Cambridge Engine Technology Series, Cambridge University Press.

Lewis, R. I. 1995: Developments of actuator disc theory for compressible flow through turbo-machines. *Int. J. Mech. Sci.*, **37**, 1057–66.

Lieblein, S., Schwenk, F. C. and Broderick, R. L. 1953: *Diffusion factor for estimated losses and limiting blade loadings in axial compressor blade elements*. NACA RM E53 D01.

Lieblein, S. 1956: Experimental flow in two-dimensional cascades. Chapter VI of *The Aerodynamic Design of Axial Compressors*. Reprinted from NASA SP36 in 1965. Originally NACA RME 56B03.

Lieblein, S. and Roudebush, W. H. 1956: *Theoretical loss relations for low-speed two-dimensional cascade flow*. NACA Tech. Note 3662.

Lieblein, S. 1959: Loss and stall analysis of compressor cascades. *Trans. ASME, J. Basic Eng.*, **81**, 387.

Lieblein, S. 1960: Incidence and deviation-angle correlations for compressor cascades. *Trans. ASME, J. Basic Eng.*, **82**, 575–587.

Marsh, H. 1966: A digital computer program for the through-flow fluid mechanics of an arbitrary turbomachine using a matrix method. *A.R.C. R. & M.*, No. 3509.

Martensen, E. 1959: Berechnung der Druckverteilung an Gitterprofilen in ebener Poten-tialstromung mit einer Fredholmschen Integralgleichung. *Arch. Rat. Mech., Anal.*, **3**, 235–270.

Massey, B. S. 1989: *Mechanics of fluids*, 6th Edition, Van Nostrand Reinhold.

Pien, P. C. 1961: The calculation of marine propellers based on lifting-surface theory. *J. Ship Res.*, Sept. 1961, 1–14.

Potts, I. 1987: The importance of S-1 stream surface twist in the analysis of inviscid flow through swept linear turbine cascades. I. Mech. E., Paper C258/87.

Potts, I. 1991: Projection techniques for quasi 3-D computation of blade-to-blade flow in axial turbomachines. *Proc. 9th Conf. on Fluid Machinery*, Budapest, Paper No. 49, p. 380.

Potts, I. and Anderson, A. 1991: An undergraduate introductory course on computational fluid dynamics. *Proc. I. Mech. E.*, **205**, Part A, *J. Power and Energy*.

Railly, J. W. 1965: Ackeret method for the design of tandem cascades. *Engineer*, London, **224** (5827), 405–416.

Riegels, F. W. 1961: *Aerofoil sections*, Butterworth.

Ringrose, J. 1963: *Compressible flow through annular actuator discs*. Ph.D. Thesis, Cambridge University.

Rogers, G. F. C. and Mayhew, Y. R. 1992: *Engineering Thermodynamics Work and Heat Transfer*, Longman Scientific & Technical.

Ryan, P. G. 1970: *Surface vorticity distribution techniques applied to ducted propeller flows*. Ph.D. Thesis, University of Newcastle upon Tyne.

Ryan, P. G. and Glover, E. J. 1972: A ducted propeller design method: a new approach using surface vorticity distribution techniques and lifting line theory. *Trans. R.I.N.A.*, **114**.

Shepherd, D. G. 1965: *Elements of fluid mechanics*, Harcourt, Brace & World.

Smith, A. M. O. and Hess, J. L. 1966: Calculation of potential flow about arbitrary bodies. *Prog. Aero. Sci.*, **8**, Pergamon Press.

Smith, S. F. 1965: A simple correlation of turbine efficiency. *Proc. Seminar on Advanced Problems in Turbomachinery*, Von Karman Institute. Also *J. Roy. Aer. Soc.*, **69**, 467.

Soderberg, C. R. 1949: Unpublished notes, Gas Turbine Laboratory, M.I.T. (see Horlock, 1966).

Stanitz, J. D. and Ellis, G. O. 1950: *Two-dimensional compressible flow in centrifugal compressors with straight blades*. NACA Report No. 954.

Stanitz, J. D. 1952: Some theoretical aerodynamic investigations of impellers in radial and mixed-flow centrifugal compressors. *Trans. ASME*, **74**, No. 4.

Stodola, A. 1927: *Steam and gas turbines*, McGraw-Hill.

Stratford, B. S. 1959: The prediction of separation of the turbulent boundary layer. *J. Fluid Mech.*, **5**.

Traupel, W. 1945: Calculation of potential flow through blade grids. *Sulzer Review*, No. 1.

Van Manen, J. D. 1962: Effect of radial load distribution on the performance of shrouded propellers. *International Shipbuilding Progress*, **9**, No. 93.

Van Manen, J. D. and Oosterveld, M. W. C. 1966: Analysis of ducted propeller design. *Trans. Soc. N.A.M.E.*, **74**, 552–562.

Weissinger, J. and Maass, D. 1968: Theory of the ducted propeller. A review. *7th symposium on naval hydrodynamics*, Office of Naval Research, Dept. of U.S. Navy.

Wilkinson, D. H. 1967: A numerical solution of the analysis and design problems for the flow past one or more aerofoils or cascades. *A.R.C. R & M.*, No. 3545.

Wilkinson, D. H. 1969: *The analysis and design of blade shape for radial, mixed and axial turbomachines with incompressible flow*. English Electric Co., Whetstone, M.E.L. Report No. W/M(3F).

Wu, Chung-Hua 1952: *A general theory of three-dimensional flow in subsonic and supersonic turbomachines of axial, radial and mixed-flow types*. NACA TN 2604.

Young, L. 1958: Runners of experimental turbo-machines. *Engineering*, London, **185**, 376.

Index

Authors' index